DR-194

CONF-750989
VOLUME I

RADIATION EFFECTS and TRITIUM TECHNOLOGY for FUSION REACTORS

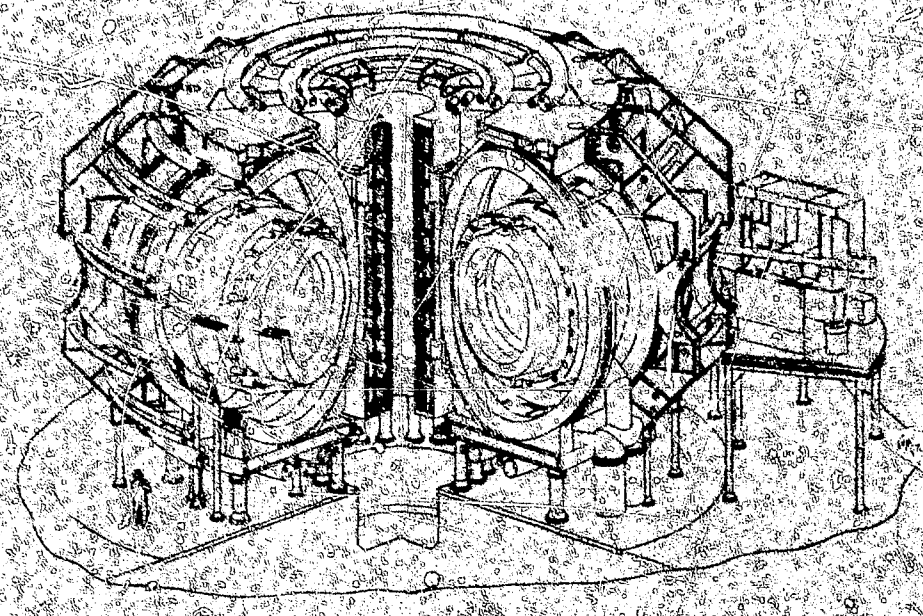

OAK RIDGE NATIONAL LABORATORY
UNITED STATES ENERGY RESEARCH AND DEVELOPMENT ADMINISTRATION
AMERICAN NUCLEAR SOCIETY
NUCLEAR METALLURGY COMMITTEE OF AIME

CONF-750989
VOLUME I

Distribution category UC-20

PROCEEDINGS OF THE INTERNATIONAL CONFERENCE HELD AT GATLINBURG TENNESSEE, OCTOBER 1-3, 1975

Sponsored By

OAK RIDGE NATIONAL LABORATORY
UNITED STATES ENERGY RESEARCH AND DEVELOPMENT ADMINISTRATION
AMERICAN NUCLEAR SOCIETY
NUCLEAR METALLURGY COMMITTEE OF AIME

RADIATION EFFECTS *and* TRITIUM TECHNOLOGY *for* FUSION REACTORS

Editors

J.S. WATSON
F.W. WIFFEN

Compiling Editors

JULIA L. BISHOP
BRENDA K. BREEDEN
OAK RIDGE NATIONAL LABORATORY

MARCH, 1976

ORGANIZING COMMITTEE

D. Steiner, ORNL, General Chairman
C. J. McHargue, ORNL, Radiation Effects
W. R. Grimes, ORNL, Tritium Technology
J. L. Scott, ORNL, Arrangements

PROGRAM COMMITTEE

Radiation Effects

F. W. Wiffen, ORNL, U.S.A.
J. L. Brimhall, Battelle-Pacific Northwest Laboratory, U.S.A.
B. L. Eyre, AERE-Harwell, U.K.
G. L. Kulcinski, University of Wisconsin, U.S.A.
H. A. Ullmaier, KFA-Jülich, Germany
R. Watanabe, National Research Institute for Metals, Japan
K. M. Zwilsky, Division of Controlled Thermonuclear Research, ERDA, U.S.A.

Tritium Technology

J. S. Watson, ORNL, U.S.A.
F. Coffman, Division of Controlled Thermonuclear Research, ERDA, U.S.A.
E. Hennelly, Savannah River Laboratory, U.S.A.
R. Hickman, Lawrence Livermore Laboratory, U.S.A.
G. McCracken, Culham Laboratory, U.K.
V. Maroni, Argonne National Laboratory, U.S.A.
L. Wittenberg, Mound Laboratory, U.S.A.

[illegible] magnetic and inertial [illegible] more realistic [illegible] significant quantities [illegible] experiments have been approved and [illegible] Test Reactor, the Joint [illegible] advanced experiments are in early [illegible] Power Reactor and Fusion Demonstration [illegible] the large, complex experiments, [illegible] technology to build and operate the [illegible] reality and follows patterns [illegible] fission, development of the [illegible] difficult, time-consuming, and expensive [illegible] concepts.

[illegible] was evident in the greater number [illegible] sessions on fusion technology, [illegible] meetings [illegible] problems.

[illegible] as a means of fulfilling [illegible] International Conference on Radiation [illegible] was held in Gatlinburg, Tennessee, [illegible] which was sponsored by Oak Ridge National Laboratory, the Energy Research and Development Administration, the American Nuclear Society, and the Nuclear Metallurgy Committee of AIME, brought together scientists and engineers to discuss the elements of fusion technology: bulk radiation effects and tritium technology. In many ways, the presentation of papers on the two subjects at this conference was like the effect of two separate conferences; however, several individuals attended sessions on both subjects. The conference was particularly timely because recent conceptual design studies of Experimental Power Reactors have shown the importance of data on both subjects. In addition, it provided an excellent opportunity for workers from throughout the world to present their most recent results and to gain insight into the remaining research needs. Judging from the quality of the papers, the number of attendees, and the interest and enthusiasm generated, the conference was eminently successful. We hope that publication of the proceedings will further enhance the benefits of the conference to all participants and also extend these benefits to others who were not able to attend.

The papers in these proceedings, which were published directly from copy supplied by the authors, are arranged in four volumes. The keynote address, delivered by R. F. Kintner of the Energy Research and Development Administration, is the first paper in Volume I. Papers concerned with radiation effects are included in Volumes I and II, while the tritium technology papers are collected in Volumes III and IV. The arrangement of the papers with regard to subject subdivision and order is the same as that used for presentation at the conference. Each of the four volumes contains a complete table of contents and author index for the entire proceedings.

The editors wish to express their gratitude to everyone who contributed to the success of the conference by assisting in the organization, chairing sessions, presenting papers, or participating in discussions throughout the conference. Special thanks are extended to J. L. Scott for conference arrangements and to D. Steiner, C. J. McHargue, and W. K. Grimes for their assistance with the organization.

J. S. Watson
F. W. Wiffen
Program Chairmen and Editors

CONTENTS

RADIATION EFFECTS

Plenary Session

Swelling and Microstructures (I)

Swelling and Microstructures (II)

Modeling and Damage Analysis

Mechanical Properties of Irradiated Metals

The Effects of Helium in Metals

Stress Effects, Magnets, and Insulators

TRITIUM TECHNOLOGY

Plenary Session

Environmental Considerations

System Design Studies

Experimental Studies, Part I

Experimental Studies, Part II

Special Topics

Permeation

AN OVERVIEW OF THE US FUSION PROGRAM

by

Edwin E. Kintner, Deputy Director
Division of Controlled Thermonuclear Research
ERDA, Washington, DC

There is much talk in this country today about "energy crisis," but there seems to be little true understanding of those words. One reason is that, even when faced with dire statistics and predictions, people find it very difficult to translate those facts into a true feeling of crisis and thence into concrete actions. We seem to be able to do that in war time, but so long as our life style flows along relatively smoothly the words "energy crisis" remain words.

Herman Kahn is reported to have said that the maximum time required for any technical development is four years. The reason for that is that four years is the approximate length of modern wars. World War II, in about four years, produced radar, jet aircraft, antibiotic medicines, and nuclear weapons. Those were major technical developments, perhaps slightly less difficult than fusion--but not much. That's what can be done in crisis. I don't see that sort of reaction to the "energy crisis" today.

There are a number of ways in which one can rank human beings into hierarchies. You can do it by salary, which is the typical one today; you can do it by academic degrees, which is probably the one used subconsciously by most of the people in this room; you can do it by the kind of automobile one drives; you can do it by the contribution an individual makes to society. One of the ways I like to do it is to consider the time span ahead on which the individual's thoughts and actions focus. "Where there is no vision, the people perish." That Old Testament proverb has a great deal of truth in it; it is that kind of view into the future that needs to be taken with regard to energy.

We <u>are</u> in a crisis. If the world were a hollow sphere filled with petroleum and the petroleum use-curve continued to grow as it has recently,

the sphere would be empty in 300 years. We are today celebrating the 200th anniversary of the United States. This is a sort of facetious comparison to make but, on the other hand, it does say something has to change. Nothing much is changing--population growth isn't changing--it's five billion today and it may level out at twelve billion. The consumption of energy in the United States took a short down-turn but then it crawled up again, and especially in the use of imported petroleum--the one fuel resource about which we should be most concerned. We are still generating about 40% of our electricity in the United States with oil and gas.

Energy is the life blood of modern industrial society. It is the resource by which we humans establish dominion over the natural world.

We face today a situation in which the United States is, in a sense, the world's food supplier of last resort. It takes about ten calories of energy in the form of fossil fuels to produce one calorie of food. Every bushel of wheat we export means deepening the shortage of fossil energy. That has implications not only for the United States but for all of mankind. If we are going to support twelve billion people on the face of this planet, we simply can't return to a pastoral society. When we had a pastoral society the Earth supported something like two or three hundred million people. In that sense, the idea which many well-trained persons have (at least well trained in terms of degrees) that we simply conserve and get back to a condition of adequate energy supplies is falacious.

We all know that a copious supply of energy has a great deal to do with our material well-being. I would like to show you several viewgraphs prepared and used by Dr. Chauncy Starr, head of the Electric Power Research Institute, which underline the very close correlation between total energy use and material well-being in this nation. (See Figures 1 through 5.)

If you talk only about electricity, not total energy, there is an equally remarkable correlation. The curve of energy use is increasing more rapidly for electrical energy than for energy in total, but the linear correlation is still apparent.

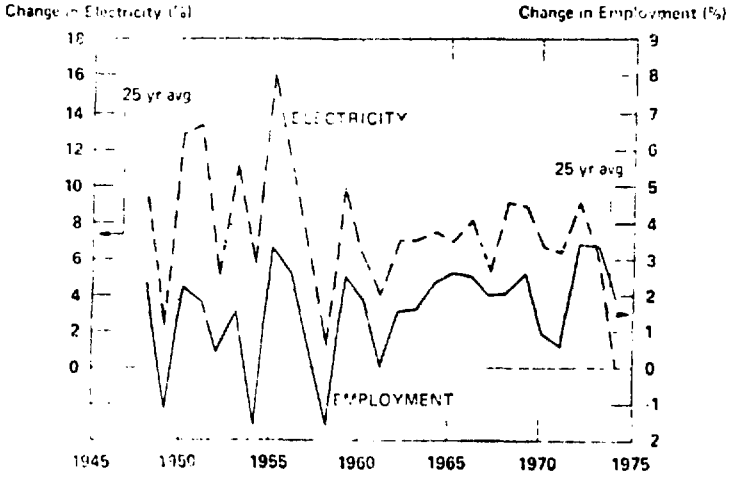

Fig. 1. Percentage Change of Electricity and Employment

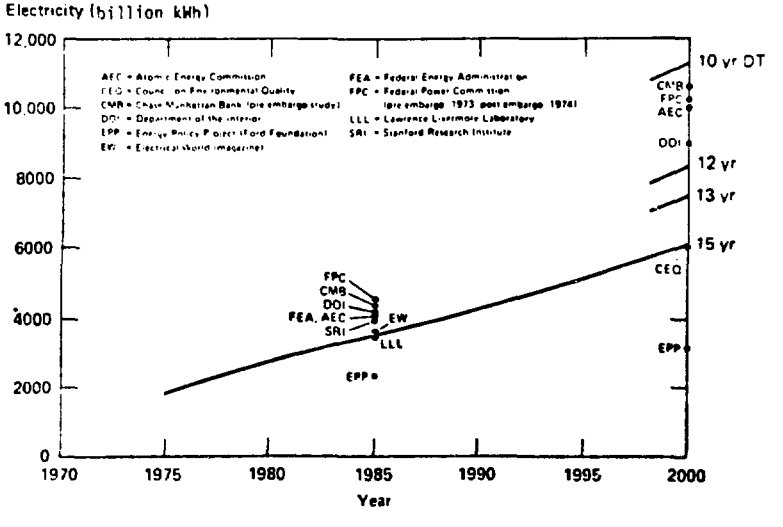

Fig. 2. Utility Electricity Demand (projected).

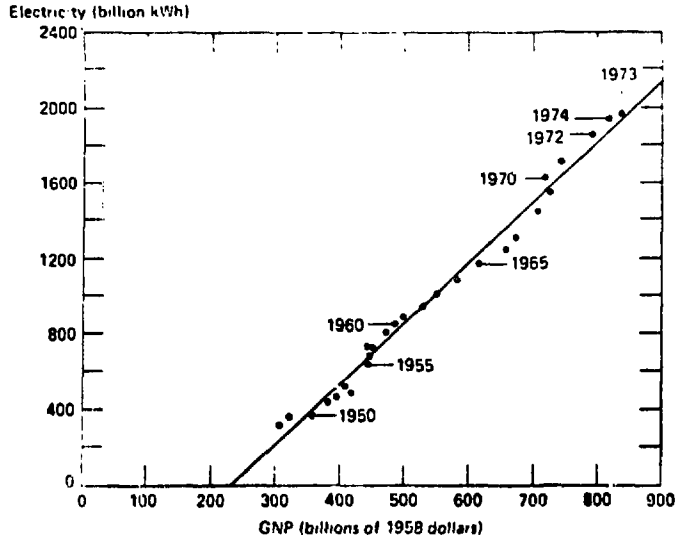

Fig. 3. GNP vs Electricity Consumption in the United States.

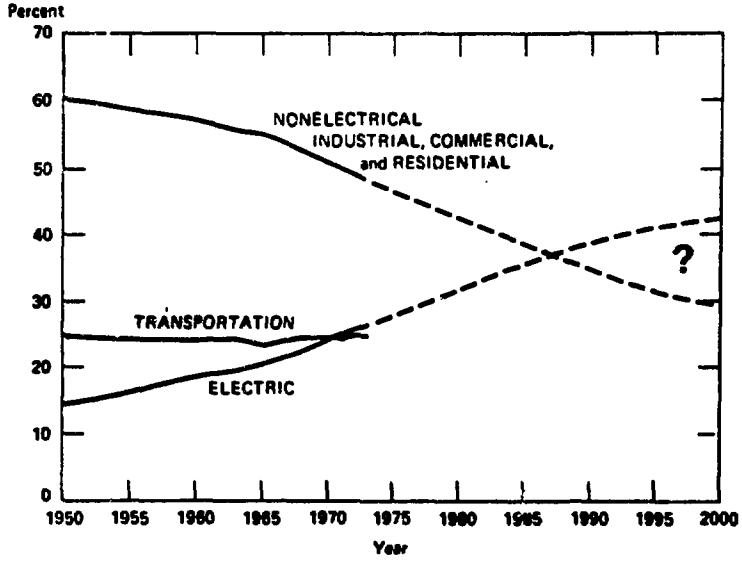

Fig. 4. Distribution of Energy Usage.

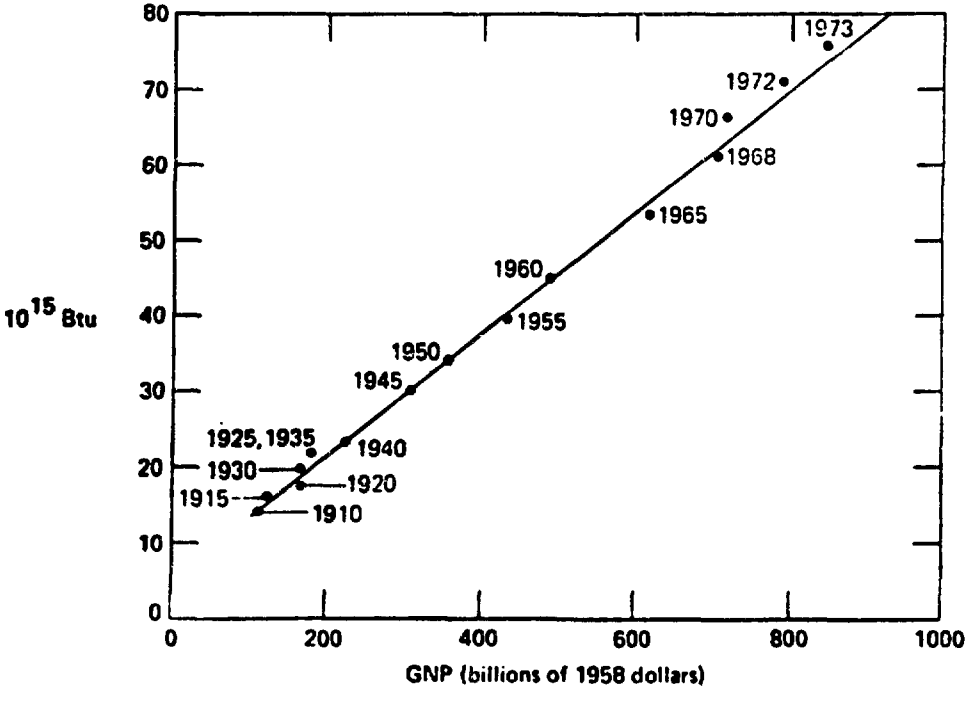

Fig. 5. GNP vs Energy Consumption in the United States.

The percentage use of electricity is increasing rapidly, from 15% in 1950 to about 25.6% today, because of the flexibility electricity provides in generation, in transmission and in use. In all ways, electricity is an extremely flexible and useful form of energy.

I know that you can argue that this is a chicken and egg proposition that the availability of energy didn't cause prosperity; that instead, increased prosperity caused an increased use of energy and electricity. That is a question--which is the chicken and which is the egg--that we ought not to answer by experiment. We ought not to determine by pragmatic means which came first, the chicken or the egg. On the other hand, we may be making that determination without meaning to do so.

We are now pumping something like 11 or 12 million barrels of petroleum a day in the U.S., and using something like 18 million; by 1985, the projection is that we will need something in the order of 25 million barrels a day and U.S. production will then be five to seven million. Those are facts generally agreed to by people working in the energy field and to which the only significant response to date has centered around whether petroleum prices are controlled or not. I think that is not looking far enough into the future.

Very recently there was a fine symposium on energy resources organized by Oregon State University and made up of working members of energy communities in all fields--fossil, nuclear, geothermal, etc. After three days of discussions, the working members (people recognized in their fields, not necessarily spokesmen for their fields and not necessarily representing the business aspects) concluded that it was probable that by 1985 this nation's status in the world would change markedly, and that it was highly likely the Western World would see social and political upheavals in ten years, solely due to the fact that energy was not available to maintain industrial society in the way it is accustomed to live.

There is really no easy way out. There are problems in every direction we turn in attempts to correct the energy situation. Petroleum, coal, geothermal, solar--all have serious limitations and penalties over the intermediate and long run.

The use of uranium has met widespread opposition which has stopped further expansion of nuclear power. In 1973, 43,000 MW of nuclear electrical plant capacity were purchased in this country. So far this year, 2000 MW were purchased, and that 2000 MW has been wiped out by cancellations of other plants, so this year's total contracting for nuclear capacity will likely be zero. As in the case of petroleum, the supply of uranium is limited, but even so, the development of the breeder reactor which would remove that limitation has been deliberately slowed from the national priority status it enjoyed four years ago to being simply a long-range option.

In this total context, we in this room must view the development of fusion as no longer a scientific investigation. Success or failure will have great practical implications for the future of mankind. Very likely fusion is a life or death matter for billions of human beings.

I would like to turn now to a discussion in some detail of the U.S. fusion program. We believe that our program planning shows a recognition of the critical nature of energy resources, that it is an aggressive one aimed at helping to answer the energy resource problem I have tried to describe to you over the last few minutes. Fusion energy is one of the most difficult technological challenges ever accepted, but the benefits which will accrue from its successful development are so great that we must attack this objective aggressively. The easily available and inexhaustible supply of fuel for the fusion process and the relatively slight environmental effects of fusion justify its consideration as the ultimate energy source for this planet. In the last several years sufficient data have been obtained to justify the conclusion that fusion is

scientifically ready for significant acceleration in the research and development applied to it. This is not to say that feasibility has been proven, but rather that now there seems to be clear paths to such proof. This conclusion is generally accepted in the scientific community world-wide. Based on that judgment, strong fusion research and development programs are under way in Japan, France, the European community, and especially in the USSR. The general plans for development of fusion are remarkably parallel in the several other national programs. During the last half of this decade, these plans propose increasingly large and advanced experiments designed primarily to further understand the underlying plasma physics. Larger fusion reactors designed to demonstrate deuterium and tritium burning are now commencing design and construction for operation in the early 1980's. This class of reactors is represented by the Tokamak Fusion Test Reactor (TFTR) being constructed at Princeton, the T-20 in the USSR, and the Joint European Tokamak (JET), which as you know is a cooperative Euratom effort.

The next objective in the fusion development program will be experimental power production in the second half of the 1980's. The U.S. plans two early power producing plants, the Experimental Power Reactors I and II which roughly parallel the Experimental Breeder Reactors I and II in the MFBR program. These plants will be extrapolated from experience gained in TFTR and in similar reactors abroad. Their design, construction and operation will require solutions to many problems on the road to practical fusion energy; they will provide the bridge between scientific feasibility and engineering feasibility.

I would like to talk now for just a moment about that bridge because I have sensed in the fusion reactor program (perhaps not so much in this group as in those who are involved and have been involved for years in plasma physics research) a serious concern--almost a reluctance--to start crossing the bridge from scientific

to engineering feasibility. They are worried that if we start crossing the bridge the scientific end will collapse under us and we will be thrown into the stream. On the other hand, there is an urgent need to get to the other side.

The next viewgraph (Table 1) repeats what I said in the last few minutes. We hope to demonstrate reactor-like conditions in hydrogen plasmas in the 1977 to 1979 period. The PLT at Princeton is about to come on-line and should contribute significantly to this objective, as will the T-10 in the Soviet Union. We hope soon to start constructing a reactor size deuterium-tritium system, TFTR, to operate by 1981. We are in the middle of the early conceptual designs of the Experimental Power Reactor, which we would still hope to get into operation by 1985, with another larger and more advanced EPR by 1990. Finally, we plan a demonstration size reactor in 1995-1997. That's the framework of planning on which the United States fusion program is placed.

About 60-65% of the total effort is on tokamaks, 15-20% on theta pinches, and 15-20% on mirrors. The budget numbers for 1975-77 are listed in Table 2. I would caution you that neither the $140 million case in 1976 nor the $212 million in 1977 are yet approved. These totals are still in the process of decision as to whether there will be $120 or $140 million in FY 1976. But, no matter what happens there is going to be a significant acceleration in the program. You can see the operating expenses go from $89 million to at least $120 million to something like $200 million in the three years 1975-77. This is an accelerating, but not a "crash," effort and if anyone wanted to spend more money on fusion research, that could be done effectively.

None of the U.S. fusion program elements is accelerating more rapidly than the Development and Technology program, which will go from $42 million in 1976 to something like $74 million in 1977. The Confinement Systems subprogram will increase from $67 million to $87.5 million in FY-1977, tokamaks from $45 to $58 million, theta pinches from $10 to $14 million, and mirrors from $11 to $14 million.

Table 1. Major Program Milestones

1. DEMONSTRATE **REACTOR-LIKE CONDITIONS** IN HYDROGEN PLASMAS IN 1977–1979.

2. DESIGN, CONSTRUCT AND OPERATE A **REACTOR-SIZED, DT SYSTEM** (TFTR) BY 1981.

3. OPERATE AN **EXPERIMENTAL ELECTRICAL POWER REACTOR** (EPR-I) BY 1985.

4. OPERATE **EPR-II** IN 1990.

5. OPERATE A **DEMO** IN 1995–1997 **TO DEMONSTRATE RELIABILITY & ECONOMICS.**

Table 2. Fusion Power Research and Development Program — Operating, Equipment, and Construction (Dollars in Millions)

		FY 1976			
	FY 1975	AMENDED EST. TO CONG.	PROG. DIV. ESTIMATES	CONG. AUTH.	FY 1977
OPERATING EXPENSES	$ 89.0	$120.0	$140.0	$140.0	$212.0
CAPITAL EQUIPMENT OBS.	19.8	16.0	18.5	20.0	43.0
CONSTRUCTION OBS.	0.2	28.7	20.2	31.8	150.3
TOTAL FUNDING	$109.0	$164.7	$178.7	$191.8	$405.3

I am sure that you here are very much interested in what happens to the materials research budget. The base program goes from $9 million to $14 million, but most significantly the construction obligations will increase from $4.5 million to $16.9 million. The reason for that is the emphasis on getting facilities into operation in which we can investigate materials at neutron energies similar to those found in fusion systems. The Rotating Target Neutron Source at Livermore is funded this fiscal year at $2.5 million and the Intense Neutron Source at Los Alamos at $2 million. The projects increase to a total of $17 million in the next fiscal year. Both of these projects are going forward vigorously with the intention of having the first in operation in 1977 and the second in operation in 1979. In addition to that, we are carrying on studies at three different locations on a D-Li source which would have capabilities roughly another order of magnitude above the INS. It is the intent in DCTR to go ahead virorously with the D-Li source. With these three sources we believe that, building on experience in materials in the fission reactor program, we will be able to go a long way towards establishing, on a reasonably sound basis, the material requirements for the experimental power reactor or any other large test reactor which may come along.

There is considerable parrallelism in the planning which is taking place in the world community in fusion development. There are three different attempts to produce reactor conditions in hydrogen and those all fall in the 1975-80 period. There are four different attempts to produce deuterium-tritium burning plasmas and those fall in the early 1980's. The different nations plan EPR's by 1990. Finally, three nations plan demonstration plants by 1995-2000.

I think one has to look at an Experimental Power Reactor project from two differing viewpoints. The first one is the benefit of design, construction and operation of the facility per se. The other is the effect on the fusion program as a whole. We can already see the focusing effect on the technology from the conceptual designs which are going

forward at three different locations. Thus, the EPR is already having a significant effect on the direction of the U. S. program.

The work in magnetic confinement fusion has been a notable example of effective international cooperation since the late 1950's when it escaped from the security blanket that had been placed over it after World War II. Numerous personnel exchanges have taken place and excellent communications and open discussions have been the rule in this program. The U.S. signed a bi-lateral agreement with the USSR in 1973 which has led to a particularly close and effective cooperation between these two countries.

This Conference is in itself an excellent example of the communication and cooperation between the nations in fusion energy. It may well be that there is an understanding of the importance and magnitude of the fusion challenge, that we in the U.S. cannot solve this problem unilaterally--that the whole world needs what we are attempting to develop, and can share in its development.

There has been a significant relative increase in the amount of effort spent on supporting technologies relative to plasma physics. There are two reasons for this. The first is that you can't build larger and larger plasma physics machines like the TFTR without doing something about the technology. Even the plasma physicists recognize that eventually they are going to want to put a superconducting magnet in a plasma physics test device. Thus, in order to allow the further intelligent development of the physics, we have to do the underlying technology to allow bigger, more powerful machines to be built. The second is that, if we presume we are going to be successful at any given time, we ought to be building the technology base now so that when that success in physics has been achieved, we can immediately turn to practical application and not wait around for another ten years to develop the technology. Therefore, it is a necessity, if fusion is going to live up to its promise on anything like the time scale we have talked about, that we proceed aggressively with the supporting technologies.

In that context the two subjects of this International Conference are in many ways the most important and the most difficult of the tasks before us. Materials determine what are in the end the things that we can and cannot do. Materials determine what we might make the difference in fission reactors and what is in the end going to make the difference in fusion reactors. Materials is the place technology of any advanced technical system. The economics eventually depend upon the materials, the reliability depends upon the materials, and safety depends upon the materials. I assure you that before we are through with fusion, the physicists will give way to the materials engineers as being the leading lights of fusion.

Many in the audience today would debate whether tritium or materials is the most important technology question we face, because tritium inventory and control is one of the socio-political questions which has plagued fission reactors and it will inevitably come into discussion in fusion, just as plutonium came to be a key question for fission reactors.

It does seem to me strange that there is so much argument about plutonium effects on mankind. Here we are some twenty-five or thirty years after the first use of plutonium, in a world in which there is something like 50,000 thermonuclear weapons, many of which contain plutonium. Yet, there is a vast national debate as to whether plutonium hurts you or not and if so, how much. The people talking about the subject are orders of magnitude apart. That's the kind of range we are debating. I hope to hell we don't have the same questions about tritium when we start using tritium in fusion power reactors. If we are, in fact, heading down that route, it's high time we change that course and find out what are the biological effects of tritium and how to evaluate its societal and environmental considerations. I am afraid that we may be heading for questions like those being debated today about plutonium. We say to ourselves that tritium

is a relatively benign radioactive material, but that's before Dr. Tamplin or his counterparts commence attacking. We had better have some facts before we find ourselves 15 or 20 years from now in a serious and debilitating debate about the biological effects of tritium.

Let me now pretend that I am Noah for a minute and, having survived the LMFBR flood, give you a few principles which I think should be followed in the development of fusion technology if fusion is to be successfully developed at an early time. These are principles which in one sense are "motherhood," but in another sense they are not "motherhood" because they are often forgotten in programs like ours.

The first thing we need to do is define the requirements. We can't develop all the interesting materials for all interesting environmental conditions at the same time. We must select several candidate materials and concentrate our efforts on those candidates for the first wall and for the other materials we are going to use in fusion reactors. Our efforts have to be concentrated on the primary goals, something that will work in the environment that we are talking about.

The second point is that we have to develop a true technical base--we have to understand thoroughly the materials and the processes in a fundamental sense if we are going to be successful in applying them to practical use. I'm sure you are saying that is exactly what we are doing--but that may not be true. Too much of what passes today for research is experimental pragmatism, too little aimed at fundamental understanding of nature. Good starts have been made in materials understandings--for example, in the LMFBR program and fusion is building upon that--but a great deal more needs to be done to understand fundamentals. Let me give you an example--ten years ago there was a large fuels and materials program for breeder reactors. It consisted--and here I am exaggerating for effect--in taking cladding of every known alloy and fuel of every known smeared density and putting them into a reactor to see what would happen. Only when there

was a concentration on a specific set of materials and a specific kind of fuel and a specific target environment and lifetime, with an attempt made to separate out the effects of the few variables associated with a specific design, did we finally obtain reasonable results. When I first became associated with LMFBR fuels, I found that the test temperatures were not known within ± 100°F--and that test powers were not known within ± 25%. That can hardly be called science. It is not "understanding the fundamentals." It was, in fact, a pragmattic approach to the problem. Problems of such technical difficulty cannot be solved that way. One might stumble onto something, he might find something better than what had been tried before. But unless we get into the deep fundamental nature of materials we are going to have a hard time in fusion because we are trying to push so much further than previously has been done in terms of application of materials.

Third, we must demonstrate our knowledge of fundamentals in actual practice, whether in prototype plants or in test facilities. That means that we have to build larger and larger devices with increasingly difficult technical requirements until we reach the characteristics of practical fusion temperature, life and stress. What is demonstrated in the laboratory is seldom precisely what is experienced in practical use. That means that bigger and more expensive and more advanced projects are going to be needed, not only for the better physics produced but for their assistance in development of fundamental technology.

Finally, throughout all this technical effort, we've got to recognize that our efforts are not ends in themselves, but means to an end. We've got to take all those steps necessary to be sure that fusion technology once developed and proven can be applied reliably, economically, and safely in the larger social and industrial context. We have to be thinking now that the objective is not the most elegant technical developments but the practical application of technology in a practical environment.

What I have tried to say over the last half-hour is that there is a vital need for what we are doing in the fusion community. The urgency and importance associated with our work will be more obvious to the general public and to those in power five or ten years from now. Correctly or not, there is a general perception that fusion holds great promise. We can consider ourselves very fortunate to have an opportunity to work in such an exciting field at this crucial time. But by accepting employment in fusion now we accept a personal commitment to something larger than our own or our laboratory's ends.

Fusion is no longer a scientific curiosity to be explored from an ivory tower. Definitive results, pro or con, are needed and they are needed soon. In no area of fusion technology is that more important than in the two subjects of this Conference.

RADIATION DAMAGE: THE SECOND MOST SERIOUS OBSTACLE TO COMMERCIALIZATION OF FUSION POWER

G. L. Kulcinski

Nuclear Engineering Department
University of Wisconsin
Madison, Wisconsin 53706

ABSTRACT

The uniqueness of radiation damage associated with 14 MeV neutrons is discussed in relation to total displacements per atom (dpa), dpa rate, gas production rate, gas to dpa ratio, and solid transmutation products. Comparisons are made with both light water and fast reactors to illustrate that it will be very difficult to use the latter facilities to provide information about high power fusion reactors. The one exception to this statement pertains to 316 SS in thermal reactors where the proper helium gas generation rate is achieved. Examination of the displacement and transmutation damage with respect to the dimensional, mechanical and physical properties of metals reveals that there is very little, if any pertinent experimental data available. Providing this data will require a massive and time consuming test program that could spread over a decade or more. Considering the shear number of radiation damage problems and their magnitude leads one to believe that their solution will be a major barrier to the commercialization of fusion power, second only to those problems associated with plasma physics.

INTRODUCTION

The production of electricity by a controlled thermonuclear reactor can be one of the most important scientific achievements in the history of mankind. However, one must also recognize that such an achievement will require the successful solution of some of the most complex problems ever encountered by the scientific community. The production and confinement of a DT plasma will be difficult, time consuming, and at times, frustrating. Once that primary carrier is overcome, there will be several other obstacles that must be surmounted before the goal of economic fusion power can be achieved. These include the successful production, handling, and containment of tens to hundreds of kgs of tritium in a fusion plant, the assurance of structural integrity over relatively long periods of time in

the face of an extremely harsh irradiation environment, and the engineering design of systems which are compatible with the resource, environmental and financial limitations that are facing every country in the world today. The object of this paper is to illustrate why it is felt that, next to the solution of the plasma physics problems, the effects of radiation damage to reactor structural components represent the second most serious obstacle to fusion power.

Such an exposure of the many materials problems is a colossal undertaking to say the least and we hope that it is done in a positive sense in this paper. The main purpose is to insure that scientists of all types, and materials scientists in particular, broaden their perspective to consider not only those problems with which they are individually acquainted with, but also those problems which so often stand between the scientific feasibility of a particular concept and the engineering feasibility of that concept.

The format of this particular paper is as follows. The anticipated irradiation environments of several types of fusion plants are first reviewed including the types and functions of various CTR materials. Next the displacement damage and transmutation characteristics are discussed, both as a function of position, and time in typical fusion systems. This is followed by a brief description of the general types of neutron damage anticipated in fusion reactors and some observations on state of the art of experimental data. Finally, the effect of these property changes on the effective lifetime of reactor components is discussed in terms of cost, resources, and long term radioactivity problems.

A final point to note is that this work will concentrate on <u>bulk</u> radiation damage by neutrons and will not be concerned with the surface damage produced by neutrons, photons, or particles leaking fron the plasma. This has been amply reviewed in previous conferences.[1-3] Such an omission should not be construed as implying surface effects are unimportant, but rather it is a result of the limited space alloted a review of this type.

OPERATING ENVIRONMENT FOR VARIOUS FUSION REACTORS

Materials

In contrast to fission reactors where there are perhaps 4 or 5 different classes of solid materials to worry about (fuel, cladding and core restraint, reflectors, control rods, and pressure vessels) there may be as many as 10 in fusion reactors. These general classes are listed below:

- Low Z liners
- Electrical insulators
- Structure
- * Solid tritium breeder material
- * Fissile breeder material
- * Neutron multipliers
- Reflectors
- Shielding material
- * Magnets
- * Optical systems

The functions of these materials have been reviewed before[4-6] and we will only briefly summarize the results here.

Tokamaks may require low atomic weight liners for plasma physics reasons (mainly to insure that excessive power is not leaked from the plasma by radiation from impurity atoms).[7-8] Such materials are placed in the vacuum region between the plasma and the first solid wall and therefore will be subjected to the most extreme temperature, charged particle, photon and neutron environments in the reactor. It is important that they last at least as long as the first structural walls in order to allow some chance for economical commercial operation.

Electrical insulators will be required in all magnetically confined systems in one form or another and in inertially confined systems (i.e. E beams). Both mirrors and tokamaks will require fueling systems (beams or pellets) which will probably rely on electrostatic acceleration. It will be difficult to shield such systems from the direct bombardment of neutrons and the associated damage to dielectric properties. Auxiliary

*only required in some systems

heating in Tokamaks may utilize RF sources which could contain dielectrics to reduce the size of the wave guides.[9] Unfortunately, such wave guides must "see" the plasma and therefore be subjected to all the radiation emanating from the plasma. Theta pinch reactors will require electrical insulators which can maintain dielectric strengths of up to 100 kV/cm while being pulsed some 3 to 10 million times per year.[10] This insulator must function at temperatures approaching 1000°C while being bombarded with copious amounts of atomic hydrogen and neutron fluences of up to 10^{22} $n/cm^2/yr$. Finally, the electrodes of E beam reactors will be subjected to very high fluxes and the associated degradation of properties has not been completely appreciated at this time.

The needs for structural vessels which provide vacuum tightness and are pulsed anywhere from 10 to 10^8 times per year are fairly well established and extremely demanding. Reflectors are required for efficient neutron utilization and protection of components outside the reactor. Shields are absolutely essential to prevent excessive radiation levels from occuring outside the reactor and to prevent damage to components not directly involved in the extraction of energy (i.e. magnets, lasers, fueling devices, etc.).

Breeding is, of course, absolutely essential for all the D-T systems. If liquid lithium is not used, then solid lithium containing compounds as Li_2O, $LiAlO_2$ or $LiSiO_2$ must be utilized.[11-12] We shall see later that these compounds have many of the same problems now facing us for fission reactor fuels with a few added features which could be quite difficult to overcome. For example, a very large fraction of the total energy is produced in these materials (normally ceramics) which promotes high temperatures and severe temperature gradients. In order to avoid large tritium inventories, the tritium must be constantly removed from the breeder. If radiation damage and high temperatures interfere with the diffusivity and/or the diffusion path of the tritium, very high tritium inventories could then occur.

The use of solid breeding compounds will almost invariably require the use of neutron multipliers such as beryllium. Ignoring the high cost per kg of Be and the lack of extensive Be reserves in the world for the

moment,[13] one finds that severe dimensional problems could occur at high temperature due to high helium gas generation rates. It has even been proposed to surround the plasma with a blanket containing fissionable and/or fertile material.[14] Presently it seems that the later is more attractive and this would mean that the associated dimensional problems of U and Th compounds need to be considered along with radioactive fission products and associated safety questions.

The critical properties of superconducting magnets for tokamaks and mirrors, and conventional magnets for theta pinches must be maintained. In the first case, the critical currents, temperatures and fields of superconducting filaments must not be significantly reduced over long periods of time by bombardment with neutrons. The cryogenic stabilizers must retain a low resistivity value to insure safe operation in the event of a quench in the superconductor. The compression coils of a theta pinch reactor will be subjected to high neutron fluxes and operate well above room temperature. Significant transmutation reactions and displacement rates will result in changes in resistivity over long periods of time. Finally, one needs to be concerned about non current carrying components of magnets such as electrical insulators or thermal insulators. Failure of any of these components could require costly repairs and unacceptable down times.

The optical systems for laser reactors (such as mirrors and windows) must maintain extreme dimensional stability (to within a quarter of the wavelength or ~3000 Å) over long periods of time in a commercial system. Very little is presently known about the effects of neutron damage on the surface roughness and the subsequent effects on the efficiency of pellet compression or, the rate at which implosions can take place. This area is almost completely lacking in prior information and it is difficult to even estimate how serious of a problem may be encountered. In the worst case, the ultimate viability of a laser reactor could critically hinge on the successful solution of such problems.

An attempt to summarize the preceding discussion has been made in Table 1 where the potential materials, their functions, operating temperatures, neutron fluxes, and critical properties are listed. A detailed

Table 1

Materials for Fusion Reactors

Function	Typical Examples	T_{op} °C	ϕt s^{-1} (MW/m^2)$^{-1}$ 14.1 MeV	ϕt s^{-1} (MW/m^2)$^{-1}$ Total	Special Comments
		GENERAL			
First Wall and Blanket Structural Components	Austenitic Steels (AISI 304,316,347,etc.)	400-650	4×10^{13}	2×10^{14}	
	Nickel Based Alloys (PE16,Inconel,Incoloy,etc.)	500-700			Low Li Corrosion Resistance
	Refractory Metals (V,Nb,Mo or alloys)	800-1000			
	Aluminum Alloys	<300			
	Other (carbon, SiC)	~1000			Low Tensile Strength
Neutron Multiplier	Be,	400-600	~1×10^{13}	1×10^{14}	High He Gas
	BeO, Be_2C	400-1000			Production
Breeding	Li	300-1000	~1×10^{13}	~1×10^{14}	High Gas
	LiAl	300-600			Production
	$LiAlO_2$, Li_2O	600-1500			
Reflection (Moderator)	Graphite (Steel)	400-1000	4×10^{12}	~2×10^{13}	High He Gas Prod in C
Radiation Shielding	B,B_4C,Pb,Steel	100-300	10^{11}	10^{13}	Thermalized Spectrum
		SPECIAL			
Electrical Insulation	Al_2O_3,MgO	500-800	4×10^{13}	2×10^{14}	~100 kv/cm pulsed operation
Optics for Laser System	Phenolics	~270	10^6	10^8	
Windows	Ge,NaCl,KCl,etc.	~100-200	up to 4×10^{13}	up to 2×10^{14}	Pulsed neutron fluxes and temp. loads
Mirrors	GaAs,CdSe,Cu,TiO_2 ZrO_2	~100	variable	variable	Extreme Dimensional Stability Req. (<3000 A)
Thermal Insulation	Mylar	~240-270	~10^6	~10^8	High susceptibility to gamma irradiation
Superconducting Stabilizing Materials	Cu, Al	~269	~10^6	~ 10^8	Periodic annealing to R.T. can remove substantial damage
Superconducting Magnet Filaments	NbTi,Nb_3Sn	~269	~10^6	~ 10^8	"
Magnet Support Structure	Austenitic Steel, Al Alloy	-200 to +30	~10^6	~10^8	High Stresses (~2/3 σ_y)
Energy Multiplication	UO_2,PuO_2	800-1500	~10^{13}	~10^{14}	Temp. Gradients
Fissile Fuel Breeding	U	<500	10^{13}	~10^{14}	Gas Swelling

discussion of these numbers is not warranted here because the quantitative numbers are somewhat design dependent. However, the reader will note the wide range of conditions and materials involved in fusion systems and can draw his own conclusions about the extent of the research program to establish engineering feasibility of CTR reactors.

Burn Cycle and Neutron Flux Effects

One of the most frustrating aspects of this type of analysis is that there are several potential (at least 5) avenues to fusion reactors and they all represent drastically different burn cycles. We will try to put all of these cycles in perspective with respect to the following quantities (see Table 2).

- time over which neutrons are produced
- time in which damage is done in materials
- time between burns

The information in Table 2 shows that the neutrons can be produced in burns which last from 10^{-9} to 10^{6} sec separated by times of 0.01 to 10^{5} sec. For all systems in which the burn time exceeds the neutron slowing down time (approximately a microsecond) the damage rate is constant over the burn time. However, in E beam or laser systems, the neutrons are produced in times much shorter than the slowing down time and consequently the damage occurs at a relatively long time after the initial burst of neutrons.

In principle, the mirror system could run in a steady state so that precise assessment of burn dynamics is not meaningful. However, it is unlikely that any system as complex as a fusion reactor could run continuously for more than a month without a mechanical failure which would require a shutdown of the reactor. Therefore, we have somewhat arbitrarily chosen 3×10^{6} seconds as a typical operating time.

The situation for tokamaks is somewhat unclear at the present time depending on the rate of buildup of impurities in the plasma, or the amount of flux swing that can be reasonably uncorporated into the transformer coils. It is quite possible that if impurity confinement times are significantly longer than fuel atom confinement times, the D-T burn

Table 2

Potential Burn Cycles for Various Fusion Reactor Concepts

Reactor Concept	Anticipated Neutron Pulse Length-sec	Time of Damage per Pulse-sec	Time Between Burn-Seconds	Number of Cycles/year 80% P.F.	Instantaneous 14 MeV Neutron Flux at an Ave. 1 MW/m^2 wall loading over burn cycle(b
Tokamak	100-5000	100-5000	10-500	5000 to $2x10^5$	$\sim 5 \times 10^{13}$
Mirror	$\sim 3 \times 10^6$(a)	3×10^6	$\sim 10^5$	10	4.5×10^{13}
Theta Pinch and Solonoids	0.3	0.3	3-10	$\sim 10^6$	$\sim 4 \times 10^{14}$
Laser	10^{-9}	10^{-6}	0.01-1	10^7-10^9	$\sim 4 \times 10^{17}$ to 4×10^{19}
E-beam	10^{-9}	10^{-6}	0.01-1	10^7-10^9	$\sim 4 \times 10^{17}$ to 4×10^{19}
LWR-Fission Reactor	3×10^6(a)	3×10^6	$\sim 10^5$	~10	2×10^{14}(c)
LMFBR-Fission Reactor	3×10^6(a)	3×10^6	$\sim 10^5$	~10	$\sim 2 \times 10^{15}$ (c)

(a) Limited by mechanical failures rather than physics considerations.

(b) Units of $n/cm^2/sec$, back scattered neutrons would increase the numbers by factors of approximately 5.

(c) Max. fluxes core center, $E > 0.1$ MeV.

cycle could be limited to as little as 100 seconds in a reactor. On the other hand, if the impurities diffuse out of the plasma at a sufficiently rapid rate, then economic limitations of incorporating flux swings of more than 500 V-sec may limit the length of the burn to a few thousand seconds before the magnets would need to be reset.

Theta pinch and solonoid reactors limit their burn times to a few hundred milliseconds due to a complex trade off between size of the plasma column, reasonable magnetic fields and rates of field buildup and assumptions on burn dynamics. It is unlikely that the burn times would be greater than one second and values of less than 10 milliseconds may be uneconomical in a magnetically confined system.

If one assumes that nominally, a time averaged 1 MW/m^2 wall loading is required for economical reactor operation, then one can obtain a rough approximation of the instantaneous 14 MeV neutron flux (in $n/cm^2/sec$) to the first wall. This ranges from ~4.5×10^{13} $n/cm^2/sec$ for mirrors and tokamaks to ~4×10^{14} for theta pinch and solonoid reactors, to as high as 4×10^{17} to 4×10^{19} for laser and E beam reactors. Of course, if back scattered neutrons are included, these values would have to be increased by factors of ~5 to get total neutron fluxes. We have included typical values for fission reactors in Table 2, which include all the fast ($E > 0.1$ MeV) neutrons. Even if the tokamak and mirror numbers were adjusted to include back scattered neutrons, we would find that the total neutron flux is considerably lower than in a liquid metal fast reactor. However, we shall see later that spectrum effects alters this picture in ways which are material dependent.

To summarize this section, we cannot state with any degree of certainty what the burn cycle and neutron flux conditions will be for the ultimate fusion system. There may be as much as a factor of 10^6 difference in damage rates not to mention the effect of annealing time between pulses on the final state of the damage. The best one can do now is to acknowledge the wide range of possible operating parameters and adjust research programs accordingly.

Spectrum Effects

The increased energy of the D-T neutron (14.1 MeV) over those typical of a fission spectrum makes the quotation of simple neutron fluxes and fluences of somewhat questionable value for fusion. Not only are there many more potential nuclear reactions to contend with (e.g. (n,n'p), (n,n'α), (n,2n)) but the primary knock on atom (PKA) energy is considerably higher. An appreciation of the spectral differences can be gained from Figure 1 where the neutron spectra from a fission reactor,[15] a typical fusion reactor,[16] a D-T neutron source[17] and a D-Li stripping source[18] are given. These numbers are plotted on an absolute scale so as to reflect the flux level as well as the energy spread of neutrons in these systems. The fusion spectrum has the traditional peak at 14 MeV followed by a down-scattered spectrum that peaks over several hundred keV. This is contrasted to the fission spectrum where the neutrons are emitted with a mean energy of ~1 MeV. Current D-T neutron sources are unable to provide sufficient backscattered neutrons to cause a significant deviation from the monoenergetic source while stripping sources such as D-Be or D-Li provide a broad range of energies which depend on the incident deuterium energy. For a 33 MeV deuterium on Be the neutron energy varies from a maximum of ~33 MeV to below 1 MeV with a maximum in flux at ~18 MeV.

The importance of such spectral effects on a few selected nuclear reactions is given in Table 3 where the spectrum averaged cross section for the helium gas reactions in metals are listed for a fusion reactor and a light water fission reactor. This table reveals that the (n,α) cross section for the metals examined here ranges from 100 to 1000 times higher in fusion reactors versus fission systems. (This is reversed for Ni containing alloys for reasons explained elsewhere.[20,21]) The ratio is even higher for the (n,2n) reaction in all metals. Such large differences are partially compensated for by the order of magnitude higher flux in fast fission reactors, but it is obvious that the magnitude of gas generation is still much higher in fusion reactors. This is also true for many other transmutations as we shall see later.

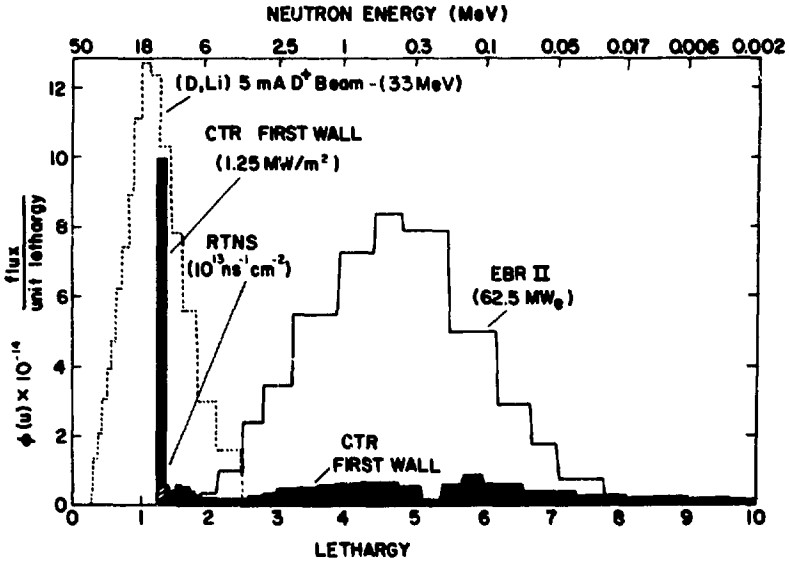

Fig. 1 - Typical Neutron Spectra for Various Nuclear Facilities

Table 3

Effect of Neutron Spectrum on Helium Production Cross Section

	Spectral Averaged Cross Section - milli barns	
Element	LWR[a]	CTR[b]
Mo	0.046	4.53
Nb	0.025	2.37
V	0.06	5.24
316SS	~60[c]	20.4
Al	0.28	32.5

(a) HFIR (High Flux Isotope Reactor) core center[19]

(b) UWMAK-I[16] First Wall

(c) Due to thermal (n,α) reaction in Ni-59[20], value here is valid after one year of exposure.

The higher neutron energy also produces a considerably different PKA spectrum as shown in Figure 2. We have used the defect production code of Gabriel et al.[22] and plotted the PKA energy of Cu atoms in (1) a light water fission spectrum, (2) a typical CTR first wall spectrum and (3) a mono-energetic 14 MeV neutron flux. The first point to note is the large number of low energy events even in the higher energy neutron case. The second point is the maximum PKA energy is ~500 keV for the fission neutrons and ~2 meV for the fusion neutrons. The effect of such high energy knock on atoms on physical processes in metals is not clear at present but it is conceivable that it could mean increased resolutioning of fine precipitates, the generation of multiple defect clusters in close proximity to each other which might be very effective dislocation barriers or in increased overlapping of displacement spikes. This question is of course of fundamental importance in assessing the validity of any simulation scheme.

In summary, it is safe to say that we do not know precisely what effect the higher neutron energy of a D-T reaction will have on the physical and mechanical properties of metals at high fluences and at high temperatures. The increased transmutation rates and the higher PKA energies are not easily incorporated into present radiation damage theories and it would n be surprising if future experimentation produces a few "surprises" in materials behavior like those of fuel pellet sintering and voids discovered in fission reactors.

Spatial Effects of Neutron Fluxes

At first glance one might think that the neutron flux and energy spectra vary only with distance into the blanket and shield measured perpendicular to the plasma. In fact, this is probably true for laser and mirror reactors which are generally spherical in geometry. It may also be true for theta pinch reactors which are either cylindrical or toroids with a very large radius of curvature. However, the small aspect ratio of tokamaks, the fact that the center of the plasma may not be the geometrical center in the toroid, and the fact that the plasma may not be completely circular all combine to produce a complex flux profile in the poloidal

direction.[23,24] A typical example is shown in Figure 3 where the wall loading* is given as a function of poloidal angle inside the cross section of a torus for the UWMAK-III reactor.[25] In this particular example (except for the divertor slots), the maximum to minimum wall loading is ~2 and the maximum to average ratio is 1.2. Such a variation is further complicated by a back scattered neutron spectrum which also varies around the poloidal direction.

The investigation of toroidal neutronics effects is rather new at this writing but it seems certain to complicate matters for damage predictions in tokamaks. We shall see later that severe displacement damage and transmutation gradients will exist in 3 dimensions throughout blanket structure. This is in contrast to essentially 1 dimensional effects in spherical and cylindrical geometries. The analysis of such damage structures in tokamaks will also be more difficult than in fission reactor cores where there is generally a 2 dimensional geometry.

DISPLACEMENT DAMAGE CONSIDERATIONS

A somewhat imperfect, but more reasonable way of comparing the potential damage rates in fission and fusion reactors is to calculate the theoretical fraction of atoms displaced per unit time of exposure in the irradiation environment. This unit, called the dpa for displacements per atom, does not include transmutation effects or the amount of spontaneous and thermal recombination of the point defects. However, it does account for the probability that reactions will take place initially and the amount of energy which will eventually be transferred to the lattice atoms in nuclear encounters. Several authors have reported displacement cross sections[22,26-28] and we have plotted some representative values in Figure 4. Note that 14 MeV neutrons have damage energies which are ~4 times those of 1 MeV neutrons and that the absolute magnitude of the dpa cross section for heavy elements differ by less than 20%. The situation for the low Z elements (e.g. C, Al) is somewhat different in that there is relatively little difference between 14 MeV and 1 MeV neutrons with respect to dpa values. This results from the

*Defined here as the uncollided 14 MeV neutron flux/4.43 x 10^{13} $n/cm^2/s$.

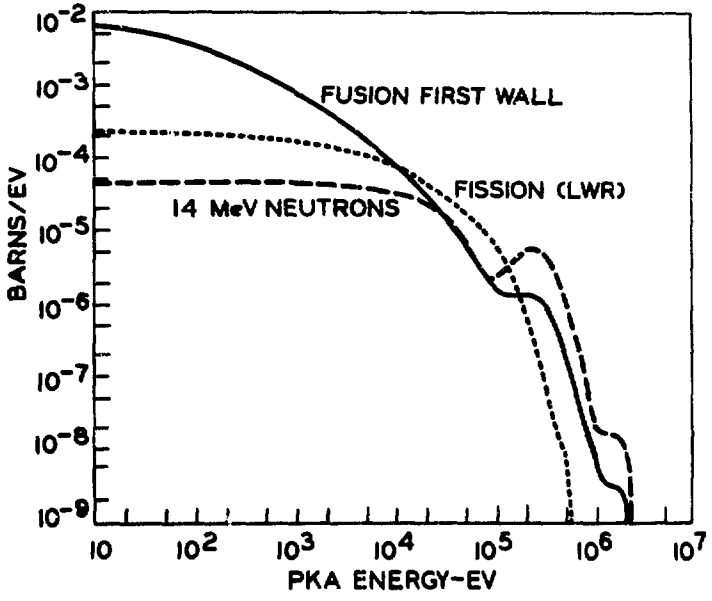

Fig. 2 — Primary Knock-On Spectra for Copper in Various Nuclear Facilities.

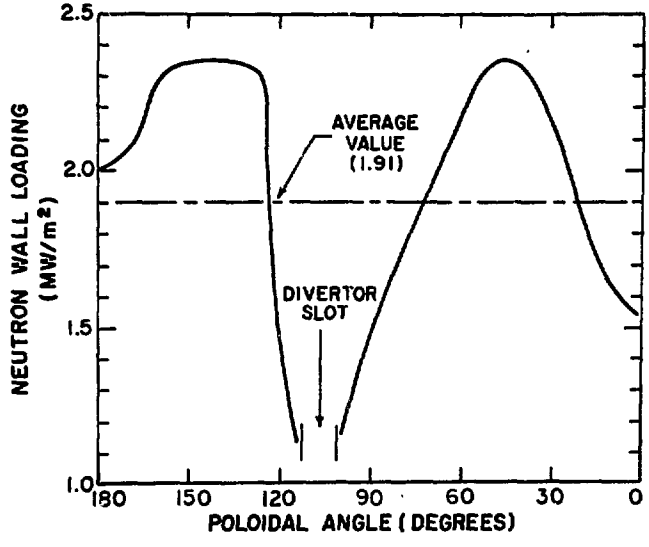

Fig. 3 — Poloidal Variation of Neutron Wall Loading in UWMAK-III.

predominance of low angle scattering and the low threshold for ionization losses in these elements. Such an effect means that, neglecting the spatial distribution of defects on a microscopic scale and transmutations, 1 MeV neutrons are nearly as damaging as 14 MeV neutrons and fission reactors probably make good simulation devices for displacement damage in low Z elements.

Coupling the dpa cross sections of Figure 4 with the neutron spectrum from a low aspect tokamak reactor like UWMAK-III [24], we can illustrate the macroscopic spatial distribution of damage in a tokamak reactor. The poloidal variation of dpa damage in the outer blanket is shown in Figure 5 and the variation in dpa with distance from the front wall is shown in Figure 6. Note that the maximum to average dpa values are close to, but not quite the same as the uncollided neutron flux due to the spectral effects mentioned earlier. It is also shown, in Figure 6, that the variation in dpa rates in the inner and outer blankets are different due to geometric consideration and different materials in each blanket of UWMAK-III. Note that displacement damage is reduced by ~1000 in 120 cm of blanket and reflector regions.

Another use of dpa calculations has to do with the calculation of the damage rates in various fusion concepts. For example, we know that the dpa rates in tokamaks are $\sim 10^{-7}$ dpa/sec per MW/m^2 and roughly the same for mirror reactors. However, the instantaneous dpa rates in a theta pinch are ~10 times higher, and those in a laser system are $\sim 10^6$ times higher. This situation (and the variation thoughout a ~1 meter blanket model) are summarized in Figure 7 for 316 SS. The displacement rates in the EBR-II reactor are also included in Figure 7 and it can be seen that they are higher than all of the values for the tokamak but actually an order of magnitude lower than those in theta pinch first walls and 5 orders of magnitude smaller than in laser (or E beam) fusion reactor blankets.

The effect of damage rates on physical processes such as void formation, creep rates, fatigue, etc., is not very well known at the present time. It can be dangerous to think that one is simulating pulsed damage in a fission reactor which can in fact produce the desired total dpa levels but only in a steady state fashion. We should be sensitive not only to the

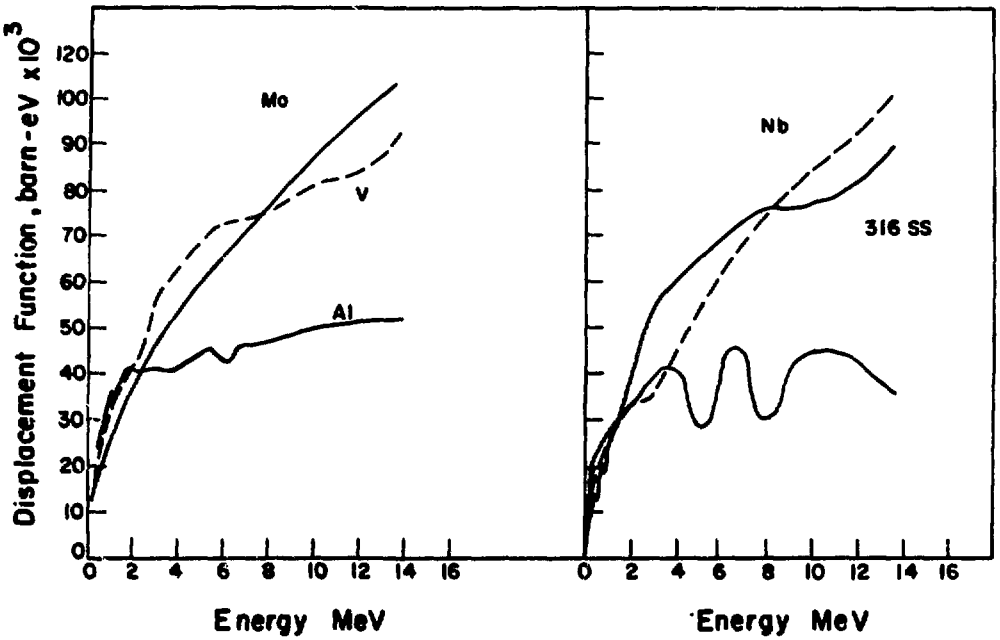

Fig. 4 — Displacement Function Values for Various CTR Materials.

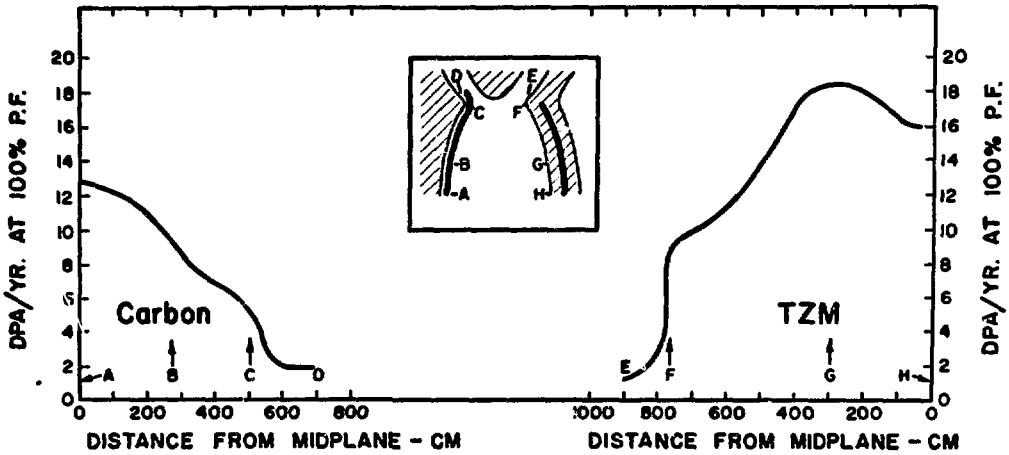

Fig. 5 — Poloidal Variation in Displacement Rate in the Tokamak Reactor UWMAK-III.

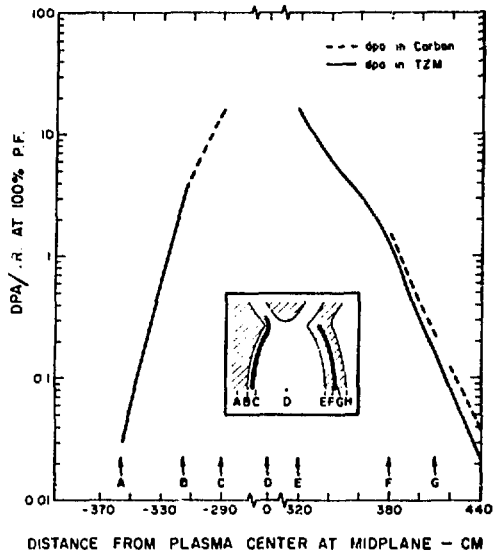

Fig. 6 - Variation of Displacement Damage in the UWMAK-III Tokamak Reactor

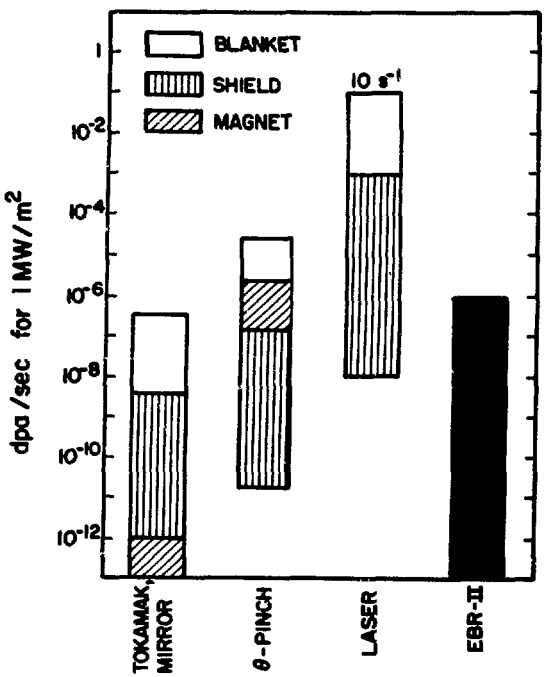

Fig. 7 - Instantaneous Neutron Displacement Rates in DT CTR First Walls

fact that some instantaneous dpa rates in fusion reactors are 10^5 to 10^6 higher than in fission reactors but also that some are actually a factor of 10 or more lower. (i.e. tokamak blankets, shields, magnets).

Recent theoretical work[29-31] shows that not only does the rate of producing damage alter such phenomena as the nucleation and growth of voids but these phenomena are also quite sensitive to the downtime (annealing time) between pulses. At the present time, there are no acceptable facilities in the world to test even the most simple of the rate theories, let alone try to incorporate the effects of the thermally induced stresses. The laser and E beam reactor concepts are the most vulnerable in this respect and a whole new field of radiation damage theories need to be developed for these concepts.

TRANSMUTATIONS

Because of the higher neutron energy in D-T fusion reactors there are a much larger variety of transmutation reactions which can take place than in a fission spectrum. We will first explore some typical transmutation rates in potential CTR materials normalized to 1 MW/m^2 wall loading, then comment on how the transmutation and displacement damage is related and finally show how the reaction rates might vary with position in a fusion blanket.

There have been several comprehensive studies on the production of gaseous and non-gaseous isotopes in CTR materials.[12,16,21,23,32,33] We will try to sumarize those results for both categories here and place them in perspective to the problems at hand. It is fairly well accepted that gaseous atoms, in particular, helium, present the greatest problem to the long term mechanical integrity of metal components. We have listed typical helium production rates in Mo, Nb, V, Al, C, and 315 SS in Table 4 for both a 1 MW/m^2 CTR spectrum and in a thermal fission reactor core. It is evident from this table that even at modest wall loadings, tens to thousands of atomic parts per million of helium can be produced per year of operation in fusion reactors. Such rates are 20-200 times higher than in fission reactors. We shall see later that at high temperatures (~0.45 to 0.5 T_m) even a few parts per million of helium can significantly reduce the ductility of metals such that safe

operation can no longer be assured. Therefore, aside from corrosion, it is reasonable to assume that the upper temperature limit for structural material will be limited by this type of embrittlement and those metals which produce the greatest amount of helium will have the shortest lives in a reactor if operated at the same high temperature limit.

One point which is often neglected in this area is a consideration of the contribution of impurities to the gas generation, especially if those impurities are low atomic numbers with low coulomb barriers (e.g. Li, C, O, N, Al, Ti). This effect can be amply illustrated by three examples:

- Pure Nb versus Nb + 2000 wtppm oxygen
- Pure Al versus Sintered Aluminum Powder ($Al + Al_2O_3$)
- "Pure" 316 stainless steel and a commercial grade alloy.

The helium production rates of these six systems in the same neutron flux are given in Table 5. Such calculations reveal that in a metal like Nb, where the annual helium production is only ~24 appm/yr, the addition of 2000 wtppm oxygen (presumably by contamination) could increase the helium production rate by 50%. Vanadium would be somewhat less sensitive to this effect because it has a higher intrinsic helium production rate (but probably the same contamination potential). The addition of oxygen to aluminum has a significant strengthening effect but the oxygen is also a potential helium producer and actually contributes twice the number of helium atoms than would the aluminum atoms it replaces. Even in a relatively complex alloy like 316 SS we find that normal commercial impurities can increase the helium production rate by ~10-15%. It is also worthwhile to point out that there is another source of helium in fusion environments, that is, the decay of tritium absorbed into the structural material. A brief example will illustrate this point. Table 6 lists the helium produced in two positions of a fusion blanket at 1 MW/m^2, the solubility of tritium at a typical operating temperature, and the amount of helium produced by the decay of that tritium. It is evident from this type of consideration that Nb and V are very susceptible to helium embrittlement in the absence of neutron irradiation and such a phenomena may pose a serious problem for ex-reactor components such as heat exchangers which presumably would never "see" a neutron.

Table 4

Helium Production Rates in Various Potential CTR Materials

	appm/year[a]	
	Fusion[b]	Fission[c]
Mo	47	2
Nb	24	1
V	57	0.3
Al	330	8
316 SS	210	5
C	3000	34

(a) 100% P.F., See Reference 21.

(b) UWMAK-I Spectrum (16), 1 MW/m^2.

(c) EBR-II Spectrum (15).

Table 5

Effect of Alloying Elements or Impurities on the Helium Production Rates in Selected CTR Materials

System	appm He/year at 100% PF and 1 MW/m_2
Nb	24
Nb + 2000 wtppm O	36
Al	365
SAP(10 Wt % Al_2O_3)	410
316 SS (pure)	210
316 SS (commercial)	235

It is now appropriate to consider the relationship between helium gas and displacement damage because it is not a function of flux (with the exception of Ni containing alloys) but only of neutron spectrum. A convenient method of assessing this relationship is to quote the ratio of gas atoms produced divided by the number of displacements produced in the same unit of time. Such a ratio is given in Table 7 for a fast reactor, a thermal reactor, a 14 MeV neutron source, a D-Li stripping source, and the first wall in a fusion reactor.*

The data in Table 7 is very important to consider when one is analyzing data from non-fusion facilities. The synergism between helium and displacement damage is not well understood, but it is well established. For example, high helium contents can increase swelling at the same dpa level especially at high temperatures.[34] It is known that voids do not even form in some metals during ion bombardment unless helium is present.[35] It is also known that helium introduced by the tritium trick does have a greater effect on the mechanical properties as does helium introduced along with some displacement damage.[36] Therefore, it is extremely important that experimenters who propose to simulate CTR damage in non-CTR devices take this synergism into account before making any conclusions about the viability, or lack of viability of CTR materials.

One last point to make on this ratio is that it will change as a function of distance in spherical and cylindrical geometries and in a poloidal sense as well for tokamaks. This is illustrated in Figure 8a and 8b where we have plotted the appm He/dpa ratio for Mo through a typical blanket. Note that even at 100 cm from the first wall the helium to dpa ratios for a fusion device are much higher than in a fission reactor. (Figure 8a and Table 7) An additional feature in the fact that this ratio can vary by a factor of 2 or more as one progresses around the poloidal angle of a tokamak reactor. Hence, the designer is going to be faced with a very complex damage situation which will require data at not only various temperatures, stresses,

* We have chosen the tokamak, UWMAK-III, for this comparison.[24]

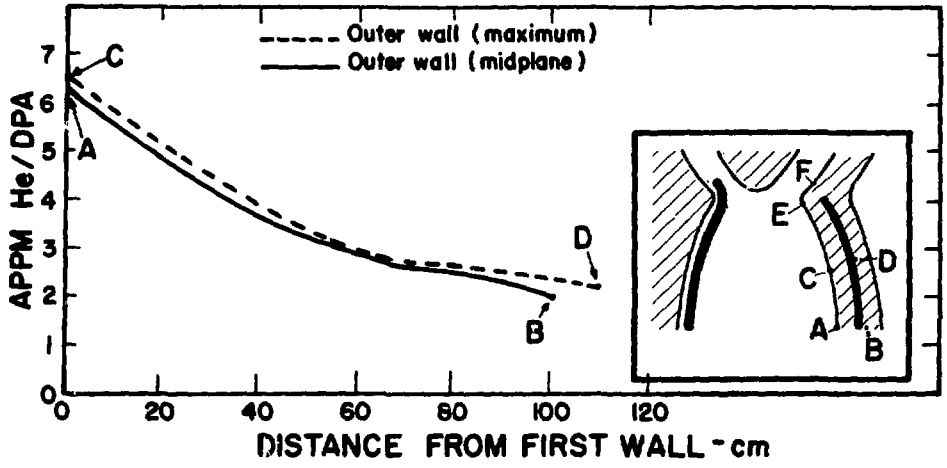

Fig. 8a - Variation in Helium Production to Displacement Ratio in UWMAK-III in the Radial Direction

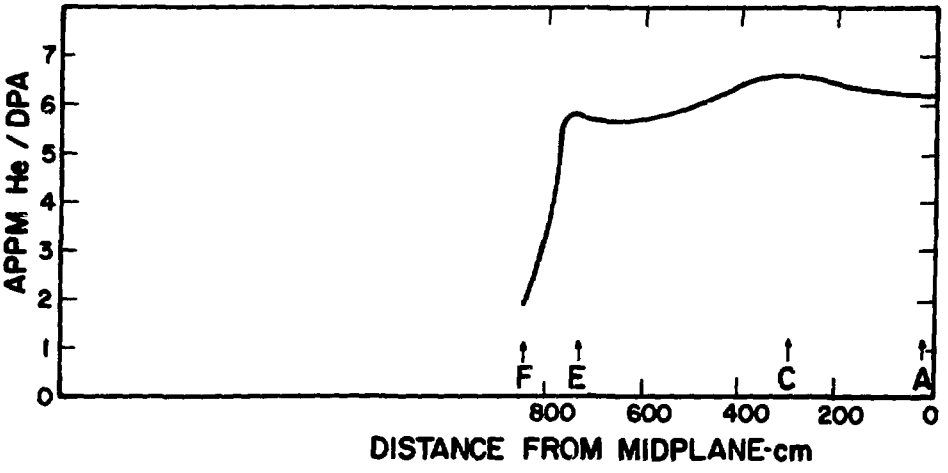

Fig. 8b - Variation in Helium Production to Displacement Ratio in the First Wall of UWMAK-III in the Poloidal Direction

Table 6

Effect of Absorbed Tritium on the Helium Production Rate in Fusion Reactors

System	appm He/yr Neutronic (a)	Typical Ave. Operating Temp. °C	appm He/yr from T_2 decay (b)	Total appm He/yr
Nb - 1st Wall	24	800	23	47
-20 cm from 1st Wall	10	800	23	33
Mo - 1st Wall	47	800	< 0.01	47
V - 1st Wall	57	600	11	68
-20 cm from 1st Wall	23	600	11	34
Al - 1st Wall	365	200	<<0.01	365
316 SS - 1st Wall	210	500-600	<0.1	210

(a) For typical neutron spectrum - UWMAK-I[16]

(b) Assuming wall absorbs the tritium to its solubility limit at the average operating temperature.

Table 7

Calculated Helium Gas to Dpa Ratio for Various Nuclear Systems

	appm He/dpa				
System	LWR (HFIR)	LMFBR (FFTF)	14 Mev Neutrons (RTNS)	D-Li (BNL) (a)	CTR (b) 1st Wall
Nb	0.073	0.033	5.4	2.5	3.3
V	0.009	0.004	9.7		4.9
Mo	0.012	0.05			5.8
Al	0.31	0.11	63		24
316SS	95 (c)	0.096	36		21

(a) BNL-20159, July 1975

(b) Ref. 24

(c) Ref. 21, after 1 year of irradiation

coolant environments, and damage levels, but at various ratios of gas atom production to displaced atoms. This will undoubtedly increase the cost of research and number of specimens that need to be examined before one can achieve the same level of confidence about a material's performance that we currently have about materials in fission reactors.

Solid Transmutation Effects

This is a very difficult area to treat in a limited discussion and the importance of such transmutations are just now being discovered. The calculation of the transmutation rates is a tedious procedure involving complex multiple reactions and decay chain considerations. However, Sung and Vogelsang[38] have devised a reasonable calculational procedure and we will quote a few of their results here.

Table 8 lists the largest transmutation rates of the host element to a different element in units of appm per year per MW/m^2, or amys for short. The major problem for Nb is the production of Zr at the rate of 700 amys. This element has a maximum solubility over the full operating temperature range of approximately 10% which could present problems if the neutron exposure exceeded 140 $MW\text{-}yrs/m^2$.

There are no serious problems with Mo except for perhaps Tc-99. The phase diagram for this system has not been established and should be investigated before any long term use of Mo is contemplated.

The generation of Si in Al could have serious consequence once the neutron exposure exceeded 2 $MW\text{-}yrs/m^2$. After that fluence, the Si would precipitate and could cause the aluminum to be brittle.

Finally, there does not appear to be any solubility problems for 316 SS but the generation of Mn, V and Ti might cause slight changes in the mechanical properties of the steel. The behaviour of this alloy is so complex that is is difficult to anticipate what effects such changes will have but experimental studies would not be difficult to perform on unirradiated 316 SS.

The synergistic effects of displacement damage, gas atom production and solid impurity atom generation need more careful study. Simple phase diagrams produced under equilibrium conditions may not be applicable to the irradiation state of a fusion reactor. If this is so, we had better know this well in advance of committing large sums of money to develop any particular metals industry (i.e. Nb or V) specifically for the production of fusion power.

SPECIFIC PROBLEMS ALREADY IDENTIFIED IN DT FUSION REACTOR DESIGNS

It will not be possible to discuss, in this paper, all of the problems related to bulk radiation damage that have been identified thus far. However, we will attempt to mention what we think are the most important problems and try to show how they may effect the normal operation of a fusion plant. It is convenient to discuss them in three separate groups; dimensional stability, mechanical properties and physical properties.

Dimensional Stability

As with most complex devices, close tolerances and high quality assurance will be required to assemble a fusion reactor. Once in operation it will be important that these dimensions are closely maintained for vacuum tightness and to prevent the generation of unreasonable stresses. Because of the sheer size of fusion devices (i.e. 1-2 square meters of surface area for every MW_e generated) even small percentage changes can result in large dimensional variations. In the UWMAK series of tokamak reactors, one finds that a 0.1% dimension change on the outer blanket structure can result in a 10 cm change in circumference. While the structure would have to be built to accomodate such strains (which might easily be imposed by thermal expansion) it is obvious that additional expansions or contractions, which may be a function of time, will be extremely difficult to predict, accomodate, and control.

Swelling Due to Voids

There is one major dimensional instability associated with metals when they are irradiated approximately 25-55% of their melting point. The generation vacancies at temperatures above which they are mobile and the preferential absorption of the associated interstitials at dislocations

produces a situation where the vacancies become highly supersaturated and tend to precipitate into voids. The metals then decrease in density with the net result that significant swelling can occur. Values up to 50% have been reported for steels. This phenomena is rather general as shown in Table 9 where we list some of the materials in which voids have been observed. Unfortunately, Table 9 includes all the potential CTR materials proposed for fusion applications so that one must prudently plan on some limited swelling if the irradiation temperature is high enough and if the damage level exceeds a few dpa. The exact magnitude of swelling to be expected may be found elsewhere from fission neutron studies[39,40] and in many papers of this conference. The basic questions for fusion reactor designers with regard to voids in metals are the following:

- What level of uniform swelling can be tolerated without compromising the vacuum integrity, or causing the flow of coolant to be reduced?
- What level of non-uniform (remember the dpa gradients) swelling can tolerated in a fusion blanket without compromising the safe operation of that reactor?
- What effect will high helium generation rates have on the data already obtained from fission reactor studies?
- What effect will lower (tokamak and mirror reactors) or higher (theta pinch, E beam, or laser reactors) dpa rates have on the nucleation and growth or voids (compared to fission reactors)?
- What effect will periodic "anneals" between burns have on the resulting microstructure?
- What effect will the solid transmutation products have in the formation of voids?

and finally,

- What effect will stress and/or the cyclic application of stress have on the resulting propensity to form voids?

None of the above questions have been satisfactorily solved or even addressed in some cases. Such gaps in our knowledge will be very costly and time consuming to fill.

Table 8

Major Chemical Changes in CTR Materials
Due to Transmutations

System	Tranmutation	$\frac{appm}{Yr\text{-}Mw/m^2}$	Approx. At. % Solubility at 0.4 Tm
Al	Mg	400	4
	Si	40	0.006
316SS	Mn	1200	60
	V	200	20
	Ti	50	~3
V	Cr	130	S. Soln
	Ti	80	70
Nb	Zr	700	10
Mo	Tc	400	?
	Ru	30	?

Table 9

Metals and Alloys in Which Neutron-Produced
Voids Have Been Observed After High
Temperature Irradiation

Pure Metals	Alloys
Al	2024-Al, 6061-Al,
Cu	
Fe	304, 316, 321, 347, 348 Stainless Steel
Ni	NiAl, Ni-Cu, Incoloy, Inconel
V	V-Ti, V-Cu-Ti
Nb	Nb-1Zr,
Mo	TZM, Mo-0.5 Ti
Ta	
W	
Pt	
Co	
Mg	

Swelling Due to Gas Bubbles

The generation of insoluble gases (in this particular case, He) inside of metals at high temperature has been known to promote bubble formation and dimensional changes associated with that phenomena. This is not too serious in most metals (except for perhaps steels and Al) because the amount of gas generated is relatively low. On the other hand, there are certain materials which have been proposed for non-structural applications in fusion devices which could have serious problems with bubbles. Some of these include, Be, B_4C, C, and Li compounds such as Li_2O, $LiAlO_2$, or $LiSiO_2$ for example. Table 10 lists the helium generation rate in these materials at different positions in a typical fusion blanket. The important points to note are the very high helium generation rates, several thousand to >15,000 appm per year at the first wall. The B_4C is unlikely to be that close to the first wall except in special "burner" designs so that values at approximately 100 cm are more appropriate Even at that spacing, several thousand ppm of helium would be generated per year of operation.

The effect of such high helium contents on the dimensional stability can be estimated as a function of bubble size and temperature from the following expression

$$\frac{\Delta V}{V_o} \% = 100\ N\ [\frac{rkT}{2\gamma} + b]$$

where N = number of gas atoms cm^{-3}
r = bubble radius
T = temperature
k = Boltzmann constant
γ = surface energy
b = Vander Waals constant

One can get an idea of how serious this problem might be by calculating the swelling in $LiAlO_2$ after one year of UWMAK-II exposure. Figure 9 shows that even if the gas atoms collect relatively few vacancies, swelling values of ~10% might be the characteristic after 1 year. Since $LiAlO_2$ is not a structural component but rather contained in cans, a

Table 10

Summary of Helium Production Rates in Non-Structural CTR Materials

Material	appm/year for 1 MW/m^2 Wall Loading[a]
Be	3050
C	2760
B_4C	3600[b]
$LiAlO_2$	15,500

(a) Use UWMAK-III Reactor, 100% P.F., maximum

(b) In Shield 100 cm from First Wall

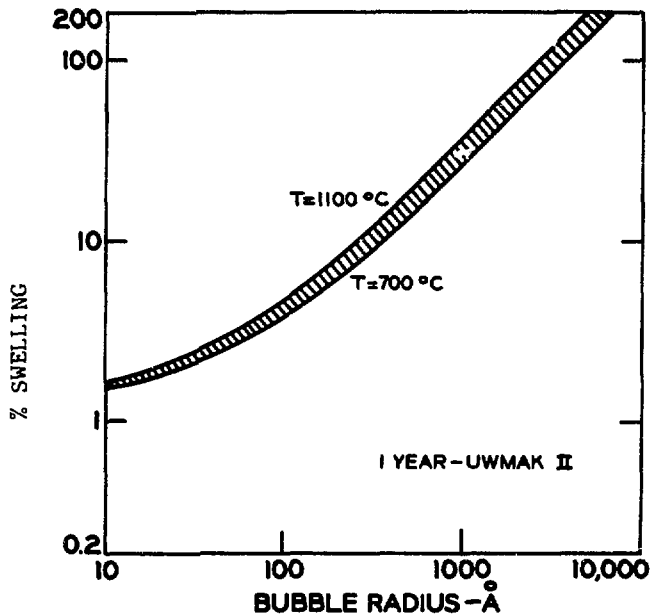

Fig. 9 - Calculated Effect of Bubble Size Temperature and Irradiation Time on the Helium Gas Induced Swelling in $LiAlO_2$

reasonable amount of dimensional instability can be tolerated. Values of 10% are not unreasonable but values of 50% may be out of the question. Such a consideration and the desire to achieve at least a one year life lifetime limits the maximum size bubble in the materials to:

	Calculated Bubble Diameter Limit for 1 year life and 50% swelling - Å
Be	10,000
B_4C	8,000
$LiAlO_2$	2,000

Previous studies in Be detected bubbles of up to 20,000 Å in dia. at 600°C and ~100 appm He.[41] Therefore, it appears that the use of Be, $LiAlO_2$ and perhaps carbon near the front walls of a D-T power reactor should be closely scrutinized. Even using B_4C closer than about 80 cm seems unadvisable above 700°C.

Dimension Change Due to Sintering

This effect would occur in CTR components which are formed by powder metallurgy techniques such as solid lithium compounds or B_4C. The main point here is that irradiation promoted sintering could initially reduce the available void space before gas bubble swelling takes place. A classic case of this phenomena is the sintering of ceramic UO_2 fuel pellets causing a shortening of the fuel column in a LWR and eventually allowing cladding collapse due to external pressures. Similar problems might arise in CTR's, especially if high pressure helium is used as a coolant.

The irradiation induced sintering also may obviate the low tritium inventory advantage that solid Li compound breeders appear to have. Because of the low diffusivity that tritium has in these compounds, they are fabricated with extremely small particle sizes (~tens of microns in diameter) to reduce the diffusion path (ℓ) the surface from where it can be

collected by a carrier gas. The design philosophy is evident from the following equation

$$\text{Tritium inventory} \propto \frac{\ell^2}{D(T)}$$

Due to the low thermal conductivity of Li ceramics the temperature profile in a breeding rod (or spherical particle) can be approximated by a parabola. (See Figure 10). When the temperature is high enough for T_2 diffusion, then there is also a tendency for sintering which increases the diffusion path. Hence, it is not clear how the inventory might change (increasing or decreasing) with temperature.

The major questions (aside from gas induced swelling) that materials scientists must answer with respect to solid breeders are:

- How does a large temperature gradient effect the overall tritium inventory?
- What effect will irradiation have on the sintering rate at high temperatures?

Other questions which need to be answered include,

- What happens in a pulsed reactor during the short, intense pulses, or - What sort of shock resistance is required to prevent fracturing?

Growth

With the increased use of carbon in D-T fusion reactors for (1) impurity control,[8] (2) radiation damage reduction,[43-45] (3) and neutron reflection, it is important to understand the nature of irradiation induced growth mechanism in that material. There have been several reviews on the effects of fission neutron irradiation on the dimensional stability of graphite[46-47] and even a few assessments of how this data might be translated to fusion reactors.[48-50] In general, neutron irradiation of carbon at elevated temperatures initially causes some shrinkage followed by expansion which eventually approaches a "run away" rate. Some typical data on nuclear grade graphite is shown in Figure 11. The purpose of calibrations, 1.4×10^{21} n/cm^2 (fission) is equal to 1 dpa. This figure shows that useful lifetimes

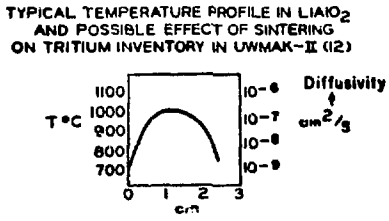

TRITIUM INVENTORY AT UNIFORM TEMPERATURE-g

AVERAGE PARTICLE RADIUS	800 °C	900 °C	1000 °C
10 μ	0.4	0.040	0.003
100 μ	40	4	0.3
1 mm	4000	400	30

Fig. 10 - Typical Temperature Profiles in $LiAlO_2$ and Possible Effect of Sintering on Tritium Inventory in UWMAK-II

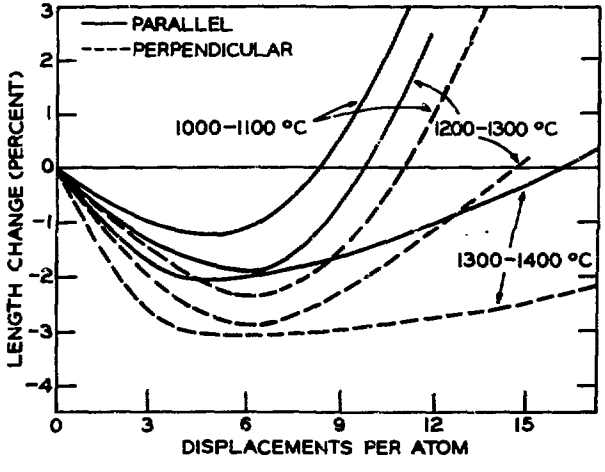

Fig. 11 - Effect of Molding Direction on Length Changes of 9640 Type Graphite

are typically 10-20 dpa at high temperatures (1000-1400°C).

Figure 12 shows the present status of experimental data from fission reactors. Also included in that figure are damage-temperature regimes that might be required for reflectors, plasma shields, or neutron spectral shifters. Note that current fission data (available from fission reactor graphite) is sufficient to almost cover the needs of the reflectors. However, only limited data is available for 1200-1400°C carbon curtain concepts (roughly 2 years of equivalent dpa levels) and there is no data available for the very high temperature ISSEC concepts.[43-45] Such information must be generated before these ideas can be implemented into real reactor designs. Intuitively, one might think that as the irradiation temperature is raised above 1300°C the increased annealing would reduce the residual damage. However, a recent paper by Van Den Berg et al.[51] suggests that such a trend may not be correct and in fact they are increasing damage rates up to 1400°C. These results are at odds with the data in Figure 11 and the bulk of previous studies on graphite. Therefore, careful research is needed to understand this mystery.

It should also be stressed that form of carbon used for fusion reactors may be considerably different that those tested for fusion reactor applications. Carbon cloths,[8] and three dimensional weaves,[8] and solid carbon walls[43-45,52] have all been proposed. The reactions of these forms of carbon to high temperature neutron irradiation may be considerably different than for fuel particle coatings (pyrocarbons), or anisotropic graphite extruded forms. A whole new irradiation program will be required to address these materials and methods (which are largely unknown now) must be found to correctly simulate CTR conditions until suitable CTR neutron test facilities can be built.

Mechanical Property Changes that Could be Important in CTR Materials

This is again one of those areas wich is extremely difficult to summarize in the limited space available here. To be complete one should cover irradiation effects on such properties as,

yield strength
ultimate strength
total elongation

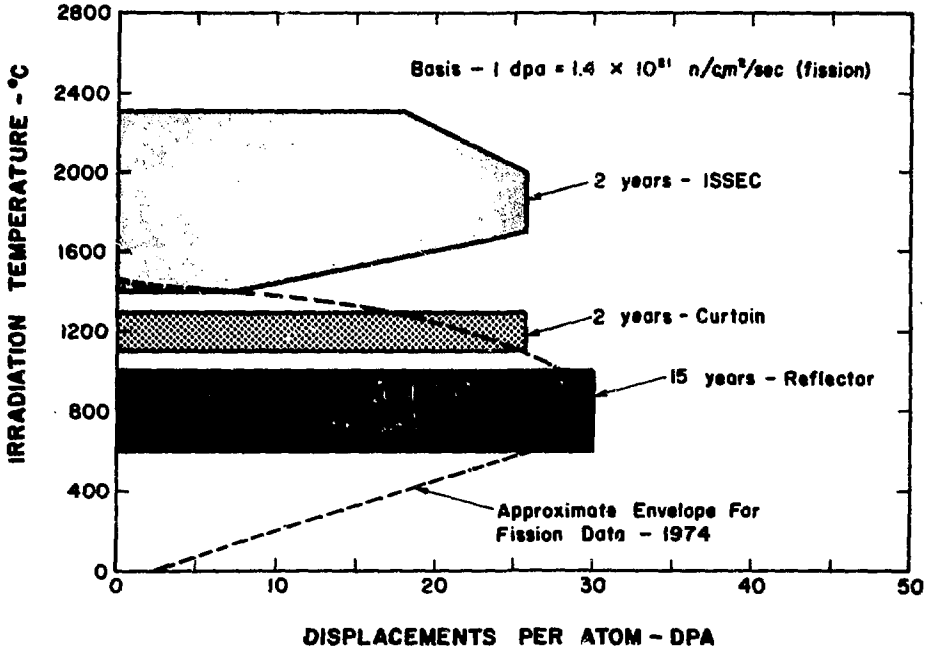

Fig. 12 - Comparison of Required Irradiation Data for Carbon in UWMAK-III to Data Available from Fission Reactors

uniform elongation
ductile to brittle transition temperatures
fracture toughness
creep
fatigue

While all of these properties are important, we will try to briefly relate uniform elongation, creep, and fatigue to the performance of a fusion reactor.

Ductility

It is absolutely essential that any massive structure such as a fusion reactor have the ability to absorb a certain amount of strain energy without plastic yielding or fracturing. This will be required to offset thermal expansion between burn cycles, finite amounts of non-uniform swelling, or simple fabrication defects. The fact that the reactor will be extremely radioactive and therefore inaccessible except for remote techniques and the high cost of having a whole power plant off the line because a single component failure means that the designers will need as big a "safety margin" as possible to keep the plant running. It is not easy to establish what that margin will be until a very detailed reactor design is available. However, we can take some lessons from the LMFBR program where it is determined that when the properties of the fuel cladding are degraded such that more than 0.4% strains will exceed the uniform elongation limit, then the component must be changed. It would be naive to simply assume the same limit applies to say a first wall of a fusion reactor which must maintain absolute vacuum tightness over a 1000 m^2 in the face of changing magnetic fields, temperatures, flow rates, damage rates, and environments. The probabilities for failure are greater and the time required to correct the fault will be longer in fusion reactors than that required to pull out a defected fuel element in a fission reactor. Intuitively, we would expect the design limit of a fusion reactor would be much more liberal than for a fission reactor, perhaps as high as 1% uniform elongation, but no one can say with certainty what it might be today.

There is only one metallic structural material for which we have

enough data to estimate what neutron irradiation at elevated temperature might do to the uniform elongation. That material is 316 SS. There is fast reactor data up to ~10 dpa (only a few appm He) at temperatures up to 650°C. This data is plotted in Figure 13. It can be seen from this information that operation up to ~20 dpa would result in U. E. values of ~0.5%. This is hard data (without the appropriate helium however) to show that the 1% limit would be reached in only a few years of 1 MW/m^2 exposure.

A very fine experiment has been conducted at ORNL to establish the effect of very high helium (~several thousand appm), high dpa (up to ~90) and high temperatures (up to 650°C) on the uniform elongation of 316 SS.[53] These results are displayed in Figure 13 also. Unfortunately, the data shows considerable scatter with some data points predicting 0.5% ductility at He levels of <50 appm He at 575°C and others showing the same or better ductility at ~90 dpa and 6000 appm He. Therefore, it is difficult to establish a definite wall life unless one were to use the most pessimistic data. Such an approach would yield 2-3 months life in a reactor like UWMAK-II. If one uses the 1% U. E. design limit, then the situation becomes much worse. In fact, it is quite possible that the wall life would be<2 years even with the optimistic data. Above 650°C there is essentially no ductility remaining after 90 dpa and 6000 appm.

The whole point of this exercise is to point out again that the high helium generation rate will probably place an upper temperature limit on the first wall life irregardless of the corrosion or straight creep behavior of the material. Secondly, it says that even for the only materia we have data on, the choice of design limit can only change an impossible situation (wall life <2 months) into a difficult one (wall life of only a few years) depending on the assumptions of tolerable ductility.

No such information on high helium contents exists for the other engineering materials (Al, Mo, Nb, V, etc.) because there is no correspondi quirk of nature such as the large thermal (n,α) cross section for Ni-59 in the other metals.[20] Therefore, we must again come up with, as to now, unkn techniques for testing these materials to provide a back up for the only

material on which we have some high helium content data. It is not a very comfortable position to be in and could require a great acceleration of the construction of D-T neutron source facilities in order to solve the problem.

Potential Creep Problems in D-T Fusion Reactors

As with any new energy source, fusion must demonstrate, among other things, that it can produce energy cheaper and with less environmental impact than fossil fuels and fission reactors. The desire for high efficiency normally means high temperatures and each new design of a fusion reactor pushes its structural material to the stress limit. It is well known that the combination of high temperatures (close to half the melting point) and high stresses will cause materials to plastically deform over long periods of time. It has also been recently demonstrated that a superposition of neutron irradiation can increase the deformation (creep) rate over the thermal values.[54] Hence, all three ingredients required for gross deformation are present in a fusion reactor blanket and we should expect that creep rupture lifes of candidate materials will have to be further lowered over their unirradiated values (Fig. 14).

Bloom and Wiffen[53] have found that creep rupture lives of 316 SS were reduced 50% compared to their non-irradiated values and there is no particular reason to expect that this would be different with the refractory metals. Therefore, if we want to have at least 2 year wall lifes (~17,000 hr) then stresses should be <10,000 psi in stainless steel. When appropriate safety factors are included (i.e. factors of ~2) then it is questionable whether a material like 316 stainless steel can withstand the thermally induced stresses in the first walls.

Even if the first walls and coolant pipes did not rupture, deformation of 0.5% may significantly complicate the maintenance procedures. For example, current reactor designs rely on periodic changing of the first walls due to radiation damage. This requires that modules can be easily removed and replaced remotely. A 0.5% shape deformation (e.g. 5 mm in a 1 meter long panel) may cause first wall panels to "stick" or make insertion of a new one an impossible job.

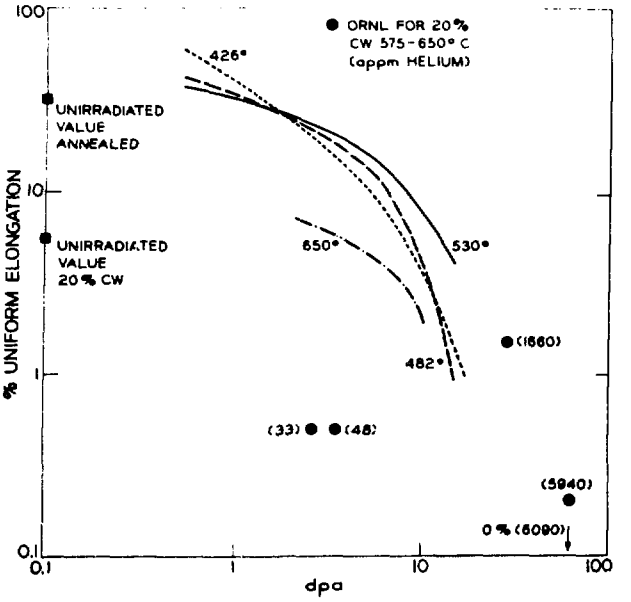

Fig. 13 - Effect of Neutron Damage on Uniform Elongation of 316 SS

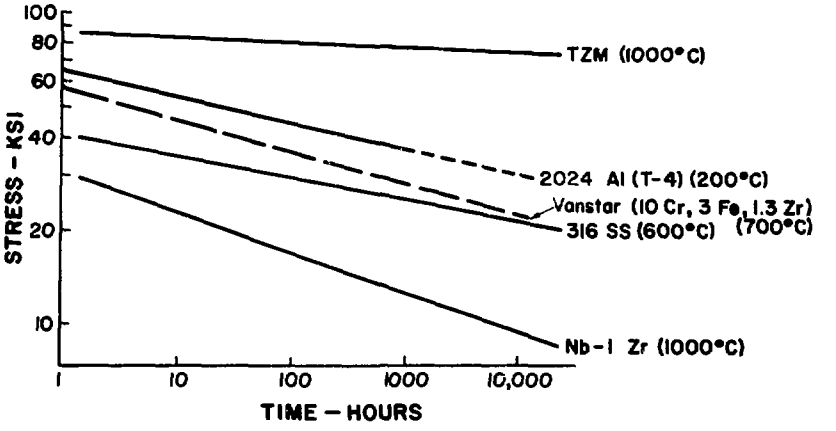

Fig. 14 - Rupture Properties of Various CTR Alloys

Since, at the present time, there is absolutely no irradiation creep data during 14 MeV neutron bombardment of any material, one must ask the following questions and set up research programs to answer these questions.

- What will be acceptable creep levels in tokamak, mirror, theta pinch E beam and laser reactors?
- What is the effect of dpa rate (from $\sim 10^{-7}$/sec steady state to $\sim 10^{-5}$ and 10^{-1}/sec instantaneously in pulsed systems) on the thermal creep rate in potential CTR metals and alloys?
- Will the high helium generation rate associated with fusion significantly reduce the creep rate in metals?
- What effect will solid transmutation products have on creep rates?
- How much of a safety factor ought one apply to creep-rupture lives (once they are determined) for fusion reactors materials where down times to replace failed components could be much longer and more expensive than in fission reactors?

One last comment on the generation of data to answer the above questions. It is relatively worthless to spend a great deal of money on post irradiation creep studies. Of all the critical mechanical properties, this one should be measured in-situ. Unfortunately, there are very few fission reactors where even one position in the core is instrumented to perform such tests. The costs of capsule design and associated equipment is also quite expensive such that the cost per data point is truly enormous. A successful irradiation creep study program needs first of all a realistic neutron source (there are none at this writing except for perhaps thermal neutron reactors for Ni containing alloys), secondly, large sums of research money (a million dollars for a capsule associated equipment and personnel for a few months of testing of one material is not unreasonable), thirdly, years of time are required to cover all the experimental conditions and materials. Such a program has not even begun as of 1975 and may represent a severe bottleneck to high power reactors (e.g. FERF or EPR) operation in 1985.

Fatigue, Perhaps the Achilles Heel of Pulsed Fusion Reactor Concepts

Fatigue, like creep is recognized by everyone as a potential problem for fusion reactors. Unfortunately, we know even less about the basic mechanisms of fatigue and the effect of irradiation on it than we do about creep, and there is even less data.

It is fairly clear where the fatigue problems stem from in tokamaks (5000-10,000 pulses per year), theta pinches (2-3 million pulses per year) or laser and E beam reactors (30-300 million pulses per year). These stresses and strains are inherent in the plasma physics of the concept and only the mirror has the potential for relatively steady state operation. Unfortunately, the quantitative stress and strain cycles for thes reactor concepts have not been clearly defined so a detailed analysis of this problem can not be made today.

Finally, the data for fatigue lives should come from in-situ tests or tests which closely resemble the operating conditions of particular reactor concepts. Such tests will again be costly, time consuming and difficult to simulate using non-fusion neutron sources. There is very little LMFBR or LWR data to build on here in contrast to the case for creep, ductility, void swelling, growth, etc. Theoretical background is almost completely lacking and standards for conducting and assessing irradiation fatigue tests are largely unknown. In short, there is a long way to go in this area and lack of success in it could prevent some fusion concepts from ever surpassing the proof of principle phase.

Some Physical Properties of CTR Materials that Depend on Radiation Damage

Most all of the physical (and thermal) properties of CTR materials will change somewhat because of 14 MeV neutron bombardment. However, only a few of them have been identified as significant (perhaps because only a few have been investigated with fission neutrons, let alone 14 MeV neutrons. We will make only a few comments here and fully expect that research in the next few years will uncover new problems and perhaps some solutions.

Electrical Resistivity

This property is mainly important for insulators and only of marginal importance for metals. A comprehensive review of the state of the art has been recently released [56] and concluded that (1) there is a general lack of data on in-situ resistivity changes for fission neutron bombardment and a complete lack of data for 14 MeV neutrons. (2) Isotropic crystal structures seem to be less susceptible to property degradation then highly anisotropic structures, (3) rate effects have not been established and (4) no information is available on the effects of high helium contents or generation of solid transmutation products.

Electrical insulators are absolutely necessary for theta pinch reactors to prevent excessive power loss in the first walls. Mirrors and tokamaks also will require insulators for neutral beam injectors or pellet injectors. It is not clear how much of a neutron exposure these insulators will experience because there may be a possibility of some shielding or placing line of sight insulators far back into the blanket where they would intercept a relatively small solid angle. There may be another insulator requirement for tokamaks if they use RF heating. Filling the wave guides with dielectrics can significantly reduce their size but such effects as high temperature gradients in thick insulator blocks remain to be investigated.[24]

The field of irradiation effects on dielectrics by high energy neutrons is not very well established or coordinated, certainly not at the level required for full fusion reactor development. Theories are essentially non-existant for the effects of helium (important because most insulators contains oxygen which has a high (n,α) cross section) on the dielectric strength. Lack of appropriate neutron sources and in-situ facilities greatly hamper a successful program in this area.

The electrical resistivity of metals is important in that one would not like to have large power dissipations in the first walls of tokamaks or theta pinches during the burn cycle. This is also true for the walls of waveguides in RF cavities. There is little high temperature-high

fluence resistivity data available from fission facilities and again, none from higher neutron facilities. Moteff et al.[57] have measured the post radiation resisitivty increase in Mo irradiated to 10^{22} n/cm^2 at temperature from 400-1200°C. It was found that at that exposure level, the irradiation induced resistivity increase was <1 micro-ohm-cm which is <3% of the electrical resistance due to thermal vibration at 1000°C. Hence, it appears that the production of voids and dislocation loops at these exposures does not cause an unmangeable resistance increase.

One word of caution before we leave this area, the electrical resistivity of metals at high temperature should be subject to transmutations and these are not adequately simulated by fission neutrons. Doping studies (in the absence of irradiation) may help understand these effects.

Radiation Damage to Superconducting Magnet Materials

This problem, which is peculiar to fusion, luckily is solvable by increased shielding in the case of tokamaks and mirrors. Of course, this means higher capital costs and adversely affects the economics of fusion power. Hence, a relatively straightforward compromise between damage to magnets and cost of increased shielding and larger magnets will have to be made in these reactors.

The radiation damage susceptibility of at least five materials will have to be examined for superconducting magnets as they are now envisioned:

Super insulation (e.g. mylar)
Structural material (e.g. austenitic steel or Al alloys
Stabilizer (e.g. Cu or Al)
Superconductor (e.g. NbTi or Nb_3Sn)
Electrical insulator (e.g. epoxy)

Previous analysis of these problems reveals that the super insulation and stabilizer are the most sensitive to radiation effects and A15 compounds like

Nb_3Sn follow closely behind. NbTi has a rather good resistance to property degradation as will be shown later.

The problem with organics such as mylar is that they become brittle and crumble. They could lose the ability to uniformly cover the cold magnets and hence result in larger refrigeration losses. Thresholds for observable effects are in the 10^7 Rad range and a 25% reduction in ductility occurs at 10^8 Rads.[58] A recent analysis[24] of a tokamak reactor shows that a 1.5 meter blanket 'leaks' $<10^6$ rads per year obviously leaving enough lifetime for even the most pessimistic designer.

The irradiation of pure metals at liquid helium temperatures has been known for some time to cause an increase in electrical resistance of these metals. Since the main function of a stabilizer in a magnet is to temporarily carry the current without significant heating in the event that a superconducting element goes normal, the increased resistance goes counter to that objective. The rates of resistivity increase for pure Al and pure copper have been determined by Horak and Blewitt [59] and are plotted in Figure 15. Note that it requires $\sim 10^{-4}$-10^{-5} dpa before the radiation damage resistance is of the same order of magnitude as the residual resistance due to impurities, imperfections and lattice vibrations at 4.2°K. Somewhat arbitrary design considerations might state that one should remove the damage (by annealing at a higher temperature) when the irradiation induced resistance exceeds the residual resistance by 10%. To relate that to real circumstances, we quote the following blanket and shield thicknesses, and the 80% plant factor dpa rates for the three most recent UWMAK reactor designs.

	Blanket and Shield Thickness-m	dpa/year at 80% P.F.	Time to Exceed ρ_0 by 10%-yr
UWMAK-I	150	5×10^{-5}	<1
UWMAK-II	190	$<10^{-6}$	<50
UWMAK-III	130	8×10^{-6}	3 (Al)

It is obvious that the damage rate in UWMAK-II is low enough so that there is no need for periodic annealing. Slight adjustments in the thickness of the stabilizer were enough to counter the higher resistivity in UWMAK-I.[16]

The next area to consider is the effect of neutron irradiation on the critical properties of superconductors. There are usually two types of

data that are reported in this regard. (1) Samples which have been irradiated at room temperature (or above) and then tested at liquid helium temperatures outside the reactor afterwards and (2) samples which have been irradiated at liquid helium temperatures and tested at the same temperature without intermittent warm-up to room temperature. Unfortunately, there is very little of the latter data and that which comes from the first situation is not always representative of the true damage state. Not only are there fewer defects remaining after the higher temperature irradiation, but the increased mobility at higher temperature will cause the defects to form clusters or loops which might not occur in the "real" case of irradiation at liquid helium temperature.

Two properties are of prime importance for superconductor in CTR magnets and those are the critical temperature (T_c) and the critical current density (J_c). The effects of fission neutron irradiation on the J_c of NbTi and Nb_3Sn are shown in Figure 16 as a function of displacement damage.[6] Considering the typical dpa rates* (appropriately adjusted for different atomic weights) one concluded that the J_c is changed by less than 10% for both alloys in typical fusion environments.

The effect of irradiation on the T_c of several alloys and compounds has been studied by Sweedler et al.[61] and is given in Figure 17.* For practically all the A15 compounds, a significant drop in the T_c occurs at 10^{-3} dpa. On the other hand, the NbTi is much more resistant to such degradation and should show no significant degradation until ~10^{-2} dpa (as ~1000 years of service in a UWMAK reactor).

In summary, appropriate blanket and shield design can reduce and even eliminate radiation damage as a major problem in CTR superconducting magnets. However, the price paid is the extra cost of materials and the larger magnet design. A special effort must be made to verify these trade offs in integral tests at liquid helium temperatures.

Side Effects of Transmutation in CTR Materials

The nuclear reactions that take place with potential CTR materials not only produce gas and impurity atoms, but they also produce considerable levels of radioactivity. This, in turn, causes high radiation fields

*For purposes of comparison 1 dpa ~3×10^{21} n/cm^2.

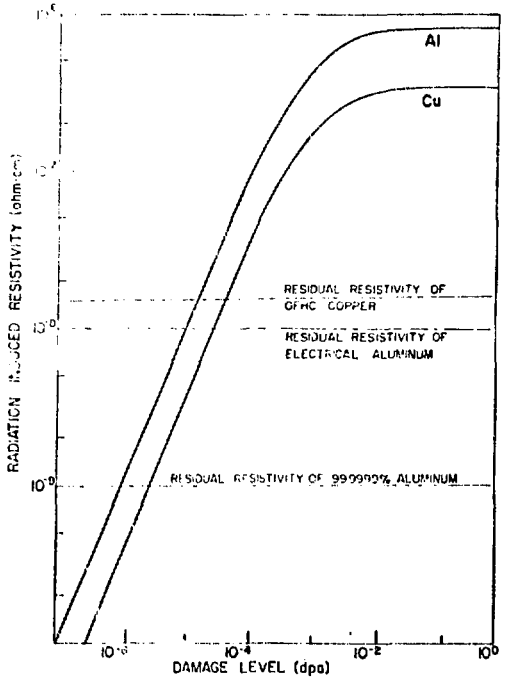

Fig. 15 - Radiation Induced Resistivity of Copper and Aluminum

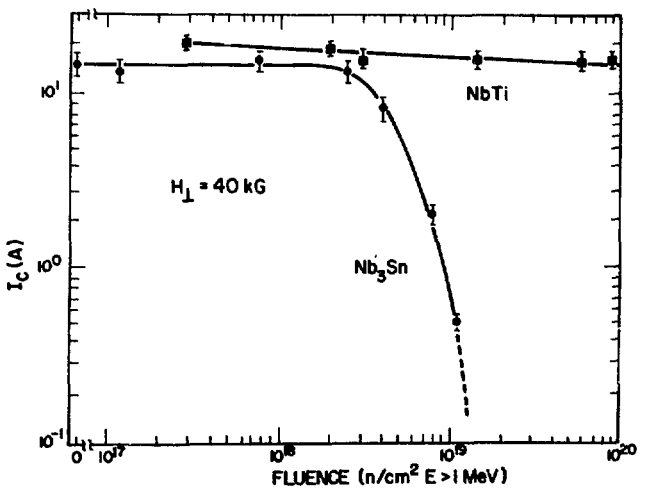

Fig. 16 - Effect of Neutron Irradiation on the Critical Current in NbTi and Nb_3Sn (60)

in the vicinity of the blanket, shield and magnets such that all normal repair and maintenance must be done remotely. The activity levels for typical CTR materials are given in Figure 18 and after two years of operation at 1 MW/m^2. The blanket configuration and total volume of material was constant in each case.[62] The first thing to note is that activities of approximately 1-5 curie/watt are typical of all materials at shutdown. Secondly, the decay of the radioactivity is fastest for the Al and V alloys, followed by Nb-Ti, TZM and 316 SS in that order. It appears that a significant amount of radioactivity will be removed a few days after shutdown such that radiation levels in Al and V systems might be "tolerable."* Unfortunately, this does not continue indefinitely and saturation occurs in some metal systems because of long lived isotopes. The major isotopes which contribute to the short and long lived activity of these metals are given in Tables 11 and 12 for reference. Contrary to popular opinion, the reader will see that there is a considerable amount of radioactivity associated with D-T fusion and society must get used to the fact that there will be some long lived isotopes which must be stored and protected from release long after fusion plants are closed.

The decay of this radioactivity causes a great deal of heat to be generated in the metal and an example of the levels associated with the radioactivity in Figure 18 are shown in Figure 19. Note that while the value is relatively high (~50 MW_t in a 5000 MW_t plant) the energy density is quite low (~0.1 $watt/cm^3$). Such low values do not present a hazard for melt down even if the coolant flow, or the coolant itself is lost.[63] This conclusion appears to be true for all currently suggested CTR materials

DISCUSSION OF THE IMPORTANCE OF NEUTRON RADIATION DAMAGE ON COMMERCIAL CTR POWER PLANTS

The degradation of materials properties by neutrons results in at least the six following major effects:

---

* This merely means that with appropriate shielding and weeks of decay, one might be able to approach the reactor to perform simple hand operations on the defected components.

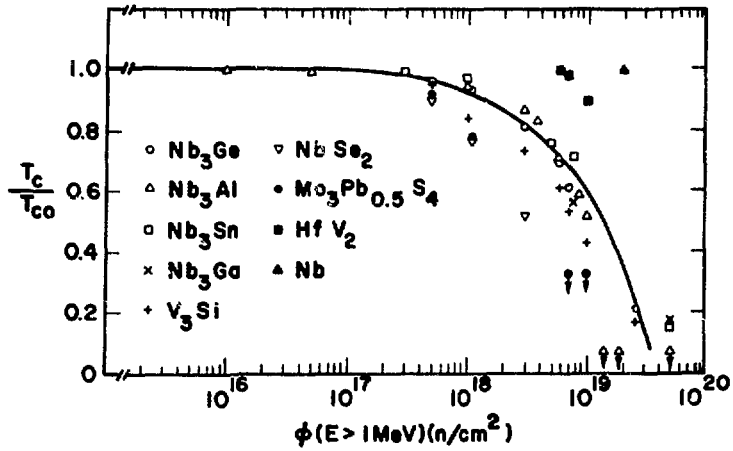

Fig. 17 - Effect of Ambient Temperature Irradiation on the Critical Temperature of Various A15 Compounds

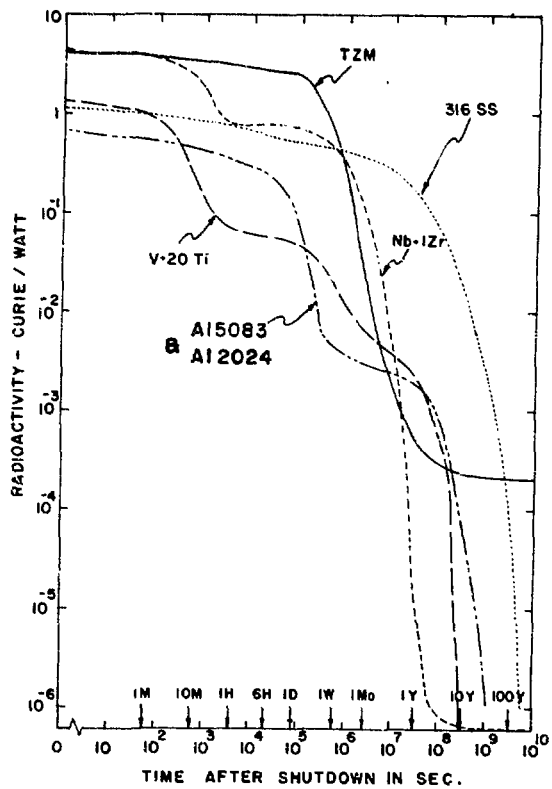

Fig. 18 - Radioactivity Induced in a CTR Blanket - 2 Year Operation - 5000 MW_t

Table 11

Summary of Major Isotopes Contributing to the Radioactivity of Potential CTR Alloys at Shutdown After 2 Years of Operation

Alloy System	Radioactive Isotope	Half-Life	Radioactivity at Shutdown (Ci/watt)
2024 Al	Na 24	15 h	.180
	Mg 27	9.5 m	.145
	Cu 64	12.8 h	.137
	Al 28	2.3 m	.0953
TZM	Mo 99/Tc 99^m	66.7 h/6 h	1.512
	Mo 101/Tc 101	14.6 m/14 m	0.441
	Mo 91	15.5 m	0.0656
	Nb 92^m	10 d	0.0213
Nb-1Zr	Nb 94^m	6.3 m	4.408
	Nb 92^m	10 d	0.720
	Nb 95	35 d	0.0168
	Y 90	64 h	0.0117
V-20 Ti	Sc 48	1.8 d	0.039
	Ti-51	6 m	0.080
	Sc-47	3.4 d	0.009
	V 52	3.8 m	1.025
316 S.S.	Mn 56	2.6 h	0.353
	Fe 55	2.6 y	0.197
	Cr 51	28 d	0.100
	Co 58	71 d	0.091

Table 12

Major Long Lived Radioisotopes in CTR Materials — 2 Yr. Operation

Major Long Lived Radioisotopes in Potential CTR Materials - 2 yr. Operation

System	Isotope	Half Life-yr.	Ci/watt at 100 yr.	BHP[(a)] at 100 yr. km^3 air/MW_e
Al-2024	Al-26	735,000	7.4×10^{-8}	0.73
316 SS	Co-60	5.2	9×10^{-9}	0.02
	Ni-63	92	1.7×10^{-5}	8.3
	Mo-93	10,000	4.2×10^{-6}	42
V-20Ti	None	----	----	----
Nb-1Zr	Sr-90	28	3×10^{-9}	0.099
	Nb-94	20,000	6×10^{-7}	0.29
TZM	Mo-93	10,000	2.1×10^{-4}	2100

(a) BHP = Biological Hazard Potential, Ci/watt divided by the maximum permissible concentration.

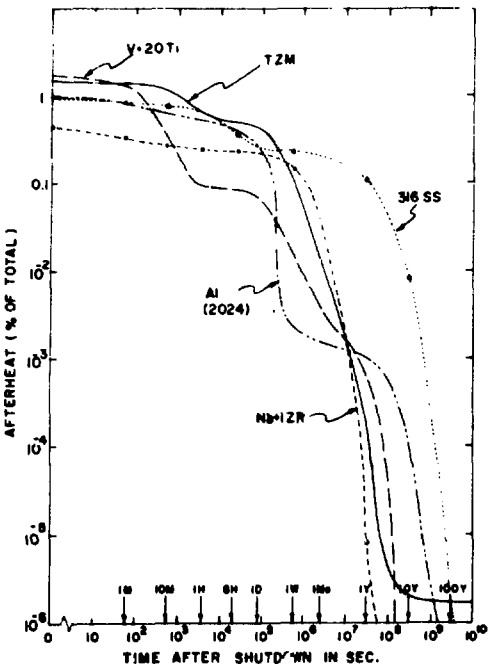

Fig. 19 - Afterheat in Potential CTR Structural Materials - 2 Year Operation - 5000 MW_t

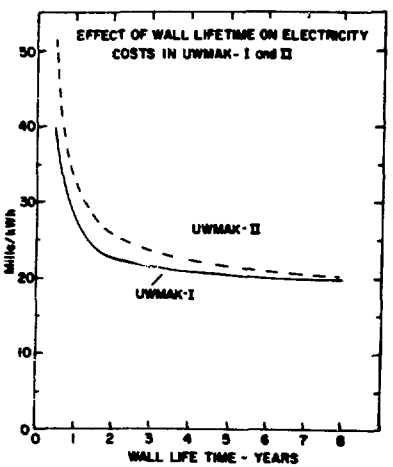

Fig. 20 - Effect of Wall Lifetime on Electricity Costs in UWMAK-I and II

(1) Reduced Efficiency - The generation of helium gas tends to reduce the maximum temperature that CTR structural, breeder and neutron multiplier materials can operate at for long periods of time. This in turn reduces allowable coolant temperatures which in turn will lower the overall plant efficiency.

(2) Reduced Plant Factors - The fact that certain components of the reactor will have to be replaced before the full lifetime of the plant is reached means that costly shutdowns must occur. The exact down time is a function of many complex considerations but some perspective on the costs can be obtained if one remembers that the revenue from a 2000 MW_e plant is approximately $1,000,000 per day at 20 mills per kw-hr. Estimates for some reactor designs predict approximately 30 days per year may be lost due to radiation damage and changing the first walls costs approximately 30 million dollars per year per 2000 MW_e plant in down time alone [64].

(3) Increased Capital Costs - Spare modules need to be purchased at the start of the plant to replace those involved in the first change out (thereafter the costs are included in operating costs). Increased remote handling equipment will be necessary to minimize the time involved in plant shutdown. Added hot cell facilities may also be required. Shielding requirements for gamma rays emitted from damaged components (or good ones for that matter) will also increase the overall plant costs. Waste storage facilities will have to be expanded beyond those required for components which fail for "conventional" reasons such as corrosion, machining faults, etc.

(4) Increased Operating Costs - Items 1, 2, and 3 combine with other costs to raise the cost of electricity as measured in mills per kw-hr. A rough idea of the sensitivity of this number to first wall lifetime is shown in Figure 20 [64] This analysis, which is detailed elsewhere for UWMAK-I and II, reveals that if the first wall lifetime gets to be less than 2 years (at a nominal wall loading of 1.2 MW/m^2) the average cost of electricity rises dramatically. It also shows that the increased cost of lowering the wall life from 8 to 4 MW/m^2 is only approximately 10% of the total.

(5) Increases the Volume of Radioactive Waste Which Must Be Processed and Stored - Most of the major reactor studies to date have made some assumptions about the first wall lifetime. These are listed in Table 13 along with the metal system and the amount of material that needs to be replaced per MW_e per year. This number is surprisingly constant considering the variation in design group, materials, and reactor power level. A reasonable average is approximately 0.4 metric tonnes/MW_e/year. If we ever do get into a large scale fusion reactor economy, such as 10^6 MW_e by 2020,[65] then this means that approximately 400,000 metric tonnes of radioactive waste would be generated per year. Clearly such a number represents a potential problem in waste management.

(6) Demand on Scarce Elements - When components become defective and radioactive at the same time, it is usually more economical to compact, process then store them until the radioactive decays to safe levels than try to refabricate them. However, we see from Figure 18 that the decay times can take hundreds, if not thousands of years. Hence, for all intents and purposes, the replacement of these components will have to come from new elements. The disposal of say 400,000 metric tonnes per year of 316 SS means that approximately 70,000 metric tonnes of Cr must be supplied per year along with appropriate amounts of Mn and Ni. In some cases, e.g. Be, there may be no choice but to reprocess the radioactive and contaminated metal because world reserves are not adequate for a "throw away" economy.

Even if all the components had the same life as the reactor, there would be the problem of what does one do with the radioactive structure when the plant becomes obsolete and a new one must be built. The blanket, shield, magnets, supports, and all equipment within 3 meters of the plasma will be too radioactive to dispose of in a conventional manner. These masses typically amount to approximately 50 metric tonnes/MW_e and will also place a severe our limited resources as the second, third, fourth, etc. generation plants are phased out in the 21st century.

Table 13

Summary of Radioactive Waste Amounts for Various CTR Reactor Designs

Reactor	System	Predicted Wall Life MW-yr/m^2	Material Replacement Metric Tonne/MW_e-yr
UWMAK-I	316SS	2.5	0.69
UWMAK-II	316SS	2.3	0.49
UWMAK-III	TZM	3.4	0.31
ORNL	Nb-1Zr	>10	0.41
BNL	Al	3.8	0.27
LASL-ANL	Nb-1Zr	10	0.33

FINAL REMARKS

This has been a rather broad look at the neutron damage problems currently envisaged for D-T reactors. Not all the problems have been discussed and indeed a whole class of conditions for fission-fusion concepts has been left out. However, it is hoped that the reader will begin to appreciate the concern of the materials science community over the growing list of problems to be solved. There will undoubtedly be more problems identified in the future. We must therefore reluctantly conclude that next to the plasma physics problems, radiation damage is the second most serious obstacle to the commercialization of fusion power.

Acknowledgment

The author wishes to thank Y. Gohar, T. Sung, H. Avci, and E. Ramer for their assistence in collecting data for this paper. Research has been partially supported by the Energy Research and Development Administration and the Wisconsin Electric Utilities Research Foundation.

REFERENCES

1. Proceedings of the First Topical Meeting on the Technology of Controlled Nuclear Fusion, CONF-740402-Vol. I & II, USAEC, 1974.

2. Proceedings of the Conference on Surface Effects in Controlled Thermonuclear Fusion Devices and Reactors, Ed. H. Wiedersich, M. S. Kaminsky and K. M. Zwilsky, J. Nucl. Mater., 53, 1974.

3. Proceedings of the International Conference on Surface Effects in Controlled Fusion Devices, San Francisco, Feb. 1975. To be published.

4. International Conference on Nuclear Solutions to World Energy Problems, Washington, D.C., Nov. 1972, ANS, Hinsdale, Illinois, 1973. See papers by R. Hancox, p. 209, R. L. Hirsch, p. 216, F. L. Ribe, p. 226, G. L. Kulcinski, p. 240 and A. P. Fraas, p. 261.

5. "Fusion Reactor Design Problems", Proceedings of an IAEA Workshop, Culham, United Kingdom, Jan.-Feb. 1974, Special Supplement of Nuclear Fusion, 1974.

6. G. L. Kulcinski, p. 251 in Volume II of "Plasma Physics and Controlled Nuclear Fusion Research, 1974", Proceedings of the 5th Int. Conf. on Plasma Physics and Controlled Nuclear Fusion, Tokyo, Japan, Nov. 1974. IAEA, Vienna, 1975.

7. D. Meade, Nuclear Fusion, 14, 289, 1974.

8. G. L. Kulcinski, R. W. Conn and G. Lang, Nuclear Fusion, 15, 327, 1975.

9. J. E. Scharer, R. W. Conn and D. T. Blackfield, UWFDM-148, Univ. of Wisconsin Report, 1976.

10. J. M. Bunch, F. W. Clinard, D. J. Dudziak, W. V. Green and R. A. Krakowski, p. 189 in the Fifth Symp. on Eng'r. Problems of Fusion Research, Princeton, N. J., 1973. IEEE Pub. No. 73CH0843-3-NPS, 1974.

11. J. R. Powell et. al., BNL-18236, 1973.

12. B. Badger, R. W. Conn, G. L. Kulcinski, M. A. Abdou, R. Aronstein, H. I. Avci, R. W. Boom, T. E. Cheng, J. Davis, J. M. Donhowe, G. A. Emmert, Y. Eyssa, N. M. Ghoniem, S. Ghose, W. Houlberg, J. Kesner, W. Lue, C. W. Maynard, A. Mense, N. Mohan, H. A. Peterson, T. Y. Sung, I. Sviatoslavsky, D. K. Sze, W. F. Vogelsang, R. Westerman, L. J. Wittenberg, T. F. Yang, J. Young and W. D. Young, "UWMAK-II, A Conceptual Tokamak Reactor Design", Nuclear Engineering Department Report UWFDM-112, October 1975. (The University of Wisconsin Madison).

13. E. N. Cameron, Trans. Amer. Nucl. Soc., 22, p. 56, 1975.

14. For Example see Review Paper by B. R. Leonard, Jr., Nucl. Tech., 20, p. 161, Dec. 1973 or DCTR Fusion-Fission Energy Systems Review Meeting, ERDA, 4, 1974.

15. Neutron Spectra from EBR-II Reactor. Obtain from HEDL Dosimetry Center. Row 2, core center.

16. Spectrum from UWMAK-I Reactor given in UWFDM 68, Vol. 1, 1974.

17. R. Booth and H. H. Barschall, Nucl. Inst. Meth., 99, 1, 1972.

18. C. M. Logan, J. D. Anderson, H. H. Barschall and J. C. Davis, To Be Published.

19. F. B. K. Kam and J. H. Swanke, ORNL-TM-3322, March 1971.

20. J. Weitman, N. Daverhog and S. Farvolden, Trans. Am. Nucl. Soc., 13, 557, 1970 and G. J. Kirouac, Nucl. Sci. Eng'r, 46, 427, 1971.

21. G. L. Kulcinski, M. Abdou and D. G. Doran, Properties of Reactor Structural Alloys After Neutron or Particle Irradiation, STP-570, 1975.

22. T. A. Gabriel, J. D. Amburgey and N. M. Greene, Trans. Amer. Nucl. Soc., 21, 67, 1975.

23. W. G. Price, Jr. and D. L. Chapin, MATT-1102, Jan. 1975.

24. B. Badger, R. W. Conn, G. L. Kulcinski, C. W. Maynard, R. Aronstein, H. I. Avci, D. Blackfield, R. Boom, A. Bowles, E. Cameron, E. T. Cheng, R. Clemmer, S. Dalhed, J. Davis, G. A. Emmert, N. M. Ghoniem, S. Ghose, Y. Gohar, J. Kesner, S. Kuo, E. Larsen, E. Ramer, J. Scharer, R. E. Schmunk, T. Y. Sung, I. Sviatoslavsky, D. K. Sze, W. F. Vogelsang, T. F. Yang and W. D. Young, "UWMAK-III, A High Performance, Noncircular Tokamak Power Reactor Design", Nuclear Engineering Department Report UWFDM-150, December 1975. (The University of Wisconsin, Madison).

25. Y. Gohar, To Be Published.

26. D. G. Doran, Nucl. Sci. Eng'r., 49, 130, 1972.

27. D. M. Parkin, To Be Published.

28. J. D. Jenkins, Nucl. Sci. Eng'r., 41, 155, 1970.

29. Y. H. Choi, A. C. Bement and K. C. Russell, To Be Published This Conference.

30. N. M. Ghoniem and G. L. Kulcinski, To Be Published.

31. J. O. Schiffgens and R. L. Simons, This Conference.

32. D. J. Dudziak and R. A. Krakowski, Nucl. Tech., 25, 32, 1975.

33. W. F. Vogelsang, G. L. Kulcinski, R. G. Lott and T. K. Sung, Nucl. Tech., 22, 379, 1974.

34. F. W. Wiffen and E. E. Bloom, ORNL-TM-4541, May 1974.

35. M. T. Sundquist, To Be Published.

36. H. Wiedersich, Unpublished Results.

37. Accelerator Based Neutron Generator, BNL-20159, July 1975.

38. T. K. Sung and W. F. Vogelsang, To Be Published.

39. Radiation Induced Voids in Metals, ed. by J. W. Corbett and L. C. Ianniello, AEC Symposium Series-26, 1972.

40. D. I. R. Norris, Radiation Effects, 14, 1, 1972 and ibid 15, 1, 1972.

41. B. S. Hickman, p. 72 in Studies in Radiation Effects , Vol. 1, Gordon and Breach, New York, ed. G. J. Dienes, 1966.

42. W. H. Culbert, Nucl. Safety, 14, 4, 356, 1973.

43. R. W. Conn, G. L. Kulcinski, H. Avci and M. El-Maghrabi, Nucl. Tech., 26, 125, 1975.

44. G. L. Kulcinski, R. W. Conn, H. I. Avci and D. K. Sze, UWFDM-127, 1975. See also Trans. Am. Nucl. Soc. 21, 50, 1975.

45. H. I. Avci and G. L. Kulcinski, This Conference.

46. G. B. Engle and W. P. Eatherly, High Temperatures-High Pressures, 4, 119, 1972.

47. J. H. Cox and J. W. Helm, Carbon, 7, 319, 1969.

48. W. J. Gray and W. C. Morgan, BNWL-B-288, June 1973.

49. W. J. Gray and W. C. Morgan, BNWL-B-289, June 1973.

50. W. J. Gray, To Be Published.

51. M. Van Den Berg, M. R. Everett and A. Kingsbury, Twelfth Biennial Conf. on Carbon, Pittsburg, July 1975.

52. J. R. Powell, O. W. Lazareth and P. Tichler, Trans. Amer. Nucl. Soc., 21, 50, 1975.

53. E. E. Bloom and F. W. Wiffen, ORNL-TM-4861, May 1975.

54. J. P. Foster, W. G. Wolfer, A. Biancheria and A. Boltax, Proc. Europ. Conf. on Irrad. Embrittlement and Creep in Fuel Cladding and Core Components, London, Nov. 1972, p. 273.

55. Fusion Power by Magnetic Confinement, WASH-1290, Feb. 1974.

56. A. A. Bauer and J. L. Bates, BMI-1930, 1975.

57. J. Moteff, To Be Published.

58. R. P. Reed, R. E. Schramm and A. F. Clark, Cryogenics, 13, 67, 1973.

59. J. A. Horak and T. H. Blewitt, Phys. Stat. Sol., 9, 721, 1972.

60. D. M. Parkin and D. G. Schweitzer, Proc. Conf. Appl. Superconductivity, 495, 1972.

61. A. R. Sweedler, C. L. Snead, L. Newkirk, F. Valencia, T. H. Geballe, R. H. Schwall, B. T. Matthias and E. Corenswit, This Conference.

62. T. K. Sung, Unpublished Results.

63. D. K. Sze, p. 599 in Reference 1.

64. G. L. Kulcinski and J. R. Young, UWFDM-140, Oct. 1975. Also, this conference.

65. G. L. Kulcinski, Energy Policy, 2, No. 2, p. 104, June 1974.

ION BOMBARDMENT SIMULATION: A REVIEW RELATED TO FUSION RADIATION DAMAGE

J. L. Brimhall
Battelle-Pacific Northwest Laboratories
Richland, Washington 99352

ABSTRACT

Prime emphasis is given to reviewing the ion bombardment data on the refractory metals molybdenum, niobium and vanadium which have been proposed for use in advanced fusion devices. The temperature and dose dependence of the void parameters are correlated among these metals. The effect of helium and hydrogen gas on the void parameters is also included. The similarities and differences of the response of these materials to high dose, high temperature radiation damage are evaluated. Comparisons are made with results obtained from stainless steel and nickel base alloys. The ion bombardment data is then compared and correlated, as far as possible, with existing neutron data on the refractory metals. The theoretically calculated damage state produced by neutrons and ions is also briefly discussed and compared to experimental data wherever possible. The advantages and limitations of ion simulation in relation to fusion radiation damage are finally summarized.

INTRODUCTION

The simulation of neutron damage by heavy ion bombardment has been used extensively in the past five years. Several excellent review articles have been written and the reader is referred to thse for details of the general technique[1,2]. The overriding justification for heavy ion bombardment studies is the ability to observe the microstructural damage after very intense particle bombardment in a rapid, direct and inexpensive manner. The swelling induced by void formation has been the major item of interest. Most work has been directed to the Fe-Cr-Ni alloy system but there has also been a number of studies in the refractory metals Mo, Nb,

and V. The latter have been mentioned as possible first wall materials for advanced fusion reactors. These studies on the refractory metals have proved valuable because of the lack of neutron data in the high fluence range. The purpose of this paper is to bring up to date the status of void swelling in refractory metals due to ion bombardment. Only brief mention will be made of the technique and some of the unresolved questions about ion bombardment. The correlation of the primary damage state between heavy ions, neutrons, and other types of particles will be discussed. Prime emphasis will be given to reviewing the experimental data on refractory metals, correlating the ion data and showing neutron correlations where possible. The relevance of the work to the CTR program and the direction of future work are finally summarized.

ION BOMBARDMENT

General Theory and Technique

The first step in determining the lattice damage from heavy ions is to calculate the energy loss due to interaction with the lattice atoms. The work of Lindhard and co-workers has been extensively used to calculate this energy loss[3], which is divided into electronic and nuclear components. Only nuclear interactions are assumed to produce displaced atoms. There have been several computer codes written to calculate the energy expended in atomic displacements[4,5]. The results for 5 MeV Ni^{++} ions in Mo computed from one of these codes (EDEP-1) is shown in Fig. 1[4]. This code also considers the energy transfers from the primary knock-on atoms (PKO) which do not result in further displaced atoms. The energy represented in Fig. 1 is, therefore, a true damage energy, i.e., that energy which results in displaced atoms. A recommended relationship is[6]:

$$N_D = \frac{.8T_D}{2E_D} \cdot N_I \ , \qquad (1)$$

where T_D is damage energy from Fig. 1, E_D is the effective threshold energy, N_I is the ion dose, and N_D is the number of displaced atoms per cubic centimeter. The number of displaced atoms/atom (dpa) in molybdenum produced by a fluence of 3×10^{16} ions/cm^2 of 5 MeV Ni^{++} ions is shown in Fig. 2.

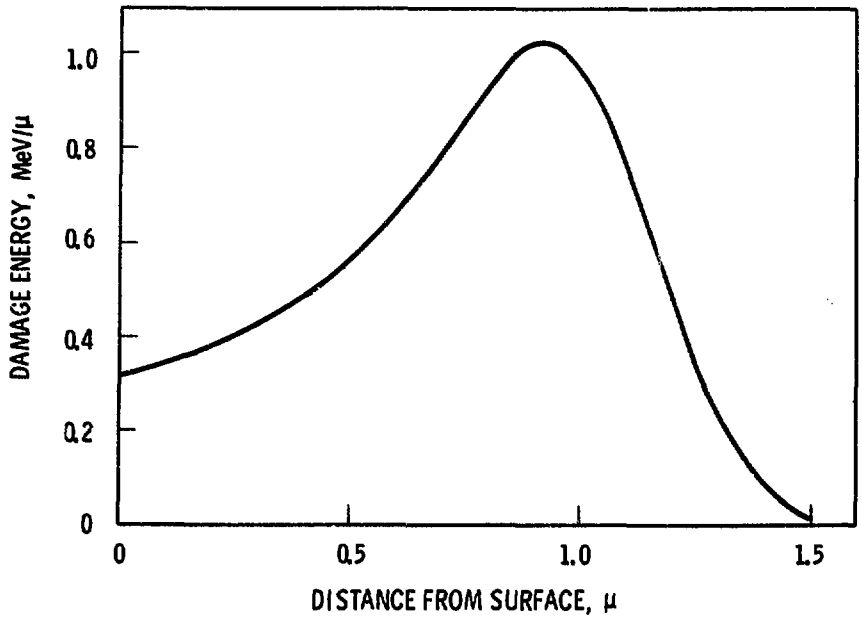

Fig. 1. Damage Energy vs. Depth for 5 MeV Ni^{++} Ions on Molybdenum.

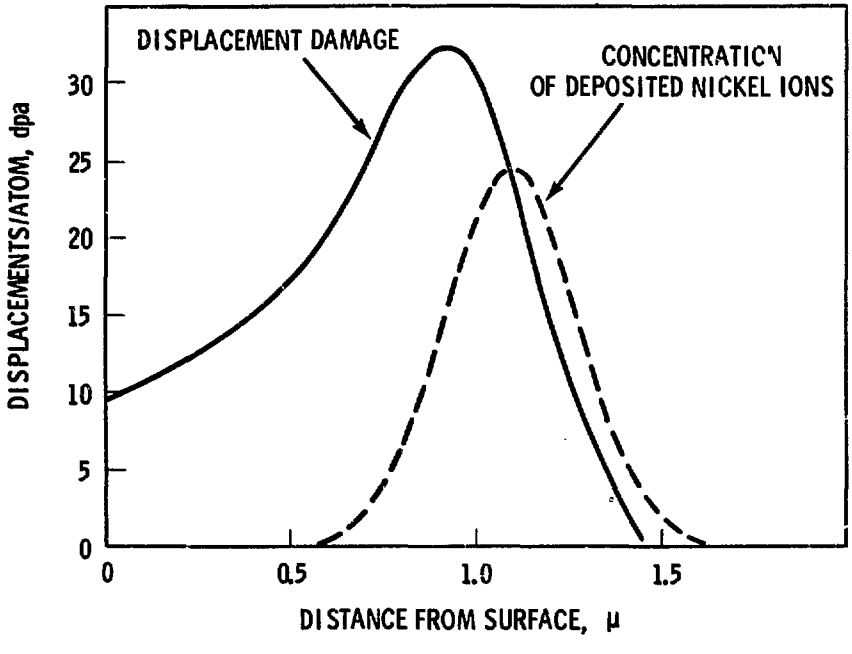

Fig. 2. Displacement Damage and Ion Concentration vs. Depth. 5 MeV Ni^{++} Ions on Molybdenum. 3×10^{16} ions/cm^2.

The curve in Fig. 2 illustrates the very small irradiation volume that one must work with in heavy ion bombardment studies. However, sophisticated techniques have been developed to extract transmission electron microscopy (TEM) specimens from the bombarded region (7-10). The location of the bombarded region as determined by the depth from the bombarded surface can be measured with an accuracy of ±500 Å. The entire damage range can also be observed by high voltage electron microscopy (HVEM) and the distribution of the damage analyzed.

Swelling due to ion bombardment has also been determined by measuring the step heights at the edge of a masked off area of the specimen surface[11] This technique and TEM are the only techniques used so far to study ion damage. Techniques utilizing x-ray analysis may become useful as the specimen preparation procedures become more sophisticated.

Problems of Heavy Ion Bombardment

Before discussing experimental results, the unique factors and problems associated with heavy ion bombardment should be mentioned. There are inherent problems which must be faced and the influence of these factors on the interpretation of the damage state must be well understood.

The extremely high dose rate used in ion bombardment is the principal advantage of the technique, but it also produces considerable difficulty in the correlation with neutron bombardment. The high dose rate produces a high supersaturation of vacancies. These supersaturations are typical of those found at lower temperatures in materials bombarded at a lower dose rate, e.g. neutron irradiation. For this reason, a "temperature shift" must be used when comparing ion bombardment results with neutron irradiation results. Some analytic expressions have been developed to calculate this temperature shift[12,13]. Sprague et al., have shown experimentally that the temperature shift is complex and it depends on whether nucleation or growth of voids is the controlling mechanism[14]. Much more experimental work is necessary to fully elucidate the precise nature of the temperature shift and the role played by all of the different parameters.

As a result of this temperature shift metallurgical changes may occur in the material at the higher ion bombardment temperature which would not

occur at the lower neutron irradiation temperature. This is particularly true in alloys in which new precipitates may dissolve at the higher temperatures. The resulting microstructural changes can affect the swelling in a manner which is not representative of neutron irradiation. This particular problem may limit the temperature range of ion bombardment studies for the certain alloys. The much shorter time at the ion bombardment temperature somewhat compensates for the higher temperature.

The possibility of a strong influence of the free surface as a point defect sink in ion bombardment studies has long been acknowledged. However, the experimental results have not shown significant defect depletion near the surface when high dose rates are used and the region observed is not directly at the surface[15,16]. Recent studies on molybdenum have shown no surface effect on microstructure in the temperature range 900-1000°C when the dose rate was greater than 1×10^{-3} dpa/sec [17]. In general, this type of surface effect will be greatest at low dose rates and high temperatures.

Other effects related to the free surface are solute segregation and stress. In alloys, radiation induced solute segregation to void and external surfaces has been observed[18]. The stress effect arises because the unswollen part of the specimen will impart a restraining force on the bombarded section as it swells. Both of these effects are potentially very important problems in particle irradiation studies.

The bombarding ion itself presents two problems in ion simulation experiments. The first is the nature of the primary knock-on spectrum produced by the ions. Very light ions will produce a considerably different PKA spectrum than heavy ions. Experimental results comparing carbon ion and nickel ion damage has shown measurable differences[16,19]. These differences were attributed to the difference in the primary knock-on spectrum produced by the two types of ions.

The second ion effect is a chemical effect due to the deposition of a foreign ion in the lattice. Many experimenters observe the structure at a depth corresponding to the peak of the damage curve (see Fig. 2). In this region, a considerable concentration of the deposited ion can result as shown by the nickel distribution curve superimposed on the damage curve in

Fig. 2. There is some experimental evidence on impurity effects arising from the deposited ions[20]. Self ions will eliminate an ion impurity problem, however, Evans has shown that self ions produce high concentrations of self-interstitials which can influence the resultant void microstructure[21]. More work is definitely needed in this area of foreign ion effects.

EXPERIMENTAL RESULTS ON REFRACTORY METALS

All studies on ion bombardment have utilized TEM to obtain data on microstructural damage. In the refractory metals, most interest has been directed toward void formation and swelling although changes in dislocation densities are also measured. The discussion of the data will include temperature dependence of swelling and the void lattice parameter, dose dependence of swelling, and effect of helium and other gases.

Temperature Dependence

The effect of temperature on void swelling for several materials is shown in Fig. 3. The swelling values have been normalized so that the maximum swelling equals one. The temperatures have been plotted as T/T_m (T_m = melting temperature). The peak swelling temperature varies from .47 to .55 T_m so in this sense there appears to be little correlation among these metals. The stainless steel shows maximum swelling at a higher temperature than any of the refractory metals. This is most probably due to the larger ratio of self diffusion energy to melting temperature in stainless steel compared to refractories. The higher dose rates used in obtaining the stainless steel curve may also account for a slightly higher temperature dependence. Niobium shows a unique double peak. This has not been found on other ion bombarded pure metals and has been tentatively attributed to an oxygen pick up within a certain temperature range[22], Nb - 1% Zr alloy also shows the double peak at the same temperatures, but the absolute magnitude of the swelling is greater[22]. A double peak has been observed in cold worked 316 stainless steel, but this was attributed to recovery of the cold work structure at higher temperature[26]. The molybdenum data show a hint of a double peak, but more data is needed to verify it. It is possible there may be a lower peak in vanadium if the data were extended to lower temperatures.

Most of the BCC refractory metals show a void lattice after high dose irradiations[27]. It is interesting, however,that none has yet been found in vanadium. The temperature dependence of the void lattice parameter in molybdenum is shown in Fig. 4 for both ion bombarded[28,29] and neutron irradiated conditions[30-32]. The curve is not linear with respect to 1/T over the entire temperature range. Both the ion bombarded and neutron irradiation show a similar increase in temperature dependence of the void lattice at higher temperatures; the ion bombardment data is just shifted to a higher temperature. The curves indicate that the temperature shift between ion bombardment and neutron data is considerably less at higher temperatures than at lower temperatures. This is in agreement with theoretical work[13]. The rather weak temperature dependence of the void lattice at the lower temperature is manifested in the weak temperature dependence of the void size and density both in ion bombarded and neutron irradiated molybdenum.

It has already been suggested that the void lattice parameter could be used as a temperature indicator in irradiation experiments if a good calibration curve of lattice parameter vs. temperature were available[33]. The temperature shift required to match the void lattice parameters as indicated in Fig. 4 may be the same as that required to match the swelling values, but this has not yet been verified.

Dose Dependence

The dose dependence of void swelling for molybdenum and niobium are shown in Fig. 5. The molybdenum shows a dose dependence $\sim(\text{dose})^{0.6}$ both at 1000°C and 900°C. The slopes of the curves from the work of Brimhall and Simonen[28,36] agree with that of Evans[21], although the absolute magntidue of the swelling is different. One possible reason for this difference is the much higher purity of the molybdenum used by Evans. Niobium shows a somewhat greater dose dependence, $(\text{dose})^{\sim.9}$, than molybdenum. There is also evidence of saturation in the swelling in niobium at higher dose levels. This has been ascribed to the formation of a well ordered void lattice. The void lattice forms in molybdenum, but the tendency toward saturation has not yet been observed. Extension to higher dose levels may be necessary. The absolute magnitude of the swelling in niobium is greater than molybdenum,

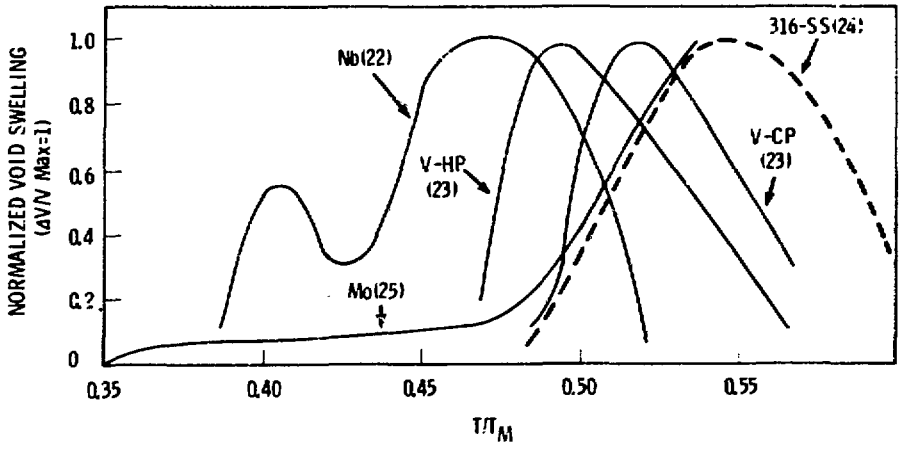

Fig. 3. Temperature Dependence of Void Swelling in Several Ion Bombarded Refractory Metals and Stainless Steel.

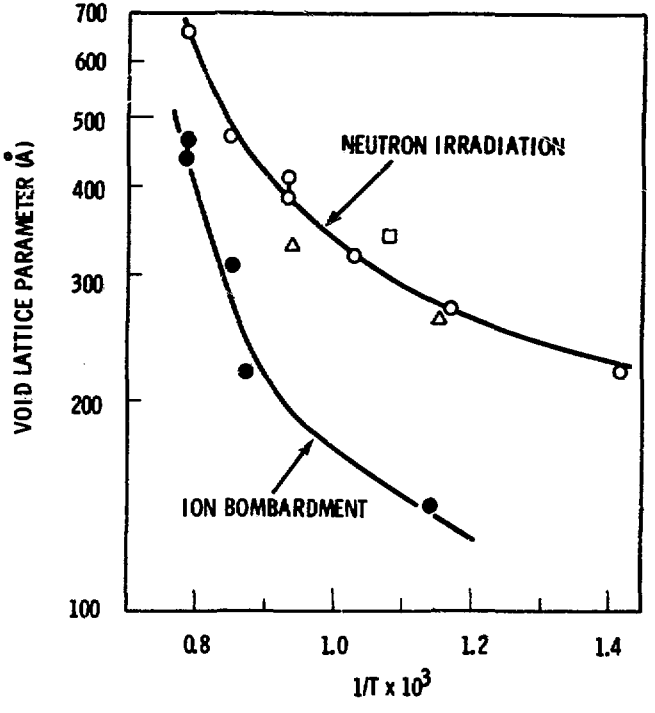

Fig. 4. Temperature Dependence of Void Lattice Parameter in Molybdenum.

however the magnitude of the swelling appears to be so strongly dependent on purity that this cannot be taken as a general rule.

Comparison can also be made between the swelling in Mo and Nb and that in stainless steel. The dependence of swelling on dose in stainless steel is much stronger than in either molybdenum or niobium. Stainless steel also shows no saturation in the void swelling. It is also believed from neutron irradiation studies that swelling in stainless steel actually shows linear dependence on dose after an incubation period, although this has not been confirmed by ion bombardment studies. In molybdenum and impure niobium, there is a higher void density but smaller void size compared to stainless steels. The maximum swelling observed in any refractory metal has been ~13% in Nb - 1% Zr alloy at 1000°C and 50 dpa. The maximum swelling in molybdenum is 3% at 1000°C after 100 dpa. Increasing the temperature during ion bombardment of molybdenum may produce swellings comparable to niobium. In general, the swelling in pure Mo, Nb, and V is considerably less than in stainless steel at high dose levels, i.e., >100 dpa.

Effects of Helium and Other Gases

The role played by helium and soluble gases such as oxygen and nitrogen is not well defined but can be substantial in certain cases. The effect of helium appears to be strongest in high purity metals. In high purity molybdenum, voids formed only part of the time without preinjected helium. With helium, voids always formed[21]. In molybdenum of lesser purity, voids always formed with or without helium[28,35]. In experiments in which the helium was injected simultaneously with the heavy ions, the helium was found to have no effect on void nucleation[37]. Fig. 6 shows the variation of void size under different conditions of helium and heavy ion bombardment. In these particular experiments the void nucleation rate in molybdenum was so high that the helium was not injected fast enough to cause an effect. In vanadium with 100 ppm pre-injected helium, a bi-modal distribution of voids was observed in which the smaller size were believed to be mainly helium bubbles[23].

The effect of helium is also dependent upon the dose rate used in the heavy ion experiments. In other experiments on vanadium, voids could not be generated in material bombarded at $<10^{-3}$ dpa/sec without the presence of

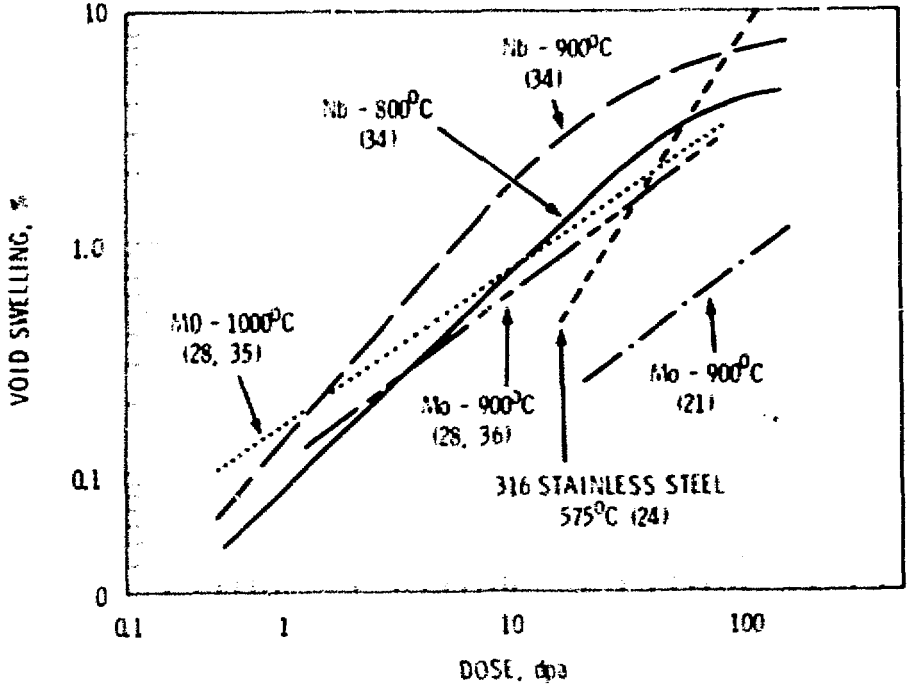

Fig. 5. Dose Dependence of Swelling in Ion Bombarded Nb, Mo, and 316 Stainless Steel.

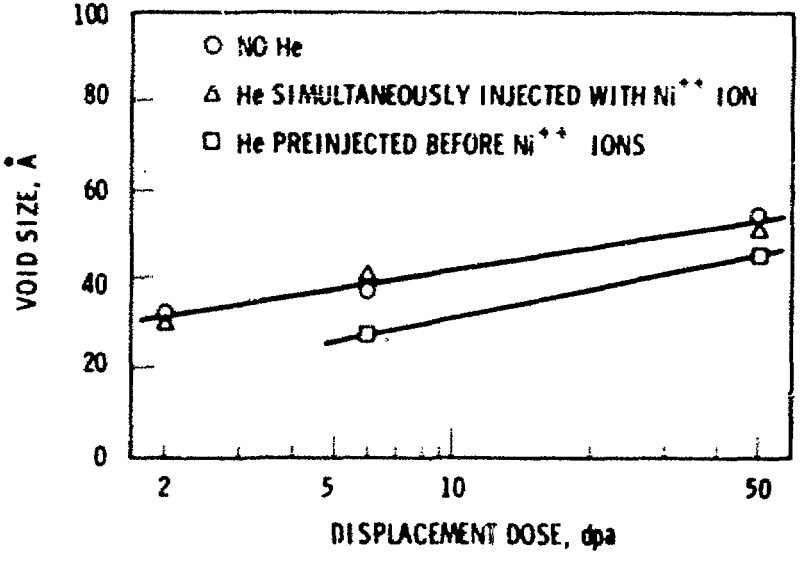

Fig. 6. Dose Dependence of Void Size in Molybdenum Bombarded under Different Conditions of He and Ni Ion Bombardment.

helium[38]. In vanadium bombarded at dose rates $\cdot 10^{-2}$ dpa/sec, voids could be nucleated without the presence of helium[38]. These experimental results are in agreement with the general theory of Wiedersich and Katz[39] dealing with the effect of insoluble gases on void nucleation.

The role of soluble gases has been studied most in niobium. Oxygen was found to increase the void nucleation in niobium[9]. Only in niobium that had a high oxygen content could the void lattice be detected. The effect of dissolved gases is also noted when comparing the void microstructure of niobium after bombardment in a poor vacuum and in a high vacuum[9,34]. In contrast to the results on niobium, molybdenum bombarded with nitrogen was expected to show some effect of the dissolved nitrogen on void nucleation; however, no systematic effect of the nitrogen was observed[21].

Correlation with Neutron Damage

Theoretical Correlation of the Primary Damage State

The ultimate goal of the heavy ion damage studies is to correlate the observed microstructure to that observed after neutron irradiation. This is currently being done theoretically by comparing the primary damage states induced by various irradiations and empirically by comparing some characteristic feature of the microstructure such as total void volume.

Doran et al., have done extensive analysis in comparing the defect spectra in stainless steel from neutrons, heavy ions, protons, and electrons[40]. In terms of number of defects per dispalcement, values for 1 MeV nickel ions are closest to those expected from a neutron spectra representative of EBR-II. Close pair recombination within the cascades (cascade annealing) had been considered in this analysis. However, Norgett has postulated that the introduction of long range replacement sequences causes the vacancies and interstititals to be separated large distances reducing cascade annealing[41].

Marwick has also compared the primary recoil spectrum in iron due to neutrons, protons, and nickel ions[42]. The nickel ions were also found to give the spectrum which best matches a fast neutron spectrum.

Marwick has recently extended this work to compare the PKA spectrum in niobium produced by niobium ions and by the neutron spectrum expected in the first wall of a CTR[43]. Fig. 7 shows the fraction of damage produced by PKA's of energy less than T. In both heavy ion and neutron irradiations, most of the damage is caused by the high energy PKA's. As in the case of fast fission reactor spectra, heavy ions give a reasonably good simulation of the primary damage state in a CTR neutron spectrum. The experimental correlation will be discussed in a later section of this review.

Bullough[45] and Bullough et al.[46] have recenlty analyzed the rate theory of swelling taking into account the different damage structure produced by heavy ions, electrons, and neutrons. They found that in order to get reasonable correlation, the effects of the cascades must be considered. The effects are accounted for by assuming that cascades collapse into vacancy loops which subsequently emit vacancies that later form voids.

Experimental Correlation with Neutrons

There has, as yet, been no systematic correlation of the experimental results from ion bombardment studies with neutron bombardment studies on the refractory metals. There have been numerous neutron studies, but a wide variety of purities and irradiation conditions (mostly low fluence) have been used.

Some correlations have been made using a very limited temperature and dose range. Eyre et al. compared the damage structure in molybdenum after 640°C neutron irradiation with that produced by ion bombardment at higher temperature[47]. Similar swelling values were obtained if a temperature shift of about 150°C was used. It was also found that the critical dose in terms of dpa for void formation was higher in the ion experiments. Further, the size was smaller and size distribution of the voids was narrower in the ion bombardment results even accounting for the temperature shift. Comparison of the swelling data from ion bombarded vanadium with that from neutron bombarded suggests a 200°C temperature shift[23]. This comparison was not made on material of the same purity, however. Studies in stainless steels and nickel base alloys generally show a temperature shift of 125-150°C.

Moteff et al. have measured the bulk density in neutron irradiated molybdenum and niobium as a function of temperature and found evidence of a double peak as shown in Fig. 8 [48]. Also shown is some of the ion bombardment data from Fig. 3. The molybdenum ion bombardment data is from the same base material as the neutron irradiated material but the niobium data is from different investigators. Also, all the ion bombardment data is obtained from TEM. The shape of the curve for neutron irradiation is the same for TEM or bulk density measurements though the absolute values are different. Qualitatively there is a reasonable correlation when the temperature shift is considered, particularly in the case of niobium. Compilation of other low fluence neutron data on molybdenum reveals a broad maximum in the swelling extending from 800°C to 1150°C (0.37 to 0.49 T_m) [48]. The ion bombardment data on molybdenum from Fig. 8 would appear to extrapolate to a maximum beyond .5 T_m.

The data does show that the temperature shift is greater at lower temperature than at higher temperatures which is in agreement with the void lattice parameter results. As a consequence of this, the swelling from neutron irradiation extends over a greater temperature range than that from heavy ion bombardment.

Correlation between ion bombardment and neutron irradiation can also be made by plotting some of the neutron data on the dose dependence curve of Fig. 5. In Fig. 9, swelling data from two temperature regimes of the neutron data for molybdenum are plotted along with the ion bombardment data at 900°C and 1000°C. Most of the neutron data are at a lower dose than the ion bombardment data [49]. Note that an extrapolation of the ion bombardment data at 900-1000°C fits reasonably well with the 600-725°C low fluence neutron data. There is a very poor fit, however, when extrapolating to the neutron data in the 900-1050°C range. This comparison implies a 200-300°C temperature shift for 900-1000°C ion bombardment temperatures.

Other differences such as swelling rate and absolute swelling magnitude may be very difficult to correlate exactly between the heavy ion and neutron irradiations. Currently there are several correlation programs being performed on both nickel and iron base alloys and on bcc refractory metals in which a reference material is bombarded with several different ions and

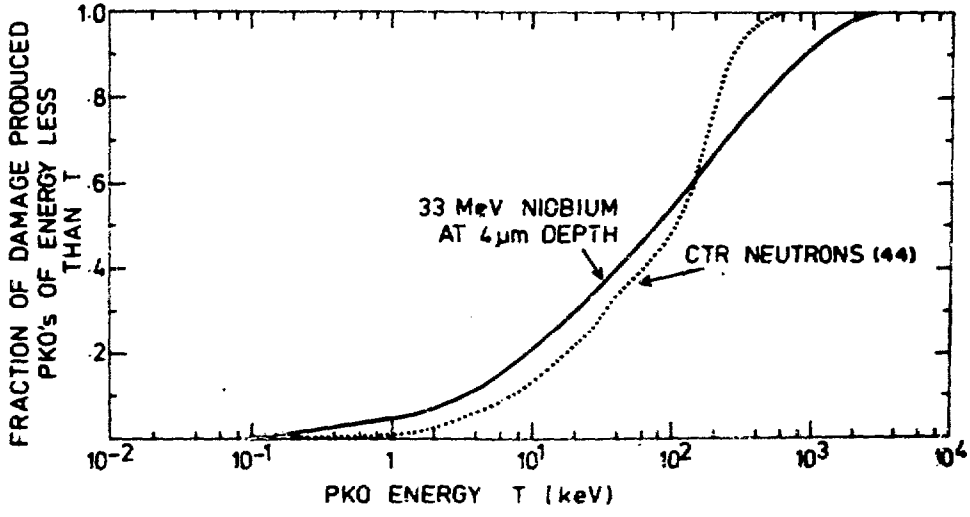

Fig. 7. The Proportion of Displacements Produced by Recoils of Less Than Energy T(KeV).

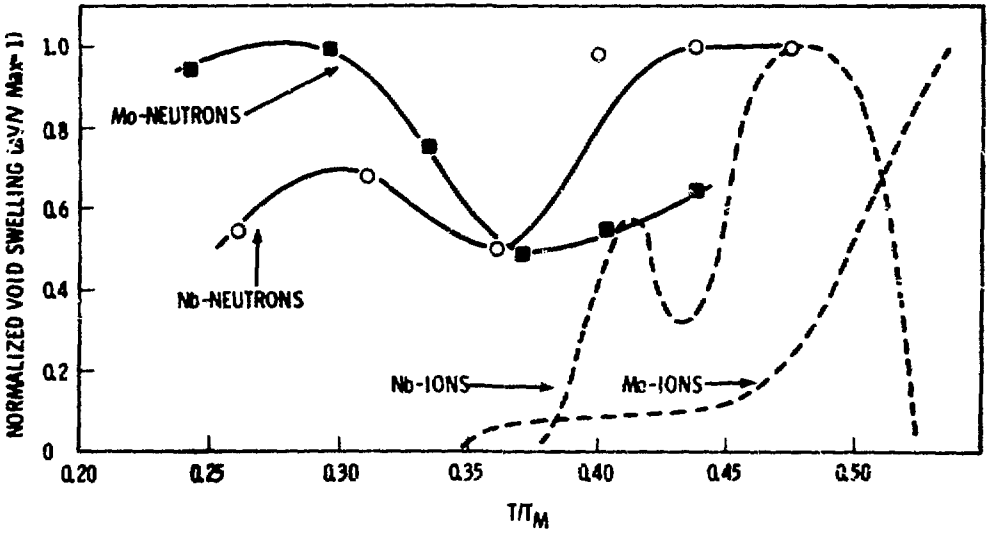

Fig. 8. Temperature Dependence of Void Swelling in Neutron and Ion Bombarded Nb and Mo.

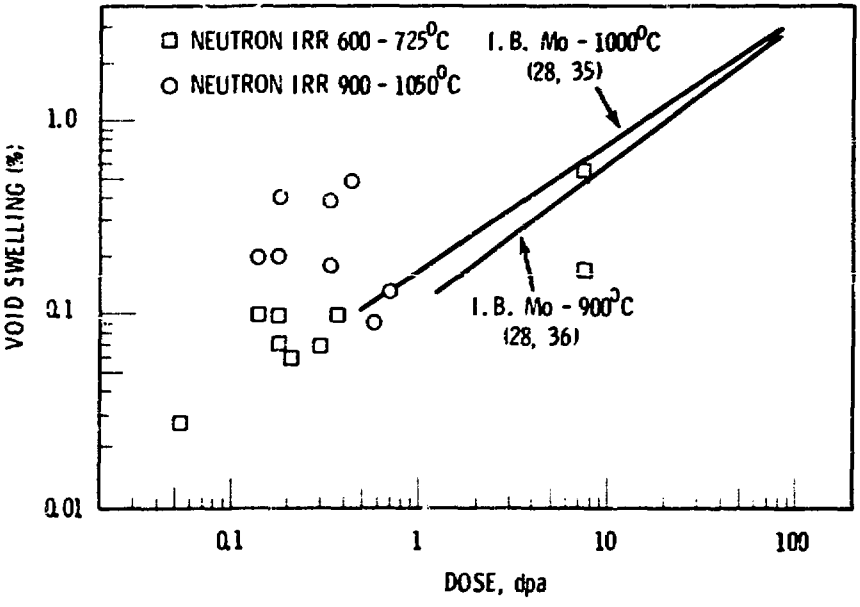

Fig. 9. Dose Dependence of Swelling in Molybdenum. Neutron Data Plotted with Ion Data from Fig. 5.

with neutrons. It is hoped that the particular conditions under which correlations can be made using the different simulation techniques can be eventually established.

There has been no correlations in the swelling between heavy ion bombardment and 14 MeV neutron or fusion spectrum irradiations. At this time, 14 MeV sources are not of sufficient intensity to provide good data to correlate with heavy ion irradiations. Since considerable data for the CTR program on bulk material behavior will probably be generated in fission reactors, it is still important to correlate the data from heavy ion irradiations with that from fission neutron spectrum irradiations.

SUMMARY OF RESULTS

Several important observations and preliminary conclusions on the damage state in refractory metals have emerged from the heavy ion studies. Theoretically, heavy ions give a good simulation of the primary damage state expected from a CTR spectrum. In the isolated experimental comparisons that have been made, the ion bombardment gives a reasonable simulation of the void swelling expected from neutron irradiation if a temperature shift is applied. The magnitude of the temperature shift will depend on the temperature of interest. The temperature dependence of the void swelling is complex with evidence of a double peak in the case of niobium. The peak swelling is generally in the realm of 0.45 to 0.52 T_m. This is significantly lower than observed in the stainless steel. These results suggest a low homologous temperature for peak swelling in neutron irradiated material but further studies will have to be done. The rate of swelling is low in the refractory metals, at least at temperatures less than 0.45 T_m. This swelling rate may depend on purity level. There is evidence of saturation in the swelling of niobium. Based on the creation of a void lattice it is expected that swelling in molybdenum would also saturate at sufficiently high dose levels. The impurities, particularly soluble gases, play a major role in determining swelling behavior. Helium is effective in promoting void nucleation under conditions of low dose rate and/or high irradiation temperature.

FUTURE DIRECTIONS

There is much basic information to be obtained from ion bombardment studies of advanced materials. The effect of cold work, precipitates, and major and minor alloying elements on the microstructural changes all need to be studied in the refractory metals. In the future these studies will be directed to more complex and commercial alloys rather than the high purity materials which have been studied so far.

Advance screening of materials in terms of their resistance to radiation damage accumulation, particularly swelling, can be done. Since some of these materials would probably not be used for a considerable time in the future, there is sufficient time to investigate a wide range of materials bombarded under a variety of conditions.

Conditions that are unique to CTR radiation environments are pulsed radiation fields and very large helium and hydrogen generation. Pulsed radiation can be simulated rather easily using heavy ion accelerators. Helium or hydrogen concentrations can also be produced by using a dual beam of heavy ions and helium ions or protons. Both of these techniques will be used more extensively in the future as the facilities become available.

Finally, correlations with neutron data must be continually updated. There is a definite need to establish the correlations over a wider spectrum of dose, dose rate, and temperature.

ACKNOWLEDGMENT

This paper is based on work performed under United States Energy Research and Development Administration Contract AT(45-1)-1830.

REFERENCES

1. R. S. Nelson, J. A. Hudson, D. J. Mazey, G. P. Walters, and T. M. Williams in: Radiation Induced Voids in Metals, J. W. Corbett and L. C. Ianniello (eds.), p. 430, CONF-710601 (April 1972).

2. G. L. Kulcinski in: Application of Ion Beams to Metals, S. T. Picraux, E. P. Eernisse, and F. L. Vook (eds.), p. 613, Plenum Press, New York, 1974.

3. J. Lindhard, M. Scharf, and H. E. Schiott, Mat. Fys, Medd. Daw Vid. Selsk 33, 3 (1963).

4. I. Manning and G. P. Mueller, Computer Physics Comm. 7, 85 (1974).

5. D. K. Brice, Sandia Laboratory Report SLA-73-0410 (April 1973).

6. D. G. Doran, J. R. Beeler, Jr.,N. D. Dudey, and M. J. Fluss, HEDL-TME 73-76 (December 1973).

7. H. R. Brager, H. E. Kissinger, and G. L. Kulcinski, Rad. Effects 5, 281 (1970).

8. W. G. Johnston, J. H. Rosolowski, A. M. Turkalo, and T. Lauritzen in: Effects of Radiation on Substructure and Mechanical Properties of Metals and Alloys, ASTM-STP 529, p. 213 (1972)

9. B. A. Loomis, A. T. Taylor, T. E. Kleppert, and S. B. Gerber in: Defects and Defect Clusters in BCC Metals and Their Alloys, R. J. Arsenault (ed.) Nuclear Metallurgy 18, 332 (1973).

10. J. A. Sprague, "An Interferometric Electropolisher for Preparing Electron Microscopy Specimens of Heavy Ion Bombarded Metals," to be published in Review of Scientific Instruments.

11. W. G. Johnson, J. H. Rosolowski, A. M. Turkalo, and T. Lauritzen, J. Nucl. Mat. 46, 273 (1973).

12. R. Bullough and R. C. Perrin in: Irradiation Effects on Structural Alloys for Nuclear Reactor Applications, ASTM-STP 484, p. 317 (1970).

13. A. D. Brailsford and R. Bullough, J. Nucl. Mat. 44, 121 (1972).

14. J. A. Sprague, J. E. Westmoreland, F. A. Smidt, Jr., and P. R. Molmberg, J. Nucl. Mat. 54, 286 (1974).

15. W. G. Johnston, J. H. Rosolowski, A. M. Turkalo, and T. Lauritzen in: The Physics of Irradiation Produced Voids, R. S. Nelson (ed.), AERE-R7934, p. 44 (1974).

16. T. D. Ryan and A. Taylor in: Application of Ion Beams to Metals, S. T. Picraux, E. P. Eernisse, and F. L. Vook (eds.), p. 675, Plenum Press, New York, 1974.

17. E. R. Bradley and J. L. Brimhall, "Effect of a Free Surface on Void Formation in Molybdenum," this volume.

18. P. R. Okamoto and H. Wiedersich in: The Physics of Irradiation Produced Voids, R. S. Nelson (ed.), AERE-R7934, p. 231 (1974).

19. R. S. Nelson, J. A. Hudson and D. J. Mazey in: The Physics of Irradiation Produced Voids, R. S. Nelson (ed.), AERE-R7934, p. 119 (1974).

20. P. R. Okamoto, A. T. Santhanam, and H. Wiedersich, Nucl. Tech. 22, 45 (1974).

21. J. H. Evans, Rad. Effects 17, 69 (1973).

22. B. A. Loomis, A. Taylor, and S. B. Gerber, J. Nucl. Mat. 56, 25 (1975).

23. A. T. Santhanam, A. Taylor, and S. D. Harkness in: Defects and Defect Clusters in BCC Metals and Their Alloys, R. J. Arsenault (ed.), Nuclear Metallurgy 18, 302 (1973).

24. W. G. Johnston, J. H. Rosolowski, A. M. Turkalo, and T. Lauritzen, J. Nucl. Mat. 48, 330 (1973).

25. J. Moteff, unpublished results.

26. H. R. Brager and J. L. Straaslund, J. Nucl. Mat. 46, 103 (1973).

27. A. M. Stoneham in: The Physics of Irradiation Produced Voids, R. S. Nelson (ed.), AERE-R7934, p. 319 (1974).

28. J. L. Brimhall and E. P. Simonen, J. Nucl. Mat. 52, 323 (1974).

29. J. H. Evans, Rad. Effects 10, 55 (1971). Also unpublished data.

30. V. K. Sikka and J. Moteff, J. Nucl. Mat. 54, 325 (1975).

31. F. W. Wiffen in: Radiation Induced Voids in Metals, J. W. Corbett and L. C. Ianniello (eds.), p. 386, CONF-710601 (April 1972).

32. B. L. Eyre and J. H. Evans in: Voids Formed by Irradiation of Reactor Materials, S. F. Pugh, M. H. Lorreto, and D. I. R. Norris (eds.), p. 323 (1971).

33. J. Moteff and V. K. Sikka, Trans. Am. Nucl. Soc. 16, 97 (1973).

34. J. L. Brimhall and G. L. Kulcinski, Rad. Effects 20, 25 (1973).

35. J. L. Brimhall and E. P. Simonen in: Defects and Defect Clusters in BCC Metals and Their Alloys, R. J. Arsenault (ed.), Nuclear Metallurgy 18, 321 (1973).

36. J. L. Brimhall, unpublished data.

37. J. L. Brimhall in: The Physics of Irradiation Produced Voids, R. S. Nelson (ed.), AERE-R7934, p. 197 (1974).

38. J. L. Brimhall and E. P. Simonen, to be published.

39. H. Wiedersich, J. J. Burton, and J. L. Katz, J. Nucl. Mat. 51, 287 (1974).

40. D. G. Doran, R. L. Simons, and W. N. McElroy in: Prop. of Reactor Structural Alloys after Neutron or Particle Irradiation, ASTM-STP 570, to be published.

41. M. S. Norgett in: The Physics of Irradiation Produced Voids, R. S. Nelson (ed.), AERE-R7934, p. 44 (1974).

42. A. D. Marwick, J. Nucl. Mat. 55, 259 (1975).

43. A. D. Marwick, J. Nucl. Mat. 56, 355 (1975).

44. C. M. Logan, J. D. Anderson, Z. A. Munier, Nucl. Tech. 22, 36 (1974).

45. R. Bullough in: The Physics of Irradiation Produced Voids, R. S. Nelson (ed.), AERE-R7934, p. 275 (1974).

46. R. Bullough, B. L. Eyre, and K. Krishan, to be published.

47. B. L. Eyre and J. H. Evans in: Effects of Radiation on Substructure and Mechanical Properties of Metals and Alloys, ASTM-STP 529, p. 184 (1972).

48. J. Moteff, V. K. Sikka, and H. Jang in: The Physics of Irradiation Produced Voids, R. S. Nelson (ed.),AERE-R7934, p. 181 (1974).

49. J. L. Brimhall, E. P. Simonen, and H. E. Kissinger, J. Nucl. Mat. 48, 339 (1973).

VOID SWELLING OF Nb, Nb-1 AT.% Zr, AND Nb-0.5 AT.% O INDUCED BY $^{58}Ni^{+}$ BOMBARDMENT*

B. A. Loomis
A. Taylor
S. B. Gerber
Materials Science Division
Argonne National Laboratory
Argonne, Illinois 60439

ABSTRACT

The void swelling of Nb, Nb-1 at.% Zr, and Nb-0.5 at.% O during 3.2-MeV $^{58}Ni^{+}$ irradiation at temperatures between 600 and 1150°C has been determined. The void swelling of Nb and Nb-1 at.% Zr determined from transmission-electron microscopy observations shows a "double peak" at 825 ± 25°C and 1000 ± 25°C. The presence of 0.5 at.% O in Nb results in a significantly reduced void swelling of Nb at all irradiation temperatures. Oxygen impurity in Nb was shown to be necessary for the formation of an ordered void array. The ordered void array is responsible for the reduced void swelling of Nb A Ti coating on Nb significantly affects the void size and void distribution.

INTRODUCTION

The void swelling of Nb caused by high-energy, heavy-ion bombardment has been a subject for recent experimental study.[1,2] The primary reason for these studies is to simulate, by the use of ion bombardment, the irradiation damage produced by neutron bombardment of Nb in either a fission or fusion reactor. The higher atom displacement rate during heavy-ion bombardment makes possible the attainment of a high irradiation damage state in a relatively short time. However, to utilize ion bombardment for simulation of the neutron bombardment of Nb, particularly at elevated temperature, consideration should be given to the interaction of intrinsic oxygen, nitrogen, and carbon impurity in Nb with the irradiation damage.[3] Furthermore, the temperature-dependence curve for void swelling in Nb during heavy-ion irradiation is displaced 200 to 300°C

*Work supported by the U.S. Energy Research and Development Administration.

higher than the temperature-dependence curve for void swelling in Nb during neutron irradiation.[1,4] Nb is particularly susceptible to oxygen and nitrogen contamination at elevated temperature under poor vacuum conditions.[5] Since the irradiation damage produced by heavy-ion bombardment is contained in a layer $\sim 10^{-4}$ cm thick, contamination effects at elevated temperature may significantly affect the state of irradiation damage aggregation.

Loomis, Taylor, and Gerber[1] have previously reported the void swelling of Nb and Nb-1%Zr as a result of $^{58}Ni^{+}$ bombardment at temperatures between 600 and 1150°C. In the present paper, we shall compare these previously reported results with recent results obtained on the void swelling of Nb containing 0.5%O. Also, we shall show the dependence of the void swelling in Nb single crystals on the depth in the irradiation-damaged layer, the effect of a protective Ti layer on Nb, and discuss the possible implications of these results as indicative of surface-contamination effects.

MATERIALS AND PROCEDURE

The Nb used for the present study was Marz-grade rod supplied by the Materials Research Corporation, and the Nb-1%Zr rod was supplied by the Haynes Stellite Company. These materials were converted to 0.13-mm-thick sheet and purified by a procedure described elsewhere.[1] Following purification, the Nb was heated at 1200°C in oxygen at 5×10^{-6} Torr for 5-15 min and then homogenized by annealing at 1200°C for 1 hr. This procedure resulted in Nb containing O concentrations up to 0.5%. The Nb-0.35%O material was coated with $\sim$1600 Å of Ti by vapor deposition.

Specimens of Nb, Nb-1%Zr, Nb-0.5%O, and Nb-0.35%O coated with Ti were irradiated at the Argonne Dynamitron facility with 3.3 ± 0.3-MeV $^{58}Ni^{+}$ at a nominal displacement rate of 5×10^{-3} dpa/s (atom displacements per atom per second). A more detailed account of the irradiation procedure is presented elsewhere.[1]

Following irradiation, a specimen for transmission-electron microscopy (TEM) observation was perforated from the unbombarded surface by electrochemical polishing in a HNO_3-HF solution. The void distribution in the bombarded layer was determined by removal of successive 2000-3000-Å sections from the bombarded surface in a 2.5% HF-5% H_2SO_4-92.5% MeOH solution. For this study, a depth of 4000-6000 Å in the damage layer was used to evaluate the void swelling parameters in the irradiated materials.

The irradiation-damaged microstructure was examined with a Siemens Elmiskop I electron microscope operated at 100 keV. The void damage was photographed at a magnification of 45000X. From photographic plates enlarged four times, the size and number of voids were determined by the use of a Zeiss particle-size analyzer. The number density of the irradiation damage was obtained by determining the thickness of the foil from stereo observation of pairs of photomicrographs obtained from different orientations of the specimens.

EXPERIMENTAL RESULTS

Effect of Section Depth

The dependence on section depth of the void volume fraction $\Delta V/V$, the average void size $\bar{\ell}_{<100>}$, and the void number density Σn_i in irradiated Nb single crystals with a {100}, {110}, or {111} surface normal to the ion beam is shown in Figs. 1-3, respectively. The void volume fraction ($\Delta V/V$) was determined from

$$\frac{\Delta V}{V} = \sum_i n_i \left[K_1(T)\, \ell^3_{<100>,i}\right] , \qquad (1)$$

where n_i is the number of voids per cm^3 in a dimension classification range with a void dimension range of 30 Å, $\ell_{<100>,i}$ is the dimension of a void in the <100> in a given dimension classification range, and $K_1(T)$ is an experimentally determined factor that takes into account the truncation of the voids in the different crystallographic directions.

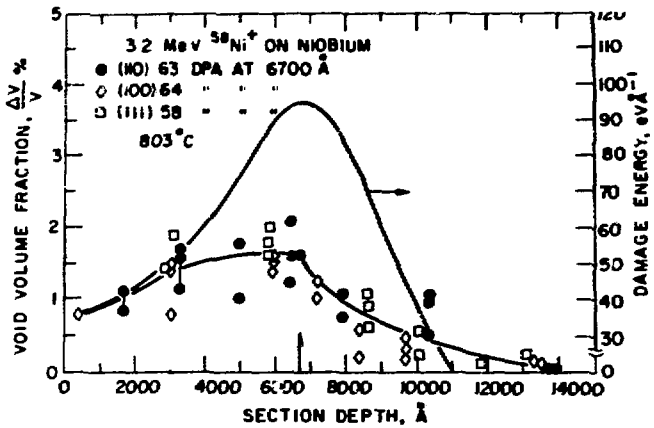

Fig. 1. Dependence of ΔV/V on Section Depth.

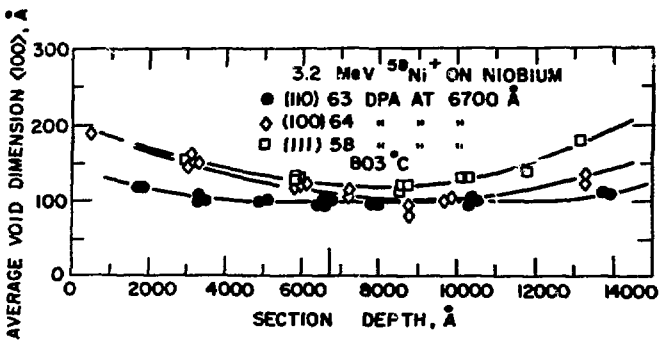

Fig. 2. Dependence of Void Size on Section Depth.

The temperature dependence of the $K_1(T)$ values for Nb and Nb-1%Zr is reported elsewhere,[1] and the $K_1(T)$ value for Nb-0.5% O was determined to be 0.64. The average void dimension, $\bar{\ell}_{\langle 100\rangle}$, was determined from the relation

$$\bar{\ell}_{\langle 100\rangle} = \left(\sum_i n_i \ell_i^3 / \sum_i n_i\right)^{1/3}. \qquad (2)$$

In Fig. 1, the deposition of damage energy with the 3.2-MeV $^{58}Ni^+$ range in Nb is also shown. The damage energy curve was shifted on the abscissa so that this curve coincided with the $\Delta V/V$ curve at the bombarded surface. In Fig. 1, the void volume fraction in Nb irradiated to ~60 dpa at 803°C appears to have no significant dependence on the crystal orientation. The maximum $\Delta V/V$ occurs approximately at the theoretically expected depth for maximum energy deposition. However, the maximum depth (~14,000 Å) in the damaged layer at which voids were observed was substantially greater than would be anticipated from the damage energy curve. The average void dimension (Fig. 2) and the void number density (Fig. 3) in the {110} oriented crystal were significantly different from the {100} and {111} oriented crystals. The maximum average void dimension in each of the crystals was observed near the surface and near the end of the ion range (~14,000 Å), whereas the maximum void density was determined to be approximately at the peak for maximum energy deposition. In a subsequent section we shall discuss the possible surface effects that these data may imply.

Temperature Dependence of Void Swelling

The temperature dependence of the void volume fraction, average void dimension, and the void number density in Nb, Nb-1%Zr, and Nb-0.5%O irradiated to 50 dpa with 3.2-MeV $^{58}Ni^+$ is shown in Figs. 4-6, respectively. The $\Delta V/V$ curves for Nb and Nb-1% Zr in Fig. 4 clearly show two swelling peaks centered at 825 ± 25°C and 1000 ± 25°C. At the temperatures for the swelling peaks, the average void dimension in Nb and Nb-1% Zr has a relative maximum value (Fig. 5), and the void number density has a relative minimum value (Fig. 6). The results of adding

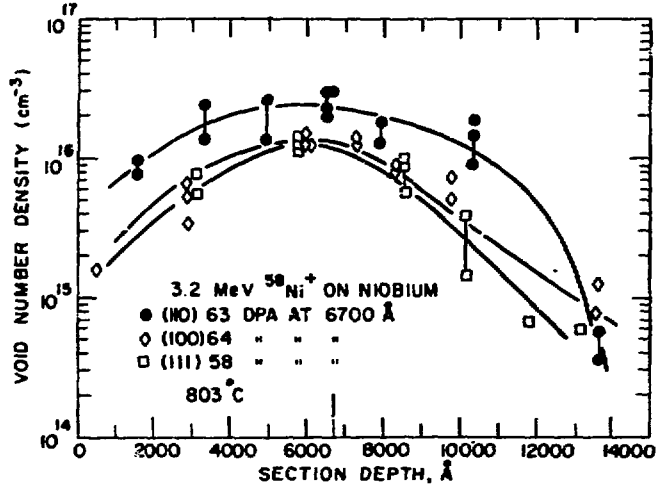

Fig. 3. Dependence of Void Number Density on Section Depth.

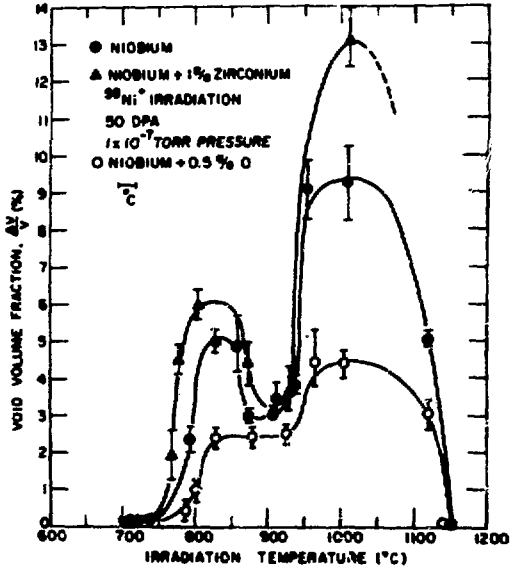

Fig. 4. Temperature Dependence of ΔV/V in Nb, Nb-1% Zr, and Nb-0.5% O.

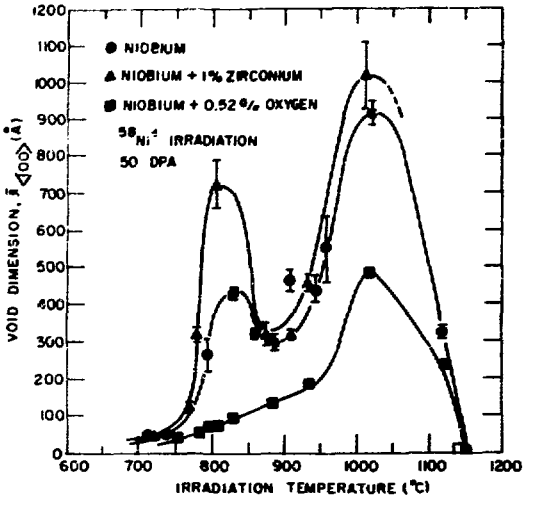

Fig. 5. Temperature Dependence of Void Dimension in Nb, Nb-1% Zr, and Nb-0.5% O.

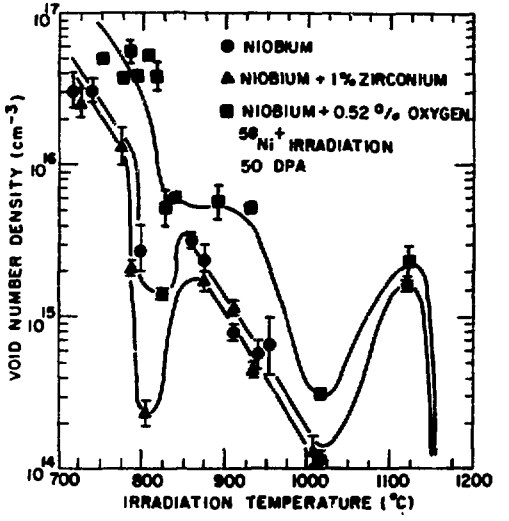

Fig. 6. Temperature Dependence of Void Number Density in Nb, Nb-1% Zr, and Nb-0.5% O.

0.5% O to Nb are clearly to reduce the average void dimension (Fig. 5) and to increase the void number density (Fig. 6). These effects result in a decrease in $\Delta V/V$ for Nb-0.5% O as compared with either Nb or Nb-1% Zr at all irradiation temperatures. These materials have also been irradiated with V^+, and, to date, we have determined no significant difference in $\Delta V/V$ from the $^{58}Ni^+$ irradiation results.

Microstructure Observations

The microstructures of a few selected irradiated Nb and Nb-0.5% O specimens, as observed by TEM, are shown in Fig. 7. A most notable affect of the presence of O impurity in Nb is to cause the formation of an ordered void array (Figs. 7d and 7e). An ordered void array was not observed in irradiated pure Nb or Nb-1% Zr. The ordered void array has a bcc superlattice that is superimposed on the host Nb bcc lattice. The lattice constant of the void array ranges from 250 Å at 750°C to 550 Å at 955°C. The perfection of the ordered void array is highest at 775 ± 25°C, with the perfection decreasing with increasing temperature for a given O concentration (Fig. 7). The ordered void array was observed in Nb containing 0.05% O irradiated at 780°C. However, with an increase in irradiation temperature, it was necessary to increase the O concentration substantially to promote perfection of void ordering. An irradiation temperature of 828°C required 0.8% O in Nb for a more perfect ordered void array. The ordered void array has also been observed in Nb-1% Zr-0.3% O material irradiated at 785°C. Furthermore, the ordered void array can be produced in Nb that has been doped with 0.25% N and irradiated at 780°C.

The effect of a 1600-Å Ti coating on Nb-0.35% O material is shown in Fig. 8. An ordered void array was observed in the uncoated material (Fig. 8d, e, and f), whereas no ordering of voids was observed in the Ti-coated material. No voids were observed in the Ti layer (Fig. 8a). In Fig. 8b, the void microstructure of the Ti-coated material is shown at a section depth (2200-3000 Å) just beyond the Ti layer. An x-ray analysis with a scanning-electron microscope at a section depth of 4900-5800 Å (Fig. 8c) showed no Ti present.

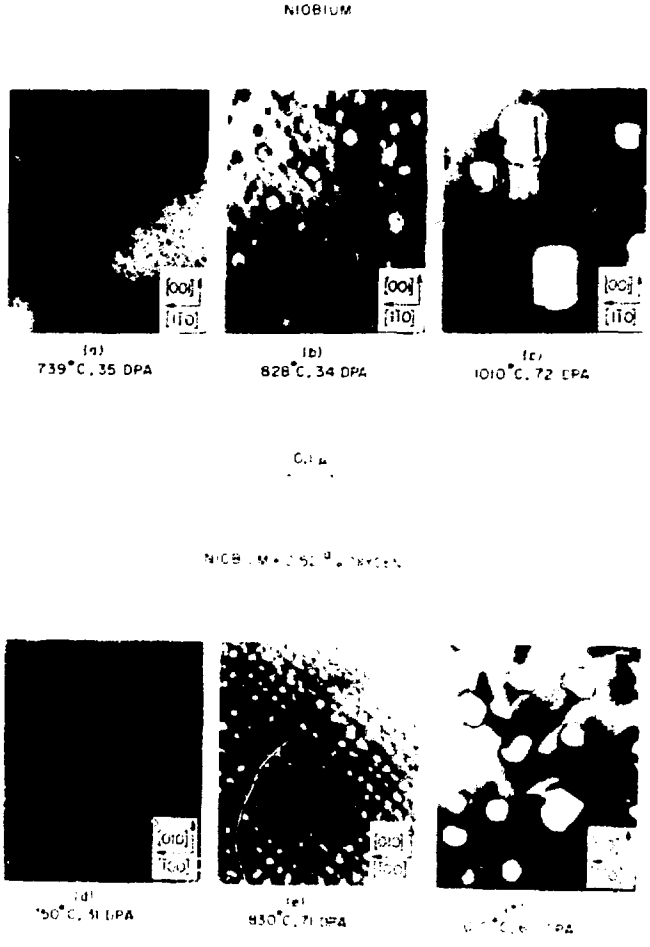

Fig. 7. Void Microstructures in Nb and Nb-0.5% After $^{58}Ni^{+}$ Irradiation at the Indicated Temperatures.

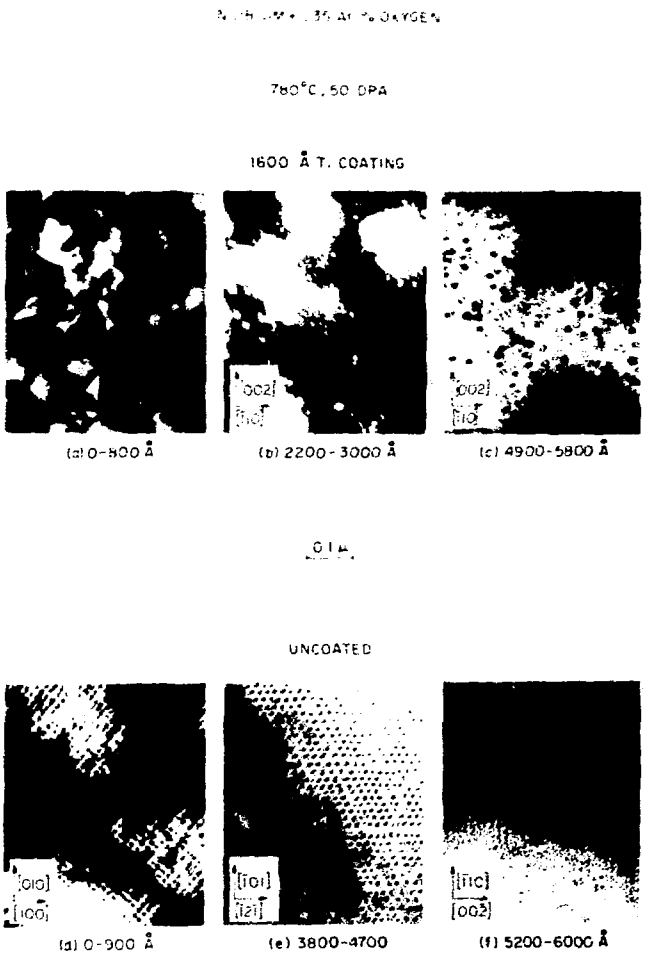

Fig. 8. Effect of a Ti Coating on Nb-0.35% O Void Microstructure.

DISCUSSION OF RESULTS

Data obtained in the present study on the temperature dependence of void volume fraction in Ni^+ bombarded Nb and Nb-1% Zr at a nominal dosage of 50 dpa over the temperature range of 600 to 1150°C show the existence of two swelling peaks for both materials, with temperature maxima at 825 ± 25°C and 1000 ± 25°C. The higher swelling of Nb-1% Zr as compared with pure Nb, particularly at the low-temperature peak, appears to be caused by a higher growth rate of voids in the alloy as seen in Fig. 5. This may be attributed to the "gettering" of O and N impurities by Zr. This interpretation is supported by the data in Figs. 5 and 6 pertaining to the Nb-0.5% O material. These data show that the presence of oxygen impurity in Nb causes increased void nucleation (Fig. 6.) and decreased void growth rate (Fig. 5) both of which result in decreased swelling (Fig. 4). These effects are clearly the result of the formation of the ordered void array. A more detailed discussion of the ordered void array in O doped Nb and Nb-1% Zr is presented elsewhere.[6]

Wiffen[4] has analyzed the available void swelling data for Nb on neutron irradiation, and this analysis shows a maximum $\Delta V/V$ at 600°C for a neutron fluence of 5×10^{21} n/cm^2. This temperature is 200-400°C less than the temperature we have determined for maximum swelling of Nb during $^{58}Ni^+$ irradiation. The results of the present study show that O impurity in Nb can have a substantial effect on void swelling. Because of the increased diffusion rate of O (and N) in Nb with increased temperature,[7] consideration should be given, therefore, to the interaction of these impurities with the irradiation damage when utilizing ion bombardment to simulate neutron bombardment.

The TEM observations of $^{58}Ni^+$ irradiated specimens always reveal the presence of an oxide (or nitride) film on the bombarded surface. We believe this film is formed during heating to the irradiation temperature (750-1000°C) and during irradiation. The poor agreement between the void volume fraction curve and the energy-deposition curve in Fig. 1 suggests that the oxide film may be a contributing effect. We have also observed for a Nb-0.5% O specimen irradiated at 808°C that the void

volume fraction is highest near the surface and progressively decreases to the peak-damage energy-deposition depth. We have no unambiguous explanation for these effects at the present time. However, if surface contamination is contributing to these effects, then the void swelling data we have obtained by ion bombardment at elevated temperature may be in error. This is because we have not determined and made correction for the thickness of the oxide (or nitride) film in evaluating the void swelling parameters at the 4000-6000-Å depth. The lower density of the oxide (or nitride) would result in a displacement of the energy-deposition profile further into the Nb. In addition, the different void size and void distribution observed in the uncoated versus the Ti-coated material suggest that the void swelling may be significantly affected by surface contamination. Surface contamination of Nb from O and N impurities is presumably minimized by the Ti coating.

CONCLUSIONS

(1) Nb, Nb-1% Zr, and Nb-0.5% O undergo void swelling on $^{58}Ni^{+}$ irradiation at temperatures between 600 and 1150°C.

(2) The swelling of Nb and Nb-1% Zr at 50 dpa has relative maximum values at 825 ± 25°C and 1000 ± 25°C.

(3) The swelling of Nb is reduced by the addition of 0.5% O.

(4) The presence of O impurity in Nb promotes void ordering.

(5) A Ti coating on Nb can significantly affect the void size and void distribution.

ACKNOWLEDGMENTS

The authors wish to acknowledge Drs. T. H. Blewitt, P. R. Okamoto, and H. Wiedersich for their helpful discussions.

REFERENCES

1. B. A. Loomis, A. Taylor, and S. B. Gerber, J. Nucl. Mater. 56, 25 (1975).
2. J. L. Brimhall and G. L. Kulcinski, Radiation Effects 20, 25 (1973).
3. B. A. Loomis and S. B. Gerber, Acta Met. 21, 165 (1973).
4. F. W. Wiffen, Proc. of the Intl. Working Session on Fusion Reactor Technology, CONF-710624, p. 139, Oak Ridge National Laboratory, Oak Ridge, Tennessee, 1971.
5. E. Fromm and H. Jehn, Vacuum 19, 191 (1969).
6. B. A. Loomis, A. Taylor, and S. B. Gerber, to be published in the Proceedings of the International Conference on Fundamental Aspects of Radiation Damage in Metals, Oct. 5-10, 1975, Gatlinburg, Tennessee.
7. G. L. Miller (ed.), Tantalum and Niobium, p. 508, Academic Press, New York, 1959.

THE INFLUENCE OF NEUTRON IRRADIATION TEMPERATURE ON THE VOID CHARACTERISTICS OF NIOBIUM AND NIOBIUM-1% ZIRCONIUM ALLOY

H. Jang and J. Moteff

Department of Materials Science
and Metallurgical Engineering
University of Cincinnati
Cincinnati, Ohio 45221

ABSTRACT

Voids in Nb and Nb-1 wt. % Zr alloy irradiated to a fast neutron fluence of $\sim 1 \times 10^{22}$ n cm^{-2} (E > 1MeV) at six different temperatures between 430 and 1050°C have been investigated. Transmission electron microscopy observations revealed the presence of voids in both Nb and Nb-1Zr at all six irradiation temperatures. The void number density and size of the niobium specimens appeared unaffected by irradiation temperatures between 430 and 700°C, but the void number density decreased and the size increased at the higher temperatures. Other observations regarding Nb were that ordered voids were observed at 800°C with the lattice parameter of 685 Å, and the maximum void swelling was $\sim$ 0.5% which occurred at 1050°C. In contrast, the Nb-1% Zr alloy specimens showed larger voids and lower number density than the corresponding Nb specimens. The void swelling of Nb-1Zr reached the maximum of $\sim$ 2% at 800°C. At the irradiation temperatures of 430, 580, and 1050°C the voids were observed only in small localized areas resulting in negligible void swelling. These results are shown to be in fair agreement, qualitatively, with immersion density data for the same materials. It has been demonstrated that a theoretical model on void swelling by Brailsford and Bullough fits reasonably well with the experimental data on Nb-1Zr, but it overestimates the swelling in Nb by a factor of up to $\sim$ 10, especially at high irradiation temperatures.

INTRODUCTION

Compared to the experimental data available for other bcc refractory metals, void swelling data for niobium and its alloys are meager in spite of their attractive mechanical and nuclear properties, and their potential use as structural materials for an advanced nuclear reactor system. Early in 1971 Elen[1] and Elen et. al.[2] have reported voids in Nb specimens irradiated to a fast neutron fluence of $\sim 10^{20}$ n cm^{-2} at temperatures between 470 and 750°C with the resulting swelling values ranging from 0.01 to 0.09%. Similarly Adda[3] has reported voids in Nb irradiated at 600°C; however, he did not observe voids in the specimen irradiated at 900°C. Wiffen[4,5] and Michel et. al.[6] have reported voids in Nb irradiated to fast neutron fluences of $\sim 10^{22}$ n cm^{-2} (E > 0.1 MeV) at temperatures between 394 and 790°C. However, their[4,5,6] work on Nb-1Zr alloy revealed voids only at 790°C and no voids were observed at the lower irradiation temperatures.

In addition to neutron irradiation, a number of charged particle irradiation experiments have been carried out on Nb and Nb-1Zr alloy.[7-12] Recently Loomis et. al.[12] have reported voids in Nb and Nb-1Zr alloy after Ni^+ bombardment at temperatures between 600 and 1150°C. They[12] observed relative maximum swelling values both in Nb and Nb-1Zr at 825 ± 25°C and 1000 ± 25°C , and they also reported higher swelling values in Nb-1Zr alloy than in Nb.

The purpose of the present study was to examine the characteristics of the void formation in Nb and Nb-1Zr alloy irradiated at temperatures between 430 and 1050°C in EBR-II to a fast neutron fluence of 1×10^{22} n cm^{-2} (E > 1MeV), and to compare with the irradiation damage that it is produced by ion bombardment.

EXPERIMENTAL PROCEDURES AND RESULTS

Commercial purity niobium and niobium-1 wt. % zirconium were used for this study. Polycrystalline rod specimens, 1.27 mm (0.05 in.) in diameter and 45 mm (1.75 in.) long of both materials were annealed in a vacuum for one hour at 1100°C to accomplish recrystallization prior to being utilized in the irradiation experiment. The specimens were irradiated in the core of the Experimental Breeder Reactor (EBR-II), row 7, in six static, inert-gas atmosphere capsules. Nuclear heating and a helium gas filled gap of different thicknesses were used to achieve the various temperatures in each capsule. The irradiation temperatures were determined by design calculations and were checked by measurements of the lattice expansion of silicon carbide detectors placed near the specimens. The calculated irradiation temperatures were 430, 580, 700, 800, 900 and 1050°C. The fast neutron fluence in Row 7 of EBR-II was calculated from the neutron spectrum presented by Kamphouse et. al.[13]. The fast neutron flux densities for E > 0.1MeV and E > 1MeV were 2.3×10^{13} and 4.2×10^{12} n cm^{-2} MW^{-1} sec^{-1}, respectively, and the calculated fast neutron fluences were $\sim 5 \times 10^{22}$ (E > 0.1MeV) and $\sim 1 \times 10^{22}$ n cm^{-2} (E > 1MeV). The irradiated specimens were cut into 0.5 mm (0.02 in.) thick discs and electropolished for the transmission electron microscopy. The electropolishing technique used in this was basically the same as that developed by Sikka et. al.[14]. The specimens were examined in a JEM 200 A transmission electron microscope operated at 200 kV, equipped with a specimen cold-finger and a 30° tilt-360° rotation stage. Voids were photographed in the under-focus condition, and the void number densities and sizes were determined from a positive print by using a Carl Zeiss particle size analyzer. For spherical voids the void diameter was measured from the diameter of the inner dark fringe, and an estimated measure was used for polyhedral

voids; i.e., the diameter of a sphere with equivalent void with an equivalent volume was determined. Voids on the foil surface (voids intersecting the foil surface) were excluded in determining the average void diameter, and only half of the surface voids were included in counting the void number density.

EXPERIMENTAL RESULTS

The microstructures of as-irradiated Nb specimens, as observed by TEM, are shown in Fig. 1. The specimen irradiated at 430°C contained black spots, dislocation loops, rafts, and dislocations (these are not shown in the figure) as well as high concentration of small voids. The voids are uniformly distributed inside the grains, and a narrow region of about 400 Å along the grain boundaries is denuded of voids. The void structures of the specimens irradiated at 580 and 700°C are similar to that of the specimen irradiated at 430°C, but the rafts were absent in these specimens. In the specimen irradiated at 800°C the voids were aligned on a bcc superlattice with the calculated lattice parameter of 665 Å. The lattice parameter of the void superlattice was determined by measuring the separation of (110) void planes and converting this value to the parameter for a bcc superlattice. At the higher irradiation temperatures the voids become larger in size and lower in number density and appear to be cubical in shape as shown in Figs. 1(e) and 1(f). The void volume fraction of the neutron irradiated Nb specimens is shown in Fig. 2. The void swelling is minimum, ~ 0.2%, at temperatures of 430 - 700°C, and then increases with the increasing temperature, reaching a maximum swelling of 0.5% at 1050°C. The microstructures of the neutron irradiated Nb-1Zr specimens are shown in Fig. 3. The microstructures of Nb-1Zr irradiated at 430, 580, and 700°C are very complex; these consist of high density unresolvable black spots which

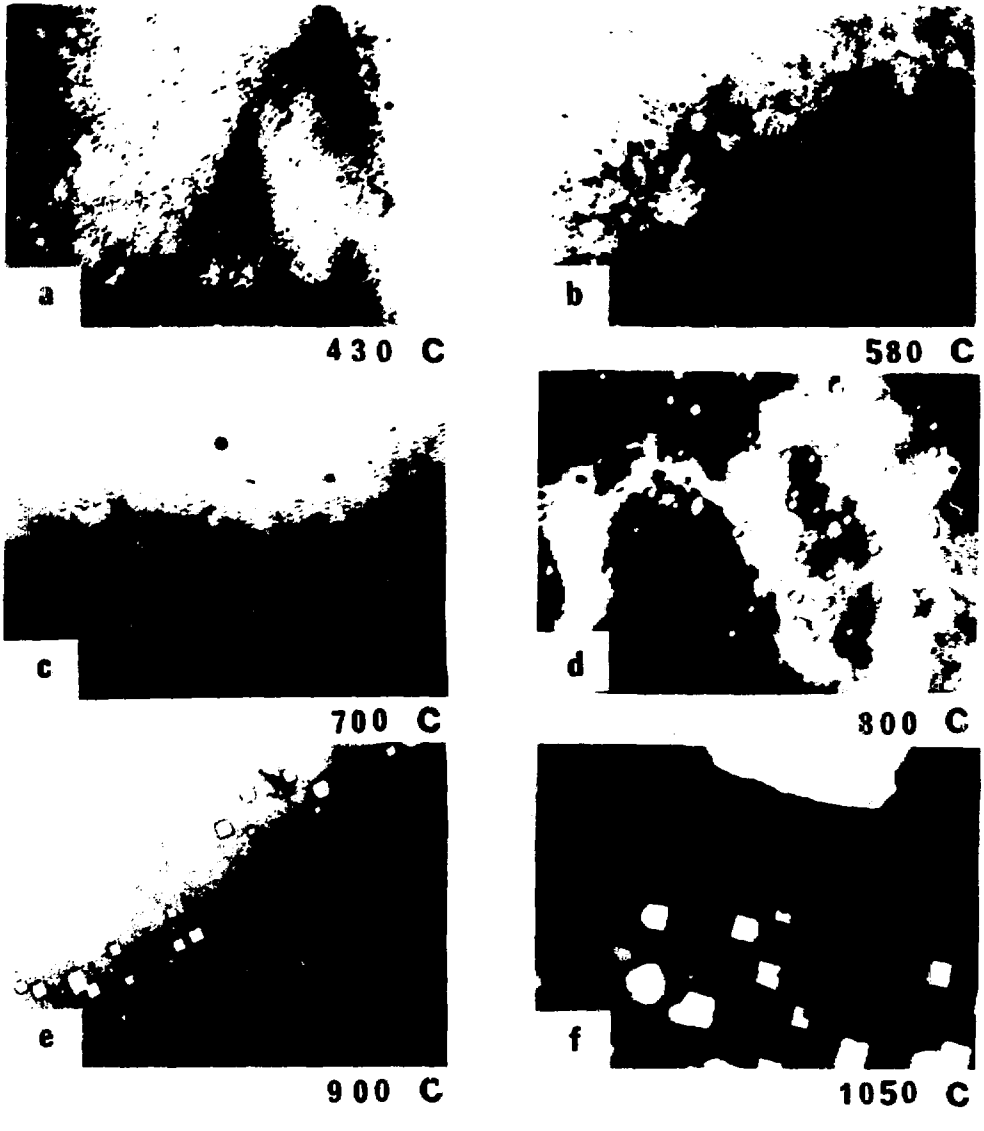

Fig. 1. Microstructures of Nb Irradiated to a Fast Neutron Fluence of 1 x 10^{22} n cm^{-2} (E > 1MeV).

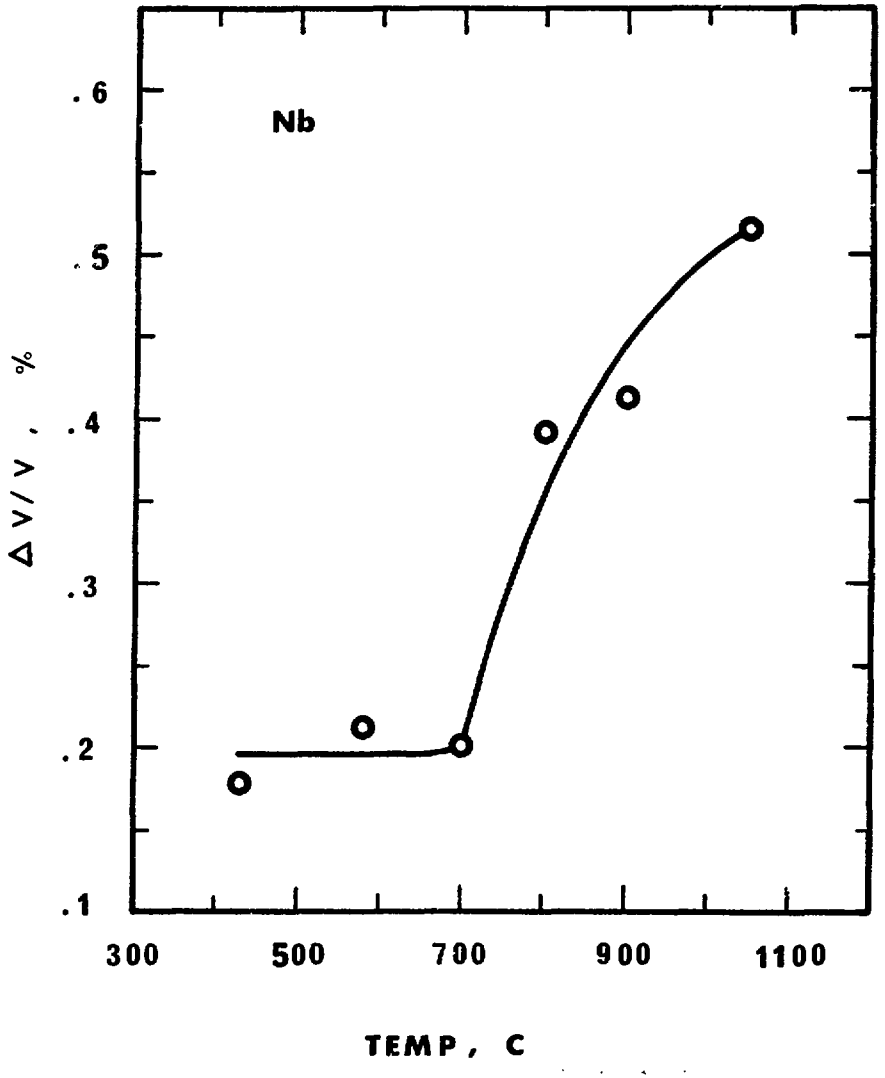

Fig. 2. Void Volume Fraction of the Neutron Irradiated Nb Specimens as a Function of Irradiation Temperature.

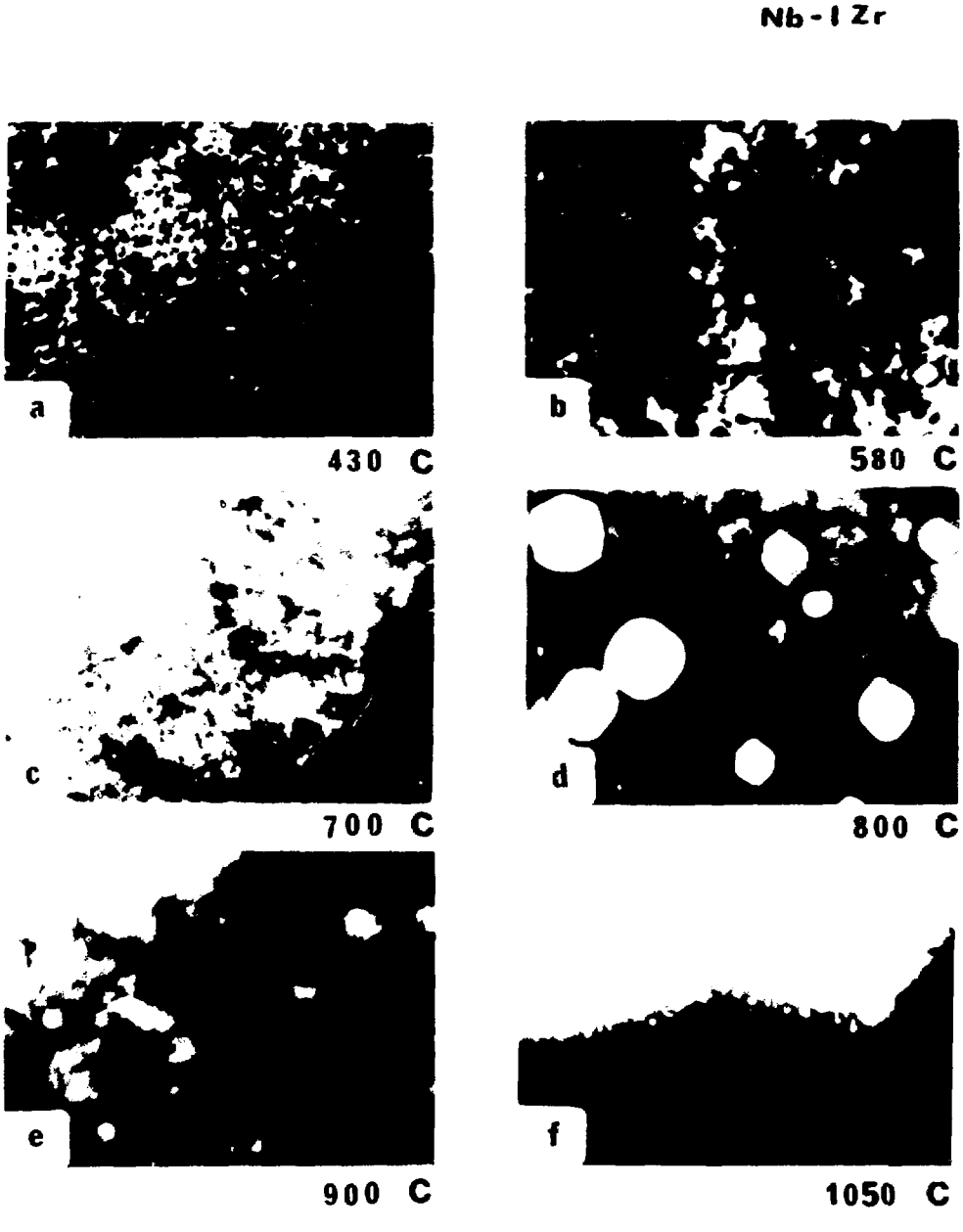

Fig. 3. Microstructures of Nb-1Zr Irradiated to a Fast Neutron Fluence of 1 x 10^{22} n cm^{-2} (E > 1MeV).

which are presumably small dislocation loops. At 430°C only a few isolated voids have been observed, and at 580°C voids have been observed in one certain area. The specimen irradiated at 700°C contains a low density of voids which are uniformly distributed throughout the grains. At the irradiation temperature of 800°C, the voids are randomly distributed throughout the specimen and no void ordering has been detected. Compared with the Nb specimen irradiated at the same irradiation temperature, the void concentration in the Nb-1Zr specimen is about one order of magnitude smaller, but the void size is bigger by a factor of three. In the specimen irradiated at 900°C, voids are non-uniformly distributed and the void size is smaller than those in the 800°C specimen. The specimen irradiated at 1050°C shows several areas characterized by high concentrations of small voids. Fig. 4 shows the void volume fraction of the Nb-1Zr specimens as a function of irradiation temperature. The swelling curve is a narrow bell shape with the maximum swelling of $\sim$ 2%, which occurs at 800°C. The swelling values at the irradiation temperatures other than 800°C are very small. For the quantitative microstructural data of the present study it is urged to refer to a forthcoming paper[15].

DISCUSSION

An attempt was made to compare the theoretical model of temperature dependent swelling proposed by Brailsford and Bullough[16] with the data obtained in the present study. The equation for the void swelling is given as:

$$\frac{\Delta V}{V} \% = S\ K\ (t-t_o)\ F(\eta)$$

where

$$F(\eta) = \frac{2}{\eta}\left[\left\{1+\eta\right\}^{1/2} - 1 - \frac{1}{2}\eta\ \exp\left\{\frac{-Q}{k}\left(\frac{1}{T} - \frac{1}{T_f}\right)\right\}\right]$$

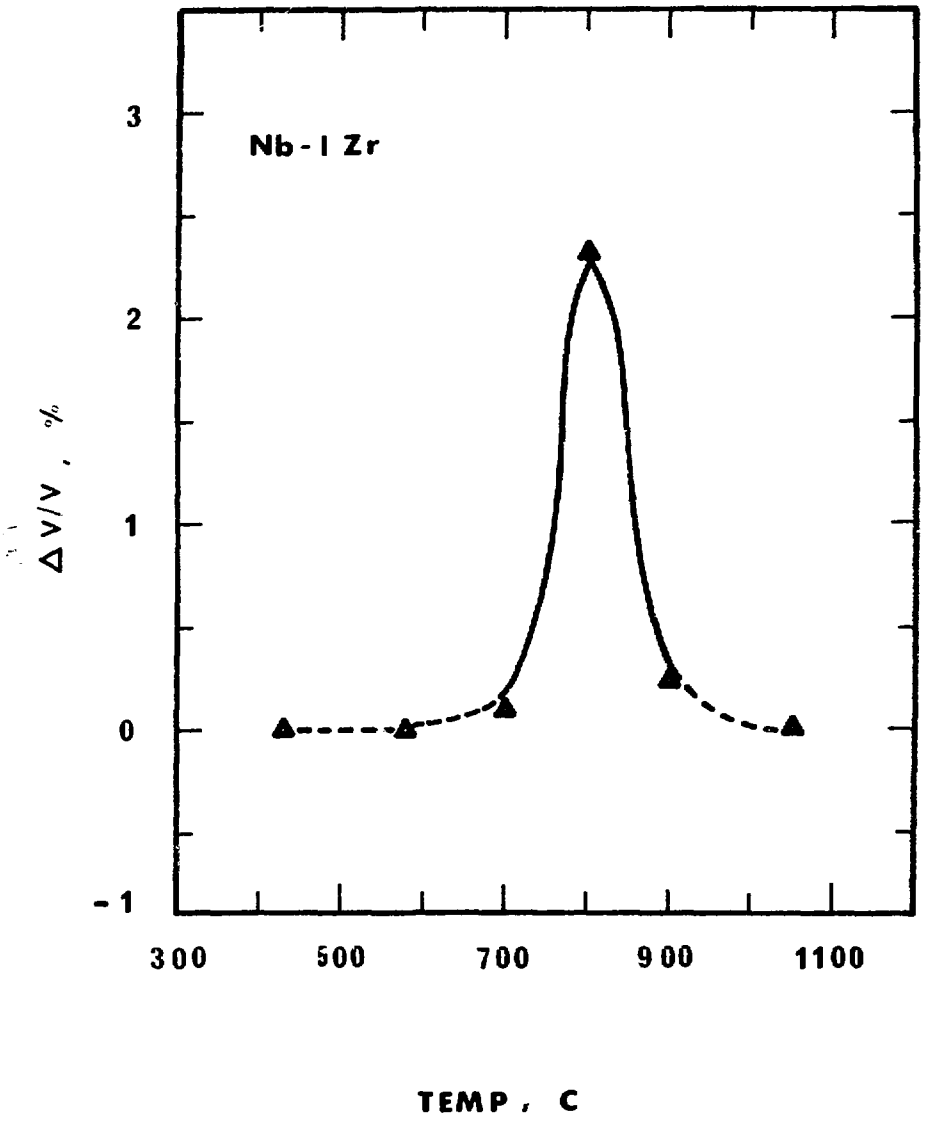

Fig. 4. Void Volume Fraction of the Neutron Irradiated Nb-1Zr Specimens as a Function of Irradiation Temperature.

$$\eta = 400 \exp\left[-\frac{E_m^v}{k}\left(\frac{1}{T_s} - \frac{1}{T}\right)\right]$$

$$S = \rho_d 4\pi r_s c_s \Big/ \left[\left(\rho_d + 4\pi r_s c_s\right)\left(\rho_d + 4\pi r_s c_s + 4\pi r_2 c_2\right)\right]$$

The definitions of the symbols used in the above equations are given in the original paper[16]. $F(\eta)$ was calculated for both Nb and Nb-1Zr using $Q = 4.06$ eV and $E_m^v = 0.68$ eV[17], and the values of T_s and T_f were estimated, based on the experimental data, to be 400 and 1400°C, respectively. The defect sink term S was determined from the experimental data[15], and the calculated swelling values are plotted, together with the experimental swelling data, in Figs. 5 and 6 for Nb and Nb-1Zr, respectively. The model overestimates the swelling in neutron irradiated Nb by a factor of up to 10, especially at high irradiation temperatures. However, a reasonable agreement is shown in neutron irradiated Nb-1Zr alloy.

The void swelling data are compared with those obtained from the immersion density measurements[15] which were carried out on the identical specimens, and plotted in Figs. 7 and 8 for Nb and Nb-1Zr, respectively. Ideally the magnitude of the volume swelling calculated from TEM void parameters should coincide with that determined from immersion density measurements. The results of this study show, qualitatively, a reasonable agreement between these two approaches. Quantitatively, however, there are significant differences between them, presumably, for the following reasons: (1) defects, other than voids might exist and contribute to the volume change, e.g., coherent precipitates, and (2) a certain portion of the voids might be too small in size to be observed under TEM.

The neutron data of the present study are compared with

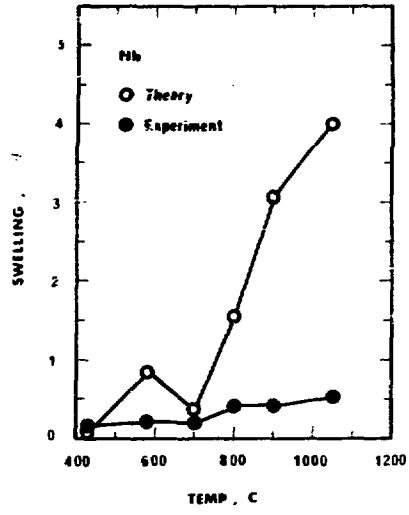

Fig. 5. Comparison Between Experimental Swelling Data and Calculated Swelling Values of Neutron Irradiated Nb.

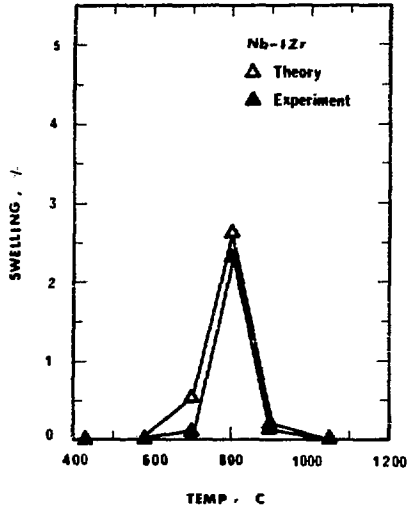

Fig. 6. Comparison Between Experimental Swelling Data and Calculated Swelling Values of Neutron Irradiated Nb-1Zr Alloy.

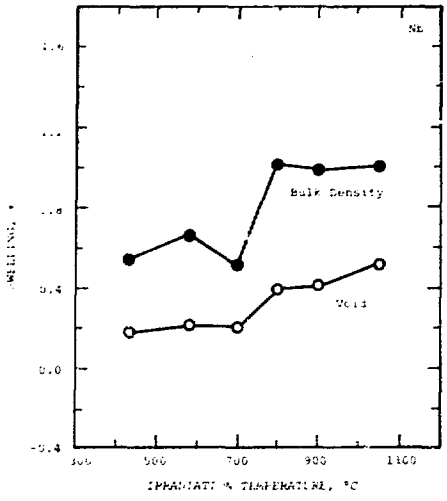

Fig. 7. Swelling Data of Neutron Irradiated Nb Determined From TEM and From Immersion Density Measurements.

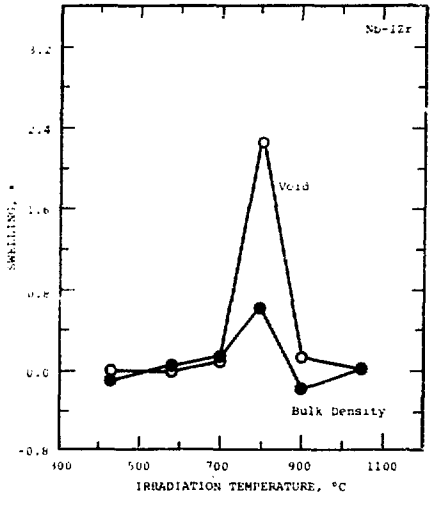

Fig. 8. Swelling Data of Neutron Irradiated Nb-1Zr Determined from TEM and From Immersion Density Measurements.

the ion data available in the literature[12], as shown in Figs. 9 and 10 for Nb and Nb-1Zr, respectively. The ion data[12] have been adjusted to a damage dose of 21 dpa by use of the linear dose dependence relationship of the void swelling, as given by Brimhall and Kulcinski[10]. Also the shift in the effective irradiation temperature was taken into account using the relationship given by Bullough and Perrin[18].

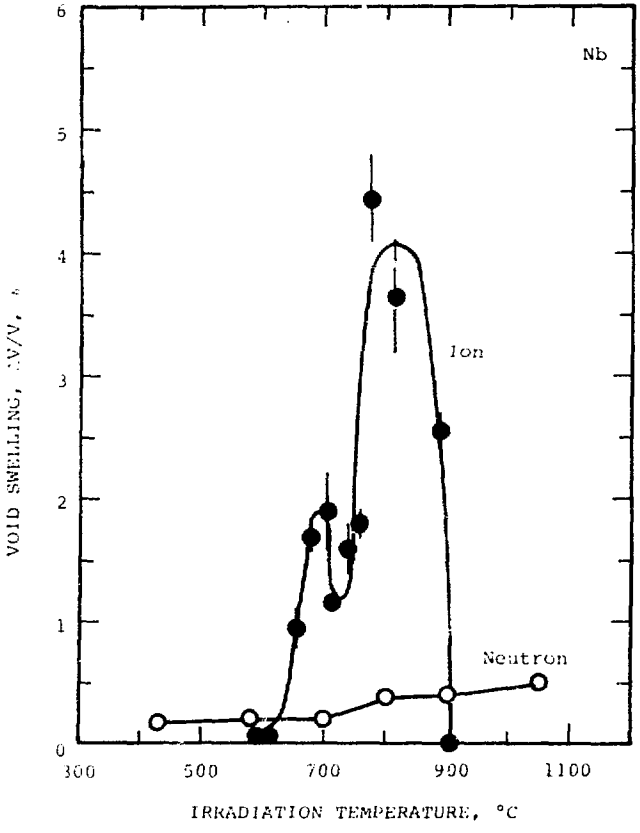

Fig. 9. Void Swelling of Neutron Irradiated and Ni^+ Ion Bombarded Nb.

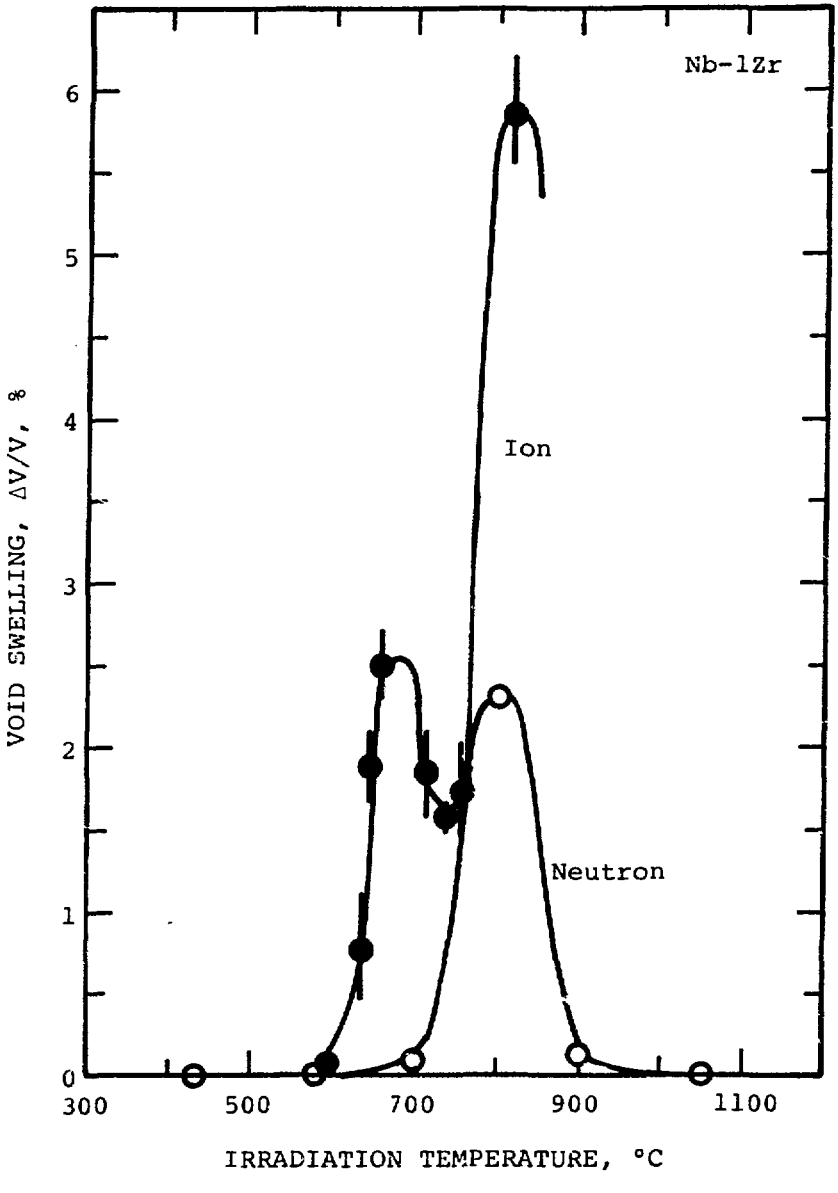

Fig. 10. Void Swelling of Neutron Irradiated and Ni^+ Ion Bombarded Nb-1Zr.

SUMMARY

(1). Voids are formed in Nb and Nb-1Zr irradiated to a fast neutron fluence of 1 x 10^{22} n cm^{-2} at temperatures between 430 and 1050°C.

(2). The maximum swellings occur at 1050°C in Nb and 800°C in Nb-1Zr.

(3). An addition of 1% Zr decreases the void swelling of Nb at the irradiation temperatures other than 800°C.

(4). A void superlattice is formed in the Nb specimen irradiated at 800°C, and the calculated superlattice parameter is 685 Å.

ACKNOWLEDGMENTS

This work was supported by the U.S. Energy Research and Development Administration under contract No. AT(11-1)-2093.

REFERENCES

1. Elen, J. D., Proceedings, Voids Formed by Irradiation of Reactor Materials, p. 51, BNES, Reading, U.K., 1971.
2. Elen, J. D., Hamburg, G. and Mastenbroek, A., J. of Nuclear Materials, 39, 194, 1971.
3. Adda, Y., Proceedings, Radiation-Induced Voids in Metals, p. 31, Albany, New York , 1971.
4. Wiffen, F. W., Proceedings, Radiation-Induced Voids in Metals, p. 386, Albany, New York, 1971.
5. Wiffen, F. W., Proceedings, Defects and Defect Clusters in BCC Metals and Their Alloys, p. 176, NBS, Gaithersburg, Maryland, 1973.
6. Michel, D. J. and Moteff, J., to be published in Radiation Effects.

7. Kulcinski, G. L., Brimhall, J.L., Trans. ANS, 14, 604, 1971.
8. Kulcinski, G. L., Brimhall, J.L., Proceedings, Defects in Refractory Metals, p. 291, Mol, Belgium, 1972.
9. Kulcinski, G. L., Brimhall, J. L., and Kissinger, H. E., Proceedings, Radiation-Induced Voids in Metals, p. 449 Albany, New York ,1971.
10. Brimhall, J. L., and Kulcinski, G. L., Radiation Effects, 20, 25, 1973.
11. Loomis, B. A.,Taylor, A. T., Klippert, T. E., and Gerber, S. B., Proceedings, Defects and Defect Clusters in BCC Metals and Their Alloys, p. 332, NBS, Gaithersburg, Maryland, 1973.
12. Loomis, B. A. Taylor, A., and Gerber, S. B., J. of Nuclear Materials, 56, 25, 1975.
13. Kamphouse, J. L., Stuart, R. L. and Moteff, J., J. of Nuclear Materials, 39, 1, 1971.
14. Sikka, V. K., Michel, D. J., and Moteff, J., J. Less-Common Metals, 31, 31, 1973.
15. Jang, H. and Moteff, J., to be published.
16. Brailsford, A. D. and Bullough, R., J. of Nuclear Materials, 44, 121, 1972.
17. Kothe, A., Proceedings, Defects in Refractory Metals, p. 125, Mol. Belgium, 1972.
18. Bullough, R. and Perrin, R. C., ASTM-STP-484, p. 317, 1970.

HIGH TEMPERATURE IRRADIATION DAMAGE STRUCTURES IN FAST REACTOR IRRADIATED NIOBIUM AND VANADIUM ALLOYS

A.F. Bartlett, J.H. Evans, B.L. Eyre, E.A. Terry and T.M. Williams
Metallurgy Division, A.E.R.E., Harwell, Didcot, Oxon., England.

ABSTRACT

The void swelling behaviour of commercial purity niobium and vanadium samples have been examined after irradiation to a dose of 3.6 x 10^{22} n/cm^2 in the Dounreay Fast Reactor at 450, 550 and 600°C. In addition the irradiation programme included samples of Niobium 5% Zirconium, Niobium 10% Zirconium, zone refined vanadium and V-15%Cr-5%Ti. The irradiated void and dislocation structures were examined using transmission electron microscopy. The most important general result was that in the alloys examined the void swelling was negligible. In the purer specimens there was a marked effect of temperature on void concentration and size but the overall effect on void swelling was small.

INTRODUCTION

The problem of void swelling in materials subject to high neutron doses at high temperatures has already been well documented in relation to Fast Breeder Reactors[1,2,3]. In the Fusion reactor the same effects could be expected with the added disadvantage that the 14 MeV peaked neutron spectrum will give considerably more displacement damage per neutron compared with the fast breeder neutron environment[4,5]. In addition, the increased production of helium from (n,α) reactors could affect the nucleation and growth of voids. Nevertheless, the behaviour of materials in Fast Breeder Reactors is one of the guides at present available to assess the comparative resistance or otherwise of fusion reactor metals and alloys to void swelling. This paper reports some initial results on Niobium and Vanadium and some alloys following neutron irradiation in the Dounreay Fast Reactor (D.F.R.).

EXPERIMENTAL DETAILS

The vanadium and niobium together with their alloys were produced as strip from which 3 mm discs were trepanned by spark-erosion. The discs were then heat-treated as indicated in Table 1. After heat-treatment the

TABLE 1. Specimen Heat Treatments

Material	Heat Treatment
Nb	1 hour at 1600°C in vacuo
Nb 5%Zr	1 hour at 1600°C in vacuo
Nb 10%Zr	1 hour at 1600°C in vacuo
V (6PZR)	1 hour at 800°C in vacuo
V (Commercial)	1 hour at 800°C in vacuo
V 15%Cr 5%Ti	1 hour at 1500°C in vacuo

discs were packed in molybdenum cans with molybdenum powder to ensure good heat transfer prior to being irradiated in the Dounreay Fast Reactor. Three temperatures were used, nominally 450, 550 and 600°C and the irradiations made to a dose of 3.6×10^{22} fast neutrons/cm^2. After irradiation specimens were electropolished to perforation and examined in a Philips EM 300 electron microscope operated at 100 KeV.

RESULTS

Vanadium

The main quantitative results available at present for the six-pass zone refined vanadium and the commercial vanadium are given in Table 2. The overall increase in void diameter and decrease in void density with the rise in irradiation temperature is very clear. In the high purity vanadium there is a tendency for the void swelling to increase with temperature but in the commercial material it is comparatively stable. However, in both materials, particularly at 550 and 600°C, the void size and concentration varied considerably from grain to grain so that it was

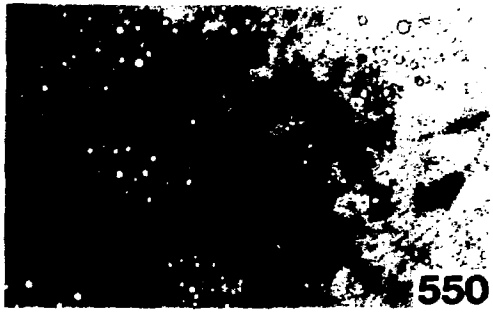

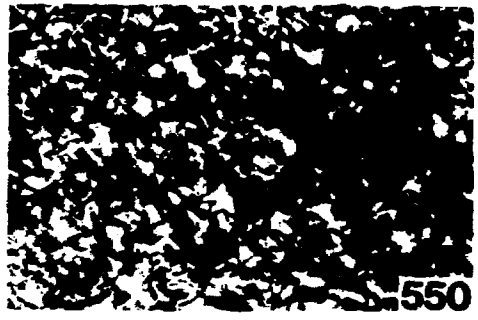

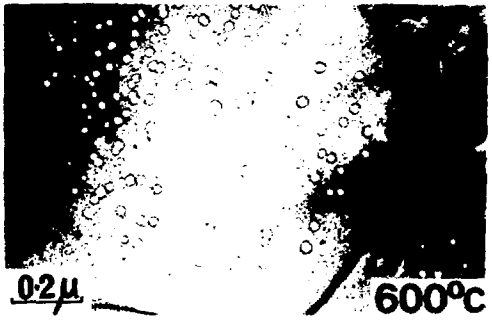

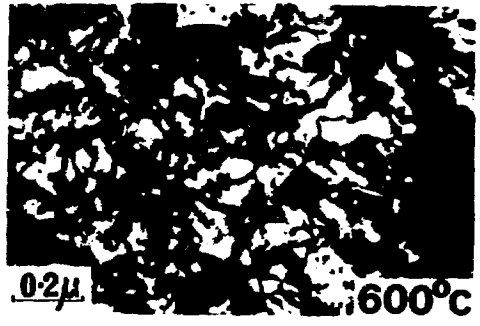

Fig. 1. Void structures in commercial vanadium after irradiation to a dose of 3.6×10^{22} n/cm^2 in DFR at 450, 550 and 600°C.

Fig. 2. Dislocation structures in V15%Cr 5%Ti after irradiation to a dose of 3.6×10^{22} n/cm^2 in DFR at 450, 550 and 600°C.

difficult to make measurements of the void parameters with high accuracy. Typical void structures for the commercial vanadium are shown in Fig. 1 where some of the inhomogeneities can be seen even within single grains. In addition, there were marked denuded zones at the grain boundaries, this effect being emphasised by the small grain sizes (between 0.5 and 0.8 microns) in the two materials.

TABLE 2. Measured Void Parameters in Vanadium

Material	Irradiation Temperature	Average Void Diameter	Void Concentration	Void Swelling
6 PZR V	450°C	60 Å	$1.35 \times 10^{16}/cm^3$	0.2%
6 PZR V	550°C	213 Å	$1.25 \times 10^{15}/cm^3$	0.6%
6 PZR V	600°C	258 Å	$9.4 \times 10^{14}/cm^3$	0.8%
Commercial V	450°C	110 Å	$1.06 \times 10^{16}/cm^3$	0.7%
Commercial V	550°C	224 Å	$1.6 \times 10^{15}/cm^3$	0.9%
Commercial V	600°C	291 Å	$3.2 \times 10^{14}/cm^3$	0.4%

In contrast to the pure and commercial vanadium the vanadium alloy, V 15%Cr 5%Ti, showed zero voidage at the three irradiation temperatures (though isolated voids were seen at 550°C). Instead the irradiated substructure was characterised by the very high dislocation content, as shown in Fig. 2. As the irradiation temperature is increased there is some coarsening of the dislocations but otherwise the structure appears to be rather stable.

Niobium

All the specimens of 1600°C heat treated niobium contained a fairly uniform distribution of voids, (Fig. 3). Mean void sizes increased and void number densities decreased with increasing irradiation temperature, (Fig. 4). Both parameters were extremely sensitive to temperature, but the changes in void size were matched by the changes in void numbers, resulting in void swelling values which, over this temperature range, were approximately constant at ~2.8%. Void ordering was not observed in any of the specimens examined.

The dislocation structure consisted almost entirely of loose tangles (e.g. Fig. 5(a)) and the dislocation density decreased from $.5 \times 10^{10}$ lines/cm^2 at 450°C to 2×10^{10} lines/cm^2 at 600°C.

In addition to voids and dislocations, the irradiated specimens also contained precipitates identified as NbC. The precipitates were either coarse (resulting in incomplete solution of carbon during pre-irradiation heat treatment at 1600°C) or relatively fine, resulting from the solubility

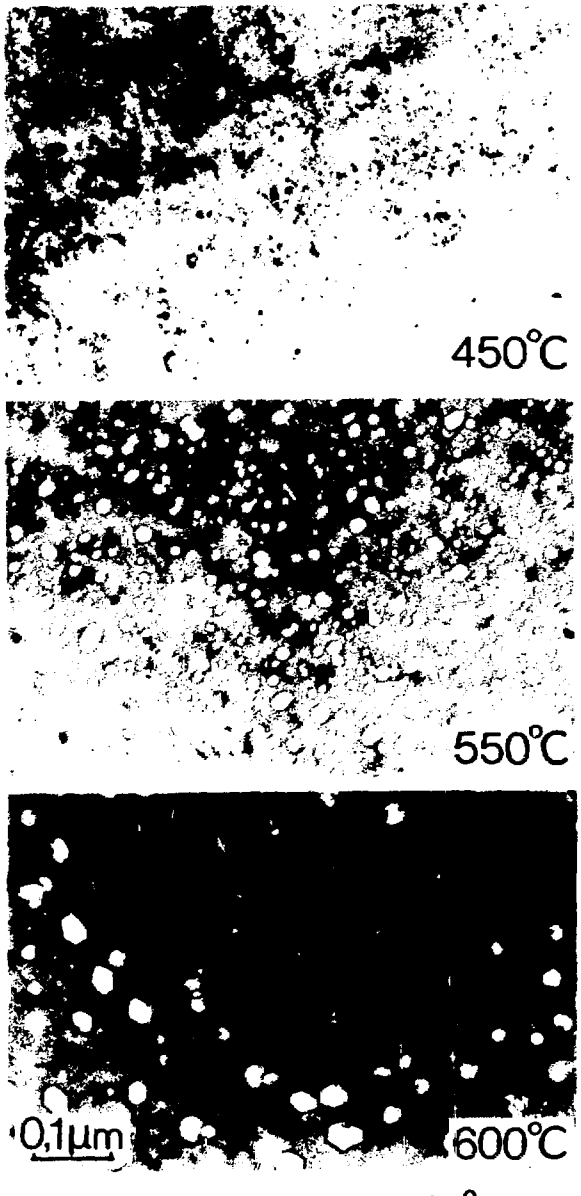

Fig. 3. Void distribution in 1600°C heat treated commercial niobium irradiated to 3.6 x 10^{22} fast neutrons/cm^2.

of carbon being exceeded at the temperatures of irradiation. This behaviour is consistent with recently published data on the solubility of carbon in niobium[6].

The irradiated Nb-Zr alloys contained either very few voids (at 550°C and 600°C) or a complete absence of voids (at 450°C). In no case was the void swelling greater than 0.05%. In this respect there was no consistent difference between the two alloys.

Unlike the niobium specimens, the irradiated alloys contained both dislocation loops and tangles, which were unevenly distributed, (Fig. 5(b)).

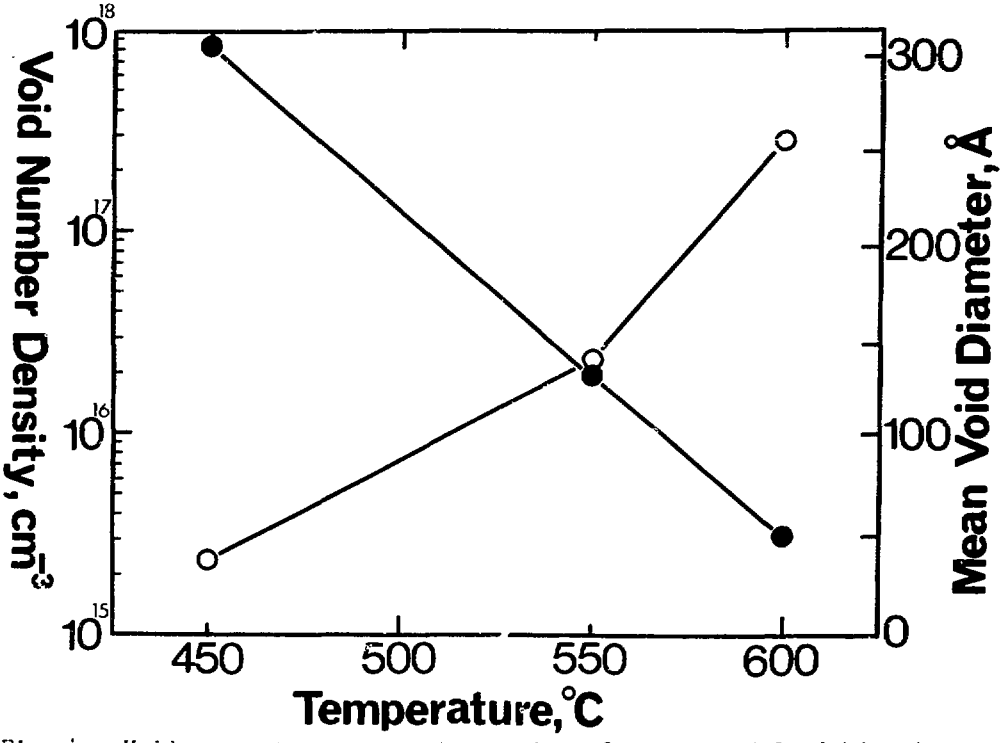

Fig. 4. Void parameters versus temperature for commercial niobium irradiated to 3.6 x 10^{22} fast neutrons/cm^2.

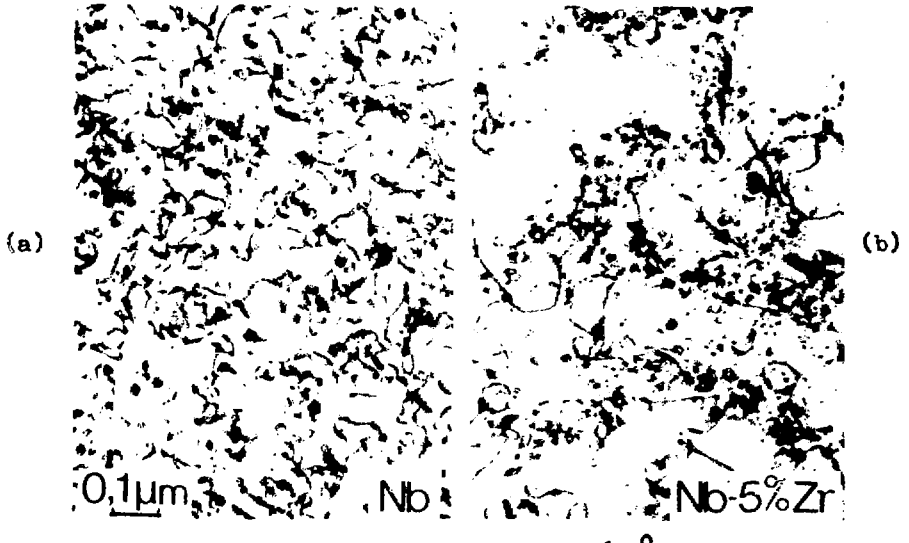

Fig. 5. Dislocation distributions in 1600°C heat treated commercial niobium and niobium - 5% zirconium irradiated to 3.6 x 10^{22} fast neutrons/cm^2 at 600°C.

DISCUSSION

The most important general result in this work is the large effect of alloying on the suppression of void swelling. As already stated, the swelling was negligible in the V15%Cr 5%Ti alloy and in the two Niobium Zirconium alloys over the temperature range studied. It is worth noting that for vanadium the 450-600°C temperature range is 0.35 - 0.41 Tm while for niobium the equivalent figures are 0.27 to 0.32 Tm. It is not clear by what mechanism the swelling is suppressed; the high dislocation densities in the alloys could be an important factor but the suppression could also be related to the high solid solubilities of niobium and vanadium for oxygen, nitrogen and carbon. The affinity of these elements for titanium and zirconium would cause a large drop in their effective concentrations and could therefore suppress void nucleation. (The presence of oxygen and nitrogen, which are surface active, can lower the surface energy and hence normally aid nucleation by minimising the probability of void shrinkage by thermal evaporation). A third possibility is the enhancement of recombination due to the presence of substitutional solute atoms.

The results on vanadium agree very closely with the work of Carlander et al[7] and Wiffen[2] who looked at a variety of vanadium alloys containing chromium and titanium and irradiated to the same dose and temperature range as in the present work. In all cases the alloys show negligible swelling and this clearly appears to be a result of technological importance. Adda[9] and Allen et al[10] have the same results on vanadium alloys but at neutron doses more than an order of magnitude lower.

Wiffen[3] and Michel and Moteff[11] have published data on niobium and niobium - 1% zirconium alloys irradiated to similar fast neutron doses as those employed here. Though the swelling values reported are considerably lower than those reported in the present paper, Michel shows that (a) the void swelling does not vary significantly with temperature between 425°C and 790°C in commercial purity niobium and (b) the addition of 1% zirconium reduces the void swelling to zero at temperatures up to at least 585°C, but results in a considerable increase at 790°C. Wiffen finds the swelling in commercial purity niobium and niobium-1% zirconium approximately equal at 790°C

Thus the trends indicated in the present work are at least in qualitative agreement with the work of Michel and Wiffen where the irradiation temperature ranges overlap, though the absolute swelling values reported here for commercial purity niobium are significantly higher.

The very marked temperature dependence of void numbers and mean sizes described here were not observed by Michel. It is possible that compositional differences between the casts of "commercial purity" niobium used in the investigations could give rise to the observed differences in void nucleation behaviour.

It thus appears that the addition of only 1% zirconium to niobium dramatically increases its resistance to void swelling at least up to ~600°C, and the void resistance is then maintained with increasing zirconium additions, at least up to 10% zirconium.

REFERENCES

1. Proceedings of the Reading Void Conference, March 1971 (Eds. S.F. Pugh, M.H. Loretto and D.I.R. Norris) British Nuclear Energy Society (1972).
2. Proceedings of the Conference on Radiation Induced Voids in Metals, Albany 1971 (Eds. J.W. Corbett and I.C. Ianniello) U.S.A.E.C. (1972).
3. Consultants Symposium, The Physics of Irradiation Produced Voids, Harwell September 1974. A.E.R.E. Report 7934.
4. J.B. Mitchell, C.M. Logan and C.J. Echer, J. Nuclear Materials, 48, 139, (1973).
5. K.L. Merkle, Nuclear Technology, 22, 66, (1974).
6. G. Horz, K. Lindenmaier and R. Klaiss, J. Less Common Metals, 35, 97, (1974).
7. R. Carlander, S.D. Harkness and A.T. Santhanam, Effects of Radiation on Substructure and Mechanical Properties of Metals and Alloys, ASTM-STP 529, American Society for Testing and Materials, (1973).
7. F.W. Wiffen, Reference 2, pg 386.
9. Y. Adda, Reference 2, pg 31.
10. J.D. Elen, G. Hamburg and A. Mastenbroek, J. Nucl. Mat., 39, 194,(1971).
11. D.J. Michel and J. Moteff, Rad. Effects,21, 235, (1974).

ION SIMULATION STUDY OF VOID FORMATION IN HIGH PURITY VANADIUM

W. J. Weber, G. L. Kulcinski, R. G. Lott, P. Wilkes, and H. V. Smith, Jr.
Nuclear Engineering Department
University of Wisconsin
Madison, Wisconsin 53706

ABSTRACT

Ion simulation techniques were used to study the characteristics of void formation in high purity vanadium bombarded with 18 MeV Cu ions. The samples were vacuum annealed at 1050°C (<5 x 10^{-8}Torr) and irradiated at temperatures from 600 to 750°C (<1 x 10^{-8}Torr) to damage levels ranging from 1 to 5 dpa. The damage rate was 3 x 10^{-4} dpa/sec in the analyzed region, approximately one micron from the front surface. The damage structure consisted of voids (<5 x 10^{14}cm^{-3}) and precipitates at low densities, dislocation loops, and dislocation networks. The precipitates were analyzed to be face-centered cubic vanadium-carbide (VC) by Auger and electron diffraction analysis. The degree of precipitation was found to depend on sample surface preparation. A description of void morphology, precipitate morphology, grain boundary denuding, and the temperature dependence of void size, shape, density and subsequent swelling is given.

INTRODUCTION

Vanadium and vanadium-base alloys are among the refractory metals considered for use as first wall material in controlled thermonuclear reactors (CTR's). The first wall of a CTR will experience high 14 MeV neutron fluxes which produce atomic displacements that can cause changes in microstructure during the irradiation. At CTR operating temperatures, these microstructural changes in the form of voids, dislocation loops and enhanced precipitation produce dimensional and mechanical property changes which may greatly affect the lifetime of the first wall and the success of the CTR as a potential energy source.

Studies of void formation in neutron irradiated vanadium are severely limited by the long irradiation times required in presently available fast reactors and the difficulty in controlling the irradiation environment. Current data[1-5] on void formation in neutron irradiated vanadium comes

from relatively low fluence studies ($<10^{22}$ n/cm^2) and is not sufficient to predict first wall lifetimes. For this reason charged-particle irradiations, with their high damage rates, are used to study void formation in potential reactor materials. Charged-particle simulation also has an advantage over reactor irradiations in that the irradiation environment is more easily controlled. This is important because of the high solubility of interstitial impurities, such as oxygen, nitrogen, and carbon, in vanadium.

Previous investigations[6-9] using charged-particles have already provided some information on vanadium. In the investigations at Battelle-Pacific Northwest Laboratory, 7.5 MeV tantalum ions were used[6], while the studies at Argonne National Laboratory were carried out with 3.25 MeV nickel[7,8] and 3.0 MeV vanadium[9] ions. In the present work, 18 MeV copper ions were employed.

EXPERIMENTAL METHODS

The high purity vanadium used in this study was obtained in sheet form from Oak Ridge National Laboratory.[10] The substitutional impurity content of the vanadium was less than 10 wt- ppm and the interstitial impurity content is given in Table 1. The carbon content of the foil was independently verified by the McDonnell-Douglas Corp.[11]

Table 1
Interstitial Impurity Level in Vanadium

Interstitial Impurity	Amount (wt-ppm)
O	48
C	50
N	71
H	3

Samples were irradiated in the form of a specially machined strip. Prior to annealing, the foil strip was cleaned and electropolished to remove approximately 25 microns from the surface thereby eliminating any surface contamination from rolling. The foil was washed

in absolute methyl alcohol and then placed in the irradiation target chamber where it was given a full recrystallization anneal at 1050°C for 1 hour in a vacuum of less than 5×10^{-8} Torr (total). The residual gas content was monitored at intervals during the anneal and, as shown in Figure 1, the main residual gases present during annealing were hydrogen (46%), carbon monoxide (40%) and water (11%). After annealing, the samples either remained in the target chamber under vacuum until they were irradiated or were taken out and electropolished again to remove a 25 micron surface layer before being placed back into the target chamber for irradiation. The target chamber, irradiation facility, and sample geometry have been described previously.[12]

The samples were irradiated with 18 MeV Cu ions at temperatures between 600 and 750°C to damage levels from 1 to 5 dpa. The residual gas content was again monitored at intervals during the irradiations. The main components of the residual gas were H_2, (81%) and H_2O (8%), but CO and CH_4 (methane) were still present with partial pressures of $\sim 3 \times 10^{-10}$ Torr (see Figure 1). The total pressure was $\sim 7 \times 10^{-9}$ Torr at 750°C and $\sim 3 \times 10^{-9}$ Torr at 600°C (the partial pressures of the residual gases dropped correspondingly). The samples were heated by means of a radiation furnace and the temperature was measured by two chromel-alumel thermocouples attached to the Ta holder. The ion-beam intensity at each specimen location was determined before, at intervals during, and after the irradiations as described in Ref. 12. The damage energy deposition as a function of depth was determined using the E-DEP-1 code of Manning and Mueller[13] and a threshold displacement energy of 26 eV.[14] The calculated displacement damage as a function of depth for 18 MeV Cu ions incident on V is shown in Figure 2; also shown is the range distribution of the Cu atoms. The dpa rate was typically 3×10^{-4} dpa/sec in the analyzed region, 0.8 to 1.8 microns from the front surface (see Figure 2).

Before the irradiated samples were prepared for transmission electron microscopy (TEM), the irradiated surface was electropolished to expose the damage at a predetermined depth. This depth was measured with a precision of 500 Å using an interference microscope. The damage analyzed was never outside the region 0.8 to 1.8 microns from the surface.

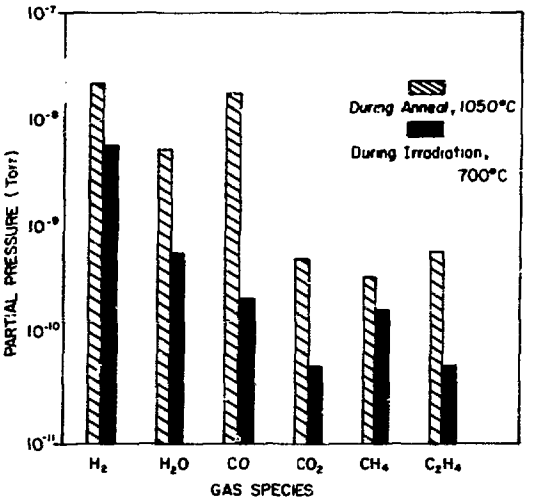

Fig. 1. Partial Pressure Analysis of the Sample Chamber Environment During the Annealing and Subsequent Irradiation of a Vanadium Sample.

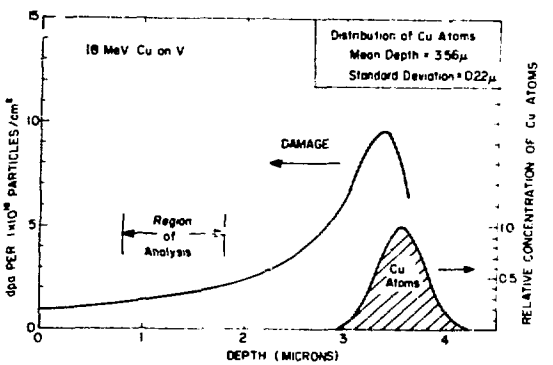

Fig. 2. Depth Distribution of Damage and Copper Atoms with 18 MeV Cu Ions Incident on Vanadium.

In this way the effect of the surface, the damage gradient, and the Cu atoms may be neglected. After the surface layer was removed, the 3 mm diameter irradiated areas were cut from the foil and the discs back-polished for TEM analysis using a single-jet electropolisher. In addition to TEM analysis, several irradiated samples were Auger analyzed to determine precipitate composition.

EXPERIMENTAL RESULTS

The main microstructural change observed was the formation of voids and precipitates in the irradiated samples (Figure 3). Both samples shown in Figure 3 were given the same anneal under identical vacuum conditions and followed the same thermal cycle during the irradiations. The sample in Figure 3a was left unirradiated whereas the sample in Figure 3b was irradiated to 1 dpa. Both samples were examined at a depth of 1.5 microns from the surface.

Significant precipitation was discovered in the irradiated specimen while no precipitates were found in the unirradiated area next to the bombarded region. The precipitates were identified through Auger and electron diffraction analysis. The Auger analysis indicated that the precipitates were carbides, but quantitative measurement of the carbon concentration was not possible. It was clear from the electron diffraction analysis that the precipitates did not contain copper. The crystal structure determined from the electron diffraction patterns was, however, consistent with face-centered cubic vanadium-carbide (VC). The orientation relationship of the precipitates was

$$(001)_V \uparrow\uparrow (001)_{VC}$$

$$[110]_V \uparrow\uparrow [100]_{VC} .$$

The precipitates usually formed as rods with their axis in the $\langle 110 \rangle_V$ direction. At this orientation, the precipitate and the matrix matched to within 3% in the (001) plane and have a misfit of 31% normal to this plane. Because of the good fit in the (001) planes, the precipitates will initially form coherently, but later become incoherent as evidenced by the high dislocation density around precipitates (Figures 4, 9, 10). In Figure 4, a bright field-dark field pair of micrographs and selected

(a)

Unirradiated

(b)

Irradiated at 600° C to 1 dpa

Fig. 3. Microstructure of Vanadium Samples with Identical Thermal Histories. The Irradiated Sample has Precipitates and Voids as a Result of the Irradiation.

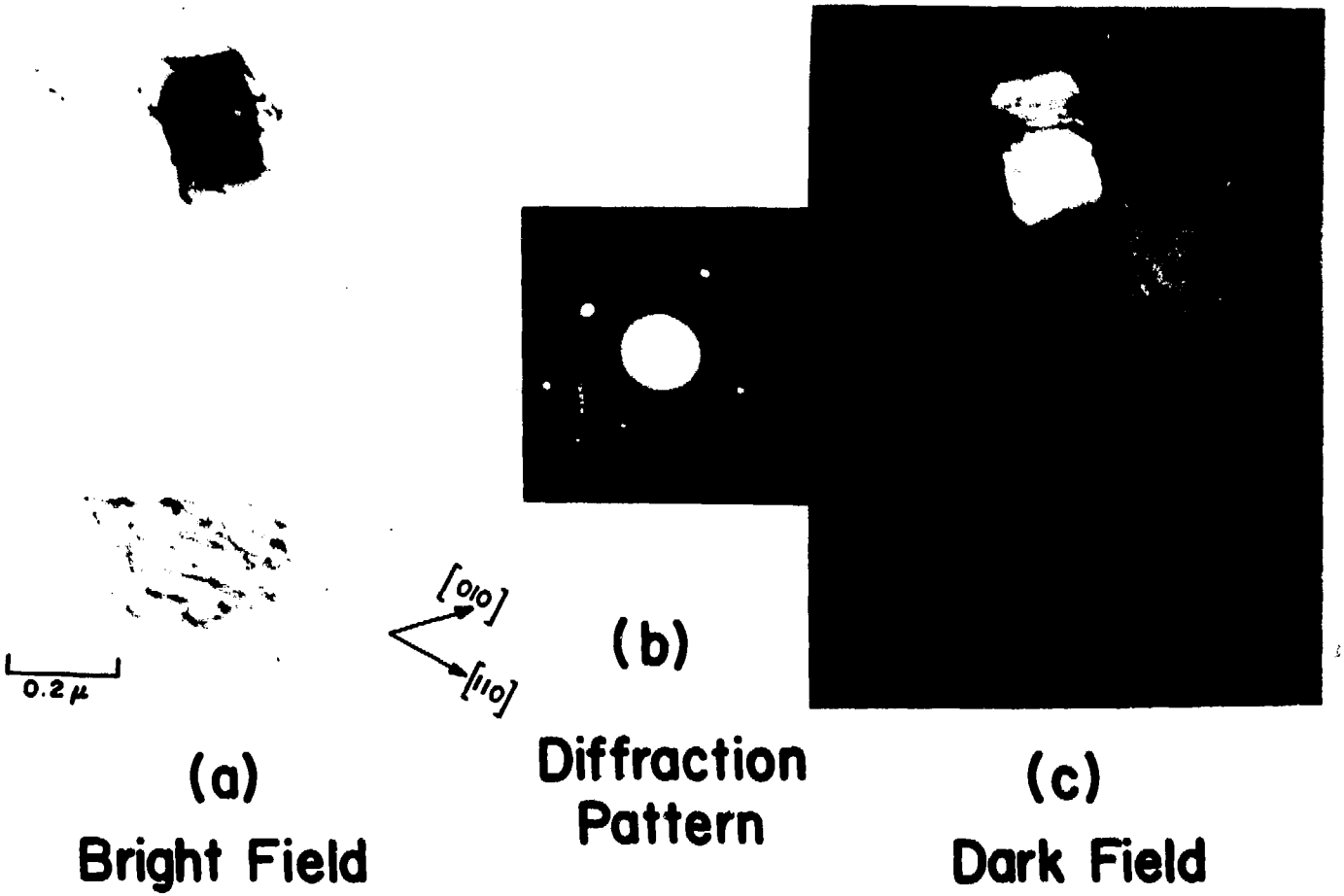

Fig. 4. Bright and Dark Field Image of Vanadium-Carbide (VC) Precipitate. The Diffraction Pattern Shows the Extra Reflections from the Precipitate.

area diffraction pattern are shown. The extra reflections in the pattern are from the precipitate shown in the figure and from precipitates in adjacent areas at different orientations.

Other microstructural features observed included void and precipitate clustering, void and precipitate denuding around grain boundaries, dislocation loops, dislocation networks, and dislocation punching. Table 2 summarizes the data for 18 MeV Cu ion irradiated vanadium. The dislocation density was less than 1×10^9 lines/cm^2 in all samples.

The estimated carbon contained in the precipitates, as indicated in Table 2, was reduced up to a factor of 50 from approximately 3500 to 60 wt-ppm as a result of removing the 25 micron surface layer after annealing and prior to irradiation. This reduced carbon contamination in the form of precipitates, and their effect on void formation, is illustrated in Figures 5 and 6.

Voids were observed at all temperatures (600-750°C), but the void distribution was noticeably more inhomogeneous at the higher temperatures. The voids were cubes with {100} faces, but some voids were truncated on either {111} or {110} planes. In the sample irradiated at 700°C with reduced precipitation, (Figure 6b), a small number of voids (~2%) were elongated with length to width ratios up to ten. The average void size increased with temperature as has been observed previously.[1-9] The average void size and the amount of precipitation decreased in the samples with reduced carbon contamination. This is evident in the micrographs of Figures 5 and 6. The shift to smaller void size as a result of removing the 25 micron surface layer is shown graphically in Figure 7. The average void size in the high and low carbon samples was 700 Å and 410 Å respectively at 700°C. It was reduced to 370 Å and 160 Å respectively at 650°C.

The peak swelling at approximately 1 dpa appeared to occur at 700°C which was in agreement with previous results.[7] The dislocation content of the samples irradiated at 700°C with different levels of carbon contamination is compared in Figures 8 and 9. The distribution of large precipitates and voids in the 700°C, 1 dpa specimen was rather inhomogeneous at times (Figure 9).

Table 2. Summary of Data for 18 MeV Cu Irradiated Vanadium

Temperature (°C)	dpa	Void Density (cm^{-3})	Average Void Size (Å)	ΔV/V (%)	Precipitate Density (cm^{-3})	Average Precipitate Volume ($Å^3$)	Estimated Carbon in Precipitates (wt-ppm)	Loop Density (cm^{-3})
600[d]	1	2.5×10^{14}	140	0.1	2×10^{14}	1×10^{8}	3500	4×10^{13}
	1.5	7×10^{13}	270	0.15	3×10^{14}	4×10^{7}	2000	4×10^{13}
650	1	1×10^{14}	370	0.5	2×10^{14}	4×10^{7}	1500	2×10^{13}
	2	1.5×10^{13}	750	0.5	7×10^{13}	4×10^{8}	5000	7×10^{12}
	5	5.5×10^{13}	760	2.5	8×10^{13}	4×10^{8}	6000	1×10^{12}
	1[a]	4×10^{14}	160	0.2	8×10^{14}	4×10^{5}	60	1×10^{13}
700	1	4.5×10^{13}	590	1.0	6×10^{13}	3×10^{8}	3500	$< 1 \times 10^{12}$
	1[c]	2×10^{13}	730	1.0	2×10^{13}[b]	1×10^{9}	3500	5×10^{13}
	3[c]	1.5×10^{12}	850	0.1	4×10^{12}[b]	4×10^{9}	3000	4×10^{13}
	1[a]	3×10^{14}	410	1.0	3×10^{14}	1×10^{6}	60	$< 1 \times 10^{12}$
750	1[c]	3×10^{11}	980	0.03	1×10^{12}[b]	3×10^{9}	600	2×10^{13}

a) These samples had a 25 μ surface layer removed after annealing.

b) These densities are only for the larger, more visible precipitates.

c) The voids and precipitates are inhomogeneously distributed in these samples.

d) Approximate

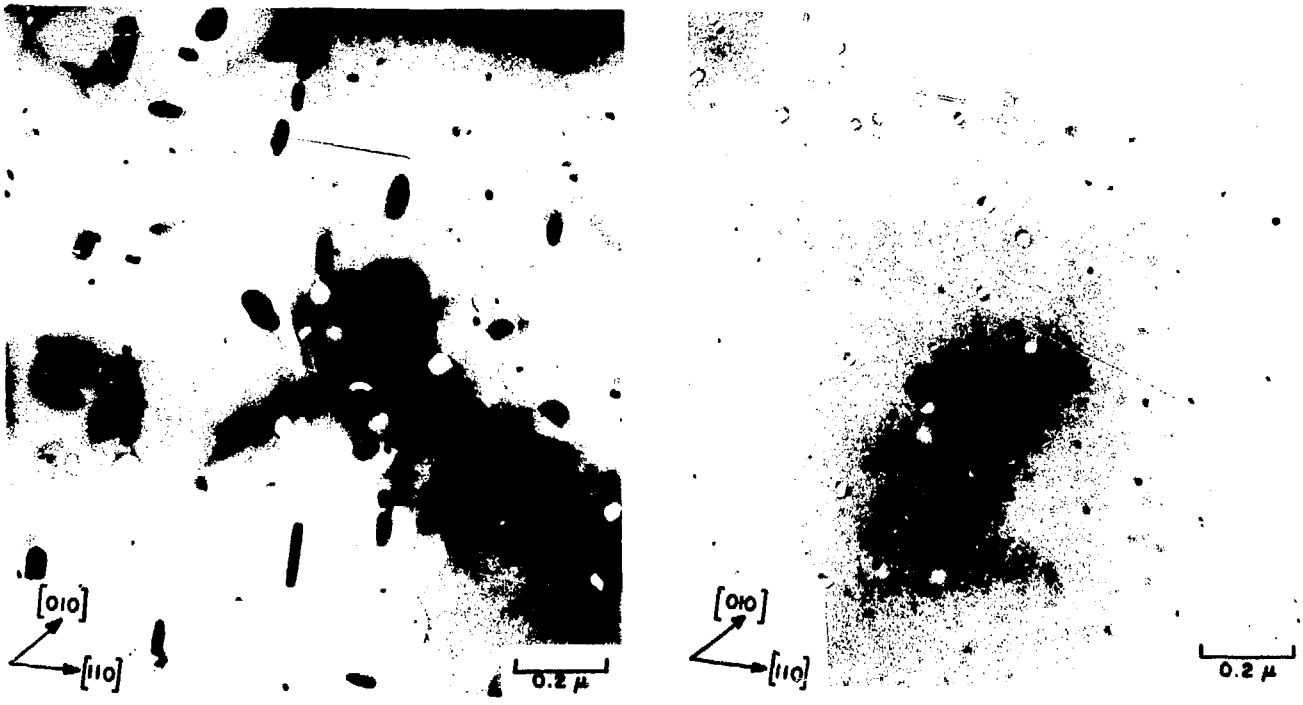

Fig. 5. Vanadium Samples Irradiated at 650°C with 18 MeV Cu Ions to 1 dpa.
5a - Sample Irradiated as Annealed.
5b - Surface Layer Removed Before Irradiation.

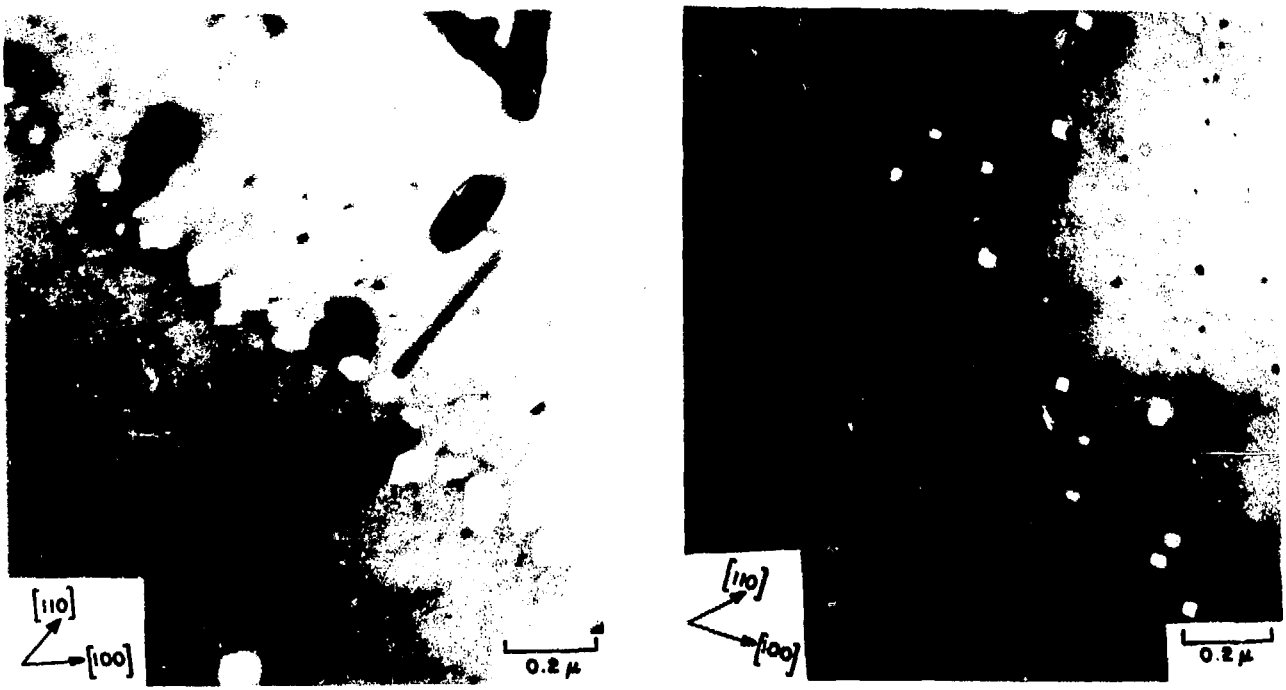

Fig. 6. Vanadium Samples Irradiated at 700°C with 18 MeV Cu Ions to 1 dpa.
6a - Sample Irradiated as Annealed.
6b - Surface Layer Removed Before Irradiation.

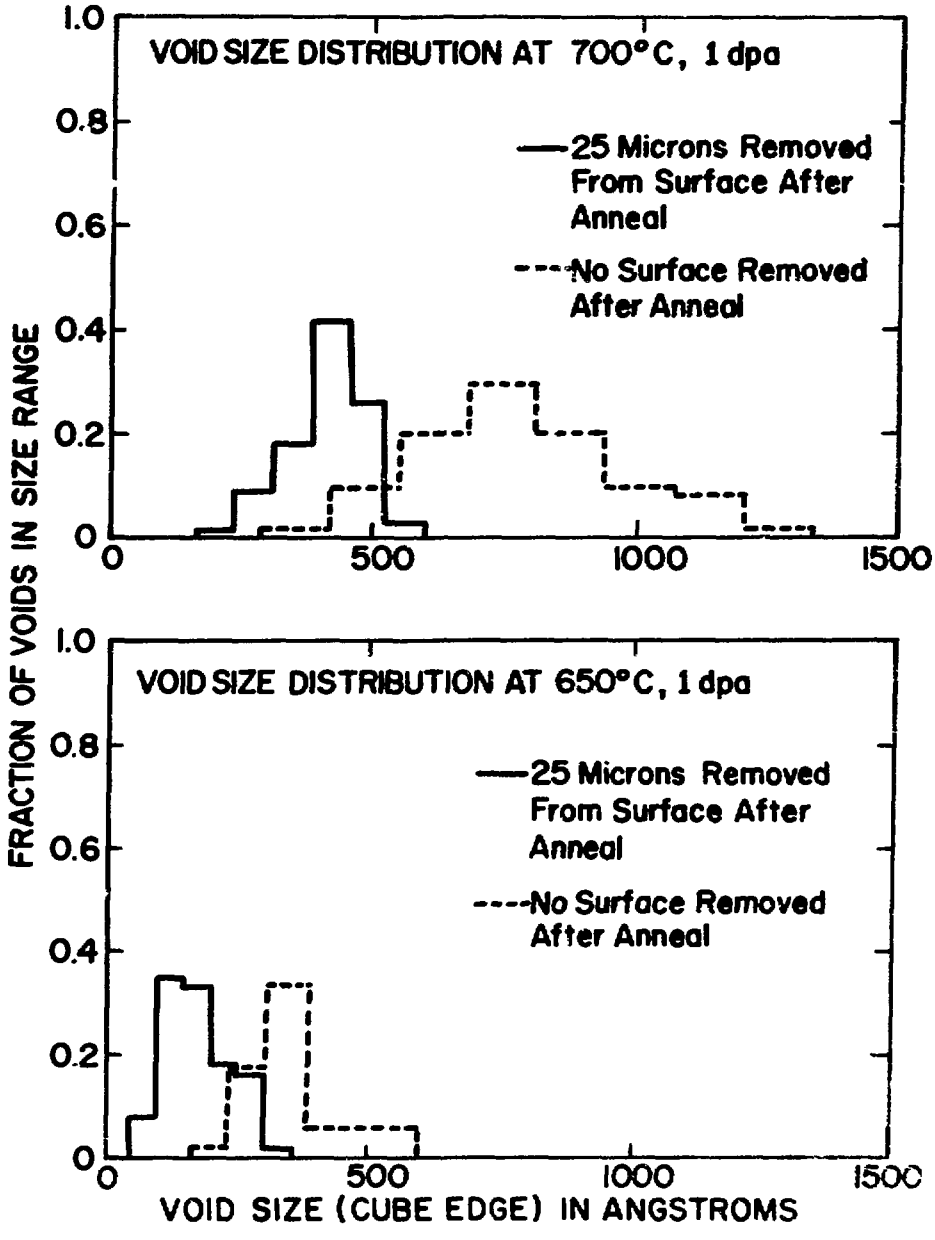

Fig. 7. Void Size Distribution for Vanadium Irradiated at 650 and 700°C after Different Post-Anneal Treatments. The Vanadium Irradiated After the Surface Layer was Removed has Considerably Less VC Precipitation.

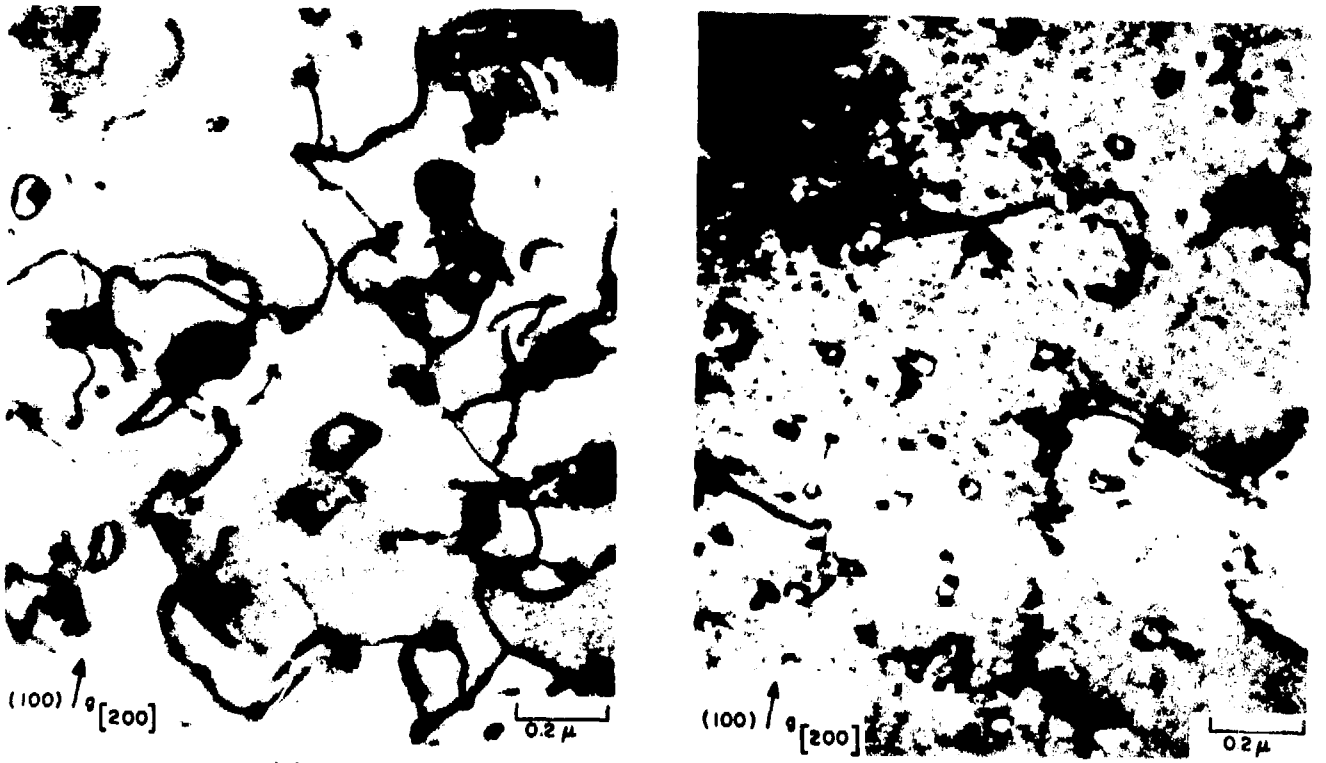

Fig. 8. Microstructure in Vanadium Irradiated at 700°C with 18 MeV Cu Ions to 1 dpa.
8a - Sample Irradiated as Annealed.
8b - Surface Layer Removed Before Irradiation.

Fig. 9. Microstructure in Vanadium Irradiated as Annealed at 700°C with 18 MeV Cu Ions to 1 dpa.

Void walls were observed in several samples which experienced extensive precipitation and one of these void walls is shown in Figure 10. Void and precipitate denuding around grain boundaries is illustrated in Figure 11.

DISCUSSION

The most significant observation in this study was the presence of a large carbon concentration (in the form of VC precipitates) whenever the samples were irradiated in the as annealed condition. The lower carbon concentration in the two samples electropolished after annealing and irradiated at 650 and 700°C suggests that the carbon contamination was associated with the large CO partial pressure (~2 x 10^{-8}Torr) observed during the anneal. The carbon impurities were probably deposited in a thin layer near the surface as evidenced by the fact that the precipitation was reduced by removing a 25 micron layer of vanadium. This conclusion was supported by the bulk analysis of the annealed vanadium which indicated no appreciable change in the bulk carbon content. The precipitation that was observed in all irradiated samples must be beam assisted since no precipitates have been observed in the samples exposed to the same vacuum conditions and temperature cycle but not irradiated (see Figure 3).

The equilibrium solubility of carbon in vanadium[15] is ~0.1 at.% in the range 700-1000°C. However, it is unlikely that such large amounts of carbon are generally present and if so, precipitation would have occured in the unirradiated region. However, the vacancy flux to voids generates strong segregation of interstitial solutes[8] so that solubility limits can be exceeded locally. In both high and low carbon content samples, small precipitates were found in association with voids (see Figures 3,5 & 6) presumably forming by this mechanism. In high carbon content samples, an additional rod type of precipitate was found which was much larger and not generally associated with voids. It is difficult to explain how the carbon solubility limit could be exceeded except by some local segregation effect associated with a defect flux to some sink. However, the precipitates are not associated with any other observable microstructural defects. One possible mechanism for the formation of the rod shaped precipitates is that they are nucleated initially near voids and as they grow they compete for the vacancy flux, eventually causing the voids to dissolve. There is some

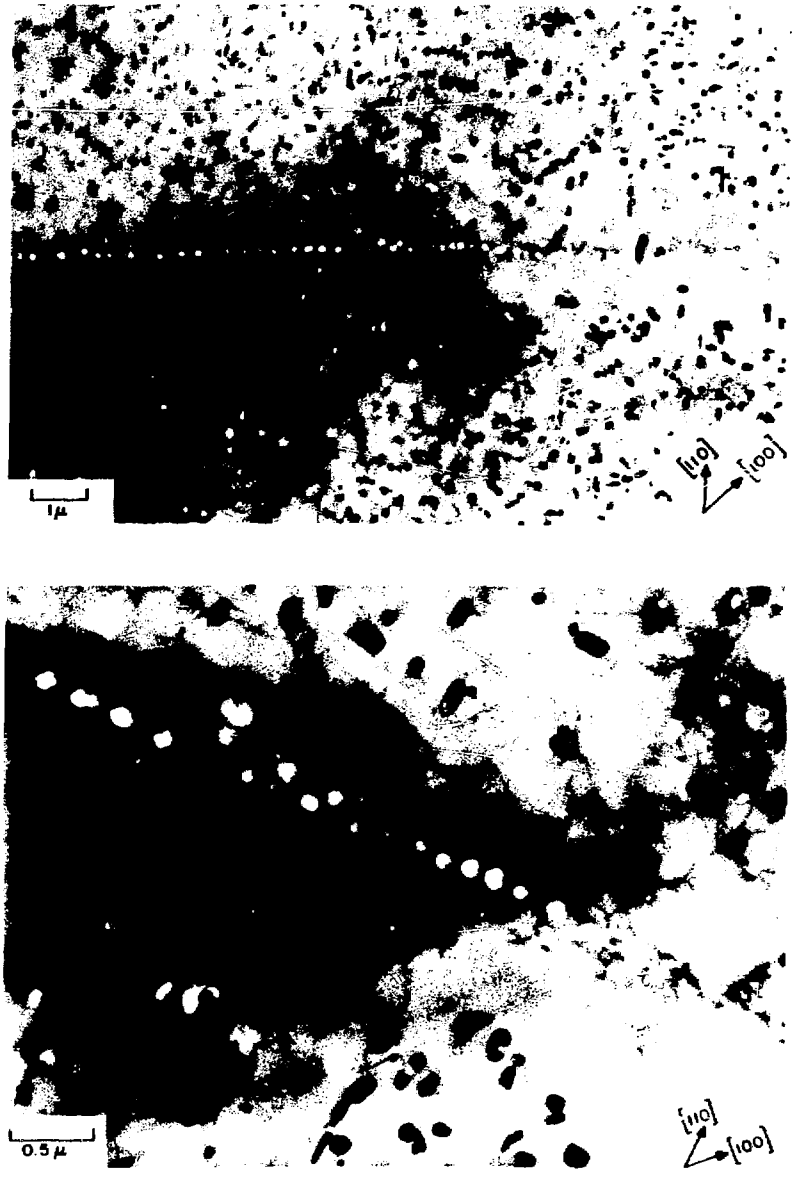

Fig. 10. Void Wall in Vanadium Irradiated as Annealed at 650°C with 18 MeV Cu Ions to 5 dpa.

Fig. 11. Void and Precipitate Denuding Near Grain Boundaries in Vanadium Irradiated as Annealed at 650°C with 18 MeV Cu Ions to 5 dpa.

experimental evidence for this in recent work by Agarwal et al.[16] This hypothesis would also be consistent with the denudation of rod shaped precipitates in the area of void walls (Figure 10).

The void wall shown in Figure 10 is similar to void walls observed in neutron irradiated aluminum by Stiegler et al.[17,18] They accounted for this by postulating that the wall of voids mark the position of a prior grain boundary that had been swept away during annealing and that the voids nucleate on impurity clusters that remain. There is no evidence to prove this assumption but, as shown in Figure 11, the grain boundaries in the vanadium are migrating either during the irradiation or during the anneal.

In general, the void morphology was observed to be cubes with {100} faces which is in agreement with previous observations in vanadium.[1-9] However, in previous investigations of vanadium[7,9] where truncation of the cubic voids was observed, the truncation was reported to occur on {111} planes. In the present study the voids were truncated on {110} planes, as is evident in Figures 5a and 6a, whenever the amount of precipitation was large and were truncated on {111} planes as shown in Figure 6b when the amount of precipitation was reduced. Truncation on both {110} and {111} planes was observed in the sample shown in Figure 5b. The elongated voids were observed only in the sample with low carbon content and irradiated at 700°C (Figure 6b). These "supervoids" typically has length to width ratios of up to ten. Approximately 2% of the voids in this sample were of this morphology when observed in a (100) orientation. The elongated voids were observed to be bounded by {100} planes and to grow in <100> directions, but their exact morphology is not known at this time. These elongated voids were not observed in the identical sample irradiated at 650°C or in any of the samples with large carbon content. A temperature threshold for rod-shaped voids has been previously reported in neutron irradiated high purity aluminum.[18,19] This could explain the absence of the elongated voids at 650°C in the sample with reduced precipitation. The absence of the elongated voids in the samples with extensive precipitation may be due to the presence of the carbon impurities.

The fact that precipitates were still observed in the samples annealed

in a vacuum of $<5 \times 10^{-8}$ Torr, electropolished to remove surface carbon contaminates, and irradiated in a vacuum of $<1 \times 10^{-8}$ Torr suggests that future irradiations of vanadium should include residual gas analysis for carbon-containing molecules. The vacuum conditions attained in the present study are to the authors' knowledge the best reported to date in ion simulation work.

CONCLUSIONS

1. Present results indicate that in vanadium irradiated at temperatures from 600 to 750°C the average void size increased with temperature while void density decreased. The maximum swelling appears to occur at 700°C for 3×10^{-4} dpa/sec, and amounted to approximately 1% at 1 dpa.
2. Beam assisted precipitation in vanadium affected void size and density.
3. Precipitation of VC in the samples was reduced two orders of magnitude by removal of a 25 μ surface layer after the anneal but before irradiation. Even then, precipitation was still observed although the partial pressure of the carbon containing molecules during irradiation was ~ 3×10^{-10} Torr.
4. At the peak swelling temperature, the voids were cubes; truncation occurred on {110} planes in the samples with extensive precipitation and on {111} planes in the samples with reduced precipitation.
5. The observed precipitates were face-centered cubic vanadium-carbide. The orientation relationship of the precipitates was

$$(001)_V \uparrow\uparrow (001)_{VC}$$

$$[110]_V \uparrow\uparrow [100]_{VC}.$$

6. Future ion simulation studies of vanadium should include the results of residual gas analysis, especially for carbon containing molecules.

ACKNOWLEDGEMENTS

The authors are grateful to the U.W. Nuclear Physics Group for use of the U.W. Tandem Accelerator and to J. B. Whitley, M. A. Sherman, and S. K. McLauren for assistance with the irradiations. This work was supported by the U.S. Energy Research and Development Administration,

Division of Physical Research.

REFERENCES

1. J. D. Elen, G. Hamburg, and A. Mastenbroek, J. Nucl Mater. 39, 194 (1971).

2. Y. Adda, Radiation-Induced Voids in Metals, ed. J. W. Corbett and L. C. Iannello, AEC Symposium Series, CONF-710601 (1972) p. 31.

3. J. L. Brimhall, H. E. Kissinger, and G. L. Kulcinski, Ibid., p. 338.

4. F. W. Wiffen, Ibid., p. 386.

5. F. W. Wiffen and J. O. Stiegler, Trans. Amer. Nucl Soc., 12, 119 (1969).

6. G. L. Kulcinski and J. L. Brimhall, Trans. Amer. Nucl. Soc., 14, 604 (1971).

7. A. T. Santhanam, A. Taylor, and S. D. Harkness, Intl. Conf. on Defects and Defect Clusters in BCC Metals and Their Alloys, ed; R. J. Arsenault, Nucl. Met., 18, 302 (1973).

8. P. R. Okamoto, A. T. Santhanam, H. Wiedersich, and A. Taylor, Nucl. Tech., 22, 45 (1974).

9. A. T. Santhanam, A. Taylor, B. J. Kestel, and C. Steves, J. Vac. Sci. Tech., 12, 538 (1975).

10. The authors wish to thank Dr. R. E. Reed for the sample material used in this study.

11. J. Davis, McDonnell-Douglas Corp., Private Communication.

12. R. G. Lott and H. V. Smith, Jr., Proceedings of the Symposium on Experimental Methods for Charged Particle Irradiations, Gatlinburg, Tenn., Sept. 30, 1975.

13. I. Manning and G. P. Mueller, Computer Physics Communication, 7, 85 (1974).

14. M. G. Miller and R. L. Chaplin, Rad. Effects, 22, 107 (1974).

15. D. R. Diercks and C. A. Wert, Met. Trans., 3, 1699 (1972).

16. S. C. Agarwal, B. O. Hall, D. I. Potter and A. Taylor, This Conference.

17. J. O. Stiegler, K. Farrell, C.K.H. DuBose, and R. T. King, Radiation Damage in Reactor Materials, Vol. II, IAEA Symposium Proceedings, STI-PUB-230 (1969) p. 215.

18. J. O. Stiegler, Radiation-Induced Voids in Metals, p. 292.

19. K. Farrell, A. Wolfenden, and R. T. King, Rad. Effects, 8, 107 (1971).

DOSE DEPENDENCE OF VOID-SWELLING IN VANADIUM IRRADIATED WITH SELF-IONS*

S. C. Agarwal
A. Taylor
Materials Science Division
Argonne National Laboratory
Argonne, Illinois 60439

ABSTRACT

The void-swelling behavior of HPV irradiated with 3-MeV $^{51}V^{+}$ ions to damage levels between 1 and 55 dpa at temperatures between 650 and 700°C has been investigated by means of transmission-electron microscopy. The results suggest that swelling increases with dose initially, attains a maximum value at some intermediate dose, and then decreases during additional irradiation. The decrease in swelling at higher doses is believed to be due to irradiation-induced precipitates.

INTRODUCTION

An investigation of the temperature dependence of the void-volume fraction of high-purity vanadium (HPV) bombarded with 3.25-MeV $^{58}Ni^{+}$ ions showed that, at a dose level of 60 dpa, the peak swelling occurs at 700°C.[1] Both at and above the peak temperature, precipitates were interspersed in the void microstructure. The work on dose dependence of swelling in this material irradiated with 3-MeV $^{51}V^{+}$ ions at 700°C was initiated by Santhanam et al.[2] in which two 4 by 4 arrays of 3-mm disks were irradiated to damage levels of 2.5-30 and 10-60 dpa, respectively. Results of the electron microscopy of samples with doses below 34 dpa have been reported. It was found that, although the void volume increased, the void number density decreased drastically as the dose increased.

*Work supported by the U.S. Energy Research and Development Administration.

Here we report on the microscopy results for the remainder of the irradiated specimens and those for another dose-dependent study carried out at 650°C. The lower temperature was chosen because it was thought that segregation effects, if present, would be more evident.

EXPERIMENTAL

Details of the preparation of annealed TEM disks and the irradiation procedure have been given in a previous paper.[3] A 4 by 4 array of specimens was bombarded with 3.0-MeV $^{51}V^{+}$ ions at 650°C to a maximum dose of 55 dpa in an ambient vacuum of 5×10^{-8} Torr. The different doses were accumulated by exposing an increasing number of specimens to the ion beam using a movable mask. Thus, all specimens experienced the same thermal history, with all the irradiations extending to the end of the time at elevated temperature. The specimens were sectioned to a depth of 8000 Å and examined in transmission with a 200-keV JOEL electron microscope. The void parameters were obtained from photomicrographs at a magnification of 150,000X.

RESULTS AND DISCUSSION

Figures 1 and 2 show the dose dependence of various void parameters and the dislocation density of the 650°C irradiation. The void-volume fraction and the average size reach a peak near 13 dpa and decrease with dose at higher doses, implying a reduction in swelling with continued irradiation. A possible qualitative explanation for this behavior may be found in Fig. 3, which shows the evolution of microstructure with dose at 650°C. It can be seen that profuse precipitation begins in the matrix at approximately the dose at which the void-volume fraction and average size exhibit a peak. The precipitates primarily form coherently on {100} matrix planes, and the precipitate density increases with dose. Occasionally, a higher multiplicity of orientations is exhibited by the precipitates, suggesting that more than one type of precipitate may be involved. Additional experiments are in progress to elucidate the nature and origin of these precipitates.

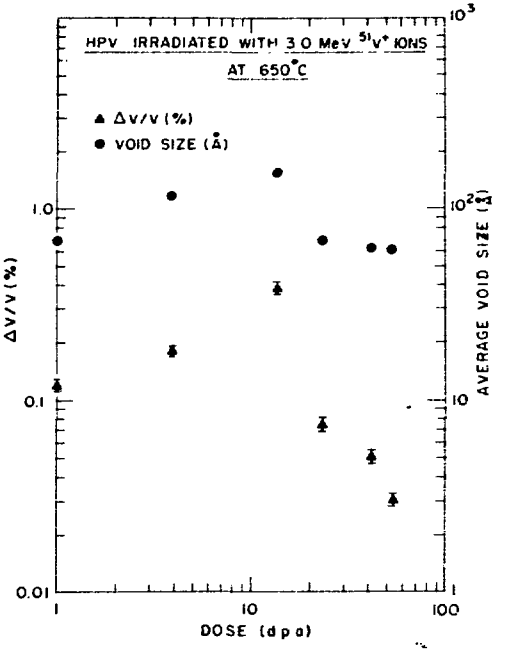

Fig. 1. Void-volume Fraction and Average Void Size as a Function of Dose.

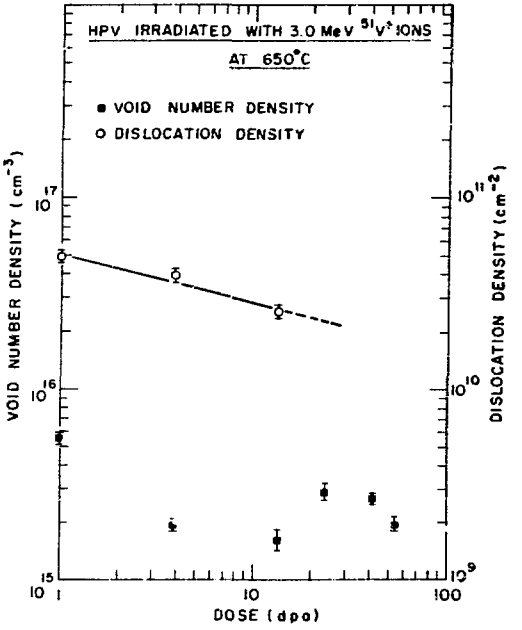

Fig. 2. Void Number Density and Dislocation Density as a Function of Dose.

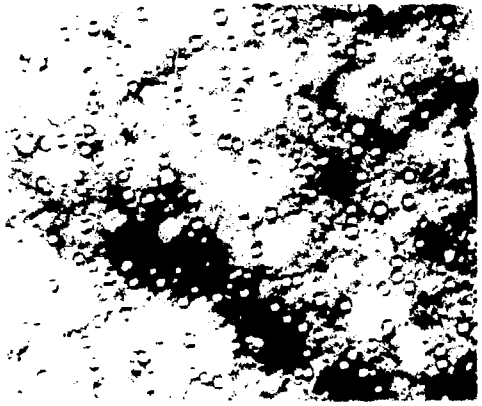

1 dpa

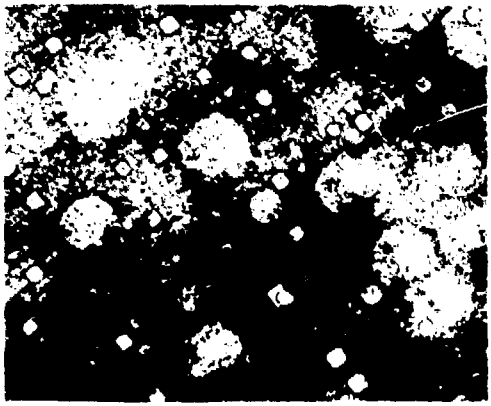

4 dpa

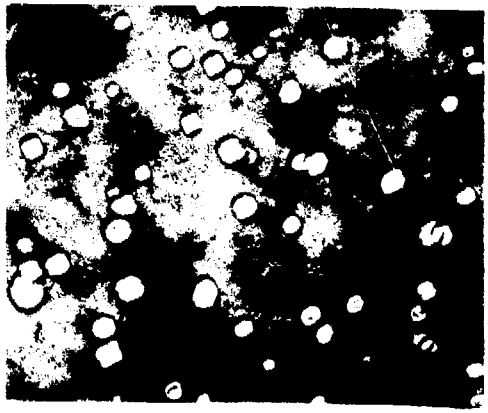

13.4 dpa

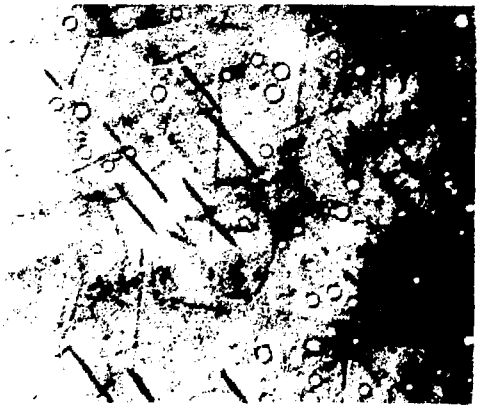

23.5 dpa

42 dpa

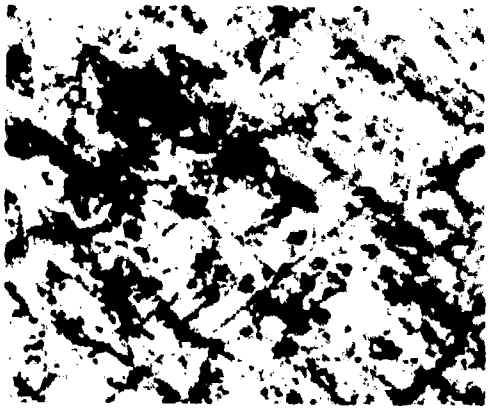

54.3 dpa

Fig. 3. Evolution of Voids and Precipitates as a Function of Dose (Mag. 150,000X).

Table 1 lists the void parameters and dislocation densities over the entire dose range (2-54 dpa) for HPV specimens irradiated at 700°C. At low doses (to ~4 dpa), the void sizes and densities are quite similar to those at 650°C. At higher doses, more scatter is evident in the 700°C data. However, the high-dose data (33-54 dpa), when combined with data published earlier,[2] show that, with continued irradiation, swelling does decrease with dose at 700°C, which is similar to that now observed at 650°C. In general, these 700°C data show higher swelling at comparable doses. This is expected because 700°C was found to be the peak swelling temperature for HPV irradiated with 3-MeV $^{58}Ni^{+}$ ions.[1] The observed dislocation densities are quite similar at both temperatures. The high density of precipitates at higher doses in the 650°C specimens makes an accurate determination of dislocation density difficult. Although precipitates were also observed in 700°C specimens, the degree of precipitation was much less than that found at 650°C. The precipitates are thought to arise from either redistribution of interstitial impurities (C, O, and N) during ion bombardment or impurities picked up during irradiation. Although the total interstitial impurity content of the starting HPV was the same (15 ppm O, 15 ppm N, and 120 ppm C, by weight) in both cases, the difference in interstitial impurity pickup during annealing and/or irradiation is probably responsible for the observed differences in the extent of precipitation. A lower precipitate density could also account for the observed increase in the average void size with dose in the 700°C specimens beyond the peak dose value (~14 dpa) at 650°C. In the 650°C case, voids that initially form at lower doses actually seem to shrink and disappear during irradiation to higher doses simultaneously with the appearance and growth of the precipitates. Finally, strain contrast and precipitation around voids observed near the peak swelling temperature in HPV irradiated with $^{58}Ni^{+}$ ions[1] were not evident in self-ion-irradiated samples at either temperature. The observed segregation in Ni ion-irradiated samples probably resulted from implantation of the bombarding ions.

Table 1. Void Parameters and Dislocation Densities for HPV Irradiated with 3-MeV Ni^+ Ions at 700°C.[a]

Corrected Dose (dpa)	Average Void Size (Å)	Void Number Density (cm^{-3})x10^{-16}	ΔV/V (%)	Dislocation Density (cm^{-2})x10^{-10}
2.4	69	6.0	0.20	3.2
4.26	101	1.84	0.25	2.3
7.0	200	0.45-0.93	0.13-0.2	-
22.2	315-375	0.15-0.34	0.9 -1.5	1.5
34.0	344-412	0.23-0.37	1.6 -2.0	0.8
42.5	218-300	0.34-0.93	0.30-0.48	-
54.4	337-425	0.3 -0.52	0.85	-

[a]Data were obtained from different areas of the same foil and the range of values are given.

Recently, one of the specimens irradiated at 650°C to a nominal dose of 47 dpa was resectioned to a depth of 14,250 Å (corresponding to ~1.1 dpa) to examine the depth dependence of damage density and swelling. Preliminary results, shown in Fig. 4, suggest an average void size of 75 Å compared with 63 Å observed at a depth of 8050 Å (~42 dpa). This would imply higher swelling at greater depths, i.e., at lower dose, than in the peak damage region.

The two most important observations that emerge from the results of the present study are:

1. Interstitial impurities play a dominant role in controlling the void-formation characteristics and associated swelling in HPV. It is, therefore, imperative that the material being examined should be unambiguously characterized in terms of interstitial impurity content at various stages during the investigation.

2. The void-volume fraction in irradiated HPV does not increase monotonically with dose but does attain a maximum at some intermediate dose level and then decreases. A reduction of swelling with increase in dose may imply reversal of the sign of the overall bias, e.g., an excess of vacancies could be required to accommodate the precipitates leaving a corresponding number of excess interstitials to shrink voids.

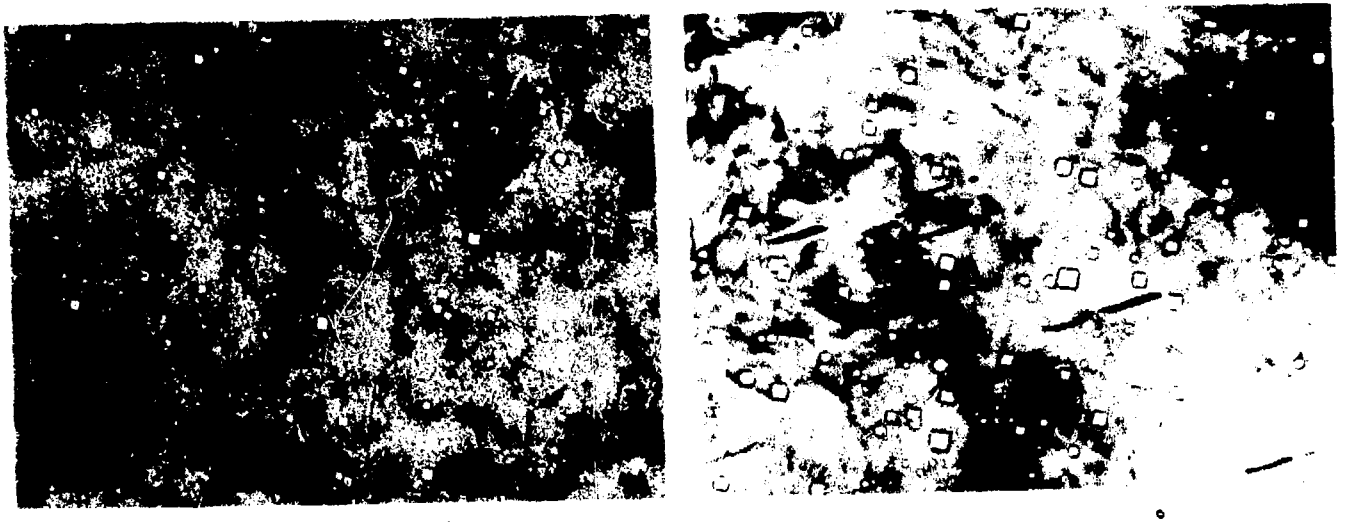

Section Depth 8050 Å
42 dpa

Section Depth 14,250 Å
1.1 dpa

Fig. 4. HPV Irradiated at 650°C with 3-MeV Vanadium Ions (Mag. 150,000X).

REFERENCES

1. A. T. Santhanam, A. Taylor, and S. D. Harkness, Proceedings of the 1973 International Conference on Defects and Defect Clusters in BCC Metals and Their Alloys, R. J. Arsenault (ed.), p. 302.
2. A. T. Santhanam, A. Taylor, B. J. Kestel, and C. Steves, J. Vac. Sci. Tech. 12(1), 528 (1975).
3. A. Taylor, J. Wallace, D. I. Potter, D. G. Ryding, and B. Okray Hall, "Argonne National Laboratory Dual-Ion-Irradiation System," this conference.

ARGONNE NATIONAL LABORATORY DUAL-ION-IRRADIATION SYSTEM*

A. Taylor
J. Wallace
D. I. Potter
D. G. Ryding
B. Okray Hall
Materials Science Division
Argonne National Laboratory
Argonne, Illinois 60439

ABSTRACT

The details of the dual 4-MV Dynamitron - 2-MV Van de Graaff ion-irradiation system at Argonne National Laboratory are described. The procedures adopted to define the ion flux, fluence, and temperature of the specimen during an irradiation are briefly presented together with a standarized specimen-preparation technique for vanadium.

INTRODUCTION

It is evident that considerable use will be made of charged-particle bombardment to investigate radiation effects in first-wall materials for prototype fusion reactors.[1] Extensive use has been made of bombardment with nickel ions to simulate the displacement damage in core components of breeder reactors.[2] In charged-particle irradiation, the general practice is to simulate the low-level helium-producing (n,α) reactions by preinjecting specimens with helium ions to levels of $\sim$10 ppm. For the first wall of a fusion reactor, which is bombarded by 14-MeV fusion neutrons, levels of $\sim$500 ppm of He can be anticipated at the end of the projected service life. At these He levels, we may anticipate that He production, concurrent with displacement damage, will influence the kinetics of void growth and nucleation. Therefore, it seems prudent to conduct irradiation studies in which He ions are simultaneously injected during a self-ion bombardment.

*Work supported by the U.S. Energy Research and Development Administration.

To facilitate such work, a 2-MV Van de Graaff accelerator has been installed at the 4-MV Dynamitron Facility in the Physics Division at Argonne National Laboratory. In addition to providing light ion injection to damage depths compatible with the Dynamitron, the beam of the Van de Graaff will also be available to probe radiation effects using backscattering and nuclear yields.[3] Because of the potential use in bcc metals and alloys in the CTR program, the vacuum system of the beam transport and the target chamber of the dual-accelerator facility has been constructed for ultrahigh vacuum (UHV) work. Both beam-line sections are instrumented so that the beam intensity profiles can be continuously monitored close to the target during the irradiations. Automatic stabilization to correct for spatial drift in the acceleration system has also been incorporated into the system. Given the intrinsic unreliability inherent in such accelerator systems, various target holders have been developed to increase information retrieval on dose-temperature dependence of irradiation-induced microstructural changes when reliable irradiations are achieved. To obtain quantitative data from these experiments, the ion fluxes, the fluence on each area of the specimen, and the specimen temperature must have been accurately characterized throughout the run.

LAYOUT OF DUAL-ACCELERATOR SYSTEM

The layout of the dual-accelerator system is illustrated in Figs. 1 and 2. The 4-MV Dynamitron, accelerator used to accelerate heavy ions, is a horizontal installation with a North-South beam axis 65 in. above the floor level of the target room. The target chamber is situated on the 8°50' West beam line some 400 in. beyond the center of the analyzing magnet. The 2-MV Van de Graaff accelerator is located on the roof of the Dynamitron vault, vertically above this analyzing magnet. Its 90° analyzing magnet is slung from a rotatable mount and can deflect the light-ion beam to all locations in the target room 24 in. above the beam from the Dynamitron. The light-ion beam is bent into the target chamber at an angle of 10° by means of a small deflector magnet. The vacuum system between the accelerators and the 10° deflector magnet is constructed with standard 2- and 4-in. HVEC beam-line components and is maintained

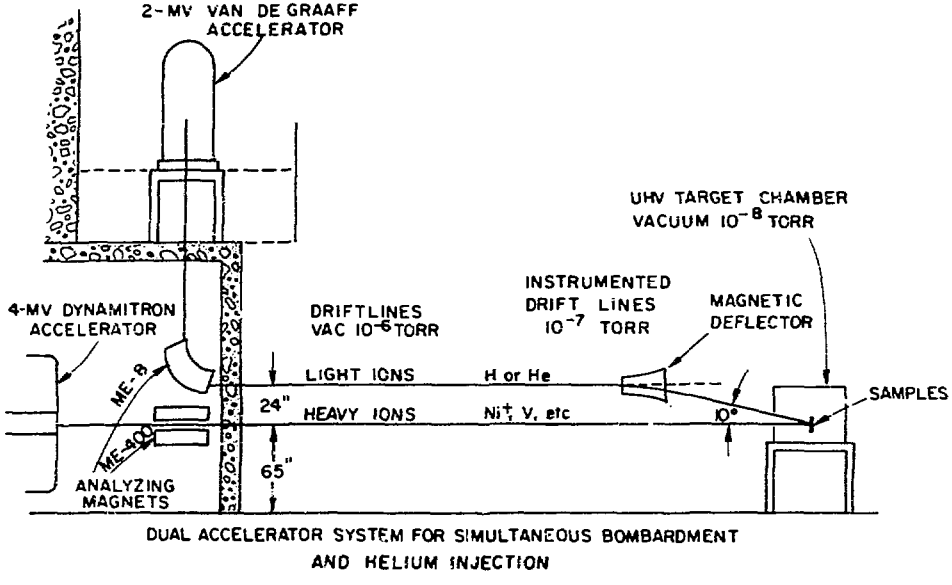

Fig. 1. Layout (looking West) of dual-accelerator system for simultaneous heavy-ion bombardment and helium injection of CTR first-wall materials.

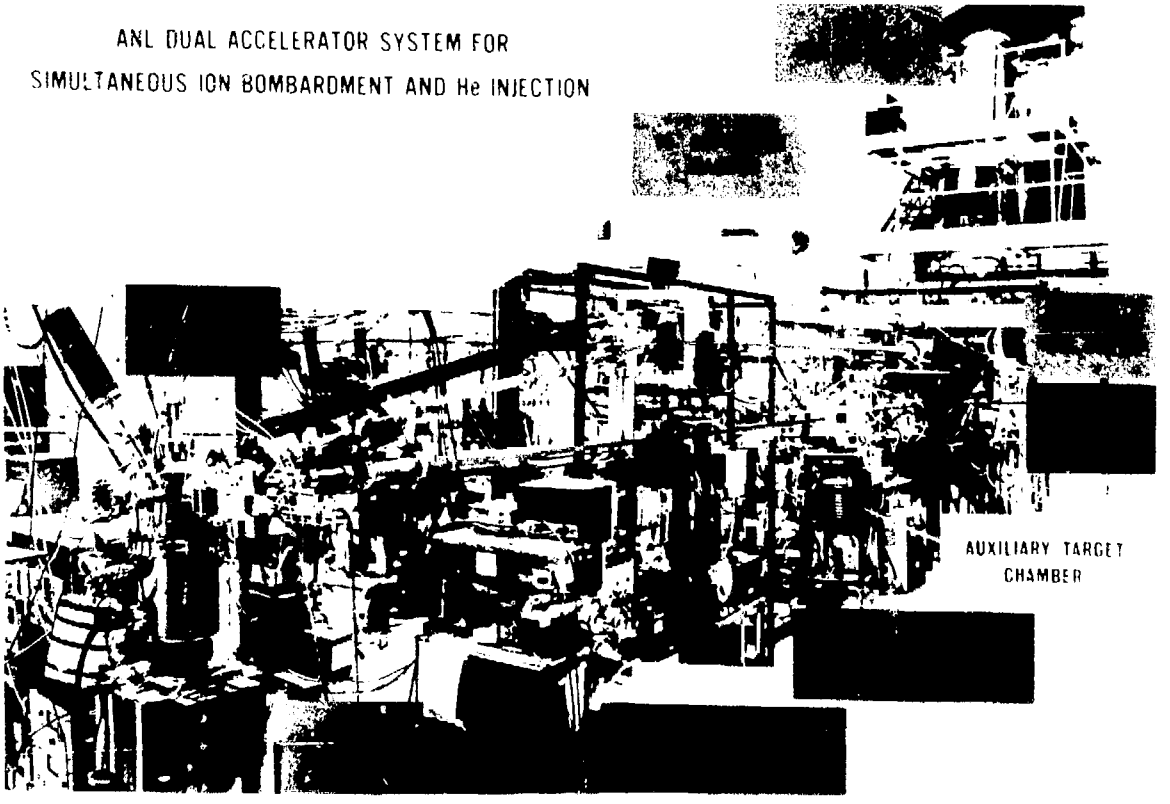

Fig. 2. Photograph of dual-accelerator systems looking Southeast.

at a vacuum of $\sim 10^{-6}$ Torr with oil diffusion pumps trapped with liquid nitrogen baffles. The beam drift-line section between the deflector magnet and target chamber, which contains the beam control and monitoring instrumentation, is a bakeable UHV system operating with a vacuum of $\lesssim 10^{-7}$ Torr. The vacuum system is divided into several zones, which, in the event of vacuum failure, are isolated by gate valves controlled from vacuum monitors attached to each section. The vacuum attainable in the target chamber is $\sim 10^{-8}$ Torr without bakeout.

HEAVY-ION ACCELERATOR

The 4-MV heavy-ion accelerator is a Radiation Dynamics Inc. Model RPEA-4 unit that has been extensively modified to meet the needs of the Physics and Materials Science programs at ANL.[4] The accelerator is equipped with twelve NEC accelerator tube sections and is joined with decoupling apertures that are 1-1/2 in. in diameter. The ion source used for heavy-ion studies consists of a modified Danyfysik type 910 with either stainless steel or graphite components. Singly charged Ni or V ions are generated efficiently using the CCl_4 method in combination with metallic elements placed behind the source filament.[5] Steel source components are used for the production of carbon ions of gaseous elements. Typically, beam currents of 1-2 μA of analyzed species at 4 MeV are obtainable, the limit is set by loading currents in the acceleration tube.

BEAM-TRANSPORT COMPONENTS

The principal components of the beam-transport systems of both the Van de Graaff and Dynamitron accelerators and the instrumentation in the target, control, and data rooms for beam control and monitoring are shown schematically in Figs. 3 and 4, respectively.

The energy-control system of the Van de Graaff consists of a conventional slit feedback system operated from the image slits of the 90° double-focusing analyzing magnet. Secondary steering and focusing elements are provided to guide and focus the beam through the 10°

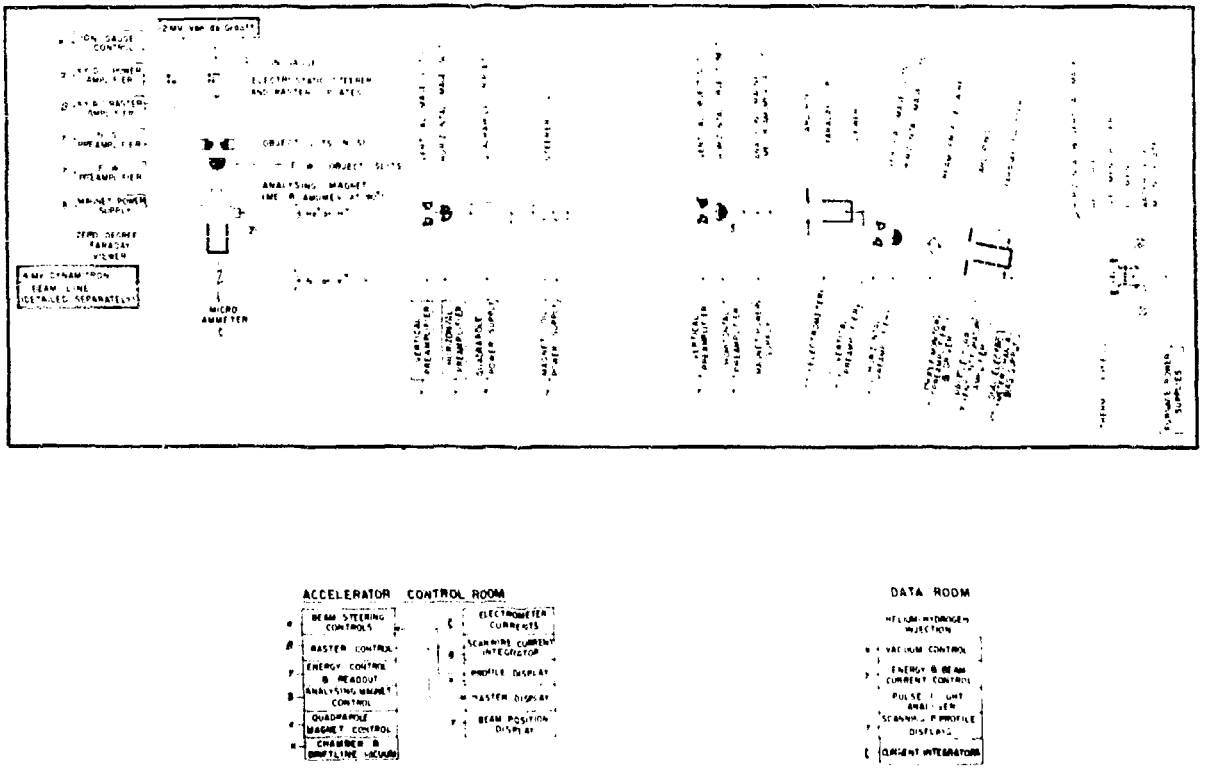

Fig. 3. Schematic of the principal components of the 2-MV Van de Graaff light-ion accelerator beam-transport section of the ANL dual-accelerator system (looking West).

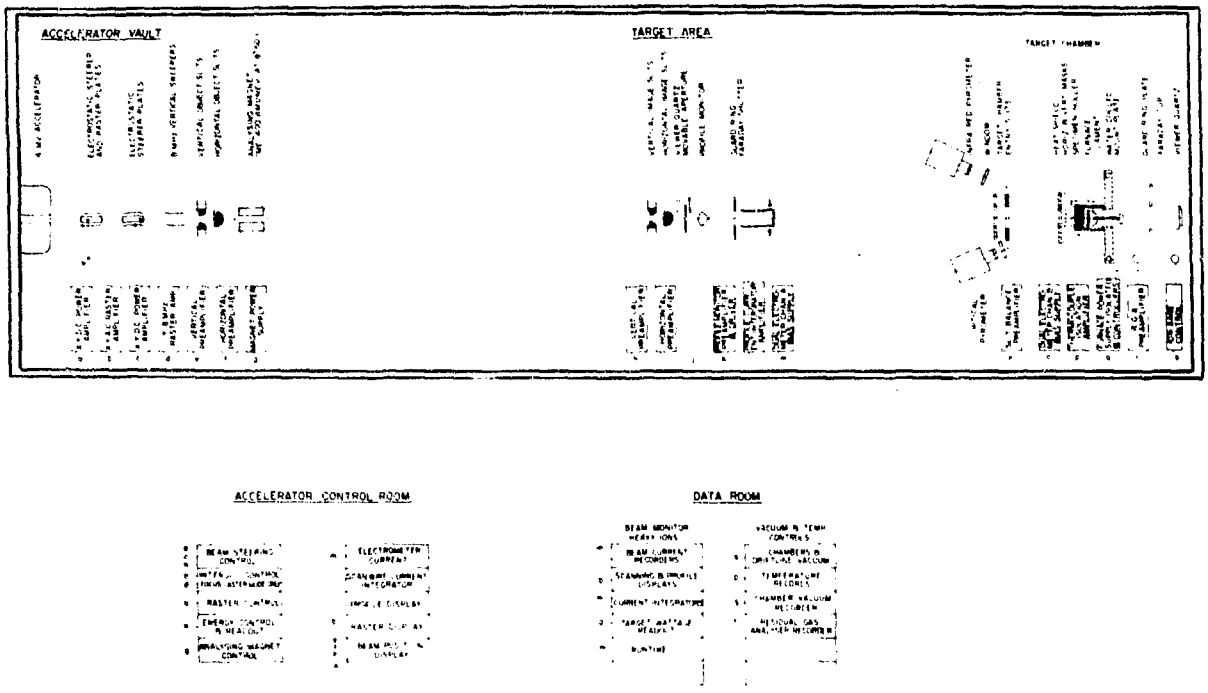

Fig. 4. Schematic of the principal components of the 4-MV Dynamitron heavy-ion accelerator beam-transport section of the ANL dual-accelerator system (looking West).

deflector magnet onto the slits in front of the target chamber. The beam is automatically centered between these vertical slits by a feedback loop that controls the current supplied to the coils of the deflector magnet. Beam profile and intensity are measured with a rotating wire beam scanner and a Faraday shutter, National Electrostatic models BPM5-45 and FCVA-6, respectively. A dc signal proportional to the current intercepted by the scanner wire is obtained from the preamplifier of the beam scanner to monitor the beam when the shutter is moved aside. To distribute the helium uniformly through the radiation damaged layer of the specimen, the helium beam is passed through a degrader foil mounted in front of the specimen slightly above the path of the heavy-ion beam.

In the heavy-ion system, two pairs of electrostatic steerer plates are used to automatically stabilize the position of the unanalyzed beam between the four-jaw entry slits of the analyzing magnet. Appropriate adjustments of the voltage levels on each set of plates provide parallel displacement and deflection of the beam to accommodate mechanical displacements of the ion source during servicing and erratic electrical deflection of the beam during machine operation. To improve the spatial uniformity of the ion flux on the target surface, one set of steerer plates is ac-coupled to the power amplifiers, which permits the beam to be wobbled* or rastered simultaneously in both the horizontal and vertical directions. Frequencies between 10 and 100 kHz, with triangular, saw tooth, or sinusoidal wave forms, could be selected to optimize the beam uniformity. A third set of vertical deflector plates provides postacceleration chopping of the beam with a minimum rise time of ∿100 ns to control the time structure of the beam during pulsed irradiation studies.

Beyond the vertical chopping plates, the beam is bent into the 8°50' west target-room drift line by an analyzing magnet and then through a four-jaw image slit system situated ∿300 in. from the target face. The

*Wobble is defined as a lateral displacement no greater than a beam half-width.

electrical pickup from these horizontal slits is fed back to the accelerator inner-loop amplifier to stabilize the ion-beam energy. Long-term drift on the generating voltmeter at the accelerator terminal is <0.05%. The dispersion of the system measured at the control slits is given by ∿46 Δp/p in. (where p is the momentum of the particle), is equivalent to a separation of 0.8 in. between the $^{58}Ni^{+}$ and $^{60}Ni^{+}$ ions. Generally, an image slit width of 0.48 in. is used such that a defocused beam would diverge to a width of 0.6 in. at the target chamber. The horizontal and vertical slits of the chamber are used to monitor the position of the beam at the target during an irradiation. Continuous monitoring of the beam profile, in both the horizontal and vertical directions, and the current transmitted to the target chamber is again provided by an oscillating wire-loop monitor, which feeds the preamplifier output signals to an oscillograph display and a dc signal to the current recorder. The total current is also read on a movable shutter that acts as the back of a biased Faraday cup. Movable quartz viewers and aperture plates are installed to facilitate the alignment and the initial set-up procedures. An intensity profile of the Ni isotopes in the focused and defocused wobbled modes is shown in Fig. 5.

TARGET CHAMBER

The target chamber (Fig. 6) consists of a standard UHV-type Auger spectroscopy stainless steel bell connected to a 500-liter/s triode ion pump and a sublimator-equipped cryoshroud. View ports (located 10 and 45° from the heavy-ion beam axis) permit optical and infrared pyrometers to be sighted onto the target surface. A Faraday cup with a fluorescent quartz screen is mounted in the rear entry port so the ion-beam current transmitted through the target chamber can be measured and viewed simultaneously. The target holder (Fig. 7) can be mounted into either of two 6-in. ID side entry points. Vertical and horizontal masks, containing both rectangular and circular apertures, are mounted in a micrometer-positioned, bellows-sealed feedthrough to facilitate the probing of the spatial distribution of the beam intensity or to mask selected specimens from the beam. The target holder mount plate has four furnace positions.

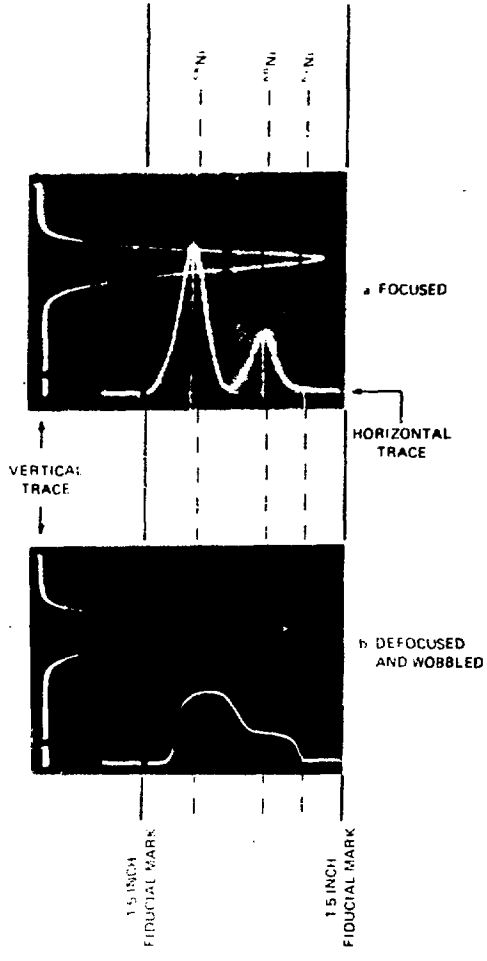

Fig. 5. Oscillographic displays of the profile of the ion beam for scanning wire traversing the beam in a vertical and horizontal direction. (Scan shows Ni isotope separations at point 100 in. closer to analyzer magnet.) (a) Beam focused (b) beam defocused and wobbled in the horizontal.

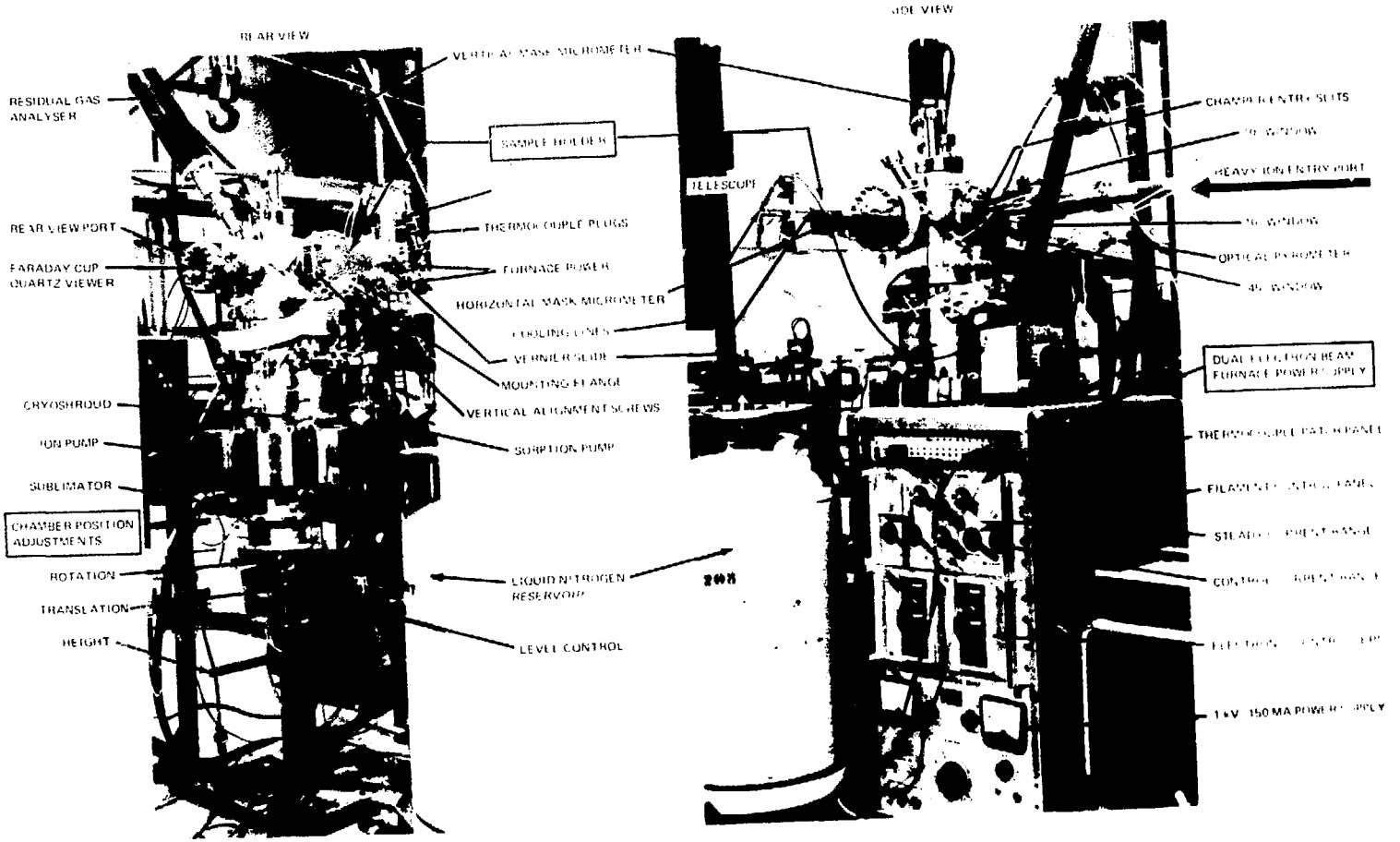

Fig. 6. Ultrahigh vacuum target chamber oblique and rear view and the dual-electron-beam furnace power supply.

During alignment procedures, the ion beam passes through the center hole in the mount plate into the Faraday cup at the rear of the target chamber. Slight misalignments between the holder centerline and the beam axis, caused by variations in the seating of the copper gasket of the mounting flange, are compensated for by adjusting the vertical alignment screws. A Veeco residual gas analyzer and a nude ion gauge are used to monitor the chamber vacuum during irradiations.

SPECIMEN HOLDERS

The specimen holder shown in Fig. 7 is constructed so that four sets of twenty microscope specimens can be irradiated at temperatures up to 1400°C. An expanded view of the specimen holders and furnace assembly is shown in Fig. 8. The tungsten specimen holder is mounted in a cylindrical alumina insulator and clamped to the water-cooled mount plate by means of a stainless steel clamp ring. The specimen holder is heated from the rear with a diffuse electron beam emitted from a thoriated tungsten filament, which is maintained at 1 kV relative to the holder. Two Chromel K stainless steel clad thermocouples are inserted into the holder block to measure and control the temperature. The dual-electron-beam furnace power supply (Fig. 6) is used to maintain the desired temperature by regulating the electron-emission current with an electronic controller. Furnace thermocouples and power leads are brought through the header assembly inside a 1-in.-dia tube and distributed to the multipin cannon plugs on the connector box. The header assembly is attached to a vernier slide, and the vacuum seal is provided by a welded stainless steel bellows, which can be extended ∿6 in.

To facilitate rapid screening of the dose-temperature dependence of radiation-induced microstructural changes, three specimen foils 0.120 by 0.605 in. can be irradiated in the temperature-gradient holder shown in Fig. 9. This holder is made of molybdenum and consists of a homogenizer block and a mask that spans two furnace positions on the specimen-holder mount plate. One side of the homogenizer block (the colder end) is heat sunk to the mount plate using a copper mounting bracket, and the high-

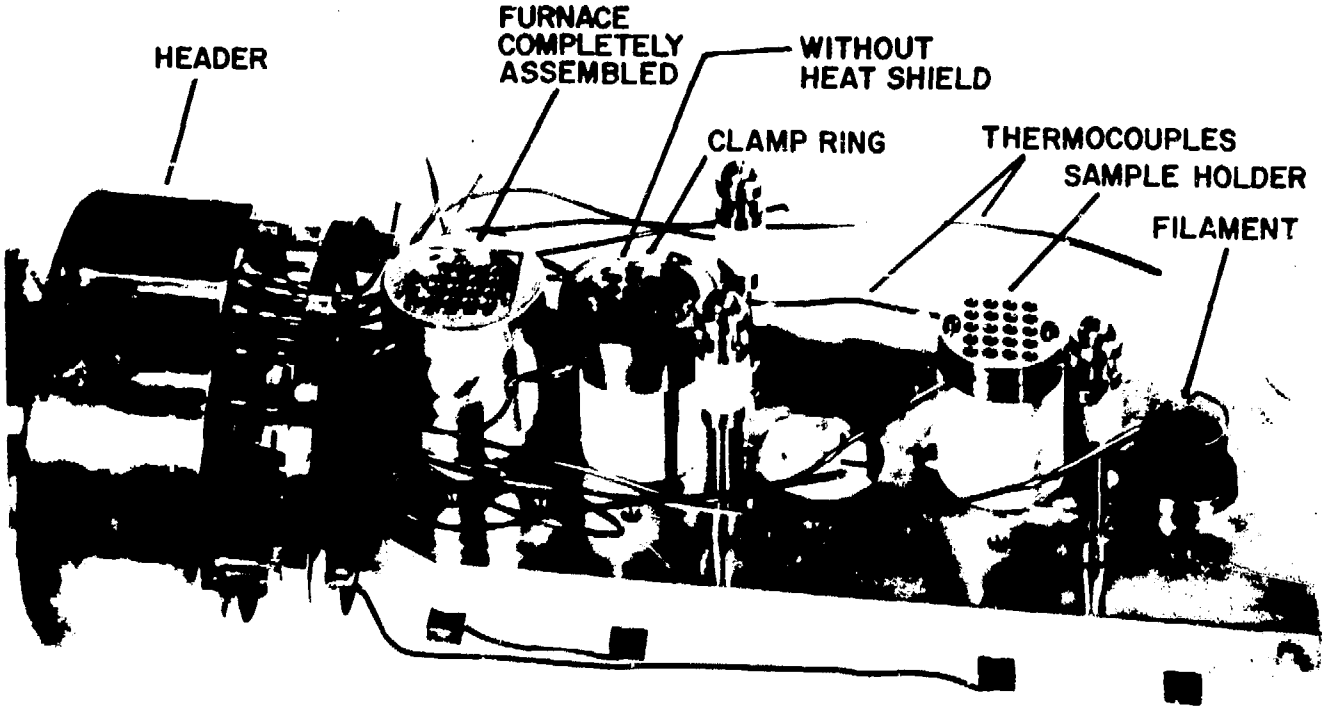

Fig. 7. High-Temperature target holder showing furnaces in various stages of assembly

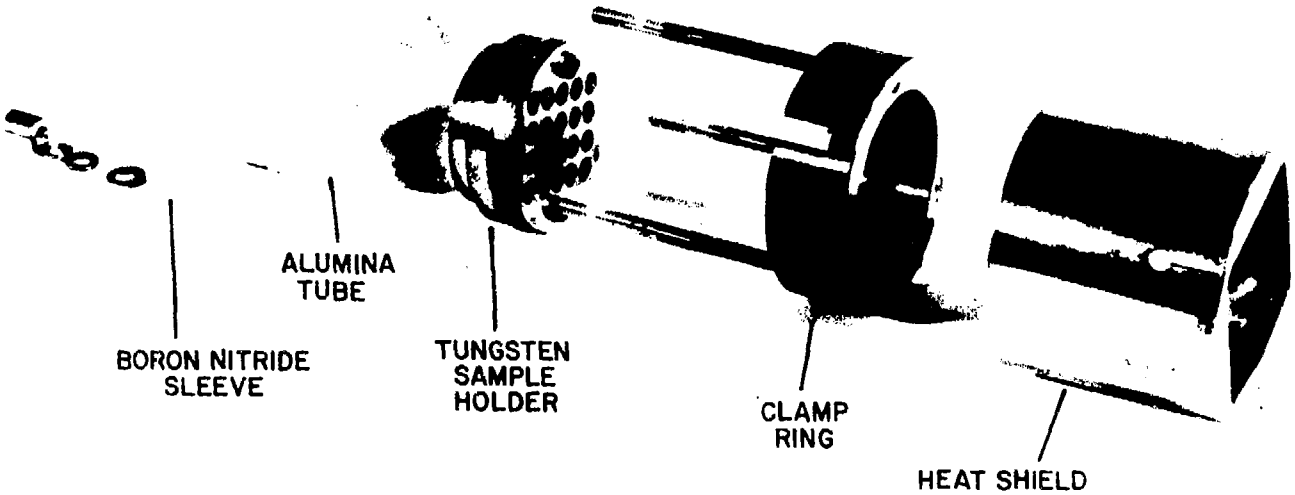

Fig. 8. Exploded view of the specimen holder and clamp ring.

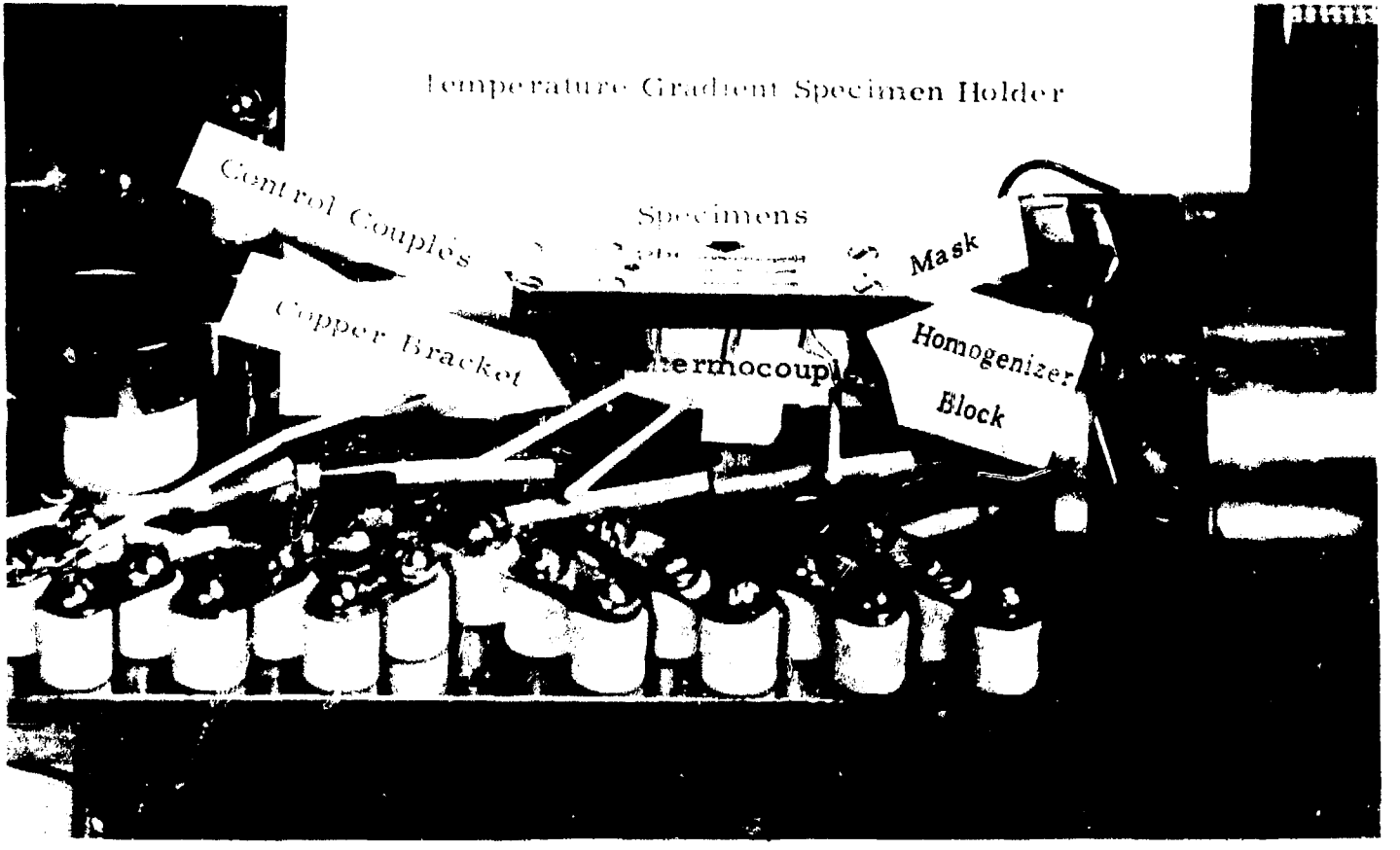

Fig. 9. Assembled view of the temperature-gradient holder.

temperature end is mounted on two thin stainless steel screws. The gradient across the specimens can be adjusted by independently controlling the temperature of each end of the holder using the dual-furnace-control unit. The temperature gradient is monitored by three Chromel K thermocouples inserted into the homogenizer block from the rear, and the optical pyrometers can be used to measure the temperature distribution of the specimens and the mask. Additional details of the system are discussed elsewhere.[6]

HELIUM INJECTION

A stationary degrader foil was designed to provide a uniform concentration of injected helium in a layer at least 3000 Å thick at a depth of ~6000 Å in vanadium. It is placed 2.3 in. before the target on the axis of the helium beam.

The foil is composed of two thicknesses of nickel and a substrate of thickness τ_1 on which a nickel layer of thickness τ_2 is randomly deposited. The thicknesses τ_1 and τ_2, the areal fraction of the deposited layer, and the helium-beam energy were chosen as follows. For a substrate thickness τ_1 and an incident-ion energy E_i, the Brice code RASE 3[7] output was used to determine the energy distribution off the back of the foil. The distribution was then fitted by a Gaussian, and the energy maximum and half-width were calculated. Moliere's Gaussian approximation[8] was used to account for multiple scattering and gave the angular distribution of ions as a function of the degraded energy. The evaluation of the mean-square spatial angle involved integrating over the intermediate energies within the foil,[9] since the energy loss suffered by the particles in traversing the foil is of the order of 70%. The Brice range and straggling results for helium on vanadium were then used in conjunction with the energy and angular distributions to determine the helium deposition profile in the sample. The range along the incident-ion direction and straggling were assumed to be unchanged for nonnormal incidence. The energy E_i of the helium beam was adjusted so that the maximum in the energy distribution transmitted through τ_1 occurred at 335 keV, (for

E_i = 1.15 MeV and τ_1 = 1.45 mg/cm^{-2}), which gave a peak in the sample deposition profile at 1.0 μm. With an additional deposited thickness τ_2 = 0.37 mg/cm^2, the output energy peaks at 135 keV, and the sample deposition peak occurs at 0.5 μm. It was found that equal areal fractions of thicknesses τ_1 and $\tau_1+\tau_2$ gave a calculated concentration, uniform within 10%, from 0.5 to 1.0 μm. The deposition profile will be checked using the ^{3}He(d,p)^{4}He reaction.[10] The fractional intensity transmitted to the sample surface for a 0.5 by 0.5-in. beam was calculated as 5%, using the Moliere scattering theory. The same type of computation was also performed for a system with a known transmitted intensity[10] and was found to agree with an experimental determination. Excessive heating of the foil occurs for beam currents above ∿1 μA, which places an upper limit on the helium deposition rate.

IRRADIATION PROCEDURE

To illustrate how the ion flux, ion fluence, and temperature are monitored during an irradiation, the specific procedures used at ANL for bombarding a 4 by 5 specimen array will be briefly described using Figs. 10-13. Figure 10 shows the completed data sheet for a $^{58}Ni^+$-ion irradiation of nickel. The sheet summarizes the irradiation conditions for each specimen. Figure 11 shows the prerun beam-profile data taken along each specimen row. An annotated portion of the temperature and ion-current recorder outputs is reproduced in Fig. 12. The oscillograph traces of the residual-gas-analyzer spectrum taken at a gauge pressure of 10^{-7} Torr and the output from the beam-profile monitor are reproduced in Fig. 13. Data recorded at each procedural step are listed in the right-hand column of Table 1.

No irradiations are performed until the entire accelerator system is stabilized, and the ion-source conditions for optimum ion yield are established. In general, this takes from 12 to 24 h of continuous operation, during which time the sample holder is installed in the chamber, outgassed, and a vacuum of $<10^{-7}$ Torr is established.

Data Sheet: Ion Bombardments Run #: [illegible]-4 Run Rating: Acc #sheets / sheets #1

Sample: 34 MeV Ni^{4+} Ion Bombardment of Ni at 600°C to a Calculated Dosage of 40 d.p.a. using a Defocussed Beam

Sample Details:
Material: H.P. NICKEL / 18-8 Si SS Origin: TMC State: Annealed C. W.
Specimen Mounting: CLAMPED Furnace Location: 3 Chamber: 2 Target Holder: 3
Appearance Before Irradiation: CLEAN FLAT S/C RESIDUE After: CLEAN, SOME RELIEF

Desired Irradiation Condition
Particle Energy 34 Flux .66 uAcm^{-2} 5x10^{-9} dpa s^{-1} Fluence 5.3 mC cm^{-2} dpa 40
Point of Injection MIDDLE Irradiate Area 4x4

Irradiation Conditions Ex: Port 0° Beam Line 60°
Accel: Differential 3/ MV:PH Setting 279.8 mV: Particle N/ Magnet Setting 87 A 34 MeV
Rasters: Vertical: Waveform: 6x10^{-2} Hz Ampl. Vernier 2.0 Pk-Pk-V 400:1 Attn 1.2
Horizontal: Waveform: 2x10^{-2} Hz Ampl. Vernier 1.0 Pk-Pk-V 40:1 Attn 5
Steerer Settings: 1st Vertical 600 Horizontal 600 2nd Vertical 600 Horizontal 580

Object Slit Settings: Upper .820 Lower .856 E .890 W .850
Image Slit Settings: Upper .815 Lower .824 E .850 W .825
Chamber Slit Settings: Upper .867 Lower .907 E .910 W .870
Half-Width Beam Integrator Attn 400 x 100 Integrator Range 3x10^{-6}
Vacuum Chamber 6x10^{-6} Torr Drift Region 4x10^{-6} Chamber 1.2
T.C. Temps Readout Block T.C.# 9 †Plug & Pins W5 Comp.# N/C mV TC mV 593 °C
Control Block T.C.# 9 †Plug & Pins 8W Comp.# N/C mV TC mV 586 °C
Surface T.C.#: †Plug & Pins W4 Comp.# N/C mV TC mV 530 °C
Surface Temp. IR Scale .6 10° Angle Incidence 60° °C †Emissivity .25
Optical Millipyro †Emissivity
Furnace # 3 Fil. Current 8A H.T. Voltage 1KV Current 60mA Total Watts 35
Furnace # N/C Fil. Current — H.T. Voltage — Current — Total Watts —

Recorders	Red Signal	mV/ind.	Zero	Blue Signal	mV/ind.	Zero
1.	T/C	5mV/in	0	[illegible]	1mV	0
2.	Ecliboy Sputter	1mV/in	0	Integrator	1mV/in	0
3.	Micro	10mV/in	0	N/C		

Current Dose Data, etc.

Operation & Clock Time	Run Time	Irrad. Time	Beam Current	Current Integrator Shutter	Mask Setting Vertical Horiz.	Mask Posit. Vertical Horizontal	Samples Exposed	Dose	Operator
Profile					1.55 1.95				
Irrad.	31.77 1906	31.77 1906	3.843 mC	1.96			c 1/2		
	64.6	32.83 1970	3.822	1.9	1.55 1.95		c 1/2/3		
	132.4	67.8 4068	3.80	1.95 1.9	1.55 1.95		c 1/2/3/4		
	160	37.60 1655	3.834	1.95 1.95	1.55 1.95		c 2/3/4		
	190		3.46 mC 1.9	1.95 1.95					

*Complete Before Run & Submit to Wallace & Taylor, MSD †Completed loading samples

SPECIMEN MOUNTING LOOKING FACE ON

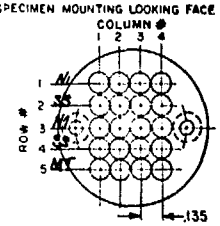

SURFACE TEMPERATURE

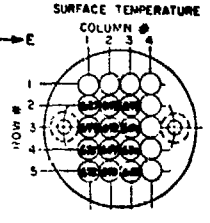

HOLDER # 3 LOAD #

Location Col.	Location Row	Composit.	Foil Section Depth Å	Dose/Dose Rate Tot. Time Secs.	Dose/Dose Rate uA/cm^2	Computations mc/cm^2	Computations dpa/sec dpa	Comment
1	1	Ni 362	3900	7825	.44	4.17	4.9x10^{-3} 38.7	
1	2	18-8 Si		7825	.505	4.79		
1	3	Ni 25A	4500	7825	.545	6.15	5.9x10^{-3} 39.6	
1	4	18-8 Si		7825	.428	4.06		
2	1	Ni 359	3900	9480	.566	5.36	4.1x10^{-3} 38.7	
2	2	18-8 Si		9480	.669	6.34		
2	3	Ni 36A	3300	9480	.682	6.46	4.6x10^{-3} 43.0	
2	4	18-8 Si		9480	.616	5.84		
3	1	Ni 339	3900	7825	.61	4.61	4.4x10^{-3} 38.7	
3	2	18-8 Si		7825	.72	5.44		
3	3	Ni 27A	3300	7825	.739	5.58	5.0x10^{-3} 37.9	
3	4	18-8 Si		7825	.692	5.23		
4	1	Ni 350	3900	5492	.410	2.31	3.0x10^{-3} 16.7	
4	2	18-8 Si		5492	.430	3.71		
4	3	Ni 28A	4600	5492	.518	2.92	3.9x10^{-3} 36.9	
4	4	18-8 Si		5492	.480	2.71		
T/C	CHECK							
#3	#9	#11						
381	402	355						
485	508	438						
590	602	525						

Fig. 10. Typical completed data sheet.

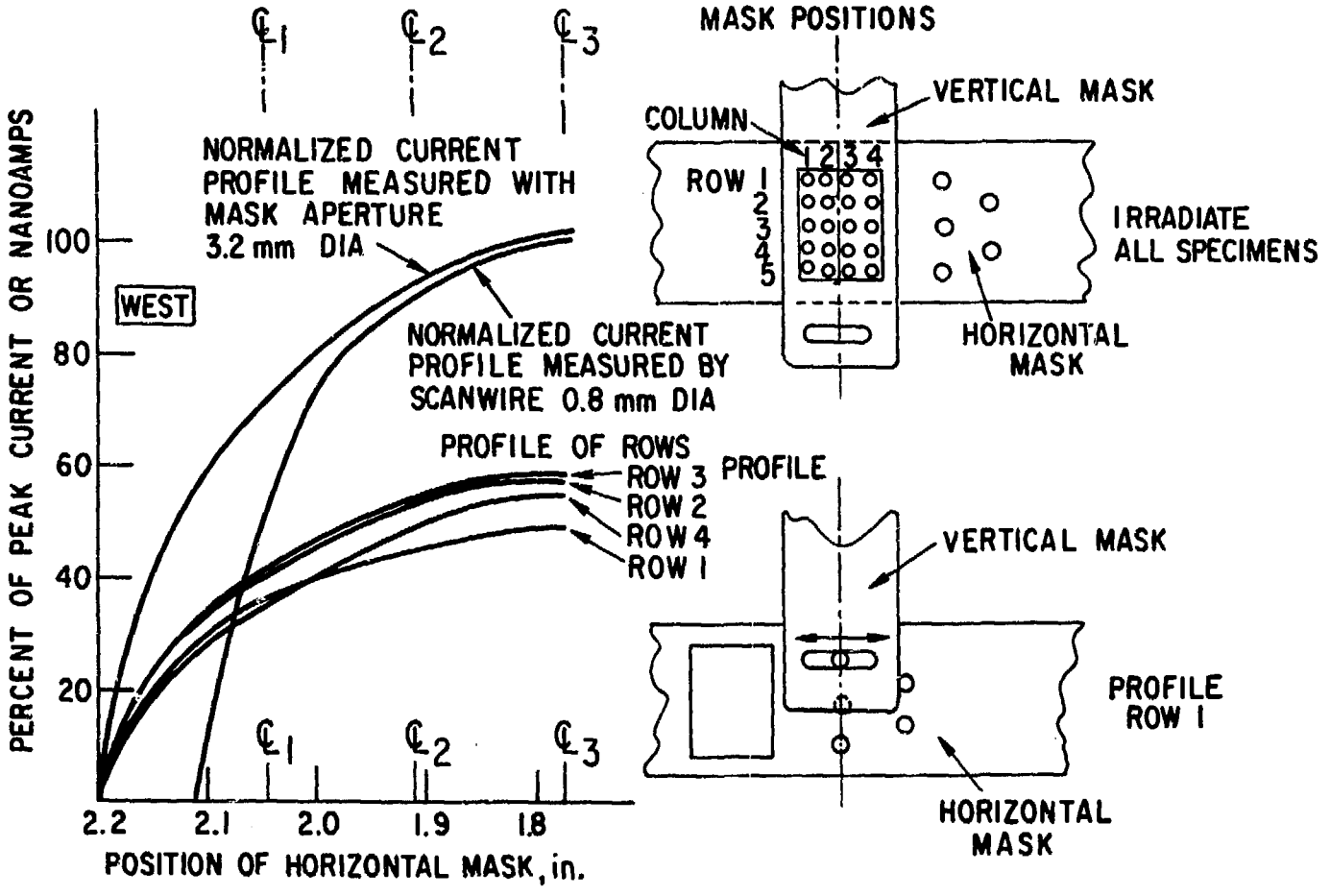

Fig. 11. A typical beam profile measured with apertures and the beam-profile monitor. The vertical and horizontal mask positions are also indicated: upper right, during run; lower right, during profile.

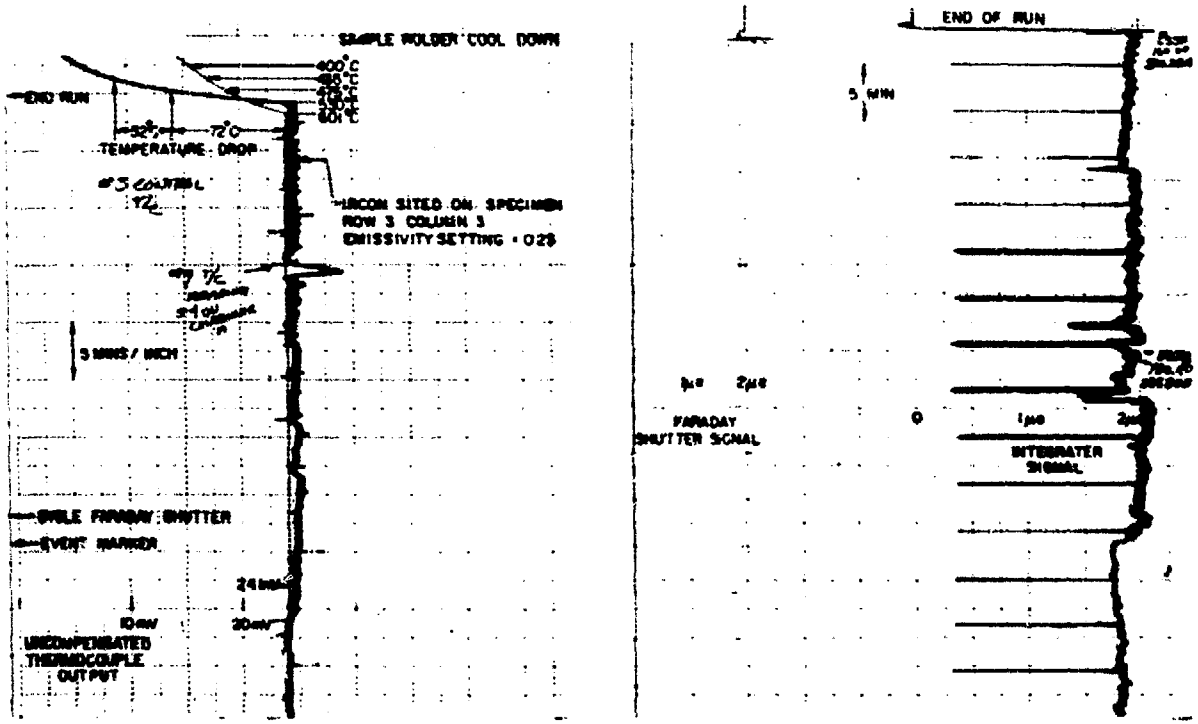

Fig. 12. Recorder Data

(a) temperature (b) current

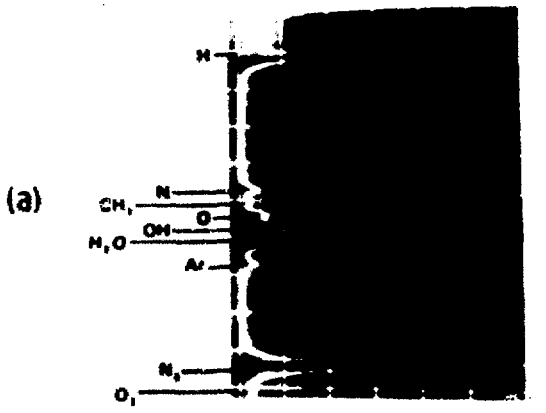

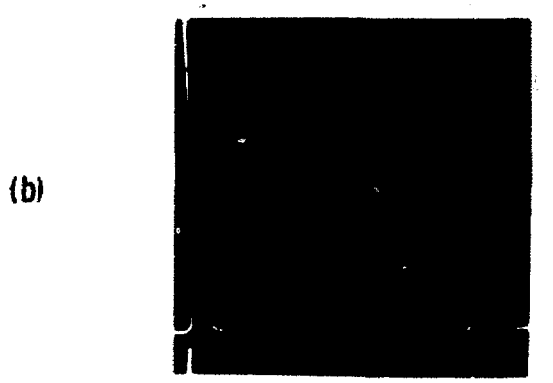

Fig. 13. Oscillographic displays of (a) Residual Gas Analyzer Spectrum. (b) Beam-profile Monitor Output.

Table 1. Irradiation Procedure

Operation	Record
1. Establish ion energy and current for desired irradiation condition	Projectile mass vs analyzing magnet current
2. Align beam through slit system to center beam in target chamber. Align telescope on beam axis	Slit settings
3. Align target holder and masks on beam axis	Target holder position; Horizontal mask position; Vertical mask position
4. Profile Beam: traverse each aperture across the beam	Current density vs horizontal position, row 1-5 (Fig. 11); Faraday shutter current (Fig. 4); Profile monitor current (Fig. 12b); Photograph beam profile (Fig. 13b)
5. Adjust beam current and defocused condition to obtain desired beam-current density. Repeat step 4 until satisfactory	
6. Heat sample holder to run temperature. Record accelerator condition. Check beam stability	Ion energy, magnet current, and steering and scanning settings; Thermocouple and pyrometer temperatures and vacuum (Fig. 10)
7. Close Faraday shutter, center furnace, set initial horizontal and vertical mask positions, and align pyrometers on appropriate specimen	Commence continuous current and temperature records (Fig. 12)
8. Commence irradiation: Survey specimen with pyrometers. Progressively expose lower-dose samples	Faraday shutter current at 5-min intervals (Fig. 12b); Start integrator count, record counts, and mask positions at successive dose steps (Fig. 10a); R.G.A. Spectrum (Fig. 13a)
9. Close shutter, commence cool down	Total time; Irradiation; Integrator counts (Fig. 10a)
10. Center target holder and mask apertures. Repeat step 4	

In procedural step 1, the desired isotope is selected using the analyzing magnet. The identification of the ion species should be confirmed from the known isotopic abundances of the various ions accelerated from the source. In step 2, the appropriate ion beam (e.g., $^{51}V^{+}$ and $^{12}C^{+}$) at the desired accelerating voltage is passed through the beam-transport system to the rear Faraday cup in the target chamber. The centering of the beam at each slit aperture is recorded by slit ratio meters; the size of the beam is reduced at each aperture to provide a signal from each slit. The beam size necessary to irradiate 20 specimens was 0.57 by 0.715 $in.^2$ At least two iterations for steps 4 and 5 of the alignment procedure are normally required at the beginning of a set of irradiations to obtain the desired mean ion current density on the required group of specimens. The beam is then profiled by traversing a circular aperture across the beam and recording the current transmitted to the Faraday cup with a function plotter. The individual profiles, total transmitted profile, beam-profile-monitor output, mask positions, and specimen locations are shown in Fig. 11. To measure the beam intensity during the irradiation, the output from the beam-profile monitor is normalized to the current transmitted to the rear Faraday cup. The Faraday shutter current is also recorded as a cross check for the normalization. The proportional current measured by the scan wire is within 1% of the current measured by the rear Faraday cup when the beam just filled the rectangular mask aperture (Fig. 11). The beam profile determined in this manner and the profile-monitor trace agreed within the resolution of the scan wire when the beam divergence from the profile monitor to the target location was taken into account. Once the desired irradiation conditions are established, all machine variables are recorded, and the sample holder is brought to the irradiation temperature. The sample holder is brought onto the beam axis (with the Faraday shutter closed). After surveying the temperatures and positioning the mask system to expose the desired specimen, the irradiation is started. The specimens are progressively exposed to the beam, with high-dose irradiation first, to avoid void-annealing effects. Because of beam heating and variations in the specimen-clamping pressures, a temperature difference of 25°C is common. The slight change

in surface temperature during the 2-s current sampling by the Faraday shutter can be seen in Fig. 12. At the completion of the irradiation, the sample holder is cooled at an initial rate of 70°C/min. Beam profiles are redetermined, and the specimen dose is calculated from the average of the prerun and postrun profile currents and normalized by the profile monitor current and/or the Faraday shutter current. The mean current density for each specimen is then scaled to the total mean current during the irradiation. The displacement rate within the TEM foil is calculated by means of the theoretical depth-dependent damage function from the Brice Codes RASE 3 and DAMG 2.[7] The total displacement dose was obtained using the known irradiation time.

PREPARATION OF VANADIUM SPECIMENS

The preirradiation specimen-preparation technique and the postirradiation sectioning, thinning, and quantitative microscopy procedure developed by the Radiation Effects Group at ANL for vanadium alloys are described below. The radiation damage in a surface layer ~1 μm is studied primarily by TEM using a JEOL 200-keV electron microscope. The swelling can also be assessed from measurements of the step height between the irradiated and unirradiated regions of the specimen surface. This technique has been used extensively for determining the swelling of ion-irradiated stainless steel,[11] and in studies of niobium that have been carried out at ANL.[12] To avoid anomalous surface effects in the TEM work and to characterize the damage at a known dose, foils are prepared from a measured depth beneath the irradiated surface.

The specimens were prepared from 0.20-mm-thick grade 1 vanadium sheet stock obtained from either Wah-Chang of Albany or Materials Research Corp. Spectroscopic and gas-analyses show that an interstitial impurity level of 500 wt ppm is typical. The sequence of steps in the specimen-preparation procedure are shown in clockwise order in Fig. 14. Disks 3 mm in diameter are punched from the sheet stock, flattened between flat steel blocks, and annealed in vacuo or high-purity argon gas for 1 h at 1100°C. The disks are mounted in resin, lapped flat, and vibratorily polished in two stages using grinding slurries of 0.3 and 0.05-μm alumina

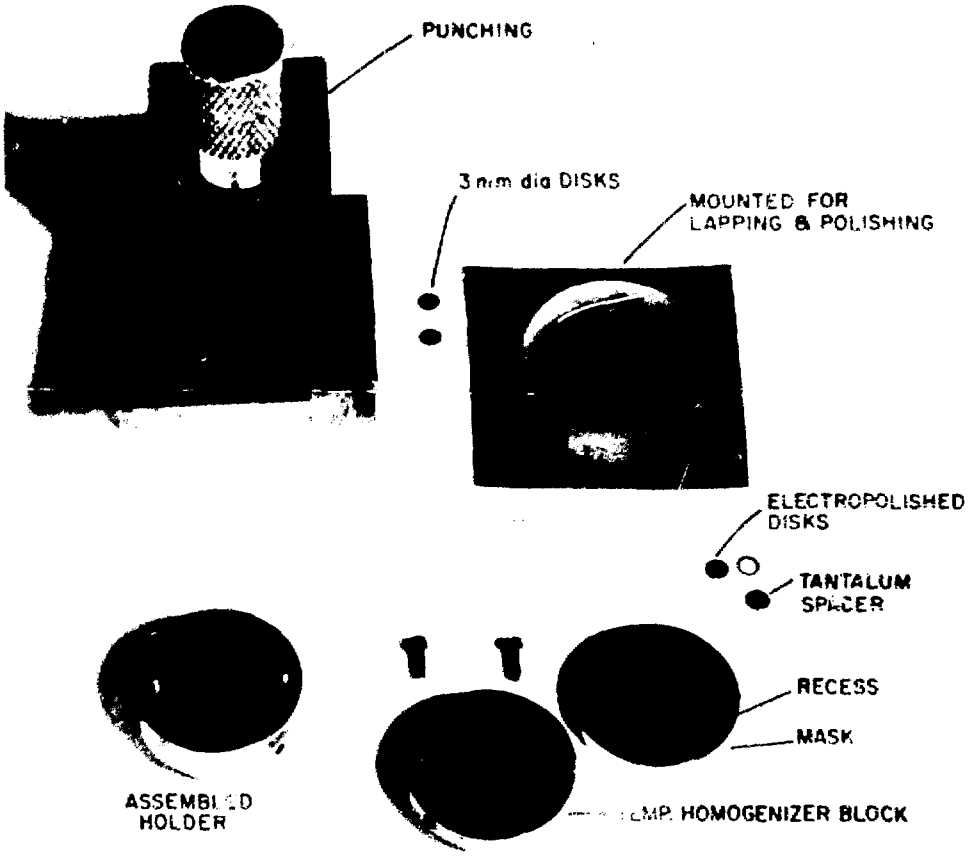

Fig. 14. Specimen preparation sequence.

grit. The specimens are demounted by soaking the mounts in acetone and then thoroughly cleaned in an ultrasonic bath containing acetone followed by rinsing in successive baths of acetone and ethyl alcohol. Mechanical polishing damage is removed by electropolishing ~1.0 μm of material from the flat surface in a 20% H_2SO_4 acid and 80% methanol solution at room temperature. This same electropolishing solution is used in subsequent electropolishing steps. The absence of surface dislocations is checked by electron microscopy. Only specimens with flat surfaces to within 0.05 μm are selected for ion irradiation.

Specimens are mounted in the counterbores of a tungsten mask. An annealed platinum wire spacer ring of appropriate diameter is placed in each hole so that the specimen protruded 0.001 in. above the back face of the mask. The temperature homogenizer block was attached to the mask with two small set screws. Additional mask-to-homogenizer block clamping pressure is provided during the irradiation by the clamp ring (Fig. 8). Each irradiated specimen is referenced by the run number and by its column and row position in a specific irradiation (Figs. 10 and 11).

POSTIRRADIATION EXAMINATION

The irradiated surface of each specimen is examined by means of an optical microscope, with particular emphasis on determining whether the sample is satisfactorily clamped and free of contamination, pitting, or scratches that might interfere with the electropolishing steps. A typical postirradiation surface microstructure of a vanadium sample irradiated at 700°C with $^{51}V^{+}$ ions to a peak dose of ~50 dpa is shown in Fig. 15. The microstructure is not significantly different from that prior to irradiation, indicating that swelling in vanadium is probably not greatly grain-orientation dependent. If it were then one would expect to observe relief of adjacent grains.

After completing the optical microscopy, a region near the edge of the irradiated surface of the specimen is protected with a thin layer

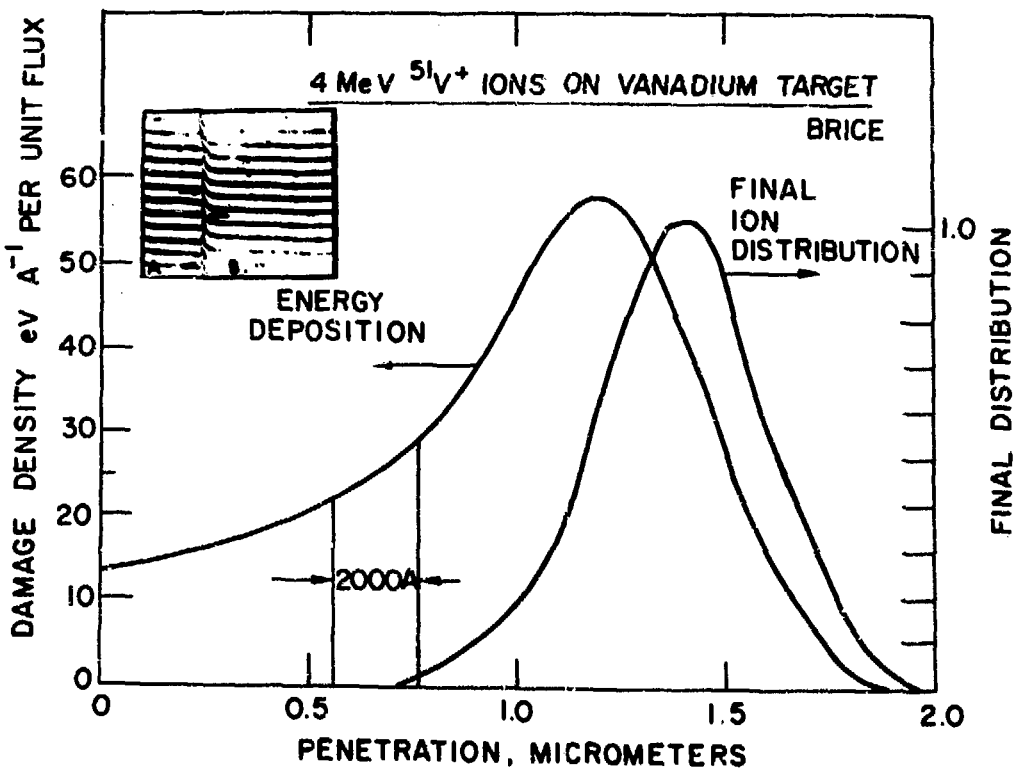

Fig. 15. The damage profile and final ion distribution of 4-MeV $^{51}V^{+}$ ions incident on a vanadium target calculated from computer codes RASE 3 and DAMG 2. The fringe pattern in the upper left illustrates the removal of 5400 Å (1.8 fringes) of material from the irradiated surface.

of Microshield.* The specimen is then electropolished at room temperature to establish a new surface ~1000 Å short of the peak damage depth. The conditions necessary to reproduce a desired sectioned depth include the precise location of the electrodes and the placement of the specimen in the stirred solution. The removal of ~8000 Å of vanadium required two or three quarter-second polishing bursts at 70 V. After each sectioning burst, the lacquer is removed in an acetone bath, the specimen is rinsed with alcohol, and the sectioned depth is determined by two-beam interference microscopy using a Zeiss interferometer. The position of the sectioned depth in relation to the calculated damage profile and a micrograph of the interference pattern produced by white light at a magnification of 400X are shown in Fig. 16. The displacement of 1.8 fringes corresponds to a sectioned depth of ~5400 Å. The straight fringe lines, remote from the step, indicate a uniform removal of the irradiated surface. The sectioned depth used in the dose calculations is based on the mean of the fringe pattern readings taken from both steps near the center band. After sectioning, the irradiated surface is lacquered, and the specimen is thinned from the rear using the electropolishing solution at 0°C. The penetration is done with a South Bay Technology model 550 Jet Thinning Instrument to produce a reasonably large region in the center of the disk that is transparent to electrons.

The electron microscopy of each foil generally included the investigation, in at least three grains, of the microstructure that develops in areas remote from the grain boundaries. In each area, stereomicrographs of the void microstructure are taken at a magnification of 55,000X under absorption-contrast-underfocused conditions such that the void edges are delineated by a dark fringe. A typical micrograph is shown in Fig. 17. The dislocation structure in the same area is imaged under a two-beam diffracting condition. In a number of instances, the microstructures that develop in the vicinity of grain boundaries are also investigated. In most high temperature irradiations (>700°C) and some low-dose

*Lacquer developed by the Michigan Chrome and Chemical Company.

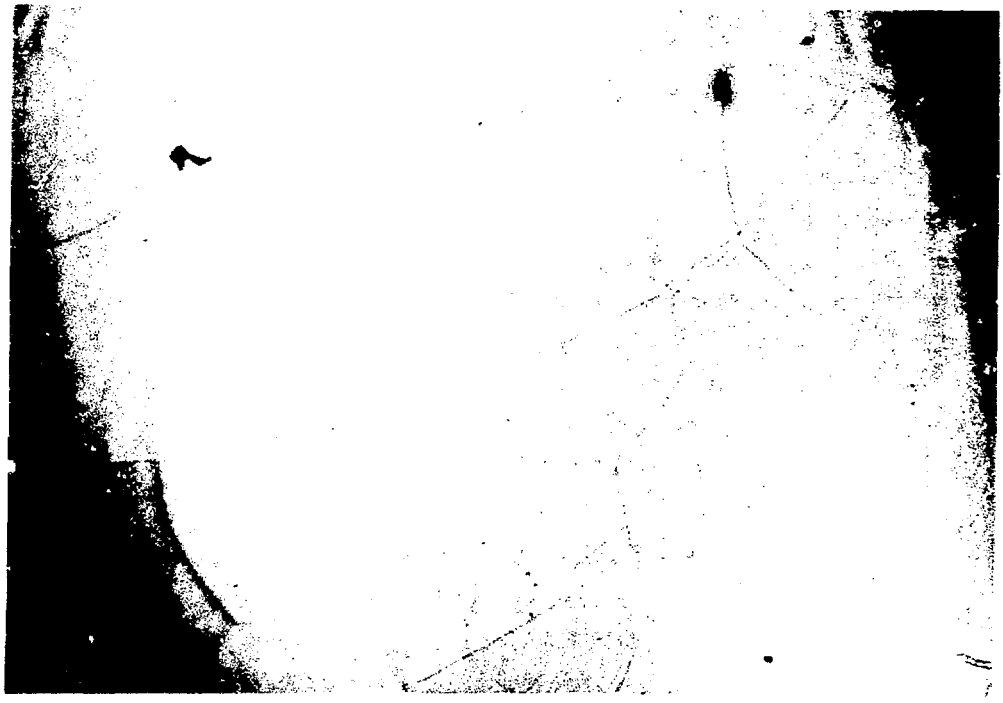

Fig. 16. Micrograph of the surface of irradiated vanadium showing slight relief of the grains.

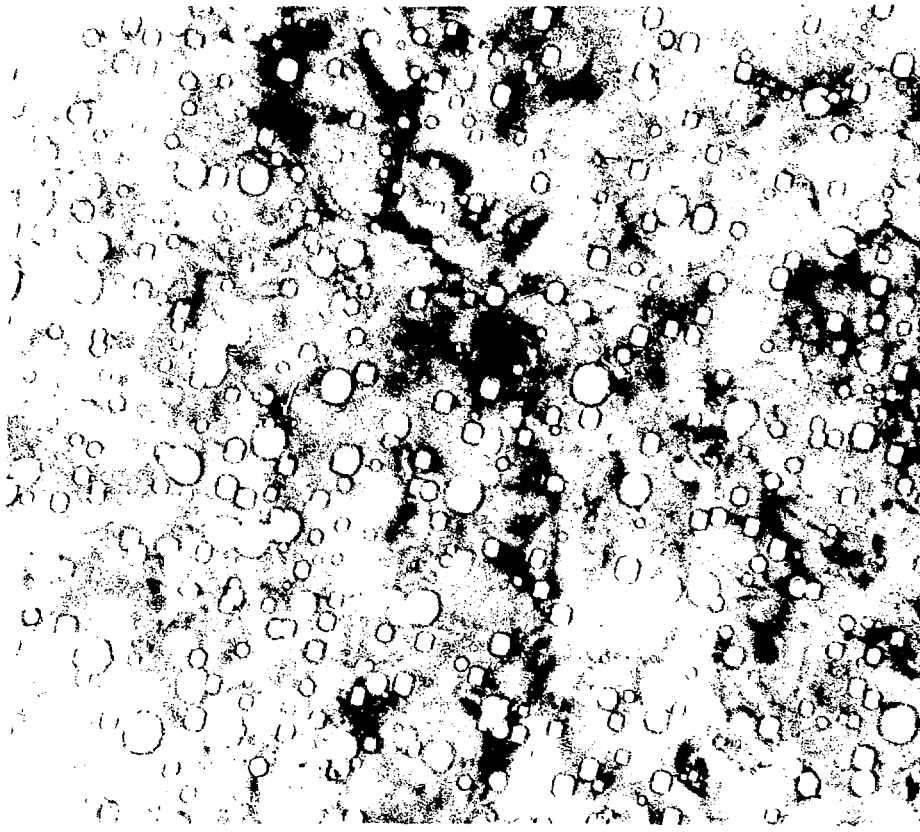

Fig. 17. Commercial-purity vanadium irradiated to ∿20 dpa at 750°C. Mag. 100,000X; ∿(331) foil orientation.

irradiations, low void-number densities necessitate the use of lower magnifications (33,000 and 15,000X) to increase the area of each micrograph and to improve the counting statistics for the swelling determination.

QUANTITATIVE METALLOGRAPHY

The quantitative metallography is carried out on stereomicrographs printed at a magnification of 165,000X. The foil thickness is determined in each area investigated using the parallax, measured with a Hilger and Watts Floating Spot Stereo Viewer, between the upper and lower foil surfaces. The tilt angle between the stereopairs and the magnification of the prints yielded the foil thickness t

$$t = \frac{P}{2M \sin \theta}$$

where R is the parallax, M is the magnification, and θ is the tilt angle, routinely 6°. The foil surfaces were identified by artifacts such as pits, electropolishing streaks, or voids that were either on or intersected the surface.

The voids present in one of the stereopairs, or possibly a lower magnification print of the same area, are counted with a TGZ3 Zeiss particle-size analyzer that has 48 size classes. The analyzer diaphragm is superimposed over the image of internal voids, approximating their polygonal shape by a circle. The edge lengths of the cubic voids are measured.

The internal void-distribution data, foil thickness, area, and magnification are used as input to the computer code "BIBELOT" which corrects the number of voids observed in each size class to account for the number that intersected the surface. The expression used is

$$n_i = \frac{n_i \text{ observed}}{1 - d_i/t}$$

where d_i is the mean diameter of size class i, and n_i is the true number

of voids in size class i. The code then calculates the mean void size and the standard deviation of the mean void size defined as

$$\sigma = \left[\frac{1}{N_T}\sum_i n_i(d_i - \bar{d})^2\right]^{1/2}$$

where $N_T = \Sigma n_i$, and $\bar{d}$ is the mean void diameter. The mass average diameter is given by

$$\bar{D} = \left[\frac{1}{N_T}\sum n_i d_i^3\right]^{1/3}$$

The void number density is calculated from the total number of voids, the foil thickness, and the foil area. The void-volume fraction is then given by

$$\frac{\Delta V}{V} = \frac{\pi}{6}\bar{D}^3 N_v$$

where N_v is the void number density.

Dislocation number densities in the foil are calculated by the line-intercept method

$$\rho = \frac{2NM\alpha}{Lt}$$

where N is the number of dislocation line intersections, L is the total mesh-line length, and α is the correction factor for dislocations not illuminated by the particular two-beam condition used.

The mean dose per unit ion flux in a given region of the foil is calculated by determining the mean energy deposited in that region, as shown by the cross hatching in Fig. 16.

ACKNOWLEDGMENTS

The authors wish to express their appreciation to the staff, A. Langsdorf, F. P. Mooring, and R. Amrein, and technicians who operate the Dynamitron Facility who have given their active cooperation in the development and operation of the system. B. Kestel and C. Steves contributed to the development of the specimen preparation techniques. The manuscript was edited by F. Adams.

REFERENCES

1. A. Taylor, Proceedings of the International Conference on Radiation Test Facilities for CTR Surface and Materials Program, July 15-18, 1975, Argonne National Laboratory, P. J. Persiani, (ed.), to be published.

2. R. S. Nelson (ed.), Consultants Symp. on Physics of Irradiation Produced Voids, Harwell, U.K., AERE-R7934 (1974).

3. S. T. Picraux, E. P. EerNisse, and F. L. Vook, (eds.), Application of Ion Beams to Metals, Plenum Press, New York, 1974.

4. F. P. Mooring, A. Langsdorf, and R. L. Amrein, IEEE Trans. on Nuclear Science, Vol. NS-22, No. 3, 1975, p. 1726.

5. A. Taylor, IEEE Trans. on Nuclear Science, Vol. NS-18, No. 3, 1971, p. 79.

6. A. Taylor, J. Stubbins, and J. Moteff, Symposium on Experimental Methods for Charged Particle Irradiations, September 30, 1975, Gatlinburg, Tennessee.

7. D. K. Brice, Sandia Laboratory Report, SLA-73-0410, (1973).

8. G. Moliere, Z. Naturf. 3a, 78 (1948).

9. W. C. Dickinson and D. C. Dodder, Rev. of Sci. Instrum. 24, 428 (1953).

10. A. Taylor and T. E. Klippert, ANS Trans. 16, 82 (1973).

11. W. G. Johnston, J. H. Rosolowski, A. M. Turkalo, and T. Lauritzen, J. Nucl. Mater. 48, 330 (1973).

12. W. G. Johnston, J. H. Rosolowski, A. M. Turkalo, and T. Lauritzen, J. Nucl. Mater. 46, 273 (1973).

13. B. A. Loomis, A. Taylor, and S. B. Gerber, J. Nucl. Mater. 56, 25 (1975).

14 MeV NEUTRON DAMAGE IN SILVER AND GOLD*

R. L. Lyles and K. L. Merkle
Materials Science Division
Argonne National Laboratory
Argonne, Illinois 60439
USA

ABSTRACT

Displacement damage due to 14 MeV neutrons predominantly take place in the form of rather energetic displacement cascades. The vacancy clusters that are directly formed in the depleted zones are observed by transmission electron microscopy in 14 MeV neutron bombarded gold and silver. The number densities and structures of cascades will be compared quantitatively with theoretical predictions and results from cascade studies using self-ion bombardment. The splitting into subcascades will be demonstrated and its importance to 14 MeV neutron damage will be discussed.

INTRODUCTION

Components of the deuterium-tritium fusion device, in particular, the first wall of the vessel surrounding the plasma, will be exposed to intense irradiation. Of the total flux a considerable fraction at the first wall will consist of 14 MeV neutrons.[1] Since these energetic neutrons have a significant amount of the total reaction energy, they are expected to be responsible for a major portion of the radiation damage incurred by CTR materials.

The results of recent investigations[2,3,4] to identify the character and nature of the materials problems encountered in 14 MeV neutron radiation damage are largely incomplete. However, these preliminary results have served as an impetus for suggestions to use proton and heavy ion radiation to simulate the effects of damage by 14 MeV neutrons. It should be noted that such energetic neutrons are able to transfer a considerable amount of kinetic energy to the lattice atoms. For simulations to be

*Work supported by the U.S. Energy Research and Development Administration.

useful, the nature of the resultant radiation damage must be similar to that found with 14 MeV neutrons. Moreover, it will be necessary to develop damage production cross sections and to obtain the necessary correlations between them.

Since all damage processes involve PKA production, information derived from comparing the primary recoil distribution and the nature of the displacement cascades of 14 MeV neutron damage with damage caused by heavy ion irradiation could increase the possibility of accurately predicting simulation conditions. In the present investigation, comparative results are developed for the cascade structures observed with 14 MeV neutron bombardments. An earlier study[5] on 14 MeV neutron irradiation of Au has found excellent agreement between the observed cross sections for the formation of visible cascades and the theoretically predicted ones based on an analysis of self-ion results. The present study fully confirms these results on Au. Therefore, the emphasis is now focussed on the development of the results in Ag and a comparison with the Au information.

Silver, in addition to Au, was chosen because the atomic number is close to that of metals of prospective first wall materials. Also, silver is better understood than Au with regards to its defect annealing characteristics. In an earlier study it has been demonstrated that vacancy clusters in Ag large enough to be visible by transmission electron microscopy can be observed as a result of energetic self-ion bombardments.[6] Although subcascades were not observed, from the correlation of the results with Au, subcascades would be expected to be found in cascade structures as energetic as that found in 14 MeV neutron bombardments. This has been confirmed in the present investigation and, in addition, subcascade formation has been observed recently by us in self-ion bombardments of Ag.

In order to make a quantitative correlation between self-ion results and the cascade formation cross section under 14 MeV irradiations, it is necessary to know the probability of formation of visible cascade structures as a function of cascade energy. This function has been well established for gold. Recent results on the self-ion bombardments of Ag indicate that the probability function is shifted to slightly lower energy

in the case of Ag. This result is also manifested in the more pronounced splitting into subcascades in Ag relative to Au for cascades of the same energy. Moreover, the cascade size in Ag is noticeably larger than in Au by a factor of 2 in diameter as predicted by the random cascade model.[7] Also, in Au the random cascade model predicts cascades which are smaller than those experimentally found. Similarly, we can expect the cascades in Ag to be larger than that which corresponds to the random cascade model.

For a comparison material, Ag is an excellent choice since the basic cascade structure is very similar to that in Au, but at the same time, since Ag is a lighter metal, there should be distinct differences in the sizes and numbers of cascades present.

The maximum energy transferred by 14 MeV neutrons in an energetic recoil is 281 keV for gold and 510 keV for silver. This major difference in maximum recoil energies offers an excellent opportunity for correlation of results and with the inclusion of the proper scaling factors, these results should be useful in studying other metals.

EXPERIMENTAL

The gold specimens were (100) thin films, which were epitaxially grown on cleaved surfaces of rock salt. The films were subsequently annealed on the rock salt in air for 30 minutes at 350°C and then mounted on Au electron microscope grids. Film thickness was accurately determined by gravimetry.

The Ag specimens were from rolled 0.005" polycrystalline foils (6 9's pure from Cominco American). Microscope grid size samples were punched out and annealed in vacuum at 600°C for 1 hour.

Each of the specimens were mounted in an Al holder. The individual specimen holders were then placed into a copper capsule such that the specimens were spaced over a distance of 56 mm to provide sampling at different fluences. After loading the samples, the copper capsule was evacuated and back-filled with 1 atmosphere of helium to suppress the recoils from outside of the specimens.

The capsules were irradiated at room temperature with 14 MeV neutrons at the Lawrence Livermore Laboratory RTNS. The capsules were positioned such that the axis of the beam was parallel to the axis of the capsules. Niobium dosimetry foils were attached to the exterior of both the front and the rear of each of the capsules. Also, sets of dosimetry foils (Nb, Ni, Au) were interspaced among the specimens. The fluences of the niobium foils on the exterior of the capsule were determined at LLL by the method described by Van Konynenburg.[8] Values for both fluence and energy were obtained from the sets of dosimetry foils inside of the capsule. These measurements were made at ANL.[9] Fluence values for the specimens ranged from 4.11×10^{16} to 6.98×10^{13} n/cm^2.

After irradiation, the specimens were kept at room temperature for several weeks and then decapsulated. The gold specimens were used directly for electron microscopy. The Ag samples were electropolished with a cyanide solution[10] in a commercial Fischrone jet polishing apparatus.[11]

All of the specimens were examined by electron microscopy under kinematical conditions. In the gold samples sharp, well defined black spots are found within a few degrees of the [001] direction.[5] Under these conditions, the most accurate measurements of spot size and position can be made. The polycrystallinity and the variations in thickness due to electropolishing in the silver made the selection of appropriate orientations more difficult. Consequently, these samples were studied under a variety of orientations. However, all of the micrographs were taken in bright field under kinematical conditions.

RESULTS

The transmission electron micrographs in Figs. 1 and 2 illustrate a comparison of the damage from 14 MeV neutron irradiation of Au and Ag. The characteristic radiation damage defect clusters are clearly distinguishable in both materials. Stereo micrographs of both Au and Ag specimens demonstrate that the individual clusters are distributed throughout the thickness of the samples. From the heavy ion results,

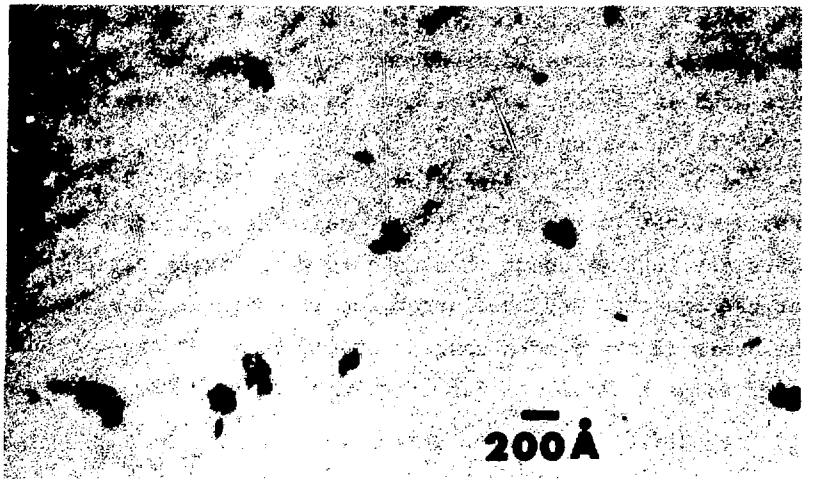

Fig. 1. An example of characteristic 14 MeV neutron damage in Au. Many distinctly separate cascades are present. The bunching of the clusters is indivative of subcascade formation.

Fig. 2. 14 MeV neutron radiation damage in Ag. Bunching of clusters exists, although not as pronounced as is observed in Au. The individual cascade size is somewhat larger than in Au.

it is inferred that these clusters are of the vacancy type and are expected to be largely Frank loops on the (111) planes. The nature of the defects in gold show a distinct bunching of individual spots. Each group of closely spaced clusters is produced in an individual cascade. At the low fluence used in Fig. 1, each cascade is distinctly separate in space, and the probability for overlap is very low. The bunching of these spots is indicative of subcascade formation. As seen in Fig. 2, the bunching still occurs in silver, although it is not quite as apparent. The individual clusters are further apart than in gold which is expected because of the larger cascade size and the larger recoil energies in Ag. In fact, even on the basis of the random cascade model,[7] the average cascade size is expected to be a factor of 3.5 larger for silver compared to Au.

If the defect structures which are observed are a direct result of the energetic displacements which caused the cascades, number densities of the defects must be directly proportional to the fluence ϕ. This applies to the number densities of cascades, as well as, the number densities of spots produced in 14 MeV bombardments. The number densities of the vacancy clusters as a function of fluence for Ag is shown in Fig. 3. The straight line plotted gives a value of 1.47 clusters per cm. The position of the gold data point shown serves to illustrate that the silver had approximately three times the number of individual clusters as found in the Au. The value for the gold data point is consistent with previously published data.

An observable difference between the defects in Au and Ag was the tendency in Ag for presence of triangular shaped defects as shown in Fig. 4. Since these defects are square-shaped near the (001) orientation and triangular-shaped near the (111) orientation, they are most probably stacking-fault tetrahedra. The smallest defect with this distinct geometry was approximately 35 Å. Other observable defects in the Ag, which were smaller than this size, appeared as the traditional black spot with no discernable shape. The cluster size distribution in Ag ranged from approximately 20 to 130 Å in diameter with an average cluster diameter of 56 Å. This is slightly larger than the 48 Å average for clusters found in Au specimens.

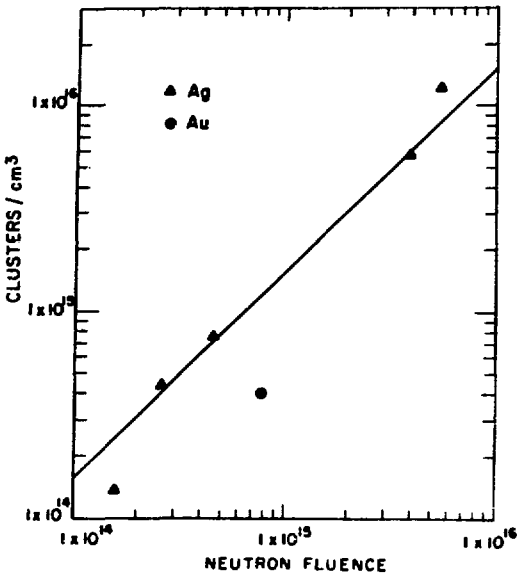

Fig. 3. Number density of defect clusters as a function of fluence ϕ.

Fig. 4. Micrograph illustrating the presence of the triangular shaped defect geometry. The smallest defect with this distinct geometry was approximately 35 Å.

ANALYSIS

To calculate the cross section for the formation of visible cascades by 14 MeV neutron bombardment, one must know the recoil density distribution as well as the criteria for the formation of visible cascades.

The latter can be obtained from self-ion bombardments. In this case, one simply determines the probability for the formation of visible clusters as a function of cascade energy. In this way a probability function W(E) for the formation of visible cascades is obtained.

Typically this function reaches a value of 1 slightly above and slightly below 40 keV in Au and Ag, respectively. Figure 5 shows an example of 10 keV self ion bombarded silver. Here only a small fraction of the cascades produce a visible cluster. On the other hand, multiple clusters are observed if the cascade energy is increased to values that lie significantly above the energy at which a unit probability for the formation of a visible cascade is reached. This splitting into subcascades is illustrated in Fig. 6. In this instance a silver foil has been bombarded with 250 keV Ag^+ ions and there exists a one to one correspondence between the bunches of clusters and the number of incident ions. Although the subcascade formation has not been studied in as much detail in Ag as in Au it is quite obvious that the subcascade formation is expected to be even more pronounced in 14 MeV neutron irradiation of Ag.

The slightly lower effective threshold energy for the formation of clusters in Ag as well as the considerably higher average recoil energies under 14 MeV neutron bombardment will tend to result in a considerably higher number of visible subcascades in the case of Ag as compared to Au.

Figure 7 shows the elastic differential scattering cross sections $d\sigma_{el}/d\Omega$ (ENDF/B data) of Ag and Au plotted against recoil energy E_R. It is seen that the Au cascades are on the average considerably less energetic. The dashed lines in Fig. 7 indicate the recoil density distribution leading to visible cascades, $W(E) \cdot d\sigma_{el}/d\Omega$. By integration the total cross section for the production of visible cascades via elastic neutron collision is obtained

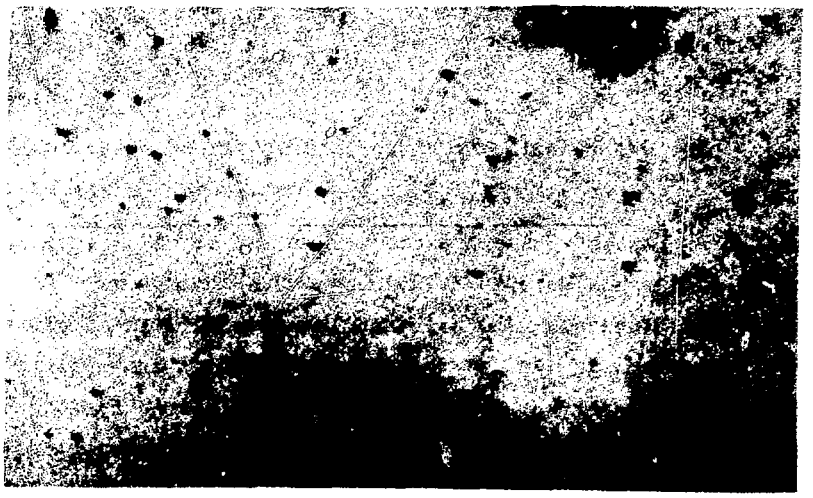

Fig. 5. An example of 10 keV self-ion bombarded Ag. Only a small fraction of the cascades produce a visible cluster and no subcascade formation exists.

Fig. 6. A silver foil that has been irradiated with 250 keV Ag^+ ions. There is a one-to-one correspondence between the cluster bunches and the number of incident ions. Subcascade splitting is very pronounced.

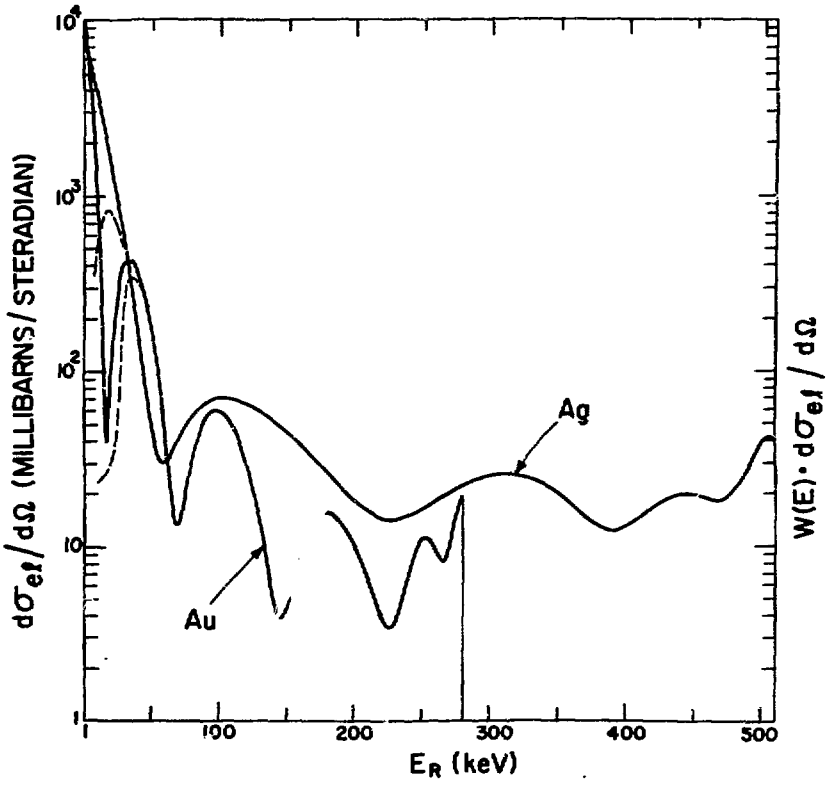

Fig. 7. Differential elastic 14 MeV neutron cross section of gold and silver from the ENDF/B files. The dashed curves indicate the recoil distribution of visible cascades and coincides with solid curves about 50 keV for gold and above 35 keV for silver.

$$\sigma_{el}^{c} = \frac{4\pi}{T_m} \int_0^{T_m} W(E) \frac{d\sigma_{el}}{d\Omega} \, dE$$

It is found that the integration gives numerically the same value for Ag and Au, namely $\sigma_{el}^{c} = 5.6 \times 10^{-25}$ cm^2.

The total elastic scattering cross sections are $\sigma_{el} = 2.71$ and 2.84×10^{-24} cm^2 for Ag and Au, respectively. Due to the strong forward scattering only a small fraction of the elasticly scattered neutrons give rise to a visible cascade. In contrast to this, all of the nonelastic scattering events lead to the formation of visible cascades. This comes from the fact that the absorption of the neutron gives rise to a recoil energy of $T_m/4$, while the secondary particle(s) will be emitted with relatively low energy, such making a reduction of the total recoil energy below about 30 keV very improbable. On the average, the nonelastic recoil energies are expected to lie near 80 and 150 keV for Au and Ag, respectively. The total cross sections $\sigma^{c} = \sigma_{el}^{c} + \sigma_{nonel}^{c}$ for the production of visible cascades are $\sigma_{Au}^{c} = 3 \times 10^{-24}$ cm^2 and $\sigma_{Ag}^{c} = 2.46 \times 10^{-24}$ cm^2.

DISCUSSION

If the total number of visible cascades can be determined experimentally, this value can be related to the number of recoils during the irradiation. The procedure that was used to determine the number of cascades consists of counting the clusters contained in a circular area of a certain diameter. For gold, this diameter was determined to be $\sim$400 Å from the heavy-ion bombardment results. In silver, a 1000 Å diameter area was chosen. The procedure is statistically accurate if the cascade density in the sample is sufficiently low such that cascade overlap is negligibly small and if the most energetic cascades are contained within these circular areas.

For gold, this method gives a cross section for the formation of visible cascade of $\sigma_c = N_c/N\phi = 3.3 \times 10^{-24}$ cm^2, where N is the atomic density and N_c is the number of cascades per cm^3.

Similarly, using a 1000 Å diameter area for silver, the cascade cross section is $\sigma_c = 1.6 \times 10^{-23}$ cm^2. This is significantly higher than the cross section calculated in the previous section from heavy ion data and the 14 MeV neutron recoil spectrum. The data for silver is in contrast to that of gold where the experimental cross section and the calculated cross section agree within experimental error.

There are 3 factors which may contribute to the high cascade density count in Ag. Firstly, the area used to discriminate between cascades in determining the cascade density may be too small. Secondly, in the case of silver, the average cascade diameter produced by 14 MeV neutron bombardment appears to be close to the maximum thickness of the specimen that can be studied with 100 keV electron microscopy. Thirdly, although linearity is observed in cluster density over 2 orders of magnitude of neutron fluences, interstitial cluster formation cannot be excluded in the bulk specimens.

In gold, a 400 Å diameter area was sufficient to discriminate between overlapping cascades. If we use the random cascade theory, we find that the diameter of a cascade for the average recoil energy observed under 14 MeV neutron irradiaton is a factor of 3.5 larger in silver as compared to gold. Therefore, an area of 1000 Å diameter is insufficient to contain all of the defect clusters of a single cascade. Since the thickness of the silver foils was approximately 1000 Å, a fraction of the cascades were not contained completely in the volume viewed by electron microscopy. This situation would also result in a high cascade count.

Since we do not expect a valid cascade cross section from the present result due to the above difficulties, we shall only discuss the effective cross section for the formation of individual clusters and compare this with the theoretically expected cascade cross section. From Fig. 3, $Ns/\phi = 1.47$ spots/cm which corresponds to an effective cluster cross section of $\sigma_s = Ns/N\phi = 2.6 \times 10^{-23}$ cm^{-2}. If this value is compared

with the calculated cross section for 14 MeV neutron bombardment of silver, the σ_s/σ_c is approximately equal to 11. This implies that, on the average, each cascade has 11 clusters. This appears to be somewhat high since the preliminary results from self-ion irradiations indicate that an energy of approximately 30 keV is necessary per subcascade. The average recoil energy in the 14 MeV neutron irradiations is expected to be close to 150 keV. Therefore, the number of subcascades observed appears to be high by roughly a factor of 2. Similar discrepancies regarding the number of subcascades existed in the results for gold also.

The size of the clusters can give an indication of the number of vacancies they contain. Figure 6 shows a typical area in a Ag specimen with several cascades. These clusters are assumed to be Frank loops on (111) planes. Since the average cluster diameter was 56 Å for silver, this corresponds to approximately 468 vacancies per cluster. In Ag, the average cascade energy, E is approximately 150 keV. The total number of vacancies produced in a cascade with 150 keV cascade energy can be calculated using a simple Kinchin-Pease expression; neglecting electronic losses the number of vacancies per cascade Nr is

$$N_V = \frac{E}{2E_d},$$

where E_d is the threshold energy for displacement. If we take 28 eV to be the threshold energy for Ag, then the average cascade should contain nearly 2700 vacancies. In the extreme, if the maximum energy, $T_m = E = 510$ keV for Ag, is used, the largest cascade should contain over 5000 vacancies.

Likewise, for gold, the average damage energy is approximately 80 keV. With a threshold energy, E_d, of 35 eV, the average cascade in Au is expected to contain about 1200 vacancies while the largest cascade, T_m = 281 keV, should have almost 4100 vacancies.

All interactions of 14 MeV neutrons with gold and silver take place as elastic and nonelastic collisions. Data for both gold and silver show that the elastic collisions are not responsible for more than 20% of the cascades observed in gold or for more than 30% of the cascade structures silver. Therefore, most of the 14 MeV neutron damage is due to nonelastic neutron scattering events. The average recoil energy is expected to be

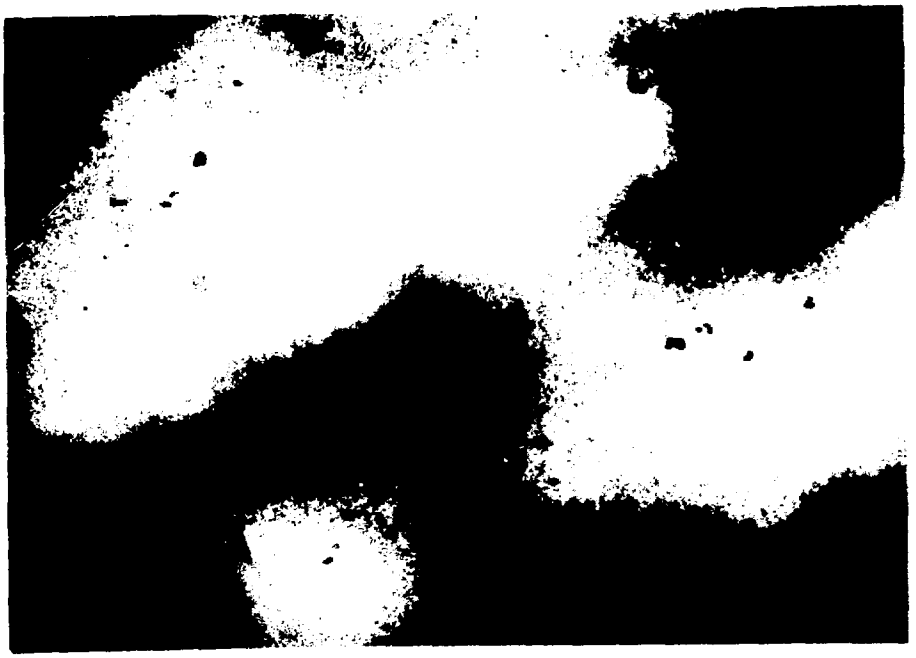

Fig. 8. A typical area in a 14 MeV neutron irradiated silver foil. Several cascades are present with 4-6 clusters.

greater than $T_m/4$ for this kind of event from the results obtained for both the gold and the silver.

CONCLUSIONS

The results of this study allow several conclusions to be made:

1. The damage observed in gold and silver from 14 MeV neutron irradiations is mainly produced in the form of energetic cascades.

2. Subcascade formation is evident in both gold and silver. From the cross sectional data, silver should have approximately 11 clusters per cascade. Also, in gold, up to six clusters per cascade was observed.

3. The number densities of the clusters agree quantitatively with previous results on gold and the elastic and nonelastic cross section data.

4. Elastic neutron scattering events do not produce more than 20% of the cascades in gold or more than 30% in silver.

5. Nonelastic collisions dominate the damage production. It is concluded that virtually every nonelastic event produces a visible cascade in gold, as well as in silver. The cascades from the nonelastic events in silver are expected to be highly split into subcascades.

6. The average cascade energy, estimated from the number of vacancies and the number of clusters per cascade are significantly higher than expected.

7. Differences between the cascades in gold and silver were manifested in the number of clusters per cascade, the size of the cascades, and the geometry of the individual clusters.

An accurate correlation between the number of visible cascades calculated for heavy-ion results and the number of cascades observed under 14 MeV bombardment seems to require a much thicker section than used in this investigation. Accurate results may also be obtained by a thin film experiment in which a protective atmosphere protects the specimen from outside recoils.

ACKNOWLEDGMENTS

The authors would like to thank R. J. Borg and R. A. Van Konynenburg for irradiating the samples at the Lawrence Livermore Laboratory 14 MeV neutron source and for performing the neutron dosimetry. The additional dosimetry performed at Argonne National Laboratory by R. Heinrick was appreciated. The technical help of J. R. Wrobel and L. R. Singer is gratefully acknowledged.

REFERENCES

1. J. D. Lee, Lawrence Livermore Laboratory, Report UCID-15944 (1971).
2. J. B. Mitchell, C. M. Logan, and C. J. Ecker, J. Nucl. Mater. 48, 139 (1973).
3. A. D. Marwick, J. Nucl. Mater. 56, 355 (1975).
4. J. B. Mitchell, R. A. Van Konynenburg, M. W. Guinan, and C. J. Ecker Phil. Mag.
5. K. L. Merkle, Nuc. Tech. 22, 66 (1974).
6. T. Schober, Phys. Stat. Sol. (a) 1, 309 (1970).
7. K. B. Winterbon, P. Sigmund and J. B. Sanders, Mat. Fys. Medd. Dan. Vid. Selsk. 37, 14 (1970).
8. R. A. Van Konynenburg, UCRL-51393, Lawrence Livermore Laboratory (1973).
9. Argonne National Laboratory - Dosimetry.
10. W. M. Hesselberger, Met. Ind. 75, 167 (1949).
11. R. D. Schoone and E. A. Fischione, Rev. Sci. Instr. 37, 1351 (1966).

HVEM QUANTITATIVE STEREOSCOPY THROUGH THE FULL DAMAGE RANGE OF AN ION-BOMBARDED Fe-Ni-Cr ALLOY

S. Diamond M. L. Bleiberg
I. M. Baron R. Bajaj
R. W. Chickering

Westinghouse Advanced Reactors Division
Box 158, Madison, Pa. 15663

ABSTRACT

The swelling of a Ni-ion irradiated Fe-25%Ni-15%Cr alloy has been investigated employing high voltage (1 MeV) electron microscopy. Helium pre-injected samples were irradiated to a maximum dose of 92 dpa with 3.5 MeV $^{60}Ni^{+}$ ions at 600, 650, 700 and 750°C. By means of quantitative stereoscopy throughout the full range of ion damage, the void morphology, swelling and dislocation morphology as functions of the distance from the ion-entry surface of the foil were obtained. The dose also varied as a function of depth and, with this technique, swelling as a function of dose was determined from a single sample at each temperature. Swelling, void concentration, and void size varied with irradiation temperature with the maximum swelling of 7.4% occuring at 700°C. Several distinct dislocation configurations could be distinguished progressing inward from the ion-entry surface. The observations suggest that nucleation and growth of voids are related to dislocation densities and possibly to dislocation structure. The swelling-dose relationships were analyzed using a linear expression for each apparent swelling regime and the results interpreted in terms of the Brailsford and Bullough statistical rate theory. Two distinct steady-state swelling regimes exist at each irradiation temperature and the difference in the rates is attributed to the different kinetic development of the dislocation structure and densities in the two stages.

INTRODUCTION

The damage produced in metals and alloys by fast neutron fluences has been simulated in many experiments[1,2] by bombardment with high energy charged particles. The void formation, swelling, and irradiation-related

microstructural evolution during these particle bombardments occur a thousand fold more rapidly than during neutron exposure. This permits rapid detailed study of the damage process and of the possible mechanisms for the avoidance or suppression of swelling, which can have an important influence on the design and economics of the first wall for CTR.

The damage from charged particles occurs typically in a band within one or two microns of the ion-entry surface of the material. Since this thickness is too great to achieve an acceptable image resolution with conventional ($\lesssim$ 200 KeV) transmission electron microscopy, a sample has to be sectioned to a predetermined depth beneath the ion-entry surface and then backthinned to obtain regions thin enough for TEM. This requires several samples to measure the damage parameters throughout the full damage region and the depth of each sectioning is subject to considerable uncertainty. However, the thickness from which acceptable image resolution can be obtained with 1 MeV electrons is greater than the thickness of the damage region in materials of immediate interest for CTR and LMFBR applications, i.e. Fe-Ni-Cr alloys, which have been irradiated with Ni ions (<5 MeV). By backthinning an ion-irradiated sample directly to the ion-entry surface, a section is obtained which includes the full damage range. High voltage electron microscopy (HVEM), quantitative stereoscopy,[3] and associated computer codes[3] can then be used on a single sample to study the swelling, void concentration, and dislocation morphology through this range as functions of the distance from the ion-entry surface.[4] The dose also varies as a function of depth and, with this technique, swelling as a function of dose can be determined from a single sample.

This work reports such a full range HVEM study in an Fe-25%Ni-15%Cr alloy irradiated with $^{60}Ni^{+}$ ions to a maximum dose of 92 dpa at four irradiation temperatures. This alloy is a base for an experimental alloy series which was designed to obtain fundamental irradiation damage information for the development of new commercial alloys for use in reactors.

EXPERIMENTAL PROCEDURE

Pre- and Post-Bombardment Sample Preparation

The composition of the alloys used in this experiment is shown in Table 1. The alloy was fabricated by International Nickel Company by vacuum melting a 100 pound heat, extruding into 15.9 mm diameter bar stock, and cutting into 30.5 cm. lengths. The material was then swaged at toom temperature to about 10.2 mm diameter, annealed at 1093°C for one hour in a H_2 atmosphere, centerless ground to 9.5 mm diameter, copper plated, and drawn into wire about 3.18 mm diameter. After the copper plating was removed from the wire, it was solution treated at 1150°C for 1 hour. Disc samples about 0.38 mm thick were cut for the ion bombardment experiment. The disc surfaces were prepared for bombardment using a multiple lapping technique. One face was ground on 600 grit abrasive. The discs were turned over and the second face (the ion-entry face) was lapped with successively finer diamond abrasive down to 0.1μ, resulting in a final sample thickness of ∿0.2 mm. Each lapping step was designed to remove all of the cold-worked surface material from the original cutting of the disc and from the previous lapping step. However, because of the extreme softness of this alloy, fine surface scratches were encountered even with these detailed lapping procedures; therefore, the surfaces to be bombarded were ion-milled, electropolished, and jetted over a 2mm. diameter in the foil center. The samples were then indium bonded to a copper plate and injected with 5 appm He to a depth of .025 mm. An additional 0.006 mm. was jetted from the sample surface to remove fine scratches which were observed after the He injection and demounting from the copper plate.

The samples were then mounted in tungsten alloy holders and irradiated with 3.5 MeV $^{60}Ni^{+}$ ions in the ANL Dynamitron at 600, 650, 700, and 750°C to a nominal peak of 90 displacements per atom (dpa). The peak dose rate was about $5x10^{-3}$ dpa per second.

After bombardment, a sample from each of the four irradiation conditions was demounted from its holder and prepared for HVEM examination by backthinning to the ion-entry surface.

Table 1. Composition Of Alloy, Wt. %

Fe	Cr	Ni	O	N	C	Co	Cu	Si	Mn
60.1	14.8	25.04	0.0154	0.0028	0.010	0.014	0.02	0.02	0.005

HVEM Technique

The irradiation-induced swelling in this alloy was measured using HVEM (on the U.S. Steel 1 MeV electron microscope) and stereomicroscopy techniques so that the entire damage range could be imaged simultaneously. This technique is summarized below.

A sample is first positioned in the HVEM in an appropriate orientation to produce the desired contrast conditions and a diffraction pattern and micrograph are recorded. The sample is then tilted through an angle of 6-9° along the selected Kikuchi band until a companion orientation with the desired contrast conditions is obtained. The diffraction pattern and micrograph in this orientation are then recorded. The two micrographs, constituting a stereo pair, are then mounted in an instrumented Hilger-Watts floating spot stereoscope and a magnified three-dimensional image of the irradiated sample is obtained. Void or precipitate coordinates along the entire damage range may be recorded on paper tape as transducer voltages from the instrumented stereoscope. The QUEST computer code is utilized to process these data and perform the following functions.

The program defines the surface plane of the foil with respect to an arbitrary origin by using the voltages corresponding to points on the foil surface. Next, the program calculates the perpendicular distance of defects from the foil surface and the defect sizes by using the voltages corresponding to two sides of each defect. From these computations the code calculates the following results:

1. Defect number density as a function of foil depth.
2. Size distribution at any foil depth.
3. Volume fraction of defects as a function of depth.
4. Swelling, in the case of voids, as a function of depth.
5. Maximum radius of defects.
6. Minimum radius defects.

7. Average defect radius.

These results are particularly useful in analyzing specimens which are ion bombarded. In such specimens, the number of displacements per atom varies as a function of depth. Therefore, the effects of radiation damage for a fixed irradiation time as a function of total displacements per atom can be determined from a single specimen.

This technique requires that a surface of the sample, such as the ion-entry surface, be observable in the stereo image so that a sufficient number of surface points may be recorded to define it mathematically and the perpendicular distance of the voids from that surface may be calculated.

In this experiment the sample surfaces, in general, were devoid of markings or stray contaminants such that they were rarely observable when the foil was imaged in absorption (void) contrast. However, when the foil was imaged in weak strain (dislocation-void) contrast, the intersection of dislocations with the surface provided a sufficient number of points to define the surface analytically. Therefore, the following procedure was used to analyze the swelling in the foil irradiated at 700°C:

A. Record two stereo pairs of a foil, one pair in absorption (void) contrast and the other in weak strain contrast.
B. Calculate the swelling in the stereo pair viewed in weak strain contrast.
C. Compare the swelling versus depth curve from this calculation to the calculated energy deposition curve.

The results obtained by this procedure are shown in Fig. 1 where the normalized swelling vs. depth is plotted for the case of weak strain contrast in which the foil surface position was measured. It can be seen that the peak in the swelling vs. depth curve occurs at $\sim$6700 Å, and is within $\pm$ 200 Å of the calculated peak in the energy deposition curve (dE/dx vs. x) calculated by the EDEP-1 Code.[5]

An alternative method was developed for approximately determining the surface plane from the measured void distribution. From the data for a stereo pair taken in absorption contrast in which the ion entry surface was

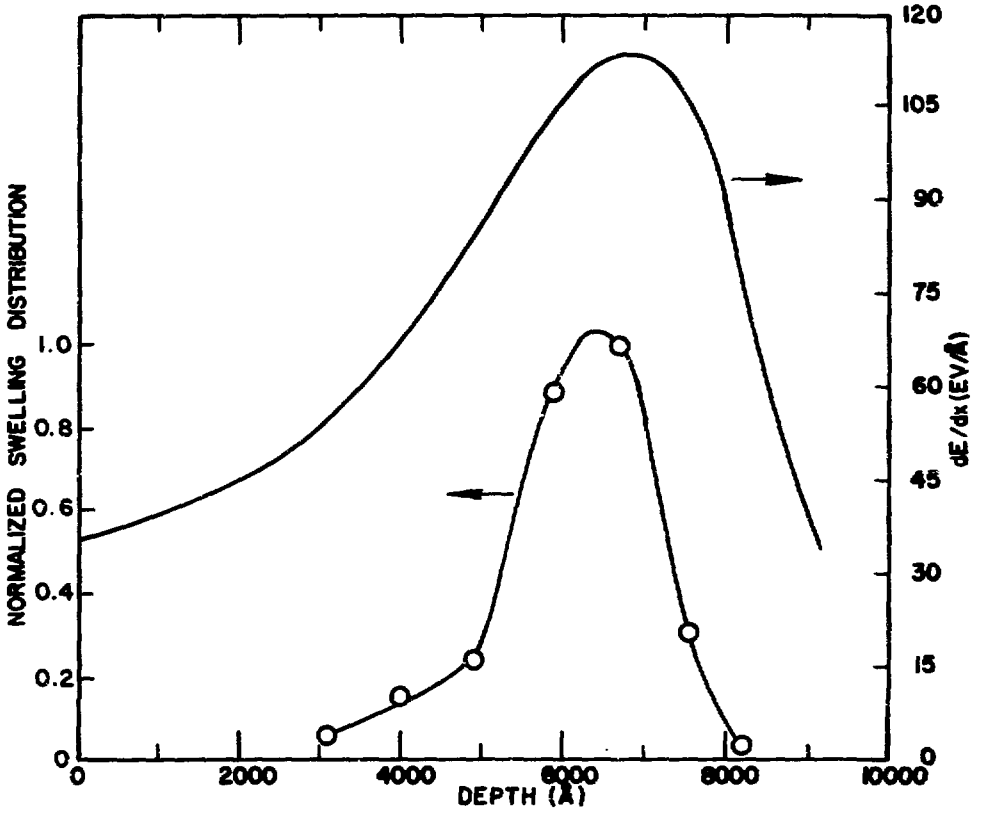

Fig. 1 Energy Deposition Curve and Normalized Swelling Curve for Voids Imaged in Void and Dislocation Contrast where Dislocation Intersections with Foil Surface Define the Surface.

observable and had been experimentally determined, the equation of another plane was calculated by a least square method which minimized the sum of the squares of the vertical distances of the voids from this latter plane. This plane was shown to be parallel to the experimentally determined surface plane to within 5°. The swelling vs. depth dependence was found by an iterative process in which the plane determined from the void distribution was translated parallel to itself until the calculated peak swelling occurred at the peak in the energy deposition curve. The functional dependence of the swelling with depth calculated by the iterative method was shown to be the same as that calculated by the method utilizing the experimentally determined surface plane. Subsequently, for those samples where the surface plane was unobservable, the swelling vs. dose dependence was calculated by the iterative method.

Stereomicroscopic observations of the general microstructure were made not in optimum dislocation contrast, but at typical deviations of 4g to 8g such that the gross features of dislocation structure and void structure were simultaneously evident throughout the imaged range.

RESULTS

Microstructural Observations

Stereo examination of the HVEM micrographs in weak strain contrast established that four distinct dislocation configurations, although spatially mixed, could be distinguished at all temperatures:

1. A coarse dislocation structure within which the path of individual dislocation line segments could be followed over large distances.
2. Relatively large, well separated faulted loops randomly oriented.
3. Relatively large unfaulted loops, randomly oriented.
4. A densely tangled, fine dislocation network.

These four elements were the major components of the observed microstructure (in addition to voids), although occasionally small loops lying within larger loops were also observed.

In those regions where the dislocation network was the dominant feature of the microstructure, the void concentrations were higher than in the regions characterized by the coarse dislocation structure.

In the weak strain contrast imaging conditions, gross changes in dislocation densities and structure and void distribution as a function of depth into the foils were relatively easy to detect visually with the stereomicroscope. Although these observations were of a qualitative nature, they indicated that nucleation and growth of voids is related to dislocation densities and possibly to dislocation structures.

Fig. 2 summarizes schematically the dislocation and void structure observed at all four temperatures for this material. In all cases, two regions with different microstructures separated by a transition region were observed. The region nearest to the ion entry surface has been termed Region I and that farthest from the ion entry surface, Region II. The transition region was relatively sharp compared to the whole imaged range in which damage was observed. The dislocation structure in Region I appeared coarser and the voids were generally fewer and smaller than in Region II. Also, the voids in Region I seemed to decorate the dislocations. Since the minimum size of the voids was of the order of 100 Å, the swelling in Region I cannot be attributed to any homogeneous or inhomogeneous incubation stage relating to void formation as is usually understood in nucleation.

SWELLING RESULTS

A micrograph of the typical void morphology observed in the irradiated samples is shown in Fig. 3. This is one-half of a stereo pair on which swelling measurements were made.

A plot of measured swelling as a function of depth below the ion-entry surface for each of the irradiation temperatures is shown in Fig. 4 along with the calculated energy deposition curve. The results of the stereo measurements are summarized in Table 2. It can be seen that the peak swelling increased, the void concentration decreased, and the void size increased with temperature up to 700°C. At 750°C the void

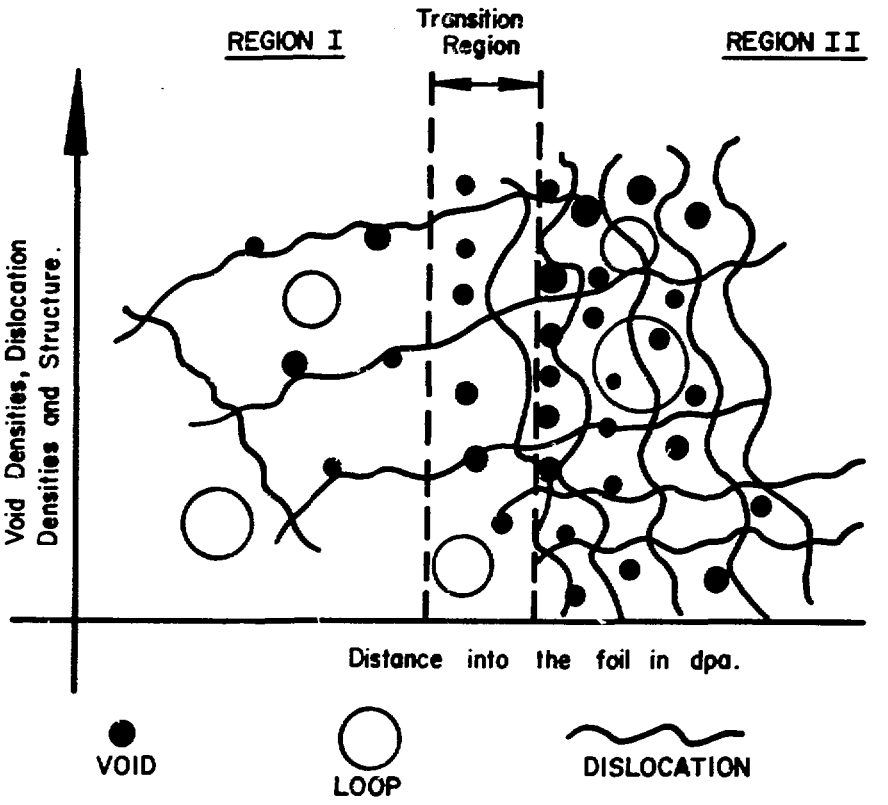

Fig. 2 Schematic Illustration of the Microstructural Features of Region I and Region II in Nickel ion Bombarded Fe-25%Ni-15%Cr

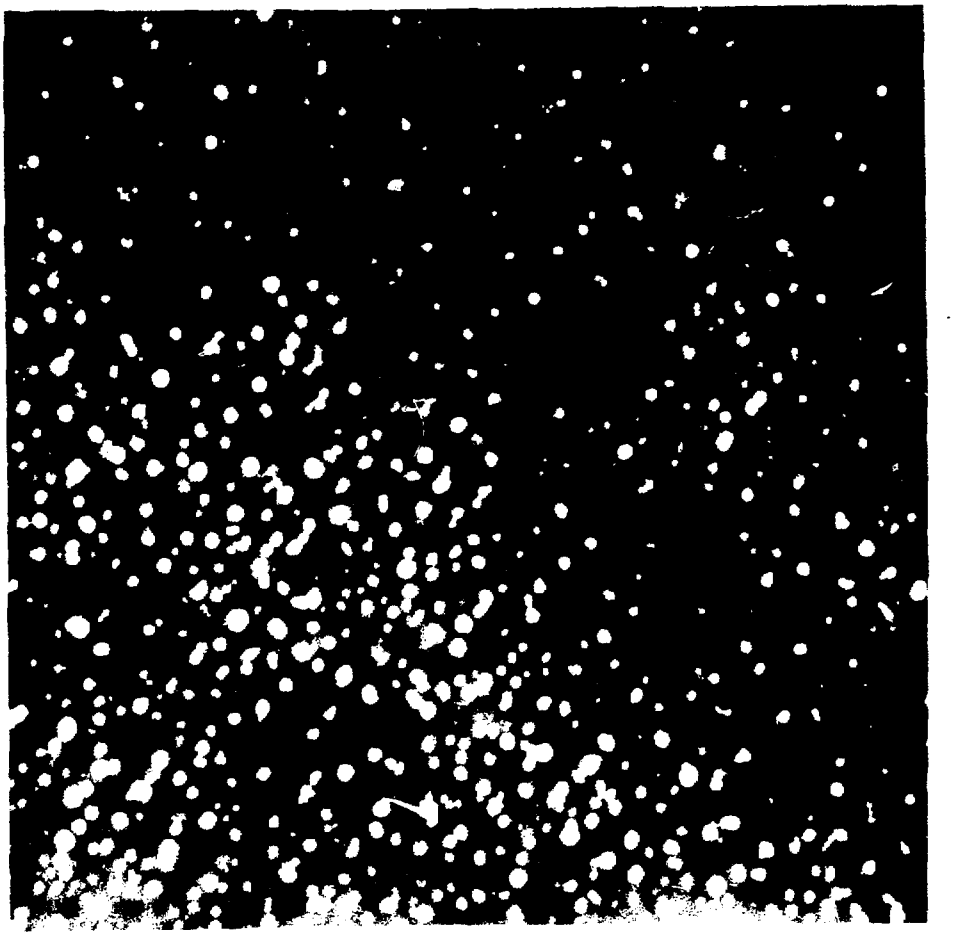

Fig. 3 Voids in Fe-25%Ni-15%Cr Alloy, Bombarded with 3.5 MeV Ni^+ at 700°C, Dose 90 dpa; 1 MeV Electron Micrograph $\vec{z} \sim [001]$, Bright field [200] Systematic $s_{8g} > 0$.

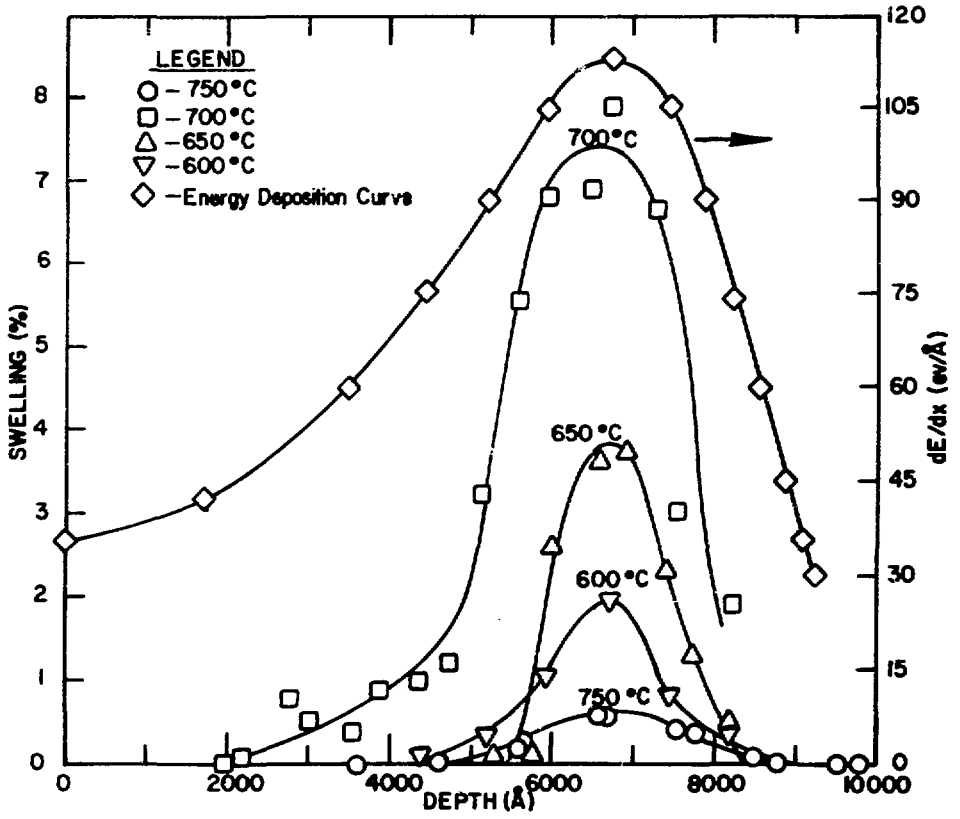

Fig. 4 Swelling vs. Depth Curves and Energy Deposition Curve for Fe-25%Ni-15%Cr Alloy Bombarded with 3.5 MeV $^{60}Ni^{+}$ at 600, 650, 700, 750°C.

Table 2. Bombardment Conditions and Results of Stereo-Measurements for Irradiated Fe-25Ni-15Cr Alloy

			AT PEAK DOSE	
TEMPERATURE (°C)	PEAK DISPLACEMENT DOSE (dpa)	AVERAGE PEAK SWELLING (% $\Delta V/V_o$)	AVERAGE VOID CONC. ($per\ cm^3$)	AVERAGE VOID DIAMETER (Å)
600 ± 15	86 ± 9	2.0	1.39×10^{15}	300
650 ± 15	83 ± 8	3.5	7.34×10^{14}	446
700 ± 20	90 ± 9	7.4	1.30×10^{14}	1003
750 ± 15	92 ± 9	0.6	1.42×10^{14}	433

concentration increased slightly but the void size was very much smaller and the swelling was thus greatly diminished. The maximum swelling of 7.4% occurred at 700°C.

Since in Fig. 4 there appears to be a correlation between the spatial distribution of the measureable damage in the form of swelling and the energy per ion deposited within the material, it was assumed that there was a statistical relationship between the measured swelling and the calculated dose. Swelling vs. dose values were determined from the experimental data for each temperature and are plotted in Fig. 5. It was further assumed that, for these ion bombardments, the relationship between swelling and dose was linear, similar to the swelling caused by neutron irradiation where it has been assumed[6] that

$$\frac{\Delta V}{V_o}\ \% = S = R\ (F - F_{th}) \qquad (1)$$

where F = the dose in displacements per atom (dpa)

F_{th} = a "threshold" dose in dpa

R = a steady-state swelling rate in % swelling/dpa

S = the observed swelling in %.

A regression analysis was performed on the data to develop the correlation between the swelling and the dose. The following are the regression equations developed by this analysis:

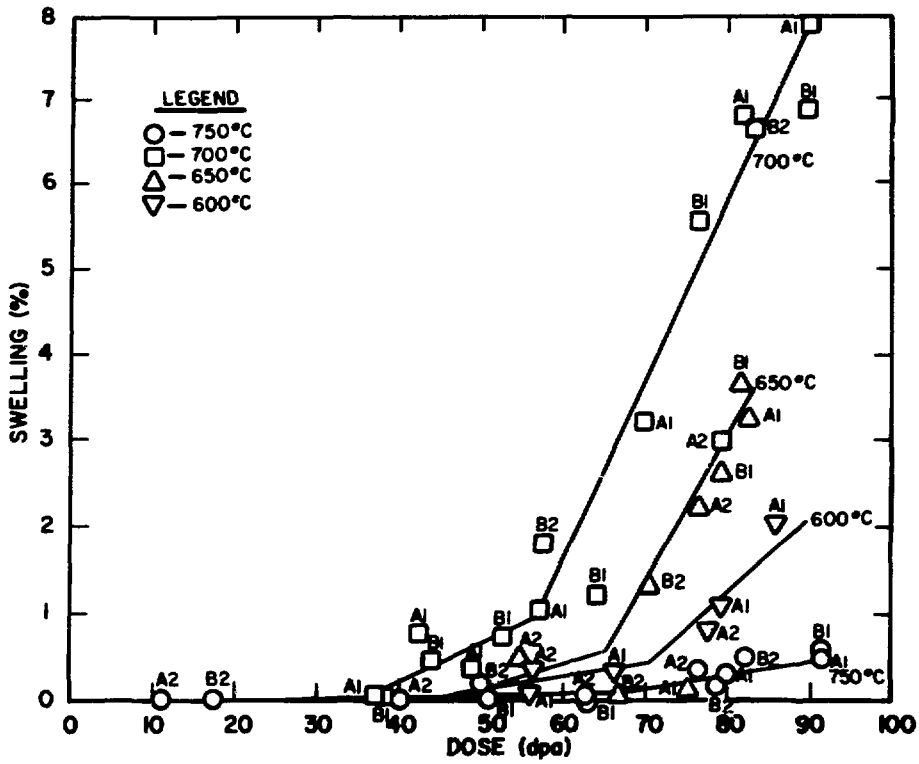

Fig. 5 Swelling as a Function of Dose and Temperature for Fe-25%Ni-15%Cr Alloy.

600°C	Stage I	$S = .0098 (F-32)$	$45 < F < 70$	$\gamma = .415$	(2A)
	Stage II	$S = .0874 (F-65)$	$70 < F < 90$	$\gamma = .95$	(2B)
650°C	Stage I	$S = .035 (F-45)$	$45 < F < 65$	$\gamma = .46$	(3A)
	Stage II	$S = .178 (F-64)$	$65 < F < 82$	$\gamma = .97$	(3B)
700°C	Stage I	$S = .0395 (F-35)$	$35 < F < 58$	$\gamma = .87$	(4A)
	Stage II	$S = .190 (F-51)$	$58 < F < 85$	$\gamma = .93$	(4B)
750°C	Stage I	$S = .007 (F-29)$	$30 < F < 70$	$\gamma = .82$	(5A)
	Stage II	$S = .0194 (F-62)$	$70 < F < 90$	$\gamma = .80$	(5B)

where S is swelling and F is dose as in Eq. (1) and γ denotes the measure of statistical correlation.[7] In Fig. 5 both the data and the regression lines are plotted. The data points are labeled with A or B indicating different areas of the foil while 1 indicates a depth less than and 2 indicates a depth larger than that at which the peak occurs. For each irradiation temperature in Fig. 5 there can be seen two distinct linear portions of the swelling vs. dose plot. The portion characterized by the lower swelling rate is hereafter referred to as Stage I and the portion of higher swelling rate, Stage II.

Interpretation of the Data

Two distinct phases in the swelling process are consistent with these data at all temperatures. To analyze the nature of the processes contributing to each phase, some assumptions on the kinetic evolution of the microstructure are necessary.

The following fairly conventional picture regarding the nucleation of loops and voids was adopted. The first sign of radiation damage in this alloy is probably the nucleation of small interstitial and, possibly, vacancy loops. However, the rate of energy deposited into displacement processes (per unit distance per incoming particle) is larger deeper within the foil (Region II) than closer to the surface of the foil (Region I). Therefore, the number of loops nucleated (per unit volume) in region II would be expected to be larger than the number nucleated in region I and the mean distance between the loops in region II would be smaller than in Region I.

The second kinetic stage probably involves nucleation of small voids in the vicinity of dislocation loops, their stabilization by helium, and growth of both voids and loops in both regions. Since the mean distance between the loops is larger in Region I, they may be considered as growing independently without effects of competition between the loops being appreciable. The loops grow and their bias[8] approaches rather quickly the bias of straight dislocation line segments.

In Region II, however, due to the presence of a large number of small loops closely spaced, the interaction between loops soon becomes important, and with it, effects of competition among loops. This in general will have the effect of "slowing down" the growth of individual loops thus increasing the relative bias over and above the value expected for a straight edge dislocation.[8] Due to the higher loop density in Region II and the larger bias (as compared with Region I), nucleation of voids will be more probable and their growth rate enhanced as compared with Region I. The final stage of microstructural evolution probably involves stabilization of the dislocation structures first in Region II and later in Region I. Eventually a "fine" dislocation netowrk will develop in Region II and a "coarse" dislocation structure in Region I.

Analysis of Swelling-Dose Relationships

Our results, in particular Eqs. 2-5, may be interpreted at all temperatures within the framework of the approximate statistical rate theory of Brailsford and Bullough (B.B.).[9] The basic theory is summarized in the following equations.

$$\frac{\Delta V}{V_o} \% = S = \alpha K (t-t_o) F(\eta) \tag{6}$$

where

$$\eta = 400 \exp \left[- \frac{E_m^v}{K_B} \left(\frac{1}{T_s} - \frac{1}{T}\right)\right] \tag{7}$$

$$F(\eta) = \frac{2}{\eta} \left[(1+\eta)^{1/2} - 1 - \frac{\eta}{2} \exp \left\{- \frac{Q}{K_B} \left(\frac{1}{T} - \frac{1}{T_f}\right)\right\}\right] \tag{8}$$

and for our case, with no precipitates,

$$\alpha = \rho_d \; 4\pi \; r_s \; C_s \; (Z_I - Z_V)/[(\rho_d + 4\pi \; r_s \; C_s)^2] \tag{9}$$

where: $\frac{\Delta V}{V_o}\,\% = S$ = swelling in percent

ρ_d = characteristic average dislocation line density

r_s = average void radius

C_s = average void density

$Z_I - Z_V$ = bias in percent

E_m^v = vacancy migration energy

k_B = Boltzman's constant

Q = activation energy for diffusion by the vacancy mechanism

T = temperature of irradiation in °K

T_s = temperature characteristic of the onset of measurable swelling

T_f = temperature characteristic of the termination of measurable swelling

K = displacement rate in dpa/sec

t = time in seconds

Kt_o = threshold dose

It is assumed that Eqs. 6-9 apply to each linear swelling regime which can be distinguished experimentally. Thus, the steady state swelling rate R appearing in Eqs. 2-5 may be thought of as being composed of two distinct factors:

$$R = \alpha \; F(\eta) \tag{10}$$

where α is a factor related to microstructure and defined by Eq. (9), and $F(\eta)$ is a phenomenological temperature dependent factor defined in Eq. (8). In practice, when a detailed numerical description of the kinetic evolution of the microstructure is not postulated, the parameters α, T_s and T_f are adjustable parameters, which are fixed for some given irradiation conditions. In Fig. 6, $F(\eta)$ is plotted as a function of temperature using the activation energy values recommended by B.B. for stainless steel

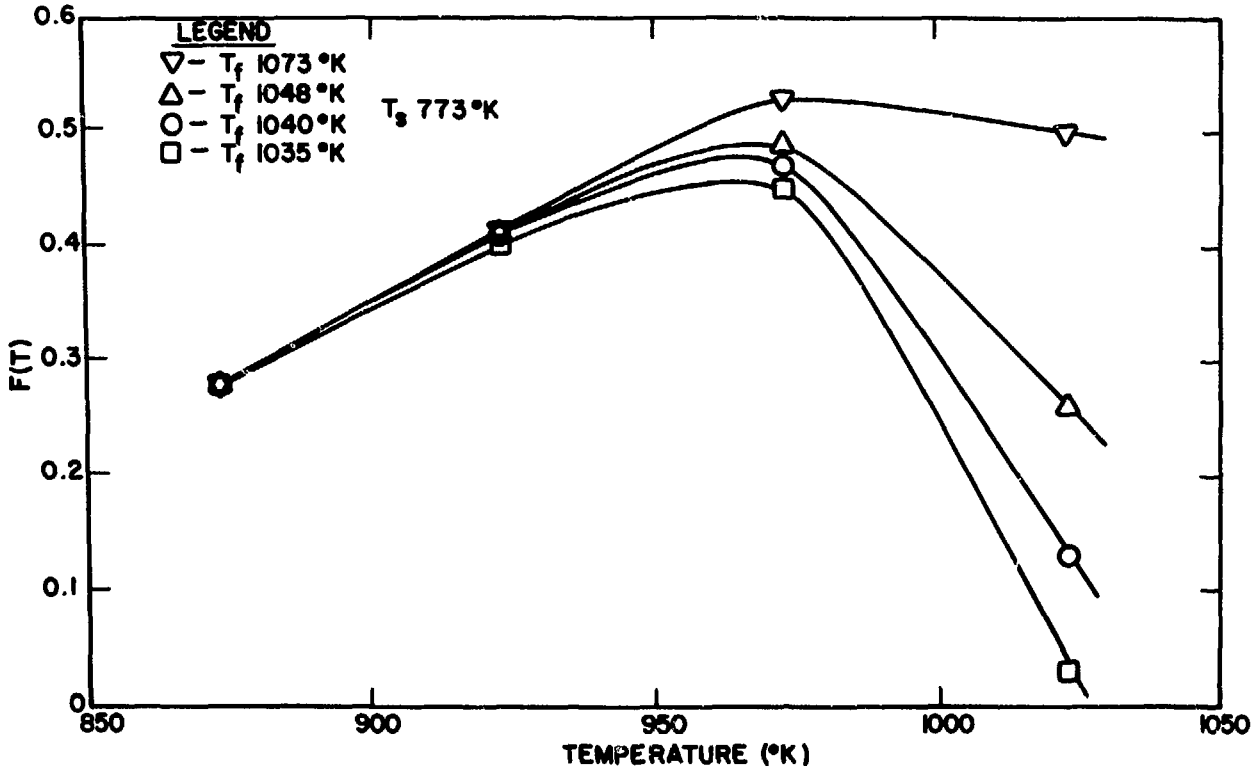

Fig. 6 F as a Function of Temperature with T_f and T_s as Indicated; E_v^m = 1.4 eV, Q = 3 eV.

(E_m^v = 1.4eV, Q = 3eV) for several plausible choices of the parameters T_s and T_f.

If Eqs. (2-5) are compared with Eq. (6), the following interpretation is suggested. At each temperature there are two distinct stages in the swelling process, both corresponding to steady state swelling. The first stage corresponds to Region I with parameters $R_1(T) = \alpha_1 F(\eta)$ and threshold dose $F_{th}(1) = K t^{(1)}$, and the second stage corresponds to Region II with parameters $R_2(T) = \alpha_2 F(\eta)$ and threshold dose $F_{th}(2) = K t_o^{(2)}$.

Microstructural observations and the dynamic picture outlined above suggest that the threshold doses as well as the two steady state rates at each temperature are associated with the dynamic evolution of the dislocation structure in Regions I and II. In other words, the difference in swelling rates R_1 and R_2 at the same temperature is a reflection of the fact that the dynamic evolution of the microstructure is different in Regions I and II. The functional dependence in Eq. (9) substantiates this observation.

Let us assume for the moment, as a working hypothesis, that Eq. (9) holds in some average sense for Stage II uniformly, i.e., independent of temperature over the range investigated here. Thus, the change in swelling rates between different temperatures in Stage II is viewed as being due solely to the temperature variation of the phenomenological factor $F(\eta)$. A similar assumption is made for Stage I.

If we then plot the experimentally measured rate in Stage I and Stage II as a function of temperature in Fig. 7, we note that the two curves have very similar temperature dependence. The form of the temperature dependence is characteristic of steady state swelling in both stages, which is a self-consistent check on our original assumption of steady state swelling in both stages. Furthermore, if we compare Fig. 7 with $F(\eta)$ (Fig. 6) the following result is found. Of all the functions $F(\eta)$ there are several which are consistent overall with both curves in Fig. 7. For example, if we base our comparison on the curve $F(\eta)$ with T_s = 773°K, T_f = 1035°K (Fig. 6), which corresponds approximately to onset

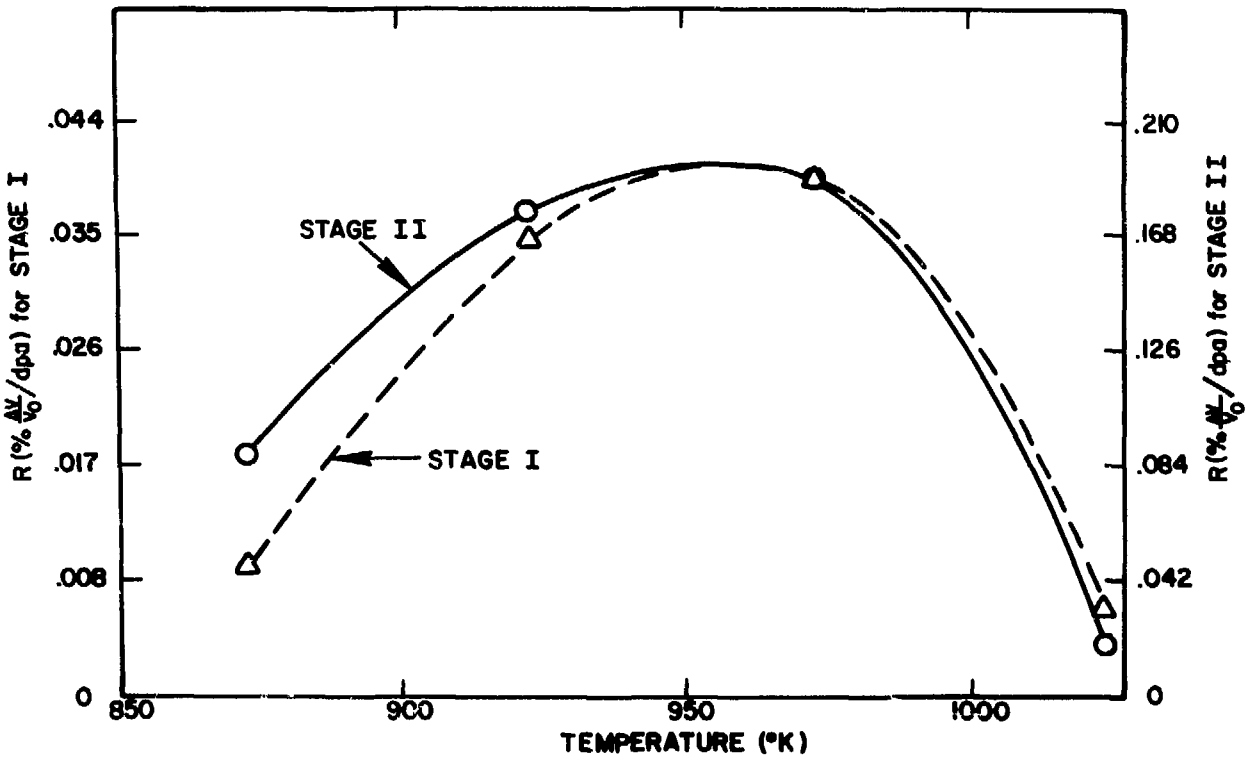

Fig. 7 Experimentally Measured Swelling Rate as a Function of Temperature for Stage I and Stage II.

of measurable swelling at 500°C and termination at 762°C (which is consistent with the experimental data), the following average values are retrieved for α:

$$\alpha_1 = \alpha(\text{Stage I}) = 1/11.39 = .09 \tag{11}$$

$$\alpha_2 = \alpha(\text{Stage II}) = 1/2.37 = .42 \tag{12}$$

If this theoretical curve $F(\eta)$ is accepted with the above parameters, we may iterate on our working hypothesis (that α_1 and α_2 are temperature independent) and allow the factor α to vary with temperature. Thus better agreement between theory and experiment may be obtained. Thus refined estimates based on $F(\eta)$ with $T_s = 773$ and $T_f = 1035$ are:

Stage I	Stage II
α_1 (750°C) = .23	α_2 (750°C) = .70
α_1 (700°C) = .09	α_2 (700°C) = .42
α_1 (650°C) = .09	α_2 (650°C) = .42
α_1 (600°C) = .03	α_2 (600°C) = .32

These results may now be used in conjunction with Eq. (9) to get a lower bound for the <u>average</u> bias parameters characterizing the dislocation structure at each temperature for each stage. This can be done by noting that in Eq. (9) the factor containing the average dislocation densities, void radii, and void concentrations is bounded by the numerical factor 0.25. Thus for each steady state swelling regime at each temperature we have

$$\alpha_{1,2}\,(T) < .25\,(z_I - z_v) \text{ or } (z_I - z_v) > 4\,\alpha_{1,2}\,(T) \tag{13}$$

Thus for Stage I

$$(z_I - z_v) > .92\% \text{ at } 750°C$$
$$(z_I - z_v) > .36\% \text{ at } 700°C$$
$$(z_I - z_v) > .36\% \text{ at } 650°C$$
$$(z_I - z_v) > .12\% \text{ at } 600°C$$

and for Stage II

$$(z_I - z_v) > 2.80\% \text{ at } 750°C$$
$$(z_I - z_v) > 1.68\% \text{ at } 700°C$$

$(z_I - z_v) \lesssim 1.68\%$ at 650°C

$(z_I - z_v) > 1.28\%$ at 600°C

Note that the average bias parameters in Stage II are consistently lower bounded by larger numbers at each temperature than the average bias parameters corresponding to Stage I. Slightly different lower bounds on the bias would be calculated if the analysis is based on F(η) with different T_s and T_f but the relationship between Stage I and Stage II remains invariant.

This may be taken as an indication of the different kinetics underlying the development of the dislocation structure in Stage I and Stage II.

These results may have major implications in the comparison of charged particle bombardments between various investigations, in the comparison of simulation data with neutron data, and in the comparison of neutron data obtained from different reactors. This work has shown that the swelling rate of Fe-25Ni-15Cr was increased by a factor of five by the change in microstructure between Stage I and Stage II. Thus, comparison of swelling results without a simultaneous comparison of microstructures is of little value. If an equivalent dose value is used, it must be equated with an equivalent microstructure. It would be expected that a "saturation" microstructure would evolve under all bombarding particles at which point swelling rates could be compared. This investigation indicates that high doses ($\gtrsim$ 70 dpa) are required to achieve this microstructure in fully annealed simple ternary Fe-Ni-Cr alloys.

CONCLUSIONS

1. An Fe-25%Ni-15%Cr alloy, Ni-ion bombarded at 4 temperatures to 90 dpa and examined by full range HVEM stereoscopy, showed maximum swelling of 7.4% at 700°C.
2. A bi-linear swelling-dose relationship appears to hold over the entire temperature range investigated.
3. The experimental results can be interpreted at all temperatures using the B.B. statistical rate theory approach to swelling in irradiated materials.

4. Application of the B.B. model indicates that the difference in the swelling rates in the two distinct swelling regimes at each temperature is the result of the different kinetic development of the dislocation structure and densities in the two stages.

ACKNOWLEDGEMENTS

We wish to acknowledge gratefully the cooperation and participation of Scott Lally and the staff at the U.S. Steel Research Laboratories in the high voltage microscopy; the assistance of A. Taylor, members of the staff of the Metals and Ceramics Division, and the Dynamitron staff at Argonne National Laboratory with the nickel ion bombardments; the indispensable efforts of T. Dimuzio in the preparation of the samples and the performance of the irradiation; the technical contribution of A. F. Rowcliffe and F. Venskytis in the pre-bombardment sample preparation and techniques; and the assistance of K. Garr of Atomics International with the helium injection of the samples. The support of the U.S. Energy Research and Development Administration for this work is greatly appreciated.

REFERENCES

1. R. S. Nelson, J. A. Hudson, D. J. Mazey, G. P. Walters and T. M. Williams,430; G. L. Kulcinski, J. L. Brimhall, and H. E. Kissinger, 449; J. S. Armijo and T. Lauritzen, 479; A. Taylor and S. G. McDonald, 499; D. W. Keefer, A. G. Pard, and D. Kramer, 511; in Radiation Induced Voids in Metals, J. W. Corbett and L. C. Ianniello, Eds., U. S. Atomic Energy Commission Office of Information Service, Washington D. C., 1972.

2. W. G. Johnston, J. H. Rosolowski, A. M. Turkalo, and T. Lauritzen, Journal of Nuclear Materials, 47, 155 (1973).

3. L. E. Thomas and S. Lentz, in Proceedings of the 32nd Annual Electron Microscope Society Meeting, St. Louis, Mo., 1974.

4. A. F. Rowcliffe, S. Diamond, M. L. Bleiberg, J. Spitznagel, and W. J. Choyke, in ASTM Symposium on The Effects of Radiation on Structural Materials, Gatlinburg, Tenn., June 1974, in press.

5. I. Manning and G. P. Muller, Computer Physics Communications, 7, 85, 1974.

6. J. I. Bramman, K. Q. Bagley, C. Cawthorne, E. J. Fulton, and W. D. J. Sinclair, in Voids Formed by Irradiation of Reactor Materials, S. F. Pugh, Ed., Proceedings of the British Nuclear Energy Society, London, 27, (1971).

7. W. Feller, An Introduction to Probability and Its Application, J. Wiley & Sons, New York, N. Y., Vol. 1, 221 (1950).

8. W. G. Wolfer, M. Ashkin, J. P. Foster, A. Biancheria, and A. Boltax in ASTM Symposium on The Effects of Radiation on Structural Materials, Gatlinburg, Tenn., June 1974, in press.

9. A. D. Brailsford and R. Bullough, Journal of Nuclear Materials, 44, 121, (1972).

THE SWELLING EFFECTS TO BE EXPECTED IN MATERIALS UNDER HIGH TRANSMUTATION GAS GENERATION RATES

R. Bullough and M.R. Hayns

ABSTRACT

The effects of high gas generation rates appropriate to the first wall of a fusion reactor on the expected swelling at the peak swelling temperature and above are discussed. The critical void size is deduced for bias driven swelling and the rate equations appropriate for the transition to gas driven swelling are outlined. Specific results of computations are presented for cold worked M316 steel for a range of temperatures and gas generation rates. Very high swelling can occur at high temperatures.

---

1. INTRODUCTION

The first wall material in a fusion reactor will be subjected to very high energy neutron damage (14 MeV) at temperatures at and above the temperature where void swelling is known to occur. The range of relevant conditions and the present state of our understanding of the expected damage processes have been surveyed by Kulcinski[1]. Since there is virtually no direct experimental observation of irradiation damage at these energies and temperatures it is particularly appropriate to use our theoretical understanding of the swelling of fission reactor components to predict the expected swelling behaviour under the fusion reactor conditions. This approach will at least provide an indication of the kind of swelling to be expected and any future discrepancy with observation can be used to refine the theoretical model and hence help to develop the necessary complete understanding of the various dominant damage processes. A physically rigorous model of the swelling and associated damage processes under fusion conditions is particularly important since relevant experimental data will largely derive from simulation experiments with high energy ions or electrons. Experience has shown that successful correlations between fast neutron data and

and corresponding simulation data can only be achieved when a rather sophisticated model of the damage process is used[2].

Although the range of expected operating conditions for the first wall is large[1] the particular differences from the fast reactor core situation are in the much higher generation rate of transmutation gas together with a higher homologous temperature (0.3 Tm - 0.5 Tm). The present discussion will therefore highlight the effects on the swelling to be expected from these differences. The required extension to the established "bias" swelling rate theory to permit a simultaneous discussion and an actual transition to gas driven swelling (such as occurs in nuclear fuels) will be outlined in section 2. The sensitivity of the critical void (gas bubble) radius, for bias driven void growth, to the production rate of transmutation gas will be explicitly derived. Finally some general effects on swelling of high gas generation rates will be surveyed, again with reference to M316 steel*.

2. THE THEORETICAL MODEL

The notation used in this section is based on the rate theory studies of Brailsford and Bullough[3,4] and has been recently extended to include recoil spectrum effects by Bullough, Eyre and Krishan[2] and simultaneous irradiation creep by Bullough and Hayns[5] and Bullough[6]. Repetition of definitions will therefore be minimised and the present account can be usefully supplemented with reference 6.

In general the effects of transmutation gas production on void growth or gas bubble growth‡ are only significant at temperatures above the peak swelling temperature; below such temperatures gas is only

---

*M316 steel was chosen for convenience only since it has been studied in great detail as a core component material for the fast reactor. The results presented should be pertinent to the refractory metals etc. at the appropriate homologous temperature.

‡The term "void" is used for a cavity containing insufficient gas to balance the surface tension force; when the gas pressure approaches or equals the surface tension force the cavity may be termed a "gas bubble".

important as a nucleating agent for the three dimensional morphology of the void embryo and its growth is unaffected by subsequent gas production. This is not the case at higher temperatures[7] and the swelling rate can become acutely sensitive to both the gas generation rate K_g and to the applied stress (if any) σ. For a general discussion of the effects of such gas the void rate equations must be supplemented by the additional gas rate equation for the rate of loss of a gas into the voids.

$$C_V \frac{d}{dt}(n_g b^3) = k_{gV}^2 D_g c_g - BC_V n_g \tag{1}$$

where n_g is the number of gas atoms per void, b^3 is the atomic volume, C_V is the volume concentration of voids, D_g is the diffusion coefficient for the gas, B is the resolution parameter[8], k_{gV} is the void sink strength (with average radius r_V) for gas atoms

$$k_{gV}^2 = 4\pi r_V C_V \tag{2}$$

and c_g is the steady state gas concentration in the material satisfying the relation

$$K_g - k_g^2 D_g c_g + BC_V n_g = 0. \tag{3}$$

In this equation K_g is the gas generation rate in atoms per atom per second (apa/sec), k_g^2 is the total sink strength for loss of gas given by

$$k_g^2 = k_{gV}^2 + k_{gD}^2 + k_{gGB}^2 \tag{4}$$

where

$$k_{gD}^2 = Z_g \rho_D \tag{5}$$

is the sink strength for gas loss to dislocations and

$$k_{gGB}^2 = \frac{6}{d}\left[k_{gV}^2 + k_{gD}^2\right]^{\frac{1}{2}} \tag{6}$$

is the sink strength for gas loss to the grain boundaries[8] when d is the

average grain diameter. The rate equation for the swelling S is[6]

$$\frac{dS}{dt} = k_{vV}^2 D_v c_v - k_{iV}^2 D_i c_i - K_V D_v \tag{7}$$

where

$$k_{vV}^2 = k_{iV}^2 = 4\pi r_V c_v \tag{8}$$

are the sink strengths* for the loss of vacancies and interstitials respectively to the voids, c_v and c_i are the respective vacancy and interstitial steady state concentrations and

$$K_V = k_{vV}^2 \bar{c}_V \tag{9}$$

is the rate of thermal vacancy emission from the voids. In equation (9)

$$\bar{c}_V = c_v^e \exp\left\{\left(\frac{2\gamma}{r_V} - p_g\right) b^3/kT\right\} \tag{10}$$

is the equilibrium vacancy concentration adjacent to a void, where c_v^e is the defect free equilibrium vacancy concentration, γ is the surface tension and

$$p_g = 3n_g kT/4\pi\left(r_V^3 - \frac{3b_v n_g}{4\pi}\right) \tag{11}$$

is the gas pressure exerted by n_g gas atoms within the void satisfying Van der Waals gas law (b_v is Van der Waals constant). The steady state concentrations c_v and c_i follow from the usual pair of non-linear simultaneous steady state algebraic equations defining the balance between the rate of formation of the intrinsic point defects with their loss at the various sinks and by recombination.

To obtain the swelling rate it is necessary to solve simultaneously the rate equations (1) and (7) together with the associated rate equations

---

*For simplicity we have omitted the second order correction terms to these sink strengths[6,9].

for the average interstitial loop* radius and for the density and average size of the vacancy loops* formed within the displacement cascades. Some results of such computations will be described in the next section for M316 cold worked steel.

Before describing these results it is interesting to simplify drastically the preceding rate equations to the situation when the only sinks present are dislocations and voids and all the transmutation gas immediately migrates to the voids (no gas-dislocation or-grain boundary trapping) and no resolution of gas. In this situation equations (1) and (3) yield for the number of gas atoms/void at time t

$$n_g = K_g t/b^3 C_V \tag{12}$$

and with the further simplification of the ideal gas law ($b_v = 0$)

$$p_g(t) = 3kTK_g t/4\pi r_V^3 b^3 C_V \tag{13}$$

With these drastic simplifications the swelling rate equation (7) becomes

$$\frac{dS}{d\Delta} = \frac{(Z_i - Z_v)\rho_D 4\pi r_V C_V}{(4\pi r_V C_V + \rho_D)^2} - \frac{D_v c_v^e \rho_D 4\pi r_V C_V}{K(4\pi r_V C_V + \rho_D)}\left[\frac{2\gamma}{r_V} - p_g(\Delta)\right]\frac{b^3}{kT} \tag{14}$$

where $\Delta = Kt$ and K is the damage rate in dpa/sec. The form of equation (14) is only valid at the peak swelling temperature or higher when recombination effects should be small.

In order to integrate (14) for the swelling S the existence of small void embryos must be assumed containing a number

$$n_g^o = 8\pi r_V(0)^2\gamma/3kT \tag{15}$$

---

*When the body is subjected to uniaxial stress we must subdivide the loop populations into aligned and non-aligned varieties since vacancy emissions is enhanced from the aligned loops. The asymmetry in the loop distributions also has an important effect on the irradiation creep at the peak swelling temperatures and above[5,6].

of gas atoms in equilibrium with the initial surface tension $2\gamma/r_v(0)$; it follows that n_g^o should be added to (12) and the appropriate incubation dose required to generate these gas atoms must be included as the starting dose for the integration.

In (14) the first term describes the bias driven growth of the voids and the second term, which is only important at high temperatures (when c_v^e is large), will be negative when $p_g < 2\gamma/r_v$ and thereby retard the void growth by vacancy emission from the voids or will be positive when $p_g > 2\gamma/r_v$ and thereby drive the growth of the voids by the excess gas pressure.

When $p_g = 0$ a cavity will grow as a void by bias driven swelling when its radius exceeds a critical radius r_v^c given by $\frac{dS}{d\Delta}(p_g = 0) = 0$; that is when

$$r_v^c = 2\gamma b^3 D_v c_v^e \rho_D / \left[kkT(Z_i - Z_v) - 8\gamma b^3 D_v c_v^e \pi C_v \right] \qquad (16)$$

As the temperature increases we see that the critical radius increases and bias driven swelling becomes more unlikely. However, when $p_g \neq 0$ and K_g is finite we see that depending on the temperature and magnitude of K_g two quite different swelling processes can occur. If the temperature is near the peak swelling temperature then a very small K_g (say 10^{-12} apa/sec) will reduce $2\gamma/r_v$ just sufficiently for the cavity to grow slowly up to its zero p_g critical radius (16); it will then grow rapidly by the usual bias driven swelling process. If K_g is larger then the critical dose and radius for swelling will be reduced but the subsequent swelling will be bias driven. On the other hand at higher temperatures, the bias driven growth, with small K_g, can only occur after a very large critical dose; if K_g is large then the second term is completely dominant and the swelling is purely gas driven. In this high temperature situation (14) becomes

$$\frac{dS}{d\Delta} = \frac{4\pi r_v C_v \rho_D}{K(4\pi r_v C_v + \rho_D)} \frac{D_v c_v^e}{kT} \left\{ \frac{kTK_g\Delta}{Kb^3 S} - \frac{2\gamma}{(3S/4\pi C_v)^{1/3}} \right\} \qquad (17)$$

To solve accurately this differential equation for S is non trivial and because we have the complete numerical solution available with all the sinks fully included it does not seem worthwhile to pursue it. However, it is worthwhile to point out that at high temperatures c_v^e will become large and thus for $dS/d\Delta$ to remain finite the resulting swelling can be obtained by equating the quantity in the curly bracket on the right hand side of equation (17) to zero; that is

$$S = \left(\frac{3}{4\pi C_v}\right)^{\frac{1}{2}} \left(\frac{K_g kT}{2\gamma Kb^3}\right)^{3/2} \Delta^{3/2} \qquad (18)$$

which is the expected high temperature, gas driven, swelling result such as occurs in nuclear fuels from the fission gases.

3. HIGH TEMPERATURE SWELLING IN M316

In this section we shall present some results obtained using the full rate equations as outlined in the previous section. The physical parameters used are those appropriate to M316 steel and are given in detail by Bullough, Eyre and Krishan[2] in their study of the correlation between the swelling in M316 under HVM, VEC and Reactor irradiation. For completeness we have also included some effects of uniaxial stress as well as variations of K_g and temperature and all the results are for a dislocation network density of 5.10^{11} cm/cm^3, corresponding to the cold worked condition; a typical fast reactor damage rate $K = 10^{-6}$ dpa/sec has been assumed.

The results for the three temperatures 500°C, 700°C and 800°C and various K_g values ranging from the typical fast reactor value of 10^{-12} apa/sec to the high value of 10^{-9} apa/sec are shown in figures 1, 2 and 3 respectively. At 500°C we see the typical high rate of swelling when $K_g = 10^{-12}$ apa/sec with a long incubation dose for the slowly growing voids to reach the critical radius. At larger K_g the critical radius is achieved at lower doses as expected. The linear swelling rate at this temperature when K_g is large indicates a rather complex admixture

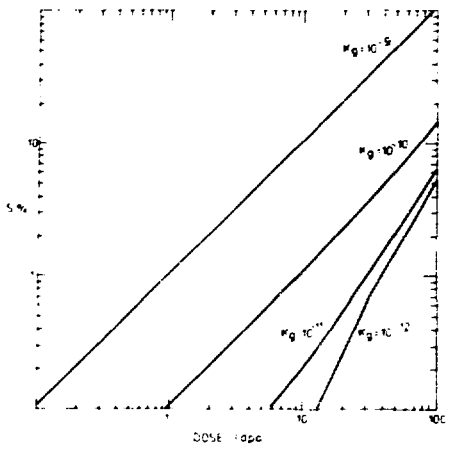

Fig. 1. The theoretical swelling at 500°C in cold worked M316 steel for a range of gas generation rates K_g. The damage rate is 10^{-6} dpa/sec and the network dislocation density is 5 10^{11} cm/cm^3. The other physical parameters are given in reference 2.

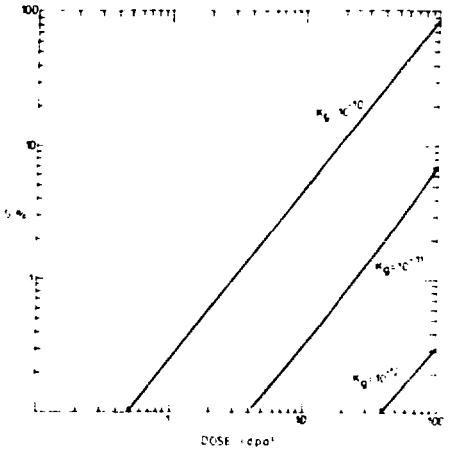

Fig. 2. The theoretical swelling at 700°C in cold worked M316 steel for a range of gas generation rates K_g. The damage rate is 10^{-6} dpa/sec and the network dislocation density is 5 10^{11} cm/cm^3. The other physical parameters are given in reference 2.

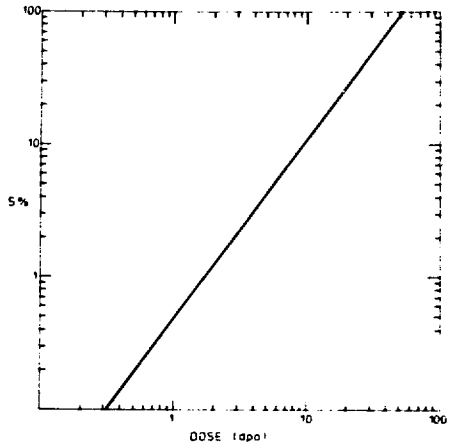

Fig. 3. The theoretical swelling at 800°C in cold worked M316 steel for a gas generation rate $K_g = 10^{-10}$ apa/sec. The damage rate is 10^{-6} dpa/sec and the network dislocation density is 5 10^{11} cm/cm^3. The other physical parameters are given in reference 2.

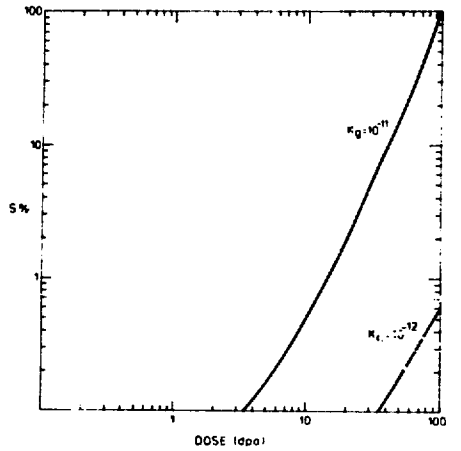

Fig. 4. The theoretical swelling at 700°C in cold worked M316 under a uniaxial tensile stress of 100 MPa and gas generation rates of 10^{-11} and 10^{-1} apa/sec. The damage rate is 10^{-6} dpa/sec and the network dislocation density is 5 10^{11} cm/cm^3. The other physical parameters are given in reference 2.

of bias driven and gas driven swelling. Thus even with $K_g \approx 10^{-9}$ apa/sec this temperature is too low for the high temperature "genuine" gas driven swelling exemplified by (18) to occur. At 800°C, on the other hand, as shown in figure 3, the swelling is gas driven and the accurate swelling in that figure is closely represented by the simple result (18). It is clear from figure 2 that increasing the gas generation rate at temperatures above the peak swelling temperature roughly decreases the critical dose and increases the absolute swelling in direct proportion to K_g. If such high K_g values are to be present in the first wall material then we expect high temperature swelling to be a serious problem.

Finally in figure 4 we show the simultaneous effect of a uniaxial stress of 100 MPa. Comparing this with the zero stress results in figure 2 we note that though the stress has only slightly reduced the critical dose its presence leads to a much greater swelling rate. Such dramatic effects of stress at high temperatures have been previously discussed by Brailsford and Bullough[7]. A realistic assessment of such stress effects must take account of simultaneous stress relaxation processes such as thermal creep that may be present at these high temperatures[7].

REFERENCES

1. G.L. Kulcinski, Fusion Design Problems, Proc. IAEA Workshop, Culham, p.479, (1974).
2. R. Bullough, B.L. Eyre and K. Krishan, Proc. Roy. Soc. (1975) to be published. Also Harwell Res. Report AERE-R 7952, (1975).
3. A.D. Brailsford and R. Bullough, J. Nucl. Mat. 44, 121 (1972).
4. A.D. Brailsford and R. Bullough, Phil. Mag. 27, 49 (1973).
5. R. Bullough and M.R. Hayns, J. Nucl. Mat. (1975) to be published. Also Harwell Res. Report TP 616, (1975).
6. R. Bullough, In Proc. of Fundamental Aspects of Radiation Damage in Metals, Gatlinburg, (Oct. 1975).
7. A.D. Brailsford and R. Bullough, J. Nucl. Mat. 48, 87 (1973).
8. M.R. Hayns and R. Bullough, Thermodynamics of Nuclear Materials, Vol. 1, p.217, (IAEA, Vienna, 1975).
9. A.D. Brailsford, R. Bullough and M.R. Hayns, to be published.

THE INFLUENCE OF PRE-INJECTED HELIUM ON VOID SWELLING IN ION-IRRADIATED STAINLESS STEELS

D. J. Mazey and R. S. Nelson
Metallurgy Division, AERE Harwell, Didcot, Oxfordshire, England.

ABSTRACT

High energy implantation of helium is used extensively to promote void formation in ion bombardment experiments designed to simulate irradiation damage effects in materials of potential use in reactors. However, the concurrent effects of radiation damage and helium production in the reactor interact to produce a complex behaviour which is difficult to simulate precisely. Such effects are expected to be more significant in a fusion reactor where helium concentrations could build up to $\sim 10^{-3}$ atom/atom. The likely effects of pre-implantation of helium at ambient and elevated temperature are discussed and related to the ideal simulation experiment in which helium injection and heavy-ion irradiation are carried out concurrently. Experimental TEM results are given for annealed AISI 316 stainless steel which had been injected with helium concentrations from 10^{-6} to 10^{-4} atom/atom at ambient temperature. These show that an interstitial loop structure evolves during annealing between 550°C and 700°C and that the retained interstitial atom fraction in the loops is the same as the injected helium concentration. This indicates a strong effect of helium on evolved structure and retained point-defects. Comparison of void swelling at 40 dpa in AISI 321 steel after pre-injection of 10^{-6}, 10^{-5} and 10^{-4} atom/atom helium at 30°C and 600°C showed that swelling is much higher in the material implanted with 10^{-4} He at 600°C. Small helium bubbles were resolved in 316 and 321 steel after implantation of 10^{-5} and 10^{-4} atom/atom helium at 600°C and the numbers of voids which formed during subsequent nickel ion irradiation to 40 dpa at 600°C were found to be similar to the initial bubble concentration. The effects on void formation of the various defect structures which result from helium implantation are discussed.

INTRODUCTION

The use of ion bombardment to simulate fast-neutron irradiation damage and void formation in both fission and fusion reactors is now widely used as a back-up to neutron data in order to select suitable materials for core and first-wall components. In both cases helium is produced within the components as a consequence of nuclear transmutation and in the fusion reactor case can build up to many hundred atomic parts per million. There is little doubt that the helium so produced has an important influence on void nucleation and irradiation damage structure, as discussed by Bloom et al [1]. In the majority of simulation studies carried out to date the helium has been implanted prior to irradiation either with samples maintained at ambient temperature or at temperatures at which the subsequent irradiation is to be carried out. Some experiments have been reported in which helium was added incrementally between ion irradiations [2]. In an ideal experiment, the helium should steadily accumulate as the irradiation damage proceeds. This can conveniently be achieved by using so-called dual irradiation facilities where two ion beams are used simultaneously; such facilities are currently being installed at a number of laboratories and some results have been obtained [3,4,5].

Helium is, in general, implanted into samples at energies in the range 100 keV to 40 MeV depending on the particular simulation experiment. In every case the helium will be associated with irradiation damage, and on average each helium ion will produce something like 100 atomic displacements. In other words for an implanted helium concentration of 10^{-3} atom/atom the damage associated with the implant will be between 0.1 and 1 displacements/atom (dpa). Such a dose will produce observable irradiation damage in stainless steels and, if heated, the point defects will interact with the implanted helium to form dislocation [6] and gas bubble [7] arrays which may well influence the formation of voids which grow during the subsequent irradiation. In addition, the dislocation and gas bubble configuration which forms after the helium injection is likely to be different depending on whether the gas is implanted at

ambient temperature and then heated, or is implanted at the elevated temperature. In either case it is of interest to establish the form of the irradiation microstructure after helium implantation and to evaluate its influence on the subsequent nucleation and growth of voids. In the present paper we wish to discuss the problems associated with the implantation of gas prior to irradiation compared with the situation which is likely to prevail during a dual irradiation and further to present results illustrating some of the points discussed.

EXPERIMENTAL DETAILS

Technique

The materials used in the experiments were stainless steels having specifications which fell within the AISI 316 and 321 standard. Cast analyses are shown in Table 1. Strip foil was prepared from plate material

Table 1 Chemical Composition of Stainless Steels (Wt%)

Alloy \ Element	C	B	Si	S	P	Mn	Cr	Ni	Mo	Ti	Fe
321 (En58B)	0.05	-	0.42	0.03	0.025	1.76	18.09	9.57	-	0.3	Bal
316 (FV555)	0.03	0.002	0.3	-	-	1.1	17.5	11.8	2.5	-	Bal

by sequentially annealing and cold-rolling with a final solution anneal (ST) at 1050°C for 20 minutes in vacuum ($< 10^{-5}$ torr) followed by a rapid cool under vacuum to 25°C. The resultant grain size was ~50 μm. Strip specimens 2.4 cm x 1.4 cm were implanted with helium at nominally ambient temperature in the Harwell Variable Energy Cyclotron (VEC) to uniform concentrations of 1, 10, 100 and 1000 appm helium. The method of implantation involves degrading the energy of a 40 MeV alpha-particle beam through a moving aluminium wedge [8]. Helium implantation at

temperature was carried out in-situ on the rocking target holder in the VEC [9]. Where possible the implanted foils were divided into two batches for each helium concentration studied; one was used to evaluate displacement microstructure and the other identical batch was used for studies of void formation under 46.5 MeV Ni^{6+} irradiation in the VEC.

The atom displacements produced during 40 MeV alpha-particle implantation were calculated by Matthews [10] using a modified version of the Manning and Mueller [11] EDEP-1 computer code with electronic stopping data taken from the Northcliffe and Schilling [12] data. A displacement energy of 25 eV was used with the displacement efficiency k = 0.8 to give the following approximate values of dpa for the relevant implanted concentrations of helium; 0.0001 dpa (1 appm He), 0.001 dpa (10 appm He), 0.01 dpa (100 appm He), and 0.1 dpa (1000 appm He). The estimated atom displacement rate during helium implantation was $\sim 0.5 \times 10^{-6}$ dpa/sec, and the helium flux into the steel $\sim 2 \times 10^{-9}$ atoms/sec. The displacement rate during Ni^{6+} irradiation was between 2 and 3×10^{-3} dpa/sec. Transmission electron microscopy (TEM) observations were carried out using Philips Em 300 and 301 electron microscopes at 100 kV. Representative electron micrographs were taken of each specimen examined and evaluation of the average bubble or void diameter ($\bar{d}$); bubble (C_B) and void (C_V) concentration, volume fraction of voids (S') and dislocation density were made using methods described previously [13].

Nature of Experiments

The experiments which were carried out were intended to check on several of the factors discussed in the introduction and comprised the following:

(i) investigation of microstructure produced in ST 316 steel by 40 MeV alpha-particle injection and the effect of post-irradiation annealing.

(ii) inspection of the microstructure in ST 316 after 100 appm He implantation at 100, 200, 300, 400, 500, 600 and 700°C.

(iii) investigation of the effect of helium pre-injection at ambient

temperature and at 600°C on subsequent void swelling in ST 321 irradiated to 40 dpa at 600°C.

(iv) the influence of pre-nucleated helium bubbles on void formation in ST 321 and ST 316 steel.

RESULTS AND OBSERVATIONS

Implantation-Induced Microstructure

Some of the TEM results obtained from experiment (i) on the microstructure produced in ST 316 steel following helium implantation at ambient temperature and subsequent annealing have been published [6,13]. These showed that a fine-scale point-defect cluster structure was resolvable initially after 100 and 1000 appm implantation, but not after doses of 1 and 10 appm helium. During post-irradiation annealing between ~550°C and 750°C for various times a structure consisting of faulted Frank interstitial loops (see Figure 1(a))and small bubbles evolved. Annealing at 700°C for periods up to 20 hours caused the interstitial loops to grow initially and then anneal away in samples injected with 100 appm He or less. In samples containing 1000 appm He the loops grew and unfaulted to createa high density of dislocations upon which small helium bubbles (diameter $\lesssim$ 50 Å) nucleated in visible concentrations approaching 10^{16} cm^{-3}. Annealing between 750°C and 1100°C produced slow growth and reduction in numbers of helium bubbles. Smidt and Pieper [6] have also observed loop and gas bubble formation in helium-implanted 316.

Additional experiments and analysis of the evolved interstitial loops in ST 316 have shown that the total calculated interstitial atom content in the Frank loops after anneals of one hour or greater correlates with the implanted helium concentration. It was found that ~1% of the calculated total number of atoms displaced during helium injection were preserved in the loops which formed during annealing. If it is assumed that for each self-interstitial atom preserved a corresponding vacancy remains then the interstitial fraction can be

Figure 1 Comparison of damage structure in ST 316 steel after helium implantation (a) Small interstitial Frank loops formed after a 9 hour anneal at 600°C following 100 appm helium injection (b) Dislocation loop defects on which precipitates and helium bubbles nucleate during implantation with 100 appm helium at 600°C. (Arrow indicates large bubbles).

considered an index of the trapped vacancy concentration. Comparing these vacancy and interstitial concentrations with the respective injected helium concentrations it is found that to a first approximation the helium:interstitial or helium:vacancy ratio is unity, as can be seen in Table 2. Helium is clearly influencing the retention and agglomeration of point-defects in 316 steel.

Table 2 Comparison of Injected Helium Atom Concentration, Retained Interstitial Atoms, and Vacancies in ST 316 Steel

Anneal Temperature	Interstitial atom concentration	Equivalent irradiation-induced vacancy concentration	Injected helium concentration
650°C	6×10^{-6} atom/atom	6×10^{-6}	10^{-5} atom/atom
650°C	1×10^{-4} atom/atom	1×10^{-4}	10^{-4} atom/atom
650°C	9×10^{-4} atom/atom	9×10^{-4}	10^{-3} atom/atom

Post-implantation annealing structure was not investigated in detail in ST 321 but it was established that an interstitial Frank loop population similar to that produced in ST 316 was formed in material annealed at 700°C following 1000 appm He injection at 30°C.

In experiment (ii) the microstructure in ST 316 after 100 appm He injection was studied as a function of implantation temperature. A summary of TEM observations is given in Table 3.

No structure was resolved up to 400°C but clusters and small loops were present after the implantation at 500°C. At 600°C small cavities were resolved in grain boundaries, on linear dislocation lines, and on small irregularly-shaped prismatic dislocation loop defects, examples of which are seen in Figure 1(b). This defect structure is different from that which evolved during annealing after room temperature implantation of helium in that the loops are not of the Frank type as seen in Figure 1(a). A high magnification micrograph illustrating the association of cavities and the dislocation

Table 3 Damage Structure in ST 316 After Hot Implantation of 100 appm Helium

Temp.	100°C	200°C	300°C	400°C	500°C	600°C	700°C
Observed Structure	None	None	None	None	Clusters & Loops (d ~100 Å) 2.0×10^{15} cm^{-3}	Clusters & dislocation loops 6.5×10^{14} cm^{-3}. Bubbles on loops & clusters (d 20-100 Å) 5×10^{14} cm^{-3}	Bubbles on dislocation and grain boundaries $\bar{d}$ ~200 Å 2.4×10^{13} cm^{-3}

defects is shown in Figure 2(a). If the sample is tilted to take the defects out of contrast it is often possible to resolve many bubbles in association with them. It is of interest to note that the number of cavities observed at 600°C correlates closely with the number of dislocation loops observed. It is likely that these dislocation defects were formed initially as loops and that helium bubbles subsequently nucleated at the periphery of the loop. There is also an indication that precipitation is occurring on the defects although extra reflexions attributable to precipitates could not be seen in high resolution diffraction patterns. Previous observations by Harkness et al [14] have shown that precipitates form in 304 steel during helium implantation, and furthermore that void and dislocation loop formation during subsequent reactor irradiation are affected by the presence of pre-injected helium.

These results show that hot implantation of 100 appm helium in the range 500°C to 700°C produces an observable defect clusters, dislocation loops and helium bubble microstructure in ST 316 which could influence the nucleation of voids etc., during subsequent irradiation within the same temperature-range. This will be discussed later.

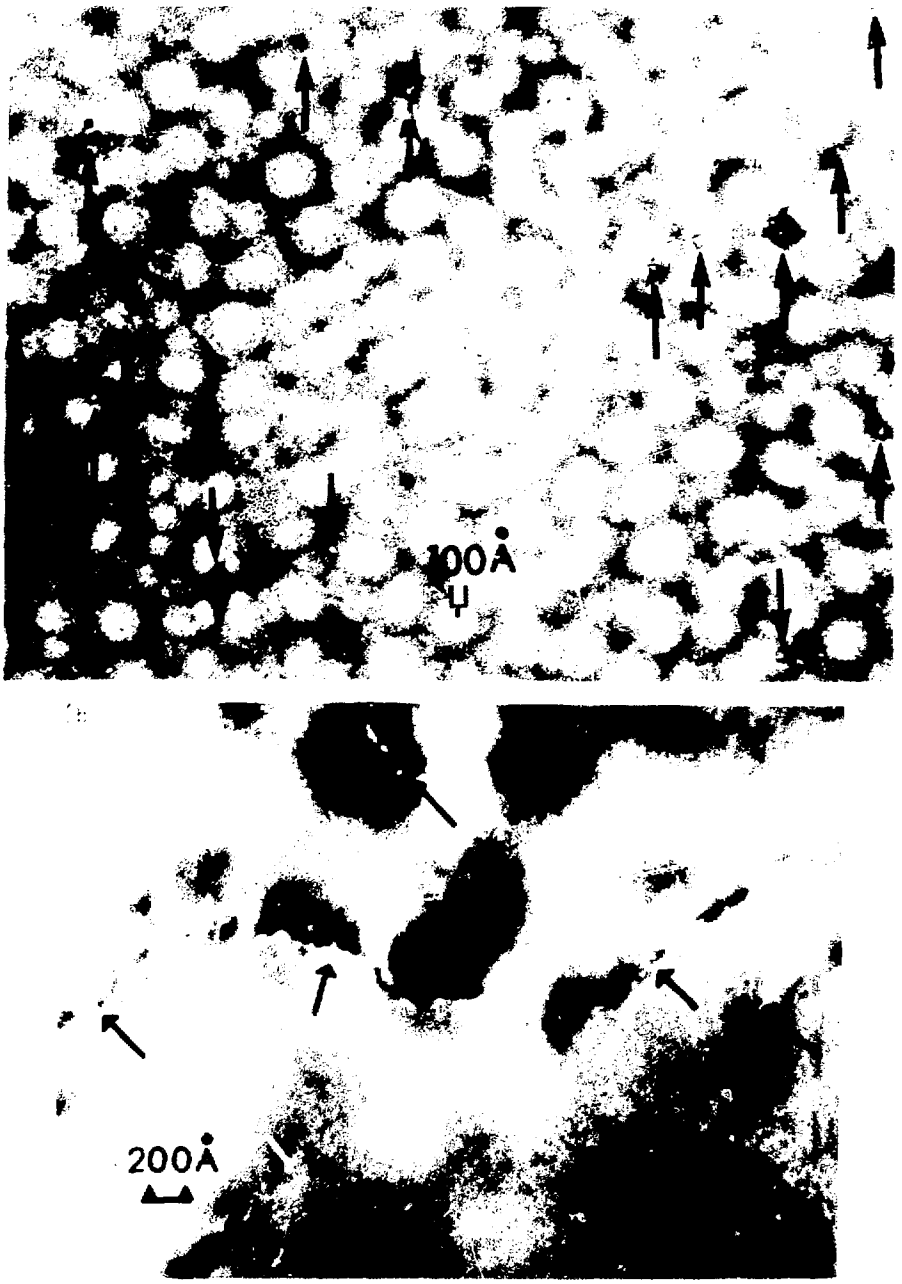

Figure 2 Electron micrograph showing helium bubbles on dislocations after implantation with 100 appm He at 600°C (a) Bubbles associated with cluster and loop defects seen in figure 1(b) in ST 316 (b) Bubbles on dislocations in ST 321.

Void Swelling Results

Foils of ST 321 containing 0, 1, 10 and 100 appm helium pre-injected at ~30°C were subsequently irradiated to 40 dpa with 46.5 MeV Ni^{6+} ions at 600°C in the VEC. Steel foils from the same parent batch were uniformly filled in-situ at 600°C on the rocking target in the VEC with 1, 10 and 100 appm He and subsequently irradiated to 40 dpa with 46.5 MeV nickel ions. The results of the TEM observations are given in Table 4.

Table 4 Comparison of Void Swelling in ST 321 Steel after 40 dpa Irradiation at 600°C Following Helium Injection at 30°C and 600°C

Helium Implantation Temperature (°C)	Implanted Helium Concentration atom/atom	Average Void Diameter $\bar{d}$ (Å)	Void Density C_v (cm^{-3})	Void Swelling S' (%)	Dislocation Density Λ (lines cm^{-2})
~30	0	420-490	$1.5\text{-}5 \times 10^{14}$	1-3	1.0×10^{11}
	10^{-6}	400	1.3×10^{15}	4.5	1.0×10^{11}
	10^{-5}	285	3.1×10^{15}	4.4	1.0×10^{11}
	10^{-4}	216	5×10^{15}	2.7	1.0×10^{11}
600	0	420-490	$1.5\text{-}5 \times 10^{14}$	1-3	1.0×10^{11}
	10^{-6}	395	6×10^{14}	2.0	6.0×10^{10}
	10^{-5}	441	9×10^{14}	4.3	9.0×10^{10}
	10^{-4}	481	2×10^{15}	13.4	1.1×10^{11}

The data relating to ambient temperature implantation of helium have been published elsewhere [15].

After the initial implantation with 10 and 100 appm He at 600°C bubbles were observed on dislocation lines (Figure 2(b)) and in grain boundaries. Resolution of bubbles after 10 appm helium implant was very difficult. Bubble size and concentration determined for 100 appm samples are given in Table 5. Typical void microstructures in 321 steel after 100 appm He implantation at 30°C and 600°C are illustrated in Figure 3. Figure 3(b) compares with Figure 2(b) where the pre-void microstructure is revealed. Figure 4 shows a graph of the void

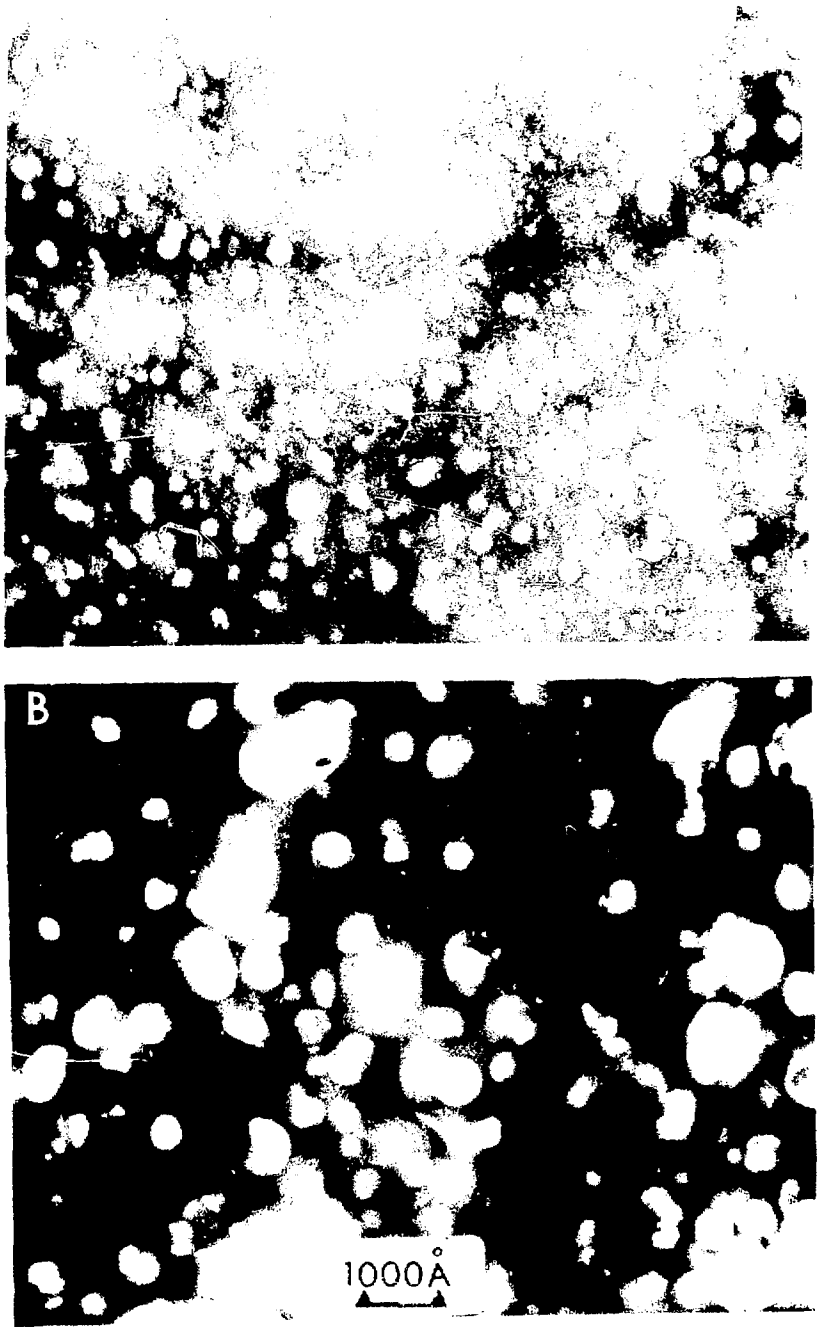

Figure 3 Typical void distribution in ST 321 after 46.5 MeV Ni^{6+} irradiation to 40 dpa at 600°C following (a) 100 appm He implantation at ~30°C and (b) 100 appm He implantation at 600°C.

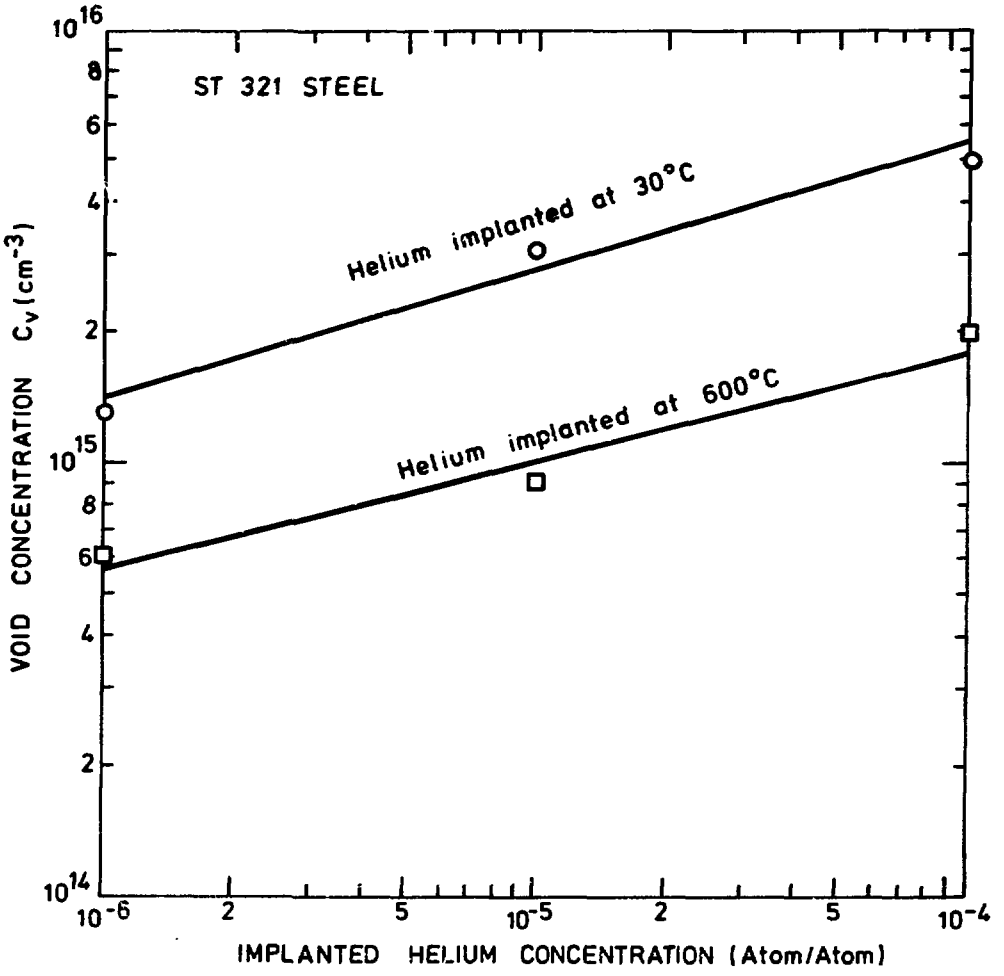

Figure 4 Graph of void concentration (C_v) versus helium concentration for constant (40 dpa) dose at 600°C in ST 321 steel.

concentration (C_v) as a function of helium concentration for the two helium implant temperatures. A lower void concentration in the hot implant experiments is clearly evident. Void swelling as a function of helium concentration for the two implant conditions is plotted in Figure 5 where it can be seen that a high swelling has resulted in the samples containing 100 appm He implanted at 600°C. Bubble size is smaller and void concentration is higher to give lower swelling in the sample injected with 100 appm He at ambient temperature.

Several results obtained from experiment (iv) on the influence of pre-formed helium bubble distributions on subsequent void formation in ST 321 and 316 are given in Table 5.

It is seen that the initial bubble (C_B) and final void (C_v) concentrations are almost identical in both 316 and 321, but the concentrations of bubbles and voids are a factor four lower in the 316 steel. This points very strongly to heterogeneous nucleation of voids on the pre-nucleated bubbles. This conclusion is substantiated by numerous observations of curved stringers of voids clearly formed on dislocation lines in a non-random manner. Note also that a high bubble concentration is only attained thermally by a long anneal at 700°C following implantation at ambient temperature. Estimate of the helium concentration in the observable bubbles was made using a modified Van-der-Waals equation of state as follows:

$$m' = \frac{2\pi\gamma\bar{d}^2/3}{(4B\gamma/\bar{d})+kT}$$

The helium content (m') for the average size bubble ($\bar{d}$) was determined using values of surface energy ($\gamma \sim 3{,}000$ ergs cm^{-2} at 600°C) extrapolated from zero-creep data for 304 stainless steel [16]. The Van-der-Waals constant for helium was taken from Tsederborg et al [17] ($B = 9.6$ cm^3 $mole^{-1}$ at 600°C). The helium concentrations calculated (Table 5) are only a rough estimate in view of the difficulty in resolution of small bubbles and assessment of true image size. The results indicate that although all the injected helium is not present in bubbles, more helium has precipitated into bubbles in 321 than in 316.

Table 5 Comparison of Initial Helium Bubble Concentration and Void Concentration after Subsequent Ion-Irradiation (100 appm He)

	Treatment		Average Cavity Diameter $\bar{d}$ (Å)	Visible Cavities (C_V, C_B) cm^{-3}	S'%	He in Bubbles appm
ST321	He implant at 600°C	Bubbles	48	1×10^{15}	-	65
	He implant at 600°C +40 dpa 600°C	Voids	461	2×10^{15}	13.4	-
ST316	He implant at 30°C +70 hrs 700°C	Bubbles	40	1.5×10^{15}	-	33
	He implant at 600°C	Bubbles	60	5×10^{14}	-	30
	He implant at 600°C +40 dpa 600°C	Voids	700	4×10^{14}	6.7	-

DISCUSSION

Although we have mainly been concerned with the possible influence of helium on void nucleation it should be pointed out that in most steels and in particular 316 steel, void formation during simulation experiments occurs readily even with no added gas. On the other hand, in 321 steel in which titanium has been added as a stabilising agent, void nucleation is somewhat limited unless helium is added. This difference has been explained in terms of dissolved oxygen - which acts as a void nucleating agent - where, in the case of 321 steel, association of oxygen with

titanium is thought to effectively limit the availability of free oxygen. Void nucleation is, therefore, expected to depend more strongly on helium content in 321 steel than in 316 steel, that is except at very high helium levels where its influence will outweigh that of the dissolved oxygen. We will, therefore, concentrate our discussion mainly on the role of helium in void nucleation in 321 steel.

Perhaps the most significant result presented in the preceeding section is to be found in Table 4 where the hot-implanted 321 steel samples show a lower void density than in the case of the ambient temperature implants. In all cases shown the void density is significantly greater than in the samples having no injected helium. These differences are thought to be a manifestation of the scale on which helium gas bubbles have been nucleated prior to the void irradiation. In this context we should take note of the pre-irradiation microstructures which exist in the 100 appm samples. At this stage it is worth pointing out that it is not possible to see all the helium bubbles which are believed to have formed prior to nickel ion irradiation, due to the resolution limit ($\sim$15 Å) of small cavities in the electron microscope. For instance, at 600°C in 316 and 321 steel it is only at 10 and 100 appm that bubbles have grown sufficiently large to be resolved and only then after the hot implant where the assumed lower helium bubble concentration compared with that of the cold implant allows the attainment of larger void sizes. The comparison is readily made in 316 where at 700°C the bubbles are clearly resolvable and observed bubble density is low after annealing or hot implantation. The general conclusion is that in the high temperature (i.e. >600°C) implant cases the pre-irradiation resolvable gas bubble density is significantly lower than in those foils which have been implanted with helium at ambient temperature and subsequently annealed to temperatures similar to those of the hot implants.

Implanted helium is thought to be highly mobile as an interstitial[18,19,20] immediately after 'slowing down' in the solid from its initial high energy injection as an ion. Such helium interstitials are then trapped at vacancies, dislocations and precipitates. At ambient temperatures the vacancies created during the implant can build up to high concentrations

in steels and these no doubt act as the major traps for the helium as the results of Table 1 suggest. If the temperature of irradiation is raised steadily, bubble precipitation can occur as a consequence of the migration of these vacancies through the lattice. The scale of precipitation will depend on the gas concentration and will occur both homogeneously, and heterogeneously on the dislocation structure which evolves. On the other hand, at irradiation temperatures such as 500°C → 650°C and above, the dynamic vacancy concentration within the lattice is extremely low relative to the dislocation density which evolves, and to the precipitate density which might exist. Gas bubble nucleation will therefore occur almost exclusively in a heterogeneous manner on such sinks, as illustrated in Figure 1(b) and 2 and as such will occur at a lower density than expected for the material annealed after room temperature helium implantation.

The above difference in nucleation density observed in the case of 321 steel has a significant affect on the total void swelling. This is shown in Figure 5 where it is seen that at high gas concentrations the two swelling curves diverge widely. This behaviour clearly results from the different sink densities which exist during the two conditions and is predicted from current theories of void swelling [21]. Experimental data at higher (>>100 appm) gas concentrations would be of interest in this context. This is particularly desirable in the light of recent neutron irradiation data [22] from 316 steel containing up to 6000 appm transmuted helium where current models failed to explain high swelling observed at 680°C.

Although the scope of the present experiments is limited to single pre-injections of helium, it is of interest to consider the implications in the case of simultaneous helium implantation and, say, nickel ion irradiation of stainless steel. Such dual irradiation experiments will almost certainly be carried out at elevated temperatures in the homologous temperature-range for void formation where the dynamic vacancy concentration is small compared with other sinks for migrating helium such as the irradiation-produced dislocation structure. Under such circumstances nucleation will occur in a similar way to that expected during a hot

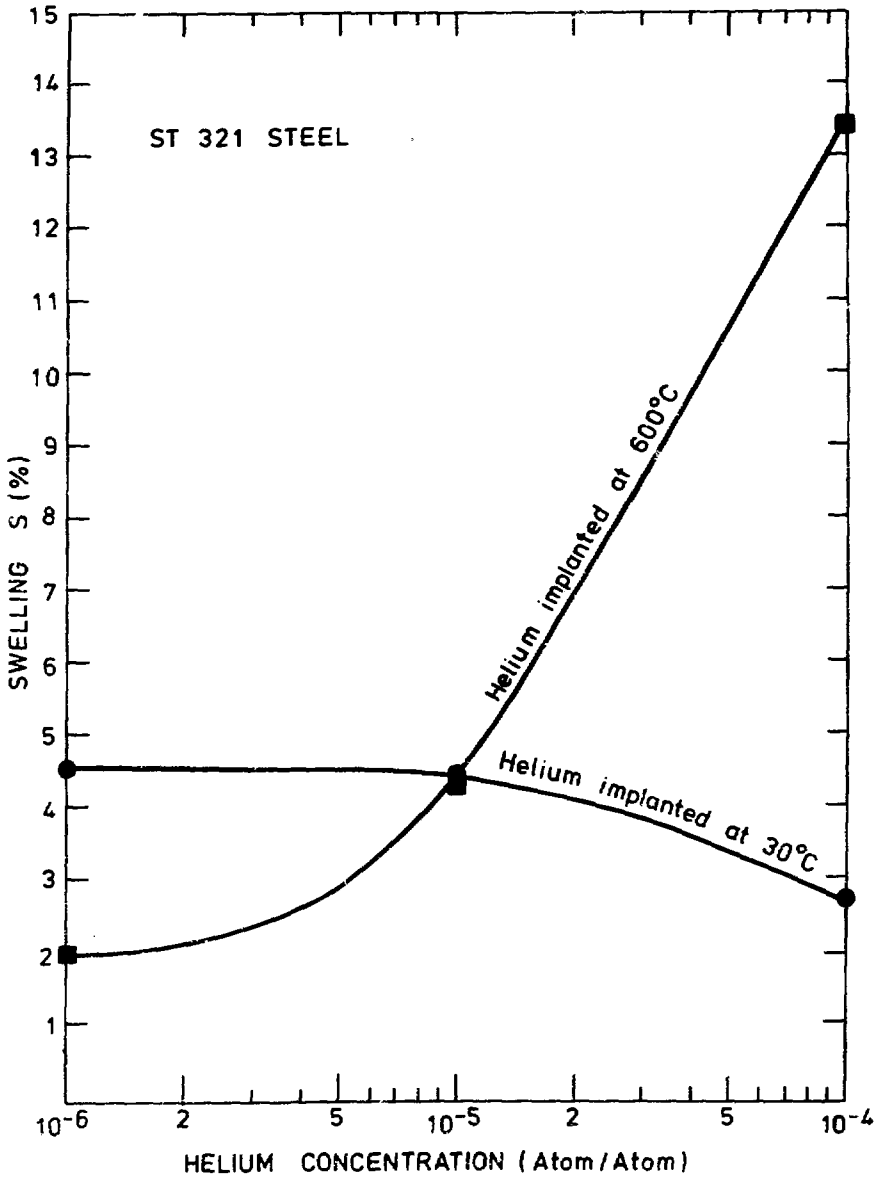

Figure 5 Graph of void swelling (S') versus helium concentration for constant (40 dpa) dose at 600°C in ST 321 steel.

implant prior to irradiation. However, the precise ratio in number density of void nuclei will probably differ [illegible] the helium atom:displaced atom ratio will be between 1 - 1 [illegible]. Thus if nucleation occurs primarily in association with [illegible] it is likely that the nucleation density would be somewhat smaller than is observed after hot helium implantation alone. From the [illegible] presented here we might expect significant differences in the [illegible] behaviour between stainless steel samples implanted prior to [illegible] and those which are irradiated concurrently with helium implantation; this will be especially so at helium concentrations in excess of [illegible].

REFERENCES

1. E. E. Bloom, K. Farrell, M. H. Yoo and J. [illegible], Proc. [illegible] Symposium 'The Physics of Irradiation-Produced Voids', Harwell, September 1974, AERE Report R7934, p[illegible], 1975.
2. D. W. Keefer and A. G. Part, J. Nucl. Mat. [illegible].
3. J. L. Brimhall, Proc. Consultant Symposium 'The Physics of Irradiation-Produced Voids', Harwell, September 1974, AERE Report R7934, [illegible], (1975).
4. J. H. Evans, S. N. Buckley and S. Mantovani, J. Nucl. Mat., [illegible], (1975).
5. S. C. Agarwal, B. O. Hall, D. I. Potter and A. Taylor, [illegible] conference (1975)).
6. D. J. Mazey and S. Francis, Proc. Consultant Symposium 'The Physics of Irradiation-Produced Voids', Harwell September 1974, AERE Report R7934, p257, (1975).
7. F. A. Smidt and A. G. Pieper, NRL Report [illegible], [illegible] Proc. ASTM Symposium on 'Effects of Irradiation on Structural Materials', Gatlinburg, Tennessee, June 1974, to be published.
8. J. H. Worth, Proc. Int. Conf. 'Uses of Cyclotrons in Chemistry, Metallurgy and Biology', Oxford 1969. Edited C. B. Amphlett (Butterworths) p282 (1970).
9. J. H. Worth, J. Inst. Nuc. En. 15, 73, (1974).

10. M. D. Matthews, Unpublished [illegible] AERE Report R[illegible] (1974).

11. I. Mannan and G. P. Mueller, [illegible], 5, 45, (1974).

12. L. C. Northcliffe and R. F. [illegible], [illegible], Vol. 5, Numbers 3-4, p. [illegible] (1970).

13. D. J. Mackey, D. Phil. Thesis, 'Ion Implantation in Metals', University of Sussex, England (1976).

14. S. D. Harkness, R. J. Kerr, [illegible], J. Nucl. Mat. 44, 153, (1972).

15. J. A. Hudson, Unpublished AERE Report R[illegible] (1974).

16. L. E. Murr, G. L. [illegible], J. Appl. Phys., Al, 1481, (1970).

17. N. V. Tsvetkov, V. N. Bykov and N. A. Matveev, Chapter 2 in 'Thermodynamics and Inner Friction in Microscopic Solids', Atomizdat, Moscow (1965).

18. W. D. Wilson and R. A. [illegible], in 'Interatomic Potentials and Simulation of Lattice Defects', Ed. Gehlen, Beeler and Jaffee, Plenum Publishing Corp., New York (1972).

19. E. V. Kornelsen, Rad. Effects, 13, 227, (1972).

20. W. D. Wilson C. L. [illegible], Rad. Effects, 13, 85, (1972).

21. A. F. Bradshaw and P. [illegible], J. Nucl. Mat., 41, 121, (1971).

22. F. W. Wiffen and B. E. Bloom, Nuclear Technology 17, 114, (1973).

[illegible] IN TYPE 316 STAINLESS STEEL [illegible] RELATED CLR CONDITIONS*

[illegible], and E. E. Bloom

[illegible] Sciences Division
[illegible] National Laboratory
[illegible], Tennessee 37830

ABSTRACT

[illegible] to 316 stainless steel were irradiated [illegible] Reactor (BFIR) to displacement damage [illegible] 36 dpa, displacements/atom) and helium contents of [illegible] at temperatures from 380 to 680°C. The samples [illegible] the annealed condition (1 hr at 1050°C) [illegible] cold condition. The microstructures of these [illegible] transmission electron microscopy (TEM). [illegible] companion split specimens of the same heat of [illegible] irradiated to approximately the same conditions [illegible] helium content, which was 15 at. ppm. [illegible] irradiated samples with high helium [illegible] remained constant with temperature from 380 to [illegible] from 500 to 650°C. Swelling in cold [illegible] was higher in annealed samples for all [illegible] 380°C. Swelling was larger at all temperatures [illegible] for the higher helium concentrations than for the [illegible] lower helium concentrations. Recrystallization [illegible] lower swelling resistance. Cold work [illegible] concentrations, decreased the cavity sizes. [illegible] [illegible] with annealed material containing [illegible] concentrations. Swelling was greatly [illegible] at temperatures above 600°C in both the [illegible] samples; the increase was due to the [illegible] cavities at the grain boundaries. Calculated [illegible] helium measured in the samples [illegible] to the helium equilibrium bubbles have [illegible] to the equilibrium helium bubbles.

[illegible] Union Carbide Corporation under contract [illegible] and Development Administration.

INTRODUCTION

Type 316 stainless steel is a candidate material for the first wall of fusion reactors. Previously, cold work had been shown effective in reducing swelling and maintaining usable mechanical properties in fast reactor irradiations.[1] Such irradiations produced low helium concentrations. The purpose of this investigation was to determine the effects of high helium contents and high dpa levels on the microstructure of both 20% cold worked and solution-annealed type 316 stainless steel to simulate accurately anticipated controlled thermonuclear reactor (CTR) operating conditions. Our experiments approximated the displacement damage produced after 6 years and the helium produced after 20 years of fusion reactor operation[2] at a wall loading of 1 MW/m^2 (Table I). This study examined the temperature dependence of microstructural changes in both annealed and 20% cold worked samples for nearly constant gas content and displacement level. Since helium acts synergistically with the displacement level to influence properties[3,4] it was important to duplicate as closely as possible the production rates of helium and displaced atoms in the first wall of a fusion reactor. In EBR-II, only about 35 dpa and 15 at. ppm He are produced per year. With alpha-particle injection techniques,[4] high displacement damage does not accompany high helium concentrations. For stainless steel or other nickel-containing alloys, a more suitable simulation can be obtained using mixed-spectrum fission reactors, taking advantage of a two-step nuclear reaction of nickel atoms with thermal neutrons to produce helium: $^{58}Ni(n,\gamma)^{59}Ni$ followed by $^{59}Ni(n,\alpha)^{56}Fe$. High-flux reactors with both thermal and fast components of the spectrum, such as the HFIR, allow the combination of continuous helium and displacement production in reasonably short irradiation times to simulate fusion reactor conditions (Table I). This paper reports the microstructural information obtained from type 316 stainless steel samples irradiated in both the 20% cold worked and solution-annealed condition at irradiation temperatures between 380 and 680°C, to exposures of 40–60 dpa, and 3000–4300 at. ppm He.

Table I. Radiation Damage Parameters for Type 316 Stainless Steel

Reactor	Rate per Year[a]	
	dpa	He (at. ppm)
CTR (1 MW/m^2)	10	200
EBR-II	35	5
HFIR[b]	35	1900[c]

[a]Calculated by Kulcinski et al. (Ref. 2).

[b]HFIR: damage flux, 1.5×10^{15} n cm^{-2} sec^{-1} (>0.1 MeV); thermal flux, 2.4×10^{15} n cm^{-2} sec^{-1}

[c]Experimentally measured value.

EXPERIMENTAL

A description of the HFIR experiments containing these samples and the swelling and the mechanical properties of these samples have been previously reported.[5,6] Microscopy disks were cut from samples that had been irradiated and then tensile tested at temperatures near the irradiation temperature. The composition of the type 316 stainless steel is as follows: 18.0 Cr, 13.0 Ni, 2.58 Mo, 1.9 Mn, 0.05 Ti, 0.8 Si, 0.05 C, 0.013 P, 0.016 S, 0.05 N, 0.0005 B, bal Fe. [Values (wt %) are averages of multiple determinations on this heat.] The tensile specimens were produced from rod stock as follows: 12.7-mm-diam (0.5-in.) hot-rolled rod was annealed at 1200°C and then swaged to 50% reduction in area. The rod was solution treated for 1 hr at 1050°C in argon and rapidly cooled. The rod was further reduced by 50% and similarly solution treated at 1050°C. Annealed specimens were machined from this material. Part of the remaining rod was cold worked to a 20% reduction in area by swaging, and specimens were machined from the rod. The specimens were 31.7 mm (1.25 in.) long, with the gage section 18.3 mm (0.72 in.) long and 2mm (0.080 in.) in diameter. The irradiation experiment was uninstrumented, and heating was accomplished by using

a helium-filled gap to provide resistance to radial flow of the heat produced by nuclear heating. Calculated nuclear heating rates were checked by using silicon carbide temperature monitors in a calibration experiment.[7] The variation in nuclear heating and in the fast and thermal flux with distance from the horizontal midplane is shown in Fig. 1. The effect of a variation in temperature axially along the specimens was minimized by cutting the TEM discs near the specimen center. The uncertainty in irradiation temperature is estimated to be ±10% of the temperature above ambient (55°C), but the relative difference in temperature between samples is thought to be more accurate than their absolute temperatures.

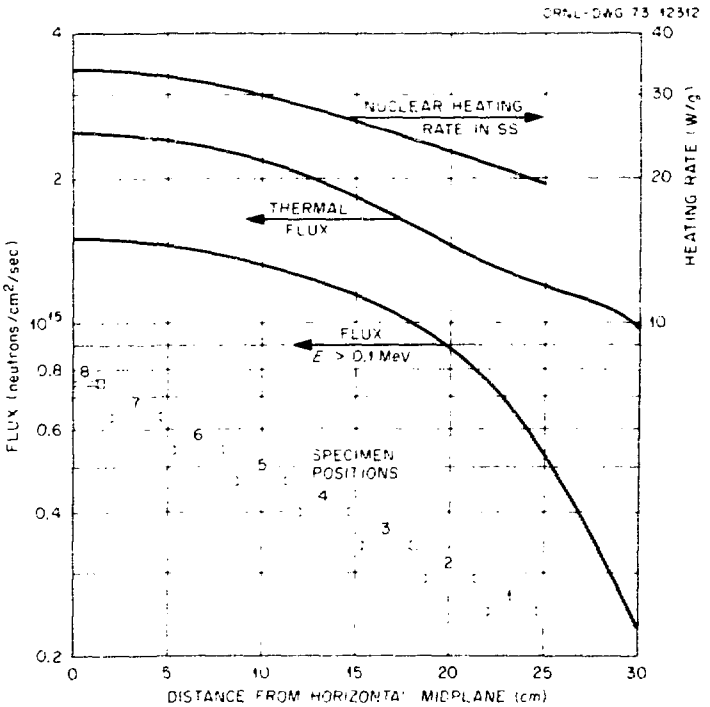

Fig. 1. Variation in Nuclear Heating Rate and Neutron Flux Along the Half Length of a HFIR Irradiated Experiment. Flux data from F.B.K. Kam and J. H. Swanks, *Neutron Flux Spectrum in the HFIR Target Region*, ORNL-TM-3322 (March 1971).

Values of helium contents were measured for selected samples, and the helium production cross sections derived from the measurements were used to calculate the helium concentrations for other samples. The dpa values were calculated using the neutron spectrum from the HFIR[8] and the displacement model recently recommended by the IAEA.[9] These helium and dpa numbers are more accurate than those previously reported on the same samples.[5,6]

Immersion density measurements and then tensile tests in air preceded the cutting of the microscopy samples. TEM disks were cut from the gage sections of selected samples, at least 3 mm (0.12 in.) from the fracture section. Because of gamma activity greater than 10 R/hr at contact, most samples were thinned remotely by a two-step procedure. Dimpling was accomplished with a solution of 120 ml of water, 700 ml of ethyl alcohol, 100 ml of ethylene glycolmonobutyl ether, and 78 ml of perchloric acid at ~20°C and a current density of about 4 A/cm^2; polishing was done with a solution of ethyl alcohol and perchloric acid at 0–10°C and a current density of about 4 A/cm^2.

The TEM samples were examined in 1-MV and 200-kV Hitachi electron microscopes. Thicknesses of the sample were determined using stereographic techniques. Cavity sizes and distributions were determined on a Zeiss particle-size analyzer. Thickness measurements and cavity counting were done on pictures taken in absorption contrast. The recommendations of Rühle[10] for determining the true cavity size from an out-of-focus image were followed while measuring the cavity sizes. Several fields of view in different grains were observed when available, and between 2000 and 5000 cavities were counted for each sample. For the stereo pairs, most pictures were taken by tilting along a Kikuchi band so that the tilt axis was known and accurate parallax determinations could be made. Foil thicknesses measured on pictures taken on the 1-MeV microscope ranged from 700 to 7000 Å. When possible, precipitate identities were determined from analysis of the diffraction patterns by comparing them with known data for various precipitate phases in type 316 stainless steel.[11,12] Dislocation concentrations were measured knowing diffraction vector and either counting ends or using the line intercept method in areas with measured foil thickness.

RESULTS

Swelling

The swelling results are given in Table II and Fig. 2. In both the annealed and cold worked material, swelling is quite insensitive to irradiation temperature in the range 380 to ~550°C and then increases very rapidly at higher temperatures. The swelling remains the same or decreases slightly as the temperature is increased for the cold worked samples from 380 to 550°C, from 2.2 to 1.4% respectively. This trend is confirmed by immersion density measurements of 1.6% at 380 to ~0.0% at 550°C. The immersion densities appear to differ from the void volume fractions by 1–2% swelling for most samples, but the former are always less than the latter. The solution-annealed material shows a fairly constant cavity volume fraction of ~8.7% at 480 and 550°C.

Data from Brager and Straaslund[13] for solution-annealed type 316 stainless steel irradiated in EBR-II, where helium levels are relatively low, show an increase in swelling with temperatures from 395°C and 17 dpa to 470°C and 21 dpa. The swelling is on the order of 1.0%. At higher temperatures a swelling maximum is reached, and the swelling decreases to nearly zero at ~680°C. Limited data from the same heat of stainless steel used in the present experiments and irradiated in EBR-II show similar behavior,[14] but shifted to a higher temperature than the Brager and Straaslund data, as can be seen in Table II. A swelling peak is not defined by this limited data. If the empirical equations developed by Brager and Straaslund are used for fluence and temperature conditions equivalent to the EBR-II data of Sklad and Bloom,[14] a swelling of ~5% in the temperature range 525 to 535°C and at a fluence of 6.6×10^{22} n/cm^2 for annealed type 316 stainless steel is predicted. This is higher than the 0.4% swelling observed by Bloom and Sklad for the present heat of steel[14] (see Table II). The swelling resistance of this heat of steel shows that it is important to compare the HFIR data with the limited EBR-II data on the same heat of steel.

Table II. Microstructural Swelling Data on Irradiated Samples

Condition	Irradiation Temperature (°C)	Neutron Fluence, >0.1 MeV (n/cm^2)	Helium Content (at. ppm)	Displacement Damage (dpa)	Immersion Density Decrease, $\Delta\rho/\rho_0$[a] (%)	Void Volume Fraction[b] (%)	Cavity Concentration[c] ($no./cm^3$)	Diameter[c] (Å)
Annealed 1 hr at 1050°C, irradiated in HFIR	480	6.10×10^{22}	2950	42		8.8 ± 1.2	$1.4 \pm 0.06 \times 10^{15}$	386
	550	6.18	2990	42		8.5 ± 1.6	$4.4 \pm 1.3 \times 10^{14}$ (1.2×10^{12})[c]	500 (3350)[c]
	680	8.74	4140	61	14.1	15.2 ± 1.7	$4.6 \pm 1.2 \times 10^{13}$ (1.1×10^{12})	1083 (6400)
20% Cold Worked after 1 hr at 1050°C, irradiated in HFIR	380	7.05	3320	49	1.6	2.2 ± 0.4	$1.8 \pm 0.4 \times 10^{16}$ (4.5×10^{12})	95 (1110)
	450	7.69	3660	54	0.80	2.0 ± 0.4	$6.6 \pm 1.6 \times 10^{15}$	170
	550	6.18	2990	42	0.0	1.4 ± 0.10	$2.4 \pm 0.4 \times 10^{15}$	210
	600	8.71	4070	60	3.3	5.0 ± 0.2	$3.3 \pm 3.0 \times 10^{14}$ (2.7×10^{12})	647 (3500)
	680	8.74	4140	61	16.8	16.8 ± 3.6	$6.3 \pm 2.6 \times 10^{13}$ (1.4×10^{12})	1100 (7100)
Annealed 1 hr at 1050°C, irradiated in EBR-II[d]	500–535	5.6	~15	31	0.37	[e]	4.9×10^{13}	485
	600–660	6.6	~15	37	1.53	[e]	6.3×10^{12}	1370
20% Cold worked after 1 hr at 1050°C, irradiated in EBR-II[d]	500–555	6.6	~15	37	~0	[e]	[e]	400–600
	600–660	6.6	~15	37	0.4	[e]	[e]	600–1500

[a] Obtained from immersion density measurements.

[b] Obtained from electron photomicrographs.

[c] The numbers in parentheses are for the large portion of the bimodal distributions observed.

[d] Data from personal communication, P. S. Sklad and E. E. Bloom, 1975.

[e] Not available.

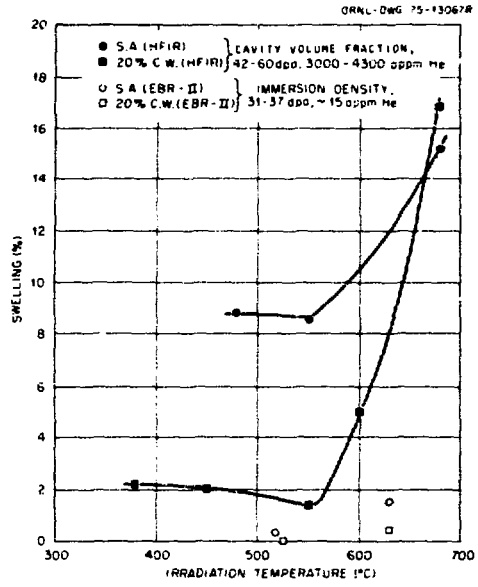

Fig. 2. Variation in Swelling as a Function of Temperature for Both 20% Cold Worked and Annealed Type 316 Stainless Steel Samples Irradiated in the HFIR. In addition, points from the same heat of steel irradiated in EBR-II are plotted for reference at low helium content.

The microstructures of the cold worked and irradiated type 316 stainless steel samples are shown in Fig. 3–7, and those of the annealed and irradiated type 316 stainless steel samples are shown in Figs. 8–10. Annealed and cold worked samples irradiated in the HFIR and EBR-II are compared in Fig. 11.

In both the annealed and the cold worked HFIR samples, swelling increased rapidly with temperature in the range 550 to 680°C. In the cold worked material, the cavity volume fraction is 5.0% at 600°C and ~17% at 680°C. It is significant to note that recrystallization of the cold worked structure had occurred at 600°C and that grain growth occurred at this temperature (see Fig. 6). Recrystallization will be discussed in more detail later. For these temperatures both optical metallography and TEM show massive σ-phase formation at the grain boundaries.

The annealed material irradiated at 680°C has a void volume fraction of 15.2%. At 680°C, swelling in the cold worked and annealed samples was comparable (see Figs. 7 and 10).

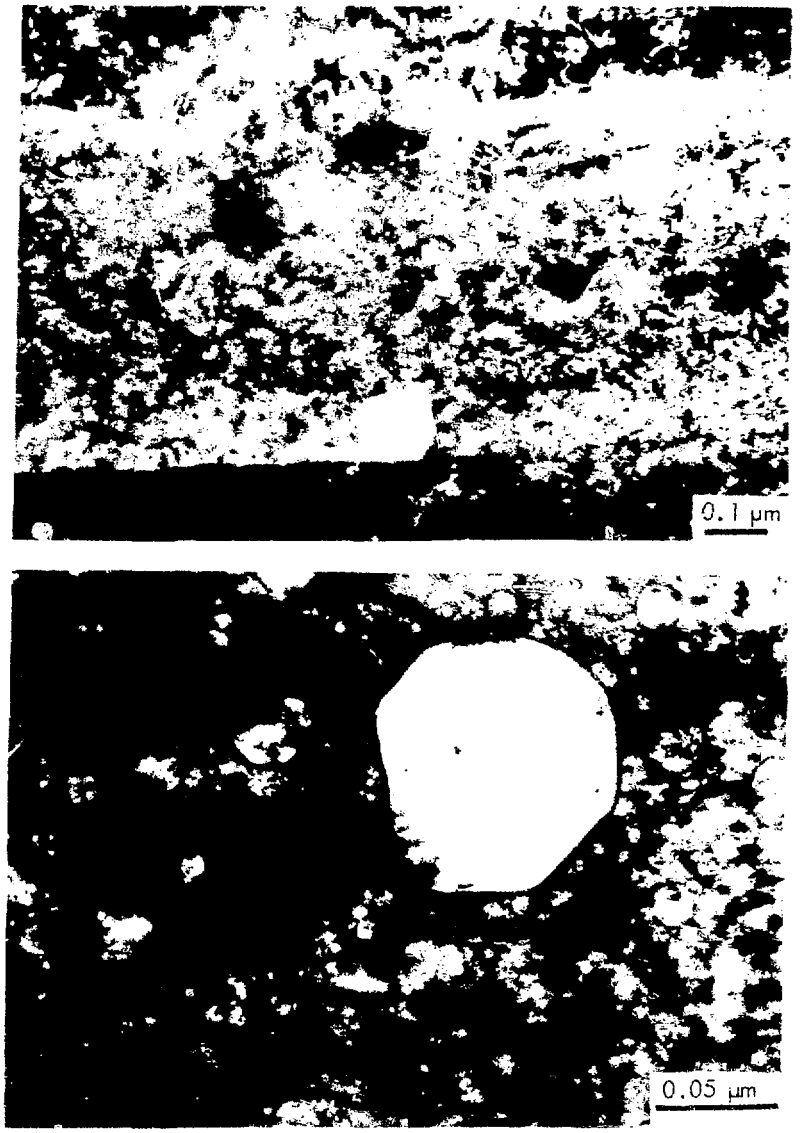

Fig. 3. Type 316 Stainless Steel, 20% Cold Worked, Irradiated at 380°C to 49 dpa and 3320 appm He. Note the high concentration of very small (diam ≈30 Å) cavities.

Fig. 4. Type 316 Stainless Steel, 20% Cold Worked, Irradiated at 450°C to 54 dpa and 3660 appm He.

Fig. 5. Type 316 Stainless Steel, 20% Cold Worked, Irradiated at 550°C to 42 dpa and 2990 appm He. (a) Cavities in the matrix; (b) cavities at the grain boundary. Note σ-phase particle labeled σ.

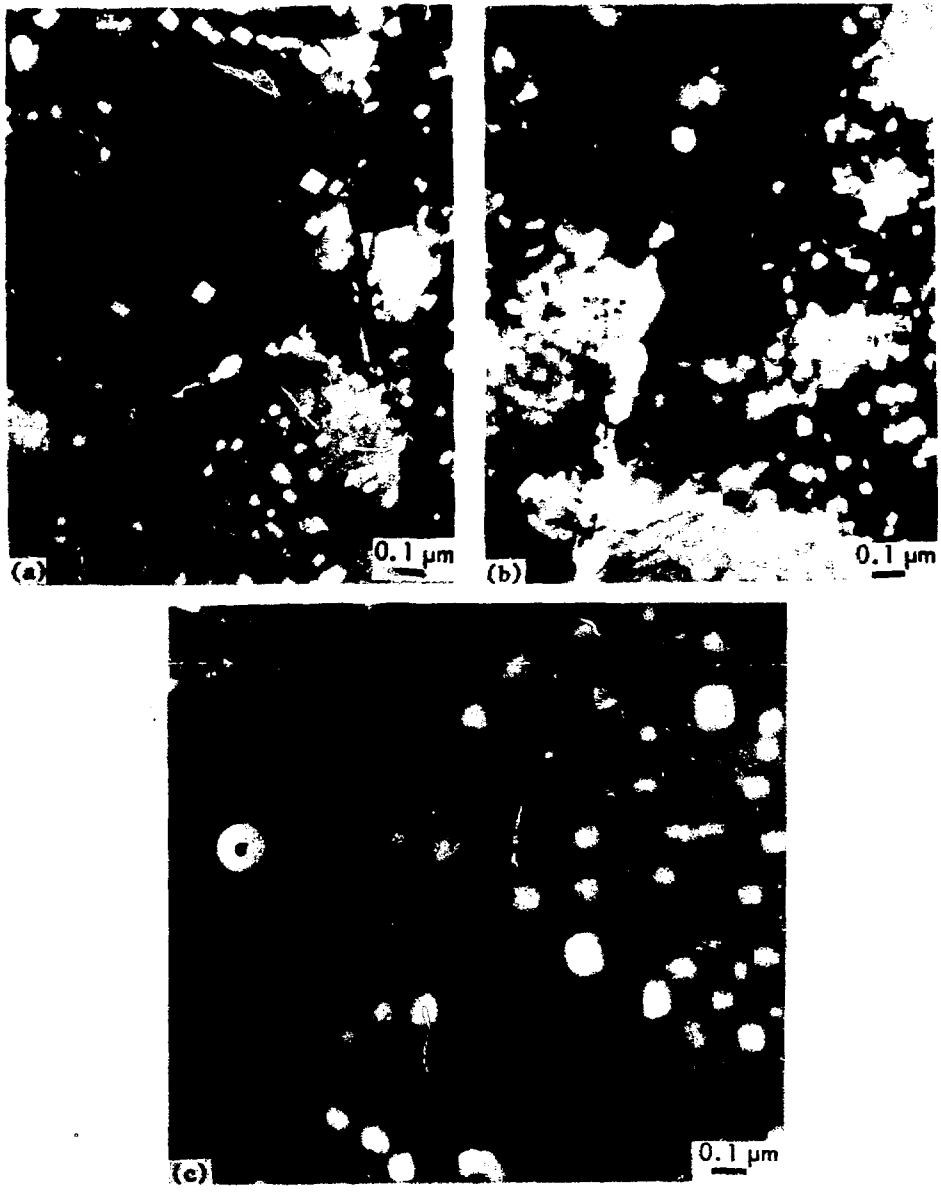

Fig. 6. Type 316 Stainless Steel, 20% Cold Worked, Irradiated at 600°C to 60 dpa and 4070 appm He. (a) Recrystallized region with cavities preferentially located at the growing grain front. (b) Austenite grain boundary with large cavities. (c) Region in which grain boundary growth has occurred. Note the large cavities at the austenite-sigma interface. Particles labeled are sigma phase.

Fig. 7. Type 316 Stainless Steel, 20% Cold Worked, Irradiated at 680°C to 61 dpa and 4140 appm He. Note the very large cavities at the grain boundaries.

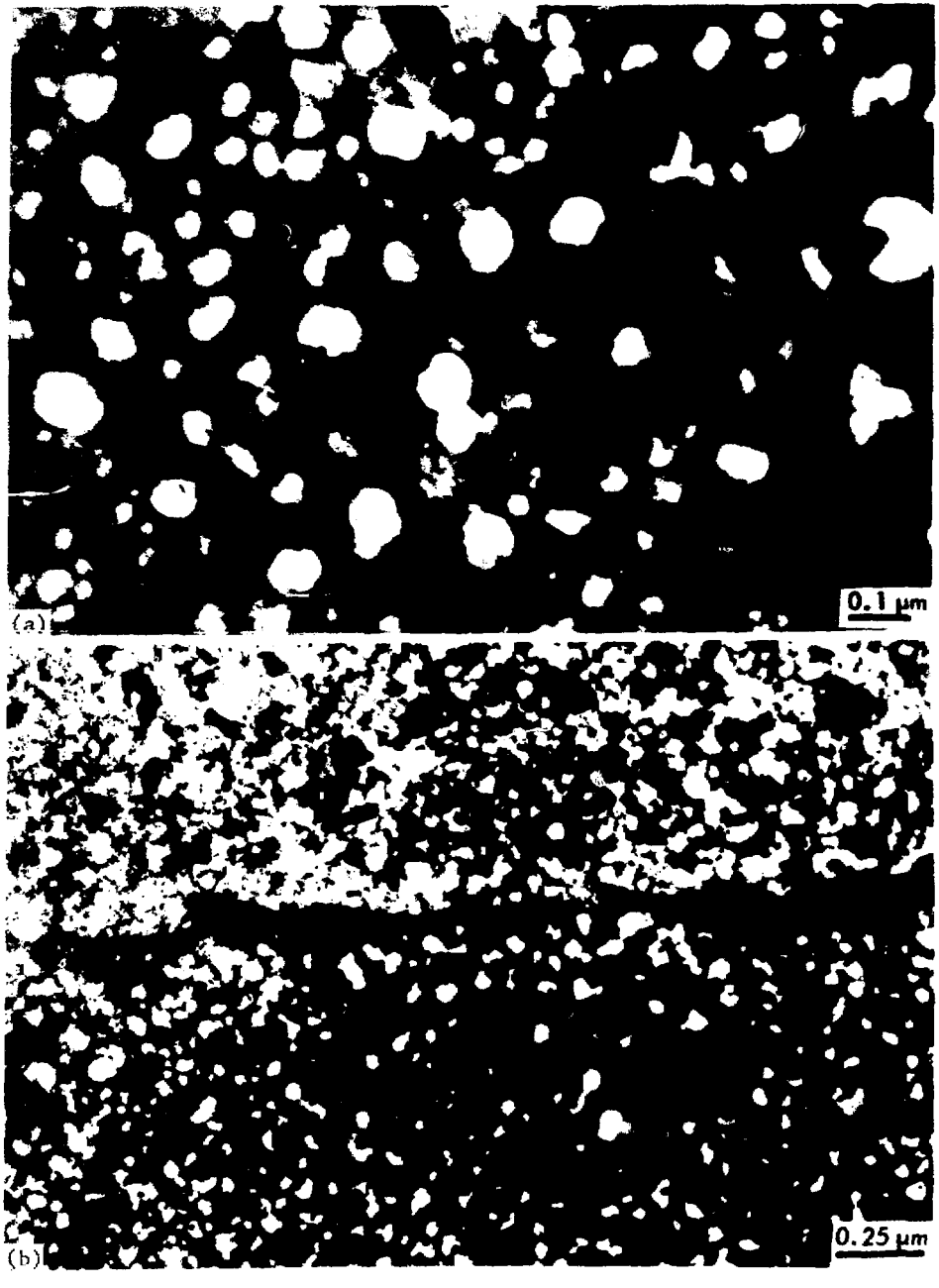

Fig. 8. Type 316 Stainless Steel, Annealed 1 hr at 1050°C, Irradiated at 480°C to 42 dpa and 2950 appm He. (a) Matrix with many cavities and precipitates. (b) Grain boundary with precipitates.

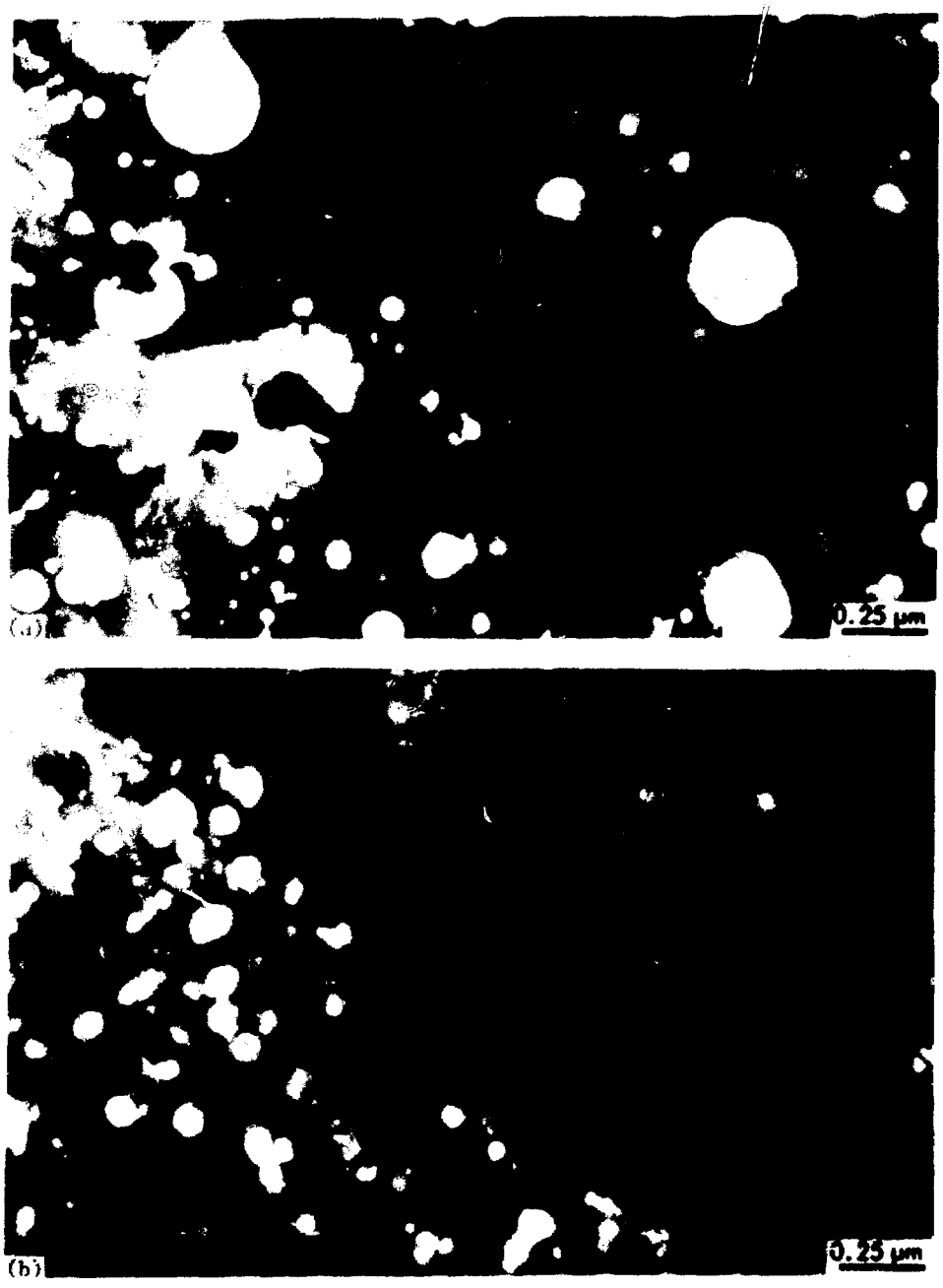

Fig 9. Type 316 Stainless Steel, Annealed 1 hr at 1050°C, Irradiated at 550°C to 42 dpa and 2990 appm He. (a) Matrix with rodlike precipitates and large cavities. (b) Grain boundary with equiaxed precipitates.

Fig. 10. Type 316 Stainless Steel, Annealed 1 hr at 1050°C, Irradiated at 680°C to 61 dpa and 4140 appm He. (a) Matrix with cubic or polyhedral cavities. (b) Grain boundary with very large cavities.

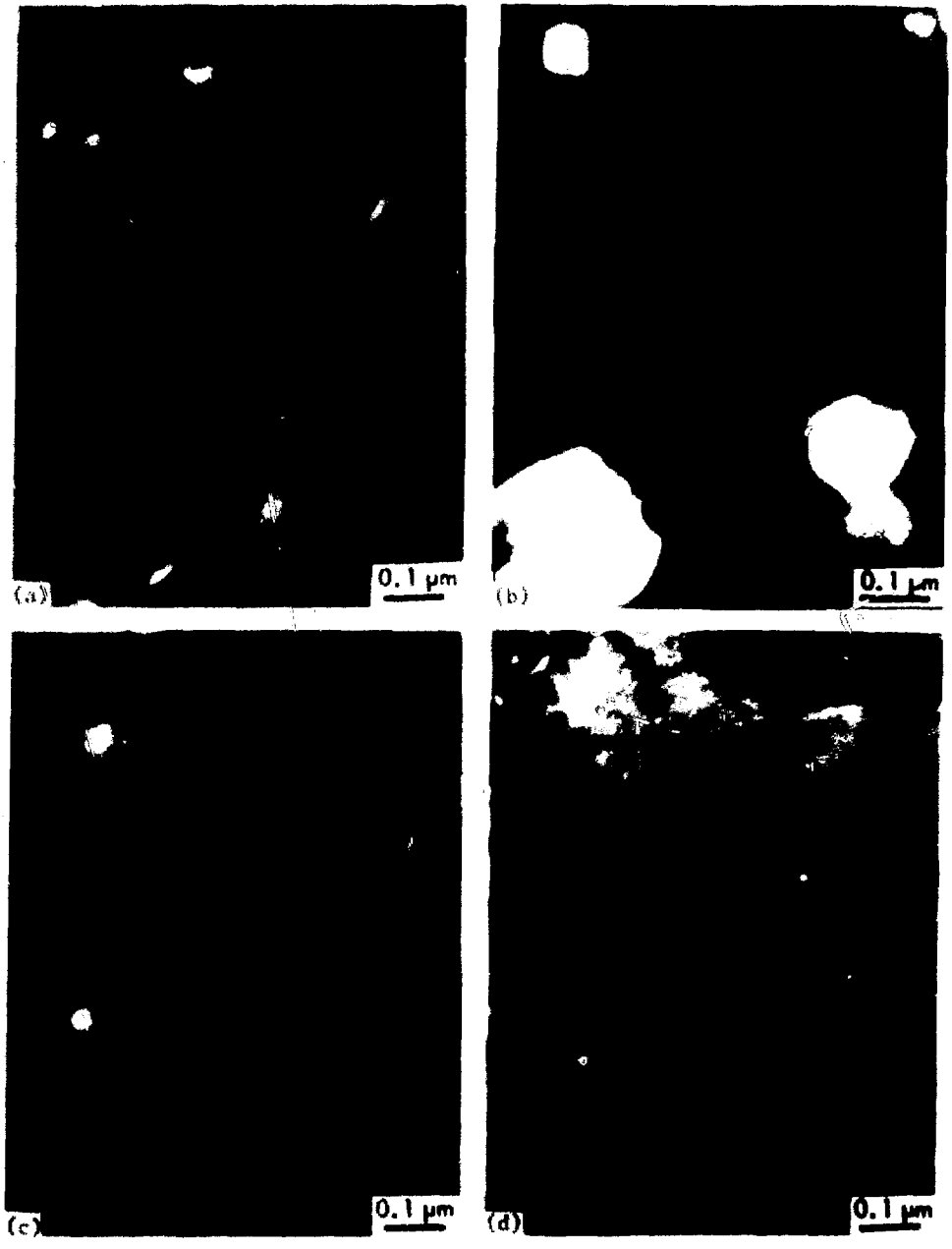

Fig. 11. Comparison of Annealed and Cold Worked Type 316 Stainless Steel Irradiated in the HFIR and EBR-II at Nearly the Same Temperature and Fluence. (a) Annealed, irradiated in EBR-II at 500–535°C to 31 dpa and ~15 appm He. (b) Annealed, irradiated in the HFIR at 550°C to 42 dpa and 2990 appm He. (c) 20% cold worked, irradiated in EBR-II at 500–550°C to 37 dpa and ~15 appm He. (d) 20% cold worked, irradiated in HFIR at 550°C to 42 dpa and 2990 appm He.

The cavity concentrations decrease with increasing temperature (see Fig. 12). The cavity concentrations are higher in the cold worked material than in the annealed material at all temperatures, with the difference becoming less at higher temperatures. Figure 13 shows that at all temperatures below 680°C, the average cavity diameter in the annealed material is more than twice that in the cold worked material (see also Table II). Samples irradiated in EBR-II have cavity diameters that are essentially the same in the cold worked and annealed material, but larger than the diameters for the corresponding cold worked samples irradiated in the HFIR. Brager[15] also found similar cavity diameters in annealed and 20% cold worked samples at each of the irradiation temperatures of 420, 475, and 580°C in EBR-II. Therefore, at low helium content, the primary effect of cold working is to reduce the cavity concentration while having little effect on cavity size and thereby to reduce swelling. For the high helium concentrations of HFIR irradiation, cold work increases cavity concentration and decreases cavity size, resulting in reduced swelling over the temperature range for which cold work is effective, up to 600°C. At 680°C, the annealed and cold worked samples containing high helium concentrations behave similarly because of recrystallization of the cold worked structure.

The samples containing high helium concentrations have larger swelling than samples with low helium for both the annealed and cold worked conditions over the temperature range 380 to 680°C (Table II and Fig. 2). The cavity diameters are about the same for the annealed samples irradiated at 550°C in either the HFIR or EBR-II, but the cavities are several times larger in EBR-II than in the HFIR for the cold worked samples (see Fig. 11). Cavity concentrations are about an order of magnitude greater for the annealed samples irradiated in the HFIR than for those irradiated in EBR-II (see Table II). Another very obvious difference is the appearance of large cavities, 6 to 7 times larger than the average cavity diameter and present in small concentrations of $1\text{–}3 \times 10^{12}$ cavities/cm^3, in the high helium samples at higher temperatures. These large cavities are exclusively attached to intragranular precipitates at 550°C

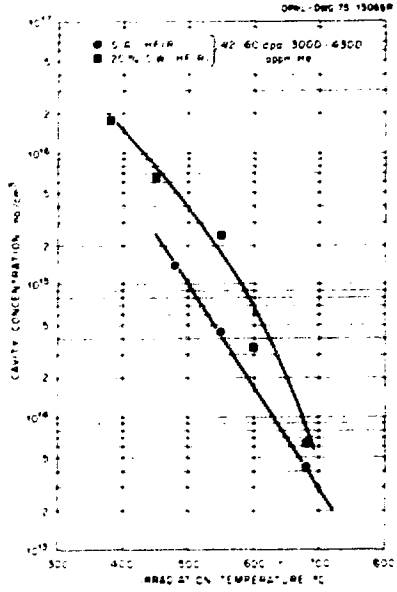

Fig. 12. Cavity Concentration as a Function of Temperature. Note that the cavity concentration for the cold worked and the annealed materials decrease with temperature, but the cavity concentration is always higher in the cold worked samples at any temperature.

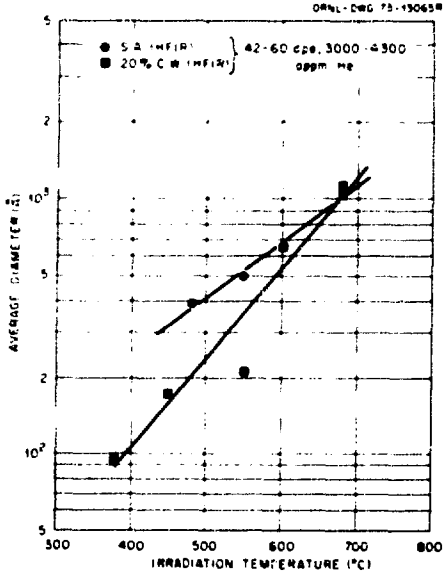

Fig. 13. Average Cavity Diameter as a Function of Temperature. Both cold worked and annealed cavity sizes increase with temperature, and they appear to converge at 680°C. This does not include the very large cavity sizes observed.

in the annealed material (see Fig. 9) and are found exclusively at the grain boundaries at 680°C in the cold worked and annealed samples (see Figs. 7 and 10). These cavities contribute about one-third of the total 8.5% swelling observed in the 550°C annealed sample and about two-thirds of the total 16–17% swelling observed at 680°C in both the annealed and cold worked samples. There is a denuded zone accompanying the large grain boundary cavities at 680°C of about 0.2 to 2 μm for both conditions.

Probably the most important difference in the samples with low and high helium concentrations is their response to irradiation temperature. While the swelling increases with temperature to a maximum at low helium concentrations, it stays fairly constant for high helium concentrations until about 550 to 600°C and then increases very rapidly with temperature. This temperature region is also significant because it is the temperature at which both the annealed and cold worked samples begin to behave similarly. These points will be discussed later. In summary, high helium levels affect the temperature dependence of swelling for both annealed and cold worked materials, increase the cavity concentrations in both annealed and cold worked samples, and decrease cavity diameters in the latter. Most importantly, high helium levels increase the swelling in both annealed and cold worked materials over the temperature range 380 to 680°C, compared to values observed during fast reactor irradiation.

Dislocation Structure

Only the annealed samples irradiated at 480 and 550°C were not tested after irradiation, and hence only these samples exhibit an as-irradiated dislocation structure. However, information on as-irradiated microstructures can be derived from the irradiated and tested materials, in some cases, when viewed in light of the mechanical properties reported previously by Bloom and Wiffen.[6] The dislocation density in the control sample solution annealed for 1 hr at 1050°C is $1.4 \pm 0.7 \times 10^8$ cm/cm^3. There were no loops observed in this sample nor in any irradiated sample where the dislocation structure was clearly evident. This is in marked contrast to observations made by Brager et al.[13] in which Frank loops were observed in annealed material irradiated at 600°C and below.

The dislocation densities in cold worked samples irradiated below 550°C and annealed samples irradiated at 480°C were very high. No Frank loops were present in any samples. The qualitative trend in the cold worked samples is for the dislocation density to decrease and form a cell structure as the temperature increases up to 600°C, at which point recrystallization occurs and grain growth begins. In the annealed series the dislocation density is higher than for the unirradiated controls and decreases as irradiation temperature increases. After irradiation at 680°C, the dislocation density is $3.0 \pm 2.3 \times 10^8$ cm/cm^3 and $5.0 \pm 1.5 \times 10^8$ cm/cm^3 for the cold worked and annealed samples, respectively. Both of these samples were tensile tested, but showed essentially no ductility. They failed at the grain boundaries with very small plastic strains, and the dislocation densities are likely little changed from as-irradiated values.

Precipitates and Grain Boundary Features

Observations made on precipitate structures are given in Table III and Fig. 14. In the annealed samples irradiated in the HFIR, the intergranular precipitate density decreases with increasing temperature up to 550°C. At 680°C no intragranular precipitates are observed by TEM, but coarse precipitation is seen in optical metallography. In the cold worked samples the intragranular precipitate density increases from 380 to 450°C, and decreases slightly from 450 to 550°C. At 680°C the cold worked sample is similar to the annealed sample. In the annealed samples the size of rod and equiaxed precipitates increases as the temperature increases up to 550°C. In the cold worked samples, rod precipitates are present for irradiation temperatures from 380 to 550°C. and equiaxed precipitates are present from 450 to 550°C.

Electron diffraction patterns indicate the presence of $M_{23}C_6$ type precipitates. It is possible that other phases are present, but they have not as yet been identified from the diffraction patterns.

Table III. Microstructural Data

Sample	Temperature (°C)	Concentration of Intragranular Precipitates/cm³	Intragranular Precipitate Description	Grain Boundary Features
Annealed 1 hr at 1050°C, irradiated in HFIR for 10,200 hr	480	1.3 ± 0.4 × 10^{17}	Small, coarse equiaxed and rod-shaped precipitates distributed throughout the grains. $M_{23}C_6$ type spots identified in the diffraction pattern. Equiaxed dimensions: 0.1 ± 0.02 by 0.12 ± 0.05 μm; rod dimensions: 0.07 ± 0.02 by 0.16 ± 0.07 μm.	Long, large precipitates, probably of $M_{23}C_6$ type, with small cavities attached to them. Precipitate dimensions: 0.12 ± 0.03 by 0.38 ± 0.12 μm.
	550	1.5 ± 0.4 × 10^{17}	Large needle equiaxed and ring native rod-shaped precipitates appear in the grains. $M_{23}C_6$ type spots are identified from the diffraction pattern. Large cavities are attached to most of the equiaxed rod-shaped precipitates. Dimensions: 0.12 ± 0.02 by 0.3 ± 0.2 μm; rod dimensions: 0.1 ± 0.02 by 0.2 ± 0.07 μm.	Large equiaxed precipitates with very small cavities adjacent to them. Probably of the $M_{23}C_6$ type. Precipitate dimensions: 0.29 ± 0.07 by 0.36 ± 0.12 μm.
	590	None	None	Large precipitates identified as γ' from the diffraction patterns. The γ' phase has flat, square, rimmed-shaped cavities in it. These are huge cavities in the grain boundaries and γ-γ' interfaces.
20% Cold worked after 1 hr at 1050°C, irradiated in HFIR for 10,200 hr	380	1.7 ± 0.3 × 10^{17}	Small equiaxed precipitates in between deformation bands. Rodlike precipitates with axes parallel to all directions, i.e., ⟨110⟩ $M_{23}C_6$ spots identified in the diffraction pattern.	Little or no precipitation and no large cavities at the grain boundaries.
	450	2.6 ± 0.4 × 10^{17}	Description is the same as at 380°C, but there are more precipitates. $M_{23}C_6$ spots identified from the diffraction pattern. Equiaxed dimensions: 0.07 ± 0.04 by 0.1 ± 0.04 μm; rod dimensions: 0.04 ± 0.01 by 0.16 ± 0.2 μm.	Small amounts of precipitate at the grain boundary were sparsely separated. Some average size cavities along the grain boundary.
	550	1.4 ± 0.4 × 10^{17}	Rodlike and equiaxed precipitates along deformation bands. Also elongated globular precipitate phases along deformation bands. *Possibly η or γ phase.* Equiaxed dimensions: 0.09 ± 0.04 by 0.2 ± 0.1 μm; rod dimensions: 0.06 ± 0.01 by 0.3 ± 0.1 μm.	Large globs of η or γ phase and slightly larger than average cavities at the grain boundaries. Dimensions: 14.0 ± 6.0 by 50.0 ± 24.0 μm.
	590	None	None	Two or three layers of large cavities at the boundaries and very large particles of γ' phase with large cavities at the γ-γ' interface.
	680	None	None	Same as 590°C annealed except *that the precipitate particles* are more numerous and not quite as large. Very large cavities at the grain boundaries and γ-γ' interfaces.
Annealed 1 hr at 1050°C and aged 10,000 hr, unirradiated	400	a	Very long swordlike precipitates in the grains. Dimensions: 0.07 ± 0.03 by 18.0 ± 9.0 μm.	No precipitates at the grain boundaries.
	650	7.4 ± 1.0 × 10^{17}	Almost all precipitates are rodlike in the grains, but some are thin rods and some are thick rods. Dimensions: 0.06 ± 0.01 by 0.06 ± 0.3 μm (thin rods). Thick rods: 0.2 ± 0.1 by 0.8 ± 0.1 μm.	Very large elongated precipitates of uncertain identity along the grain boundary with a few chunklike precipitates similar to those in the matrix. Dimensions: 0.8 ± 0.6 by 20.0 ± 10.0 μm.

[a]Not available.

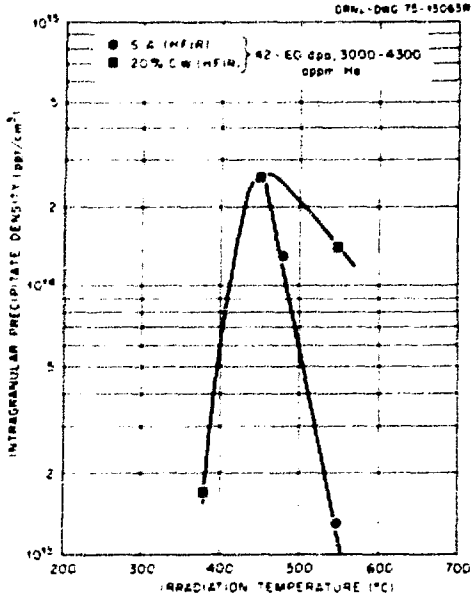

Fig. 14. Intragranular Precipitate Density as a Function of Irradiation Temperature. Note that for the cold worked material, precipitate concentration initially increases as a function of temperature, reaches a peak, and then decreases.

The grain boundary precipitates observed in the annealed sample at 680°C and the 600 and 680°C cold worked samples were identified by electron diffraction as an Fe(Cr-Mo) σ phase similar to that observed by Weiss and Stickler.[12] This intermetallic phase contains flat, diamond-shaped cavities and has very large cavities, on the order of 6000–7000 Å in diameter, at the interface of the σ and the austenite (see Figs. 6, 7, and 10).

The grain boundaries of the annealed samples indicated at 480 and 550°C have precipitates on them, probably $M_{23}C_6$, which becomes more equiaxed and larger as the temperature increases. Only the smallest cavities in the cavity-size distribution are seen adjacent to the grain boundary precipitates. At 550°C, large cavities are attached to rod-shaped intragranular precipitates. Large cavities do not appear at the grain boundaries at 550°C (see Fig. 9).

The cold worked sample irradiated at 550°C has large particles, either σ or χ, appearing along prior deformation bands. This precipitate microstructure is similar to that of a 20% cold worked sample aged 10,000 hr at 650°C. (The samples irradiated in the HFIR were at temperature for about 16,000 hr.) Irradiation in the HFIR enhanced precipitation in the cold worked and the annealed materials. It also appears from Fig. 11 that the precipitation behavior in HFIR irradiation is different from that in EBR-II.

The important points are: (a) there are large cavities at the grain boundaries in both the annealed and cold worked materials at 600°C and above; (b) the precipitate behavior in the annealed and irradiated samples and the precipitate and recovery behavior in the cold worked and irradiated samples are enhanced relative to unirradiated and aged control samples; (c) when there are carbides at the grain boundary, they are accompanied by large cavities which appear attached to precipitates in the grains.

Recrystallization

The cold worked sample irradiated in the HFIR at 600°C exhibits regions that are recovered, some that are just recrystallized, and some cellular areas plus massive particles of σ phase (see Fig. 6). The grain boundaries and the σ-γ interfaces have large cavities. It appears that growing dislocation cells are sweeping the area free of cavities and helium and collecting them at σ-γ interfaces, or former austenite grain boundaries, or wherever growing cells meet. The portions of the sample that show considerable grain growth appear very much like the grains at 680°C in both the annealed and cold worked material (see Figs. 7 and 10). They have large cavities at their boundaries and have cubic-shaped cavities in the grains that are larger and of lower concentration than those in areas where grain growth has not yet occurred. It is in this manner that the cold worked material makes its transition from a low-swelling microstructure to a microstructure similar to that of annealed material. The cavities at the grain boundary probably coalesce to form the larger cavities seen at the grain boundaries in samples irradiated at 680°C.

In summary, recrystallization sets a temperature limit of about 550°C on the effectiveness of 20% cold work as a means of controlling swelling during high-fluence irradiation of type 316 stainless steel.

Cavity Nature

The question naturally arises as to whether or not the cavities are equilibrium helium bubbles. Barnes[16] gives the relationship between gas pressure in a cavity and the surface energy as $P = 2\gamma/r_0$, where P = gas pressure in ergs/cm^3, γ = specific surface energy in ergs/cm^2, and r_0 = cavity radius in cm for the stress-free state. The van der Waals gas equation can be expressed as $m' = 8\pi\gamma r^3/3(kTr_0 + 2\gamma b)$, where m' = the number of gas atoms in a bubble of radius r_0. This reduces to the perfect gas law for cavities greater than ~1000 Å in radius; but many of the cavities were less than that size, so that the van der Waals reduced equation must be used. Recent work by Tsederberg et al.[17] has shown that b is temperature dependent and ranges from 1.84×10^{-23} cm^3/atom at 380°C to 1.57×10^{-23} cm^3/atom at 680°C. The results of calculations over the measured cavity size distributions, using an assumed constant surface energy of 1500 ergs/cm^2,[18] are shown in Table IV. The amount of gas necessary to stabilize equilbrium bubbles is divided by the amount of gas actually measured in the sample, to give a "void bubble" ratio that would be unity if the cavities were equilibrium bubbles, and would approach zero if the cavities were voids. In the cold worked series, this ratio stays fairly constant with temperature from 380 to 680°C and is nearly unity. The greatest deviation from unity is in the annealed sample irradiated at 480°C. The value approaches unity for annealed samples irradiated at 550 and 680°C.

In the case of the annealed sample irradiated at 480°C, the ratio is only 0.37, but this could be unity if a lower surface energy, on the order of 500–600 ergs/cm^2, is assumed. The surface energy could be lower than the 1500 ergs/cm^2 assumed if surface segregation of impurities is occurring, so annealing studies will be conducted to investigate this possibility.

Table IV. Helium Analysis Data

Sample	Temperature	Measured Helium (at. ppm)	Calculated[a] Helium (at. ppm)	Ratio of of Measured to Calculated Helium
Annealed 1 hr at 1050°C	480	2950	7949	0.37
	550	2990	4422	0.68
	680	4140	4282	0.97
20% Cold work after 1 hr at 1050°C	380	3320	3815	0.87
	450	3660	4773	0.77
	550	2990	2613	1.14
	600	4070	4976	0.82
	680	4140	5926	0.70

[a]Calculated amount of helium required to stabilize the observed cavity population in the irradiated samples. Calculation procedure described in text.

DISCUSSION

The effect of helium produced continuously during irradiation of type 316 stainless steel is to increase the cavity concentration in both the annealed and cold worked conditions as compared with samples irradiated in a fast reactor with much lower helium production rates. The effect of cold work is markedly different in the two cases. In fast reactors, cold work reduces cavity concentration with no effect on size. At high helium concentrations the cavity size is reduced and the cavity concentration increased. As a result the cold worked materials swell less than the annealed material in both cases. The high dislocation density in the cold worked steel provides cavity nucleation sites, presumably by trapping helium, since most cavities are observed to be attached to dislocations. The high helium concentration in the cold worked material stabilizes the many nuclei provided by the high dislocation density. For low helium concentration EBR-II irradiations, there is not enough helium to stabilize a large number of nuclei. Hence, only a few random cavities grow in areas of low dislocation density [see Fig. 11(c)]. Once the cavities are stable

in the high helium case, they apparently compete for vacancies and grow more slowly than in cold worked material with low helium concentrations or in annealed material.

There are cavities at the grain boundaries in the cold worked material at 500°C. As recrystallization occurs, grain growth sweeps the cavity and helium to the grain boundaries and σ-austenite interfaces. Once there, they coalesce to form the very large cavities observed. Grain growth does not occur in the annealed samples; thus the cavities observed on the grain boundaries must nucleate and grow due to helium migrating to the grain boundaries.

Rough estimates of the amounts of $M_{23}C_6$ and σ phase can be obtained from TEM and optical metallography and the aging studies done by Weiss and Stickler.[12] Precipitation can affect the measured density of the steel. Calculated densities of σ and $M_{23}C_6$ based on the composition and structure data of Weiss and Stickler[12] give the amounts of the alloying elements removed from the matrix by their precipitation. Taking into account the density change of the precipitates and using the formula for the density of the type 316 stainless steel as a function of the various alloying components given by Straaslund and Bates,[19] a densification of 0.93% was calculated. This would help explain the discrepancy between immersion density and cavity volume fraction at 550°C; since the major contribution to the calculated densification is the precipitation of σ phase, it also helps explain the swelling discrepancy at 600°C. The effect of precipitation on the cavity concentration is also important, because precipitation changes the composition of the matrix, and compositional changes have an important effect on cavity formation and growth.[20] Hence, type as well as composition of the precipitates present in the microstructure must be considered and will be studied further.

There is a question as to whether or not the as-irradiated microstructures are the same as in the as-irradiated and mechanically tested microstructures. Annealing studies of irradiated type 304 stainless steel have shown that only minor changes are produced in the microstructure on annealing at temperatures up to 100°C above the irradiation temperature.[21,22] It can be assumed that the mechanical tests at temperatures

near the irradiation temperature produced no annealing of the as-irradiated microstructures. It can also be assumed that the mechanical tests did not cause much growth in the large cavities because of the close agreement between the immersion density measured before the tests and the cavity volume fractions measured by TEM after the tests. Where plastic deformation occurred, however, the dislocation densities can be expected to have changed.

In a CTR, large amounts of helium will be produced simultaneously with displacement damage. These results have shown that the helium strongly influences the microstructural changes produced during irradiation, and thus the mixed spectrum irradiation such as in the HFIR better simulates CTR conditions than does fast reactor irradiation such as in EBR-II. We have shown that prior cold working can significantly reduce swelling up to 550°C for high displacement and high helium levels. Cold working also has been shown to improve the mechanical properties as compared with annealed material for the same irradiation conditions up to 550°C.[6]

CONCLUSIONS

1. A major effect of high helium concentrations on the microstructure of irradiated type 316 stainless steel is to increase cavity nucleation and overall swelling in the temperature range 380 to 680°C, as compared with fast reactor irradiations.

2. High helium concentrations in cold worked material increase cavity nucleation and reduce cavity sizes compared with annealed material. The net result is decreased swelling with respect to annealed material, but increased swelling with respect to irradiated cold worked material of low helium content.

3. Cold work produces reduced swelling under irradiation conditions producing high helium contents and high dpa levels for irradiation temperatures below about 550°C.

4. Swelling in both the annealed and cold worked materials is only slightly temperature dependent up to 550–600°C. Swelling increases rapidly with temperature in both conditions for irradiation temperatures beyond 600°C.

5. Recrystallization occurs in cold worked materials during long-term irradiations between 550 and 600°C and results in loss of swelling resistance.

6. The large cavities associated with grain boundaries and precipitates at irradiation temperatures above 600°C in both the annealed and cold worked material are responsible for a large portion of the swelling.

7. The cavities observed in most samples are probably equilibrium bubbles.

ACKNOWLEDGMENTS

Appreciation is expressed to J. T. Houston and L. T. Gibson for their expert work in thinning the samples and to the hot-cell operations personnel for their care and help with specimen handling. Thanks are due J. O. Stiegler for many helpful suggestions and discussions and to K. Farrell and L. K. Mansur for review of the manuscript. For perseverance and fortitude in manuscript preparation, we also want to thank JoAnne Zody and Julia Bishop.

REFERENCES

1. J. L. Straalsund, B. R. Brager, and J. J. Holmes, "Effects of Cold Work on Void Formation in Austenitic Stainless Steel," *Irradiation-[illegible] for Metals*, ed. J. W. Corbett and L. C. Ianniello, AEC Symp. Ser. 26, CONF-710601, 142 (1972).

2. G. L. Kulcinski, D. G. Doran, and M. A. Abdou, "Comparison of Displacement and Gas Production Rates in Current Fission and Future Fusion Reactors," to be published in *Proceedings of the ASTM [illegible]*, Gatlinburg, Tennessee, ASTM-STP-570.

3. E. E. Bloom and J. O. Stiegler, "The Effects of Helium on Void Formation in Irradiated Stainless Steel," *J. Nucl. Mater.* 36, 331 (1970).

4. D. Kramer, K. R. Garr, A. G. Park and C. G. Rhodes, "A Survey of Helium Embrittlement of Various Alloy Types," p. 109, *Irradiation [illegible] for Fast Breeding and Fusion Components*, British Nuclear Energy Society, London, 1973.

5. F. W. Wiffen and E. E. Bloom, "Effect of High Helium Content on Stainless-Steel Swelling," *Nucl. Technol.* 25, 113 (1975).

6. E. E. Bloom and F. W. Wiffen, "The Effects of Large Concentrations of Helium on the Mechanical Properties of Neutron-Irradiated Stainless Steel," *J. Nucl. Mater.* 58, 171 (1975).

7. E. E. Bloom, J. W. Woods, and A. F. Zulliger, *Measurement of Nuclear Heating Rates in FFTF-PF and HFIR*, unpublished (September 1969).

8. F.B.K. Kam and J. H. Swanks, *Neutron Flux Spectrum in the HFIR Target Region*, ORNL-TM-3322 (March 1971).

9. "Recommendations for Displacement Calculations for Reactor/Accelerator Studies in Austenitic Steel," C. Z. Serpan, Jr., Chairman, Working Group on Reactor Radiation Measurements, *Nucl. Eng. Des.* 33, 91 (1975).

10. M. R. Rühle, "Transmission Electron Microscopy of Radiation-Induced Defects," *Radiation Induced Voids in Metals*, ed. J. W. Corbett and L. C. Ianniello, AEC Symp. Ser. 26, CONF-710601, 255 (1972).

11. K. W. Andrews, D. J. Dyson, and S. R. Keown, *Interpretation of Electron Diffraction Patterns*, Plenum, New York, 1971.

12. B. Weiss and R. Stickler, "Phase Instabilities During High-Temperature Exposure of 316 Stainless Steel," *Metall. Trans.* 3, 851 (1972).

13. H. R. Brager and J. L. Straalsund, "Defect Development in Neutron Irradiated Type 316 Stainless Steel," *J. Nucl. Mater.* 46, 134–158 (1973).

14. P. S. Sklad and E. E. Bloom, personal communication, 1975.

15. H. R. Brager, "The Effects of Cold Working and Preirradiation Heat Treatment on Void Formation in Neutron-Irradiated Type 316 Stainless Steel, *J. Nucl. Mater.* 57, 103 (1974).

16. R. S. Barnes, "Theory of Swelling and Gas Release for Reactor Materials," *J. Nucl. Mater.* 11, 135 (1964).

17. N. V. Tsederberg, V. N. Poper, and N. A. Morozona, *Thermodynamic and Thermophysical Properties of Helium*, translation TT 70-50096, 1971, available from U.S. Dept. of Commerce, National Technical Information Service, Springfield, Va.

18. D. R. Harries, "Neutron Irradiation Embrittlement of Austenitic Stainless Steels and Nickel Base Alloys," *J. Br. Nucl. Energy Soc.* 5, 74 (1966).

19. J. L. Straalsund and J. F. Bates, "Partial Molar Volumes and Size Factor Data for Alloy Constituents of Stainless Steel," *Metall. Trans.* 5, 493 (1974).

20. J. I. Bramman, K. Q. Bagley, C. Cawthorne, and E. J. Fulton, "Void Formation in Cladding and Structural Materials Irradiated in DFR," *Irradiation-Induced Voids in Metals*, ed. J. W. Corbett and L. C. Ianniell AEC Symp. Ser. 26, CONF-710601, 125 (April 1972).

21. H. R. Brager and R. E. Robbins, "Stabilized Cavities in Irradiated Austenitic Stainless Steel," *Trans. Metall. Soc. AIME* 242, 2010 (1968).

22. E. E. Bloom and J. O. Stiegler, "The Effects of Large Fast Neutron Fluences on the Structure of Stainless Steel," *J. Nucl. Mater.* 33, 173 (1969).

NUCLEATION OF VOIDS IN A NEUTRON ENVIRONMENT

R.M. Mayer, Atomic Energy Board, Pretoria, South Africa
and L. M. Brown, Cavendish Laboratory, Cambridge England

ABSTRACT

A model of void nucleation in a neutron environment is formulated based on chemical rate theory. The resulting set of first order differential equations is numerically integrated using a computer. The swelling due to voids in nickel, copper, alpha iron and molybdenum is then compared with experiment.

INTRODUCTION

The major feature of high temperature irradiation in metals is the swelling due to the agglomeration of vacancies into voids. Vacancies as well as interstitial atoms also agglomerate into two dimensional platelets called loops. Any theory of void nucleation must take all these competing processes into account.

NUCLEATION PROCESSES

It is known that in many metals both the vacancy and interstitial loop concentrations increase with irradiation time. These loops cannot be homogeneously nucleated because homogeneous nucleation leads to a saturation of loop density within a short irradiation time.[1]

There is strong evidence that the vacancy loops arise from vacancy agglomerates formed at the end of the track of the primary knock-on atom[2]. Since vacancy loops are normally

observed rather than three-dimensional agglomerates, there must be a collapse process which converts the latter into the former. In this paper, the collapse time of the vacancy cluster is taken to be the square of the number of vacancies in the cluster divided by the jump frequency of the divacancy.

Not all the vacancies in the cluster will be in the loop resulting from the cluster's collapse. The ratio of vacancies in the loop to those in the original cluster is called the cascade efficiency and its value will depend on how efficiently the focussed collision sequences separate the interstitials from the vacancy cluster. On the basis of evidence from electron microscopy, we have taken the size of a freshly formed vacancy loop to be 20Å. Specifying the cascade efficiency then gives the initial size of the vacancy cluster.

Our theory treats these nucleation processes phenomenologically, i.e. every PKA has a certain probability ('defect yield') of creating a vacancy cluster or interstitial loop. We take the defect yield for vacancy clusters to be unity. Interstitial loops are allowed to nucleate by random agglomeration of two interstitials and by athermal production in the damage cascade. The yield of the latter is taken to be zero, but we have also considered a yield proportional to time to the one third power[1]*.

The total defect generation rate has been derived from the formulae described by Robinson[3,4] in accordance

---

* This does not affect the results presented here in any significant manner.

with the proposals of the IAEA working party. The partition of the defects into single defects and clusters is fixed by the parameters discussed above.

ROLE OF GAS ATOMS

Hydrogen and helium are generated via (n,p) and (n,α) transmutation reactions. We assume that whilst single vacancies can act as shallow traps, the uncollapsed vacancy agglomerates will act as sinks. From a variety of evidence, it is accepted that the gas stabilises the agglomerate. We shall assume that one gas atom is sufficient to prevent the agglomerate collapsing thereby nucleating a void. Thereafter the void can absorb gas atoms up to the number required to form an equilibrium gas bubble; this is included in the programme explicitly.

Whereas hydrogen will diffuse interstitially, helium diffuses substitutionally, which is a much slower process, and we therefore assume hydrogen to be the nucleating agent.

What is the role of the gas present initially in the material? If it is bound to other atoms or at pre-existing sinks it will be immobile. If the gas is mobile however it could assist the void nucleation process in the same way as we assume hydrogen to do.

RESULTS

We shall describe elsewhere the formulation of the equations[5] and their numerical integration using a computer[6]. Whilst the theory can be applied to any material, we consider here the irradiation of four pure metals, copper and nickel (fcc) and alpha iron and molybdenum (bcc). A homologous temperature (i.e. the ratio of the irradiation to

the melting temperature expressed in degrees absolute) of 0.40 has been taken for Fe, Cu and Ni and 0.25 for Mo.

The variation in void density and void radius with time is similar for all these metals (fig. 1). The rate of nucleation of voids is constant with time and decreases as soon as the voids start to grow. The void growth increases monotonically after a certain period ('incubation time') at which time the vacancy flux (defined in the usual way as the product of the vacancy concentration and its velocity) exceeds the interstitial flux into the void nucleus.

The incubation time is critically dependent on the preferential drift, Z, of interstitials over vacancies to dislocations, and on the cascade efficiency. In order to obtain void growth after a reasonable time interval we have assumed a cascade efficiency of 0.5 and taken Z to be in the range 1.2 - 1.4.

The nucleation rate depends upon the gas generation rate. Ni, Fe, Mo and Cu have successively decreasing (n,p) cross-sections and inspection of fig. 1 shows that at short times the nucleation rate decreases in the same order. A further indication of the importance of gas generation rate is to increase it by a factor of ten - the nucleation rate is also increased though the incubation time for growth is unaltered (fig. 2).

DISCUSSION

We have used chemical rate equations to describe the various interactions between point defects, defect clusters and gas atoms. The set of first order differential equations (16 of them) need on average only five minutes to be numerically integrated up to a dose of $10^{23} n/cm^2$, and the output is in a form which is directly comparable with experiment.

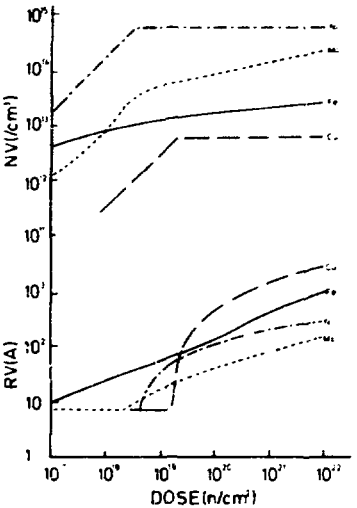

Fig. 1 Computed variation in void density and radius with time for a fast flux of 10^{14} n/cm^2 at the following irradiation temperatures - Cu 250 C, Ni 417 C, Fe and Mo 450 C.

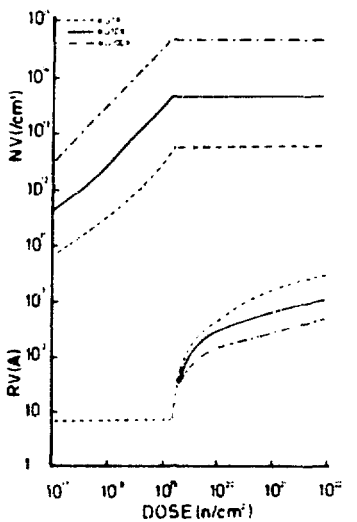

Fig. 2 Computed variation of void density and radius with dose in copper irradiated at 250 C for different gas generation rates.

The variation of void density with time is similar to that found experimentally - for Ni and Cu where data at low doses exist, the initial slope is linear and then decreases[7] whilst for Mo[8] the void density increases as time to the one-half power round 10^{20} n/cm^2.

The variation of void radius with time is also similar to that observed experimentally. Often a linear variation of the swelling with dose is found, which means that the void radius increases to the one-third power if the void density is constant or less if the void density slowly increases.

In view of the good qualitative agreement between theory and experiment, one must comment on the absolute values as well. A full analysis must await a detailed survey of this formulation[5], but it is readily discernible that the predicted void density is three orders of magnitude too low in Mo and two orders of magnitude too low in Cu, whilst for Ni and Fe there is reasonable agreement.

The only sustainable conclusion is that extra gas is available to nucleate the voids over and above that generated in the transmutation reactions. Both Cu and Mo are known to contain gas. In Mo where the solid solubility is high, there seems no reason why this gas should not be available to stabilise vacancy clusters from collapsing. In Cu where the solid solubility is very much lower, the gas is more likely to be bound to impurity atoms. If we suppose that there is 1 ppm gas, then the displacement rate of these gas atoms will be two orders of magnitude higher than that due to the (n,p) reaction.

Increasing the gas generation rate does not alter the variation of void density with time, but increases the nucleation rate (fig. 2). The incubation time before void growth commences is unaffected whilst the void size is

if anything less at high doses.

A feature of chemical reaction rate theory applied to the void problem is the crucial importance of the incubation time before void growth commences. This time depends upon the difference between the vacancy and interstitial flux, and depends mainly upon temperature, dislocation preference for interstitials, and the cascade efficiency. Anything which affects the relative mobility of vacancies and interstitials plays an important role; in principle, alloying elements can be chosen either to increase or to decrease the incubation time.

CONCLUSIONS

1) It appears probable that chemical rate theory can be developed to predict the swelling of materials in high neutron fluxes as a function of temperature and dose. The critical assumption is that the void nucleus consists of one gas atom in an uncollapsed vacancy cluster.

2) The equations reflect our current state of knowledge regarding fundamental radiation damage processes. Current knowledge seems capable of explaining a wide range of experimental data.

3) The essential input data consist of the binding energies and energies of motion for the various defects. The output data are the void number and size as a function of dose.

The effect of varying all other parameters of the radiation can be studied.

We acknowledge the labour of Mr. P. B. Kruger in programming this set of equations over an extended period of time.

REFERENCES

1. Brown, L.M. and Mayer, R.M. (1975) Proceedings of International Conference on Fundamental Aspects of Radiation Damage in Metals, Gatlinburg, Tennessee, Oct. 1975, in press.
2. Eyre, B.L. (1973) J. of Physics F 3 422-70
3. Robinson, M.T. (1972) Radiation Induced Voids in Metals, CONF-710601, p 397-429
4. Robinson, M.T. (1974) AERE - R 7934, p 18-36
5. Brown, L.M. and Mayer, R.M. (1976) to be published.
6. Kruger, P.B. and Mayer, R.M. (1976) to be published.
7. Levy, V. (1974) AERE - R 7934, p 50-70
8. Bentley, J. (1974) Ph.D. thesis, University of Birmingham.

SUPPRESSION OF VOID FORMATION IN NEUTRON IRRADIATED TZM

J. Bentley*
Department of Physical Metallurgy
University of Birmingham, England

B. L. Eyre
Metallurgy Division
A.E.R.E.
Harwell, England

M. H. Loretto
Department of Physical Metallurgy
University of Birmingham, England

ABSTRACT

A TEM study of the damage structures in Mo (2 purities) and TZM alloy neutron irradiated in the temperature range 330°C to 850°C to fluences of 1 to 3 x 10^{20} fission n · cm^{-2} has revealed that at the lower irradiation temperatures the structures in all three materials consist of a fine distribution of voids plus a dislocation component of loops and networks. The structures generally coarsen with increasing irradiation temperature but in TZM this tendency is reversed at irradiation temperatures of 750 and 850°C where the damage structure consists of a high concentration (~3 x 10^{15} cm^{-3}) of dislocation loops (~200Å diameter) with an almost complete absence of voids and thus a very low value of swelling. Contrast experiments have shown that these loops are, remarkably, vacancy in nature. A number of observations - the presence of vacancy loops as the major component of the damage structure in the alloy only, the stability and shrinkage behavior of the loops during postirradiation annealing and TEM observations which suggest both slight modifications of the loop strain fields and an increased value of the loop glide stress - all imply a strong interaction between impurities and the dislocation loops. The observations can be understood in terms of segregation of oversize alloying elements to the dislocation cores. The very low value of swelling is an important result for CTR technology since it occurs in a candidate material for the first wall at typical proposed operating temperatures.

---

* Presently at Metals and Ceramics Division, Oak Ridge National Laboratory, Oak Ridge, Tennessee 37830 USA

INTRODUCTION

In a detailed and systematic series of experiments performed at Harwell,[1,2,3,4,5] the behavior of the damage structure in molybdenum neutron irradiated at 77 and 473°K was shown to depend sensitively on material purity and irradiation conditions. A study of the recovery of these structures on postirradiation annealing again revealed a strong dependence on these parameters as well as annealing conditions. The experiments have been extended to higher irradiation temperatures and the range of materials broadened to include TZM.[6,7,8] In this paper we report observations of the structures in TZM and show how they differ from molybdenum particularly for high irradiation temperatures.

EXPERIMENTAL

The starting material for this investigation was "Climelt" arc-cast molybdenum rod and TZM alloy rod supplied by the Climax Molybdenum Company. From the molybdenum rod high-purity single crystals were grown and, together with the as-received material, were annealed in high-purity oxygen to reduce the carbon content. The TZM specimens were given a recrystallization anneal of one hour at 1600°C. The materials were fully characterized by electron microscopy, spark source mass spectrometry, and gamma activation techniques. Disc specimens of all three materials were irradiated at 330, 475, 575, 650, 750, and 850°C to integrated fluences of ~1 and ~3 x 10^{20} fission neutrons cm^{-2} in the PLUTO reactor at AERE Harwell. Specimens were packed in molybdenum tubes and these, together with iron flux monitors, were sealed under one atmosphere of helium in stainless steel containers. The containers were mounted in fully instrumented irradiation rigs which were equipped with heaters and loaded into hollow fuel elements. The temperatures of the containers were monitored continually by thermocouples. On some specimens post-irradiation annealing was performed under a vacuum of ~5 x 10^{-7} torr, the specimens being first electropolished briefly and wrapped in tantalum foil. Disc specimens were thinned for examination by TEM using a two

stage technique of first dimpling with a jet of electrolyte and then thinning to perforation in a bath of 25% sulphuric acid in 75% methanol at ~8V. Thinned specimens were examined in Philips EM 300 (100 kV) and AEI EM7 (high voltage) electron microscopes both equipped with ±30° double tilt stages.

RESULTS

The more important features of the development of the rather complex damage structures in the irradiated samples are described first. In the 4PZR Mo there is a general coarsening of the damage structure with increasing irradiation temperature. The dislocation substructure develops from one consisting of "rafts" plus a fine distribution of small mainly vacancy-type loops to one of large resolvable interstitial loops plus network dislocations (see Fig. 1). Voids are observed at all irradiation temperatures, the concentration decreasing and the size increasing with increasing irradiation temperature. The behavior of the AR Mo is similar to that of the 4PZR Mo except that the dislocation substructures occur on a finer scale and the voids are larger and occur on a coarser scale. The behavior of the TZM, however, does not follow the same pattern as the molybdenum. With increasing irradiation temperature the dislocation substructure initially coarsens from "rafts" plus fine loops to large resolvable interstitial loops plus networks, but at irradiation temperatures of 750 and 850°C the dislocation substructure becomes finer again, consisting of a high concentration of small dislocation loops plus a very low density of network dislocations (see Fig. 1). In the regions near the grain boundaries the loops are larger and in higher concentration than in the grain interiors with a denuded zone immediately adjacent to the grain boundary as shown in Fig. 2. In TZM significant void formation is limited to the intermediate irradiation temperatures; in particular at irradiation temperatures of 750 and 850°C voids are virtually completely absent.

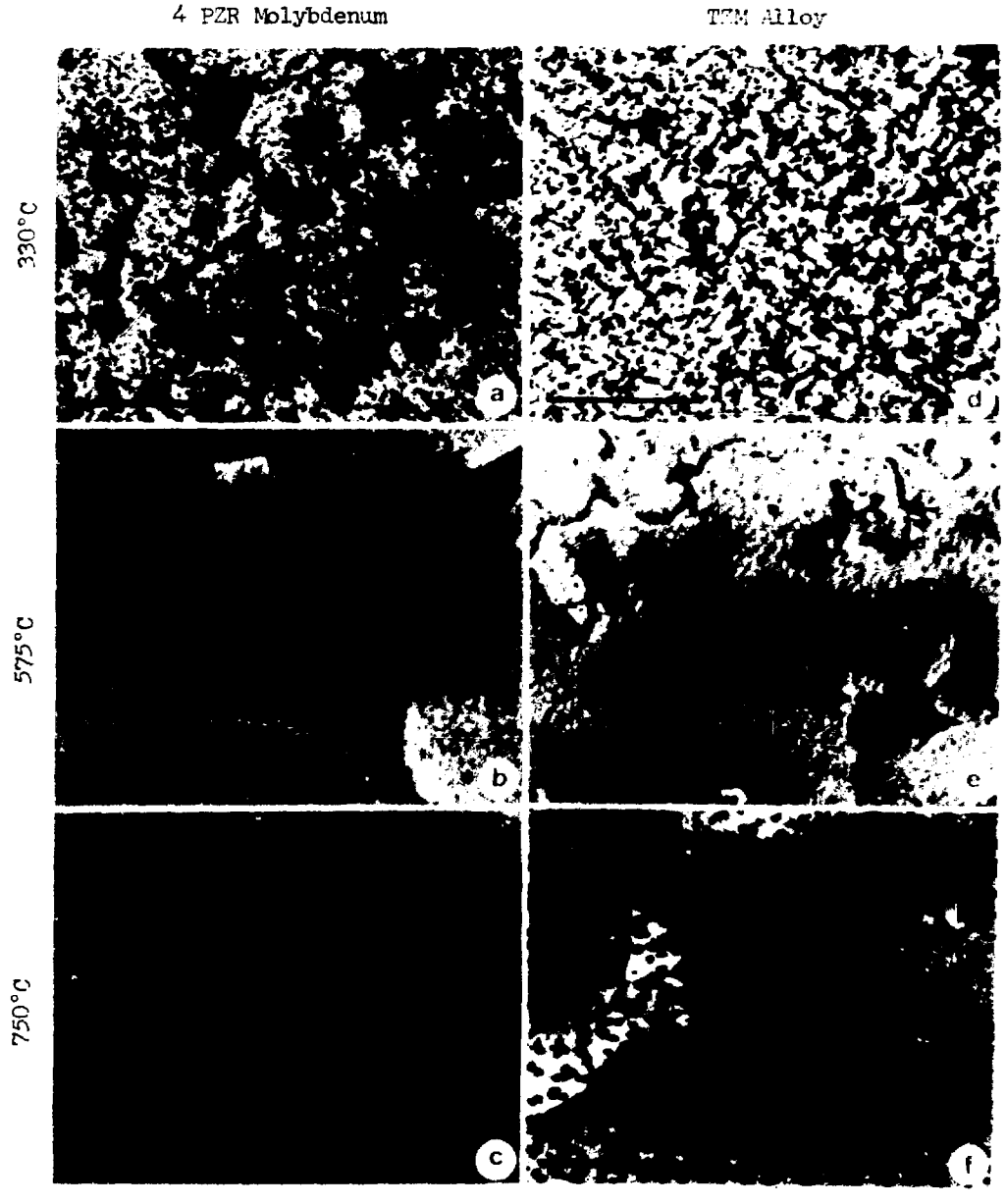

Fig. 1. Electron-micrographs Showing the Dislocation Substructure in Zone Refined Molybdenum (a to c) and TZM Alloy (d to f) Irradiated to ~3 x 10^{20} n.cm^{-2} at Temperatures of 330°C (a and d), 575°C (b and e) and 750°C (c and f). Diffracting conditions, $\underline{z}$ = [023], $\underline{g}$ = [200], $w_g > 0$. Fig. 1 (a,b,d,e,f), 100 keV, t = 8 ξ_{110} (~1600 Å). Fig. 1c, 600 keV, t ~ 1 μm. Scale markers = 0.5 μm.

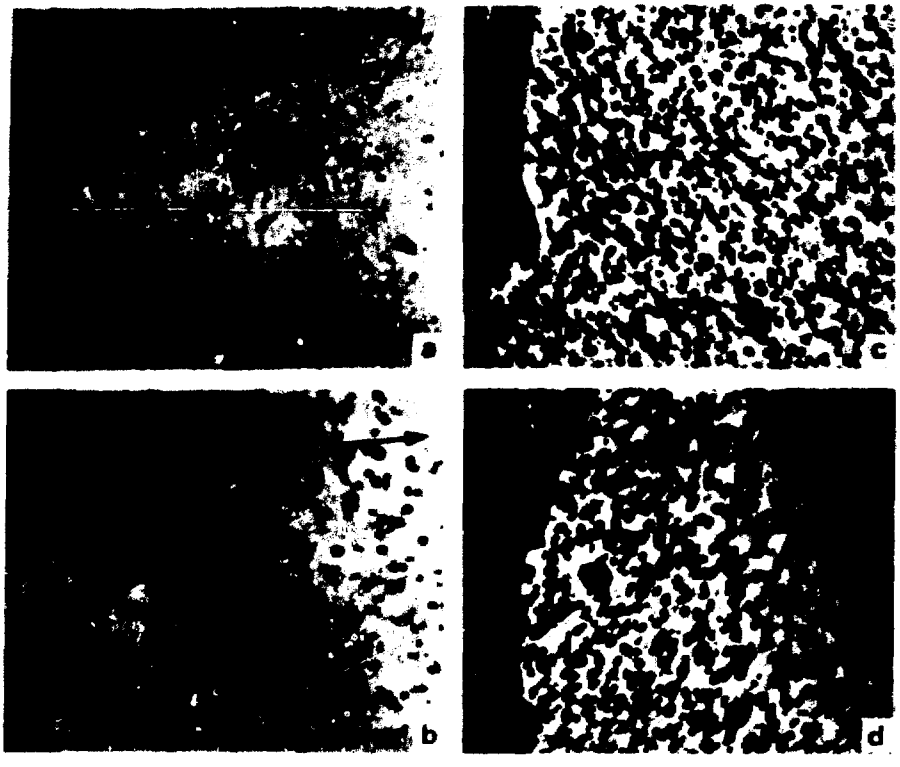

Fig. . . Electron-micrographs Showing Typical Dislocation Substructures Formed Near Grain Boundaries in TZM After Irradiation at 750°C (a and c) and 950°C (b and d). Diffracting conditions, z = [3], g = 220, w, > , 1 keV, scale marker = 0.5 μm. (a and b) ~2 x 1 n.cm and t = 5 s (~1000). (c and d) ~2 x 10 n.cm and t = s (~160).

The size distributions and concentrations of the dislocation loops occurring in TZM irradiated at 750 and 850°C were obtained. Data were obtained for the regions near the grain boundaries where enhancement of loop formation occurs as well as for regions within the grain interiors. A summary of the results is presented in Table 1. It can be seen that within experimental error there is no great difference between the structures following irradiation at 750 and 850°C for a given dose but there is a significant increase in the loop concentration with increased dose.

Analyses of the dislocation loops were carried out following the principles of Maher and Eyre.[1] ⟨110⟩ and ⟨211⟩ diffracting vectors were used to obtain the direction of $\pm\underline{b}$ from $\underline{g} \cdot \underline{b} = 0$ invisible or residual contrast images. Both $+\underline{g}$ and $-\underline{g}$ diffracting vectors were used so that the invariance in position and strength of contrast of images satisfying $\underline{g} \cdot \underline{b} = 0$ conditions could be confirmed. ⟨310⟩ diffracting vectors which gave $\underline{g} \cdot \underline{b} = 2$ conditions for the appropriate loops were used for the inside/outside contrast experiments to determine the sense of $\underline{b}$ and thus the nature of the loop. For the smaller loops $\underline{g} \cdot \underline{b} = 2$ weak beam images with diffraction conditions ⟨310⟩ (⟨620⟩) with $s_{\langle 310 \rangle} = 2.4$ to 2.9×10^{-2} Å^{-1} (Ewald sphere intersecting the reciprocal lattice 1/4 to 1/2 of the distance between the ⟨620⟩ and ⟨930⟩ points) were employed for the inside/outside contrast.[9] More than 300 loops were analyzed and in all analyses the loops were found to have $\underline{b} = 1/2$ ⟨111⟩ and to be vacancy in nature.

The observation of weak "anomalies" in the loop contrast together with the unexpected result of the loops being of vacancy type prompted a full investigation into the detailed contrast behavior of the loops but this failed to reveal observations of stacking-fault type fringes or indeed of any contrast which would be inconsistent with vacancy loops having $\underline{b} = 1/2$ ⟨111⟩.

In view of the surprising result of the loops being of vacancy type, annealing treatments were performed primarily to obtain data on the thermal stability of these loops. Bulk postirradiation anneals were

Table 1. Measured Loop Parameters for As-Irradiated TZM

Irradiation Temperature °C	Fluence (fission n.cm^{-2})	near grain boundaries		grain interiors	
		loop concentration (cm^{-3})	mean loop radius[a] (Å)	loop concentration (cm^{-3})	mean loop radius[a] (Å)
750	1 x 10^{20}	1·9 x 10^{15}	100	1·6 x 10^{15}	52
750	3 x 10^{20}	4·4 x 10^{15}	130	4·1 x 10^{15}	76
850	1 x 10^{20}	2·3 x 10^{15}	115	1·0 x 10^{15}	80
850	3 x 10^{20}	3·4 x 10^{15}	125	3·1 x 10^{15}	72

[a]Radius of loop of mean area.

performed on specimens of TZM irradiated at 750°C to 3 x 10^{20} fission neutrons cm^{-2} each for one hour at temperatures of 900, 1000, 1100, and 1200°C. Micrographs of the structures formed on annealing are presented in Fig. 3. The size distributions and loop concentrations were obtained, a summary of the data being presented in Table 2.

Table 2. Measured Loop Parameters For Irradiated-Annealed TZM

Annealing Temperature (°C)	near grain boundaries		grain interiors	
	loop concentration (cm^{-3})	mean loop radius[a] (Å)	loop concentration (cm^{-3})	mean loop radius[a] (Å)
		Small Loops		
as irradiated	4.4×10^{15}	130	4.1×10^{15}	76
1000	4.3×10^{15}	126	3.9×10^{15}	71
1100	4.2×10^{15}	142	3.5×10^{15}	45
1200	3.7×10^{15}	86	4.2×10^{15}	31
		Large Loops		
1100			2.9×10^{13}	360
1200	1.3×10^{14}	460	2.2×10^{13}	520

[a]Radius of loop of mean area.

From Fig. 3 and Table 2 it can be seen that little change occurs at annealing temperatures up to 1000°C. Following annealing at 1100°C, however, it is noticeable that the size of the majority of the loops in the grain interior has decreased ("small loops") while the size of a limited number has increased markedly ("large loops") so that a double population develops. On increasing the annealing temperature to 1200°C the size of the small loops continues to decrease, their concentration remaining approximately constant. The concentration of large loops in the grain interiors also remains approximately constant, but their size increases. Near the grain boundaries this same type of behavior of the small loops shrinking and the large loops growing is also apparent after

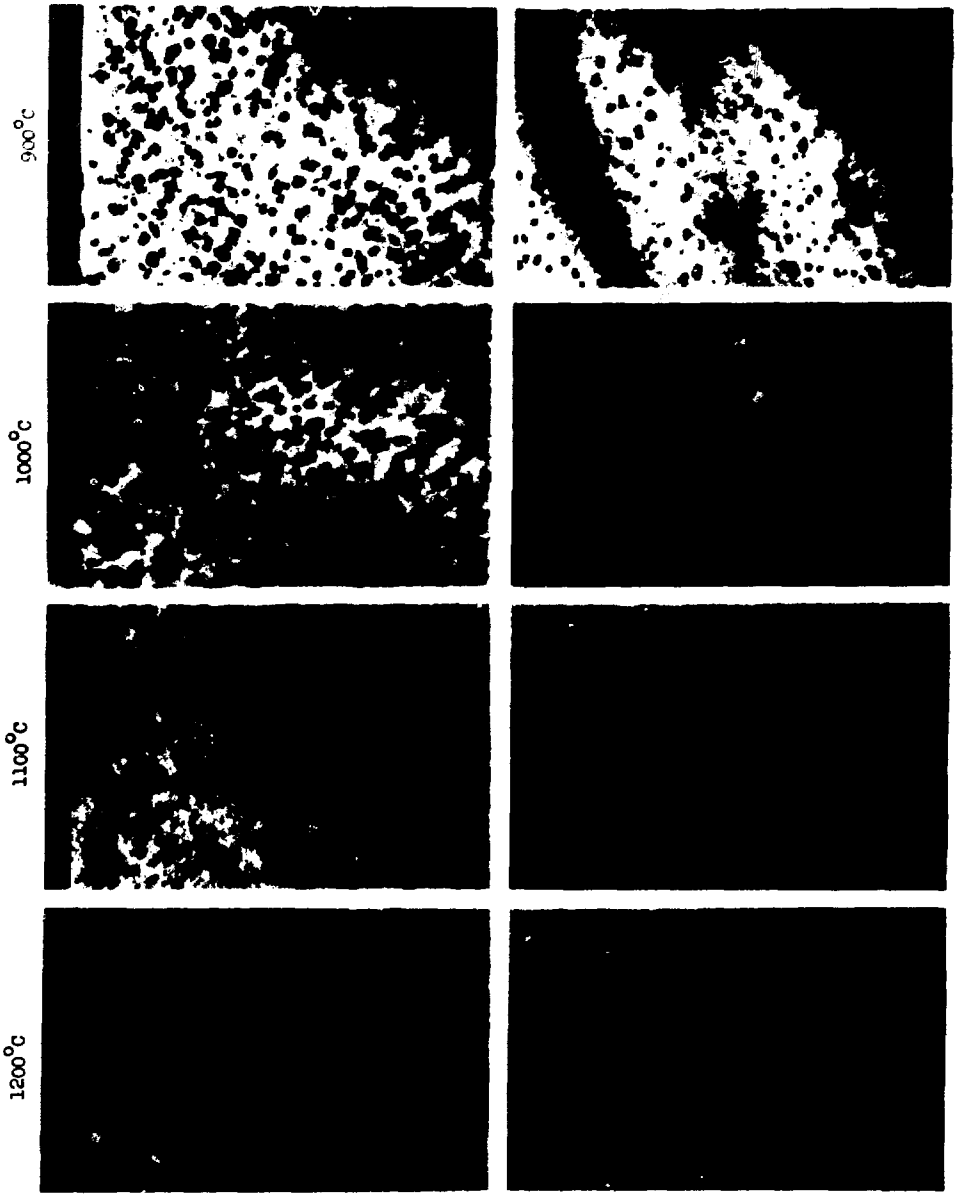

Fig. 3. Electron-micrographs Showing Typical Structures Formed Near Grain Boundaries and in Grain Interiors After Annealing TZM (neutron irradiated at 750°C to ~3 x 10^{20} n.cm^{-2}) For 1 Hour at 900°C (a and b), 1000°C (c and d), 1100°C (e and f), 1200°C (g and h). Diffracting conditions $\underline{z}$ = [023], $\underline{g}$ = [200], $w_g > 0$, 100 keV, scale marker = 0·5 μm.

annealing at 1200°C. A new component to the structure within the grain interiors also appears in the form of a uniform coarse distribution of voids. Figure 3 also shows several examples of large loops intersecting the foil surface. Loop analyses carried out on the irradiated-annealed specimens showed that both large and small loops were of vacancy type with $\underline{b} = 1/2\ (111)$.

A thinned specimen of TZM which had been bulk annealed for 1 hr at 1200°C was annealed for a further 15 min at 1000°C under the same conditions as used for the bulk anneals in an attempt to observe directly any loop shrinkage. Deterioration of the specimen condition was very marked. However, loops present before the anneal could be identified after the anneal and their image diameters compared to pre-anneal measurements obtained under identical imaging conditions [$\underline{g}$, $\underline{g}$ (sense) and w_g all constant]. In all cases no measurable differences could be found either for large or small loops.

Finally, specimens of TZM neutron irradiated at 750 and 850°C were irradiated with 1 MeV electrons at room temperature in the HVEM. At this temperature interstitials are mobile but vacancies are not. Although a high concentration of black spots formed, presumably small interstitial loops, shrinkage of pre-existing vacancy loops did occur.

DISCUSSION

The formation of vacancy loops in TZM irradiated at elevated temperatures has not previously been observed although voids in TZM have been observed following ion irradiations[10,11] at temperatures in the range 600 to 1000°C, following neutron irradiation[12] at temperatures in the range 465 to 680°C, and in a Mo–0.5% Ti alloy following neutron irradiation[13] at temperatures in the range 585 to 790°C. Brimhall et al.[14] observed void formation after irradiation to $\sim 5 \times 10^{20}$ neutrons cm^{-2} at 635°C whereas after irradiation at 720°C no voids were formed but high densities of small defects were observed which exhibited black-white contrast when imaged at the Bragg condition and which Brimhall et al. concluded were precipitates. These results show some, although not exact, measure of agreement with the present more detailed observations.

The mean size of the loops (~ 1[illegible] Å radius) is such that they could not form as a result of the collapse of single cascades since the maximum number of vacancies expected in the largest cascades on a Kinchin and Pease[1] model is only ~ 1[illegible] whereas a loop of 120 Å radius contains ~ 2[illegible] vacancies. This implies that even if the loops form initially by cascade collapse they must undergo further growth. The growth of vacancy loops, especially when they are the major component of the damage structure, seems to contradict the corner stone of void growth theory, namely that dislocations attract more interstitials than vacancies and indicates that the preference term has been reversed. These dislocation loops therefore attract more vacancies than interstitials. The observation that this behavior occurs only in TZM and that the behavior of the PZR and AR molybdenum irradiated under identical conditions is normal, (in the sense that voids and a dislocation substructure consisting mainly of networks is observed), suggests that impurities are having a marked effect on the clustering of point defects in TZM. A comparison of the materials analysis results shows that the only major difference between the compositions of TZM and AR molybdenum is that the alloying elements Ti (0.5%) and Zr (0.08%) and a much higher proportion of carbon are present in the TZM.

The contrast associated with these vacancy loops suggests that the strain field may be slightly modified from that expected for a loop with $\underline{b} = 1/2\ \langle 111 \rangle$. However the majority of the observations of the contrast behavior of the loop images — the appearance of residual images, the occurrence of strong contrast and large image shifts when $\underline{g} \cdot \underline{b} = 2$ and the absence of any stacking-fault fringes when examined under bright-field and weak-beam imaging conditions — all suggest that any change in the strain field from that expected for loops with $\underline{b} = 1/2\ \langle 111 \rangle$ is very small.

The structures formed following bulk post-irradiation annealing treatments of TZM irradiated at 750°C to 3×10^{20} fission neutrons cm^{-2} showed that the loops were very stable. No observable changes in the structure (even near grain boundaries) occurred at annealing temperatures of $\leq$ 1000°C. This is to be contrasted with the observations in molybdenum

of Eyre et al.[5,6] who observed large changes in irradiated structures involving vacancy loop growth at an annealing temperature of 900°C. Another important feature of the annealing results is that at temperatures of 1100 and 1200°C although many of the loops shrink and feed the large loops (and voids at 1200°C) the number of small defects remains approximately constant (i.e., the loops shrink to a small size but do not disappear). This contrasts with the normal behavior occurring in an "Oswald ripening" type diffusion controlled growth mechanism in which the smallest defects shrink the fastest and disappear so that the concentration of defects decreases.

One other interesting feature observed in the bulk-annealed specimens is that many examples were observed of large loops intersecting the foil surfaces. This contrasts with the structure of TZM irradiated at lower temperatures (475 to 650°C) which also contained large loops but in which no loops intersecting the surface were observed. This behavior of loop loss near the foil surfaces is usually attributed to loops gliding to the surface under the action of image forces and so the value of the glide stress for the large loops in the bulk-annealed specimens appears to be very large compared with the value of the glide stress for interstitial loops of the same Burgers vector in the same material.

Although no actual loop shrinkage was observed in the thin foil annealing experiment, using the experimental error in measuring the size of the loop as a maximum value of shrinkage implies an activation energy for self-diffusion of > 5 eV when the rate-controlling factor is self-diffusion.[16,5] This result should be compared with the value[17] in molybdenum of 4.1 eV and with the analysis of the results of the kinetics of vacancy loop growth in molybdenum occurring on bulk annealing at 900°C where the results[5] fitted a value of ~ 4 eV. The present results thus imply a vacancy-impurity binding energy of > 1 eV which is very high. Observations of the widths of grain boundary denuded zones suggest a more reasonable value of ~ 0.1 eV. It is more likely, therefore, that the rate-controlling process for shrinkage of these loops in a thin foil is not self-diffusion but rather the emission of the vacancies from the loop.

The observations and preceding conclusions can all be understood in terms of segregation[18,19] of oversize alloying elements to the dilatation side of the vacancy loop cores (the Goldschmidt atomic radii of Mo, Ti, and Zr are 1.4, 1.47, and 1.60 Å, respectively), as outlined in Table 3.

Table 3. Explanation of Observed Vacancy Loop Behavior in Terms of Solute Segregation

Observation	Deduction	Explanation
Vacancy loop growth	Bias reversed	Interstitial flow to core decreased
Loop contrast	Modified strain field	Modified strain field
Thermal stability	Emission controlled	Difficult jog nucleation and/or propagation
Loops intersect surface	High glide stress	Peierls stress increased
Shrinkage	Stable loop nucleus	Impurity cluster

Interstitial atoms are attracted and approach the core of the dislocation from the dilated side whereas vacancies approach from the compressive side. The presence of the large impurity atoms is then to reduce the ease with which the interstitials are able to approach the dislocation core and be annihilated whereas the vacancies are practically unaffected. Thus the model can explain the reversal in the preference term and makes dislocations with these associated oversize impurity atoms more efficient sinks for vacancies than for interstitials. The strain fields around the loops will not be too drastically affected by the segregation of impurities since the large impurity atoms would be expected to be in substitutional positions, the regions near the core on the dilatation side of the dislocation then being more "close-packed" than the equivalent region in pure molybdenum. The stability of the loops upon annealing can also be explained by the presence of segregated impurities making jog nucleation and/or propagation difficult. The same impurities would also be expected to lead to a higher value of the loop glide stress due to increases in

the Peierls stress. Finally, the observation that the loops do not shrink completely when annealed can be understood as the formation of a highly concentrated nucleus of impurity atoms remaining in the central dilated region of the small dislocation loop and preventing further shrinkage until the temperature is high enough to overcome the binding energy of the impurity atoms to the dislocation and so cause the impurity atoms to diffuse away.

It is to be emphasized that the above model is only very simple and that the real situation is expected to be very much more complex, possibly involving Ti-Zr-C vacancy complexes. However, on the basis of the limited data the present model appears to be reasonable and capable of explaining the observations. The formation of vacancy loops as the major component of the visible damage structure and the associated suppression of swelling is an important result for CTR technology since it occurs in a candidate material for the first wall at typical proposed operating temperatures. Whether the suppression will continue at higher fluences and in the presence of higher helium production rates remains to be seen but it would seem that the formation of impurity stabilized vacancy loops may be an effective way to reduce swelling.

ACKNOWLEDGMENTS

The authors wish to thank A. F. Bartlett and E. A. Terry for their assistance in this work and one of us (JB) wishes to acknowledge the UKAEA, AERE, Harwell, for financial assistance during the course of this work in the form of a research studentship.

REFERENCES

1. D. M. Maher and B. L. Eyre, Phil. Mag. 23, 409 (1971).

2. B. L. Eyre, D. M. Maher, and A. F. Bartlett, Phil. Mag. 23, 439 (1971).

3. D. M. Maher, M. H. Loretto, and A. F. Bartlett, Phil. Mag. 24, 181 (1971).

4. D. M. Maher, B. L. Eyre, and A. F. Bartlett, Phil. Mag. 24, 745 (1971).

5. B. L. Eyre and D. M. Maher, Phil. Mag. 24, 767 (1971).

6. J. Bentley, B. L. Eyre, and M. H. Loretto, Eighth Intern. Congr. on Electron Microscopy, Vol. 1, Canberra, 1974, p. 612.

7. J. Bentley, Ph.D. Thesis, University of Birmingham, 1974.

8. J. Bentley, B. L. Eyre, and M. H. Loretto, to be published in Proc. Intern. Conf. on Fundamental Aspects of Radiation Damage in Metals, Gatlinburg, Tenn., October 5–1[illegible], 1975.

9. R. C. Perrin and B. L. Eyre, J. Microscopy 98, 200 (1973).

10. J. H. Evans, Rad. Effects 1[illegible], [illegible] (1973).

11. G. L. Kulcinski, J. L. Brimhall, and H. E. Kissinger, Radiation-Induced Voids in Metals, p. [illegible], ed. by J. W. Corbett and L. C. Ianniello, AEC Symposium Ser. [illegible], CONF-710601, April 1972.

12. B. L. Eyre, Defects in Refractory Metals, p. 311, ed. by R. deBatist, J. Nihoul, and L. Stals, SCK CEN Mol, Belgium, September 1971.

13. F. W. Wiffen, Radiation-Induced Voids in Metals, p. 386, ed. by J. W. Corbett and L. C. Ianniello, AEC Symposium Ser. 26, CONF-710601, April 1972.

14. J. L. Brimhall, H. E. Kissinger, and G. L. Kulcinski, Radiation-Induced Voids in Metals, p. 338, ed. by J. W. Corbett and L. C. Ianniello, AEC Symposium Ser. [illegible], CONF-[illegible]601, April 1972.

15. G. H. Kinchin and R. S. Pease, Rep. Progr. Phys. 18, 1 (1955).

16. P. S. Dobson, P. J. Goodhew, and P. E. Smallman, Phil. Mag. 16, 9 (1967).

17. J. Askill and D. H. Tomlin, Phil. Mag. 8, [illegible] (1963).

18. T. R. Anthony, Radiation-Induced Voids in Metals, p. 630, ed. by J. W. Corbett and L. C. Ianniello, AEC Symposium Ser. 26, CONF-710601, April 1972.

19. D.I.R. Norris, The Physics of Irradiation Produced Voids, p. 134, ed. by R. S. Nelson. AERE-R[illegible]34, September 1972.

DAMAGE STRUCTURE IN NEUTRON IRRADIATED TZM

A. G. Pard
K. R. Garr

Atomics International
A Division of Rockwell International
Post Office Box 309
Canoga Park, California 91304

ABSTRACT

Transmission electron microscopy (TEM) has been used to study the damage structure of TZM after irradiation in EBR-II to fluences of 3.8 x 10^{26} and 8 x 10^{26} n/m^2 (E > 0.1 MeV) at temperatures of 500°C and 600°C. The damage structure consists of individual defect clusters, rafted defect clusters, dislocation loops and line segments, and voids. Swelling was negligible in all cases. The nature and disposition of the damage structure as a function of irradiation temperature and fluence is discussed.

INTRODUCTION

The formation of defects and defect clusters in stainless steel and some fcc metals has been extensively studied in recent years. Quantitative data on the effects of irradiation temperature and fluence caused by neutron and high energy particle irradiations is voluminous[1]. Meanwhile, the study of irradiation induced defects and defect clusters in refractory metals has been mainly limited to relatively low neutron fluences ($\lesssim 3 \times 10^{26}$ n/m^2) and heavy ion bombardment to simulate high fluence neutron damage[2-6]. In this paper we present some TEM observations on TZM, a dilute molybdenum alloy, irradiated to a relatively low and a moderately high neutron fluence.

EXPERIMENTAL

The TZM specimens used in this study were in the form of thin sheets (3.7mm x 3.7mm x 0.127mm thick). The vendor's chemical analysis is listed in Table 1. Prior to irradiation, the specimens were annealed in vacuum for one hour at 1400°C. Specimens were irradiated in EBR-II (S/A X100) to fluences of 3.8 and 8 x 10^{26}n/m^2 at 500°C and 600°C. Fluences quoted in this report are for E > 0.1 MeV except where noted. After irradiation, the foils used for electron microscopy were obtained by jet thinning in the usual manner. All electron micrographs were taken using an AEI EM6G electron microscope, operated at 100 kV, equipped with a goniometer stage.

RESULTS AND DISCUSSION

The preirradiation microstructure contains few dislocations and a heterogeneous distribution of precipitate particles, see Figure 1. The average grain size is approximately 60 microns.

Results of the microstructural examination are summarized in Tables 2 and 3. Voids were observed in the specimen irradiated at 600°C to a fluence of 3.8 x 10^{26}n/m^2 and in both specimens irradiated to a fluence of 8 x 10^{26}n/m^2. Typical void structures are presented in Figures 2, 3 and 4. Generally, the void array is random in the specimens irradiated to a fluence of 8 x 10^{26}n/m^2. Exceptions to this can be found in the specimen irradiated at 600°C; some local areas, though small in comparison to the total specimen examined, do show evidence of void alignment, see Figure 4. The typical ordered void structure is present in the specimens irradiated at 600°C to 3.8 x 10^{26}n/m^2, see Figure 2. No voids were observed in the specimen irradiated at 500°C to a fluence of 3.8 x 10^{26}n/m^2.

The planar defect structure is summarized in Table 3. The predominant damage structure in the specimen irradiated at 500°C to a fluence of 3.8 x 10^{26}n/m^2 is the rafting of small defects and black spot clusters, see Figure 5. The specimen irradiated to the same fluence at 600°C has

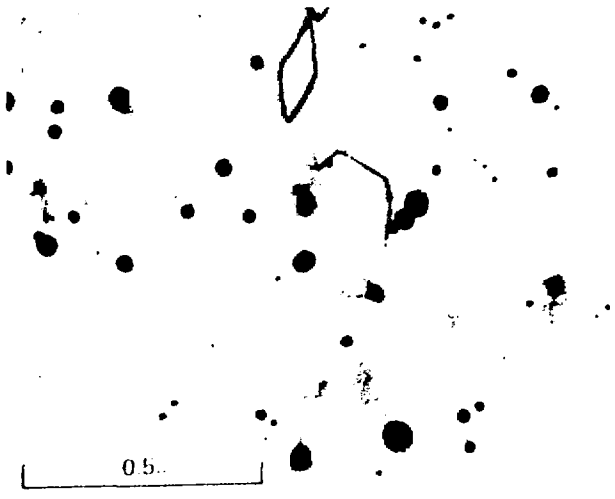

1 Micrograph showing typical preirradiation microstructure of TZM.

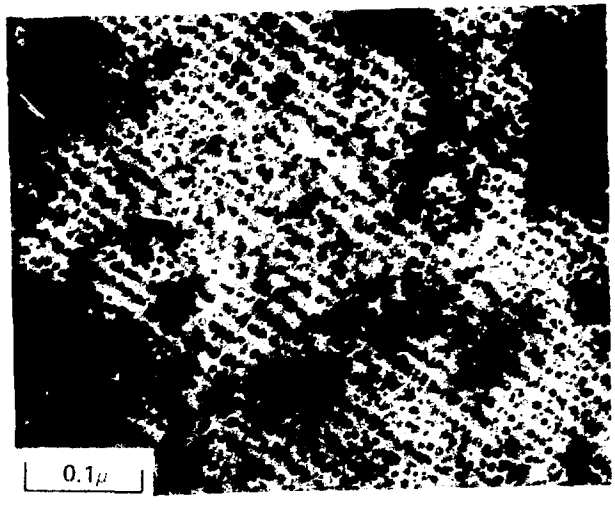

2 Micrograph showing ordered void structure in TZM irradiated in EBR II at 600°C to a fluence of 3.8×10^{26} n/m^2. ($E > 0.1$ MeV).

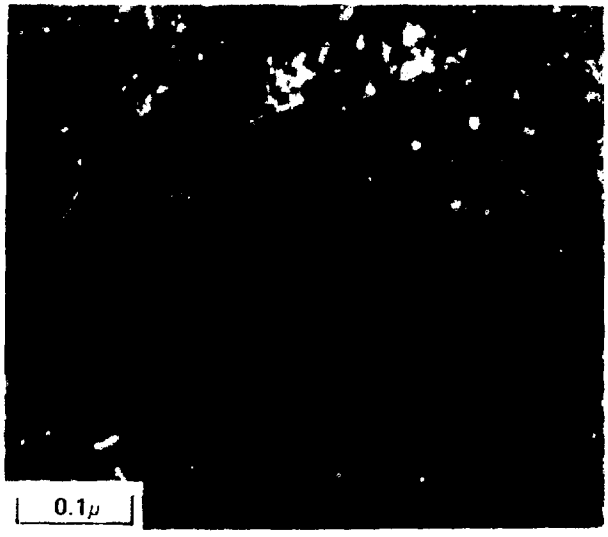

3 Micrograph showing random void structure in TZM irradiated in EBR II at 500°C to a fluence of 8×10^{26} n/m^2 (E > 0.1 Mev).

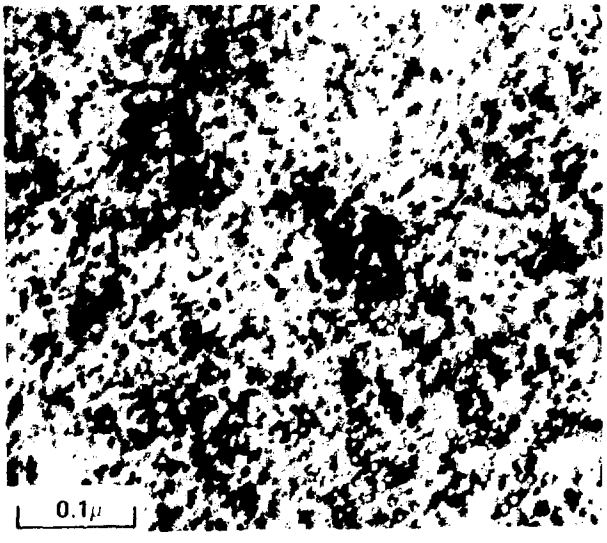

4 Micrograph showing random void structure in TZM irradiated in EBR II at 600°C to a fluence of 8×10^{26} n/m^2 (E > 0.1 Mev,. Note area of ordered voids near bottom right corner.

5 Micrograph showing rafted and clustered defects in TZM irradiated in EBR II at 500°C to a fluence of 3.8×10^{26} n/m^2 (E > 0.1 Mev).

an obvious decrease in the number and size of rafts and clusters present. Upon close examination, one can see many small loops in strong diffraction contrast, see Figure 6. Rafting and clustering of individual defects at 500°C and 600°C at the higher fluence, 8 x 10^{26}n/m^2, is minimal, see Figures 7 and 8, respectively. In all cases, an obvious decrease in number density of precipitate particles, compared with the control specimen, was observed.

If one assumes TZM to be very impure molybdenum, then the present results compare favorably with those of other investigators[2-6]. The swelling values are in good agreement with those reported by Sikka and Moteff[5], Brimhall et al[4], and Eyre and Bartlett[6]. The ordering of voids in the specimen irradiated at 600°C to a fluence of 3.8 x 10^{26}n/m^2 is not unexpected since the tendency for void ordering in refractory metals[7-10] is well established.

Although no loop analysis was performed, it is reasonable to assume that the planar defects are interstitial in nature. Arguments that suggest their interstitial nature are given in work reported by Sikka and Moteff[5] and Eyre and Bartlett[6]. Growth of these defects is both by diffusion of other interstitials to existing defects and loop coalescence as a result of glide and climb. Work reported by Eyre and Maher[11] has shown that growth by the latter process is dependent on the lattice impurities present because of their influence on the loop mobility. The high impurity concentration in our material could easily account for the high number density and size of the planar defects present.

CONCLUSIONS

1. The defect structure of TZM irradiated in EBR-II to neutron fluences of 3.8 and 8 x 10^{26}n/m^2 (E >0.1 MeV) at 500°C and 600°C consists of a high density of planar defects.
2. Voids were observed in all specimens except the one irradiated at 500°C to a fluence of 3.8 x 10^{26}n/m^2 (E >0.1 MeV).

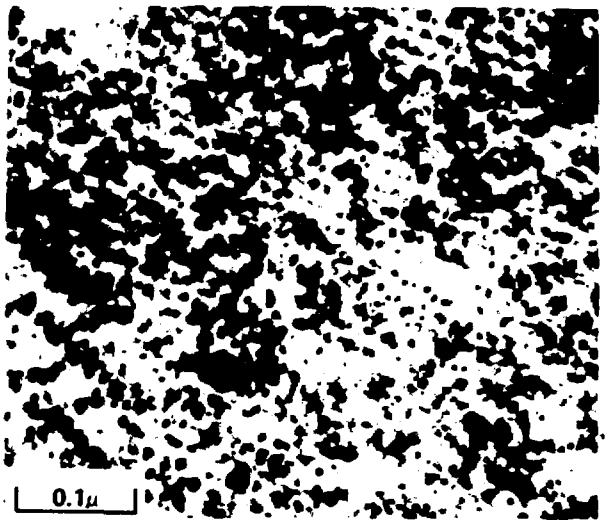

6 Micrograph showing planar defects in TZM irradiated in EBR II at 600°C to a fluence of 3.8×10^{26} n/m^2 (E > 0.1 Mev).

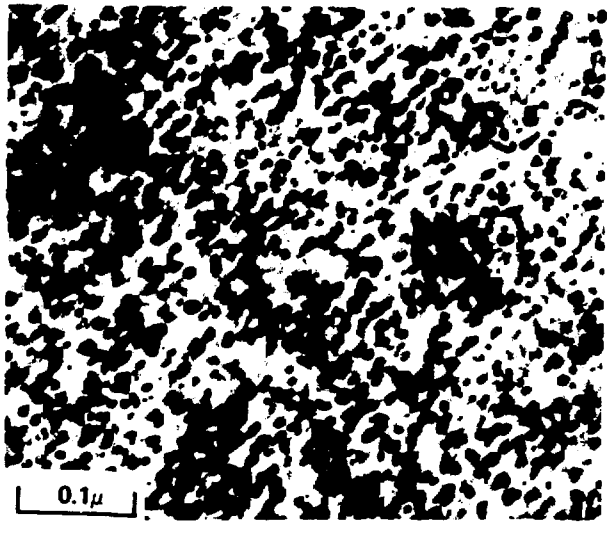

7 Micrograph showing planar defects in TZM irradiated in EBR II at 500°C to a fluence of 8×10^{26} n/m^2 (E > 0.1 Mev).

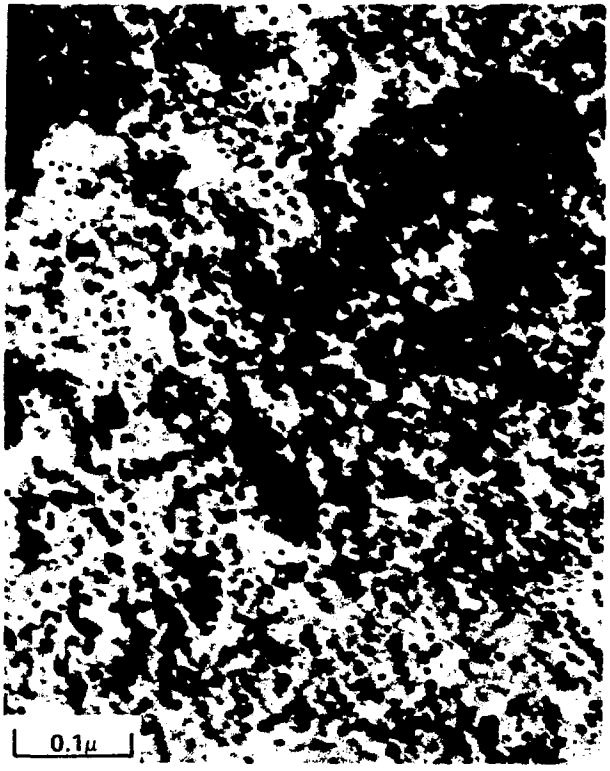

8 Micrograph showing planar defects in TZM irradiated in E3R II at 600°C to a fluence of 8 x 10^{26} n/m^2 (E > 0.1 Mev).

3. A comparison of these results with those obtained by other workers from purer molybdenum shows that the impurity content has some influence on the number density and size of the planar defects.

ACKNOWLEDGEMENTS

The authors thank Dr. D. W. Keefer and Mr. D. Kramer for critical reading of the manuscript and Mr. H. Hori and Miss M. D. Ellis for experimental assistance. This work was supported by the U.S. Energy Research and Development Administration under Contract AT(043)-701.

Table 1. Chemical Analysis of TZM

Element	Mo	Ti	Zr	C	O^2	H^2	N^2	Fe	Ni	Si
Wt ppm	Bal	5100	960	160	5	<1	1	<10	10	20

Table 2. Void Data in Neutron Irradiated TZM

Temp (^oC)	Fluence (n/m^2 E >0.1 MeV)	Void Density $/m^3$	Void Size (nm)	Swelling (V/V_o)
500	3.8×10^{26}	a	-	-
600	3.8×10^{26}	7.6×10^{22}	5.4	0.79
500	8×10^{26}	0.3×10^{22}	3.2	0.01
600	8×10^{26}	b	b	-

a - None were observed.

b - Most voids were too small to obtain meaningful data.

Table 3. Summary of Planar Defects in Neutron Irradiated TZM

Nature of Defect	Fluence n/m^2 ($E > 0.1$ MeV)			
	3.8×10^{26}		8×10^{26}	
	500°C	600°C	500°C	600°C
Rafts	Many	Some	Some	Some
Clusters	Many	Some	Some	Some
Loops	High Density/ very, very small	High density/ very small	High density/ small	High density/ very small
Dislocation Segments	None Observed	Some	Some	Some
Voids	None Observed	Ordered	Random	Random*

* Generally random but some local areas where ordered voids are present.

REFERENCES

1. See selected papers in: International Symposium on Properties of Reactor Structural Alloys after Neutron or Particle Irradiation, ASTM STP 570, in press.

   International Symposium on Radiation Effects on Structural Materials, ASTM STP 529 (1972)

   Radiation-Induced Voids in Metals, ed., J. W. Corbett and L. C. Ianniello, AEC Symposium Series, CONF-710601, Albany, New York (1971)

   Voids in Reactor Materials, ed., S. F. Pugh, D. I. R Norris and M. H. Lorretto, Proceedings of British Nuclear Energy Society Conf., Reading (1971)

2. See selected papers in: International Conference on Defects and Defect Clusters in B.C.C. Metals and Their Alloys, ed., R. J. Arsenault, Gaithersburg, Maryland (1973)

   Defects in Refractory Metals, ed., R. DeBaptist, J. Nihoul and L. Stals, Pub., SKN/CEN (Mol, Belgium, 1972)

3. B. L. Eyre and J. H. Evans in: International Symposium on Radiation Effects on Structural Materials, ASTM STP 529 (1972), Page 184

4. J. L. Brimhall, E. P. Simonen and H. E. Kissinger, J. Nucl. Mater. 48 (1973), Page 339

5. V. K. Sikka and J. Moteff, J. Nucl. Mater. 54 (1974), Page 325

6. B. L. Eyre and A. F. Bartlett, J. Nucl. Mater. 47 (1973), Page 143

7. B. L. Eyre and J. H. Evans in: Voids in Reactor Materials, ed., S. F. Pugh, D. I. R. Norris and in M. H. Lorretto, Proceedings of British Nuclear Energy Society Conf., Reading (1971), Page 323

8. F. W. Wiffen, in: Radiation-Induced Voids in Metals, ed., J. W. Corbett and L. C. Ianniello, AEC Symposium Series CONF-710601, Albany, New York (1971), Page 386

9. J. H. Evans, Nature 229 (1971), Page 403

10. G. L. Kulcinski and J. L. Brimhall, International Symposium on Radiation Effects on Structural Materials, ASTM STP 529 (1971) Page 258

11. B. L. Eyre and D. M. Maher, Phil. Mag. 24 (1971), Page 767

KINETIC STABILITY AGAINST VOID COARSENING IN MOLYBDENUM

E. P. Simonen and J. L. Brimhall
Battelle-Pacific Northwest Laboratories
Richland, Washington 99352

ABSTRACT

The measured rate of increase of void size in molybdenum with annealing time is found to be slower than expected from the Wagner analysis of diffusion-controlled coarsening. The Wagner theory of surface-reaction-control is also compared with ripening data. The determined surface kinetic parameters are compared with vacancy diffusivities and are found to be not unrealistic. Furthermore, a measured decrease in void volume during annealing indicates that total void volume is not conserved. These observations support the conclusion that void coarsening is influenced by more than one rate controlling mechanism. A numerical solution to the void annealing problem is obtained and the specific role of volume diffusion, surface kinetics, and annealing of vacancies to sinks other than voids is calculated.

INTRODUCTION

Radiation induced voids and the associated metal swelling has been a subject of concern in high fluence reactor material applications[1,2]. The growth and dissolution of voids in metals is dependent on both the irradiation environment and material properties. Although the principal concern in modeling void behavior has been void growth during irradiation[3], some consideration has been given to the response of voids during post irradiation annealing[4,5]. Annealing in the absence of irradiation is of interest for the practical reason that CTR first wall materials will be subject to periods of irradiation and post irradiation annealing. Furthermore void annealing experiments present a unique opportunity to study void kinetic behavior in the absence of self interstitials and in the presence of a low

vacancy supersaturation. The purpose of the present work is to study the response of void size distributions to post irradiation annealing so as to determine rate controlling mechanisms. The Wagner[6] analysis of particle coarsening for volume-diffusion-control and surface-kinetic-control is compared with annealing data. In addition, a numerical solution of the same problem is obtained and compared with data assuming measured size distributions, combined volume-diffusion and surface-kinetic-control, and the influence of vacancy sinks other than voids.

THEORY

The Wagner[6] theory of particle coarsening describes the kinetics of small particles dissolving at the expense of large particles due to the higher surface to volume ratio of smaller particles. Both volume-diffusion-control and surface-reaction-control were considered by Wagner. The analysis includes the assumption that the particles are the only sinks present in the matrix and, in addition, the total particle volume is conserved. A quasi-steady-state distribution and ripening rate is predicted after an initial incubation period. The rate of coarsening for volume diffusion control is given by

$$\bar{r} = \bar{r}_o \left[1 + \frac{8\gamma D_s \Omega\, t}{9\bar{r}_o^{\,3} k_B T}\right]^{1/3} . \qquad (1)$$

$\bar{r}$ is the average void radius at time t and $\bar{r}_o$ is the initial average radius. The surface energy, self diffusivity, and atomic volume are represented by γ, D_s, and Ω, respectively. The absolute temerature is T and Boltzman's constant is k_B.

Surface-kinetic-control is described by

$$\bar{r} = \bar{r}_o \left[1 + \left(\frac{8}{9}\right)^2 \frac{\gamma \bar{K}_v c_e \Omega\, t}{\bar{r}_o^{\,2} k_B T}\right]^{1/2} . \qquad (2)$$

$\bar{K}_v$ is the vacancy transfer velocity across a void surface and c_e is the equilibrium vacancy concentration. Thus coarsening behavior by either volume diffusion or surface-kinetic-control is characterized by the shape

of the size distribution and the rate of increase of the average particle size with annealing time.

In the present analysis of void coarsening and annealing some difficulties with the above analytical models are encountered. Firstly, the coarsening conditions are such that the incubation period may not be complete thus the long-time solutions shown in Eqs. (1) and (2) may not be appropriate. Secondly, an observed reduction in total void volume during annealing suggests that vacancies are lost to sinks other than voids. Finally the influence of volume diffusion, surface-reaction-kinetics and annealing to alternate sinks will have a combined control resulting in kinetic behavior not expected by any of the single controlling mechanisms. To deal with the above difficulties a numerical description of the void size distribution was used.

Central to the particle coarsening problem is the calculation of the time rate of change of the particle size distribution function, f, subject to the expression

$$\frac{\partial f}{\partial t} = - \frac{\partial (f\dot{r})}{\partial r} , \tag{3}$$

where the void radius, r, has a first derivative with respect to time, $\dot{r}$. In the numerical solution to Eq. (3), a forward difference equation was used to describe the distribution of dissolving voids and a backward difference equation was used to describe the distribution of growing voids. This procedure results in boundary conditions at the critical size, and thus no boundary restrictions are placed on the smallest or the largest void size considered in the calculation.

The forward difference equation for dissolving voids is

$$f(r,t+k) = f(r,t) - \frac{k}{h} \{f(r+h,t)\dot{r}(r+h,t) - f(r,t)\dot{r}(r,t)\}, \tag{4}$$

where $r < r_c - h$. The time interval is k and the size interval is h. Here r_c represents the critical void radius. The backward difference equation for growing voids is

$$f(r,t+k) = f(r,t) - \frac{k}{h} \{f(r,t)\dot{r}(r,t) - f(r-h,t)\dot{r}(r-h,t)\}, \tag{5}$$

when $r > r_c + h$. As a boundary condition for dissolving voids the following restriction applies to the largest size class of dissolving voids:

$$f(r,t+k) = f(r,t) + \frac{k}{h} f(r,t)\dot{r}(r,t) \tag{6}$$

for $r_c - h < r < r_c$.

Similarly, the smallest size class of growing voids obeys

$$f(r,t+k) = f(r,t) - \frac{k}{h} f(r,t)\dot{r}(r,t) \tag{7}$$

for $r_c < r < r_c + h$.

Eqs. (6) and (7) represent boundary conditions at the critical void size. These conditions are consistent with the restriction that a void of critical size, r_c, neither grows nor dissolves.

Solutions for Eqs. (4) through (7) can be obtained if the time rate of change of void radius, $\dot{r}(r,t)$, is known. The rate is determined from the void sink efficiency and a vacancy flux balance at the void surface. The equilibrium concentration of vacancies, c_v^r, at a void having a radius, r, is given by

$$c_v^r = c_e(1 + \frac{2\gamma\Omega}{rkT}). \tag{8}$$

From the void growth model of Brailsford and Bullough[3], it can be shown that for a finite vacancy transfer rate at a void surface the sink efficiency of voids, S_v, is given by

$$S_v = 4\pi r\rho_v/[1 + D_v/r\bar{K}_v]. \tag{9}$$

D_v and ρ_v are the vacancy diffusivity and the void number density, respectively. A vacancy flux balance at the void surface results in

$$\dot{r}(r,t) = -\frac{2\gamma D_s \Omega}{r^2 k_B T}[1 - \frac{r}{r_c}]/[1 + \mathcal{D}_v/r\bar{K}_v]. \tag{10}$$

The critical radius, r_c, is determined from Eq. (8) and is

$$r_c = \frac{2\gamma\Omega c_e}{(c_v - c_e)k_B T}. \tag{11}$$

The matrix vacancy concentration, c_v, is obtained from an expression of conservation of vacancies

$$\sum_n \left[\frac{4\pi f_n r_n \rho_v (c_v - c_v^{r_n})}{1 + D_v / r_n K_v} \right] + (c_v - c_e) k_v'^2 = 0, \qquad (12)$$

where $k_v'^2$ represents the sink efficiency of all vacancy sinks excluding voids. The first term in Eq. (12) represents the net vacancy loss to voids and the second term represents the net vacancy loss to alternate sinks. Hence, from Eq. (12) the matrix vacancy concentration is

$$c_v = c_e \left\{ \frac{k_v'^2 + \sum_n \frac{4\pi f_n r_n \rho_v}{1 + D_v / r_n K_v} \left[1 + \frac{2\gamma\Omega}{r_n k_B T} \right]}{k_v'^2 + \sum_n \frac{4\pi f_n r_n \rho_v}{1 + D_v / r_n K_v}} \right\}. \qquad (13)$$

Eqs. (4) through (13) describe void annealing behavior for the combined influence of volume diffusion, void surface kinetics, and annealing to alternate sinks.

Solutions to the finite difference equations Eqs. (4) through (7) are stable if $k < |h/\dot{r}_{max}|$ where $\dot{r}_{max}$ is the largest dissolution rate used in the calculation. The time interval is thus a function of the smallest void size included in the solution. In the present analysis a radius of 6.67 Å was the smallest considered with h equal to 1.67 Å. The largest void considered in the analysis was approximately twice the largest void observed in the particular experimental size distribution of interest. For the 1100°C anneal k was chosen to be 3 seconds and at 1000°C, k equal to 40 seconds was used. With these choices of time and size increments, the solutions were found to be stable. A discontinuity in the distribution function occurs at the critical radius in this finite difference treatment. The magnitude of the discontinuity vanishes, however, as the size interval, h, is reduced.

EXPERIMENTAL RESULTS

Three samples were bombarded with Ni^{++} ions to a dose of 6 dpa at 1000°C. The as irradiated void microstructure consisted of 6×10^{16} voids/cm^3 having an average size of 38 Å. The dislocation density was approximately 3×10^9 cm^{-2}. A two hour vacuum anneal at 900°C resulted in no microstructural change, whereas at 1000°C the annealed void size increased to 45 Å with no significant change in the void number density after a six hour anneal.

The neutron irradiated specimens were irradiated to a fluence of 3×10^{19} n/cm^2 (E > 1 MeV) at 800°C. The as irradiated microstructure consisted of a dislocation density of about 3×10^9 cm^{-2}, an average void size of 53 Å, and a void number density of 1×10^{16} voids/cm^3. One specimen was annealed at 1100°C for two hours and another was annealed for twenty hours. The two hour anneal resulted in an average void size of 65 Å and a number density of 2×10^{15} voids/cm^3, whereas the twenty hour anneal resulted in an average void size of 67 Å and a number density of 2×10^{14} voids/cm^3. The two anneals at 1100°C were considered separately in the analysis due to the large uncertainty in the measured void size.

ANALYTICAL INTERPRETATION

The analytical model of Wagner[6] describes the rate of coarsening of particles for volume diffusion control as described by Eq. (1). Table 1 indicates the choice of self diffusivity that would rationalize the observed coarsening for the three annealing conditions considered. A surface energy of 1000 ergs/cm^2 was assumed throughout this investigation. The observed ripening kinetics are less than expected based on experimentally determined self diffusivities of molybdenum[8].

The Wagner interpretation of surface-kinetic-control for $r\bar{K}_v << D_v$ was considered using Eq. (2). The results for surface-reaction-control indicate that the activation energy for vacancy transfer is greater than that for vacancy migration by an amount shown in Table 1. ΔE_m is defined by the relationship

Table 1. Results of Analytical Calculations

Anneal Conditions	Control	$\frac{D_S(\text{predicted})}{D_S(\text{experimental})}$	ΔE_m (eV)
2 hrs 1100°C	Volume Diffusion	1.78×10^{-1}	
	Surface Reaction		0.520
20 hrs 1100°C	Volume Diffusion	2.15×10^{-2}	
	Surface Reaction		0.773
6 hrs 1000°C	Volume Diffusion	2.31×10^{-1}	
	Surface Reaction		0.416

$$\bar{K}_v = \frac{D_v}{b} \exp(-\Delta E_m/k_B T), \quad (14)$$

where b is the jump distance. It is assumed that the surface influence increases the activation energy for a vacancy jump at the surface by an amount ΔE_m. Surface kinetic control could account for the retarded coarsening kinetics for transfer kinetics defined by Eq. (14) and ΔE_m values from Table 1.

NUMERICAL INTERPRETATION

A numerical analysis of the void data was undertaken to describe the incubation period for coarsening and to include the combined control of volume diffusion, surface kinetics, and annealing to alternate sinks. The incubation period for void coarsening was accounted for by calculating the increase in average void radius numerically for volume diffusion control using measured size distributions. The predicted self diffusivities are shown in Table 2. It is noted that the predicted diffusivities from the numerical analysis, Table 2, are nearly the same as predicted from the analytical analysis, Table 1. This indicates the slower than expected experimental rates are not due to the nature of the initial distribution, i.e., the incubation period.

A second difficultly with the coarsening analysis is the annealing out of vacancies to alternate vacancy sinks. This effect is included with the sink term $k_v'^2$ in Eq. (13). The alternate sink strength was determined from the observed increase in void size and decrease in total void volume with annealing for assumed infinite surface kientics. The calculated alternate sink strengths and self diffusivities are shown in Table 2. The measured dislocation sink strength in the neutron irradiated sample was 3×10^9 cm^{-2} in the as irradiated condition. This sink strength when compared with the predicted strength for volume diffusion and alternate sink control suggests that for this interpretation of coarsening all dislocations would have to be effective vacancy sinks. This is unrealistic, thereby indicating a possible influence of surface kinetics.

Table 2. Results of Numerical Calculations

Anneal Conditions	Control	$\frac{D_S(\text{predicted})}{D_S(\text{experimental})}$	$k_v'^2$ cm^{-2}	ΔE_m (eV)
2 hrs 1100°C	Volume Diffusion	2.25×10^{-1}	0	0
	Volume Diffusion Alternate Sink	3.03×10^{-1}	2.5×10^{9}	0
	Volume Diffusion Surface Kinetics Alternate Sink	1.0	5.0×10^{8}	0.375
20 hrs 1100°C	Volume Diffusion	2.50×10^{-2}	0	0
	Volume Diffusion Alternate Sink	4.54×10^{-2}	4.0×10^{9}	0
	Volume Diffusion Surface Kinetics Alternate Sink	1.0	2.0×10^{8}	0.640
6 hrs 1000°C	Volume Diffusion	2.78×10^{-1}	0	0
	Volume Diffusion Alternate Sink	2.78×10^{-1}	$<2.0 \times 10^{9}$	0
	Volume Diffusion Surface Kinetics Alternate Sink	1.0	$<5.0 \times 10^{8}$	0.300

The influences of surface kinetics, ΔE_m, and alternate vacancy sinks, $k_v'^2$, were determined simultaneously from the experimental change in void size and total void volume with annealing. The experimental self diffusivities of molybdenum were assumed. The annealing behavior of voids in molybdenum are rationalized using the parameters shown in Table 2 for volume diffusion, surface kinetic, and alternate sink control. These results were obtained with only a small fraction of the total dislocation density acting as effective vacancy sinks. The increase in activation energy for a surface vacancy jump compared to a matrix vacancy jump was determined to be a few tenths of an electron volt. Fig. 1 shows the change in void radius, void number density, and fraction of void volume as a function of time for the two hour anneal at 1100°C. An alternate sink strength of 5×10^8 cm^{-2} and ΔE_m equal to 0.375 eV were assumed. The predicted size distribution compares well with the measured size distribution in Fig. 2. A slight discontinuity referred to earlier is seen in the distribution function at the critical radius. If the alternate sink strength, 5×10^8 cm^{-2}, and the activation energy increase, 0.375 eV, from the two hour anneal are used to calculate the void parameters after twenty hours of annealing, the magnitude of annealing out of void volume is greatly overestimated.

It is necessary in the above interpretation that vacancies anneal out to dislocations in preference to voids. Fig. 3 illustrates the void radius which results in equilibrium between a void and a dislocation of a given radius of curvature, R_d. A void and dislocation are in equilibrium with each other from surface creation and line tension considerations if

$$r_v = \frac{2\gamma R_d}{\mu b \ln(R_d/5b)}, \tag{15}$$

where μ is the shear modulus. The initial void radius for the 1100°C anneals was 26 Å. Fig. 3 indicates that voids with radii smaller than 26 Å can anneal out to dislocations having radii of curvature greater than 900 Å. Hence, it does appear reasonable that some fraction of the total dislocation density could act as effective vacancy sinks.

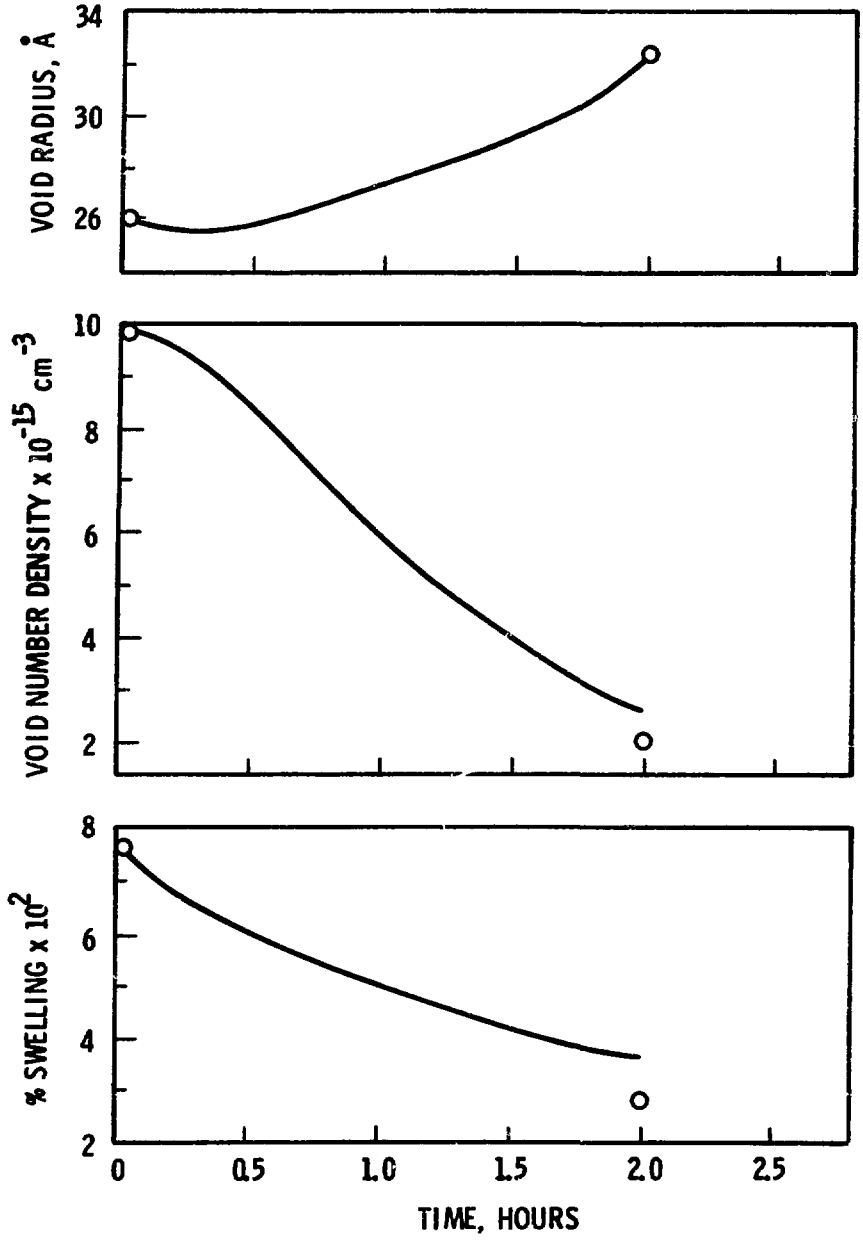

Fig. 1. Void radius, number density and volume as a function of annealing time at 1100°C. The alternate sink strength is 5 x 10^8 cm^{-2} and ΔE_m equals 0.375.

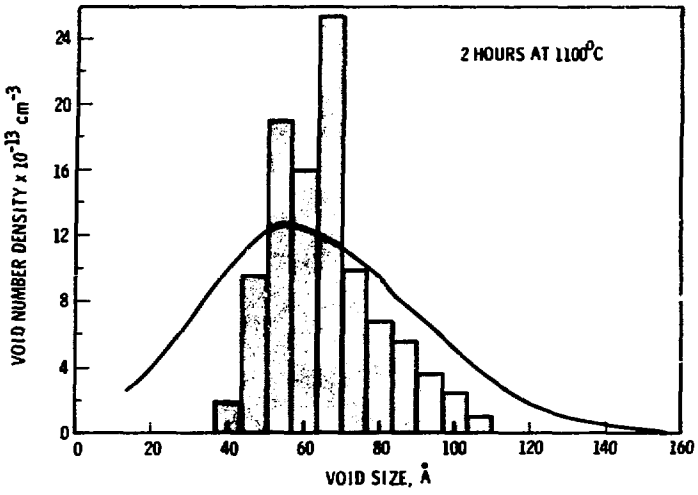

Fig. 2. The predicted and measured void size distributions after a two hour anneal at 1100°C, for the combined influence of volume diffusion, surface kinetics, and alternate vacancy sinks. The critical void size is 82 Å.

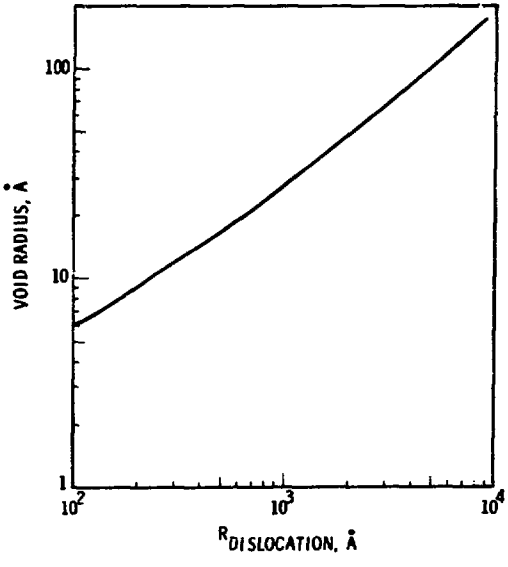

Fig. 3. Void radius which results in equilibrium, as calculated by Eq. (15), between a void and a dislocation having a radius of curvature, $R_{dislocation}$.

CONCLUSIONS

The preceding analysis suggests the following conclusions:

1. Volume diffusion control does not adequately describe void coarsening in molybdenum when void volume is not conserved during annealing;
2. Alternate vacancy sinks can account for the observed decrease in total void volume and increase in void size during annealing if void surface kinetics are included in the analysis;
3. Dislocations can annihilate vacancies but are inefficient sinks due to line tension; and
4. With the present interpretation, the transfer rate of vacancies has an activation energy a few tenths of an electron volt greater than that for vacancy migration in the matrix.

ACKNOWLEDGMENT

This paper is based on work performed under United States Energy Research and Development Administration Contract AT(45-1)-1830.

REFERENCES

1. J. W. Corbett and L. C. Ianniello (eds.), Radiation Induced Voids in Metals, proceedings of the 1971 Intl. Conf. at Albany, New York, June 9-11, 1971.
2. Effects of Radiation on Substructure and Mechanical Properties of Metals and Alloys, ASTM STP 529, American Soc. for Testing Materials, Philadelphia, 1973.
3. A. D. Brailsford and R. Bullough, J. Nucl. Mater. 44, 121 (1972).
4. T. E. Volin and R. W. Balluffi, Phys. Stat. Sol. 25, 163 (1968).
5. C. Cawthorne in: Consultant Symposium - The Physics of Irradiation Produced Voids, R. S. Nelson (ed.), p. 78, AERE-R 7934(January 1975).
6. C. Wagner, Z Elektrochem 65, 581 (1961).

7. J. L. Brimhall and B. Mastel, Rad. Effects 3, 203 (1970).

8. J. Askill in: Diffusion in Body-Centered Cubic Metals, p. 247, Amer. Soc. for Metals, Metal Park, Ohio, 1965.

THE EFFECT OF THE FREE SURFACE ON VOID FORMATION IN ION BOMBARDED MOLYBDENUM

E. R. Bradley and J. L. Brimhall
Battelle-Pacific Northwest Laboratories
Richland, Washington 99352

ABSTRACT

Heavy ion bombardment is currently being considered as a technique to simulate neutron damage in CTR components, especially the first wall structure. The use of heavy ion bombardment as a neutron simulation technique has been criticized due to the damage zone being near a free surface (i.e., ≤1 micron for 5 MeV Ni^{++} ions in molybdenum). The purpose of the present investigation was to examine the microstructure of ion bombarded molybdenum at and below the bombarded surface utilizing transmission electron microscopy to determine the influence of the free surface on void formation. Single crystal molybdenum discs were bombarded at 1000° ± 25°C with 5 MeV Ni^{++} ions at surface dose rates of 3×10^{-4}, 1.8×10^{-3}, and 8×10^{-3} dpa/sec. The void size and density were determined as a function of depth below the bombarded surfaces. Voids were observed within 100 Å of the bombarded surfaces and no significant indications of surface-related effects were observed. The variations in void size and density are discussed in terms of the total dose and dose rate at the various regions of examination and the results compared with existing ion bombardment and neutron irradiation data.

INTRODUCTION

The use of high energy, heavy ion bombardment of metal specimens to simulate the damage produced by neutrons in fission or fusion reactors has received considerable interest in recent years[1,2]. Although ion bombardment has been widely used for this purpose, there is still some uncertainty as to the influence which the free surface has on the development of the irradiation induced microstructure, especially in specimens where the damage zone is less than one micron from the free surface[3,4].

Regions denuded of voids have been commonly observed adjacent to grain boundaries in neutron irradiated materials and near the surfaces in HVEM irradiations[5]. The width of the denuded regions increases with increasing temperature and decreases with increasing damage production rate. The high dose rates associated with heavy ion bombardment are thought to adequately suppress the influence at the surface, but no systematic study of surface denuding in ion bombarded materials has been reported.

This paper reports on the characterization of the void microstructures in ion bombarded molybdenum, at and below the bombarded surface. The microstructure was evaluated as a function of dose rate at constant temperature and ion dose.

EXPERIMENTAL PROCEDURES

Single crystal molybdenum discs approximately 0.25 mm thick and 3 mm diameter were used in these experiments. The discs were ground flat, mechanically polished to a smooth finish and electropolished to remove any residual surface damage. All specimens were then annealed at 1700°C for 2 hours in a vacuum of $\sim 1 \times 10^{-7}$ torr.

The specimens were irradiated in a tandem Van de Graaff accelerator using 5 MeV Ni^{++} ions at a temperature of 1000° ± 25°C. The vacuum in the specimen chamber varied between 1×10^{-6} and 5×10^{-6} torr during the irradiation. Nickel ion currents of 1×10^{12}, 5.9×10^{12}, and 2.6×10^{13} ions/cm^2-sec were used which correspond to atom displacement rates of 3×10^{-4}, 1.8×10^{-3}, and 8×10^{-3} dpa/sec at the bombarded surfaces. The total nickel ion dose was 2×10^{16} ions/cm^2 corresponding to ~ 6 atom displacement per atom (dpa) at the surface.

The displacement damage as a function of penetration has been calculated and is shown in Fig. 1. The energy deposition of the Ni^{++} ions was calculated using the EDEP-1 computer code of Manning and Mueller[6] and the atom displacements were calculated using a modified Kinchin and Pease relation. The β factor was taken as 0.8 and the effective threshold energy for atomic displacement in molybdenum was assumed to be 62 eV in accordance with current recommendations for displacement calculations[7].

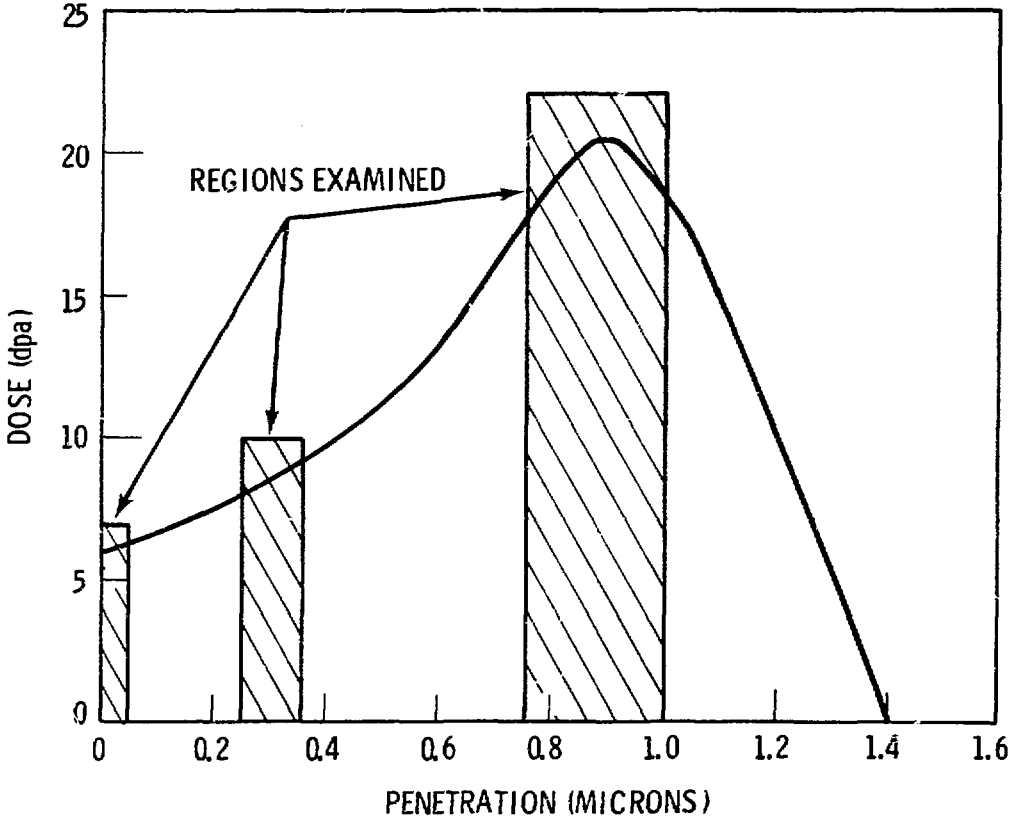

Fig. 1. Displacement Damage in Molybdenum as a Function of Distance from the Bombarded Surface after Bombarding with 5 MeV Ni^{++} Ions to a Total Dose of 2×10^{16} ions/cm^2.

Electron microscopy specimens were prepared by the standard two step technique of dimpling and final polishing. The bombarded surfaces were painted and the specimens were perforated from the back side. Following examination of this region, approximately 0.3 μm ± .05 μm of metal was removed from the bombarded surface and a new perforation was made from the back side. The amount of material removed from the surface was determined by measuring the step height at painted off regions. A series of consecutive surface removals and microscope examinations followed until the entire damage zone had been examined. The peak damage region was taken as that region where the void density was a maximum.

The void size and number density were measured from electron micrographs using stereo techniques to determine the foil thickness. The larger voids have a cubic shape and this shape was assumed for the smaller voids also. The void volume fraction was calculated using the relation:

$$\frac{\Delta V}{V}\ (\%) = 100 \left(\frac{\Sigma_i N_i d_i^3}{\Sigma_i N_i} \right) \times (\text{void concentration}), \qquad (1)$$

where N_i is the number of voids of cube edge d_i.

RESULTS

The void data were obtained from three regions of examination: at the bombarded surface; approximately 3000 Å below the surface; and near the peak damage zone as shown schematically in Fig. 1. The void microstructures at the various regions of examination are shown in Fig. 2 for each of the three dose rates. The spatial distributions of voids in the vicinity of the bombarded surfaces were determined by stereo microscopy for the intermediate and low dose rate specimens and are shown in Fig. 3. As can be seen, the measured denuded region was ∿50 Å wide in the specimen bombarded at the intermediate dose rate and ∿100 Å for the low dose rate specimen. The above distributions are based on measurements of approximately 100 voids in each specimen. Surface contamination and small void size prevented stereo examination in the high dose rate specimen.

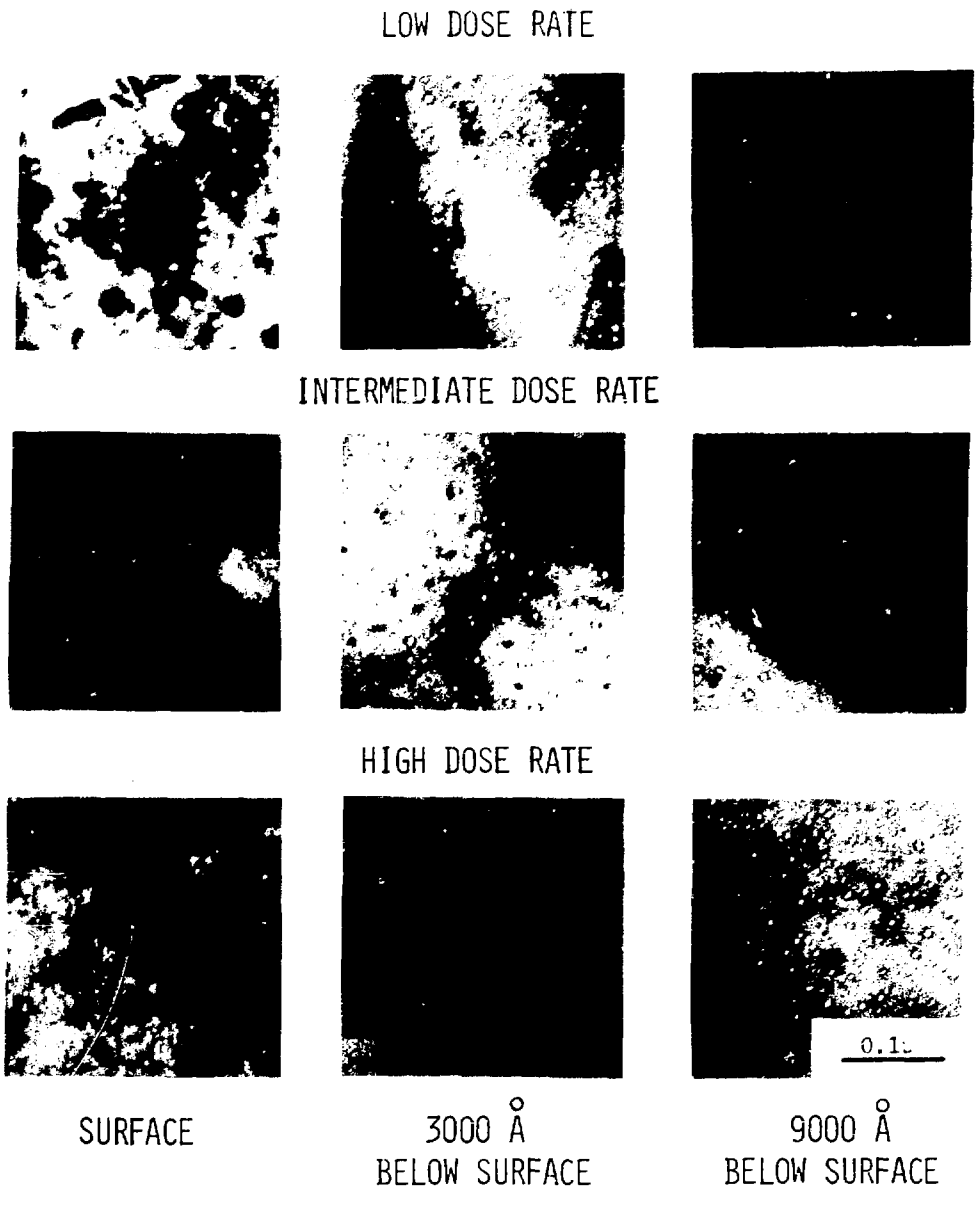

Fig. 2. Void Microstructures at Three Regions of Examination in Molybdenum Bombarded with 5 MeV Ni^{++} Ions at Ion Currents of 1 x 10^{12}, 5.9 x 10^{12}, and 2.6 x 10^{13} ions/cm^2-sec.

The void data from the three regions of examination for each ion current used are given in Table 1 and can be summarized as follows:

i. The void size increases with decreasing dose rate at equivalent dose levels.

ii. The void density increases with increasing dose rate at equivalent dose levels.

iii. The void size remains relatively constant for the low and intermediate dose rate specimens and increases slightly in the high dose rate specimen as a function of depth below the bombarded surface.

iv. The void density increases with increasing depth below the bombarded surface.

DISCUSSION

Surface Denuding

Boundaries are known to act as sinks for point defects and thus lower the defect concentration in their vicinity. This depletion of point defects has been used to explain void denuding at grain boundaries in neutron irradiated metals and surface denuding during HVEM irradiations. The defect concentration profile adjacent to free surfaces have been calculated by several investigators[8,9] and used to estimate the width of the void denuded zones in HVEM irradiations. These calculated zone widths are often found to be less than the experimetally measured denuded zone widths[5].

The vacancy concentration profiles near the free surface for molybdenum at 1000°C as a function of dose rate have been calculated using the solution of Lam et al., for a semi-infinite solid[10]. Assuming an initial dislocation density of 10^8 cm/cm^3 and a vacancy migration energy of 2 eV, the above calculations give denuded zone widths of 1900 Å and 1200 Å, respectively, for dose rates of 3×10^{-4} dpa/sec and 1.8×10^{-3} dpa/sec when Foreman's criteria[8] of a 5% depression of the vacancy concentration is used for defining the denuded zone boundary. These calculated widths are a factor of twenty greater than the experimentally measured widths and this large

Table 1. Void Parameters as a Function of Depth Below the Surface in Molybdenum Bombarded with 5 MeV Ni^{++} Ions at Currents of 1×10^{12}, 5.9×10^{12}, and 2.6×10^{13} ions/cm^2-sec.

Region of Examination	Dose (dpa)	Dose Rate (dpa/sec)	Void Size (Å)	Void Density (cm^{-3})	Void Volume Fraction (%)
Surface	6	3.0×10^{-4}	60	-	-
∿3000 Å	8	4.0×10^{-4}	54	3.0×10^{16}	.47
Peak Damage Zone	20	1.0×10^{-3}	59	4.8×10^{16}	.98
Surface	6	1.8×10^{-3}	43	-	-
∿3000 Å	8	2.4×10^{-3}	47	3.2×10^{16}	.33
Peak Damage Zone	20	6.0×10^{-3}	44	7.4×10^{16}	.63
Surface	6	8.0×10^{-3}	30	-	-
∿3000 Å	8	1.0×10^{-2}	36	4.6×10^{16}	.21
Peak Damage Zone	20	2.7×10^{-2}	41	9.4×10^{16}	.65

discrepancy is difficult to rationalize on the basis of experimental uncertainty.

Surface oxidation of stainless steel has been found to greatly reduce or eliminate the surface denuded regions during HVEM irradiations[4] and may offer an explanation for the small denuded regions observed in the ion bombarded specimens. The vacuum in the specimen chamber varied between 1×10^{-6} and 5×10^{-6} torr during the irradiations and may not have been adequate to prevent oxidation of the surfaces. The surfaces were found to be contaminated as shown in Fig. 2, but it is impossible to determine if the contamination was present during the irradiations or introduced during cooling and subsequent handling of the specimens.

A comparison of width of the denuded regions adjacent to grain boundaries in neutron irradiated molybdenum with the surface denuding in the ion bombarded specimens should provide an indication as to whether surface contamination influenced the ion results. Such a comparison is possible by utilizing the relation[4]:

$$L \sim \left(\frac{D_v}{P}\right)^{1/2} \tag{2}$$

where L is the denuded zone width, D_v is the vacancy diffusion coefficient and P is the dose rate.

Using Sikka et al.[11], data for neutron irradiated molybdenum at 1000°C and a dose rate of 1×10^{-6} dpa/sec, the above relation predicts denuded zone widths of 20 Å and 50 Å for the intermediate and low dose rates used in the present investigation. These predicted widths are a factor of two smaller than the experimentally measured widths but the agreement is rather good when the uncertainties in the dose rate calculations, irradiation temperatures, and experimental measurements are considered.

Although the agreement between denuded zone widths in the neutron irradiated and ion bombarded molybdenum indicates that surface contamination did not influence the present results, final resolution of surface denuding in ion bombarded materials requires better control of the irradiation atmosphere.

Void Microstructure vs. Depth of Observation

Comparison of the void microstructure at various depths in ion bombarded specimens is complicated by the fact that both total dose and dose rate increase with increasing depth below the surface. Void size generally increases with increasing dose and decreases with increasing dose rate while the void density increases with dose rate and can increase, saturate, or decrease with dose depending on the dose level.

Void size as a function of dose in ion bombarded molybdenum at 1000°C has been reported by Brimhall et al., and the data can be approximated by a dose dependence of $(\text{dose})^{0.2}$. Using this relation to normalize the present data to a constant dose level of one dpa, the void size dependence on dose rate is shown in Fig. 4. The data show a relatively smooth decrease in size with increasing dose rate up to $\sim 10^{-2}$ dpa/sec and an apparent dose rate independence at higher rates. This independence of void size on dose rate at high rates is in qualitative agreement with neutron data where void size is reported to be independent of temperature at low temperatures[11].

The dose rate dependence on void size in molybdenum has not been previously reported such that comparison with the present results is not possible. However, the major significance of the relationship shown in Fig. 4 is that the data from all three regions of examination fit on the same curve. This implies that the void size was not influenced by the free surface nor by the presence of the implanted nickel ions near the peak damage zone.

An increase in void density with both dose and dose rate is required to account for the increase in void density with depth observed in the present investigation. Brimhall et al.[12], have reported that the void density in ion bombarded molybdenum saturates at a dose level of ~5 dpa while Evans[13] data show the void density increases up to ~100 dpa. These conflicting results prevent any definite conclusions on the variation of void density with depth of observation to be made.

Comparison with Neutron Data

Since the primary purpose of elevated temperature ion bombardment studies is to simulate the damage produced by neutron irradiations, it is

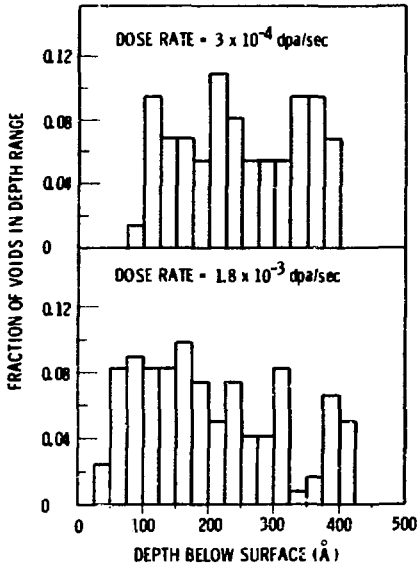

Fig. 3. The Spatial Distribution of Voids Near the Bombarded Surface in Ion Bombarded Molybdenum.

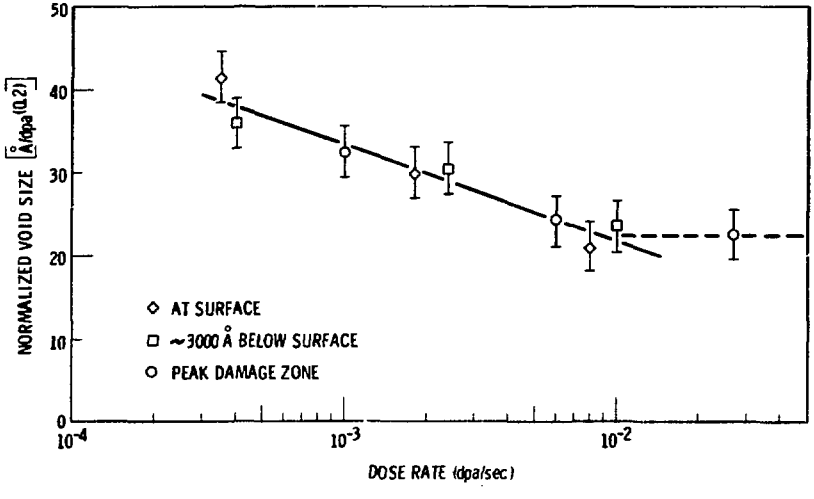

Fig. 4. The Normalized Void Size Data from Three Regions of Examination as a Function of Dose Rate in Ion Bombarded Molybdenum.

of interest to compare the results of the present investigation with the available data from high fluence neutron irradiations. Only the data of Sikka et al.[11], Wiffen[14], and Eyre et al.[15], have sufficient displacement dose* to enable meaningful comparisons to be made. The Bullough-Perrin[16] temperature shift was applied to the ion bombardment data in order to compare the data as a function of the effective irradiation temperature. A displacement rate of 1×10^{-6} dpa/sec was assumed for the neutron irradiations and the self diffusion energy for molybdenum was taken as 4 eV in the temperature shift calculations.

Figs. 5, 6, and 7 show the void size, void density, and void volume fraction, respectively, as a function of the effective irradiation temperature for the ion and neutron irradiations. The void volume fraction data shown in Fig. 7 have been adjusted in order to be consistent with the cubic shape assumed in the present investigation and have also been normalized to a dose of 10 dpa using the dose dependence reported by Brimhall et al.[12] (i.e., $\frac{\Delta V}{V} \propto (\text{dose})^{0.6}$). Additional ion bombardment data[13,17,18,19] are also included in Fig. 7.

There are large variations in the neutron irradiated data as can be seen in Figs. 5 and 6. The void size data from the ion bombarded specimens are somewhat smaller but agree reasonably well with the void sizes reported by Sikka et al. A smaller size is expected in the present investigation since the smallest projected length was measured rather than the largest projected length as reported by Sikka et al. The void densities measured in the present investigations are in better agreement with Wiffen's data than with the data of Sikka et al., as shown in Fig. 6. Neither of the above comparisions have considered the variations in total dose but the corrections should be rather small.

The correction for dose variations is included in the plot of void volume fraction as a function of effective irradiation temperature and, as can be seen in Fig. 7, the scatter in the neutron irradiation data is still

*The dose values reported by the various investigators were corrected to be consistent with the dose calculations of the present investigation. The corrected values being ∿10 dpa for Sikka et al., and Eyre et al., and ∿12 dpa for Wiffen's data.

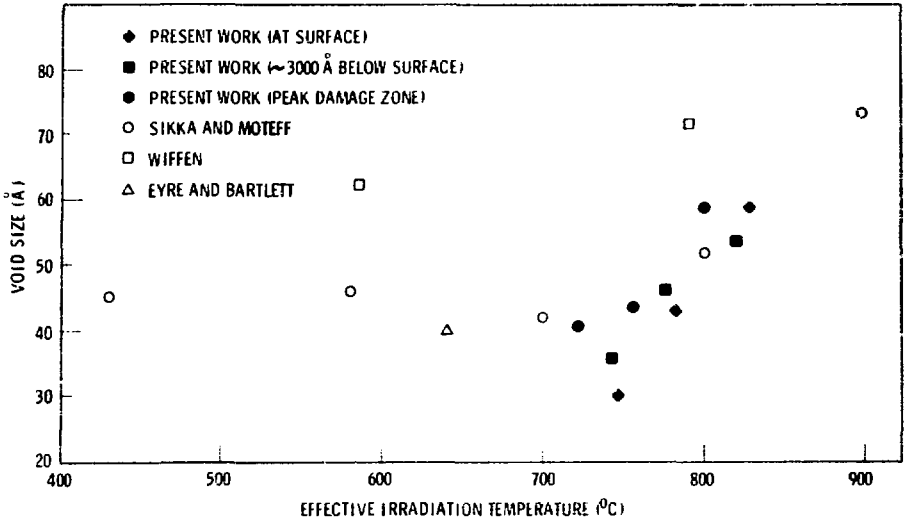

Fig. 5. Comparison of the Temperature Dependence of Void Size in Ion and Neutron Irradiated Molybdenum.

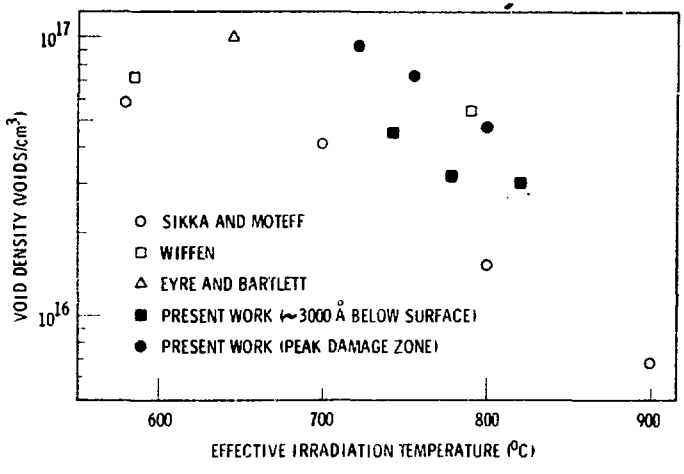

Fig. 6. Comparison of the Temperature Dependence of Void Density in Ion and Neutron Irradiated Molybdenum.

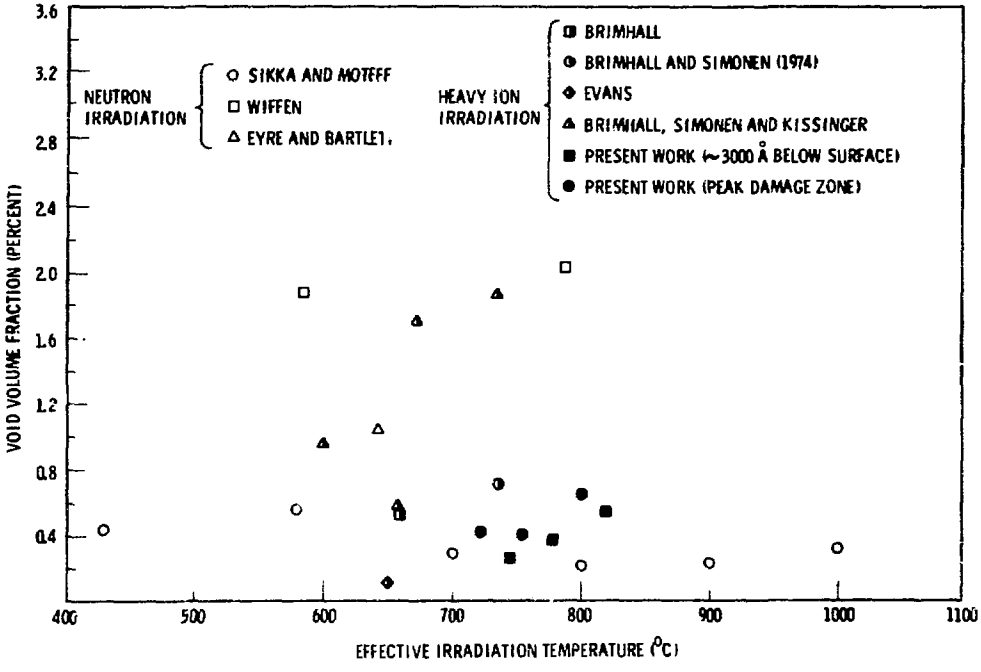

Fig. 7. Comparison of the Temperature Dependence of Swelling in Ion and Neutron Irradiated Molybdenum.

very large. The majority of the ion bombardment data are within the scatter of the neutron data and generally approach the lower limit established by Sikka et al. However, the large scatter in both the ion and neutron data make quantitative comparisons difficult.

CONCLUSIONS

1. The width of the surface denuded regions in ion bombarded molybdenum decreases with increasing dose rate and is less than 100 Å for dose rates greater than 3×10^{-4} dpa/sec. The magnitude of the surface denuded regions is in reasonable agreement with grain boundary denuding in neutron irradiated molybdenum when the difference in dose rate is included.

2. The variation in void microstructures as a function of depth below the bombarded surfaces can be qualitatively explained by the increase in dose and dose rate with increasing depth below the bombarded surface. Sufficient data are not available for quantitative evaluation, but there dose not appear to be a significant surface effect on the void microstructures.

3. The ion bombardment data are in reasonable agreement with neutron irradiation data when the Bullough-Perrin temperature shift is included. However, the large scatter in both the neutron and ion data prevent quantitative comparisons from being made.

ACKNOWLEDGMENT

This paper is based on work performed under United States Energy Research and Development Administration Contract AT(45-1)-1830.

REFERENCES

1. G. L. Kulcinski in: Applications of Ion Beams to Metals, S. T. Picraux, E. P. Eernisse, and F. L. Vook (eds.), p. 613, Plenum Press, New York, 197

2. J. L. Brimhall, this conference proceedings.

3. R. S. Nelson, J. A. Hudson, D. J. Mazey, G. P. Walters, and T. M. Willians in: Radiation Induced Voids in Metals, J. W. Corbett and L. C. Ianniello (eds.), p. 338, AEC Symposium Series CONF-710601, Albany, New York, 1971.

4. F. Garner and L. E. Thomas in: Effects of Radiation on Substructure and Mechanical Properties of Metals and Alloys, p. 303, ASTM 529, Philadelphia, 1973.

5. D. I. R. Norris, Rad. Effects 15, 1 (1972).

6. I. Manning and G. P. Mueller, Computer Phys. Comm. 7, 85 (1974).

7. D. G. Doran, J. R. Beeler, Jr., N. D. Dudey, and M. J. Fluss, Report on the Working Group on Displacement Models and Procedures for Damage Calculations, HEDL-TME 73-76 (December 1973).

8. A. J. E. Foreman, Rad. Effects 14, 175 (1972).

9. K. Urban, M. Wilkens, and A. Seeger in: Radiation Induced Voids in Metals, J. W. Corbett and L. C. Ianniello (eds.), p. 550, AEC Symposium Series CONF-710601, Albany, New York, 1971.

10. N. Q. Lam, S. J. Rothman, and R. Sizmann, Rad. Effects 23, 53 (1974).

11. V. J. Sikka and J. Moteff, J. Nucl. Mater. 54, 325 (1974).

12. J. L. Brimhall and E. P. Simonen in: Defects and Defect Clusters in B.C.C. Metals and Their Alloys, R. J. Arsenault (ed.), p. 321, Nuc. Metallurgy, Vol. 18, Natl. Bureau of Standards, 1973.

13. J. H. Evans, Rad. Effects 17, 69 (1973).

14. F. W. Wiffen in: Radiation Induced Voids in Metals, J. W. Corbett and L. C. Ianniello (eds.), p. 386, AEC Symposium Series CONF-710601, Albany, New York, 1971.

15. B. L. Eyre and A. F. Bartlett, J. Nucl. Mater. 47, 143 (1973).

16. R. Bullough and R. C. Perrin in: Irradiation Effects on Structural Alloys for Nuclear Reactor Applications, p. 317, ASTM 484, Philadelphia, 1970.

17. J. L. Brimhall, E. P. Simonen, and H. E. Kissinger, J. Nucl. Mater. 48 339 (1973).

18. J. L. Brimhall in: The Physics of Irradiation Produced Voids, R. S. Nelson (ed.), p. 197, AERE-R7934, Harwell, 1975.

19. J. L. Brimhall and E. P. Simonen, J. Nucl. Mater. 52, 323 (1974).

IRRADIATION HARDENING AND ANNEALING IN IRONS AT A HIGH NEUTRON FLUENCE

T. Takeyama H. Takahashi

N. Yokoya H. Kayano

ABSTRACT

The purpose of the present study is to obtain basic information for irradiation effect on two kinds of iron with different carbon content; specimen A (Fe-0.002 wt%C), specimen B (Fe-0.012 wt%C). The behavior of the lattice defects occurring due to neutron irradiation was investigated through electron microscopy and mechanical examination.

After the irradiation, specimen A showed voids of about 500 Å in size. The void density obtained through direct observation was about 1.0×10^{14} /cm^2. On the contrary, in specimen B the void was hard to observe. It was concluded that for the formation of voids by irradiation, specimens with less carbon atoms were desirable. The intriguing observation obtained through void formation showed that the yield stress of specimen A was higher than specimen B of high carbon content. The mechanism operating there may have much to do with the hardening is caused by void formation.

INTRODUCTION

Void formation has been studied in 304 stainless steel and a number of pure metals and alloys.[1] It is reported that irradiation temperature, fluence, and material purity have deep influence on the formation of defects, especially, of voids. In general, the void occurs in the temperature region from about 0.3 Tm to 0.55 Tm, where Tm is the absolute melting temperature. This temperature will be essentially determined by the behavior of vacancy and interstitial. The threshold fluence level also seems to be an important factor in forming voids by neutron irradiation. The effect of purity on void formation has been studied in several metals. Namely, the void is formed in pure metals, but not formed in low purity metals under the same irradiation conditions. However, Wiffen showed that, in vanadium irradiated at 395°C, the void density was

increased by an increase in the interstitial impurity content of the material.[2,3] In the case of pure iron, the void was observed at 450°C in the EBR-II reactor to a fast neutron fluence and it was suggested that the threshold fluence is likely to lower as the purity of the metal was increased.[4] The interstitial impurity level in bcc metals has a very strong influence on the void formation produced by irradiation, but much more data is required to determine the behavior.

The purpose of the present study is to obtain the basic information for the irradiation effect of the two kinds of iron which have different carbon contents under the same conditions of fast neutron fluence at the same irradiation temperature. The void formation resulting from the degree of purity and the effect of the void for irradiation hardening were studied.

EXPERIMENTAL METHOD

The iron used in this investigation is a re-electrolytic pure iron produced by Showadenko Co. Ltd. Two specimens were prepared by vacuum melting. The chemical analysis of the specimens was given in the Table 1. The material was cold-rolled into sheets of 0.2 mm thickness. It was then cut into pieces of 15 x 100 mm. The specimens were solution-treated one hr at 730°C in a vacuum of 5×10^{-5} Torr, and then quenched into iced water.

They were irradiated at estimated temperatures of 500 ∿ 550°C with fast neutrons (E > 1 MeV) to a fluence of 1.2×10^{21}nvt.

For electron microscopy, thin films were prepared by jet-electro-polishing.[5] They were then examined in a JEM 200 electron microscope operating at 150 ∿ 200 kV.

The tensile test specimens were cut into pieces, 5 x 15 mm. They were then derusted with dilute hydrochloric acid. Tensile deformation was performed by using an Instron-type tensile testing machine at a strain rate 3.2×10^{-4} sec^{-1}. The testing temperatures were -196, -78, room temperature, 150, and 200°C. Isochronal post-irradiation annealing carried out for one hr in the temperature region between at 100 and 800°C and specimens were examined at room temperature. More details concerning

experimental methods and techniques can be found in other publication.

RESULTS AND DISCUSSION

Typical void distribution in specimen A containing 20 ppM carbon atoms was shown in Fig. 1.(a). As the projected shape of the dots was not so clear, it was difficult to determine the morphology of the voids but, many black and white dots from 200 to 800 Å in size were seen rather uniformly on the matrix. The black and white contrast varied critically with the diffraction conditions. These dots could be the voids formed by the clustering of the vacancies. Besides the voids, no precipitates or point defect clusters were observed. The void density obtained by direct observation was about $1.0 \times 10^{14}/cm^3$. This number was calculated for an average foil thickness of 2000 Å. The size distribution and number of voids were shown in Fig. 2.

On the contrary, the microstructure of the irradiated specimen B of 120 ppM carbon content was shown in Fig. 1.(b). The precipitates possibly formed either during irradiation or subsequent cooling were observable, and also the dislocations developed due to the growth of the precipitates. The voids as observed in specimen A were not clear. Accordingly, for void formation by irradiation it is desirable that the specimen has less carbon atoms of the interstitial type.

The yield stress of the irradiated specimens A and B derived from the stress-strain curves were plotted against the temperature as shown in Fig. 3. In the whole range of the test temperature, the values were greater in specimen A than in specimen B. This is an intriguing observation indicating that hardening is caused by void formation.

Both the irradiated specimens A and B were then annealed at temperatures from 100 to 800°C and yield stress was obtained as a function of annealing temperature. Fig. 4. shows the annealing temperature dependence on the yield stress in the irradiated irons. The high value of the yield stress in specimen B observed at about 200°C annealing is probably due to the precipitation of ε-carbide. It is obvious that the yield stress of specimen A in which voids were formed during irradiation was, as a whole, higher than that of specimen B. This effect seems to be caused

Table. 1

Specimen	C	Si	Mn	P	S	Ni	N (wt%)
A	0.002	0.0025	0.0015	0.0011	0.004	0.0059	0.0013
B	0.012	0.0035	0.0005	0.0011	0.005	0.0061	0.0010

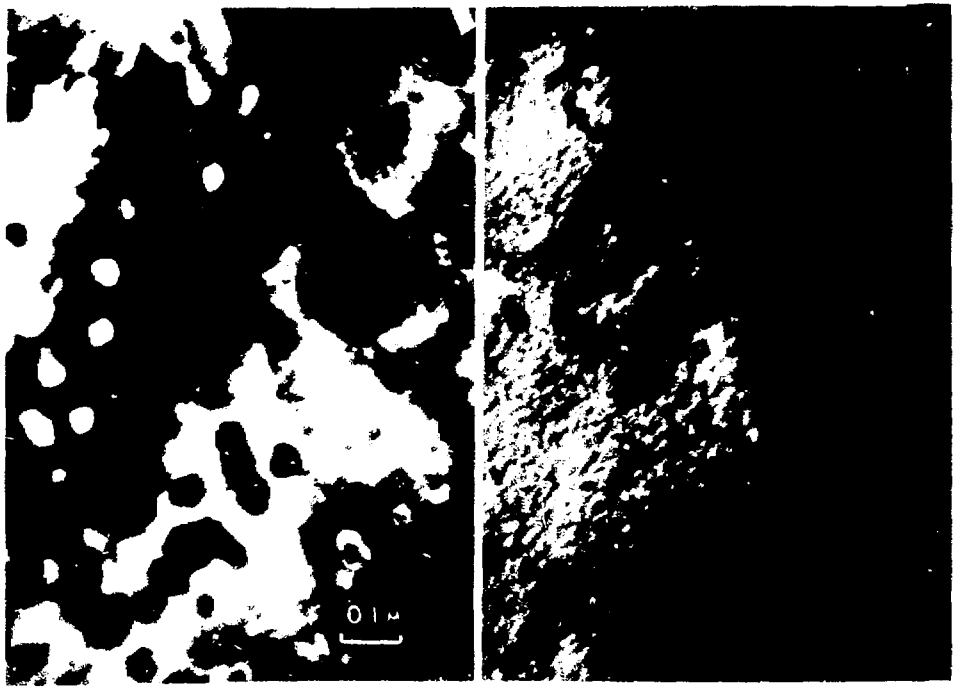

(a) (b)

Fig. 1. (a) Void distribution in an irradiated specimen A.
(b) Absense of voids in an irradiated specimen B only with precipitation of carbides.

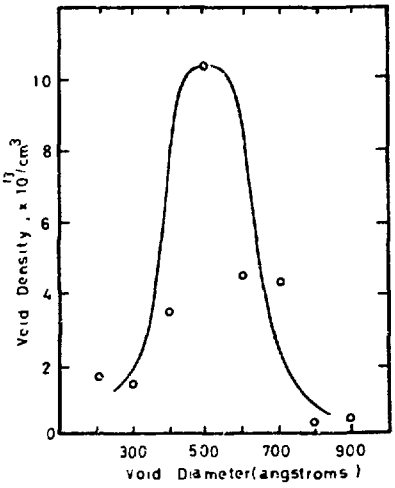

Fig. 2. The size distribution and number of voids within grains of specimen A.

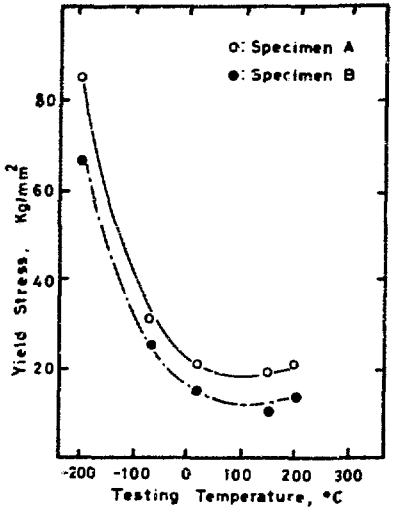

Fig. 3. Yield stress as a function of testing temperature for irradiated specimens A and B.

by void distribution. Microstructural changes of both specimens occurring during post-irradiation annealing at 200 and 600 C were examined by transmission electron microscopy. Fig. 5.(a) shows the typical void structure viewed in {012} of specimen A after post-irradiation annealing at 200°C. The voids with cubic shape were distributed fairly randomly within the grains, and no specific changes were observed in the structure of the irradiated specimen A after post-irradiation annealing. It showed that the size and morphology of void were not affected at 200°C. Consistent morphology of void shapes in iron could not be determined. Fig. 6. shows the voids having strain contrast around them. At the higher annealing temperature of 600°C, large voids of low density were observed due to coarsening as shown in Fig. 5.(b). The size of the voids increased to about 2000 Å and the number of the voids decreased with the rise of the annealing temperature. Visible aggregates of defect complex besides the large voids also did appear in the matrix. On the other hand, no voids were observed in specimen B with high carbon content as shown in Fig. 7. (a) and (b).

The effect of solute atoms and point defects has been already studied on iron irradiated by electrons of high voltage electron microscope. The carbon atoms dissolved in iron act as a trap for vacancy and interstitial.[6] V-C pair is the simplest complex and is considered to have the lower binding energy. The de-trap temperature of the V-C pair was estimated at 240°C.[7] Above this temperature, carbon atom and vacancy can migrate due to de-trap from the pair. However, the larger complexes which consist of various V_m-C_n with different value of m and n and having higher binding energies could be formed during irradiation. The dissociation temperature of the V_m-C_n complexes is probably higher than that of the V-C pair, and some of them may be stable even at the irradiation temperature. At the irradiation temperature of 500 ∿ 550°C, although no pairing occurs between the vacancy and carbon atom, the more stable complexes (V_m-C_n) could be formed for a long irradiation period. In a specimen B, with higher carbon content, the number of such complexes becomes greater. Therefore, in the specimen with higher carbon, reduction of free-vacancy might be expected for the same neutron flux. Furthermore, some of carbon

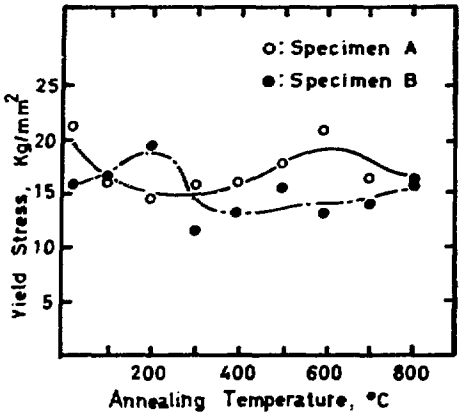

Fig. 4. Yield stress as a function of post-irradiation annealing temperature for specimens A and B.

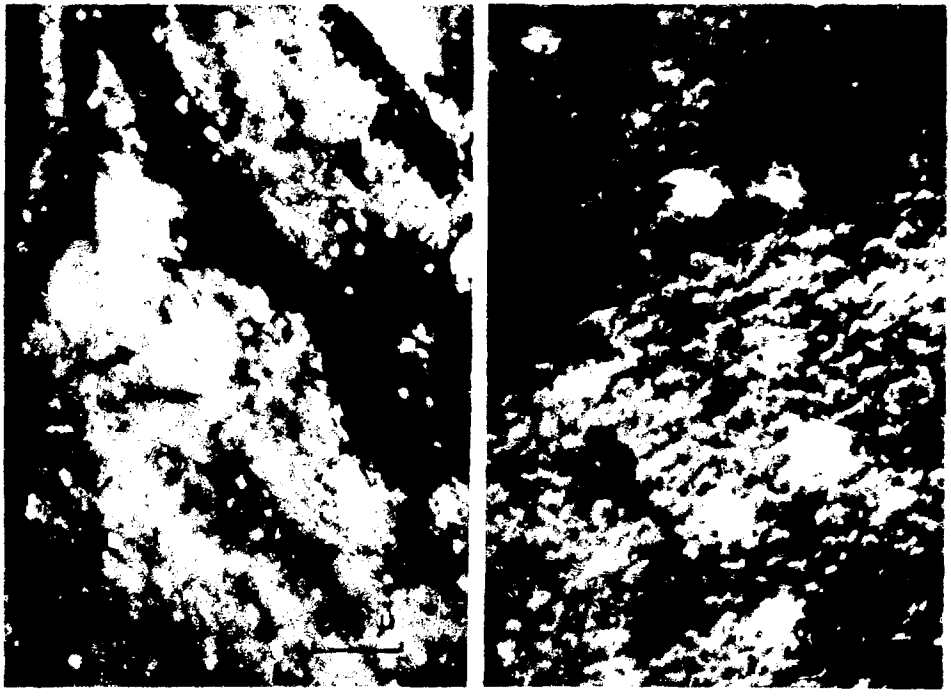

(a) (b)

Fig. 5. (a) Specimen A annealed 1 hr at 200°C, showing no coarsening of voids.
(b) Specimen A annealed 1 hr at 600°C, showing coarsening of voids.

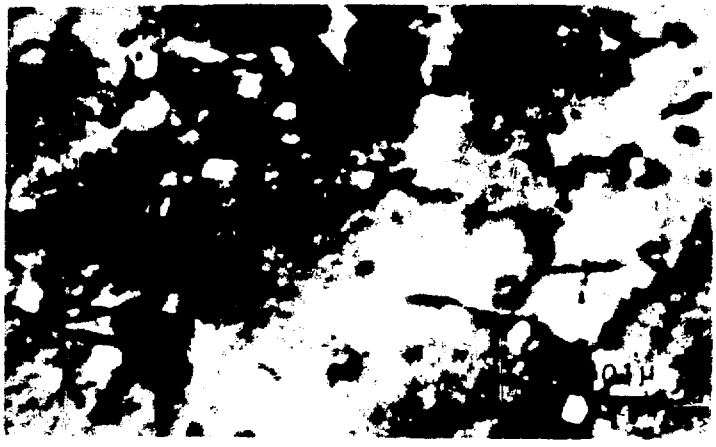

Fig. 6. Specimen A annealed 1 hr at 200°C, showing strain contrast around voids.

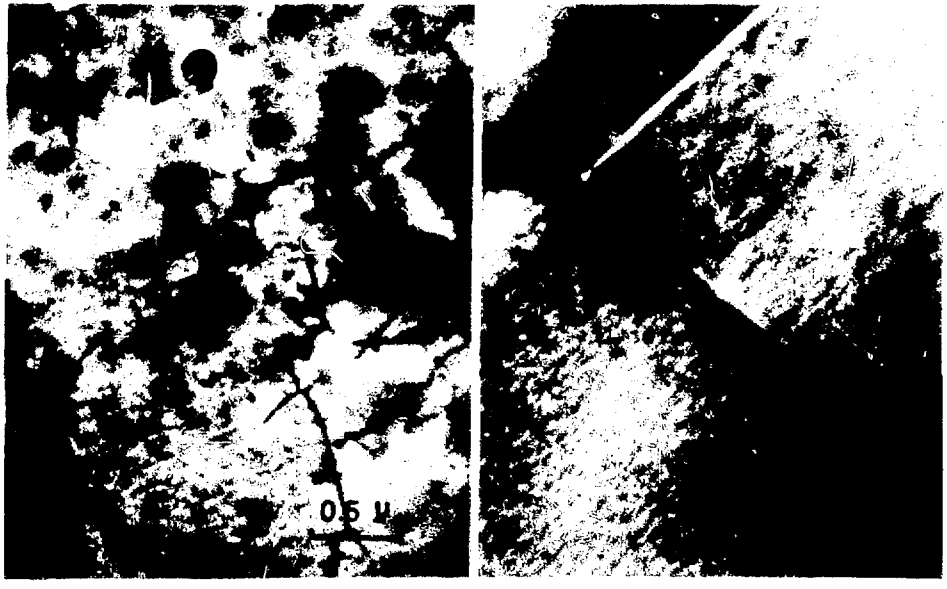

(a) (b)

Fig. 7. (a) Specimen B annealed 1 hr at 200°C, showing no structural change.
(b) Specimen B annealed 1 hr at 600°C, showing no structural change.

atoms can freely move in the lattice at the irradiation temperature and nucleate the cementite and/or aggregate on the already formed particles of cementite. Vacancy may be absorbed on to the cementite-matrix interface and act to relieve the coherent strain developed during the growth of the precipitate. Consequently, the interface can serve as sites for vacancy annihilation and concentration of free vacancy which is available for the formation of voids, may decrease more and more. Swelling should be avoided or delayed to much higher fluences.

SUMMARY

Two kinds of iron with different carbon content, specimen A with 20 ppM and specimen B with 120 ppM, were irradiated to a fluence of $1.2 \times 10^{21} n/cm^2$ ($E > 1$ MeV) at $500 \sim 550°C$.

1. Voids were clearly seen in the specimen A, but they were not distinct in the specimen B.

2. The void was stable after one hr of post-irradiation annealing at 200°C. The void density decreased and the size increased with increasing temperature.

3. Interstitial carbon atoms stabilized the void-nucleation process. The suppression of void-nucleation in iron may result from reaction at the interface of cementite and the formation of C_m-V_n complex.

4. Due to hardening caused by void formation, the yield stress of specimen A was greater than that of specimen B.

ACKNOWLEDGMENT

The authors wish to express their cordial thanks to Professor Seishi Yajima, Director of the Oarai Branch, The Research Institute for Iron, Steel and Other Metals, Tohoku University.

REFERENCES

1. C. Cawthorne and E. J. Fulton, Nature, 216, 575 (1967).

2. D. I. R. Norris, radiation effects 14, 1 (1972).

3. J. W. Corbett and L. C. Ianniello (editors), Radiation Induced Voids in Metals, U.S. Atomic Energy Commission (1972).

4. G. L. Kulcinsky, B. Mastel, and J. L. Brimhall, radiation effects, 2, 57 (1969).

5. T. Takeyama, M. Hachinohe, and Y. Sato, J. Electron Microscopy, 15, 269 (1966).

6. F. E. Fujita and A. C. Damask, Acta Met. 12, 331 (1964).

7. T. Takeyama and H. Takahashi, J. Phys. Soc. Japan, 35, 939 (1973).

COLLISION CASCADES IN IRON AND NIOBIUM

J. R. Beeler, Jr. M. F. Beeler C. V. Parks

North Carolina State University
Raleigh, North Carolina

ABSTRACT

Defect production by collision cascades in fcc iron and niobium was studied using a computer experiment approach. Cascades with energies up to 975 keV and 594 keV were studied for iron and niobium, respectively. In the case of iron, the primary defect state produced directly by each cascade was subjected to short-term annealing (STA) simulation at 566°C. Recipes for the numbers of free defects, defect clusters, microvoids and interstitial loops after STA, as functions of cascade energy, were constructed from the annealing computer experiment results. In the case of niobium, the primary defect state is described. For a given PKA* energy, the displacement production in niobium was about 18% smaller than that in iron. The cascade size in niobium was about the same as that in iron up to 100 keV.

INTRODUCTION

The intent of this paper is to describe the defect state produced in fcc iron and niobium by fusion reactor radiation at elevated temperatures. This description is based on computer experiment results. Attention is centered on the nature of the defect states produced by neutron and heavy ion irradiation. The discussion is self-contained so far as ion irradiation is concerned. In the case of neutron irradiation, however, knowledge of the PKA distribution in space and energy is a prerequisite for full utilization of the defect production results given here. Parkin and Goland[1] have developed a computer program that gives the PKA energy distribution produced by an arbitrary neutron irradiation energy distribution. The defect types considered are free vacancies, free interstitials, immobile vacancy clusters, immobile interstitial clusters, microvoids and interstitial dislocation loops.

*Primary knock-on atom. See second section, SCHEMATIC OVERVIEW.

The maximum energy for PKA produced by 14.1 MeV neutrons in elastic collision events is 975 keV in iron and 594 keV in niobium. These upper limits are larger than the effective PKA energy upper limits for fission reactor neutron irradiation. In the FBR-II reactor, for example, the effective upper limits on PKA energies in iron and niobium are about 300 keV and 188 keV, respectively. The more energetic PKA associated with 14.1 MeV neutron irradiation initiate cascades whose structures are substantially different from those of cascades initiated by the PKA produced by fission reactor neutron irradiation. This difference should be an important consideration in damage simulation and analysis studies for fusion reactor materials.

SCHEMATIC OVERVIEW

Fig. 1 is a schematic diagram of the general radiation-induced defect production process in a metal. Primary radiation particles (PRP) from either an external or an internal source collide directly with constituent atoms of the irradiated material. Atoms directly struck by a PRP are called primary knock-on atoms (PKA). In this paper, PRP include neutrons and heavy ions. Each PKA that receives enough kinetic energy from a PRP to be ejected from its normal atom site initiates a collision cascade. A cascade is a localized dynamic disturbance that is active for a brief time (about 10^{-12} seconds) and then dies out. Some cascades produce vacancies and interstitials that remain after the cascade has died out.

Each additional vacancy-interstitial pair produced is called a displacement event. Given an ejection direction $\underline{D}$, there is a threshold energy $E_d(\underline{D})$ for displacement production. If the PKA energy exceeds $E_d(\underline{D})$, at least one displacement will be produced; if $E \leq E_d(\underline{D})$, a displacement event is not possible. When a cascade produces one displacement, the result is called a Frenkel pair. When a cascade produces two or more displacements, the result is a displacement spike. This distinction arises because the stability rules for a single vacancy-interstitial pair are different from those for a collection of multiple pairs. The threshold energy for displacement spike production will be denoted as $E^u(\underline{D})$. Starting with PKA energy in the range $E_d(E) < E \leq E_i^u(E)$, only one displacement

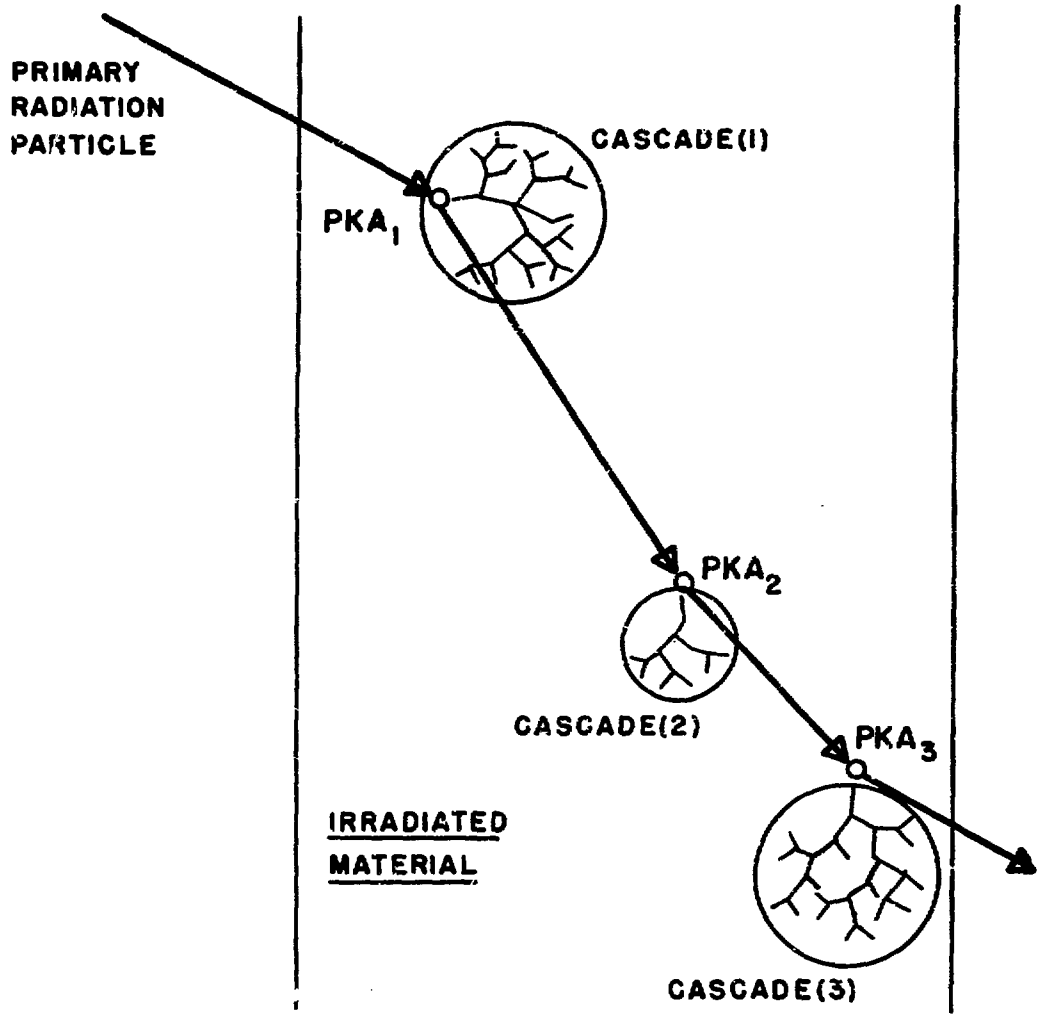

Fig. 1 PKA production by a primary radiation particle (PRP). PKA production sites are represented by small open circles. The collision cascade initiated by each PKA is represented schematically. The PRP concerned in this paper are electrons, heavy-ions and neutrons. Each type of primary radiation gives a different distribution of cascade sizes and distances between cascades.

is produced. For $E > E^{u}(\underline{D})$, two or more displacements are produced.

COMPUTATIONAL MODELS

Cascade Simulation

Two different cascade simulation programs were used in this study. One was the CASCADE Program[2], and the other was the COLLIDE Program[3]. The CASCADE Program considers only elastic atomic collisions but subtracts 8 eV at each collision to represent energy dissipated in extracting a struck atom from its site in the crystal. All CASCADE simulations were for cascade energies of 20 keV or less. COLLIDE treats both elastic and inelastic atomic collisions. The inelastic collision treatment is based on the revised Firsov model developed by Robinson and Torrens[4]. The COLLIDE Program simulates atomic collisions in an amorphous model of the metal concerned whenever the knock-on atom (KA) energy is above $E^{u}(\underline{D})$. At lower KA energies, COLLIDE adopts a crystalline model of the metal concerned and locates the vacancy and/or interstitial associated with the ejected KA at positions given by a dynamical, many-body atomic collision model. The dynamical model results are taken from a catalog of Frenkel pair production results given by the DYNAM Program[5]. The results obtained from these two different models are surprisingly similar. This result supports the view of Robinson and Torrens that directional aspects of cascade evolution are not important at high KA energies. The computational time for COLLIDE is much less than for the fully crystalline solid model program. The direction dependent displacement results for KA with energy below 100 eV in fcc iron were computed using the Erginsoy-Vineyard potential[6]. In the case of niobium, the direction dependent displacement results for low-energy KA were obtained by scaling Erginsoy's results for bcc iron using the ratio of the melting temperatures ($T_m(Nb)/T_m(Fe) = 1.5$). The results are given in Table 1.

The Erginsoy-Vineyard potential was used in the binary collision approximation portion of the cascade simulation for iron. In the case of niobium, the Moliere potential was used in the binary collision approximation portion of the simulation.

Displacement Spike Annealing Simulation

Displacement spike annealing simulations were performed using the RINGO Program[7]. RINGO simulates the simultaneous correlated random walks of up to 1000 vacancy and interstitial defects in a bcc or fcc metal. The random walk jump histories of each defect are followed on a cubic crystal atom site lattice. The interaction radii for vacancy-interstitial annihilation, vacancy clustering and interstitial clustering are those indicated by variational method and dynamical method computer experiments on defect interactions in a discrete lattice system.

CASCADE STRUCTURE

Cascade structure in iron is described by the series of figures, Fig. 2-6. Structurally, a collision cascade consists of a principal trajectory line from which emanate secondary trajectory lines. The principal trajectory line is initiated by the PKA which sets off the cascade. Each secondary trajectory line is initiated by a secondary knock-on atom (SKA) that is ejected in a collision with the PKA that initiated the cascade. This is the fundamental structural motif for a collision cascade in metals.

The collection of collisions associated with a particular secondary trajectory line is called a subcascade. Individual differences in the radiation effects produced by cascades of different energies are the result of differences in the density and energy of their subcascades. This comes about because the elemental defects produced by separate subcascades can interact during displacement spike production. This interaction can take place either by way of focussed collision chains or by way of elastic displacement field overlap. Interactions among subcascades determine the defect content and the physical size of the displacement spike produced by a cascade.

Fig. 3 is a diagram of the subcascade arrangement for a 20 keV cascade in fcc iron. Each circle represents the extent of a subcascade projected onto the plane of the figure. The central line from which each circle diameter emanates is the principal trajectory line of the cascade. The direction of each circle diameter is the initial direction of the

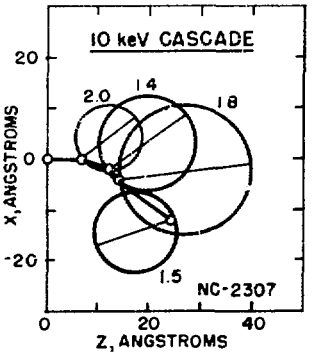

Fig. 2 Structure of a 10 keV cascade in fcc iron. When the cascade energy is less than 15 keV, division into cascade subregions seldom occurs.

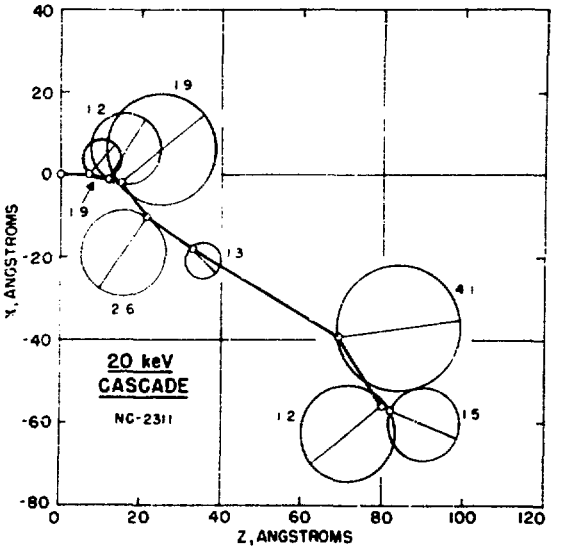

Fig. 3 Structure of a 20 keV cascade in fcc iron. This cascade has divided itself into two cascade subregions. Each circle represents the extent of a subcascade. The number at each circle is the subcascade energy in keV.

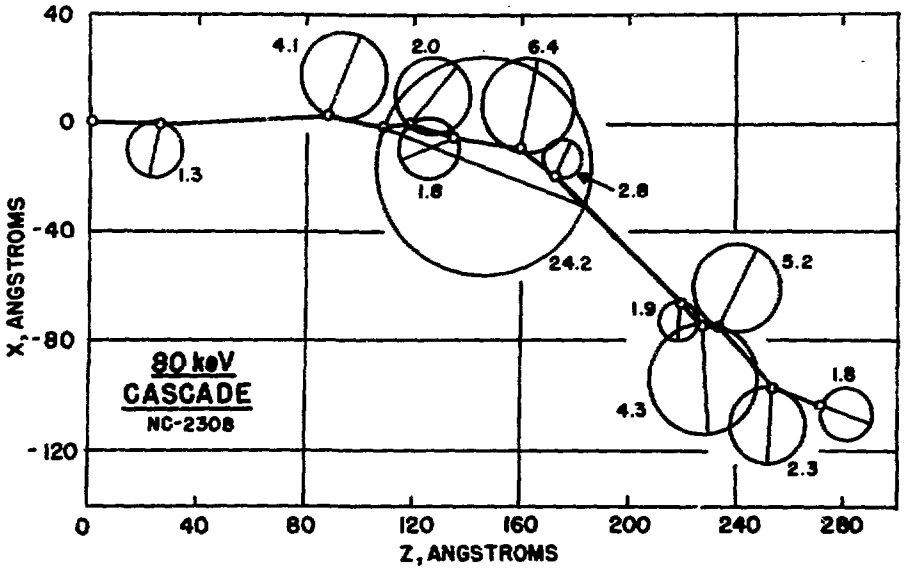

Fig. 4 80 keV cascade in fcc iron.

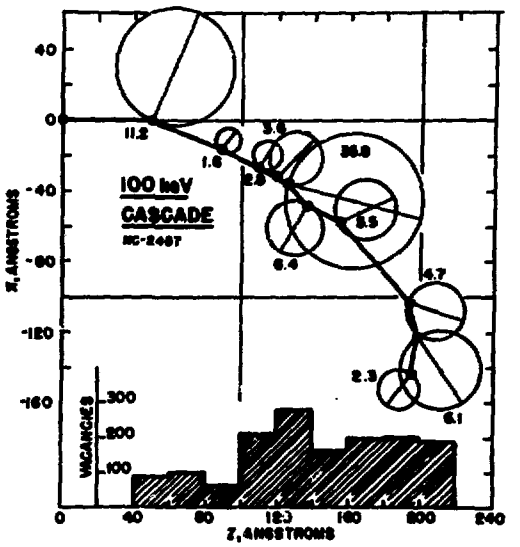

Fig. 5 100 keV cascade in fcc iron.

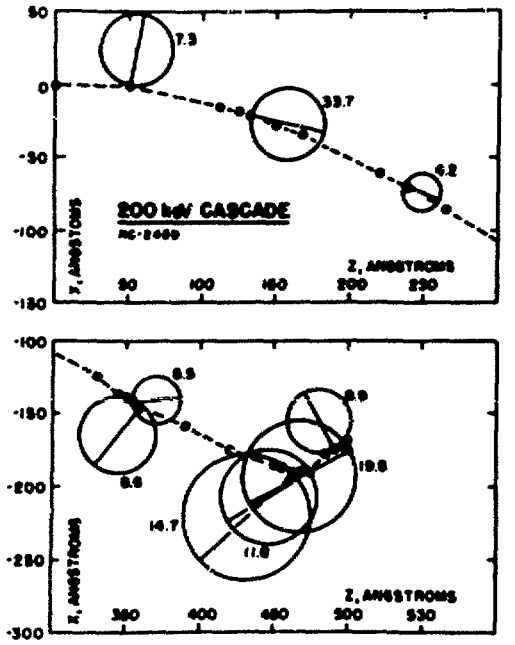

Fig. 6 200 keV cascade in fcc iron.

secondary trajectory line for the subcascade projected onto the plane of the figure. A number appears beside each circle; this number is the subcascade energy in keV. Only subcascades with energy above 1 keV are shown. This particular cascade divided into two groups of closely adjacent and/or overlapping subcascades. Each such group is called a cascade subregion. Cascades with energies above about 10 keV usually divide into two or more cascade subregions, whereas those with energies below 10 keV usually consist of a single group of closely positioned subcascades. The 10 keV cascade in Fig. 3 illustrates this point. The length of the principal trajectory line in a cascade whose energy is 10 keV or less is about the same as the diameter of the subcascades that are produced. For larger energies, however, the principal trajectory line length exceeds the diameter of a typical subcascade and it is possible for distinct cascade subregions to appear.

As the PKA energy rises above 20 keV in iron, the probability for inelastic collisions rises also, and that for elastic collisions decreases. This circumstance leads to an increase in the distance between cascade subregions at the beginning of a cascade with increasing PKA energy. Fig. 4-6 illustrate this effect. The histogram insert in Fig. 5 describes vacancy production by a 100 keV cascade as a function of position along the initial direction of the principal trajectory line.

The structure for the 200 keV cascade shown in Fig. 7 nicely illustrates the kind of cascade structure most often seen for cascades with energies up to 5 MeV in iron. Well separated individual subcascades occur along the initial part of the principal trajectory line. As the initiating PKA slows down, the distance between subcascades decreases progressively and cascade subregions begin to appear. For the maximum energy (975 keV) PKA produced by 14.1 MeV neutrons in iron, the length of the principal trajectory line ranges from 2000 Å to 4000 Å, and the cascade appears as a long string of cascade subregions.

At this writing, the work on cascade structure in niobium is not complete. The cascades which have been examined, however, show a structure pattern similar to that described for iron but with a somewhat smaller spatial extent along the principal trajectory line for energies above

100 keV.

DISPLACEMENT SPIKE ANNEALING IN IRON

Thermally activated defect migration immediately begins to alter the defect distribution and population of a fresh displacement spike. Any spike produced in the cubic metals from vanadium to niobium with energy above 2-3 keV is transformed by thermal annealing into a collection of a few immobile defect clusters that is surrounded by a peripheral array of several mobile defects. The immobile clusters may be either point defect clusters or dislocation loops formed from large, mechanically unstable point defect clusters. It appears as if loops seldom form in iron unless the spike energy is 30 keV or greater. The mobile defect configurations contain from one to three elemental defects. Each peripheral mobile defect soon becomes sufficiently far removed from both the other peripheral defects and the central immobile clusters that it is free of significant interactions with other defects. The subsequent migration of these free defects can be described adequately by diffusion theory models.

The displacement spike annealing regime during which a centralized set of immobile defect clusters and an array of peripheral free defects develop is called short-term annealing (STA). The basic measure for the duration of STA is the average number of migration jumps per surviving mobile defect required. Typically, 5×10^4 to 10^5 jumps per surviving mobile defect are needed to complete STA. In iron, at room temperature, this corresponds to about 4000 microseconds; at 650°C it corresponds to about 0.6 microseconds. Interactions among defects are sufficiently strong and frequent during STA that ordinary diffusion theory continuum models are not appropriate. Atomistic model computer experiments are needed to describe STA events.

The primary defect state in a 30-Å-thick section of a 50 keV displacement spike in iron appears in Fig. 7. The defect state in this same section after STA appears in Fig. 8. The dashed rectangular outline in Fig. 8 indicates the region where the defects in Fig. 7 were located at the beginning of STA. The annealed state contains an interstitial loop

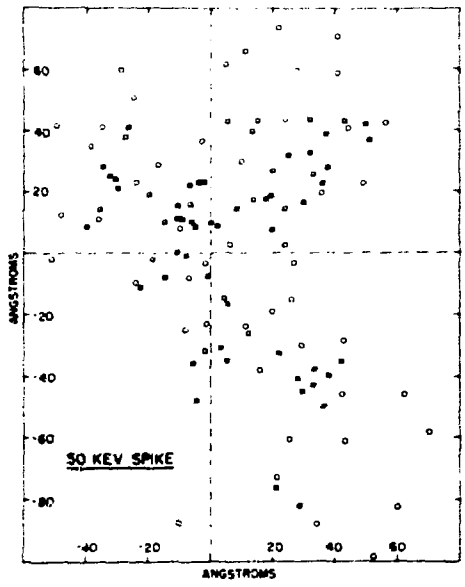

Fig. 7 Fresh 50 keV displacement spike in fcc iron.

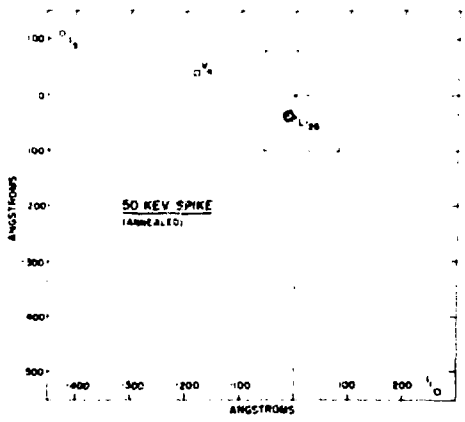

Fig. 8 Annealed 50 keV displacement spike in fcc iron.

(LI_{26}) containing 26 interstitials, a cluster of three interstitials (I_3), a single interstitial (I_1), and a cluster of four vacancies (V_4). This particular section is clearly interstitial-rich. Other sections, not shown here, were vacancy-rich and contained microvoids.

Figures 9 and 10 describe computer experiment annealing of a 20 keV displacement spike in bcc iron, as given by a RINGO Program simulation. These figures illustrate why 10^4-10^5 jumps per surviving mobile defect constitute the duration of STA for displacement spikes. The number of vacancies NVAC is plotted as a function of the number of jumps per mobile defect in Fig. 9. Note that the data points fall along two trend lines, L1 and L2, which intersect at A, corresponding in this instance to 10^3 jumps per mobile defect. The number of jumps (annealing time) asscciated with A correlates with the beginning of a separation between interstitial defects and vacancy defects, and also a separation between mobile defects and immobile defects. The number of vacancies and hence also the number of interstitials changes very little after 10^3 jumps per surviving mobile defect. This indicates that nearly all annihilation events during STA occur during the first 10^3 jumps per surviving mobile defect.

Fig. 10 gives the fraction of elemental defects in immobile clusters as a function of the number of mobile defect jumps during STA. Most interstitial clustering activity occurred during the first 10^3 jumps, indicating that the segregation of mobile and immobile interstitial defects was established during this interval. Vacancy clustering continued until 10^4 jumps, however, indicating a slower segregation of mobile and immobile vacancy defects. Supplementary computer experiments showed that the belated segregation of mobile and immobile vacancy defects is a general trait of displacement spike annealing at reactor temperatures. It arises solely from the initial centralization of the vacancy population in a fresh spike and is independent of the interstitial clustering interaction range and the vacancy jump rate provided the vacancy jump rate is finite.

Isolated displacement spike STA behavior for 1-100 keV spikes exhibits the same principal aspects seen in the 20 keV spike STA example described above. In the interval 10^3-10^4 jumps per surviving mobile defect,

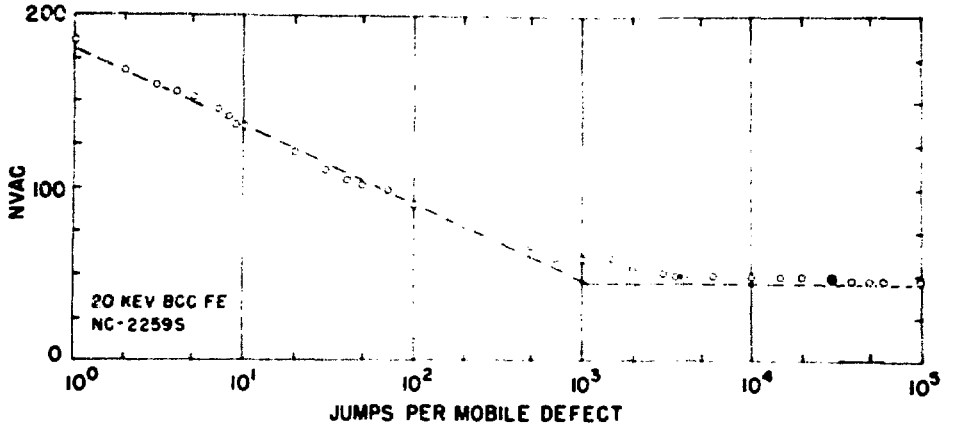

Fig. 9 Number of vacancies (NVAC) during short-term annealing of a 20 keV displacement spike in bcc iron. Annihilation and separation of vacancy and interstitial defects occurs in the region associated with trend line L1. Defect clustering is the main activity in the region associated with trend line L2.

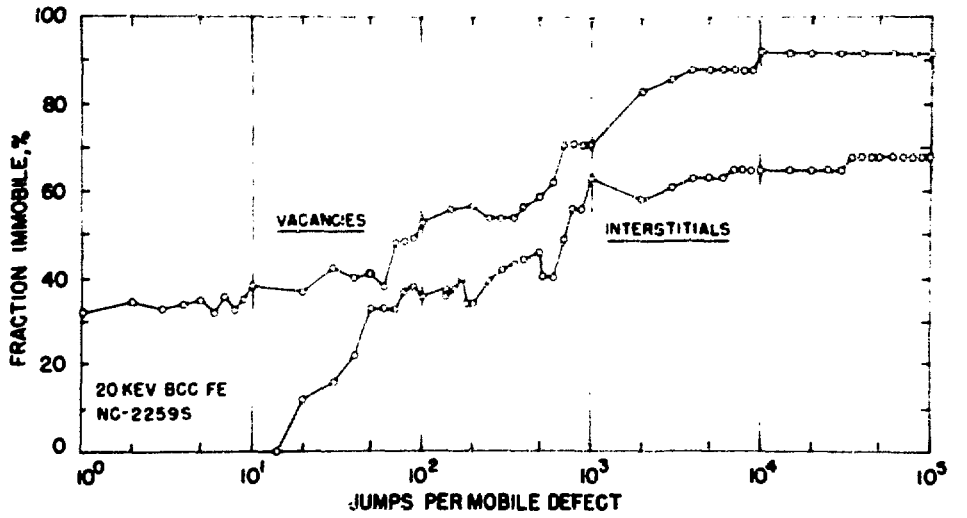

Fig. 10 Fraction of the surviving elemental defects contained in immobile defect configurations during short-term annealing of a 20 keV displacement spike in bcc iron.

the vacancy population becomes separated from the interstitial population to such an extent that the mobile vacancy and mobile interstitial defects existing at this time can be considered as being free defects whose future migration history can be well-approximated by a continuum theory diffusion model.

The annealing process for the free defects remaining after STA is called long-term annealing (LTA). Free defects can undergo extensive diffusion excursions during LTA, whereas defect migration during STA is primarily a localized process. For this reason, LTA is most efficiently described using a diffusion theory continuum model simulation method. The defect source for LTA is the free defect production rate density contributed by STA. The LTA defect sink system consists of all extended defects, immobile defect clusters, and impurity atom configurations in the host metal (alloy). The nature of the defect sink system means that the boundary conditions for LTA are determined by the manufacturing process and the service history of the structural component concerned. Hence, the outcome of LTA nearly always is strongly dependent on the specific engineering application concerned. This sensitivity of LTA results to the particulars of a reactor component's life history as a solid material introduces a statistical aspect into radiation effects forecasting that has not yet been explored systematically.

DISPLACEMENT SPIKE ANNEALING PRODUCTS IN IRON

This section summarizes the results of computer experiments on the products of displacement spike STA in fcc iron at 566°C. Fig. 11 shows the total number of surviving vacancies, free vacancies and free interstitials. Recipes, gotten by fitting the plotted data points and by counting the numbers of different defect structures at the end of STA provide a computational summary of these results. The recipes are as follows:

1. Total Vacancies(TV): $N(TV,E) = 3.7E^{0.83}$ $E > 0.3$ keV
2. Free Vacancies(FV): $N(FV,E) = 1.23E^{0.48}$ $E > 0.3$ keV
3. Free Interstitials(FI): $N(FI,E) = 2.09E^{0.48}$ $E > 0.3$ keV

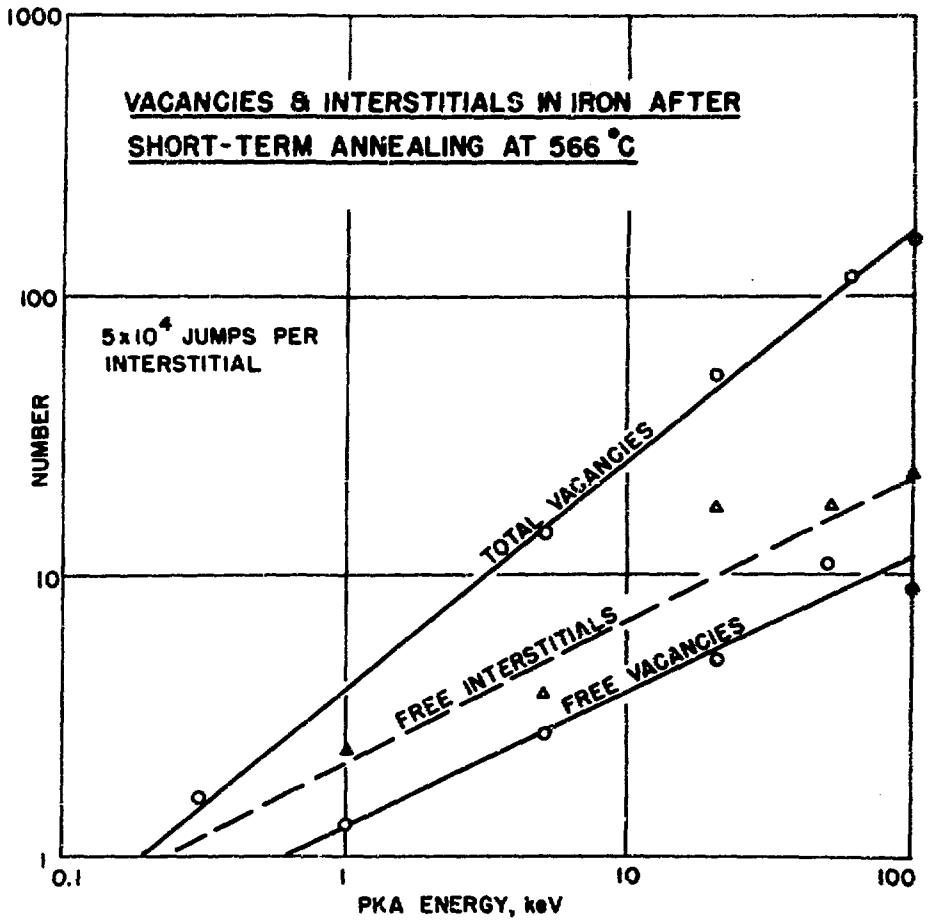

Fig. 11 Total vacancies and free vacancies and interstitials present after displacement spike short-term annealing in fcc iron.

4. Interstitial Loop Nuclei(LI):

N(LI,E) = 0	E < 30 keV
N(LI,E) = 1	30 ≤ E < 40 keV
N(LI,E) = 1-2	40 ≤ E < 100 keV
N(LI,E) = 2-4	100 ≤ E < 200 keV

5. Vacancy Loop Nuclei(LV): Computer experiments for fcc iron indicate that vacancy loop nuclei are not formed during isolated displacement spike STA. If formed, these loops are produced during LTA.

6. Microvoids(MV):

N(MV,E) = 0	E < 20 keV
N(MV,E) = 0.4-1	20 ≤ E < 30 keV
N(MV,E) = 1-1.5	30 ≤ E < 100 keV
N(MV,E) = 1.5-2.1	100 ≤ E < 200 keV

7. Immobile Vacancy and Interstitial Cluster Populations: The number of clustered vacancies is N(TV)-N(FV), and the number of clustered interstitials is N(TV)-N(FI).

8. Displacement Spikes in the Energy Range (E_1,E_2): The displacement spike production rate density for cascades initiated by PKA with energies in the interval (E_1,E_2) is:

$$n(DS) = \int_{E_1}^{E_2} y(E)dE \qquad E > 0.070 \text{ keV}$$

Item No. 8 gives the number density of spikes per unit time. All other items give the defect production per displacement spike. The total number of vacancies, and the number of free vacancies and interstitials remaining in fcc iron after STA of a displacement spike are plotted in Fig. 11.

PRIMARY DEFECT STATE IN NIOBIUM

Short-term annealing computer experiments have not yet been performed for displacement spikes in niobium. This section briefly describes the number of vacancies produced by a cascade in niobium and the projected extent of the vacancy distribution along the initial direction of the

principal trajectory line, i.e., the type of vacancy production extent shown in Fig. 5 for a 100 keV cascade in iron.

Table 2 lists the damage energy, damage energy per vacancy, and the effective displacement energy for niobium cascades. Note that the damage energy per vacancy and E_d increase with increasing PKA energy up to about 100 keV. Above 100 keV, they are constant. This is associated with the transition from a "low-energy" cascade structure to a "high-energy" cascade structure that is illustrated in Fig. 2-6 for iron. The number of vacancies (NVAC) produced and the damage energy fraction $\eta(E)$ are listed in Table 3 along with the vacancy production extent ZV along the principal trajectory line initial direction. For a given PKA energy, vacancy production in niobium is 76% and 87% of that produced in fcc iron at 100 keV and 1 keV, respectively. If roughly the same STA annealing survival fractions apply to niobium as to iron, then about 15% of the vacancies produced by a 100 keV cascade will survive, and about 37% of those produced in a 1 keV cascade will survive STA in niobium. These data enable one to make an approximate total vacancies line on a log-log plot for niobium (see Fig. 11). Table 4 compares vacancy production extent for niobium and iron cascades. Below 100 keV the vacancy extent figures are about the same. Above 100 keV the niobium production range is more compact that that for iron.

CONCLUDING REMARKS

Perhaps the most versatile approach to either forecasting or analyzing irradiation effects in metals proceeds by using the PKA production rate density $y(E)$ as the weighting function for the kinds of defects which survive short-term annealing of a displacement spike produced by cascades of energy E. This approach applies to any type of primary radiation particle field. $y(E)$ for neutron irradiation can be obtained using the Parkin-Goland program. The defect production recipes given in this paper for iron appear to be good approximations for niobium as well.

Table 1. Displacement energy used in the low-energy (< 100 eV) knock-on atom portion of cascade simulation in niobium. $\underline{D}$ is the KA ejection direction region and $E_d(\underline{D})$ is the displacement energy threshold for that region. Prob($\underline{D}$) is the probability for KA ejection in direction region $\underline{D}$.

$\underline{D}$	$E_d(\underline{D})$[a]	Prob($\underline{D}$)
[100]	27	.2466
[110]	57	.1010
[111]	60	.3904
[ran]	90	.2620

[a]The direction dependent displacement energy was approximated by multiplying that for α-Fe by $T_m(Nb)/T_m(Fe) = 1.5$.

Table 2. Damage energy (EDAM) and damage energy per vacancy (EDAM/NVAC) for cascades in niobium. E is the PKA energy and E_d is the effective displacement energy for use in the recipe, NVAC = 0.8 EDAM/$2E_d$.

E,keV	EDAM,keV	EDAM/NVAC	E_d,eV
1	0.90	93	40
5	4.65	105	42
20	18.4	108	43
100	85.7	112	45
200	163	113	45
400	301	112	45
600	432	112	45

Table 3. Vacancy production (NVAC), damage energy fraction (η(E)) and projected extent of vacancy production (ZV) for cascades in niobium. E is the PKA energy.

E,keV	NVAC	η(E)	ZV,Å
1	9	-	15
5	44	0.97	40
20	170	0.94	92
100	760	0.87	360
200	1450	0.82	600
400	2690	0.76	1100
600	3840	0.72	1550

Table 4. Comparison of projected extent of vacancy production by cascades in niobium and iron. E is the PKA energy and ZV is the projected extent.

E,keV	ZV(Nb),Å	ZV(Fe),Å
1	15	-
5	40	-
10	58	65
20	95	90
50	180	175
100	330	320
200	604	660
400	1100	1250
600	1550	∿1900

ACKNOWLEDGMENTS

This work was supported by U.S. Atomic Energy Commission Contract AT-(40-1)-3912, and by computer funds supplied by North Carolina State University.

REFERENCES

1. D. M. Parkin and A. N. Goland, Analysis of Radiation Damage in Fusion Simulation Neutron Spectra, Proceedings of this Conference.

2. D. G. Besco and J. R. Beeler, Jr., USAEC Report GEMP 252 (1964).

3. J. R. Beeler, Jr., USAEC Report ORO-3912-21.

4. M. T. Robinson and I. M. Torrens, Phys. Rev. B 9, 5008 (1974).

5. R. H. Evans, Jr., Ph.D. Thesis, North Carolina State University (1973).

6. C. Erginsoy, G. H. Vineyard, and A. Englert, Phys. Rev. 133, A595 (1964).

7. J. R. Beeler, Jr., USAEC Report ORO-3912-19.

PROTON SIMULATION OF 14 MeV NEUTRON DAMAGE AND LOW TEMPERATURE RECOVERY OF 16 MeV PROTON IRRADIATED IRON*

D.A. Thompson J.E. Robinson

R.S. Walker A.M. Omar

A.B. Campbell

Department of Engineering Physics
and
Institute for Materials Research
McMaster University, Hamilton
Ontario, Canada L8S 4M1

ABSTRACT

The Total Damage Energy deposited into iron bombarded with 14.3 MeV and 17.6 MeV protons, and 14 MeV neutrons has been computed using scattering theory. The results suggest the validity of using high energy protons to simulate 14 MeV neutron damage. Measurements are reported of resistivity change and recovery in α-iron bombarded at 68°K with 16 MeV protons. The results are compared to fast fission neutron data and the calculated damage energies.

INTRODUCTION

In recent years, interest in controlled fusion as a future energy source has rapidly accelerated. Consequently a major emphasis is being placed upon solving the technical problems related to the development of fusion power. Of immediate concern is maintaining the structural integrity of the "first-wall" materials that face the D-T plasma. One of the major aspects under consideration is the high flux of 14 MeV neutrons to which the wall material will be exposed. Currently, considerable effort is being placed in the development of the high flux neutron sources necessary to study this problem. In parallel to this,work is underway using simulation techniques such as ion bombardment.

*Research supported by Atomic Energy of Canada Ltd. and the National Research Council of Canada.

One simulation technique, proposed by Logan and Anderson[1], suggests ∿16 MeV protons to simulate the elastic and non-elastic collision events. Calculations[1] have indicated the recoil energy spectra due to 14 MeV neutrons on niobium are closely approximated by the recoil spectra resulting from 16.4 MeV protons. The major discrepancy would appear to be larger component of low energy recoils resulting from the proton small angle coulomb scattering. However, the defects resulting from these low energy recoils should be relatively simple and anneal out at typical "first-wall" operating temperatures.

Comparison of recent investigations of wall erosion by sputtering infers the validity of this simulation techniques. Experimental studies have reported sputtering yields varying from 0.25 ± 1[2] to 1.5×10^{-5}[3] for 14 MeV neutron irradiated Nb. Studies of Fe, Nb and Au bombarded with the 16 MeV protons[4] were in good agreement with the above neutron lower value and with the calculated sputtering yields.

In this paper we report the results of scattering calculations for 14 MeV neutron and high energy proton bombardment of iron. This is presented in relation to resistivity change and recovery measurements for α-iron bombarded at 68°K with 16 MeV protons.

SCATTERING THEORY

The objective is to determine the fraction of the incident particle energy that is dissipated in the creation of lattice disorder, i.e. the Damage Energy. These calculations assume the occurence of no defect annealing effects.

The procedure is to (i) determine the total primary recoil energy spectrum from the elastic and non-elastic scattering cross-sections, (ii) determine the fraction of the primary recoil energy that goes into atomic collision processes, which allows the Damage Energy Spectrum to be obtained, then (iii) integrate the Damage Energy Spectrum to obtain the total Damage Energy.

Elastic Collisions

For 14 MeV neutrons, the elastic differential scattering cross-sections calculated from otpical potentials by Wilmore and Hodgson[5] were used. The corresponding data for protons (14.3 MeV and 17.0 MeV) were taken from the results of the optical model used by Perey[6] over the range $15^\circ \lesssim \theta_{cm} \lesssim 175^\circ$. For scattering angles greater than 175° the data has been extrapolated. The differential cross-sections for scattering angles less than 15° were obtained using the Rutherford cross sections $(d\sigma/d\Omega)_R$, multiplied by the ratio $(d\sigma/d\Omega)/(d\sigma/d\Omega)_R$ from Melkanoff et al.[7] Using the relationship

$$\frac{d\sigma}{dE_2} = \frac{d\sigma}{d\Omega} \cdot \frac{4\pi}{E_{2(max)}} ,$$

where E_2 is the primary recoil energy and $E_{2(max)}$ is the maximum transferred recoil energy to a target atom by the incident particle, the primary recoil energy spectra were determined. These spectra are shown in Fig. 1.

Non-Elastic Collisions

The non-elastic primary recoil energy spectra, for protons and neutrons with incident energies, E_1, greater than 10 MeV, were obtained following the method described by Grimes et al[8]. The values of the parameters used in the calculations are given in Table 1. Fig. 2 shows the resultant non-elastic primary recoil energy spectra in iron bombarded with 14 MeV neutrons and 14.3 and 17.0 MeV protons. Since the most likely non-elastic event is one in which the ejected particle has almost zero energy, the most probable primary recoil will have energy $E_{max}/4$[8]. This can be clearly be seen in Fig. 2. The contribution from other reactions (e.g. (n,α), $(n,2n)$, (p,α)) were neglected in these calculations since they are relatively low[10].

In Fig. 3 the elastic and non-elastic primary recoil energy spectra were added to obtain the total energy spectra. These total primary recoil energy spectra were converted into Damage Energy Spectra by multiplying by the primary recoil energy weighted by that fraction

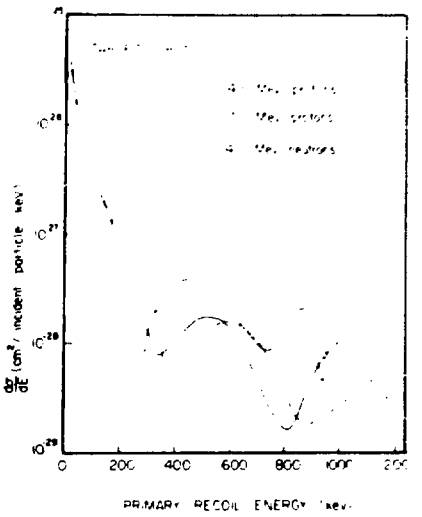

Fig. 1 Primary recoil energy spectra in iron resulting from elastic collisions.

Table 1. Parameters used in calculation of Primary Recoil Spectra for (p,n) and (n,n) non-elastic reactions with iron.

Reactions	E_1(MeV)	σ_R(mb)	$F^{(9)}$	$n^{(9)}$	T_n(MeV)$^{(9)}$
(p,n)	14.3	982	0.11	2	1.2
(p,n)	17.0	1005	0.11	2	1.2
(n,n)	14.0	1460$^{(10)}$	0.15	2	1.1

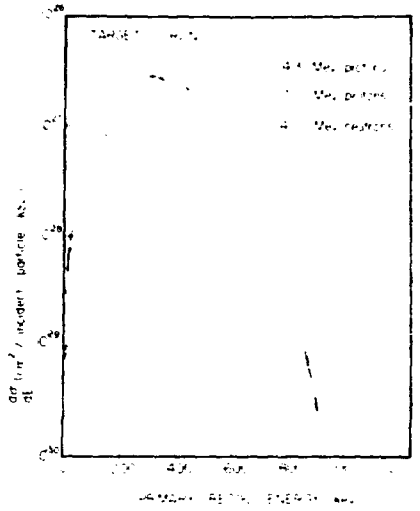

Fig. 2 Primary recoil energy spectra in iron resulting from non-elastic collisions.

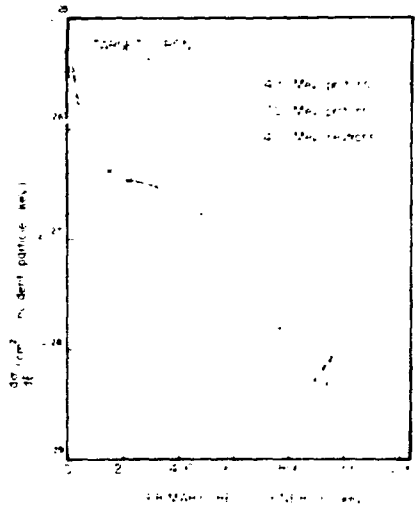

Fig. 3 Total primary recoil energy spectra in iron.

of the recoil's energy that goes into atomic collision processes. The remainder is lost in electron excitation. This fraction is determined, as a function of energy, using an approximation[11] based upon Lindhard's theory[12]. Integration of the Damage Energy Spectrum gives the Total Damage Energy. This is given in Table 2 for various lower energy limits of the integration. Excellent agreement is obtained between 14.3 MeV proton and 14 MeV neutron Damage Energies if only recoils with energy greater than 10 keV are considered. The rapidly increasing proton elastic cross-section for small energy transfer collisions causes recoils with energies < 10 keV to contribute significantly to the Damage Energy. However, as the recoil energy decreases the complexity of the defects will decrease. Hence at elevated temperatures, where only the more complex defect clusters survive, it is expected that the contribution from the small scattering angle proton elastic processes will be significantly reduced.

EXPERIMENTAL

The above infers that the damage effects in iron bombarded with 14 MeV neutrons can be closely simulated using 14-17 MeV protons, especially for higher temperature irradiations. However, since the calculated proton induced Damage Energy is partitioned approximately equally into damage processes resulting from high energy primary recoils (> 10 keV) and low energy primary recoils (< 10 keV) it is significant to obtain information on the effects of the simpler defects. In fact, reference to Table 2 shows that ∿7% of the Total Damage Energy for 14-17 MeV protons goes into the production of recoils with energies < 50 eV, i.e. into the direct formation of single interstitials and vacancies. One method of studying the simplest of these defects is by electrical resistivity measurements. Also, since the defects will be mobile except at low temperature, it was necessary to carry out the irradiation at temperatures below significant recovery stages. Samples of 0.002 in high purity (Marz grade) iron wire were irradiated at 68°K with 16 MeV protons from the McMaster Tandem Van de Graaff, for a total dose of 5.3×10^{17} cm^{-2}. A cryocooler was used to cool the sample to

Table 2. Total Damage Energy calculated down to various lower recoil energy limits.

Lower Limit of Integration (keV)	Damage Energy (barn-keV)		
	Neutron E_1 = 14.0 MeV	Protons E_1 = 17.0 MeV	E_1 = 14.3 MeV
972.2	0	2.97	0.73
600	23.9	20.0	12.3
300	127.4	109.1	81.9
100	217.0	178.7	156.0
10	236.8	271.2	236.2
1	236.8	374.7	259.7
0.5	236.8	405.9	396.9
0.05	236.8	509.3	520.3
0.035	236.8	525.4	539.5
0.025	236.8	540.5	557.5

the base temperature. Two identical samples were mounted on the target holder, one for irradiation and the other to serve as a standard. The resistance was measured using an a.c. technique employing a lock-in amplifier. Resistance changes $\sim 10^{-3} R_o$ (R_o = initial resistance) could be measured. After irradiation, the sample was subjected to 5 minute isochronal anneals up to $\sim 250°K$. The temperature was measured using a calibrated Au(+0.02%Fe)-Chromel thermocouple.

RESULTS AND DISCUSSION

The resistivity increase ($\Delta\rho$) at 68°K as a function of 16 MeV proton dose is shown in Fig. 4. $\Delta\rho$ is observed to increase linearly up to a dose $\sim 2.7 \times 10^{17}$ p/cm^2. For higher doses, a departure from linearity indicates that overlap of defect zones is occuring. Using the modified Kinchin and Pease model[13], and the results of the present Damage Energy calculation (Table 2) it is possible to determine the defect pair concentration (N_D) from the expression

$$N_D = \frac{0.42\ E_D N \phi}{E_d},$$

where E_D = the calculated total Damage Energy for a lower integration limit of 25 eV.,

ϕ = the proton dose,

N = the atomic density,

E_d = the displacement energy.

For 16 MeV protons in iron, E_D has been interpolated from Table 2 as 546.8 barn-keV. Using E_d = 24 eV[14] and a total dose of 2.7×10^{17} p/cm^2, $N_D = 2.2 \times 10^{20}$ defect pairs/cm^3. For this dose, the observed resistivity change is 0.8 μΩ-cm (Fig. 4). Hence the resistivity change/atomic % defect pairs, $\Delta\rho_D$, is 3.1 μΩ-cm. Previous observations[15] for fission neutron irradiation of iron have given $\Delta\rho_D$ = 13 μΩ-cm/atomic % defect pairs. This difference is consistent with the higher-order defect structures, resulting from the more energetic proton bombardment, contributing a smaller resistivity change per defect pair within the cluster than would be expected for the lower-order clusters due to fission

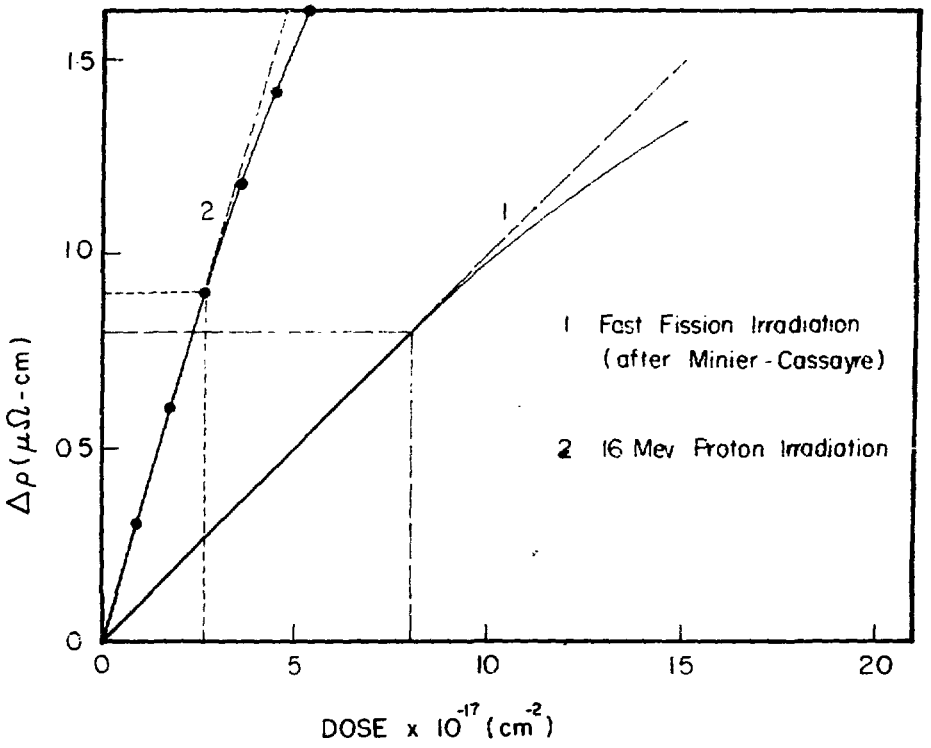

Fig. 4 Measured resistivity change in iron bombarded at 68°K with 16 MeV protons as compared to the resistivity change for fast fission neutron irradiation at 77°K

neutrons. Moreover, the measured value of $\Delta\rho_D$ for electron irradiation is 19 μΩ-cm/atomic % defect pairs[16], the trend being consistent with the above argument.

Also shown in Fig. 4 are the results of Minier-Cassayre[15] for fast fission neutron irradiated iron at 80°K. Damage saturation effects are seen to occur at about the same resistivity change as for the 16 MeV protons. Over the linear region ($\phi \lesssim 8\times10^{17}$ n/cm^3) a resistivity change/fast neutron of 9.8×10^{-19} μΩ-cm/(n/cm^2) is observed. This is a factor ∿3.5 smaller than that for 16 MeV proton bombardment where the resistivity change/proton is 3.3×10^{-18} μΩ-cm/(p/cm^2).

The results of carrying out 5 min. isochronal anneals are shown in Fig. 5. Three distinct recovery stages are observed. Approximately 55-60% recovery of the damage induced resistivity occurs at 120°K. Additional recovery occurs in two steps at ∿180°K and ∿210°K. After 250°K anneal, the total observed recovery is ∿90%. These recovery peaks agree with those observed by Horak and Blewitt[17] for fast fission neutron irradiated Fe, where three similar recovery stages are observed, but at slightly lower temperatures (stage I at 115°K, and stage II in substages at 167°K and 195°K). The magnitudes of the recovery in the fast neutron damage case are ∿40-45% for stage I and a total recovery of ∿80-85% after 250°K anneal. Since these recovery stages have been attributed to the anneal of simple defect structures[15,18], then ∿90% of the observed resistivity increase after 16 MeV proton bombardment results from these simple defects. If these simple defects contribute 19 μΩ-cm/atomic % defect pairs[16], and their observed resistivity contribution is 0.9x3.1 μΩ-cm/atomic % defect pair, then the fraction of the total damage in the form of simple defects is ∿15%. This compares reasonably well with the calculated ∿7% simple defect production.

SUMMARY

1. Comparision between the measured resistivity change per defect pair created by 16 MeV protons at 68°K and fast fission neutrons at 80°K suggests that higher order defect clusters dominate the proton induced damage, these clusters making a relatively small contribution to the

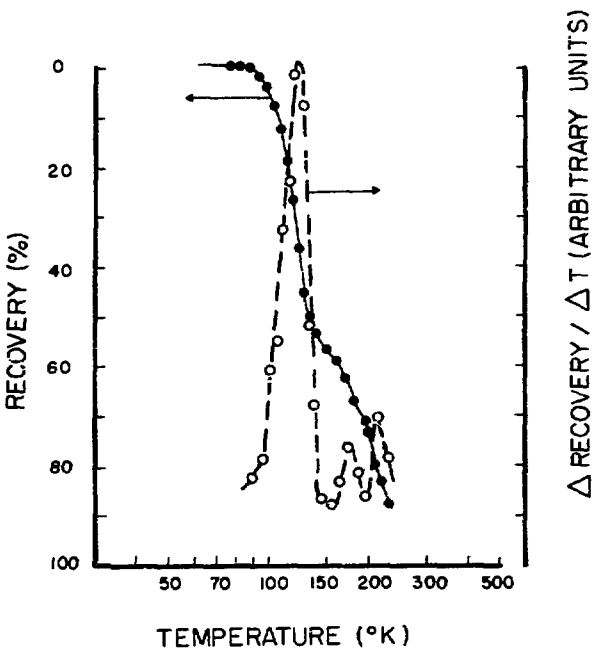

Fig. 5 Recovery and differential recovery spectra for iron bombarded with 16 MeV protons at 68°K

resistivity change. Anneal studies show that simple defects account for most of the observed resistivity change since ∿90% recovery occurs by 250°K.

2. Calculations based on scattering theory in iron show that 14-17 MeV proton damage is a good simulation of fusion neutron damage considering only primary recoils > 10 keV. However the calculations show deviations occur in the range where simpler defects would be produced directly by the bombarding proton. Measurements of these simpler defects produced are in reasonable agreement with the calculated values.

3. The 16 MeV proton induced resistivity recovery agrees well with that resulting from fast fission neutron irradiation.

REFERENCES

1. C.M. Logan and J.D. Anderson, Proceedings of the International Conference on Defects and Defect Clusters in B.C.C. Metals and Their Alloys, Gaithersburg, Md. (1973) p.383.
2. M. Kaminsky, J.H. Peavey and S.K. Das, Phys. Rev. Lett. 32, 599 (1974).
3. O.K. Harling, M.T. Thomas, R.L. Brodzinski and L.A. Rancitelli, Phys. Rev. Lett. 34, 1340 (1975).
4. J.E. Robinson and D.A. Thompson, Phys. Rev. Lett. 33, 1569 (1974).
5. D. Wilmore and P.E. Hodgson, Nucl. Phys. 55, 673 (1964).
6. F.G. Perey, Phys. Rev. 131, 745 (1963).
7. M.A. Melkanoff, J.S. Nodvik, D.S. Saxon and R.D. Woods, Phys. Rev. 106, 793 (1957).
8. S.M. Grimes, J.D. Anderson, B.A. Pohl, J.W. McClure and C. Wong. Phys. Rev. C. 4, 607 (1971).
9. S.M. Grimes, Lawrence Livermore Laboratory, private communication (1975).
10. M.D. Goldberg, V.M. May and J.R. Stern, "Angular Distribution in Neutron Induced Reactions", BNL 400, 2nd ed., Vol. II, Brookhaven National Laboratory (1962).
11. M.T. Robinson, Proceedings of the British Nuclear Energy Society Conference on Nuclear Fusion Reactors, Abingdon (1969) p.364.
12. J. Lindhard, V. Nielsen, M. Scharff and P.V. Thomsen, Kgl.Danske Videnskab,Selskab, Mat.-Fys. Medd, 33, No. 10. (1963).

13. P. Sigmund, Appl. Phys. Lett. 14, 114 (1969).
14. R.G. Lucasson and R.M. Walker, Phys. Rev. 127, 485, 1130 (1962).
15. C. Minier-Cassayre, O.R.N.L. Report No. 668 (1965).
16. A. Lucasson, P.G. Lucasson and R.M. Walker, Proceedings of the International Conference on Reactor Materials and Radiation Damage, p.83, Butterworth, London, 1962.
17. J.A. Horak and T.H. Blewitt, J. Nucl. Mater. 49, 161 (1973/74).
18. S. Takamura, H. Maeta and S. Okuda, J. Phys. Soc. Japan, 26, 1125 (1969).

MODELING OF SYNERGISTIC EFFECTS OF DISPLACED ATOM AND TRANSMUTANT DAMAGE IN FISSION AND FUSION ENVIRONMENTS

G. R. Odette
S. C. Langley

University of California
Santa Barbara, California 93106

ABSTRACT

The effect of simultaneous production of displaced atoms and transmutant helium on damage microstructural evolution is studied. A range of helium generation rates which encompasses both fission and fusion reactor environments is treated. The effect of helium on the damage microstructure at the end of the nucleation stage is discussed qualitatively and treated in a growth calculation parametrically. Diffusion limited rate equations are used to model the growth at bubbles, voids and loops for various nucleation microstructures and irradiation conditions. The results of the calculations indicate that void formation and growth may be severely restricted in fusion environments at temperatures near or above the normal swelling peak. This is due to formation of a high density of small bubbles at high helium generation rates which serve as point defect sinks and enhance void vacancy emission. At lower helium generation rates characteristic of fission reactors, or at lower temperatures, the influence of transmutant helium on total void swelling is less.

INTRODUCTION

Significant variables which influence irradiation behavior of structural materials include composition and microstructure, temperature, particle type, flux, fluence, and energy spectrum. Of these, only neutron flux spectra characteristic of fusion reactor conditions cannot be reasonably duplicated in existing facilities*. In hard controlled thermonuclear reactor (CTR) spectra, production rates of hydrogen and helium

*It is recognized that the periodic nature of some CTR irradiations may be an important factor in influencing damage behavior. However, in the work reported here only continuous irradiations are considered.

from threshold reactions are generally high relative to those in fission reactors. These gases may act alone or synergistically with displaced atom damage to produce radiation damage. Displaced atom defect generation rates in most conceptual CTR designs do not exceed those in present fission reactors. Hence, a major difference in fission and fusion environments is the ratio of helium (and hydrogen) to displacement production rate which is distinctly higher in CTRs[1].

Therefore, it is important to estimate the consequences of He production rates on damage microstructural evolution, and hence on dimensional stability and mechanical properties. Although the models are only approximate, they are useful: in assessing possible qualitative differences in behavior in various environments; in testing and developing damage correlation procedures; in estimating the relevance to the CTR program of available environments; in suggesting useful experiments; and in analyzing data as it becomes available.

PHENOMENALOGICAL DESCRIPTION OF THE MODEL

Nucleation Microstructure

The model is based on the premise that a nucleation microstructure composed of voids, gas filled helium bubbles, and dislocation loops forms early in irradiation. The total number density of voids and bubbles, and also loops is assumed to be constant thereafter. Such behavior has been indicated in nucleation calculations because of the reduced point defect supersaturation and the lowering of the probability of forming new nucleation sites resulting from the buildup of irradiation induced sink microstructure.

A model of coupled bubble and void nucleation and growth has been previously reported[2] and an advanced version has been developed and is undergoing testing. Hayns[3] has reported nucleation calculations for dislocation loops. Both the previous calculations and preliminary runs using the advanced model are consistent with the following qualitative description of the nucleation microstructure for temperatures at or slightly above the normal swelling peak (nominally ~550°C).

1. At relatively low helium generation rates, G_{He}~10^{-13} apa/sec, and low displacement rates, G_d~10^{-6} dpa/sec, a low density of bubbles nucleate and grow to the size where they act as void nucleation sites. A large fraction of the bubbles transform to voids after a time delay associated with bubble growth and nucleation incubation time. Homogeneous nucleation is not significant but other heterogeneous nucleation sites may contribute voids. When heterogeneous nucleation sites are exhausted and point defect concentrations decreased by the prior irradiation induced sink microstructure, nucleation ceases and the microstructure is primarily composed of voids, C_v~10^{13}-10^{14} void/cm^3, and loops, C_ℓ~10^{13}-10^{14} loops/cm^3. Such behavior is characteristic of calculations for fission reactor environments.

2. At low displacement rates, G_d~10^{-6} dpa/sec, and high helium generation rates, G_{He}~10^{-11} apa/sec, which would be found in a fusion reactor environment, a significantly higher bubble density form. Crude theory predicts the density to vary approximately as the square root of the generation rate[4]. At high densities effectiveness of the bubbles as defect sinks is enhanced relative to a similar helium content at lower densities. Thus lower point defect concentrations result in lower nucleation rates and increased incubation times for void formation. Hence, these microstructures tend to be characterized by a high density of bubbles, C_b~10^{15} -10^{16}/cm^3, and a low concentration of voids, C_v<10^{14}/cm^3, and loops, C_ℓ<10^{14}/cm^3.

3. At very high displacement rates, G_d>10^{-4} apa/sec, which might be found in charged particle irradiations voids readily nucleate and grow with or without the presence of helium, although preinjected helium can result in a somewhat higher void density. However, a very high density of small bubbles might at moderate displacement rates, G_d~10^{-4}-10^{-6}, suppress nucleation by lowering defect concentrations without themselves serving as nucleation sites.

At high temperatures (600°C) a low density of bubbles nucleates and grows with little void swelling. At low temperatures (<500°C) a high density of bubbles forms and serves as void nucleation sites. At still lower temperatures helium is essentially immobile and has little effect on void nucleation (however, lattice helium might trap vacancies, hence enhance recombination).

Of course, the specific calculational results are dependent on the choice of material parameters and model assumptions. Critical factors appear to include the activation energy for helium diffusion, taken as ~1.5-2.0 eV, and the assumption that a di-helium atom cluster is the stable bubble nucleus. Since the nature of helium mobility in solids under irradiation is not well understood and helium-vacancy cluster parameters ill-defined, additional experimental and theoretical work is needed to clearly establish the influence of helium on nucleation microstructures.

Growth Calculations

The description of the nucleation microstructure based on calculations given above is generally in qualitative agreement with experimental observations. However, due to the model uncertainties noted above, the nucleation microstructure is treated parametrically in this work by assigning some initial density (and size) to bubbles, voids and loops as input into a growth calculation. These densities are varied along with other relevant parameters to study the effect of helium on microstructural evolution.

• Bubbles are initially taken to be nearly in equilibrium, i.e., internal gas pressure plus excess vacancy chemical stress is balanced by surface tension. Conversely, voids are not completely stabilized by internal gas pressure but, having previously nucleated and grown, are of sufficient size to undergo continued stable growth.

This behavior is schematically illustrated in Figure 1, where growth rates of helium vacancy clusters are plotted as a function of cluster radius. Curve 1 shows a case where the net vacancy flux (vacancies minus interstitials) at neutral sinks (i.e., bubbles) result in a stable bubble size r_b and critical void size r_v^*. A fraction of the bubbles can grow

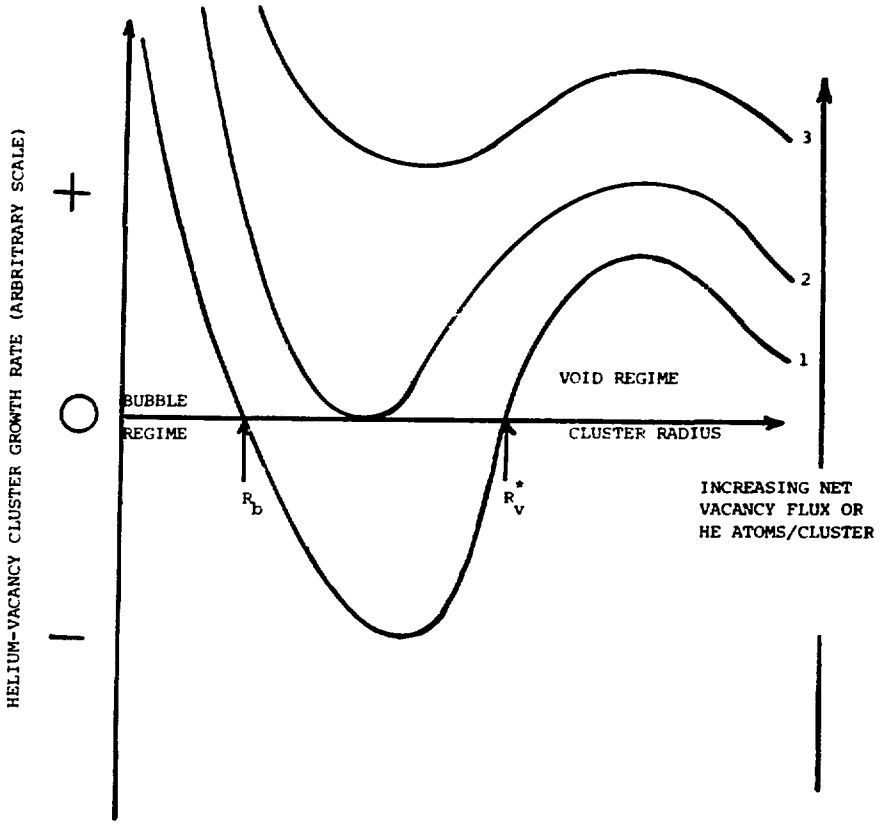

Fig. 1. Schematic illustration of growth velocities of bubbles and voids as a function of cluster radius.

from r_b to r_v^* by statistical nucleation. However, the nucieation rate is assummed to be negligable in these calculations. Beyond r_v^* is a region of continuous void growth. The other curves show the effect of increasing either the net vacancy flux or the number of helium atoms in a cluster. Curve 2 illustrates a situation where the stable bubble and void size are the same (i.e., there is no nucleation barrier) and curve 3 the case when only void growth is possible.

As irradiation proceeds bubbles grow at a rate controlled by the addition of helium, and voids grow at a rate primarily determined by the net vacancy flux. Void and loop* growth rates are determined from the rate equations for diffusion limited swelling. Stable bubble radii are calculated as a function of the number of helium atoms and net vacancy flux. Bubbles can grow to the point where they transform to voids, or conversely voids may shrink to bubbles (in cases where the helium generation rate is very high, voids may refill with gas and grow as driven bubbles).

Helium generated is partitioned between the various sinks according to the relative sink strengths.** Vacancy and interstitial concentrations are taken at steady state levels as determined by generation rates and total existing sink strength. Biased sinks include initial network and radiation induced Frank loop dislocations. Neutral sinks are bubbles and voids (other sinks such as precipitates and grain boundaries can be easily added but should not alter the qualitative results of the calculations).

QUANTITATIVE MODEL DESCRIPTION

Rate equations for diffusion limited defect growth have been derived by a number of workers[5-7]. The treatment here closely parallels the method of Brailsford and Bullough[7].

---

*Different procedures may be used to specify the dislocation sink strength as discussed in the next section.

**Simple partitioning of helium between sinks is not good approximation at low temperatures when the helium is immobile. In such circumstances the model would tend to overestimate the influence of helium on void and bubble growth.

Vacancy and interstitial concentrations c_v and c_i found by the solution of

$$G_v' - D_v c_v S_v - \alpha c_i c_v = 0 \tag{1a}$$

and

$$G_i - D_i c_i S_i - \alpha c_i c_v = 0 \tag{1b}$$

Here D_i and D_v are the interstitial and vacancy diffusivities, S_v and S_i the vacancy and interstitial sink strengths, and α the lattice recombination coefficient. The effective vacancy generation rate G_v' includes both surviving displacement defects, G_d, and vacancy emmission from clusters as

$$G_v' = G_d + D_v \left\{ \sum_j 4\pi r_j C_j \bar{c}_j + 2\pi r_\ell C_\ell \bar{c}_\ell + \rho_d^\circ \bar{c}_\ell \right\} \tag{2}$$

Here the summation is over the various helium-vacancy clusters (bubbles and voids and dislocations) where r_j and r_ℓ are the cluster and loop radii, and C_j and C_ℓ are the cluster and loop densities, and ℓ_d° the initial network dislocation density. The factor $\bar{c}_i$ is the vacancy concentration in equilibrium at the surface of a cluster

$$\bar{c}_j = c_v^e \exp\left[(2\gamma/r_j - P_j)\,\Omega/kT\right] \tag{3a}$$

for bubbles and voids, and

$$\bar{c}_\ell = c_v^e \exp\left[-(\gamma_{sf} + F_{e\ell})\Omega^{2/3}/kT\right] \tag{3b}$$

for dislocation loops. P_i is the gas pressure in the cluster, γ the surface energy, Ω the vacancy volume, T temperature, c_v^e the thermal equilibrium vacancy concentration, γ_{sf} the loop stacking fault energy and $F_{e\ell}\Omega^{2/3}$ the elastic energy opposing loop growth where

$$F_{e\ell} = \frac{\mu b^2}{4\pi(r_\ell + b)} \ln\left(\frac{r_\ell + b}{b}\right) \tag{3c}$$

Here b is the Burgers vector and μ the shear modulus. The ideal gas law is used to determine P_i and the interstitial generation rate G_i is defined as $G_i=G_d$.

The sink parameters S_i and S_v are defined as

$$S_i = Z_i \left(\rho_d^\circ + 2\pi r_\ell C_\ell\right) + \sum_j 4\pi r_j C_j \tag{4a}$$

and

$$S_v = \rho_d^\circ + 2\pi r_\ell C_\ell + \sum_j 4\pi r_j C_j \tag{4b}$$

The factor Z_i which is greater than one reflects the dislocation bias for interstitials.

The growth rate of voids of class j is given by

$$\frac{dr_j}{dt} = \frac{G_d}{r_j}\left\{D_v c_v - D_i c_i - D_v \bar{c}_j\right\} \tag{5a}$$

Other methods of specifying dislocation sink density are available, including a constant value throughout irradiation. Helium is partitioned between the sinks as

$$\frac{dHe_j}{dt} = G\left\{\frac{r_j C_j}{\sum_j r_j C_j}\right\} \tag{6}$$

where He_j is the number of helium atoms in the j'th cluster. These equations are numerically integrated starting at time zero using a Hammings predictor corrector method for a given set of cluster densities and initial sizes. Loop density is also specified and the initial loop radius calculated assuming the excess interstitials corresponding to the initial swelling are distributed uniformly between the loops.

If the cluster is not growing except via the addition of helium it is a stable bubble. The bubble radius is found by determining the smallest root of the equation

$$f\left[He_j, r_j, (D_v c_v - D_i c_i)\right] = \ell n\left[\frac{D_v c_v - D_i c_i}{D_v c_v e}\right] + \left(P_j - \frac{2\gamma}{r_j}\right)\frac{\Omega}{kT} \tag{7}$$

A test is made at each time step to see if bubbles have converted to voids in which case Eq. (7) has either zero or one finite root.

The swelling behavior for various situations is studied. Parameters which can be varied include nucleation microstructures (initial void, bubbles and loop densities and sizes); irradiation conditions (temperature and helium and displacement generation rates); and material parameters (including bias factors, network dislocation densities, surface energy, migration energies). In the work reported here bubble and void densities, helium generation rates, and temperature are varied over ranges characteristic of fission and fusion irradiation environments. Displacement rates are set at 10^{-6} dpa/sec which is nominal for both CTRs and fission reactors. Material parameter values are those frequently used in the literature, and nominally representative of nickel. An additional constraint that clusters specified as voids have a radius large enough to give a positive initial growth rate is imposed. The run parameters are given in Table 1. Although the quantitative results are certainly sensitive to the particular set of parameters selected, the qualitative trends resulting from altering nucleation microstructures and irradiation conditions should be physically realistic.

However, it must be emphasized that the parametric treatment of the nucleat microstructure does not imply that the entire range of cluster densities or initial sizes are physically appropriate in all the circumstances studied. Rather, the parametric treatment seeks to indicate: ranges of potential behavior; the sensitivity of swelling to the model parameters; and the implications of existing uncertainties in specifying these parameters.

To further facilitate understanding of growth phenomena a continuous monitor of the fate of radiation induced vacancies is included in the calculations. The following quantities are tabulated:

1. Vacancies lost due to lattice recombination.
2. Total vacancies which go to voids.
3. Total vacancies which go to bubbles.
4. Total vacancies which go to dislocations.
5. Void vacancies lost due to the interstitial flux.
6. Void vacancies lost due to thermal emission.

RESULTS AND DISCUSSION

Two series of runs are included involving different treatment of dislocation sinks. In the first one initial loop density of $C_\ell = 10^{13}/cm^3$ is specified and loop growth is calculated as discussed previously. The helium generation rate is varied between 10^{-13} to 10^{-11} apa/sec, temperatures between 450 and 550°C, void densities between 10^{13} and $10^{14}/cm^3$, and bubble densities between 10^{14} to $10^{16}/cm^3$. A displacement rate of 10^{-6} is used in all runs. Initial bubble radii are specified at 2Å (typically, 20-30 helium atoms/cluster) and voids at 50Å. Results are fairly insensitive to the specific choice of these parameters providing the void character is initially preserved*. All calculations are carried out to 10 dpa.

Figure 2 shows plots of calculated swelling at 10 dpa as a function of G_{He} for various nucleation microstructures at 550°C. It is evident that an increase in bubble density decreases swelling substantially. Also, in some cases of intermediate to high bubble densities, increasing helium generation rate decreases swelling further.

At lower temperatures no effect of helium generation rate was observed. Figure 3 shows swelling at 10 dpa as a function of total void and bubble concentrations for $G_{He}=10^{-11}$ apa/sec. It can be seen that increasing the cluster density first increases then decreases total swelling depending on the temperature. Figure 4 shows swelling at 10 dpa as a function of temperature for various bubble and void densities and helium generation rates. The temperature dependence of swelling is clearly effected by the nucleation microstructure and in some cases by the helium generation rates, with peak swelling temperature decreasing with increasing cluster density.

By examining the fate of the vacancies in detail, further insight can be gained as to what physically meaningful conclusions can be drawn from these calculations as opposed to effects which are largely artifacts of the model. A number of examples of such vacancy fates are tabulated in Table 2. Final cluster radii, helium contents and the dose at bubble to void conversion (if this occurs) are also listed in Table 2.

*However, because of this factor and potential errors in the integrations the results should be considered numerically accurate only to about ±10%.

Table 1. Fixed Parameters Used in the Study*

Vacancy diffusivity D_i	0.6 exp (-1.4/kT) cm^2/sec
Vacancy equilibrium concentration C_V^e	exp (-1.5/kT) atomic fraction
Interstitial diffusivity D_V	exp (-1.09/kT) cm^2/sec
Dislocation Interstitial Bias Factor, Z_i	1.1
Surface Energy, γ	1000 ergs/cm^2
Loop Density, C_ℓ	$10^{13}/cm^3$
Stacking fault energy γ_{SF}	15 ergs/cm^2
Initial dislocation density ρ_d^o	$10^9/cm^2$
Shear modulus, μ	$4x10^4 MN/m^2$
Recombination coefficient α	10^{17} D_i
Atomic volume Ω	$1.07x10^{-23} cm^3$**
Burgers vector b	2.5Å
Displacement rate G_d	10^{-6} apa/sec

* These values in general correspond to those suggested by Brailsford and Bullough [8].

** For runs with a constant dislocation density at $\rho_d = 10^{10}$, Ω was taken as $.8x10^{-23}$ and b as 2Å following Brailsford and Bullough [8].

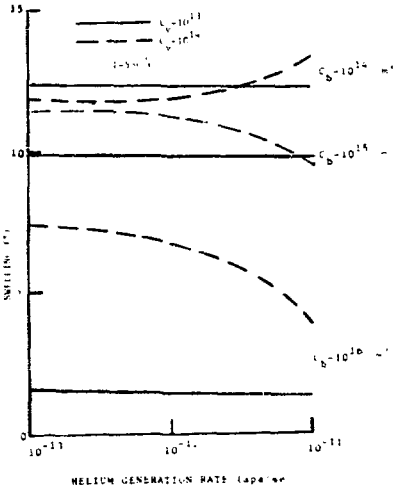

Fig. 2. Swelling as a function of helium generation rate for various nucleation microstructures at 550°C.

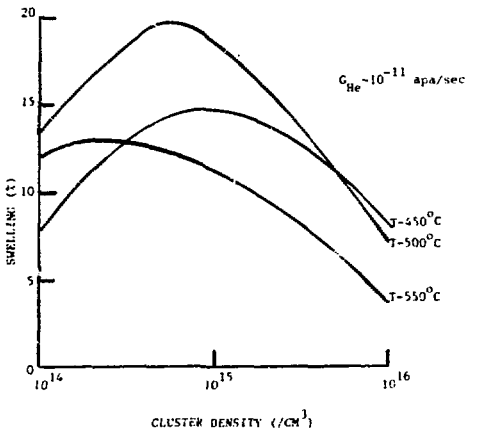

Fig. 3. Swelling as a function of cluster (void plus bubble) density for various temperatures for $G_{He} = 10^{-11}$ apa/sec.

KEY

CURVE	C_b^*	C_v^*	G_{He}^{**}	CURVE	C_b	C_v	G_{He}
A	10^{14}	10^{14}	10^{-11}	E	10^{16}	10^{14}	10^{-13}
B	10^{14}	10^{13}	10^{-11}	F	10^{16}	10^{14}	10^{-12}
C	10^{15}	10^{14}	10^{-13}	G	10^{16}	10^{14}	10^{-11}
D	10^{15}	10^{13}	10^{-11}	H	10^{16}	10^{13}	10^{-11}

*-/CM^3 **-apa/sec.

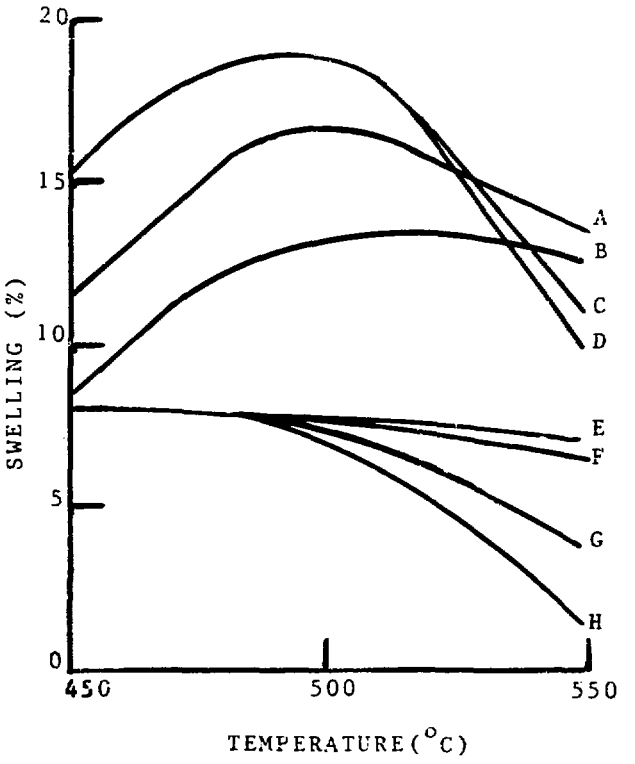

Fig. 4. Swelling as a function of temperature for various nucleation microstructures and helium generation rates.

Table 2. Detailed Results of Swelling, Vacancy Fate and Final Cluster Parameters for Selected Cases[1]

Run No.	Run Parameters					Initial Vacancy Distribution to Sinks Vacancies lost to: %				Void vacancies lost to: %[2]				
	T	C_b	C_v	G_{He}	Swelling at 10dpa	Recombination	Voids	Bubbles	Dislocations	First to Interstitial Flux	Remaining to Emmission	Dose at Bubble Conversion[3]	Final Radii	Final Cluster He Content
5	450	10^{16}	10^{13}	10^{-11}	8	8	83	0	9	99	4	0	124 135	661 1011
3	450	10^{15}	10^{13}	10^{-11}	15.8	28	46	0	26	96.5	1	0	334 338	6354 6899
1	450	10^{14}	10^{13}	10^{-11}	8.3	58	13	0	29	93.5	6	0	566 567	58123 59458
54	550	10^{16}	10^{14}	10^{-13}	7.3	10	18	10	62	92.8	44	NC	2 560	29 619
53	550	10^{16}	10^{13}	10^{-13}	1.5	14	3	13	70	92.3	32	NC	2.2 712	32 1428
49	550	10^{14}	10^{13}	10^{-13}	12.4	12	27	0	61	92.6	38	0	636 646	608 769
42	550	10^{16}	10^{14}	10^{-11}	3.7	8	13	22	57	93.6	57	NC	8 446	420 24854
41	550	10^{14}	10^{13}	10^{-11}	12.3	12	27	0	61	93.6	37	0	638 644	57213 58320
37	550	10^{15}	10^{13}	10^{-11}	9.8	4	64	0	32	93.4	79	0	283 285	6361 6525

1) VHITS: dose-dpa; T-°C; C_b, C_v-#/cm^3; G_{He} -apa/sec; swelling-%; radii-Å; He content-#/cluster.

2) For example for run 54 at 10 dpa ~1.8 dpa originally go to voids; of these 92.8% are annihilated by interstitials leaving ~0.13 dpa; of these 44% are lost via emmission leaving .073 dpa or 7.3% swelling.

3) NC-No conversion at 10 dpa.

Examination of these results suggests that at least five factors interact to determine the net swelling including:

1. At higher void (and bubbles which quickly convert to void) densities, the fraction of vacancies going to voids increases relative to loss to dislocations and lattice recombination. The absolute magnitude of recombination decreases. These factors tend to increase swelling. This is shown in Table 2 if run number 1 is com- to compared to run 5.
2. At higher void densities the ratio of interstitial to vacancy fluxes at neutral sinks increases. This tends to decrease swelling. This is also illustrated by comparing runs 1 and 5.
3. At higher void densities vacancy emission from voids increase in relative importance, tending to decrease swelling. This can be seen by contrasting runs 37 and 41.
4. Bubbles act as defect sinks decreasing swelling, but themselves contribute little to swelling. Increased bubble size due to the addition of helium enhances this sink effect. This is shown in going from run 42 to run 54, and by comparing final void and bubble radii.
5. Helium which ends up in voids contributes little in increased or decreased swelling.

The effect of higher void densities in increasing void to dislocation sink strength ratios may be artificial since the treatment of dislocations is certainly not rigorous. However the effect at lower temperatures of reducing lattice recombination appears to be physically appropriate.

There is also little physical basis for expecting a range of nucleation microstructure as large as utilized here to be representative of all conditions of helium and displacement generation rates and temperature. At lower temperatures, for example, helium may be effectively immobile and have little influence on the void density formed on available heterogeneous sites. If small bubbles form at lower temperatures they would tend to act as void nucleation sites, thus not retain their bubble identity (actually this is indicated in the growth calculations when 2Å bub-

effect of transmutant helium at lower temperatures would be at most, an increase in void density ($C_v > 10^{14}/cm^3$). The approximate growth model described previously predicts increased swelling with increasing void density in the range of 10^{13}-10^{15} voids/cm^3, and decreasing swelling for C_v~10^{15}-10^{16} (see Figure 3). However, the caveat regarding the treatment of dislocation sink growth should be considered in evaluating the physical validity of the void density effect at lower temperatures. Reduction in lattice recombination at high void densities would also tend to enhance swelling.

Although the precise choice of initial bubble and void sizes does not appear to be too critical to the calculated swelling at 10 dpa, the assumption that a microstructure consisting of very small and very large initial clusters is artificial and is useful only in illuminating ranges of potential swelling behavior.

For example, at higher temperatures and helium generation rates substantial reduction in early void nucleation and growth would be expected. Therefore, for these situations assigning high concentrations (C_v>~$10^{13}/cm^3$) of initially large voids (r_v~50Å) is not physically realistic. Thus these calculations can be viewed as tending to predict a maximum swelling, thus minimizing the effect of helium, when high densities of small bubbles initially form. Conversely at lower helium generation rates a high assigned density of bubbles is not appropriate. Thus the effect of helium on decreasing total void swelling is probably overestimated in this case.

However, within the limits of the model assumptions discussed above some physically based effects of helium are apparent. At higher temperatures the increased emission from smaller voids and lowering of defect concentrations due to a high density of bubble sinks is likely to reduce swelling. Since bubbles are small and grow slowly only with the addition of helium, they contribute little to the overall swelling. They can, however, effect the annihilation of vacancies which would otherwise go to voids. The additional helium introduced at high generation rates can therefore enhance this bubble sink reduction in swelling.

That is, more vacancies that would have otherwise reached voids are annihilated due to the addition of a helium atom at a bubble, than is swelling increased by the helium atom itself.

It is also possible for bubbles to convert to voids via the addition of helium. This occurs both at high helium generation rates and at the lower temperatures. In some cases bubbles convert quickly to voids and rapidly catch up to void size, and little effect of bubbles or helium on swelling is observed. In contrast, in other cases bubbles are slow to convert or grow very slowly after conversion, due to high emission rates, substantially reducing swelling. Very slowly growing small voids produce much the same effect as bubbles.

A series of calculations in which dislocation density as fixed at $\rho_d=10^{10}/cm^2$ illustrates these effects. In this case Ω is taken as 0.8 x $10^{-23}/cm^3$ instead of $1.07 \times 10^{-23}/cm^3$ and the voids are started at a 10Å radius. The general behavior is consistent with the results shown in Figures 2 to 4. Figure 5 shows swelling versus dpa for some cases in this second series of calculations. Curve 1 shows a case ($C_b=C_v=10^{14}$, $G_{He}=10^{-11}$) where bubbles convert to voids quickly and void growth proceeds normally. Curve 2 illustrates the situation when bubbles remain stable throughout irradiation. ($C_b=10^{16}, C_v=10^{14}, G_{He}=10^{-12}$). Curve 3 is the result of a quick bubble to void conversion followed by slow void growth due to vacancy emission ($C_b=10^{16}, C_v=10^{13}, G_{He}=10^{-11}$). Curve 4 is a case when bubbles convert to voids only after a relatively long irradiation time ($C_b=10^{15}, C_v=10^{13}, G_{He}^{-13}$) but grow relatively quickly after conversion.

These results suggest that the helium generation rate can influence void swelling through the nucleation microstructure which it affects, and in some circumstances directly during the void swelling stage. Higher helium generation rates would initially form higher bubble densities. At temperatures near the peak in swelling the high sink density resulting from these small bubbles would tend to suppress void nucleation and slow void growth should they form. One or both of two mechanisms is responsible for this, including vacancy loss to slowly growing sinks and enhanced void vacancy emission.

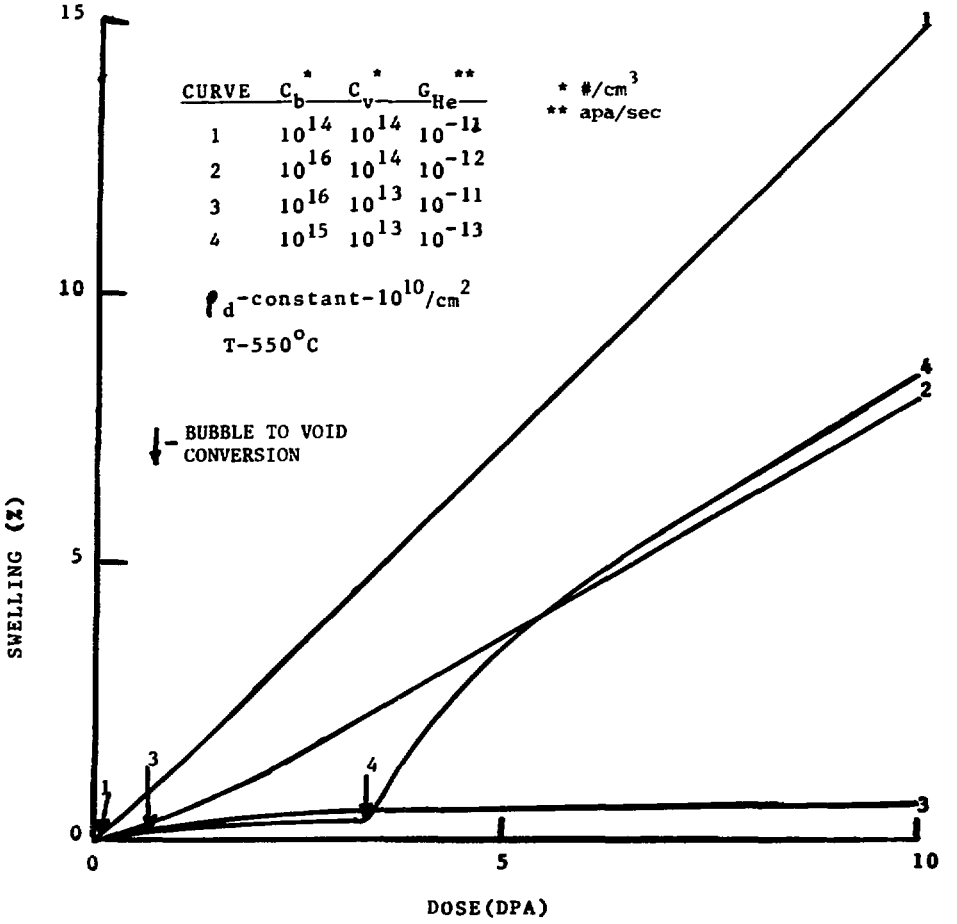

Fig. 5. Dose dependence of swelling for various nucleation microstructures and helium generation rates.

At lower temperatures and helium generation rates or higher displacement rates, transmutant helium might assist nucleation but would be expected to have less influence on total swelling.

By parametrically treating a wide range of nucleation microstructures in growth calculations it is possible to estimate bounds on the influence of helium on void swelling. Figure 6 shows both limiting and nominal behavior of swelling schematically as a function of helium generation rate and temperature. Although even these broad estimates are to some extent model and parameter dependent, they are largely based on the physically sound components of the model discussed above. The counter-intuitive prediction of decreased void swelling at high helium generation rates may have important implications to CTR development.

There is some other theoretical and experimental work which bears on the question of the influence of helium on void swelling. Brailsford and Bullough have discussed the effect of helium on enhanced stress assisted swelling above the normal peak swelling temperature[8]. In some accelerator experiments, swelling appears to be suppressed if there is a fine distrubtion of bubbles due to prior helium injection[9,10]. Other accelerator experiments show little effect of helium on total swelling[11]. Forman and Makin have also discussed the effect of higher void densities in lowering swelling[12]. Thermal reactor irradiation of stainless steel which has a high helium generation rate due to the two stage nickel (n, α) reaction seems to show predominately bubble swelling, although the data is not conclusive[13]. None of these findings appear to be inconsistent with the results of this study.

SUMMARY AND CONCLUSIONS

The very large number of complex and interacting phenomena in a material under irradiation clearly demonstrate the need to develop better and more complete models, and to collect new and relevant experimental data. We are currently carrying out such model development and hope to work closely with experimentalists so that much needed data can be obtained and analyzed. (It is noted, however, that some of the unexplained discrepancies between current calculations and experiments might be resolved by closer examination of the implications of model

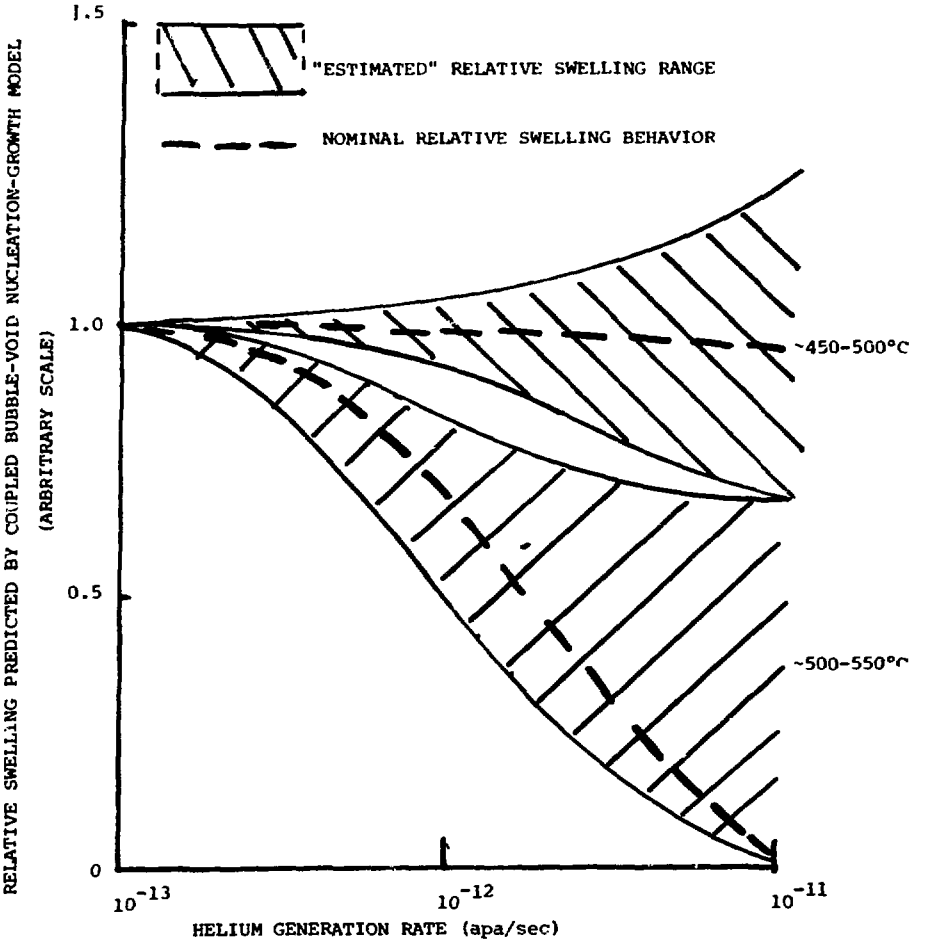

Fig. 6. Schematic representation of estimated bounds and nominal swelling as a function of the helium generation rate based on coupled bubble-void nucleation-growth phenomenological model.

assumptions and the accuracy of the data.) In particular, it is apparent that more needs to be done in characterizing the nature and the stability of the nucleation microstructure as influenced by helium generation; and the development of the dislocation microstructure during irradiation.

However some tentative conclusions regarding CTR radiation damage seem warranted. At temperatures near and slightly above that are normally associated with peak fission reactor swelling, void formation and growth might be substantially suppressed in CTRs if a high density of small bubbles initially form. However, the resulting lattice strengthening coupled with increased helium grain boundary embrittlement would indicate that severe ductility reductions, rather than dimensional instability, will be a major CTR first wall concern. At higher temperatures pure bubble swelling and stress assisted swelling and/or helium assisted creep coupled with severe helium embrittlement might be expected to impose the major CTR design limitations. At temperatures significantly below the normal swelling peak, helium is expected to have little effect on total swelling.

The most significant phenomenological aspect of this model is the prediction that high helium generation rates lead to high bubble densities. Since the nature and stability of the nucleation microstructure as influenced by helium is not precisely understood the conclusions outlined above should be taken as tentative. For example, bubble nucleation may, in practical circumstances, be controlled by a pre-existing density of heterogeneous sites, resulting in a bubble density which is independent of helium generation rate. This, however, suggests that metallurgical treatments to control bubble nucleation might be an effective means of controlling swelling in CTRs. A controlled distribution of helium trapped in a high density of small bubbles in the lattice would also tend to mitigate the helium grain boundary embrittlement problem.

In conclusion, the calculations carried out in this study indicate that irradiation induced microstructural evolution may be significantly different in CTRs than in fission reactors due to altered transmutant helium generation rates. Further study of this effect should have important implications to the development of safe and efficient fusion power.

REFERENCES

1. G. Kulcinski, D. Doran and M. Abdou, Proc. of International Conference on Irradiation Effects in Reactor Metals, Gatlingburg, Tennessee (1974) to be published.

2. G. Odette and M. Frei in Proc. of First Topical Meeting on Technology of Controlled Nuclear Fusion V. II p. 485 CONF-740402-P2 (1974).

3. M. Hayns, Journ. of Nuc. Mat., 56, 267 (1975).

4. G. Greenwood, A. Foreman and D. Rimmer, Jour. of Nuc. Mater. 4, 305 (1959).

5. H. Wiedersich, Radiation Effects, 12, 111 (1972).

6. S. Harkness and C. Lee, Met. Trans., 2, 1457 (1971).

7. A. Brailsford and R. Bullough, Journ. of Nucl. Mater., 44, 212 (1972).

8. A. Brailsford and R. Bullough, Journ. of Nucl. Mater., 48, 87 (1973).

9. J. Delaplace, N. Lams and L. LeNeour, Journ. of Nucl. Mater., 47, 278 (1973).

10. A. Santhanan, T. Taylor and S. Harkness, Defects and Defect Clusters in B.C.C. Metals and Alloys, AIME Nucl. Metallurgy V. 18, 302 (1973).

11. J. Brimhall, Proceedings of AIME Meeting, Detroit, Mich. (1974).

12. A. Foreman and M. Makin in Physics of Irradiation Produced Voids AERE-R7934, 313 (1974).

13. T. Wiffen, E. Bloom, Nucl. Tech. 25(1), 113 (1975).

ACKNOWLEDGEMENTS

We would like to thank D. Doran and R. Simons of the Hanford Engineering Development Laboratory for helpful discussions. The work was partially supported by the Westinghouse Hanford Company Contract Number YSA-544-23344.

ANALYSIS OF RADIATION DAMAGE IN FUSION-SIMULATION NEUTRON SPECTRA*

Don M. Parkin
Los Alamos Scientific Laboratory
Los Alamos, New Mexico 87545

and

Allen N. Goland
Brookhaven National Laboratory
Upton, New York 11973

ABSTRACT

During the next decade experiments will be performed at a number of neutron sources in an effort to discover and alleviate radiation effects in fusion reactors. Comparison of experimental results obtained after irradiations in diverse neutron spectra will require a versatile analysis method such as the one we have developed. Various parameters which are relevant to an understanding of radiation effects in metals have been evaluated utilizing available neutron spectrum information for several existing sources, e.g. EBRII, HFIR, and LAMPF, as well as the hypothetical spectrum at a fusion reactor first wall, and measured Li(d,n) spectra. Recoil energy distributions were calculated for several metals including Al, Cu, and Nb. The recoil energy range was divided into groups, and the fraction of recoils occurring in each energy group was compared with the fraction of the damage energy contributed by that group. From this comparison it was possible to conclude that the significant recoil range differs by about an order of magnitude between fission and fusion sources. The analysis further confirms that basic defect production characteristics depend upon the neutron spectrum, and that integral calculations of radiation-effect parameters do not provide a complete description of the dependence. This is equally true for comparisons between fusion-related spectra or fission-reactor spectra independently. Four recoil-dependent parameter functions which describe different aspects of radiation damage were used in the calculations. The relative effectiveness of neutron sources was found to depend upon the choice of parameter function. Fission-reactor spectra comparisons are relatively insensitive to the parameter functions used whereas spectra with an appreciable component of high-energy neutrons are much more sensitive.

INTRODUCTION

The potential materials problems caused by the extreme radiation environment in future fusion reactors have been outlined in many publications.[1] The new ingredient arising from the use of the D-T fusion reaction is the presence of high-energy neutrons with energies up to $\sim$ 15 MeV. These neutrons are responsible for generating high-energy recoil atoms and for inducing nonelastic reactions which lead to the production of impurity atoms in the materials surrounding the reaction chamber. The simultaneous generation of high-energy recoil cascades, transmutation products and gaseous impurities at high rates will have important implications for the structural integrity of a fusion reactor. Therefore, because of the accelerated schedule which has been adopted for the construction and operation of fusion-test reactors[2] even more rapid development of neutron sources for materials research and testing is warranted. In all likelihood, a variety of sources will be employed, each characterized by its own neutron-energy spectrum. It is, therefore, imperative that methods be developed for comparing the radiation effects induced by these sources on the basis of relevant parameters. In this paper one particular approach[3,4] which has so far proved useful is outlined.

There are three kinds of input required for calculations of the type to be described: first, nuclear data consisting of accurate flux spectra, detailed cross section information and models for nuclear-reaction kinematics; second, solid-state information in the form of a theory of the stopping power of solids for energetic-recoil atoms with energies up to a few hundred keV; and third, models which relate the production of energetic-recoil atoms to observed changes in measured physical properties or other characteristics of solids.

In previous papers[3-7] we have dealt mainly with the first two kinds of information. This paper is intended to emphasize the latitude available in the choice of models for comparing predictions with experimental results. The central idea is that a different model may be best suited for comparison with each kind of experimental result. The choice

of a particular model requires some insight into the nature of the damage process in each case, and as experience is gained, a library of useful models will be accumulated.

In the next section a brief review of the computational method is given in order to make clear what approximations have been made. The third section describes the results of recoil-energy-spectrum calculations for various metals. Section four deals with the interpretation of radiation-effects experiments in terms of several models[8] relating energy deposition to such factors as defect-cluster formation, and Frenkel pair production per recoil atom. The final section summarizes the status of this type of analysis, as well as the future directions of the research.

REVIEW OF COMPUTATIONAL METHOD

Neutron Spectra

A neutron-energy grid corresponding to the input neutron spectrum is used in generating the necessary data for subsequent calculations. Between group boundaries for multigroup neutron data, the calculations do not utilize an energy-weight function because its application to all spectra of interest may not be justified. Hence for both histogram and pointwise data linear interpolation is used between energy-grid points.

It should be noted that the calculational accuracy of all quantities derived from the neutron spectrum is determined in part by the energy-grid mesh and in part by the accuracy of the neutron spectrum data. The finer the energy grid, the more accurate the results; however, using an energy grid finer than that on which the neutron spectrum is specified would be unwarranted. It is in this manner that neutron dosimetry ultimately affects the validity of radiation-effects calculations.

Nuclear Models

Neutron-scattering models[3,9,10] are used to calculate the probability, $K_i(E,T)$, that a neutron with lab energy, E, will produce a primary atom recoil with lab energy between T and T + dT via the i^{th} scattering process. This probability function, when multiplied by the corresponding scattering cross section, is the recoil probability cross section,

$$\sigma_i(E)K_i(E,T)dT$$

for the i^{th} scattering process. This cross section forms the basis for all calculations in DON.[3] Except where noted, all nuclear data required to calculate the recoil probability cross section are obtained from the ENDF/B library.[11] For materials with resonance-elastic-scattering data, a smooth elastic-scattering cross section was generated external to DON.[12]

The total recoil probability cross section is the sum of the partial cross sections for each of the scattering processes and can be written as

$$\begin{aligned}\sigma(E)K(E,T)dT = \sum_i \sigma_i(E)K_i(E,T)dT = \{&\sigma_{el}(E)K_{el}(E,T) \\ &+ \sum_r \sigma_r(E)K_r(E,T) + \sigma_{n,2n}(E)K_{n,2n}(E,T) \\ &+ \sum_n \sigma_n(E)K_n(E,T) + \sigma_x K_x(E,T)\}dT \quad ,\end{aligned} \tag{1}$$

where the subscripts have the following meaning:

el ≡ elastic scattering

$\sum_r$ ≡ inelastic resolved level scattering

(n,2n) ≡ (n,2n) scattering

$\sum_n$ ≡ other remaining nonelastic scattering processes included (see Table 1)

x ≡ high-energy model scattering.

Table 1. Nonelastic Cross Sections Used in Calculations

n	Cross Section
1	Inelastic Continuum
2	(n,p)
3	(n,d)
4	(n,t)
5	(n,^{3}He)
6	(n,α)

The functional forms of $\sigma_i(E)K_i(E,T)dT$ in Eq. (1) are given in Ref. 3.

Cross section data and the recoil probability cross section are used to compute the following integrals:

1. Generalized Parameter Cross Section.

$$G(E) = \int\sigma(E)K(E,T)g(T)dT \quad , \tag{2}$$

where g(T) is the recoil-dependent parameter function that can be used to relate recoil energy to observable radiation effects. For example, in part of the following discussion we have used the damage energy form of the recoil-dependent parameter function

$$g(T) \equiv e(T) = \begin{cases} 0, & T < T_o \\ TL(T), & T_o \leq T \leq T_1 \\ 0, & T > T_1 \quad . \end{cases} \tag{3}$$

L(T) is the Lindhard efficiency factor[13] as approximated by Robinson[14] in simple analytic form. Thus,

$$L(T) = [1 + K_L f(\omega)]^{-1} \quad ,$$

$$K_L = 0.133745\ Z^{2/3}\ A^{-1/2} \quad ,$$

$$\omega = TE_L^{-1} \quad , \qquad (4)$$

$$E_L = 86.931\ Z^{7/3}\ \text{eV} \quad ,$$

$$f(\omega) = \omega + 0.40244\ \omega^{3/4} + 3.4008\ \omega^{1/6} \quad .$$

With this choice of g(T), we obtain the damage energy cross section

$$E_D = \int_{T_o}^{T_1} \sigma(E)K(E,T)e(T)dT \quad , \qquad (5)$$

for the recoil-energy interval $T_o \leq T \leq T_1$. If T_o is set equal to the displacement-threshold energy, say 25 eV, and T_1 is taken as the maximum possible recoil energy for a given incident-neutron energy then Eq. (5) is the expression for the total damage energy cross section.

2. Neutron Energy-Spectrum-Dependent Integrals.

(a) normalized primary recoil energy spectrum,

$$P(T) = \frac{\int \sigma(E)K(E,T)\phi(E)dE}{\int \sigma(E)\phi(E)dE} \qquad (6)$$

where $\phi(E)dE$ is the differential neutron spectrum.

(b) spectrum-averaged parameter cross section,

$$\langle G(E) \rangle = \frac{\int G(E)\phi(E)dE}{\int \phi(E)dE} \quad . \qquad (7)$$

(c) spectrum-averaged neutron cross section,

$$\langle \sigma(E) \rangle = \frac{\int \sigma(E)\phi(E)dE}{\int \phi(E)dE} \quad . \qquad (8)$$

(d) spectrum-averaged parameter

$$\bar{G} = \frac{\int G(E)\phi(E)dE}{\int \sigma(E)\phi(E)dE} = \frac{\langle G(E) \rangle}{\langle \sigma(E) \rangle} \quad . \qquad (9)$$

The spectrum-averaged cross section for each of the processes used is calculated using the data available in ENDF/B. However, to calculate probabilities at energies above which detailed data are available from ENDF/B, typically 15-20 MeV, a simple evaporation model was used to represent all scattering. This model was adopted on the basis of nuclear systematics,[15] and the assumption that for most materials of interest the major contribution to the generalized parameter cross section above the ENDF/B energy limit, E^*, comes from nonelastic-scattering events.

In earlier calculations[3,4] the high-energy scattering cross section was assumed to be energy independent, and was defined so that it yielded the correct parameter cross section $G(E^*)$ at the energy limit E^*, i.e.

$$\sigma_x(E) = \frac{G(E^*)}{\int K_x(E^*,T)g(T)dT} \quad , \tag{10}$$

where

$$K_x(E,T) = K_1(E,T) \quad \text{(subscript 1 refers to inelastic continuum)}$$

with

$$\theta(E) = 3.22 \times 10^3 \sqrt{E(eV)/A} \quad , \text{ the nuclear temperature.}$$

Except near reaction thresholds, the calculations are relatively insensitive to the magnitude of the nuclear excitation, Q. Therefore, the value of Q_x was arbitrarily chosen to be 1 MeV.

The results reported in subsequent sections have been obtained with a new high-energy model in which the nuclear-cross sections are individually extended to higher energies by assigning to each cross section its value at the ENDF/B energy limit. This has the effect of removing any discontinuity in the recoil probability distribution at the ENDF/B limit. A comparison of numerical results obtained with both high-energy models reveals that they differ by at most a few percent from one another. Thus, our previously published values for radiation-damage parameters are still reliable.[3-7] Nevertheless, the new model should yield the more accurate values for the recoil probability distributions, P(T), and they are quoted in the next section.

CALCULATED RECOIL SPECTRA

One way of comparing neutron sources is an integral method in which spectral averages are calculated over the full range of neutron energies, E, and allowed recoil energies, T.[3,4] A more detailed method involves restricting the limits of integration on T to intervals small enough that it becomes effectively a differential calculation. When this approach is applied to the general parameter average, $\bar{G}(E)$, it is possible to determine what fraction of $\bar{G}(E)$ is associated with each member of a set of specified recoil energy groups. For example, if $\bar{G}(E)$ is taken to be $\bar{E}_D$, the spectrum-averaged damage energy, then the fractional damage energy in each recoil-energy group can be obtained. The distribution of recoil atoms among the same energy groups is directly given by the normalized primary recoil-energy spectrum, P(T), which is always computed. It is instructive to compare the fraction of primary recoils with the fraction of damage energy in each energy group.

This comparison has been made for Al (ENDF/B Material 1193), Cu (1087) and Nb (1164) in five different neutron spectra corresponding to existing or hypothetical sources: EBRII - midplane, row 7,[16] HFIR,[17] "14-MeV" (13.5 - 14.9 MeV), BENCH (a hypothetical fusion-reactor first-wall spectrum),[18] and Li(d,n) (30-MeV deuteron).[19] The numerical results are given in Tables 2-4.

The first point which is immediately apparent is the importance of recoils in the last energy group, i.e. above 100 keV in the three fusion-related spectra (last three columns). Better than 60 percent of the damage energy is contributed by these primary recoils. Moreover, the results are strikingly similar for the three metals. The Li(d,n) neutron spectrum produces recoil and damage energy fractions in good correspondence to those produced in the "14-MeV" neutron spectrum, and is thus a good simulation source. The fission-reactor spectra, on the other hand, emphasize lower energy recoils and the distributions are somewhat different in EBRII and in HFIR. In the former, about 50 percent of the damage energy is attributable to

Table 2. Al (1193) - Recoil-Energy and Damage-Energy Spectra

Recoil Energy (keV)	EBRII-7		HFIR		BENCH		"14 MeV"		Li(d,n) 30 MeV	
	P(T)	$\%E_D$	P(T)	$\%E_D$	P(T)	$\%E_D$	P(T)	$\%E_D$	P(T)	$\%E_D$
0 - 0.1	0.7%	0.	30.4%	0.	0.8%	0.	0. %	0.	0. %	0.
0.1 - 1.0	6.1	0.2	7.4	0.2	6.0	0.1	0.4	0.	0.4	0.
1.0 - 5.0	24.1	4.7	13.7	2.3	22.2	2.0	1.6	0.	1.9	0.1
5.0 - 10.0	18.1	8.3	8.4	3.4	14.7	3.1	1.8	0.	2.2	0.1
10.0 - 50.0	41.6	51.0	24.3	29.0	32.9	19.1	11.2	1.9	13.8	2.6
50.0 - 100.0	6.9	21.5	8.3	23.6	8.7	12.7	7.9	2.9	10.3	4.3
100.0 - T_{max}	2.5	14.3	7.5	41.5	14.7	63.0	77.1	95.0	71.4	92.9

Table 3. Cu (1087) - Recoil Energy and Damage-Energy Spectra

Recoil Energy (keV)	EBRII-7		HFIR		BENCH		"14 MeV"		Li(d,n) 30 MeV	
	P(T)	$\%E_D$	P(T)	$\%E_D$	P(T)	$\%E_D$	P(T)	$\%E_D$	P(T)	$\%E_D$
0. - 0.1	3.8%	0.	63.4%	0.1	5.5%	0.	0.2%	0.	0.2%	0.
0.1 - 1.0	23.2	1.7	15.0	1.3	25.2	0.5	1.5	0.	1.6	0.
1.0 - 5.0	35.0	12.1	7.7	4.5	26.5	2.7	6.1	0.2	6.3	0.2
5.0 - 10.0	15.3	14.5	3.4	5.5	10.3	2.9	6.3	0.4	6.8	0.5
10.0 - 50.0	20.5	51.4	7.6	38.1	19.5	16.7	24.3	4.7	28.5	6.6
50.0 - 100.0	1.7	13.2	2.0	27.3	3.6	9.2	6.9	3.4	11.1	6.6
100.0 - T_{max}	0.5	7.1	0.9	23.2	9.4	68.0	54.7	91.3	45.5	86.1

Table 4. Nb (1164) - Recoil-Energy and Damage-Energy Spectra

Recoil Energy (keV)	EBRII-7		HFIR		BENCH		"14 MeV"		Li(d,n) 30 MeV	
	P(T)	$\%E_D$	P(T)	$\%E_D$	P(T)	$\%E_D$	P(T)	$\%E_D$	P(T)	$\%E_D$
0 - 0.1	3.8%	0.	57.2%	0.1	4.4%	0.	0.3%	0.	0.3%	0.
0.1 - 1.0	22.8	2.2	11.4	1.1	20.6	0.5	2.9	0.2	3.1	0.
1.0 - 5.0	40.3	18.7	12.1	7.3	30.3	3.7	11.0	0.4	11.4	0.4
5.0 - 10.0	16.4	20.4	6.4	10.3	13.2	4.4	10.1	0.8	10.2	1.0
10.0 - 50.0	15.9	48.8	11.0	51.0	19.8	18.0	21.4	4.8	23.6	6.5
50.0 - 100.0	0.7	7.4	1.6	21.6	2.9	8.9	6.2	4.9	12.2	11.0
100.0 - T_{max}	0.1	2.5	0.3	8.6	8.8	64.5	48.1	88.9	38.7	81.1

recoils in the 10-50 keV energy group with other major fractions at lower energies. In the latter, the 10-50 keV range is also important, but damage-energy fractions associated with recoils above 50 keV are considerably larger. Neither source is especially suited to simulation of a fusion-source spectrum from this point of view.

In HFIR from 30 to $\sim$ 60 percent of the recoils have energies below 100 eV and contribute a negligible fraction to the total damage energy. However, in EBRII-7 less than 4 percent of the recoils are in this lowest energy group. At the high-energy end of the recoil spectrum the opposite situation arises. There are twice as many recoils above 50 keV in HFIR as in EBRII-7. It is interesting to note that the recoil-energy spectrum produced by the BENCH fusion-reactor spectrum is similar to that produced in EBRII-7 below 50 keV in all three metals. The recoil spectrum in this energy range in the BENCH spectrum is determined mainly by the neutrons returning from the blanket. The 14-MeV source current is represented by the recoil component above 50 keV. It is this component, however, that imparts more than 70 percent of the damage energy to each material.

The reason for the good simulation of 14-MeV recoil and damage energy spectra by Li(d,n) neutrons is that for 30-MeV deuterons the most probable neutron energy is about 13 MeV. Therefore, the majority of the neutrons have energies close to the desired value for fusion-related damage studies.

The character of the initial damage production processes plays a role in determining important parameters such as interstitial and vacancy survival rates and cluster formation. The defect density per cascade and the spatial distribution of the cascades depend upon the recoil-energy ranges which contribute the majority of the damage energy. The observations made in this section clearly demonstrate that

(1) basic defect production characteristics can be strongly spectrum dependent, and

(2) integral results previously published do not provide an adequate description of this energy dependence.

PARAMETER FUNCTION COMPARISON

To estimate the effects of radiation on a material in one neutron spectrum relative to those in another, it is necessary to select a particular form of the recoil-dependent parameter function, g(T), to use in the calculation. In principle one would like to have an appropriate g(T) to represent or describe the particular form of damage of interest. The damage energy form of g(T) was used in the above discussion of recoil-energy spectra because of its wide acceptance as a relevant damage parameter although it does not represent all forms of damage. Neutron spectral data help to identify the recoil-energy ranges in which it is most important to have detailed knowledge of a parameter function. Therefore, it is important in using or developing parameter functions to know what recoil-energy range or parameter function is valid or has been tested.

Two approaches to the development of parameter functions that have been utilized are theoretical calculations, including computer simulation,[20,21] and empirical damage function unfolding.[22-24] The computer calculations have generally concentrated on estimating the number of Frenkel pairs, excluding temperature effects, produced by primary recoils. Some attempts, however, have been made to include irradiation temperature and defect clustering.[25-27] At present, the results of theoretical calculations form the basis of most of the irradiation simulation studies.

The damage-function-unfolding technique[22-24] utilizes measured physical property changes in samples irradiated under known conditions as a basis for deriving parameter cross sections representative of the type of damage causing the property change measured. Property-change measurements are made on samples irradiated in several known neutron spectra. The measurements and the neutron spectra in conjunction with a trial solution typically based on a theoretical calculation are used as input in an unfolding computer code which produces a parameter cross section.

The damage-function-derived parameter cross sections have two general characteristics of importance to the present discussion. First, over the neutron-energy range $\sim 10^{-2}$ -5 MeV which is responsible for about 90 percent of the damage in a typical fission reactor the derived parameter cross sections have neutron-energy dependencies very similar to recoil energy or damage-energy trial functions. Second, outside this energy range large differences between trial functions and derived solutions are seen. This fact is due in part to the lack of solution sensitivity outside the range of significant damage. These differences, however, are very important in estimating damage effects for fusion applications. The difference between trial functions based on theoretical calculations and derived parameter cross section above $\sim$5 MeV indicates the range of uncertainty in using these functions in calculations of damage effects in fusion spectra.

In neither case, theoretical calculations nor damage function unfolding do we have an adequate basis for extrapolating damage parameters into the recoil-energy or neutron-energy range most important for fusion spectra damage. One method of illustrating the magnitude of extrapolation uncertainties as well as indicating the types of simulation experiments that may be the most effective in developing new damage parameters is to compare several spectrum-averaged parameter cross sections representative of different forms of damage in a number of diverse neutron spectra.

Spectrum-averaged parameter cross sections using four parameter functions were calculated for Al, Cu and Nb. In addition to the damage-energy function, e(T), (see Eqs. (3) and (5)), the following parameter functions were used:

(a) Total recoil energy

$$t(T) = T \quad , \tag{11}$$

(b) radiation-hardening parameter

$$h(T) = \begin{cases} 0 & T \leq T_\ell \\ T - T_\ell & T_\ell \leq T \end{cases} \quad , \tag{12}$$

(c) Robinson-Torrens model 3[20]

$$r(T) = e(T)/(58 + 1.22 \times 10^{-3} e(T)) \qquad (13)$$

Equation (12) for h(T) is based on the computer calculations of Beeler,[21] and on the damage function results of Odette and Ziebold[23] for changes in yield stress in Fe. The function h(T) represents the relative probability of producing a defect cluster of sufficient size during the displacement cascade to act as an obstacle to dislocation motion. It has been found by Mitchell et al.[28] to compare favorably with the measured relative hardening rate for reactor neutrons and 14-MeV neutrons incident on Cu.

The Robinson and Torrens model-3 formula, r(T), (Eq. (13)), is derived from the results of computer simulation of displacement cascades in Cu. Their expression indicates that the number of Frenkel pairs produced is not directly proportional to damage energy. The calculations upon which r(T) is based covered a damage-energy range up to 10 keV whereas in the calculations of Parkin and Green[8] and the present calculations, r(T) has been extended to damage energies in the MeV range. Although this may be a "foolhardy" extrapolation into an untested recoil-energy region, for the present interests r(T) has been used since it provides a parameter function similar to damage energy for low recoil energy and extrapolates to values less than the damage energy at high recoil energies.

We can compare t(T), h(T) and r(T) using the damage-energy-parameter function as a reference. t(T) and r(T) are similar to damage energy at low-recoil energy whereas at high-recoil energy they diverge, t(T) becoming greater than and r(T) less than the damage energy. h(T) is less than the damage energy at low-recoil energy and greater than the damage energy at high-recoil energy.

For 9 neutron spectra the spectrum-averaged parameter cross sections for the four parameter functions normalized to their respective values in the EBRII-7 spectra are given in Table 5. The first five spectra are fission-type spectra whereas the last four have significant

Table 5. Normalized Parameter Cross Sections

	Damage Energy	Recoil Energy	Radiation Hardening	Modified Damage Energy
Nb (1164)				
HFIR	0.8	0.8	1.0	0.6
LPTRE-1	1.0	1.0	1.1	0.9
EBRII-7	1.0	1.0	1.0	1.0
EBRII-2	1.4	1.5	1.6	1.3
U235	2.6	2.7	3.6	2.1
M-LAMPF	2.0	2.3	3.0	1.3
BENCH	3.4	3.9	5.3	1.8
30 MeV	8.6	10.3	15.1	3.5
"14 MeV"	9.7	11.5	16.9	3.7
CU (1087)				
HFIR	0.8	0.8	0.9	0.6
LPTRE-1	1.0	1.0	1.1	0.8
EBRII-7	1.0	1.0	1.0	1.0
EBRII-2	1.4	1.4	1.6	1.3
U235	2.6	2.8	3.4	1.9
M-LAMPF	1.8	2.2	2.7	1.2
BENCH	3.1	3.80	4.7	1.6
30 MeV	8.0	10.5	13.8	3.1
"14 MeV"	8.4	11.2	14.5	3.0
Al (1193)				
HFIR	0.6	0.7	0.8	0.5
LPTRE-1	0.9	1.0	1.0	0.8
EBRII-7	1.0	1.0	1.0	1.0
EBRII-2	1.3	1.4	1.5	1.2
U235	1.9	2.5	2.8	1.5
M-LAMPF	1.2	2.0	2.2	1.0
BENCH	1.7	3.5	3.9	1.1
30 MeV	3.2	8.9	10.2	1.4
"14 MeV"	3.4	10.5	12.0	1.5

high-energy-neutron components. The first, third and seventh thru ninth spectra were described in Section III. The remaining four spectra are: LPTR-E-1, irradiation position E-1 in the Livermore Pool Type Reactor;[29] EBRII-2, row 2 midplane in the EBRII;[16] U235, ^{235}U fission spectrum;[30] and M-LAMPF, calculated spectrum for the Los Alamos Meson Physics Facility irradiation effects facility.[31]

One general observation based upon the data in Table 5 is that in the four reactor spectra, the results are essentially independent of the parameter function used, and further that the relative cross sections are similar for all three materials. These similarities point out a difficulty in using only reactor irradiations to study material and spectral-dependent radiation damage. The differences between the form of damage production in EBRII-7 and HFIR are illustrated by using parameter functions t(T) and r(T) which respectively emphasize or de-emphasize high-energy recoils. The results are consistent with the discussion in the preceding section regarding the fractional damage energy associated with various recoil-energy groups in different neutron source spectra.

Results for the remaining five spectra on the other hand are sensitive not only to the choice of parameter function, but to material as well. The sensitivity to parameter function increases as the high-energy component in the neutron spectrum increases, the maximum variations occurring at "14 MeV".

The largest variations as a function of material are seen in the two damage-energy-dependent models, e(T) and r(T) whereas the recoil-energy models t(T) and h(T) give more similar results. This difference is due to the inclusion of electronic losses in the damage energy function. The most striking example of this effect is found in Al. Using r(T) we find almost no spectral dependence in the damage.

For a given material the largest difference (2-10) occurs between h(T) and r(T) or e(T). The last two represent simple Frenkel-pair production, while h(T) is used here to represent radiation hardening. Both e(T) and h(T) have been used in comparative analyses of irradiation

experiments performed in reactor-neutron spectra and in a 14-MeV neutron flux. Parkin and Snead[32] have used damage energy in comparing neutron and charged-particle induced changes in critical current in Nb_3Sn. They find that for 14-MeV neutrons compared to reactor neutrons the experimental damage effectiveness is less than or equal to the ratio of the damage-energy cross sections calculated using e(T). The radiation-hardening data of Mitchell et al.[23] for copper give relative hardening rate ratios about the same as shown in Table 5 for copper using h(T).

SUMMARY AND CONCLUSIONS

In this paper we have tried to show, by means of some simple examples, that radiation-damage parameters are sensitive to the shape of the incident-neutron spectrum. A good way to exhibit the differences between spectra is to calculate the magnitude of the contribution to a given damage parameter that is to be associated with primary recoil atoms in each one of a set of energy groups. The damage energy is one such parameter, and the results shown in Tables 2-4 exhibit the essential differences between a first-wall-fusion spectrum and a nearly pure "14-MeV" spectrum (13.3 - 14.9 MeV).

The ultimate goal of these studies is to discover models which relate recoil-damage production to changes in the physical properties of solids. In the preceding section we reported the results of using different recoil-dependent parameter functions to compare various neutron sources. The entries in Table 5 lead us to draw two conclusions:

(1) The relative effectiveness of the sources depends upon the choice of parameter function. Different choices undoubtedly will be appropriate for different kinds of experiments.

(2) Fission-reactor spectra comparisons are relatively insensitive to the models used here. However, spectra with an appreciable component of high-energy neutrons are much more sensitive.

The models we have used are extremely rudimentary. Appreciable additional understanding of radiation damage will be forthcoming after theorists have developed more sophisticated parameter functions which

can be introduced into the calculations. Even then, we will continue to rely upon semiempirical methods to establish functional forms which are physically meaningful.

ACKNOWLEDGEMENTS

The authors wish to gratefully acknowledge the invaluable programming assistance of H. C. Berry (BNL) and M. L. Simmons (LASL) throughout the course of their work.

REFERENCES

1. See for example, "Proc. 1st Topical Meeting on the Technology of Controlled Thermonuclear Reactors", 16-18 April 1974, San Diego, Cal.
2. See for example, K. M. Zwilsky, in Surface Effects in Controlled Fusion, Eds. H. Wiedersich, M. S. Kaminsky and K. M. Zwilsky, North-Holland Publ. Co., Amsterdam, 1974, p. viii.
3. D. M. Parkin and Allen N. Goland, Brookhaven National Laboratory Report BNL-50434 (1974).
4. D. M. Parkin, A. N. Goland, and H. C. Berry, in "Proc. 1st Topical Meeting on the Technology of Controlled Thermonuclear Reactors", 16-18 April 1974, San Diego, Calif., CONF-75-502, p. 339.
5. D. M. Parkin and A. N. Goland, Trans. Am. Nucl. Soc. 19, 23 (1974).
6. A. N. Goland and D. M. Parkin, Bull. Am. Phys. Soc. 20, 351 (1975).
7. D. M. Parkin and A. N. Goland, Rad. Effects (to be published).
8. D. M. Parkin and W. V. Green, Bull. Am. Phys. Soc. 20, 351 (1975).
9. J. D. Jenkins, Nucl. Sci. Eng. 41, 155 (1970); see also Oak Ridge National Laboratory Report ORNL-TM-2706 (1970).
10. D. G. Doran, Nucl. Sci. Eng. 49, 130 (1972).
11. O. Ozer and D. Garber, ENDF/B Summary Documentation, Brookhaven National Laboratory Report BNL-17541 (ENDF-201) (1973).
12. O. Ozer, INTEND, a computer program for generating group-averaged cross sections from pointwise data, Brookhaven National Laboratory, private communication.

13. J. Lindhard, V. Nielsen, M. Scharff and P. V. Thomsen, Kgl. Dansk, Vidensk. Selsk., Mat-Fys Medd. 33, No. 10 (1963).
14. M. T. Robinson, in Nuclear Fusion Reactors, British Nuclear Energy Soc., London, 1970, p. 364.
15. S. Pearlstein, Nucl. Sci. Eng. 23, 238 (1965).
16. N. D. Dudey and R. R. Heinrich, EBRII data, Argonne National Laboratory, private communication.
17. F.B.K. Kam and J. H. Swands, HFIR PTP location data, Oak Ridge National Laboratory Report, ORNL-TM-3322.
18. A. Aronson, First-wall Spectra Using ORNL Benchmark Design, Brookhaven National Laboratory, private communication.
19. A. N. Goland, C. L. Snead, Jr., D. M. Parkin, and R. B. Theus, IEEE Trans. Nucl. Sci. 22, 1776 (1975).
20. M. T. Robinson and I. M. Torrens, Phys. Rev. B9, 5008 (1974).
21. J. R. Beeler, Jr., J. Appl. Phys 37, 3000 (1966).
22. W. N. McElroy, R. E. Dahl, Jr., and C. Z. Serpan, Jr., Nucl Appl. Technol. 7, 561 (1969).
23. G. R. Odette and T. O. Ziebold, Nucl. Sci. Eng. 49, 72 (1972).
24. R. L. Simons, W. N. McElroy, and L. D. Blackburn, Hanford Engineering and Development Laboratory Report HEDL-TME 73-85 (1973.
25. D. G. Doran, Rad. Effects 2, 249 (1970).
26. J. R. Beeler and M. F. Beeler, Nucl Metallurgy 18, 581 (1973).
27. I. M. Torrens and M. T. Robinson in "Radiation-Induced Voids in Metals" USAEC Conf. 710601, p. 739.
28. J. B. Mitchell, R. A. van Konynenburg and D. M. Parkin, this conference.
29. R. A. van Konynenburg, Lawrence Livermore Laboratory, private communication.
30. Obtained from Radiation Shielding Information Center, Oak Ridge National Laboratory.
31. D. J. Dudziak, M. L. Simmons and G. J. Russell, Trans. Am. Nucl. Soc. 19, 465 (1974).
32. D. M. Parkin and C. L. Snead, Jr., (to be published).

* Research supported by the Energy Research and Development Administration.

THE RESPONSE OF ISSEC PROTECTED FIRST WALLS TO DT AND DD PLASMA NEUTRONS

Halil I. Avci
G. L. Kulcinski

Nuclear Engineering Department
The University of Wisconsin
Madison, Wisconsin

ABSTRACT

It has been demonstrated that the displacement damage and gas production rates can be reduced in CTR first walls by employing passive carbon shields. Reductions in displacement damage range from 3 to 5 for 12.5 cm shield thickness and from 7 to 14 in gas production rates with the same carbon thickness. The factors of reduction are 8 to 20 for the displacements and 17 to 80 for the gas production if a 25 cm shield is used. Depending on whether the isotopes causing the radioactivity are produced as a result of fast or thermal neutron activation, the first wall radioactivity can either go up or down with the increasing carbon shield thickness. It has been found that at shutdown radioactivity in 316 SS, Al, and Nb first walls is reduced with increasing carbon thickness while the activities in V and Ta is increased. Long term radioactivity displays the same trends in Al, 316 SS and Ta as short term radioactivity. However, the long term activity in Nb increases and that in V decreases with increasing shield thickness.

It has also been found that systems operating on a D-D plasma cycle have higher displacement rates than respective D-T cycle systems. Gas production rates are slightly lower in D-D systems except for He production in 316 SS. This is due to the higher Ni^{59} (n,α) cross sections for thermal neutrons.

INTRODUCTION

The use of passive carbon shields to protect the plasma and the metallic first walls of a fusion reactor has been recently proposed.[1,2] Carbon curtains were shown to reduce the plasma energy losses due to impurity atom buildup, while at the same time protecting the first wall from erosion due to plasma ion induced blistering and sputtering. It was also demonstrated that increasing the thickness of the curtain degrades the neutron spectrum sufficiently such that displacement damage and gas production rates are

reduced in various CTR first wall materials.[3] The latter study revealed that short and long term radioactivities may either go up or down with increasing shield thickness depending on whether the activity is produced by thermal or high energy neutrons. The general concept was given the acronym ISSEC, for Internal Spectral Shifter and Energy Converter.[2]

Temperature and heat transfer characteristics of ISSECs have also been extensively analyzed in a previous paper.[4] It was shown that an upper temperature of about 2000°C would be imposed on the graphite ISSEC because the vapor pressure of graphite at this temperature becomes comparable to the pressure in the vacuum chamber, i.e. $\sim 10^{-5}$ torr. Two separate ideas have been developed as a result of these studies; the full ISSEC and the partial ISSEC. In the case of full ISSEC, the carbon extends all the way around the plasma and the plasma is never exposed directly to the first wall. In the partial ISSEC concept, carbon is used to protect only the inner blanket, nearest to the axis of a Tokamak where access and maintenance is most difficult. It was also shown that 2000°C maximum temperature would limit the full ISSEC thickness to ~6 cm and partial ISSEC thickness to ~30 cm at 1 MW/m^2 neutron wall loading and 10 $watts/cm^2$ surface heat load in a Tokamak reactor operating on a D-T plasma cycle.

The purpose of this paper is to expand the ISSEC concept to reactors operating with a D-D plasma and to compare the results with the D-T fuel cycle. We will not discuss the concept of internal tritium breeding as this is treated elsewhere.[2]

CALCULATIONAL PROCEDURES

The one dimensional-homogeneous blanket design used for this work is shown in Figure 1. A variable thickness carbon zone was placed between the plasma and the first wall. A density factor (D.F.) of 1.0 was used for the neutronic calculations although in practice a D.F. of ~0.7 would be more reasonable and would result in a thicker ISSEC region. However, the neutron "optical" thickness would be the same in both cases. The first wall thickness of 1 cm at a D.F. of 1.0 is intended to cover most reactor design cases. Again, lower D.F.'s and increased thickness would be used in practice to include coolant (which we assumed to be helium gas) and void spaces. The first wall is followed by a 60 cm thick reflector-

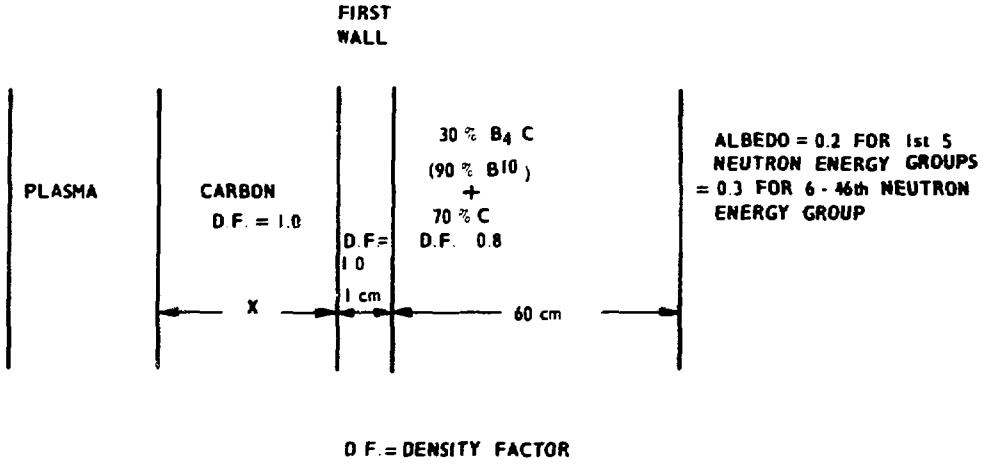

Figure 1 Model Blanket Design Used to Study the Effect of Graphite Spectral Shifter on the Radiation Damage Parameters in the First Wall.

shield region composed of 30% B_4C (enriched to 90% B-10) and 70% carbon. An albedo of 0.2 was used to simulate the final shield for the first five neutron energy groups (9 to 14.9 MeV) and an albedo of 0.3 was used for neutrons of lower energy. Obviously, no attempt was made to breed tritium in this reactor design but only to highlight the anticipated structural materials responses to the degraded neutron spectra.

The nuclear performance of this type of reactor design was studied by solving the discrete ordinates form of the neutron transport equation for a slab using the ANISN[5] program with a S_4-P_3 approximation. It has been shown elsewhere[6] that this approximation is adequate to predict integral parameters such as tritium breeding and gas production rates to within approximately 2% of a higher order calculation like the S_{16}-P_5. The neutron multigroup cross sections (except for gas production in molybdenum) were processed using the program SUPERTOG[7] from nuclear data in ENDF/B3.[8] Gas production cross sections for Mo were calculated by Pearlstein.[9] The displacement cross sections were calculated from a computer code developed by Doran[10,11] and the values used in these calculations are given in Appendix A. All calculations were performed using 46 energy groups.

The reactions considered for the radioactivity calculations, along with appropriate branching ratios and half lifes are given in reference 3, The radioactivity and appropriate decay factors for 316 SS were calculated using a special computer program developed at the University of Wisconsin.[12] The composition of 316 SS was assumed to be 70% Fe, 18% Cr and 12% Ni for all calculations except radioactivities.

All the calculations are done for two different reactors operating with deuterium-tritium (D-T) and deuterium-deuterium (D-D) plasma cycles. The blanket structure shown on Figure 1 was used for both calculations. All the results are normalized to 1 MW/m^2 of neutrons passing through the first wall (or inner ISSEC surface). In D-D case, it is assumed that all the tritium that is produced through one branch of the D-D fusion reaction is consumed in the reactor, As a result, the energy of 50% of the neutrons generated in D-D plasma is 14.1 MeV and the energy of the other half is 2.45 MeV. In the D-T case, all neutrons are of 14.1 MeV energy. With this assumption in mind, we can calculate the incident neutron fluxes corresponding to the 1 MW/m^2 neutronic wall loading in the two cases. In the D-T case,

$$(14.1\ \frac{MeV}{n})(1.602\times10^{-19}\ \frac{MW\text{-}sec}{MeV})(4.43\times10^{13}\ \frac{n}{cm^2\text{-}sec})(10^4\ \frac{cm^2}{m^2})=1\ \frac{MW}{m^2}(neutronic)$$

In the D-D case,

$$(\frac{14.1+2.45}{2}\ \frac{MeV}{n})(1.602\times10^{-19}\ \frac{MW\text{-}sec}{MeV})(7.56\times10^{13}\ \frac{n}{cm^2\text{-}sec})(10^4\frac{cm^2}{m^2})=1\ \frac{MW}{m^2}(neutronic)$$

The incident flux required to give a 1 MW/m^2 neutronic wall loading is 4.43×10^{13} n/cm^2-sec for the D-T reaction and in the D-D case, it is 7.56×10^{13} n/cm^2-sec (3.78×10^{13} n/cm^2-sec of 14.1 MeV and 3.78×10^{13} n/cm^2-sec of 2.45 MeV neutrons).

RESULTS AND ANALYSIS

Reduction of Displacement Damage

Typical 316 SS first wall neutron spectra for D-T and D-D plasma cases with 0, 12.5 cm and 25 cm ISSEC thicknesses are tabulated and plotted in Appendix B. The combination of such neutron spectra with displacement cross sections in Appendix A yield the displacement rates listed in Table 1 and displayed in Figures 2 to 4.

The reader should be cautioned that it is the relative and not absolute rates of damage which are important. This is because one can not accurately compare one element with another on dpa values alone; the homologous temperature of irradiation has as much or more influence on the final damage state as does the total damage level.

A few interesting observations can be made from Table 1. For the same neutronwall loading, even though the number of 14.1 MeV neutrons incident on the first wall from the D-D plasma is approximately 85% as much as from a D-T plasma, the displacement rates are higher in D-D systems by 20-35%. The reason for this is that (1) the 2.45 MeV neutrons will cause considerable displacement damage compared to 14.1 MeV neutrons (~80% as much despite the factor of 6 difference in energy) and (2) more total neutrons (~70%) are requred to achieve a neutronic wall laoding of 1 MW/m^2. However, the relative effect of the ISSEC in reducing displacement damage is about the same.

It is also observed that the ISSEC has a greater effect in reducing the displacement damage in high Z elements as compared to low Z elements.

Table 1

Factors of ISSEC Produced Reduction in Displacement Damage in Various CTR First Wall Materials in D-T and D-D Fusion Environments

	dpa/year[(a)]			
		D-D Fusion		
Material	No ISSEC	12.5 cm C	12.5 cm C Damage Ratio	25 cm C
Al	19.8	4.8	0.24	1.32
V	18.4	5.8	0.32	2.22
316 SS	16.8	3.2	0.19	0.86
Nb	10.8	2.14	0.20	0.54
Mo	12.2	2.34	0.19	0.6
Ta	10.5	2.08	0.20	0.52
		D-T Fusion		
Al	12.7	3.4	0.27	
V	12.9	3.8	0.29	
316 SS	11.3	2.50	0.22	
Nb	8.48	1.64	0.19	
Mo	9.47	1.77	0.19	
Ta	8.42	1.60	0.19	

(a) 1 MW/m^2 neutron wall loading and 100% Duty Factor

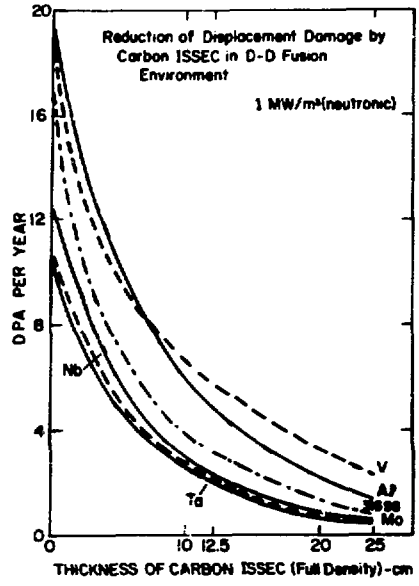

Figure 2 Reduction of Displacement Damage by Carbon ISSEC in the First Wall of a D-D Fusion Reactor.

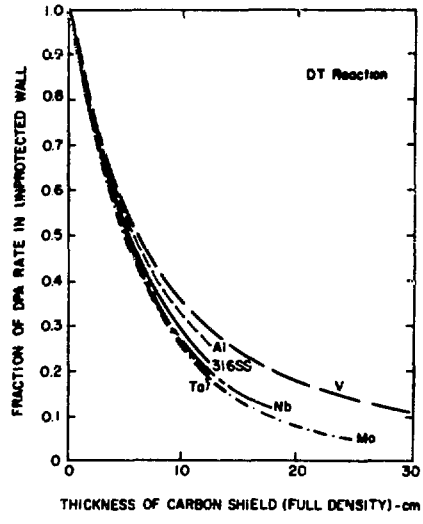

Figure 3 Normalized dpa Rate in ISSEC Protected D-T Systems.

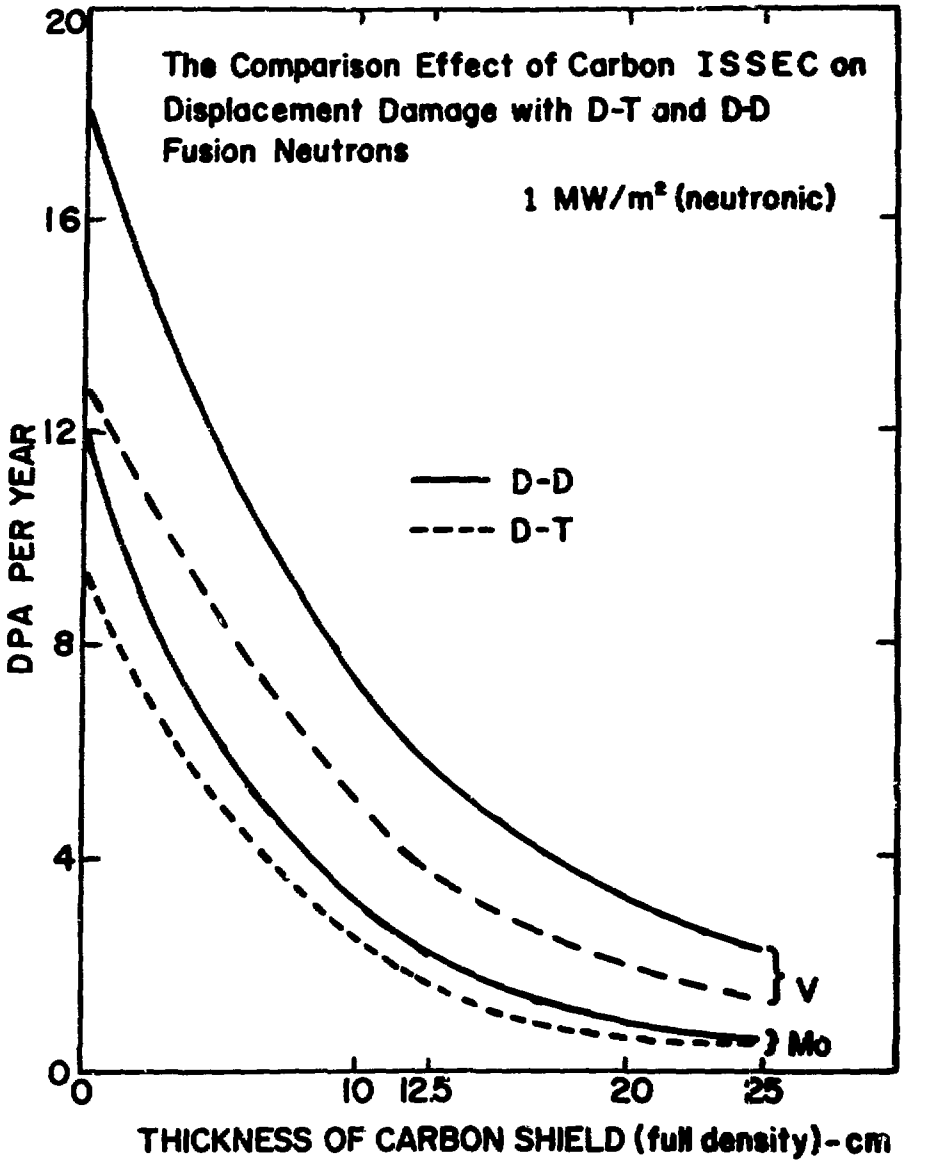

Figure 4 The Comparison Effect of Carbon ISSEC on Displacement Damage with D-T and D-D Fusion Neutrons.

The reason is complex but can be roughly explained by the low ionization threshold in low Z elements.[13] This means that the primary knock on atoms in Al lose much less energy in elastic (displacement) collisions than do the PKAs in Nb. For example, in Al 107 keV is lost to displaced atoms per PKA produced by 14 MeV neutrons and 51 keV from 1 MeV neutrons (a ratio of 2.1). The elastic energy lost by an average PKA in Nb is 213 keV from 14 MeV neutrons and 56 keV from 1 MeV neutrons (a ratio of 3.8). Hence, the reduction in neutron energy by the ISSEC is more effective in Nb than in Al.

It should be noted here that the displacement cross sections treat charged particle-out reactions [(n,p), (n,α), etc] as (n,n') reactions. Recent analysis shows that this underestimates damage done by higher energy neutrons by the following factors[14]

	% Underestimate of Damage at 14 MeV
Al	16
V	5
316 SS	17
Nb	3
Mo	No data
Ta	0.06

The inclusion of these contributions would increase the dpa level in the low Z elements for the case of no ISSEC, but would have little effect on the dpa values in ISSEC protected systems. This would tend to make the ISSEC somewhat more effective for low Z elements than stated here. However, even including these correction factors, there still would be a slight advantage to using ISSECs with high Z as compared to low Z elements.

Turning to relative reduction in displacement damage as a function of carbon thickness, we see in Figure 3 that a reduction of 3-5 can be achieved using 12.5 cm of carbon while reductions by a factor of 20 can be accomplished by using 25 cm of carbon ISSEC in front of Mo. The significance of this observation is that if the wall life is predominantly determined by the level of the total displacement damage (without regard to the spatial configuration of defects) then one might extend the wall life due to radiation damage alone by factors of 5-20 in Mo and similar

values in other systems. The relative reduction in dpa rate achieved with the D-D system are within 10-30% of the D-T case and are not presented graphically here.

Reduction of He and H Production Rates

Table 2 lists the effect of carbon ISSEC on He gas generation rates in potential CTR first wall materials subjected to neutrons from D-D plasma and Table 3 gives the results for hydrogen production. The same results for the D-T plasma are shown in Table 4. Analysis of the cross section data reveals that almost all the helium and hydrogen production reactions in the materials considered for this study have thresholds over 2.5 MeV. This means that the helium and hydrogen production rates in the D-D plasma case are lower than in the D-T case by a factor almost identical to the reduction in the 14.1 MeV component of the incident flux per 1 MW/m^2 neutronic wall loading; namely by the factor of 4.43/3.78 (1.17).

The absolute effect of carbon ISSEC on helium generation in metals for the D-T case is shown on Figure 5. The same general behavior holds true for the D-D neutrons. The absolute effect here is much more pronounced than in the case of displacement damage. Reductions in helium gas productions range from 7 to 14 for 12.5 cm carbon and from 7 to 11 for hydrogen production with the same carbon thickness. The factors of reduction are 27-80 and 17-55, respectively for a 25 cm carbon ISSEC. Except for V and Al, the reduction in He production is always greater than that for the reduction in hydrogen production. The reduction in helium gas production in Ta is a factor of 2 more than the reduction in V. This is due to the lower threshold for (n,α) reactions in V (~7 MeV) than for Ta (11 MeV).

The relative reduction values are plotted in Figure 6 and it is to be noted that on a linear scale, there is little difference between the elements. If there is a discernable trend, it is that the relative reduction is greater for high Z elements than for low Z elements. This is undoubtedly due to the high coulomb barrier (and therefore higher threshold energies) for (n,α) reactions in the high Z elements.

There is one major thing missing in the data we have presented so far as the helium generation in 316 SS is concerned. As we increase the

Table 2

Effect of Carbon ISSEC on the Helium Gas Production Rate in Potential CTR Materials in D-D Fusion Environment

	Appm He/Year[a]		
Material	No ISSEC	12.5 cm C	25 cm C
Al	405	42.8	8.90
V	67.0	9.72	2.46
316 SS[b]	239	22.8	4.6
Nb	27.8	2.82	0.58
Mo	62.0	5.94	1.2
Ta	6.42	0.46	0.08

(a) 1 MW/m^2 neutron wall loading, 100% Duty Factor.

(b) Neglecting helium from Ni^{59}.

Table 3

Effect of Carbon ISSEC on the Hydrogen Gas Production Rate in Potential CTR First Wall Materials in D-D Fusion Environment

	Appm H/Year[a]		
Material	No ISSEC	12.5 cm C	25 cm C
Al	944	95.2	20.0
V	122	24.4	7.32
316 SS	675	88.4	20.6
Nb	93.6	10.7	2.32
Mo	127	11.7	2.32
Ta	0	0	0

(a) 1 MW/m^2 neutron wall loading, 100% Duty Factor.

Table 4

Effect of Carbon ISSEC Thickness on the Gas Production Rates in Potential CTR Materials(a)

	D-T Plasma					
Material	appm He/yr No ISSEC	12.5 cm ISSEC	Damage Ratio	appm No ISSEC	H/year 12.5 cm ISSEC	Damage Ratio
Al	476	50.1	0.11	1110	111	0.10
V	78.6	11.4	0.15	143	28.6	0.20
316 SS	280	26.8	0.10	736	100	0.14
Nb	32.7	3.32	0.10	110	12.6	0.11
Mo	72.6	6.95	0.10	149	13.7	0.09
Ta	7.52	0.55	0.07	0	0	-

(a) 1 MW/m^2 neutronic wall loading, 100% Duty Factor

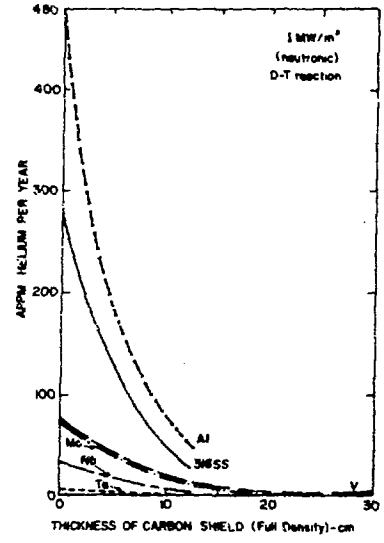

Figure 5 Reduction of Helium Generation Rates with Carbon ISSEC in D-T Systems.

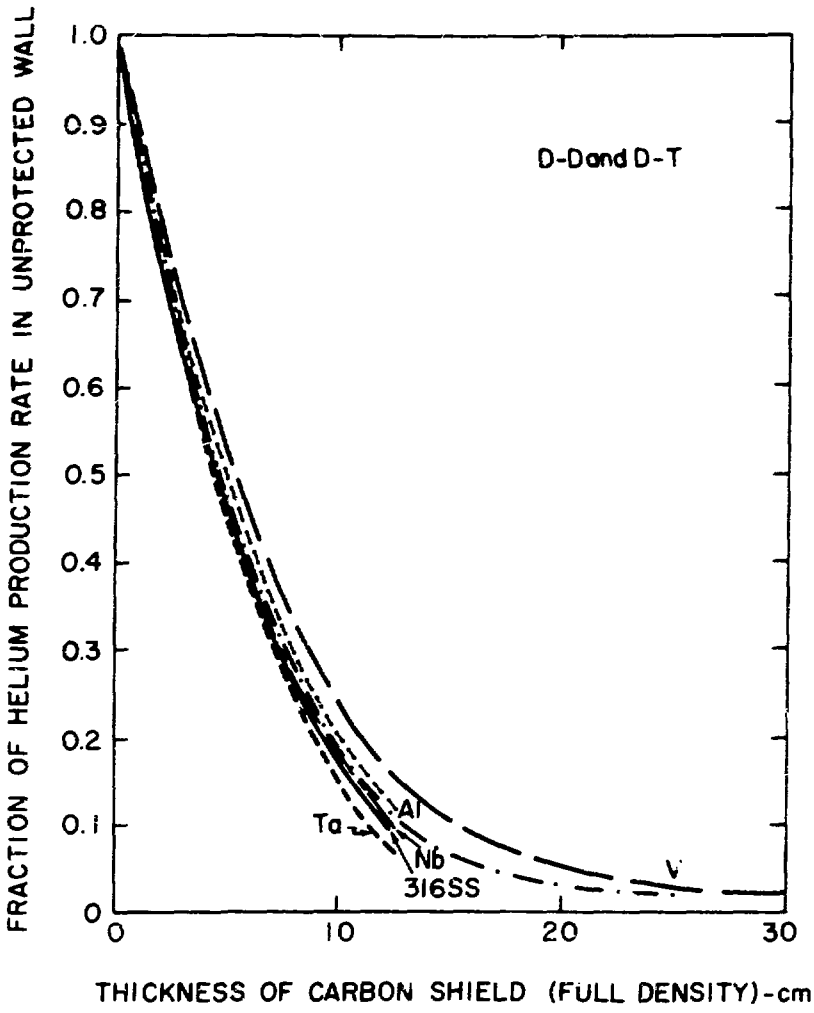

Figure 6 Normalized Helium Production Rates in ISSEC Protected Systems. D-D and D-T.

thermal components of the flux in the first wall by putting carbon in front of it, the $Ni^{58}(n,\gamma)$ $Ni^{59}(n,\alpha)$ reaction sequence plays an important role and the helium generation in 316 SS increases dramatically. We have calculated this effect and the results are given in Table 5 for various plant operating times, with 100% duty factor, and for different ISSEC thicknesses. The calculational procedure for this is given in Appendix C. Table 6 lists the total amount (due to thermal and high energy neutron reactions) of He generated in 316 SS first wall. The results are also plotted in Figure 7. It is apparent that while this thermal neutron induced helium generation is negligible when we have no ISSEC in both D-D and D-T cases, it becomes increasingly important as the carbon thickness and the first wall lifetime increases. This is especially true in D-D because of the larger number of neutrons and the softer spectrum.

For the D-T case with 12.5 cm of ISSEC, the amount of helium generated from $Ni^{58}(n,\gamma)$, $Ni^{59}(n,\alpha)$ reactions never quite catches up with the amount of helium generated from (n,α) reaction with fast neutrons even after 20 years of operation. But in the D-D case, the thermally produced α's over-ride the fast neutron produced α's after about 4 years with 12.5 cm ISSEC, and after about 6 months with 25 cm of ISSEC.

Effect of ISSECs on the Neutron Induced Radioactivity

The effect of ISSECs on the neutron induced radioactivity depends on whether the isotopes causing the most radioactivity are produced as a result of fast neutron or thermal neutron activation. One may even get reversal of the trends depending on the half lives of the isotopes.

Table 7 lists the levels of neutron induced radioactivity in potential CTR first wall materials at various times after shutdown for a two year operating time in a D-D system. The results are tabulated for bare wall and two different ISSEC thicknesses. Table 8 lists the radioactivity after 20 years of irradiation time. Two year irradiation results are plotted in Figures 8, 9 and 10 at shutdown, 1 year after shutdown and 100 years after shutdown, respectively. At shutdown and 100 years after shutdown, results for D-T plasma case are given in Tables 9 and 10 along with the D-D results for comparison. The D-T neutronic calculations were done for only 0 and 12.5 cm ISSEC thicknesses. For

Table 5

Appm He* Generated in 316 SS from $Ni^{58}(n,\gamma)$, $Ni^{59}(n,\alpha)$ Reaction Sequence Only

D-D

Operation Time (years)	No ISSEC	12.5 cm C	25 cm C
1	0.0052	5.65	28.2
2	0.0212	22.6	113
5	0.133	141	704
10	0.531	565	2820
20	2.12	2260	11260

D-T

	No ISSEC	12.5 cm ISSEC
1	0.0023	1.14
2	0.0093	4.55
5	0.059	28.5
10	0.23	114
20	0.94	455

* Per 1 MW/m^2 neutron wall loading, 100% Duty Factor

Table 6

Total Appm He Generated in 316 SS*

D-D

Operation Time (Year)	No ISSEC	12.5 cm ISSEC	25 cm ISSEC
1	239	28.5	32.8
2	477	63.2	122
5	1190	255	727
10	2390	793	2861
20	4770	2720	11400

D-T

	No ISSEC	12.5 cm ISSEC
1	280	27.9
2	560	58.2
5	1400	163
10	2800	382
20	5600	991

* Per 1 MW/m^2 neutron wall loading, 100% Duty Factor and includes threshold and thermally produced gas.

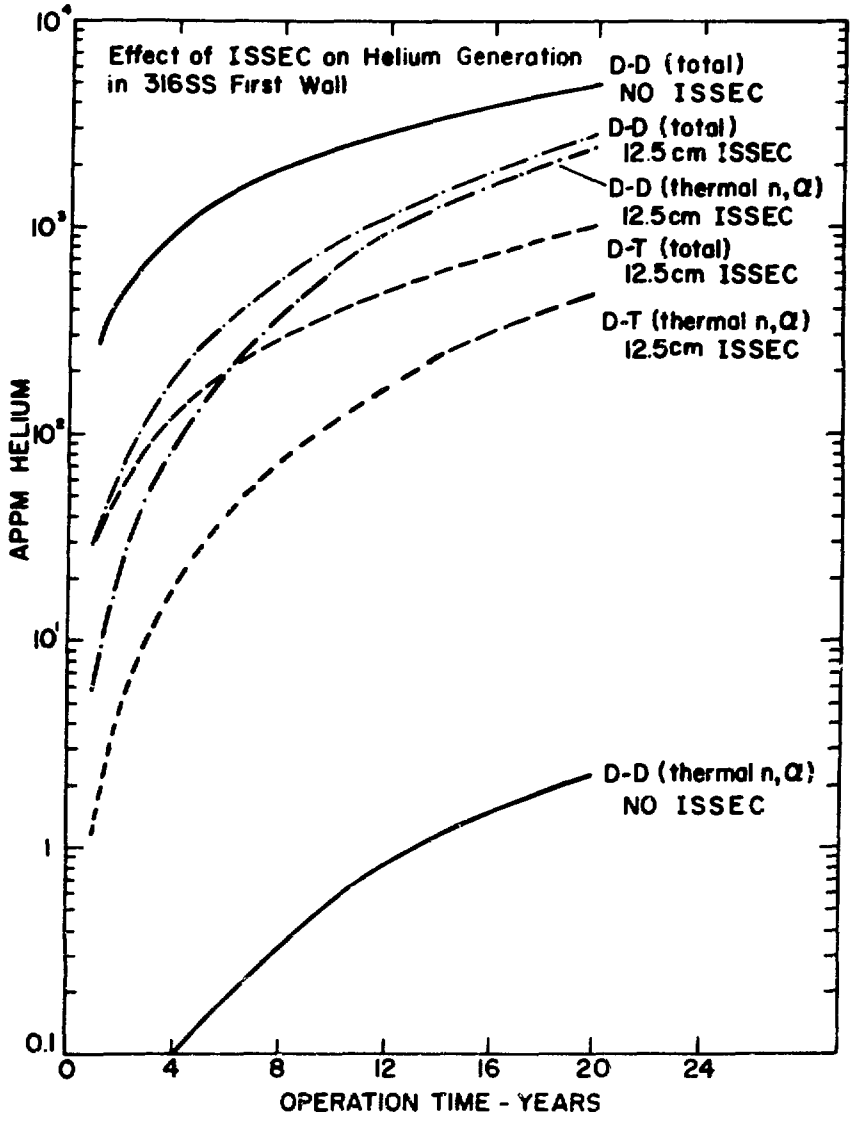

.gure 7 The Comparison Effect of Thermal $Ni^{59}(n,\alpha)$ Reaction on the Helium Production in 316 SS First Wall in D-D and D-T ISSEC Systems.

Table 7

Level of Neutron Induced Radioactivity at Various Times After Shutdown in the First Wall of a Carbon ISSEC Protected System After 2 Years of Operation/DD Plasma

		Curies/cm^3 (a)					
		Shutdown	1 day	1 week	1 year	20 years	100 years
	No ISSEC	39.8	6.84	8.8×10^{-3}	1.3×10^{-5}	1.3×10^{-5}	1.3×10^{-5}
Al	12.5 cm ISSEC	11.2	0.72	9.4×10^{-4}	7.7×10^{-7}	7.7×10^{-7}	7.7×10^{-7}
	25 cm ISSEC	17.9	0.15	1.9×10^{-4}	1.3×10^{-7}	1.3×10^{-7}	1.3×10^{-7}
	No ISSEC	27.2	5.52	.56	~0	~0	~0
V	12.5 cm ISSEC	95.4	.4	.04	~0	~0	~0
	25 cm ISSEC	345.4	.1	1.3×10^{-2}	~0	~0	~0
	No ISSEC	183.4	146.4	96.6	1.9×10^{-3}	1.9×10^{-3}	1.9×10^{-3}
Nb	12.5 cm ISSEC	122.2	12.9	8.5	8.4×10^{-3}	8.4×10^{-3}	8.4×10^{-3}
	25 cm ISSEC	126.2	2.5	1.64	9.6×10^{-3}	9.6×10^{-3}	9.6×10^{-3}
	No ISSEC	497	164.8	120.8	13.9	9.0×10^{-18}	~0
Ta	12.5 cm ISSEC	1951.	1270.	1221.	140.6	9.2×10^{-17}	~0
	25 cm ISSEC	2478	1632	1573	181	1.2×10^{-16}	~0
	No ISSEC	83.5	58.1	--	25.5	2.1(b)	2.1×10^{-3}
316 SS	12.5 cm ISSEC	26.3	23.0	--	4.9	0.42(b)	1.81×10^{-4}
	25 cm ISSEC	47.0	45.2	--	7.9	0.71(b)	$1.[illegible] \times 10^{-5}$

(a) Per 1 MW/m^2 neutronic wall loading, 100% Duty Factor.

(b) Values at 10 years after shutdown

Table 8

Level[(a)] of Neutron Induced Radioactivity at Various After Shutdown Times in the First Wall of an ISSEC Protected System After 20 Years of Operation/DD Plasma

Curies/cm^3 (a)

		Shutdown	1 Day	1 Week	1 Year	20 Years	100 Years
	No ISSEC	39.8	6.84	9.0×10^{-3}	1.3×10^{-4}	1.3×10^{-4}	1.3×10^{-4}
Al	12.5 ISSEC	11.8	0.72	9.4×10^{-4}	7.8×10^{-6}	7.8×10^{-6}	7.8×10^{-6}
	25 cm ISSEC	17.9	0.15	2.0×10^{-4}	1.3×10^{-6}	1.3×10^{-6}	1.3×10^{-6}
	No ISSEC	27.2	5.52	.56	~0	~0	~0
V	12.5 cm ISSEC	95.4	.4	.04	~0	~0	~0
	25 cm ISSEC	345.4	.1	1.3×10^{-2}	~0	~0	~0
	No ISSEC	183.4	146.4	96.6	.019	.019	.019
Nb	12.5 cm ISSEC	122.2	12.9	8.58	.084	.084	.084
	25 cm ISSEC	126.4	2.58	1.74	.096	.096	.096
	No ISSEC	498.4	166.4	122.2	14.1	9.2×10^{-18}	~0
Ta	12.5 cm ISSEC	1966	1286	1236	142.4	9.2×10^{-17}	~0
	25 cm ISSEC	2498	1651	1592	183.2	1.2×10^{-16}	~0
	No ISSEC	125.5	99.6	--	57.2	5.2[(b)]	0.019
316 SS	12.5 cm ISSEC	32.1	28.8	--	11.3	1.02[(b)]	1.67×10^{-3}
	25 cm ISSEC	46.6	45.1	--	17.8	1.6[(b)]	3.14×10^{-4}

(a) units are curies/cm^3 per 1 Mw/m^2 neutron wall loading at 100% duty factor.

(b) values at 10 years after shutdown

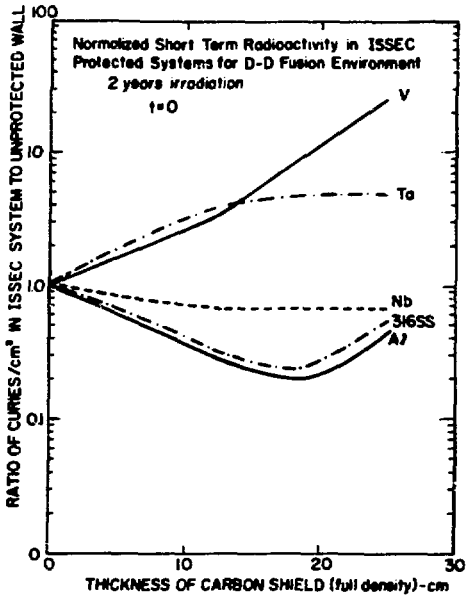

Figure 8 Normalized Short Term (Shutdown) Radioactivity in ISSEC Protected D-D Systems After 2 Years of Irradiation.

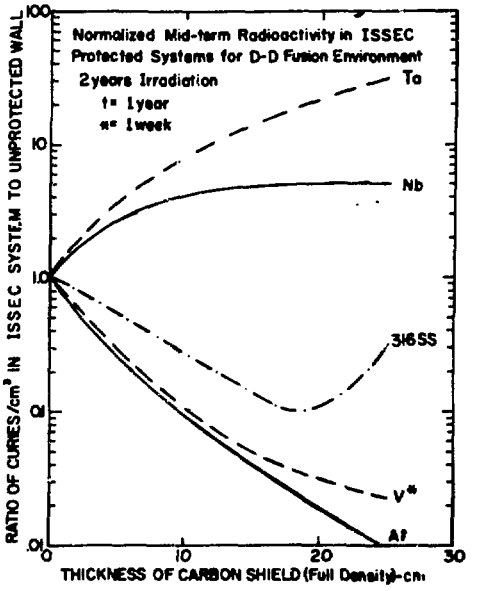

Figure 9 Normalized Mid-term (1 year) Radioactivity in ISSEC Protected D-D Systems after 2 Years Irradiation.

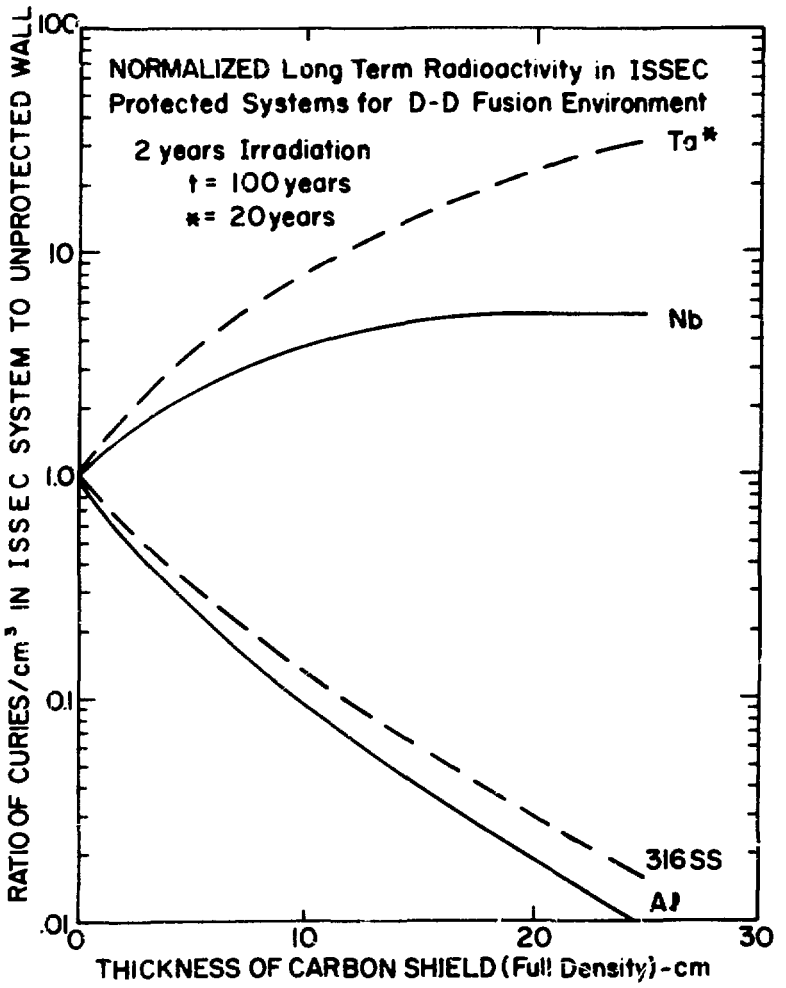

Figure 10 Normalized Long Term (100 years) Radioactivity in ISSEC after 2 Years Irradiation.

Table 9

Level of Neutron Induced Radioactivity at Shutdown in First Wall in an ISSEC Protected System After 2 Years of Irradiation

D-T Plasma[a]

Material	No ISSEC	12.5 cm ISSEC	Fraction of Unprotected First Wall Values
Al	47.4	20.4	0.43 (decrease)
V	13.3	32.8	2.44 (increase)
316 SS	91.2	15.3	0.17 (decrease)
Nb	138	60.4	0.43 (decrease)
Mo	NA	NA	---
Ta	471	925	1.96 (increase)

D-D Plasma[a]

Material	No ISSEC	12.5 cm ISSEC	Fraction of Unprotected First Wall Values
Al	39.8	11.2	.28 (decrease)
V	27.2	95.4	3.51 (increase)
316 SS	83.5	26.3	.32 (decrease)
Nb	183	122	.67 (decrease)
Mo	NA	NA	---
Ta	497	1950	3.93 (increase)

(a) curies/cm^3 per 1 MW/m^2 neutron wall loading at 100% duty factor

NA - Not Available

Table 10

Level of Neutron Induced Radioactivity 100 Years After Shutdown in the First Wall of ISSEC Protected System After 2 Years of Irradiation

Material	No ISSEC	D-T Plasma[a] 12.5 cm of ISSEC	Fraction of Unprotected First Wall Values
Al	1.49×10^{-5}	9.14×10^{-7}	0.06 (decrease)
V	$<10^{-15}$	$<10^{-15}$	0.15[b] (decrease)
316 SS	3.42×10^{-3}	2.05×10^{-4}	0.06 (decrease)
Nb	0.001	0.0038	3.85 (increase)
Mo	NA	NA	----
Ta	$<10^{-15}$	$<10^{-15}$	8[c] (increase)

Material	No ISSEC	D-D Plasma[a] 12.5 cm of ISSEC	Fraction of Unprotected First Wall Values
Al	1.3×10^{-5}	7.7×10^{-7}	0.06 (decrease)
V	$<10^{-15}$	$<10^{-15}$	0.07[b] (decrease)
316 SS	2.1×10^{-3}	1.81×10^{-4}	0.09 (decrease)
Nb	1.9×10^{-3}	8.4×10^{-3}	4.42 (increase)
Mo	NA	NA	----
Ta	$<10^{-15}$	$<10^{-15}$	10.2[c] (increase)

(a) curies/cm^3 per 1 MW/m^2 neutronic wall loading, 100% duty factor
(b) value 1 week after shutdown
NA - Not Available
(c) values 20 years after shutdown

both D-D and D-T cases the trends are the same. The short term radioactivity decreases for Nb, 316 SS and Al, but it increases for V and Ta as the thickness of the carbon shield is increased to 12.5 cm. When one considers the long term radioactivity, V and Nb switch places and Ta and Nb have higher radioactivities while 316 SS, V and Al have lower radioactivities than with 12.5 cm of ISSEC than they do with no ISSEC.

As the thickness of the ISSEC is increased over 12.5 cm, some interesting things start to happen. In Al and 316 SS those isotopes produced as a result of thermal neutron activation gain importance and the radioactivity curves start to rise. Nb and Ta total activities saturate but V keeps increasing. At 1 year after shutdown, 316 SS curve still has the same shape but Al radioactivity keeps decreasing because of the short half lives of those isotopes thermally produced. The Nb and Ta activities again tend to saturate. At 100 years after shutdown in 316 SS, the thermally activated radioisotopes have decayed away and the total radioactivity continues to decrease with increasing carbon thickness.

It should also be noted in Tables 9 and 10 that the ISSEC is more effective in reducing neutron induced radioactivity at shutdown in 316 SS and Nb for D-T than for D-D. It is also apparent that the ISSEC is more effective for Al in the D-D case than for the D-T case. At 100 years after shutdown, the reduction in radioactivity in 316 SS is less in the D-D system. The reduction factor is about the same in Al for both cases. At long times after shutdown radioactivity in V decays to insignificant levels. However, at 1 week after shutdown, it is reduced more in D-D system than in D-T. Long term radioactivities in Nb and Ta increase more for the D-D than the D-T case because long lived radioisotopes in Nb and Ta are produced as a result of thermal (n,γ) reactions.

Radiation Damage in the ISSEC

The reduction in metallic damage properties is partially taken up by the increased radiation damage in the carbon. The most serious questions have been assessed elsewhere[2] and they are:

1. Will any displacement damage survive at irradiation temperatures of 1500-2000°C (0.5-0.66 T/Tm)?

2. What will the generation of large amounts of He (several thousand

appm) do to the carbon at high temperatures?
Unfortunately, there is no experimental evidence to answer these questions now, but the authors tend to think that the displacement damage will anneal at these high temperatures, but the helium may collect into bubbles causing dimensional instabilities. Some recent work done by Bauer et al.[15] give some reason to hope that little permanent damage will be done due to this high helium generation. It was found that the remission rate of helium bombarded carbon was very high (essentially 100%) at temperatures of 1200°C. If this holds true for the carbon in an ISSEC, then perhaps there is little cause for concern about the several thousand appm of helium generated per year of operation at 1 MW/m^2 neutron wall loading. Obviously, more work is needed in this area.

DISCUSSION

All the results presented so far in this paper and elsewhere[2,3] have been normalized to 1 MW/m^2 neutronic wall loading. When one considers only one type of reactor with a certain plasma cycle, this way of normalizing the radiation damage results is quite convenient. The response of different materials to neutron spectral shifting, provided the same blanket structure is used in all cases, is also straightforward. However, when one considers two different plasma reactions as we have, another way of comparing the radiation damage results might be to normalize on the basis of MW of power. In the real case, the difficulty is that one needs to breed tritium for the DT cycle whereas in the D-D cycle, this is not required. Therefore, it is quite probable that two completely different blanket structures would be used and the neutron energy multiplication, as well as γ heating, can be much different for the two cases. All the present calculations were done with the same non-breeding blanket scheme shown in Figure 1, so any comparison made on the basis of total power generation would not be meaningful.

Another way of quoting the damage would be to normalize it on the basis of a megawatt of power generated in the plasma. Such a comparison requires a knowledge of the burnup of tritium and He-3 atoms produced by the D-D reactions. Miley[16] has shown that at 30 keV, essentially all the tritium produced is consumed and approximately 20% of the He-3 is "burned".

The reactions taking place and the energies of various products (MeV) in a D-D plasma are given below.

$$D + D \rightarrow T(1.01) + p(3.03)$$
$$D + D \rightarrow He^3(0.82) + n(2.45)$$
$$D + T \rightarrow He^4(3.52) + n(14.06)$$
$$D + He^3 \rightarrow He^4(3.67) + p(14.67)$$

If we use the results of Miley, we can calculate the neutron flux associated with a 1 MW/m^2 wall loading based on the thermal power produced in the DD plasma.

$$1\ MW/m^2(\text{plasma thermal}) = (\text{const.}) \times \left(\frac{4.04+3.27+17.60+0.2\times18.3}{2}\right) \frac{MeV}{n} \times (4.34 \times 10^{13}\ n/(cm^2\text{-sec})$$

In the D-T case,

$$1\ \frac{MW}{m^2}\ (\text{plasma thermal}) = (\text{const.}) \times 17.6\ \frac{MeV}{n} \times 3.55 \times 10^{13}\ \frac{n}{cm^2\text{-sec}}$$

where the conversion factor (const.) has a value of 1.602×10^{-15}. It appears that if we wanted to normalize our results to 1 MW/m^2 (plasma thermal), the D-T results (dpa, gas production, activation, etc.) would be approximately 20% less than presented here and the D-D results would be 43% less. These reductions tend to make the displacement rate equal in both systems and increase the advantage of the DD spectrum with respect to helium and hydrogen production.

For illustration, results for 316 SS are reproduced in Table 11 for the two normalizations. In this table, dpa and hydrogen production results are lower when they are normalized on the basis of plasma thermal by the factors given above; namely 20% in D-T and 43% in D-D cases. The same conclusions can be drawn about the other materials considered here.

Analysis of this work leads us to the observation that the radiation damage incurred in protected or unprotected D-D systems is almost the same as for the D-T systems. For example, as we see in Table 11 the displacement damage is higher in D-D systems when neutronic wall loading normalization is used, but this becomes about the same in the two systems when plasma thermal normalization is used. Gas production results are 10

Table 11

A Comparison of Possible Normalization Procedures for DD&DT Fusion Systems - 316 SS First Wall

		1MW/m^2 Neutronic			1MW/m^2 Plasma Thermal		
		D-D	DT	$\frac{DD}{DT}$	DD	DT	$\frac{DD}{DT}$
dpa/yr	No C	16.8	11.3	1.49	9.64	9.06	1.06
	12.5 cm C	3.2	2.5	1.28	1.97	2.0	0.99
	25 cm C	0.86		--	0.49		
Appm He 10 yrs.	No C	2387	2800	0.85	1370	2240	.61
	12.5 cm C	793	381	2.08	317	305	1.04
	25 cm C	2861			956		
Appm H/yr	No C	675	736	0.92	388	590	.66
	12.5 cm C	88.4	100	0.88	50.8	80.1	.63
	25 cm C	20.6	--	--	11.8	--	--

to 15% lower in D-D with 1 MW/m^2 (neutronic)normalization. This difference in gas production rates goes to 30-40% for the second normalization but it still is not much of an improvement over the D-T system.

CONCLUSIONS

A few general conclusions can be gathered from these studies about both DT and DD carbon ISSEC systems.

- Reduction in displacement rates of 3-5 can be obtained with 12.5 cm of carbon and 25 cm can reduce displacement damage by a factor of 8 to 20.
- With the exception of 316 SS, helium production can be reduced by factors of 7 to 14 with 12.5 cm of carbon and by factor of 27 to 80 with 25 cm of carbon.
- The use of carbon ISSEC to soften the neutron spectrum to 316 SS initially decreases the helium production rates by a factor of 8-10 for 12.5 cm (1 year). However, due to build-up of Ni-59 which has a high thermal (n,α) cross section, the total amount of helium generated after 10 years of operation is actually greater in D-D ISSEC system than that in an unprotected first wall.
- Depending on the mode of activation and time after shutdown the ISSEC systems can increase or decrease the induced radioactivity. In general, it decreases the short term radioactivity of Al, 316 SS, and Nb. It actually increases the activity in V and Ta. The behavior is somewhat different for long term activities in that the activity of V is decreased and that of Nb is increased over the unprotected case. (The rest of the values stay the same).

There are also several conclusions we can state for DD versus DT ISSEC protected systems that produce the same neutron power and have it passing through the same wall area.

Advantages of D-D ISSEC

. The helium production rates are approximately 15% lower for all elements except those containing Ni regardless of the ISSEC thickness.

. The short lived radioactivities is reduced without an ISSEC in Al (16%) and 316 SS (9%). Behind a 12.5 cm ISSEC this reduction is 45% for Al.

. The long lived radioactivity is reduced without an ISSEC in Al (13%) and 316 SS (39%). Behind a 12.5 cm ISSEC, it is reduced by 16% in Al and 12% in 316 SS.

Disadvantages of a D-D ISSEC

. The displacement damage is increased, without an ISSEC, in Al (56%), V (43%), 316 SS (49%), Nb (27%), Mo (29%), and Ta (25%). Behind 12.5 cm ISSEC the rates are still higher than in a DT system for Al (41%), V (53%), 316 SS (28%), Nb (30%), Mo (32%), and Ta (30%).

. The helium production from Ni^{59} is increased by a factor of 5 behind a carbon ISSEC.

. The total helium production is 2% greater after one year of DD neutrons and 270% greater after 20 years of irradiation for 12.5 cm ISSEC.

. The short lived radioactivity without an ISSEC is increased in V (105%), Nb (33%), and Ta (1%). Behind a 12.5 cm ISSEC, the same radioactivity is increased in V (188%), Nb (103%), Ta (111%) and 316 SS (72%) over the similar DT case.

. The long lived radioactivity is increased in the unprotected wall for Nb (90%) and Ta (61%). Behind a 12.5 cm ISSEC it is also increased for Nb (121%) and Ta (115%).

The above conclusions for the displacement rates will be altered by ~29% if the results are calculated on the basis of total power generated in the plasma. In general, this will tend to make the displacement rates about the same for both DT and DD systems and make the DD system more advantageous from the standpoint of helium and hydrogen production by high energy reactions. The exception is that the total amount of helium produced in Ni containing alloys will still be greater in DD as compared to DT systems.

The conclusions about the short and long lived activity will be the same except for one exception, the short lived activity of Ta without an ISSEC will be decreased, not increased.

An overall conclusion is that a DD system does <u>not</u> represent a significant advantage over a DT system unless relative difference of 20% in the amount of He produced in non-Ni containing alloys is a critical feature. Certainly a DD system represents no significant advantage over the DT case

with respect to dpa, He and induced radioactivities in 316 SS.

ACKNOWLEDGEMENT

This research was partially supported by the Energy Research and Development Administration and the Wisconsin Electric Utilities Research Foundation.

REFERENCES

1. G. L. Kulcinski, R. W. Conn and G. Lang, Nucl. Fusion 15, 327, 1975.

2. R. W. Conn, G. L. Kulcinski, H. Avci and M. El-Maghrabi, Nuclear Tech. 26, 125, 1975.

3. G. L. Kulcinski, R. W. Conn, H. I. Avci, D. K. Sze, "Protection of CTR Metallic First Walls by Neutron Spectral Shifting," Nuclear Engineering Dept. Report UWFDM-127, June 1975. Also Trans. Am. Nucl. Soc. 21, 50 (1975).

4. D. K. Sze, R. W. Conn, "Heat Transfer and Neutronics of ISSEC and Partial ISSEC Blanket Designs" Nuclear Engineering Dept. Report UWFDM-128, June 1975. Also Trans. Am. Nucl. Soc. 21, 34 (1975).

5. W. W. Engle, Jr., "A Users Manual for ANISN", K-1693, Oak Ridge Gaseous Diffusion Plant.

6. D. J. Dudziak, "Fusion Reactor Nuclear Analysis Methods and Applications," 8th Symp. on Fusion Technology, Noordijkerhout, The Netherlands, June 1974. p.

7. R. W. Wright, et al., "SUPERTOG, A Program to Generate Fine Group Constants and Pn Scattering from ENDF/B", ORNL-TM-2679, Oak Ridge National Laboratory (1969).

8. M. K. Drake, Ed., "Data Formats and Procedures for ENDF Neutron Cross Section Library", BNL-50279, Brookhaven National Laboratory (1970). See also). Ozer and D. Garber "ENDF/B Summary Documentation" BNL-17541 and ENDF-201, Brookhaven National Laboratory (July 1973).

9. S. Pearlstein, private communication, See also S. Pearlstein, J. Nuclear Energy, 27, 81, (1973).

10. D. G. Doran, Nucl. Sci. Eng. 52, 398, 1973. See also Nucl. Sci. Eng. 49, 130, 1972.

11. G. L. Kulcinski, D. G. Doran, and M. A. Abdou, to be published, ASTM Proceedings of Radiation Effects on Structural Materials, Gatlinburg, Tenn., June 1974.

12. T. Y. Sung, Unpublished work.

13. M. T. Robinson, "The Energy Dependence of Neutron Radiation Damage in Solids" B.N.E.S. Nucl. Fus. React. Conf., Culham Laboratory, Sept. 1969.

14. D. G. Doran, G. R. Odette and N. J. Graves, p. 2 in Hanford Engineering Development Laboratory Report, HEDL-TME-75-24, February 1975.

15. W. Bauer and G. J. Thomas, to be published, International Conf. on the Application of Ion Beams to Materials, Warwick, England, September 1975.

16. G. Miley, Univ. of Illinois, private communication.

17. W. C. Morgan, J. Nuclear Energy. 51, 509, 1974.

Appendix A

Displacement Cross Sections - Used in this Work

				Barns		
Group	316 SS	Mo	Nb	V	Al	C
1	2225	1751	1717	2279	1924	1254
2	2078	1670	1613	2169	1909	1378
3	1993	1557	1518	2097	1883	1364
4	1955	1561	1435	2056	1823	1015
5	1913	1362	1372	2009	1733	1107
6	1903	1281	1305	1973	1710	1038
7	1898	1254	1238	1938	1710	1704
8	1848	1156	1165	1899	1695	789
9	1763	1108	1088	1861	1568	966.5
10	1703	1048	1010	1816	1703	829.7
11	1660	965	935	1752	1658	914.7
12	1623	916.2	863	1690	1620	1047
13	1560	887	797	1626	1549	1512
14	1493	843.2	737	1566	1568	1519
15	1410	780	683	1502	1538	1855
16	1375	759	637	1457	1500	1101
17	1295	741.1	610	1379	1474	1428
18	1275	711.9	610	1346	1556	844.6
19	1070	639.2	569	1073	1379	867.8
20	788	534.6	500	967.1	1211	915.5
21	634.4	442.1	461.6	849.8	1068	985.4
22	462.8	378.4	425.8	581.6	1023	1013
23	398.3	342.6	373.5	463.2	860.8	997.1
24	373	287.3	256	387.9	831.4	941.9
25	301.4	247.6	173.7	382.2	601.5	863
26	195.6	201.2	138.5	309.4	511.8	763
27	196.8	164.8	109.6	285.8	545.6	647
28	180.3	128.9	87.3	285.8	597.4	560
29	120.8	93.5	68.1	190.6	330.7	547
30	68.6	44.5	34.3	109	136.9	358

Appendix A

Displacement Cross Sections - Used in this Work

Group	316 SS	Mo	Nb	V	Al	C
31	93.1	20.1	17.6	212.6	231.5	193.5
32	26.3	13.8	9.3	106.3	132.1	99.4
33	15.8	6.7	5.2	146.5	97.4	49.5
34	5.2	3.6	1.9	8.44	32.5	24.6
35	3.56	2.2	1.5	.51	14.7	12.0
36	1.04	1.9	1.3	.26	6.3	5.8
37	.13	1.1	1.3	.36	2.7	2.8
38	.19	2.0	1.3	.36	.64	1.4
39	.27	8.0	1.3	.37	.88	0
40	.4	1.4	1.1	.54	1.11	0
41	.58	.41	.045	.78	1.41	0
42	.84	.19	.065	1.1	2.7	0
43	1.2	.23	.095	1.65	3.8	0
44	1.79	.33	.14	2.4	4.5	0
45	2.6	.48	0.2	3.5	8.3	0
46	5.3	1.0	0.4	6.83	14.6	0

The above 46 group displacement cross sections for 316 SS, Mo, Nb, V and Al are condensed from the 100 group cross sections given in references 8 and 9. The displacement threshold energies used are 24, 37, 36, 24 and 16 eV for 316 SS, Mo, Nb, V, and Al, respectively.[11] The secondary displacement function used is:

$$\nu(T) = \beta \frac{L(\varepsilon)}{\varepsilon} \frac{T}{2E_d}$$

where E_d is the effective displacement energy, taken to be 5/3 times displacement threshold energy,

$\varepsilon = A_L T$ and for pure materials of atomic number Z and atomic weight A,

$$A_L = \frac{0.01151}{(Z)^{7/3}} \text{ eV}^{-1}$$

$$L(\varepsilon) = \frac{\varepsilon}{[1 + K_L g(\varepsilon)]}$$

where $g(\varepsilon) = \varepsilon + 0.40244\ \varepsilon^{3/4} + 3.4008\ \varepsilon^{1/6}$

and $K_L = \frac{0.1334\ (Z)^{2/3}}{A^{1/2}}$

$\beta = 0.8$

The carbon displacement cross sections are from W. C. Morgan, ref. 17.

APPENDIX B

46 Group Neutron Fluxes at the First Mesh Point in the 316 SS First Wall Normalized to 10^{15} n's/cm^2-sec Incident

Group #	D-T Reaction		D-D Reaction		
	No ISSEC	12.5 cm ISSEC	No ISSEC	12.5 cm ISSEC	25 cm ISSEC
1	2.3259 + 15*	1.4262 + 14	1.1630 + 15	7.1309 + 13	1.1786 + 13
2	1.1157 + 14	5.3754 + 13	5.5786 + 13	2.6877 + 13	6.4653 + 12
3	7.1843 + 13	3.2674 + 13	3.5922 + 13	1.6337 + 13	4.0183 + 12
4	7.1850 + 13	2.6311 + 13	3.5925 + 13	1.3156 + 13	3.4260 + 12
5	4.5608 + 13	1.4463 + 13	2.2804 + 13	7.2314 + 12	2.0268 + 12
6	6.2184 + 13	3.63 + 13	3.1092 + 13	1.8146 + 13	4.7694 + 12
7	5.5999 + 13	2.8585 + 13	2.2995 + 13	1.4292 + 13	3.0461 + 12
8	4.1854 + 13	3.708 + 13	2.0927 + 13	1.8540 + 13	6.4088 + 12
9	3.2641 + 13	2.202 + 13	1.6316 + 13	1.1010 + 13	3.4242 + 12
10	3.9763 + 13	3.0527 + 13	1.9882 + 13	1.5263 + 13	5.1483 + 12
11	3.4660 + 13	2.4321 + 13	1.7330 + 13	1.2161 + 13	4.3510 + 12
12	3.7632 + 13	2.619 + 13	1.8816 + 13	1.3095 + 13	4.6437 + 12
13	3.7388 + 13	2.373 + 13	1.8694 + 13	1.1865 + 13	4.2978 + 12
14	3.8695 + 13	2.0927 + 13	1.9348 + 13	1.0464 + 13	3.7237 + 12
15	3.8637 + 13	1.7992 + 13	1.9319 + 13	8.9960 + 12	2.9962 + 12
16	4.6361 + 13	2.5186 + 13	2.3181 + 13	1.2593 + 13	4.2887 + 12
17	5.3827 + 13	2.5719 + 13	2.6914 + 13	1.2860 + 13	4.1963 + 12
18	7.3905 + 13	3.7625 + 13	1.3012 + 15	5.2485 + 13	9.7131 + 12
19	2.6462 + 14	1.2979 + 14	6.1531 + 14	1.5594 + 14	3.4937 + 13
20	3.1852 + 14	1.4280 + 14	5.7805 + 14	1.7685 + 14	4.1899 + 13
21	3.3476 + 14	1.4062 + 14	4.7819 + 14	1.7416 + 14	4.3548 + 13
22	3.2365 + 14	1.3157 + 14	3.8235 + 14	1.6134 + 14	4.2282 + 13
23	3.1759 + 14	1.2479 + 14	3.4328 + 14	1.5177 + 14	4.1311 + 13
24	2.6452 + 14	1.1129 + 14	2.7944 + 14	1.3558 + 14	3.8236 + 13
25	2.5470 + 14	1.0689 + 14	2.6271 + 14	1.3343 + 14	3.7916 + 13
26	1.9964 + 14	9.5222 + 13	2.0284 + 14	1.1671 + 14	3.4966 + 13
27	1.5899 + 14	8.6641 + 13	1.6136 + 14	1.0685 + 14	3.3019 + 13
28	1.3552 + 14	8.2045 + 13	1.3766 + 14	1.0181 + 14	3.2428 + 13
29	1.6988 + 14	1.4102 + 14	1.7222 + 14	1.7686 + 14	5.9809 + 13
30	9.8586 + 13	1.4172 + 14	1.0139 + 14	1.7994 + 14	6.5620 + 13
31	5.0216 + 13	1.3015 + 14	5.5265 + 13	1.6697 + 14	6.5834 + 13
32	2.3768 + 13	1.1606 + 14	2.7266 + 13	1.4983 + 14	6.3376 + 13
33	1.0200 + 13	1.0957 + 14	1.1779 + 13	1.4212 + 14	6.4468 + 13
34	2.8255 + 12	9.2384 + 13	3.2466 + 12	1.9780 + 14	5.8018 + 13
35	6.4045 + 11	7.9846 + 13	7.2662 + 11	1.0409 + 14	5.3751 + 13
36	1.5887 + 11	7.4086 + 13	1.7246 + 11	9.6718 + 13	5.3051 + 13
37	3.8813 + 10	6.9059 + 13	3.8855 + 10	9.0236 + 13	5.2371 + 13
38	9.1479 + 09	6.4237 + 13	7.6487 + 09	8.3988 + 13	5.1422 + 13
39	2.4159 + 09	5.9756 + 13	1.6621 + 09	7.8163 + 13	5.0374 + 13
40	3.4589 + 08	5.5683 + 13	2.3594 + 08	7.2856 + 13	4.9335 + 13
41	5.1950 + 07	5.1885 + 13	3.4355 + 07	6.7901 + 13	4.8236 + 13
42	9.4679 + 06	4.8350 + 13	5.8077 + 06	6.3283 + 13	4.7106 + 13
43	1.7284 + 06	4.5004 + 13	9.9778 + 05	5.8909 + 13	4.5900 + 13
44	2.0936 + 05	4.1743 + 13	1.2089 + 05	5.4644 + 13	4.4526 + 13
45	2.4277 + 04	3.8506 + 13	1.4075 + 04	5.0410 + 13	4.2932 + 13
46	2.2899 + 03	4.6434 + 14	1.3989 + 03	6.0794 + 14	1.5575 + 15

* Numbers in this table should be read as $a^{+}_{-} n = a \times 10^{+n}_{-n}$

EFFECT OF CARBON ISSEC ON NEUTRON SPECTRUM FROM A D-D PLASMA - 1 MW/m²

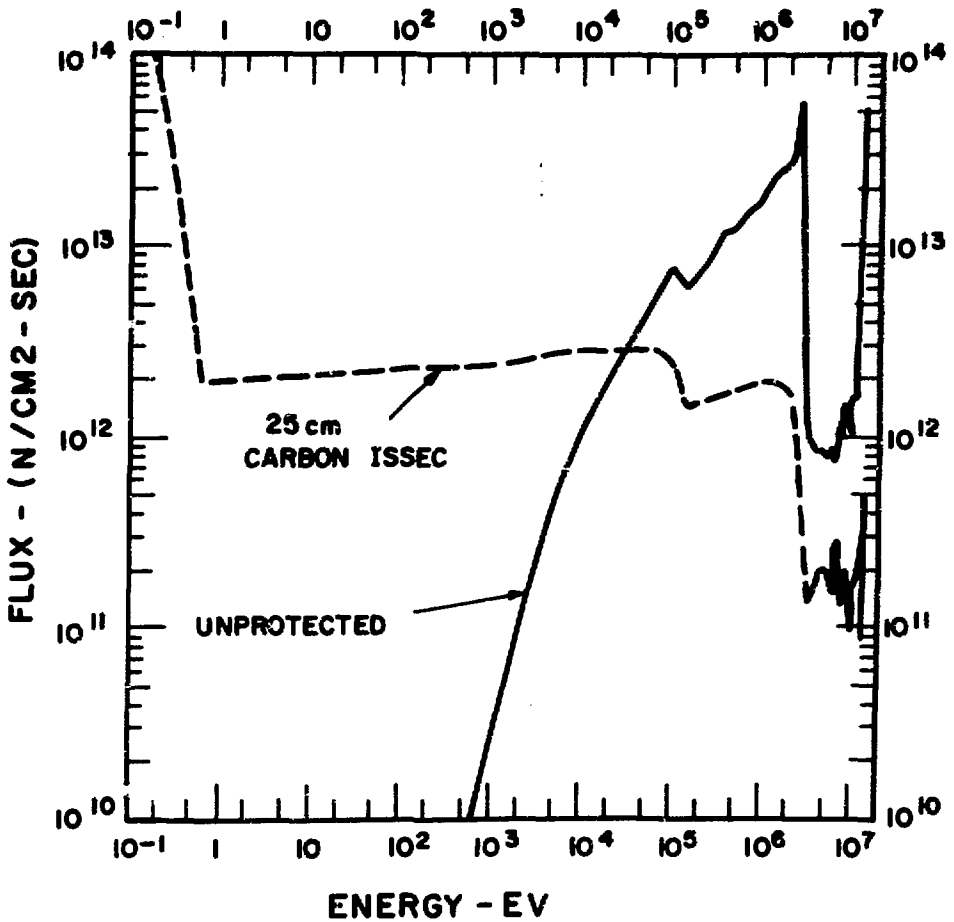

APPENDIX C

It has been known for some time that anomalous helium production occurs in Ni because of $^{58}Ni(n,\gamma)\ ^{59}Ni(n,\alpha)$ reaction sequence. Therefore, calculations were performed to test how important the ^{59}Ni reaction is to helium production in 316 SS first wall with the comparatively softer spectrum characteristic of 12.5 and 25 cm of ISSEC. Ignoring the burnout of ^{58}Ni atoms, the number of ^{59}Ni atoms as a function of time, N^{59}, due to a concentration of N^{58} of ^{58}Ni atoms undergoing (n,γ) reaction with a cross section σ^{γ}, is

$$N^{59}(t) = \sum_i N^{58}\sigma_i^{\gamma}\phi_i t,$$

where ϕ_i is the neutron flux in the i^{th} energy group. The number of helium atoms, N^{He}, produced in time, T, is then

$$N^{He} = \int_0^T \sum_j N^{59}(t)\sigma_j^{\alpha}\phi_j \, dt$$

$$= \frac{N^{58}T^2}{2} \sum_j \sum_i \sigma_i^{\gamma}\sigma_j^{\alpha}\phi_i\phi_j$$

where σ^{α} is the (n,α) cross section for ^{59}Ni. A more precise treatment would show that as the ^{59}Ni concentration reached steady state, N^{He} would be proportional to T, rather than T^2, which means the results presented here will give a pessimistic estimate of helium production. The (n,α) cross section of Kirouac (Nucl. Sci. Eng., 46, 427, 1971) was used.

STRESS EFFECTS IN ION BOMBARDMENT EXPERIMENTS*

F. A. Garner
G. L. Wire
E. R. Gilbert

Hanford Engineering Development Laboratory, Richland, WA

ABSTRACT

Ion bombardment is employed to simulate the neutron damage that will occur in fusion reactor structural materials. These experiments usually involve specimens whose thickness is large compared to the ion range. The correct interpretation of such experiments requires inclusion of the impact of swelling-induced stresses, which arise from the rigidity of the non-swelling region beyond the ion range. An initial low level of swelling is accommodated by elastic compression of the voided region, giving rise to anisotropic stresses whose deviatoric components lead to plastic deformation by various irradiation creep mechanisms. Swelling generates the stresses which lead to creep, which in turn limits the magnitude of stress. The hydrostatic stress along the ion range eventually saturates at a level which reduces the swelling rate from the anticipated stress-free value. The swelling is fully anisotropic, two-thirds of the deformation having been diverted from directions normal to the ion beam. Crystalline anisotropy further modifies the relative rates of creep processes, and radiation-hardening of the lattice imposes an additional fluence dependence. Stress reversal at denuded zones leads to second-order stress effects. The use of step height measurements allows observation and measurement of these phenomena. Estimates of the stress levels and swelling rates can be made using swelling and creep coupling coefficients derived from fission reactor data. A significant reduction in swelling rate is predicted by this analysis.

---

* Based on work performed by Hanford Engineering Development Laboratory, Richland, Washington, operated by Westinghouse Hanford Company, a subsidiary of Westinghouse Electric Corporation, under United States Energy Research and Development Administration Contract E(45-1)-2170.

INTRODUCTION

Charged particle irradiations at accelerated rates are currently employed in the simulation of neutron environments. However, in the analysis of simulation experiments, care must be taken to identify all of the relevant variables, particularly if undetected variables might play a major role in the environment being simulated. A pertinent example is the role of the stress state on swelling, which is known to be important in neutron environments but inadequately characterized in simulation experiments. Other authors[1] have noted that the stress state in ion bombardment experiments is probably atypical of the reactor environment, and should be studied to determine the impact of stress on the evolution of the data and its interpretation. In this report the role of stress in ion bombardment experiments will be examined in detail. Proper consideration of the role of stress will ensure that we are not inadvertently observing stress-affected behavior and interpreting the results as typical of stress-free behavior.

Stress fields can arise from a variety of sources such as external restraints or forces, differential swelling, temperature gradients, and unrelieved internal stresses generated by prior thermal-mechanical treatments. In a small unrestrained stress-relieved reactor specimen, there are no substantial gradients in temperature or flux, and the swelling that occurs should be isotropic and unaffected by stress. In simulation experiments, however, there can exist large displacement and temperature gradients which can give rise to swelling gradients, which in turn generate stress fields. It is expected that various creep mechanisms then react to the local deviatoric stresses in such a manner as to tend to relieve the stresses.

There is a growing body of evidence that points to the interrelationship of swelling and irradiation creep. In effect, these two phenomena are separate but related manifestations of the same process: the response of a crystalline lattice to the large point defect fluxes generated by irradiation. The details of the response are dependent, of course, on variables such as the stress state and temperature. If

swelling is non-uniform, the resultant induced stresses are also non-uniform. If the stress field is spatially anisotropic, we expect creep relief processes to react in an anisotropic manner. In addition, the magnitude of swelling has been shown to be related to the local hydrostatic stress level.[2,3] The net result is that both the magnitude and directional response of both swelling and irradiation creep are coupled through the stress environment in which they evolve and help generate.

OBSERVATIONS FROM EXPERIMENTAL STUDIES

The development of step-height measurement techniques has led to a substantial reduction in the manpower required to analyze ion-induced swelling data.[4] Using a partial mask, some regions of which are opaque to ions, a surface step develops between swelling and non-swelling regions. This allows a direct measure of the swelling integrated along the ion path. Much more importantly for this analysis, however, it demonstrates that swelling in these experiments is fully anisotropic. While we would expect swelling in a cubic structure to be isotropic in the absence of constraint, Lauritzen and coworkers[5] report that they observe (at 140 dpa) a step height of ∿60 Å per percent swelling (measured at the peak damage region) in 300 series stainless steels. It is very easy to show that this relationship requires complete anisotropy of swelling.

If we assume isotropic deformation to result from swelling, then the step height Δh would be defined by

$$\Delta h = \frac{\bar{S}\, R_{max}}{3} = \frac{1}{3} \int_0^{R_{max}} S(x)\, dx \,, \qquad (1)$$

where $\bar{S}$ is the mean swelling* along the full ion range defined by R_{max}. Assuming a simplified version of the current bilinear forms** for

---

* S and $\bar{S}$ are expressed here as fractions, rather than the conventional percentage increases in original volume.

** Documented in Reference 6.

swelling S with dose d for a fixed temperature,

$$S(d) = C\,[d - f(\alpha,\tau,d)]\ , \qquad (2)$$

where $f(\alpha,\tau,d)$ is a delay term that models an incubation period which precedes the linear swelling regime. The terms τ, α, and C are temperature dependent parameters that describe the void incubation period, transition to steady state and the final swelling rate, respectively. The incubation period is essentially complete when $d = \tau$. Since the dose profile is a direct function of distance x into the target, we can integrate Eq. (1) using relationship (2). Figure 1 shows the behavior of this integral with increasing dose. There will be no Δh until $d \gtrsim \tau$ at the peak damage depth. When d(x) exceeds τ everywhere along the ion path, then $\Delta h_o = \Delta h/S_{max}$ will rise steeply and eventually level off at a value of $\frac{1}{3} R_{max} (\bar{d}/d_{max})$, where $\bar{d} = R_{max}^{-1} \int_0^{R_{max}} d(x)\, dx$. Saturation of $\Delta h/S_{max}$ will occur when $d(x) >> \tau$ everywhere along the ion path. Graphical integration of the displacement vs. depth curve for a 5 MeV Ni^+ ion into 316 stainless shows that $\bar{d} = 0.45\, d_{max}$. Since $R_{max} = 15{,}000$ Å, this means that $\Delta h_o(\infty)$ for isotropic swelling is 22.5 Å per 1% swelling observed at the peak damage region. The discrepancy between 22.5 and 60 Å means that the assumption of isotropic swelling is incorrect. Fully anisotropic swelling, however, would lead to $\Delta h'(\infty) = 3\, \Delta h_o(\infty) = 67.5$ Å/peak swelling.* The disparity between the values 60 and 67.5 Å/% is due to denuded zones which do not contain the expected void volume contribution and the fact that τ is not a negligible fraction of d(x) for all values of x when $d_{max} = 140$ dpa.

Johnston[1] also shows that TEM and step height measurements are consistent over a large range of swelling, implying that there is no measurable time lag between deformation due to creep and swelling. We can then assume that void growth and the resultant redistribution of

---

* This value of $\Delta h'$ will change for each ion energy, identity and target composition. For example, a 3.5 MeV Ni^+ ion in an Fe-15Cr-25Ni alloy yields $\Delta h'(\infty) = 58$ Å/%.

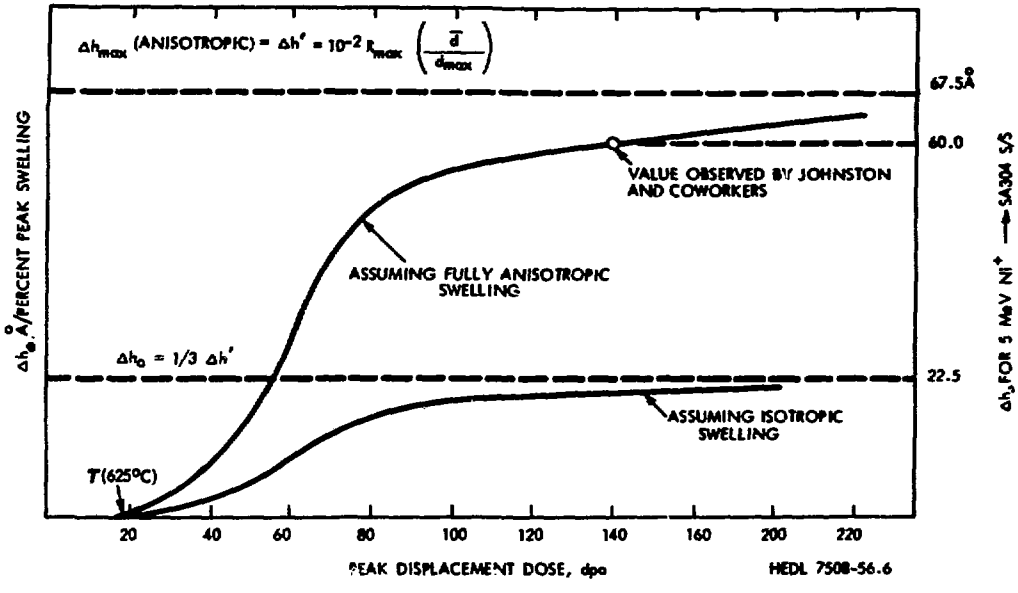

Fig. 1. Schematic Illustrations of the Magnitude of the Step Height per Unit Swelling. Note variation with dose for various assumptions about the partition of mass.

mass proceed at comparable rates. Another way of stating this point is that the swelling necessary to generate the stress field is very small and remains so throughout the irradiation.

THE ORIGIN OF THE STRESS FIELD

We are now faced with the necessity of describing the origin of a stress field which is capable of redirecting (from coordinates normal to the beam) two-thirds of the mass flow expected in an isotropic environment. We also anticipate that stress levels required for such redirection of mass flow may be sufficient to control the magnitude of swelling.

Early discussions on the origin of the stress field centered on the possibility that the non-swelling portions of the target (located on the specimen surface under the mask) provided a rigid lateral restraint which limited the expansion of the swelling material to one coordinate only. The thickness of the swollen region is very small (≈1 micron) compared to the diameter of the non-swelling restraint, however, and this assumption is incorrect. The swelling is constrained laterally by the non-swelling material beyond the ion range, which typically comprises ninety-nine percent or more of the total specimen thickness. In effect, the situation here is analogous to that of the bimetallic strip used to measure temperature changes. Differential expansion between the two components of the strip generates stresses which are relieved by bending. In the ion case, however, the non-swelling portion is so thick as to be rigid, and the stresses cannot be relieved by bending of the composite foil.

An important consequence of the above argument is that swelling should be identical in companion experiments which differ only in the presence or absence of a mask. The stress state to be described here is an inherent feature of ion irradiations of relatively thick targets.

Since irradiation creep is constantly working to relieve swelling-generated stresses almost instantaneously, the driving force that generates and maintains the stress is not the total local swelling or even

the swelling rate. The driving force is the level of swelling which can be accommodated by elastic compression of the lattice prior to the effective activation of creep processes. Once the lattice reaches a stress state such that a critical stress level is exceeded for a given creep mechanism, the swelling-induced stress saturates. The swelling level at which this occurs is very small. If we assume this level to be 0.1% swelling in annealed 304 stainless steel (bulk modulus of 1.5 x 10^{12} dynes/cm^2),[7] this would imply a hydrostatic pressure on the order of ~30 ksi, well above the level known to activate creep processes under irradiation. We can therefore safely assume the driving force (designated as "unrelieved swelling") to be much less than 0.1% swelling.

Figure 2 illustrates the expected time-dependent behavior of the hydrostatic stress at various positions along the ion range. The swelling rate $\dot{S}$ is position-dependent because the damage rate $\dot{d}$ is also position-dependent. The local stress begins to rise when the dose at that point exceeds the incubation dose ($\sim\tau$); this occurs first at the peak damage region at time = $\tau/\dot{d}_{max}$. All other points begin to develop swelling-induced stresses at later times, but follow the same basic behavior. Once swelling occurs, the local hydrostatic stress quickly rises to the critical level σ_c and remains at that level unless the lattice later hardens or softens its resistance to plastic flow with continued irradiation.

METHOD OF ATTACK FOR DERIVATION OF THE STRESS STATE

The problem will be examined in six parts:

(1) Steady-state swelling with a uniform displacement profile and no surface denuded zone.

(2) Steady-state swelling with a typical ion profile and no denuded zone.

(3) Stress states near denuded zones.

(4) Transient considerations.

(5) Effect of crystal orientation.

(6) Perturbations of the analysis near swelling boundaries produced by the mask, grain and twin boundaries, etc.

Problem 1: Uniform Displacement Profile

As shown in Figure 3, parallel plate geometry is assumed with the z coordinate axis coinciding with the ion beam axis. The ion beam is uniform and covers the entire xy plane at normal incidence. The displacement rate and therefore the swelling rate are assumed for this simple case to be uniform from z = 0 to z = -t. The incident, rear and side surfaces are unrestrained, and since t <<L, the lower surfaces of the swelling volume are restrained by shear components at the non-swelling interface. Displacements at this interface are elastic in nature only, and the atomic layers above the interface are likewise restrained since the flow required to relieve stress in such short dimensions would require impossibly large shear strains.

To obtain the distribution of stresses in the swelling region requires solution of the viscoelastic equations modified for void swelling, subject to considerations of compatibility in strain rates, equilibrium in stresses and boundary conditions.

$$\dot{\varepsilon}_{xx} = B\,[\sigma_{xx} - 1/2\,(\sigma_{yy} + \sigma_{zz})] + \frac{\dot{S}}{3}$$

$$\dot{\varepsilon}_{yy} = B\,[\sigma_{yy} - 1/2\,(\sigma_{xx} + \sigma_{zz})] + \frac{\dot{S}}{3} \qquad \text{Normal strain rates} \qquad (3)$$

$$\dot{\varepsilon}_{zz} = B\,[\sigma_{zz} - 1/2\,(\sigma_{xx} + \sigma_{yy})] + \frac{\dot{S}}{3}$$

$$\dot{\gamma}_{xz} = 3\,B\,\tau_{xz}$$

$$\dot{\gamma}_{yz} = 3\,B\,\tau_{yz} \qquad \text{Shear strain rates} \qquad (4)$$

$$\dot{\gamma}_{xy} = 3\,B\,\tau_{xy}$$

Note here that the void volume increase rate along any one coordinate is considered isotropic, as expressed by $\dot{S}/3$. Void volume per se cannot

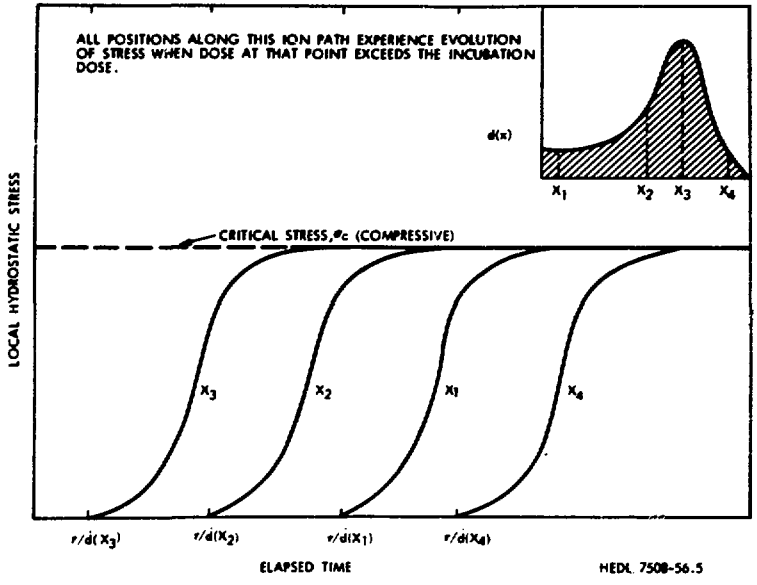

Fig. 2. Schematic Illustration of the Time and Position-Dependent Development of the Hydrostatic Stress Level Along the Ion Path. Note that the stress at all positions eventually saturates at the same level, independent of the swelling rate.

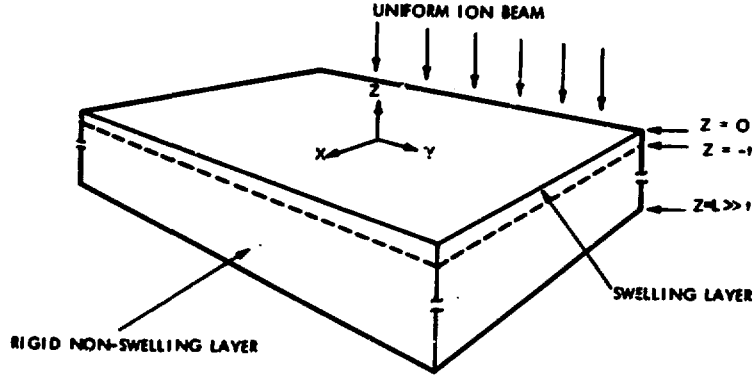

Fig. 3. Coordinate System Employed for Analysis of the Stress State in Ion-Bombarded Foils.

confer any anisotropy, as minimum surface energy requirements redistribute vacancies on the void surface to maintain near-spherical voids.

Boundary conditions: (a) $\tau_{xy} = 0$ by symmetry

(b) $\tau_{xz}, \tau_{yz} = 0, \sigma_{zz} = 0$ at $z = 0$

(c) τ_{xz}, τ_{yz} are uniform at $z = -t$

(d) $\dot{\varepsilon}_{xx} = \dot{\varepsilon}_{yy} = 0$

If we consider a typical element near $z = 0$ where shear stresses are unimportant, then boundary conditions (b) and (d) require

$$\begin{aligned} B\,(\sigma_{xx} - 1/2\,\sigma_{yy}) &= -\frac{\dot{S}}{3} \\ B\,(\sigma_{yy} - 1/2\,\sigma_{xx}) &= -\frac{\dot{S}}{3} \end{aligned} \tag{5}$$

and therefore

$$\sigma_{xx} = \sigma_{yy} = \frac{-2\dot{S}}{3B} . \tag{6}$$

Solving for the creep rate normal to the specimen surface,

$$\begin{aligned} \dot{\varepsilon}_{zz} &= \frac{-B}{2}\left(-\frac{2\dot{S}}{3B} - \frac{2\dot{S}}{3B}\right) + \frac{\dot{S}}{3} \\ \dot{\varepsilon} &= \dot{S} \end{aligned} \tag{7}$$

Eq. (7) expresses the already experimentally observed fact that the swelling-induced deformation is fully anisotropic with no appreciable time lag involved.

The hydrostatic stress σ_H is defined by $\sigma_H = 1/3\,(\sigma_{xx} + \sigma_{yy} + \sigma_{zz})$ and yields

$$\sigma_H = \frac{-4\dot{S}}{9B} \tag{8}$$

At first glance, relation (8) appears to be incompatible with the earlier statement that the stress level σ_c at which each point saturates is independent of the swelling rate. We will shortly show that B

is directly proportional to $\dot{S}$ and that σ_H is not actually dependent on the swelling rate, but equals $\frac{-4}{9D}$ where D is defined in Eq. (10). Assuming a typical value[8] of D from fast reactor data of 0.05 ksi^{-1}, then σ_H is -8.9 ksi. This in turn implies that the driving force expressed as "unrelieved swelling" is $\sim$0.03% $\Delta V/V_o$.

The concern was expressed earlier that the swelling rate $\dot{S}$ might be reduced substantially from the expected stress-free swelling rate. If we accept the relationship[3] that $\dot{S} = \dot{S}_o (1 + P \sigma_H)$, then

$$\dot{S}/\dot{S}_o = 1 - \frac{4}{9} \frac{P\dot{S}}{B} \tag{9}$$

The creep rate coefficient B is normally thought to be composed of several components which operate in the absence of swelling, and another larger component which is proportional to the swelling rate $\dot{S}$.[8]

$$B = B_o + D\dot{S} \tag{10}$$

For this application, the stresses are generated almost exclusively by swelling and

$$B \simeq D\dot{S} \tag{11}$$

Therefore

$$\dot{S}/\dot{S}_o \cong (1 - \frac{4}{9} \frac{P}{D}) \ * \ , \tag{12}$$

where $\dot{S}/\dot{S}_o$ may be defined in this case as the suppression ratio, and

$$\sigma_H \cong \frac{-4}{9D} \ . \tag{13}$$

The parameters P and D may be thought of as coupling coefficients between swelling and irradiation creep, through their mutual interaction with the stress field. Current studies[8] on 300 stainless steels indicate

---

* Note that this equation applies only for the boundary conditions established previously.

that P and D are of the same magnitude in fast reactor neutron irradiations. This implies that $\dot{S}/\dot{S}_o$ is on the order of 0.5, suggesting a factor of two reduction in the swelling rate. (We are explicitly assuming here that P and D retain their relative relationship at the higher displacement rates at which these experiments are conducted.) The origin and physical significance of the P and D coefficients are still under study, but if these parameters can vary independently with changing material properties, there exists the possibility that the suppression ratio $\dot{S}/\dot{S}_o$ may vary with material composition and microstructure.

Problem 2: Typical Ion Displacement Profile

Typical ion displacement profiles are not uniform as suggested by the insert in Figure 2. Eq. (7) requires that the creep rate parallel to the beam axis is directly equal to the swelling rate, but Eqs. (12) and (13) imply that the local hydrostatic stress and swelling suppression ratio are independent of the swelling rate. We therefore expect that the total displacement rate $\dot{U}_{zz} = \int \dot{\varepsilon}_{zz}\, dz = \int \dot{S}(z)\, dz$, and the results are therefore equally applicable to nonuniform displacement profiles.

Problem 3: Stress State Near Denuded Zones

Two types of denuded zones bound the swelling volume. The first of these is the rigid mass beyond the ion range which provides the shear stresses. There is no radiation-induced point defect field here and the material just beyond the ion range exists in a state of tension. At the front surface, however, there is a very thin region of depth $z_D(T)$, (~600 Å thick at 650°C, according to Johnston[9]) in which proximity of the surface sink lowers the point defect concentrations below the level necessary to nucleate voids. This layer is also under tension. It cannot relieve these stresses by bending because of material continuity considerations and the rigidity of the composite layers previously described. Shear stresses now exist at the denuded zone boundary

and must vanish at the front surface. This means that the hydrostatic stress level is compressive in the swelling region, approaches zero at the denuded zone boundary, and becomes tensile in nature between the denuded zone and the surface. Since $\dot{S} = \dot{S}_o (1 + P \sigma_H)$, this means that $\dot{S}$ approaches $\dot{S}_o$ in a small transition region near the denuded zone. Assuming no appreciable displacement gradient in this region, the net result would be an increase in the swelling rate on the swelling side of the denuded boundary. The interaction between the stress reversal and the influence of the surface sink will establish the final position of the denuded boundary and may account for the subsurface bumps or "double hump" swelling profiles described by Johnston.[9]

Problem 4: Transient Considerations

The combined effect of the incubation dose τ and the nonuniform dose rate profile $\dot{d}(x)$ lead to an evolution of the compressive hydrostatic stress in a manner such that it first appears at the point where $\dot{d}_{max}$ occurs. As the dose increases, this compressive region then expands toward both the front surface and toward the rear until all material between $z_D(T)$ and R_{max} exists at σ_c. As this stress front proceeds, the stress reversal mentioned in the previous position accompanies it and accelerates the void growth in the stress boundary vicinity. This tends to reduce the time required for propagation of the compressive zone to reach the zero growth boundaries at $z_D(T)$ and R_{max}. The net effect is that if swelling is bilinear with dose in the stress-free state, and the time-integrated swelling suppression ratio is constant, a bilinear relationship is retained in the stressed state. From Eq. (2), we can therefore write for an ion bombardment experiment

$$s(d,\sigma) = \left(1 - \frac{4}{9}\frac{P}{D}\right) C \left[d - f(\alpha,\tau,d)\right] , \qquad (14)$$

preserving the bilinear swelling law.

This analysis ignores the possible dependence of P and D on void growth and other radiation-induced mechanisms which might harden the lattice. Changes in various elastic moduli with void growth have been

documented[7] for 304 stainless steel.

Problem 5: Effect of Crystal Orientation

The preceding analysis assumes an isotropic lattice with creep relief occurring on the plane of maximum shear. For the stress state described in Problem 1, the plane of maximum shear is actually a 45° cone of revolution about the beam axis ($\tau_{max} = S/3B \approx 1/3D$). In a crystalline lattice, however, plastic deformation occurs due to climb and glide of components of the irradiation-produced dislocation network along specific crystalline planes and directions. The network forms obstacles to climb of its components, and other obstacles exist due to precipitates, impurity atoms and voids. The manner in which these obstacles are surmounted involves certain crystalline directions also. In the early stage of radiation-induced microstructural growth, interstitial loops form and these have preferred habit planes. The net result of the foregoing considerations is that the total response of the crystal is a complex interaction involving the various plastic deformation mechanisms and the projection of the stress field components on the crystal vectors associated with those mechanisms.

An analysis of the crystalline response is proceeding and the detailed results will be reported in a later paper. The objective here is to determine the rate-controlling mechanism of irradiation creep by comparing the experimentally observed step height relationships between grains which present different crystal vectors parallel to the beam axis. It is expected that crystal orientations which are most favorably aligned with the maximum operating shear stress will have a lower σ_H for the lattice, allowing a maximum value of the suppression ratio $\dot{S}/\dot{S}_o$. Other orientations will require a higher σ_H in order for the critical stress value (τ_{max} resolved on the operating crystal vector) to initiate creep relief. It is therefore anticipated that grains of differing orientation will have different suppression ratios and therefore different swelling rates. This is in fact the experimental observation.[1,10]

We are presented here with a problem, however. The preceding analysis expresses the suppression ratio in terms of the coupling coefficients P and D only, both of which are derived from bulk-integrated data. Further analysis efforts will require a redefinition of the coupling coefficients to include crystalline angular relationships. If we assume that the rate controlling step in the irradiation creep sequence requires a critical shear stress τ_c in a specific crystalline direction, then a value of $\tau_{max} = \tau_c/\cos\theta$ is required on the cone of maximum shear. The angle θ is measured between the rate-controlling vector and cone of maximum shear. For fcc and bcc systems these angles are usually small (<15°) for any conceivable choice of vectors. We can now redefine Eq. (12) in terms of a bulk creep coefficient D', modulated by the cos θ.

$$\frac{\dot{S}}{\dot{S}_o} = \left[1 - \frac{4}{9}\frac{P}{D' \cos\theta}\right] . \qquad (15)$$

Note that $D' = \frac{1}{3\tau_c}$, defining the creep coefficient in terms of the rate-controlling shear stress, which may change as the microstructure evolves.

Problem 6: Perturbations Due to Boundaries

It is expected that this analysis will be perturbed by the presence of various crystalline discontinuities such as mask-induced swelling boundaries, grain and twin boundaries. At grain boundaries, Johnston[1] has noted pronounced ridges indicating either nonuniform "extrusion" of mass or increased swelling. This observation may be explained by the possible presence of additional creep relief mechanisms in the vicinity of grain boundaries and therefore a lower local σ_H and different suppression ratio. Johnston[10] has also observed that twinned regions can exhibit either lower or higher step heights than the grain in which they are located. This observation is not inconsistent with previous HVEM observations[11] demonstrating that there is a strong local variation in the incubation periods between various points within a grain, adjacent twinned regions, and between various grains. There is insufficient evidence to date to indicate whether the interaction between the crystal

orientation and the stress field would lead to a change in either the incubation period τ or the suppression ratio $\dot{S}/\dot{S}_o$ for the twin-matrix combination.

In the vicinity of the swelling interface created by the presence of the mask, the material moving toward the surface will obviously experience a drag or shear force as it passes along the nonswelling boundary. However, observation of the step height profile shows that the deviation of the step height from the mean of the entire swelling region relaxes in a very small distance, implying that the analysis is not perturbed substantially by this consideration.

DISCUSSION

We have shown that swelling in a typical ion bombardment irradiation proceeds at a reduced swelling rate due to local compressive stresses on the order of 10 ksi. There is a natural temptation to equate the effect of the suppression ratio ($\sim$0.5) to the observed displacement efficiency ratio between 5 MeV Ni^+ ions and neutrons (which is also $\sim$0.5). This ratio measures the relative efficiency of void formation per initial displaced atom. Before accepting this correlation, however, more work is required.

Several questions require more analysis. Can the bulk response of the material, as measured in the D coefficient, be expressed in terms of a spatial integration over the allowable crystalline vectors? Can the rate controlling interactions for irradiation creep be identified from the relative step height and crystal normal relationships? Is it possible that P and D can vary independently of each other, leading to suppression ratios which are dependent on microstructure and composition? Can the stress reversal at denuded zones be invoked to explain the "double hump" phenomenon discussed in Problem 3? As the microstructure evolves with irradiation, does the critical stress level change? These questions are currently being studied and the answers will be reported in a separate document.

One major conclusion from this work is that ion bombardment experiments are as much a simulation of irradiation creep mechanisms as they are of void formation, and proceed in a manner such that the stress states are probably determinate.

REFERENCES

1. W. G. Johnston, J. H. Rosolowski, A. M. Turkalo and T. Lauritzen, Void Swelling Produced by 5 MeV Nickel Ions, General Electric Report 74CRD291 (Nov. 1974).

2. W. G. Wolfer, J. P. Foster and F. A. Garner, Nucl. Tech. 16, 55-63 (1972).

3. F. A. Garner, W. G. Wolfer, A. Biancheria and A. Boltax, The Effect of Stress on Radiation-Induced Void Growth, Proceedings, 1971 International Conference on Radiation-Induced Voids in Metals, Albany, New York.

4. W. G. Johnston, J. H. Rosolowski, A. M. Turkalo and T. Lauritzen, J. Nucl. Mtl. 46, 273 (1973).

5. W. G. Johnston, J. H. Rosolowski, A. M. Turkalo and T. Lauritzen, J. Nucl. Mtl. 54, 28-40 (1974).

6. F. A. Garner, HEDL Quarterly Technical Report, October-December 1974, HEDL-TME 74-4, 1, p. D-34.

7. J. L. Straalsund and C. K. Day, Nucl. Tech. 20, 27-34 (1973).

8. G. L. Wire and J. L. Straalsund, Irradiation-Induced Stress Relaxation of Previously Irradiated 304 Stainless Steel in a Fast Flux Reactor, HEDL Semiannual Report (June 1975).

9. W. G. Johnston, et al., Depth Distribution of Void Swelling Produced by 5 MeV Nickel Ions, Proceedings, EMSA, St. Louis, pp. 358-359 (Aug. 1974).

10. W. G. Johnston, J. H. Rosolowski, A. M. Turkalo and K. D. Challenger, Scripta Metallurgica 6, 999-1006 (1972).

11. J. J. Laidler, B. Mastel and F. A. Garner, Swelling in Electron-Irradiated 316 Stainless Steel, Proceedings, ASTM 7th International Symposium on Radiation Effects on Structural Materials, Gatlinburg, Tennessee, June 11-13, 1974.

THE INFLUENCE OF DISPLACEMENT GRADIENTS ON THE INTERPRETATION OF CHARGED PARTICLE SIMULATION EXPERIMENTS*

F. A. Garner
G. L. Guthrie

Hanford Engineering Development Laboratory

ABSTRACT

Neutron flux and spectrum gradients are negligible within a single grain of structural materials in fusion reactors. In charged particle simulation, however, substantial gradients exist in the flux of displaced atoms (dpa) along the ion path, which is typically several microns or less in length. In interpretation of such experiments, one must account for the influence of variables that are atypical of the simulated environment. Experimental and modeling studies show that dpa gradients lead to gradients in microstructure, which in turn modify the effect of diffusion on the effective growth environment of voids and other defects. For some ions, these effects are overwhelmed by a phenomenon designated the "internal temperature shift." Although the physical temperature is relatively invariant along the ion path, the temperature regime of swelling shifts as the displacement rate changes. The swelling vs. depth profile is altered substantially from that expected from the dpa profile, and the type of modification is dependent on the relation of the irradiation temperature to the peak swelling temperature at the mean displacement flux. Swelling profiles for a variety of simulations were analyzed and found to include the influence of surface denuded zones, incubation effects, diffusion, swelling-generated stresses and internal temperature shifts. The impact of the latter imposes restrictions on the interpretation of step height measurements and full range intercorrelations for high energy ions.

---

* Based on work performed by Hanford Engineering Development Laboratory, Richland, Washington, operated by Westinghouse Hanford Company, a subsidiary of Westinghouse Electric Corporation, under United States Energy Research and Development Administration Contract E(45-1)-2170.

INTRODUCTION

Neutron flux and spectrum gradients are negligible within a single grain of structural materials employed in fusion and fission reactor designs. In charged particle simulation of void growth in neutron environments, however, substantial gradients can exist in the rate of atomic displacement along the ion path, which is typically several microns or less in length. In the interpretation of such experiments one must account for the influence of such gradients, as well as other variables which are atypical of the simulated environment. This report summarizes a series of studies related to the origin and nature of typical displacement gradients, and their subsequent impact on the design, conduct and interpretation of void growth experiments.

ORIGIN OF DISPLACEMENT GRADIENTS

As a charged particle traverses a material, it loses energy by various interactions with the electrons and atomic nuclei of the material. Energy lost by electronic interactions is usually deposited in insufficient quantities to cause subsequent atomic displacements; but nuclear interactions can lead to atomic displacements, providing the energy transmitted to an atom is above the threshold for ejection from its potential well. A description of the various energy loss mechanisms is well documented elsewhere, and only the details pertinent to this analysis need be reviewed here. For most charged particles of interest in void simulation studies, the majority of the energy loss is electronic in nature. Electronic energy losses therefore exert the major influence on the total path length of the original particle. Nuclear interactions increase in importance as the ion energy decreases, particularly near the end of range. The nuclear interactions also cause deflections from the original particle trajectory, and the resultant "straggling" leads to a distribution of projected ranges. A typical displacement versus depth curve is shown in Figure 1 for the integrated behavior of the distribution of ranges. The principles involved in the energy deposition calculations are covered in detail by Manning and Mueller[1] and the

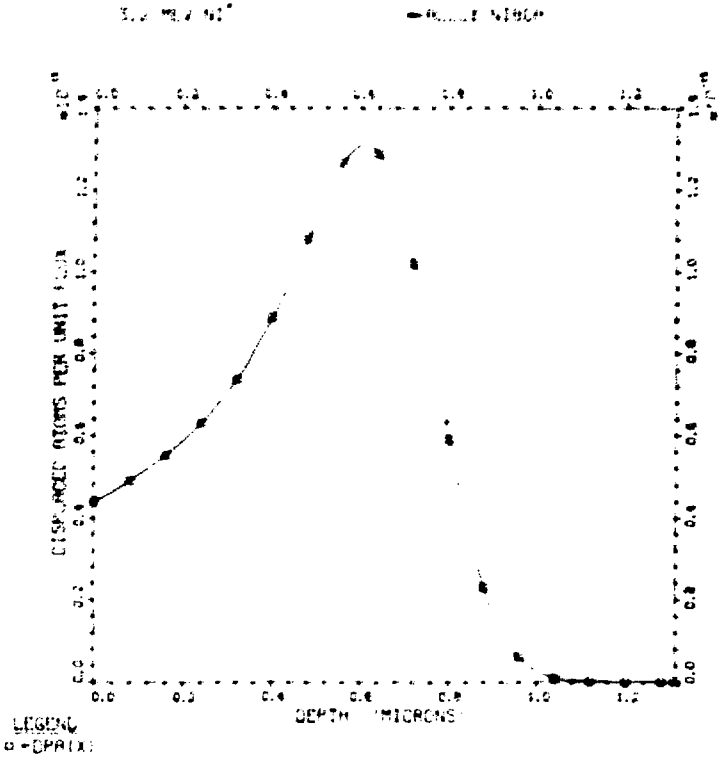

DPA(X) IS THE CURVE OF DISPLACED ATOMS
PER UNIT FLUX WHERE FLUX IS MEASURED IN
IONS PER SQUARE CENTIMETER PER SECOND.

Fig. 1. Displacement Profile for 3.2 MeV Ni^{+} Ions Incident Normal to Front Surface of Nimonic 80A Target. This profile was calculated using the EDEP-1 code described in Reference 1.

subsequent calculation of atomic displacements is treated by Doran, et al.[2]

There are three types of gradients inherent in the profile illustrated in Figure 1; these occur in the angular divergence of the collision event, the mean energy transfer per event, and the total energy deposition. Most ion beams are directed toward the specimen surface with negligible angular divergence, and the angular divergence of the ion beam increases thereafter with increasing penetration. The angular distribution of primary knock-on atoms (PKA) therefore also increases with depth, but this factor is thought to have no great impact on the total number of displaced atoms or their subsequent survivability. The average energy transfer per PKA event, $\bar{T}$, also changes with depth as shown in Figure 2. The efficiency of energy transfer by nuclear processes increases continuously with decreasing ion energy, but eventually the total energy of the ion is diminished to the point where the energy transfer per PKA declines abruptly. Since the energy distribution is heavily weighted toward low energy transfers, many of the nuclear interactions result in subthreshold events. The calculated mean PKA energy is therefore quite sensitive to E_d, the displacement energy threshold. However, over the normal range of E_d (25 to 50 eV), the variation of the mean PKA energy with depth is insufficient to influence the point-defect survivability substantially.

The major gradient with depth therefore lies in the total energy deposition by nuclear interactions, and the subsequent generation of vacancies and displaced atoms.

RELATIONSHIP OF SWELLING PROFILES TO DISPLACEMENT PROFILES

Stereomicroscopy of the volume contained within the ion range has been employed by Thomas[3] to determine the density and size distribution of voids produced by a combination of ion and electron irradiation. Norcliffe, et al.[4] have also employed stereomicroscopy techniques on specimens bombarded with ions only. Other full range studies have been performed using sectioning techniques instead of stereomicroscopy.[5,6]

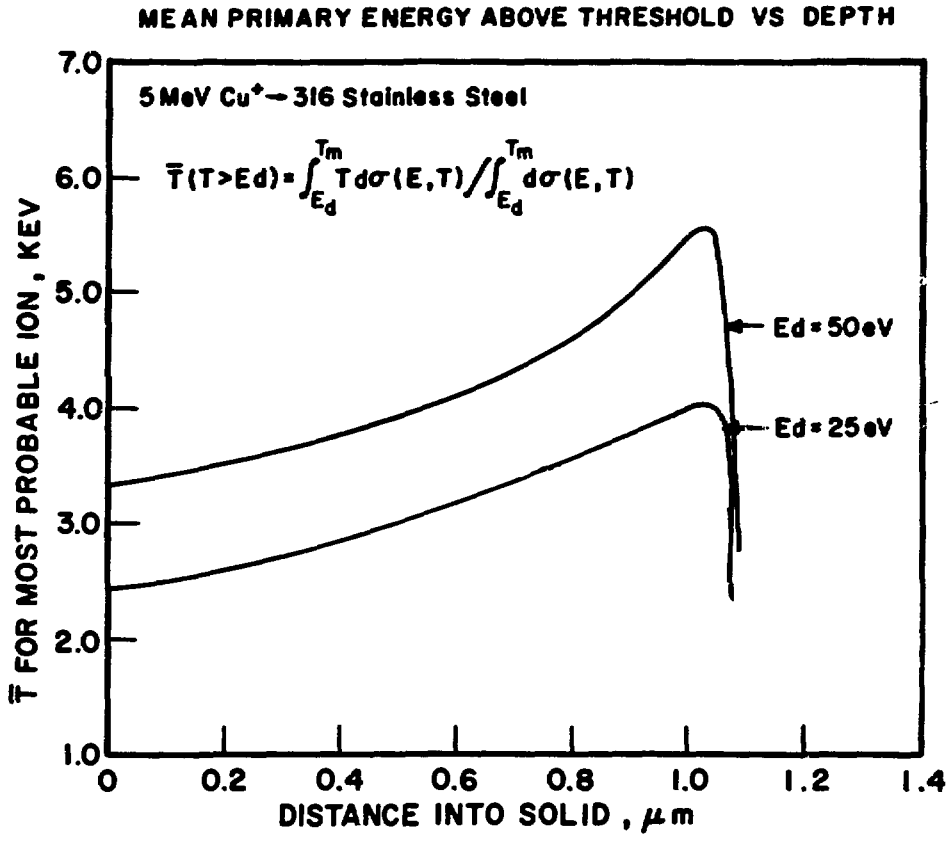

Fig. 2. In Typical Ion Irradiations, the Mean Displacement Energy $\bar{T}$ for the Primary Displacement Event Varies with Depth.

There emerges from these studies the conclusion that the depth dependence of swelling does not always bear a straightforward relationship to the displacement profile. In general, the depth dependence of swelling is not directly proportional to the depth dependence of the displacements per atom (dpa) profile. A knowledge of the relationship between the two profiles is necessary, however, in order to correctly interpret and exploit the potential of full range data. This same consideration is equally important in the interpretation of step-height measurements of the swelling integrated over the ion range.[7]

The studies summarized in this report show that almost all facets of observed swelling profiles can be explained in terms of diffusion effects, void incubation behavior, and rate effects related to the presence of displacement rate gradients. For high levels of swelling (>10%) there exists an additional factor related to the influence of accumulated voidage on the displacement rate profile.

DIFFUSION EFFECTS

Intuitively one would expect that the driving force for void growth would be modified somewhat by point defect diffusion, smoothing out steep gradients in deposited dose. However, diffusion tends to modify the void growth environment even in the absence of steep displacement gradients. Most ion-induced dpa gradients are usually very small near the incident surface, but the surface also functions as a strong sink for the point defects generated in its vicinity. This leads to a suppression of steady-state defect concentrations and subsequent void growth near the surface. This effect in turn generates the denuded zones observed in both electron[8] and ion[5] irradiation experiments.

Papers previously published by other authors have presented theoretical calculations of the steady-state[9,10] and time-dependent[11] spatial distributions of point defects near free surfaces. However, none of these efforts have considered the effects of biased dislocation sinks, which are thought to provide the origin of the driving force for void growth. Since void growth occurs in an environment composed of both

interstitials and vacancies, it is the net flow of defects across the void surface which determines the growth rate. In our studies, the net flow has been designated the growth fluid ξ, defined by $D_v (C_v - C_v^*) - D_I C_I$. This term contains the diffusivities and concentrations of both vacancies and interstitials, as well as the equilibrium vacancy concentration at the void surface, which is dependent on the void radius. In our studies, biased dislocation sinks have been included, and the growth fluid profile for small voids has been shown to be influenced by surface sinks to a much greater depth than are profiles of the vacancy or interstitial concentrations.[12] Figure 3 shows the influence of the surface on the growth environment of 50 Å voids when no dpa gradients exist and the dislocation density is temperature-dependent and typical of that observed in electron irradiations. For smaller voids the effect is even more pronounced, and accounts for the formation of void denuded zones. The growth profiles in Figure 3 were generated by the discrete-ordinate computer code CREED[12] which calculates the depth-dependence of the growth fluid for gradients in the microstructure, dose rate and hydrostatic pressure. The dislocation sinks are considered to have a bias or preference of 1% toward acceptance of interstitials over vacancies. The CREED program has been employed to study the combined influence of diffusion, surface sinks, and displacement rate gradients for typical ion bombardment experiments.

The variables investigated to date have been the dislocation density, peak dose rate and irradiation temperature. Typical values chosen were 10^9-10^{11} dislocations/cm^2, 1 x 10^{-3} to 2 x 10^{-2} dpa/sec, and 400-900°C, respectively. The model represented by these calculations is shown in Figure 4, where 5.0 MeV Ni^+ ions are incident normal to the front surface of a 316 stainless steel target. The peak damage rate occurs at a depth of approximately one micron and the rear surface is assumed to be at 2.5 μm, at which position the point defect gradients are required to be zero. The surface energy was assumed to be 1000 ergs/cm^2 and the energy of self diffusion has been experimentally determined to be 4.65 x 10^{-12} ergs. The initial estimate of the vacancy formation energy was taken to be 2.2 x 10^{-12} ergs. The dislocation density was assumed to be uniform throughout and the growth fluid

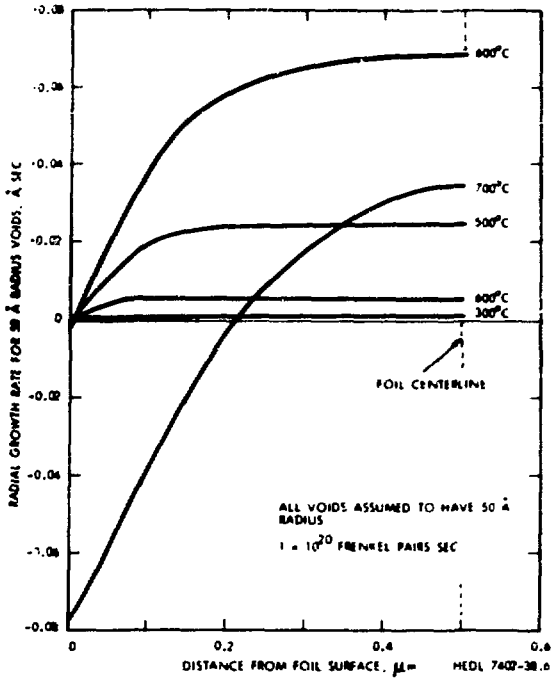

Fig. 3. The Growth Rate of Voids is Sensitive to Both the Irradiation Temperature and Proximity to the Foil Surface. Even in the absence of displacement gradients, diffusion of point defects to the foil surface will lead to gradients or total suppression of void growth behavior.

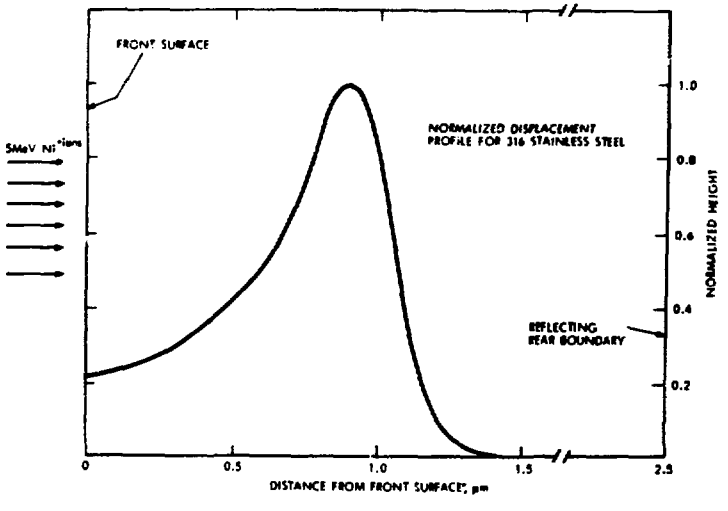

Fig. 4. Displacement Profile Employed in Computer Modeling of Ion-Induced Growth Fluid Profiles Shown in Figures 5 and 6.

profiles were calculated for a test void whose diameter was 100 Å. Otherwise, no voids were included in the first stage of analysis.

For a dislocation density of 10^9 cm^{-2} the growth fluid curve is altered greatly by diffusion of defects to the front surface and the material beyond the ion range. There is little resemblance of this profile to that of the ion damage profile. A typical profile is shown in Figure 5(a). Also shown in Figure 5(b) are the peak values of the growth fluid for various temperatures and dose rates. Surprisingly, the depth dependence of these profiles exhibits the same shape at all temperatures and displacement rates investigated; only the elevation and magnitude of the curves changed. At higher temperatures the growth fluid over its range is partially or always negative, dependent on the generation rate. The influence of the surface sink increases with temperature, manifesting itself in reduced or negative values of growth fluid near the front surface.

At a dislocation density of 1×10^{11} cm^{-2} the growth fluid profiles tend to approach the shape of the displacement profiles. However, the growth fluid profiles tend to become steeper with increasing temperature, as shown in Figure 6, rather than broader as might be expected from diffusion considerations.

The decreasing influence of diffusion at higher dislocation densities is not unexpected, however. The intervening sinks tends to screen the influence of the surface and unirradiated material beyond the ion range, thereby increasing the relative influence of the local source. This effect can be assessed in terms of relaxation distances for each parameter of interest. If there exists a local perturbation which changes C_v, C_I or ξ, then the perturbation extends into surrounding regions. The 1/e relaxation length for this perturbation is χ, where

$$\chi_{C_v} = (S+D_I C_I R)^{-1/2},$$

$$\chi_{C_I} = (S+D_v C_v R)^{-1/2},$$

and $$\chi_{\xi} = (S)^{-1/2},$$

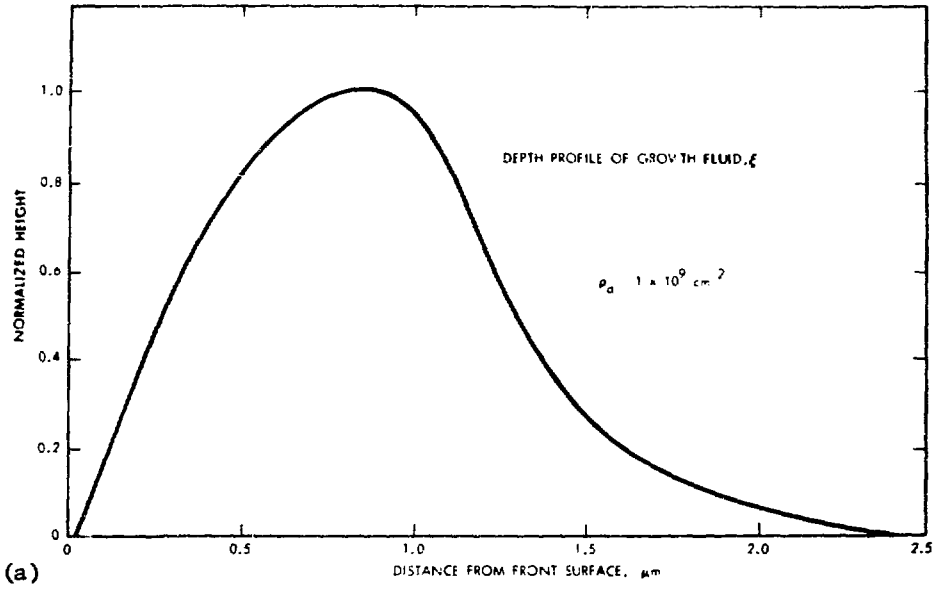

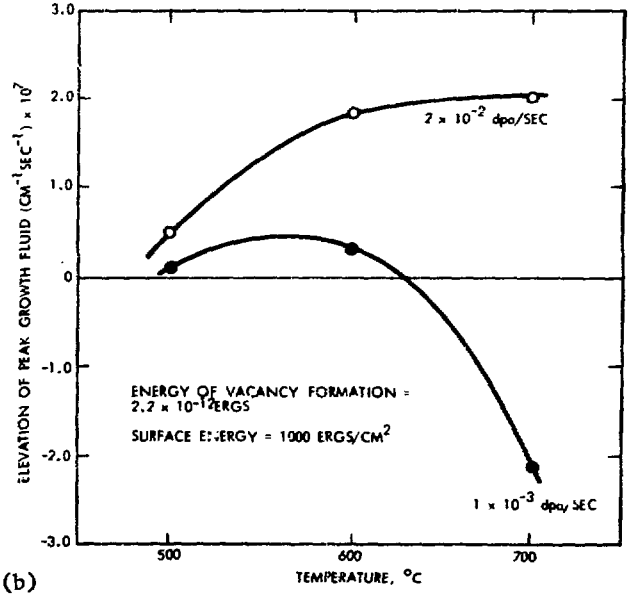

Fig. 5. (a) Depth Dependence of Growth Fluid Profile at Low Dislocation Density. (b) The Temperature and Dose Rate Dependence of Peak Growth Fluid at Low Dislocation Density, as Sensed by a Void of 100 Å Diameter.

and R is the recombination coefficient and S is the trapping coefficient due to sinks other than recombination. The coefficient S is defined by

$$S = \rho_d Z_v + 4\pi \rho_v r_v C \ .$$

The void and dislocation densities ρ_v and ρ_d represent the physical traps, where r_v is the void radius and C is a factor which represents competition effects between voids whose sphere of influence overlaps. Z_v is the vacancy bias factor for dislocations.

For this model, χ_ξ reduces to an inverse square root dependence on ρ_d since no voids are assumed in this calculation. Therefore, local perturbations are relaxed faster for higher dislocation densities. The impression implied by Figure 6 is somewhat misleading, however, since ρ_d is not constant with temperature and the presence of voids will also alter the profile. The full temperature-dependence of growth fluid profiles must allow a temperature dependent ρ_d and ρ_v, and also allow for depth-dependence of these quantities. Although typical reactor structural materials may initially have a relatively low dislocation density, irradiation quickly produces a high dislocation density. Therefore, diffusion is not expected to alter the effective growth environment profile substantially from that generated by the dpa profile, with the exception of the surface-dominated region.

VOID INCUBATION EFFECTS

If void swelling were to increase in a linear fashion with total displacement dose and not exhibit an incubation period, then the swelling profile would be directly proportional to the dpa profile. Electron irradiation experiments[13] have shown that swelling in some materials is linear with dose after a rather large incubation period. Figure 7 demonstrates the predicted relationships of swelling and dpa profiles, using an equation developed for 20% CW 316 stainless steel based on neutron data.[14] The 5 MeV Ni^+ dpa profile for Type 316 stainless steel has been used and a temperature assumed of 530°C.

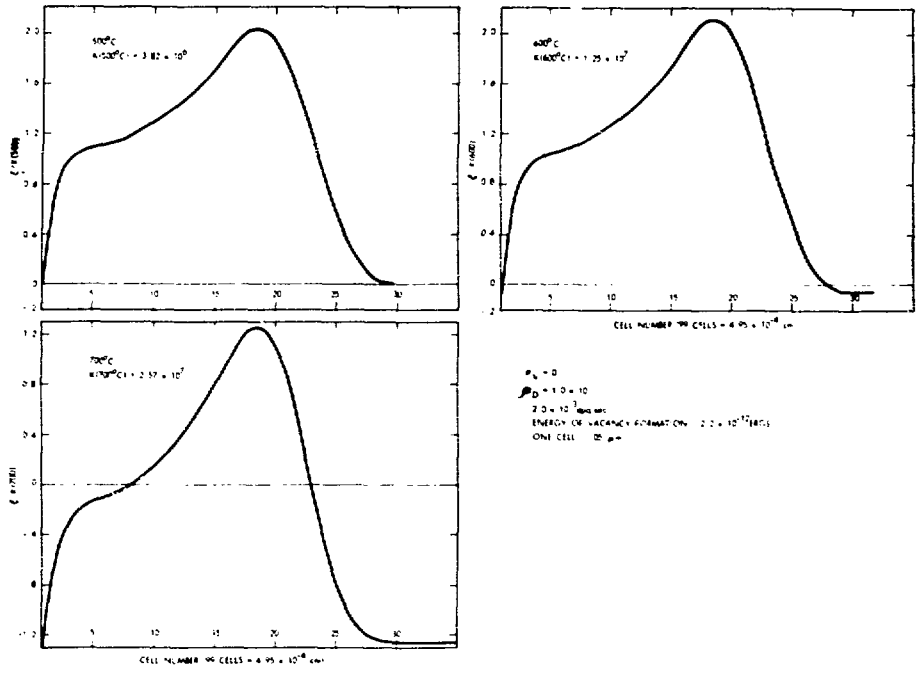

Fig. 6. Depth Dependence of Growth Fluid Profile at High Dislocation Density, as Sensed by a Void of 100 Å Diameter. Profiles tend to become steeper with increasing irradiation temperature.

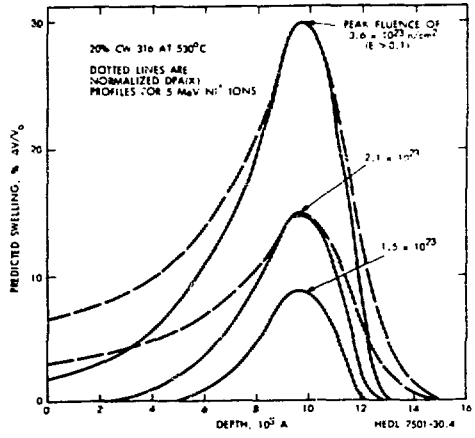

Fig. 7. Illustration of Incubation Effects on The Modification of Ion-Induced Swelling Profiles Using Current 20% CW 316 Neutron-Induced Swelling Equation. Note that the divergence from the displacement profiles decreases with increasing fluence.

In the early stages of irradiation, swelling is suppressed, giving the appearance of a surface-depressed zone of considerable depth. Obviously, this effect is only a consequence of the incubation period and gradually disappears with increasing dose. The prediction for the 2.1×10^{23} n/cm^2 case appears to be related to the input fluence profile in a manner quite comparable to the ion-induced profile observed by Rowcliffe and coworkers[4] in this material at 650°C, which is a comparable temperature considering the higher displacement rate employed. Evaluation of the relationship of the swelling profile shown in Figure 8(a) and the dpa profile show that a linear-after incubation swelling curve can be extracted from these data as shown in Figure 8(b).

DISTORTIONS OF SWELLING PROFILES DUE TO RATE EFFECTS

Although the temperature gradient within the ion range is very small, it is quite possible to have a shift in the temperature regime of swelling along the ion path. Although the physical temperature along the ion path is invariant, the swelling regime inhabits a temperature range which varies with the flux of displaced atoms. For 5 MeV Ni^+ ions incident on Fe-Ni-Cr alloys, there is a factor of about four in the magnitude of the displacement rate from the front surface to the region of the peak displacement rate.

For some ion experiments, however, the displacement flux changes much more substantially over the ion path. The peak to front surface displacement ratios for 45 MeV Ni^+ and 20 MeV C^+ ions in nickel are about 25 and 70, respectively. The temperature shift involved over the range of such experiments is substantial. Figures 9 and 10 illustrate the principles involved. For a given displacement flux, we observe a swelling rate distribution which peaks with temperature at $T_p(\phi_1)$ and ranges from $T_s(\phi_1)$ to $T_f(\phi_1)$. As the flux is increased, we observe an increase in all three characteristic temperatures. The rate-dependent temperature shift ΔT is usually measured at the peak swelling temperature, and should be of comparable magnitude when measured at T_s and T_f also.

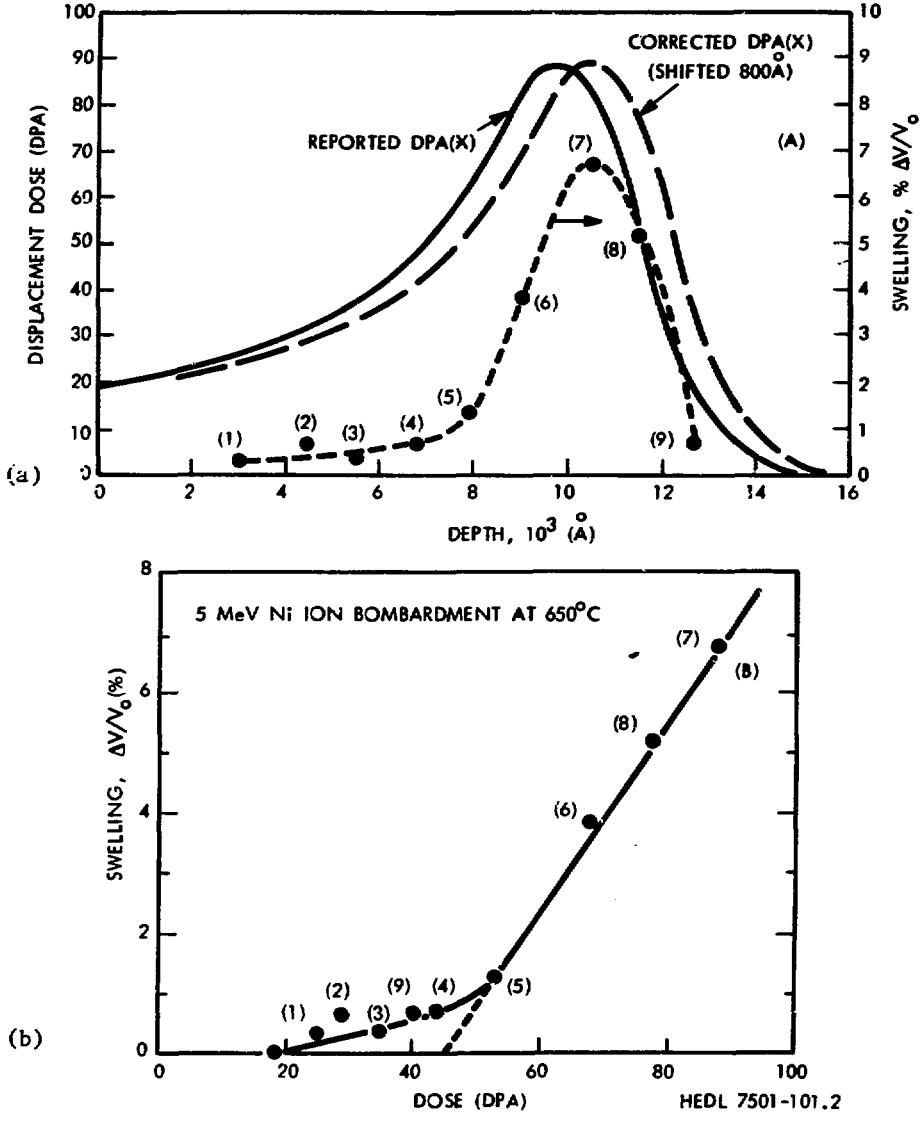

Fig. 8. (a) Swelling Profile Observed in Nickel-Ion Irradiated 20% CW 316 Stainless Steel[4] and Various Estimates of the Displacement Profile that Produced the Swelling. (b) A Linear After-Incubation Swelling Curve is Easily Extracted from the Data Shown in Figure 8(a).

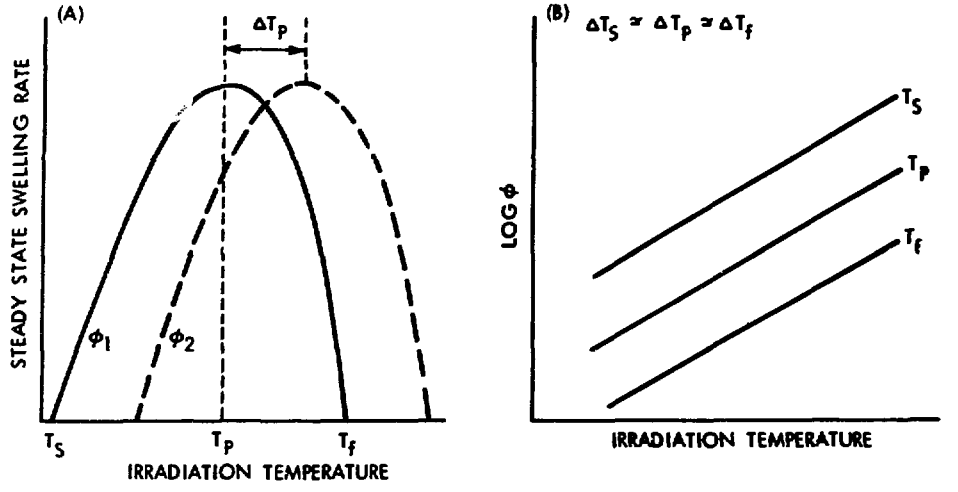

Fig. 9. Schematic Representation of the Shift of the Swelling Regime to Higher Temperatures with Increasing Displacement Flux ($\phi_2 > \phi_1$).

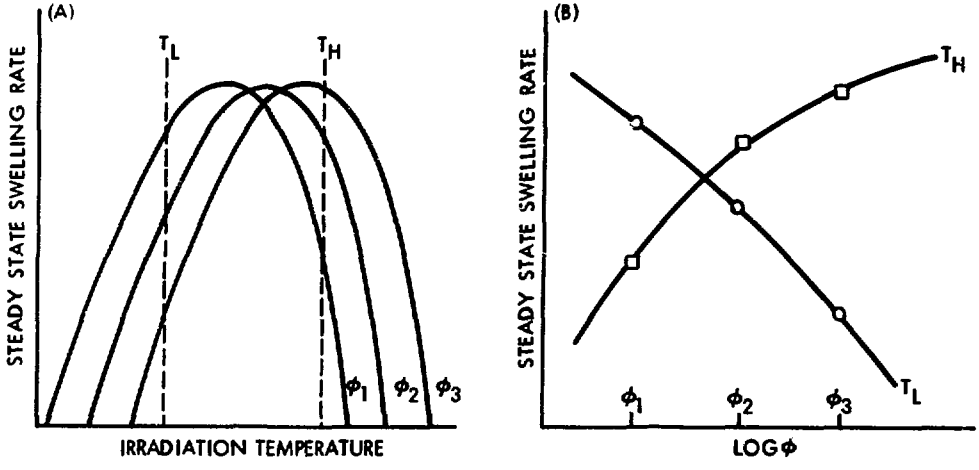

Fig. 10. Schematic Representation of the Change in Swelling Rates that Occur as the Displacement Flux Increases Along an Ion Path ($\phi_3 > \phi_2 > \phi_1$). This leads to the process described as an "internal" temperature shift." T_L and T_H represent two possible irradiation temperatures which yield different rate dependencies of swelling.

In Figure 10, we see that if an experiment is conducted at a fixed temperature such as T_L or T_H, the steady-state swelling rate can either rise or fall as the displacement rate increases. Figure 11(a) demonstrates the modification of the swelling profiles that would be expected. Note that the resultant swelling curve can be broadened or made steeper (compared to the dpa curve) depending on whether the physical temperature was relatively low (T_L) or relatively high (T_H) with respect to $T_p(\bar{\phi})$, the peak swelling temperature for the mean displacement rate along the ion path. This distortion of the void growth profile due to changes in the displacement rate has been designated the "internal temperature shift" phenomenon.

In several publications,[15,16] it was noted that the calculated dpa profile and the experimentally determined swelling profile for 46.5 MeV Ni^+ ions were significantly different from each other at 525°C. As shown in Figure 11(b), the swelling profile derived for pure nickel is much less peaked than is the dose profile. This appears to correspond to the T_L irradiation condition shown in Figure 11(a). Before we accept this hypothesis, it must be shown conclusively that the swelling profile is indeed broader than the dose profile. Figure 11(b) reproduces the normalized data set as reported in Reference 15, and it shows that a great deal of scatter is involved. If the scatter arises due to a normalization procedure based on assumptions about swelling that are not true for a varying displacement rate, then it is better to examine the individual swelling curves prior to normalization. Hudson[15] supplied the individual curves shown in Figures 12(a) and 12(b). Note that each swelling vs. depth curve appears to be broader than the dose profile.

It must be shown that the 525°C, 46.5 MeV Ni^+ → nickel irradiation was performed at a temperature below $T_p(\bar{\phi})$, since the modification observed led to broadening of the swelling profile relative to the displacement profile. In Figure 13, the reported peak swelling temperatures have been plotted for pure nickel under neutron and various energy ion experiments. The data sources used are listed in Table 1. No correction is made for the various methods of calculating displacement

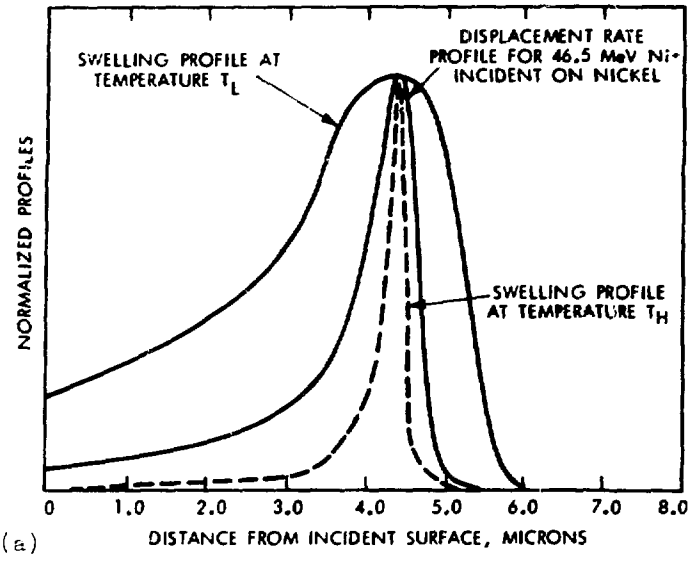

(a)

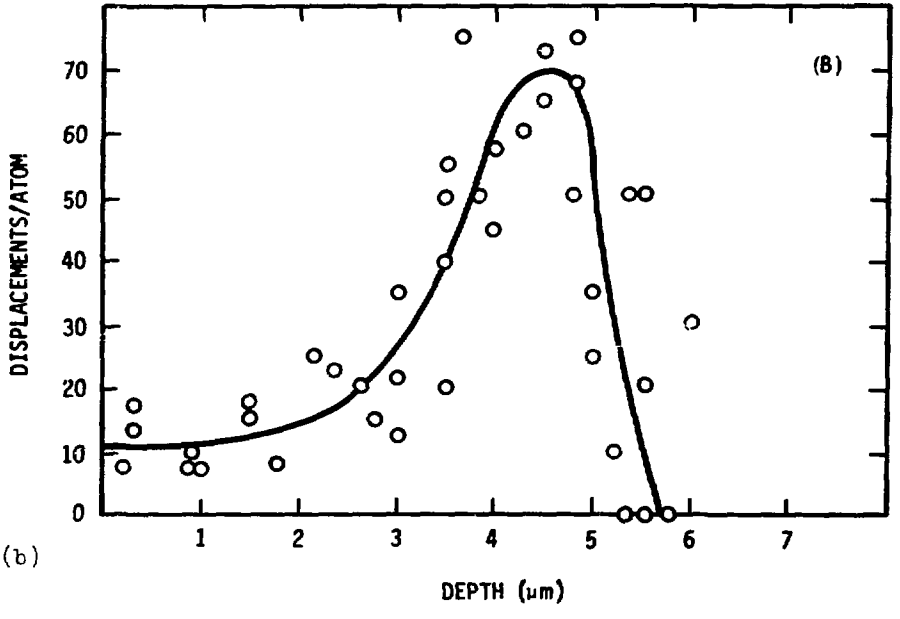

(b)

Fig. 11. (a) Schematic Representation of the Swelling Profiles that Evolve for Various Irradiation Temperatures when the Displacement Profile Involves Relatively Large Gradients. (b) Normalized Swelling Data Set of Hudson[6,15] for 46.5 MeV Nickel Ion Bombardment of Nickel at 525°C, Composed of Data from Six Separate Irradiations at Different Ion Fluences. The solid line is the calibration curve of Hudson.[15]

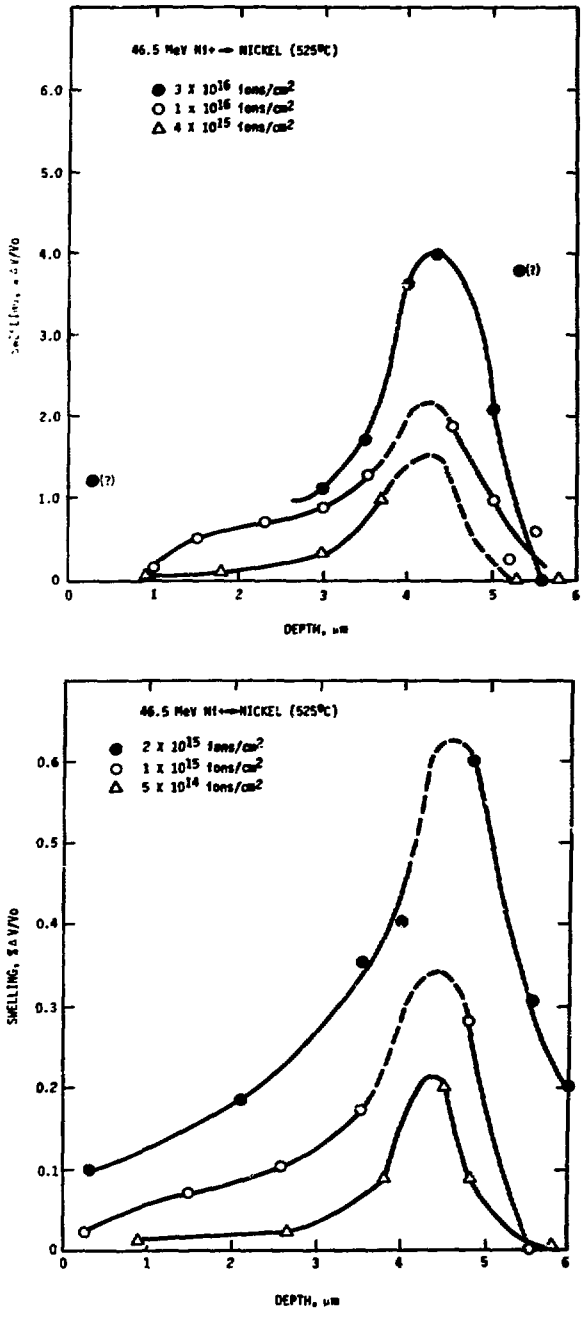

Fig. 12. Individual Swelling Profiles Prior to Normalization Procedures used in Figure 11(b).

Table 1. Nickel Ion Swelling Peak Data Used in Figure 13

Bombarding Particle	Damage Rate (dpa/sec)	Peak Swelling Temperature (°C)	Comments	Reference
500 keV Ni^+	1×10^{-3}	625	25 dpa	19
4 MeV Ni^+	2.5×10^{-3}	600	10 dpa, 5 ppm He	18
2.8 MeV Ni^+	7×10^{-4}	550	13 dpa	17
2.8 MeV Ni^+	7×10^{-2}	625	13 dpa	17
Neutrons	$\sim 1 \times 10^{-6}$	500	5×10^{19} n/cm^2	21
Neutrons	$\sim 1 \times 10^{-6}$	500	2.3×10^{20} n/cm^2	20

rates, which are known to vary by roughly a factor of two. The solid line represents a best fit to all the data, while the dotted line represents a rate shift determination performed by researchers at NRL. Note that the 46.5 MeV Ni^+ ion experiment lies well below either line, and represents an irradiation at a temperature $T_L < T_p(\bar{\phi})$. This confirms the supposition that the modification arises primarily due to an internal temperature shift, rather than from diffusional modification of the growth fluid profile.

Theory[22] predicts a temperature shift based on the upper end of the swelling regime such that

$$\Delta T_f(\phi_1,\phi_2) \approx \Delta T_p \approx T_1^2 \frac{K}{E_v} \left[\frac{1}{1 + \frac{KT_1}{E_v} \ln \frac{\phi_2}{\phi_1}} \right] \ln \frac{\phi_2}{\phi_1} ,$$

where T_1 is the peak swelling rate temperature in Kelvin at ϕ_1, K is Boltzman's constant, and E_v is the self diffusion energy.

For small enough changes in ϕ, the denominator term in the brackets tends to balance out the T_1 dependence and we can assume

$$\Delta T_p \approx J \ln (\phi_2/\phi_1) .$$

From Figure 13 we can derive $J \propto 25°C$ per factor of ten in flux from the entire data set, and 38°C per flux decade from the NRL temperature shift data. Since the 46.5 MeV Ni^+ experiment and most 5 MeV Ni^+ experiments are performed in the 10^{-3} to 10^{-2} flux regime, and the NRL experiment is the only self-consistent determination of flux effects, the latter value will be used. For the 46.5 MeV Ni^+ experiment, the internal temperature shift is 49°C, while the shift for the 20 MeV carbon ion experiment is at least 70°C. Even for 5 MeV Ni^+ ion bombardment experiments, the internal temperature shift is 22°C. The internal temperature shift phenomenon is not as obvious in the 5 MeV Ni^+ CW 316 data set shown in Figure 8.[4] This is not only due to the smaller rate change in this experiment but also due to the fact that swelling occurred over less than the total range. Part of the internal temperature shift effect was therefore submerged under the incubation effect.

The program CREED was employed to model this effect, taking into account diffusion as well. The results are shown in Figure 14 for 46.5 MeV Ni^+ ions incident on a pure nickel target. Note that the growth fluid profiles are much broader than the dpa profiles at low temperatures and much steeper at high temperatures.

There are several consequences of the internal temperature shift problem: (1) For 46.5 MeV Ni^+ and 20 MeV C^+ ions, a dose calibration curve, based on the premise that "equal dose requires equal swelling" everywhere along the path of the ion, cannot be satisfactorily performed, as has been the practice in the past for 20 MeV C^+ and 46.5 MeV Ni^+ irradiations. "Rocking" the beam will not quite alleviate the problem, as the effect will be equivalent to the presence of a time-dependent temperature history at any point along the ion path. (2) For specimens extracted at a given depth and compared only with other irradiations from the same depth, there is no "internal" temperature shift problem. (3) For integrative techniques such as step-height measurements and stereo depth-analysis of full-range swelling, there will be some distortion of the results, and the impact of the distortion will vary at each irradiation temperature.

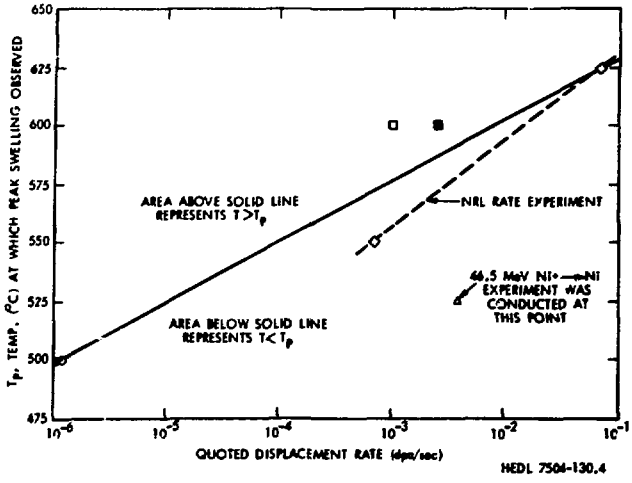

Fig. 13. Reported Peak Swelling Temperatures are Shown for Various Neutron and Nickel Ion Irradiations of Pure Nickel. Note that the 46.5 MeV Ni^+ → nickel experiment occurs well below either estimate of the peak swelling temperature.

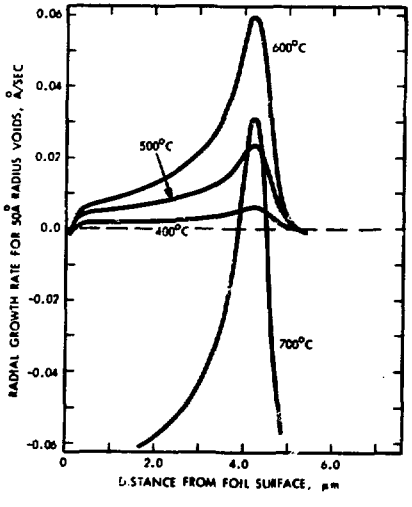

Fig. 14. Computer Simulation of the Internal Temperature Shift Phenomena in 46.5 MeV Ni^+ Ion Irradiation of Pure Nickel. Note that the growth fluid profiles (expressed in terms of a radial growth rate) are very broad at low irradiation temperatures and become increasingly steeper at higher temperatures. At 700°C the steepness is accentuated by the onset of void instability, evidenced by negative growth rates. The dislocation density for this example was 1×10^{10} cm^{-2}, the test void radius was 50 Å and the displacement rate was 1×10^{-3} dpa/sec.

EFFECTS OF SWELLING ON DISPLACEMENT GRADIENT

As swelling accumulates along the ion path, each successive ion must travel a larger distance before coming to rest. As a consequence, the displacement profile will steadily decrease in peak magnitude and increase in total depth. The effect of swelling on the instantaneous displacement curve has been treated by Odette and coworkers.[23] As shown in Figure 15, the net effect at any fixed position is to cause the displacement rate to change with time, with the sign of the change dependent on where the position under examination was located with respect to the original displacement peak. The total displacement dose at any position (measured relative to the surface) is therefore the time integral of the displacement profile as affected by swelling and requires knowledge of the dose dependence of swelling. This consideration was not covered in Reference 23.

In a previous section it was noted that swelling in 300 series stainless steels is linear after an incubation period. Confirmation of this swelling law for a given material leads to a method of using full range data even when the dpa profile is distorted by swelling. Figure 16 is a reproduction of two swelling profiles observed by Johnston.[5] Using the displacement profile of Figure 4, the swelling versus dose curves of Figure 17 were extracted. The divergence from the linear behavior is consistent with the behavior predicted in Figure 15. The steady-state swelling rate can be extracted from the low dose portion of the curve and used to calculate the time-integrated dpa levels seen by regions near the original position of the peak displacement rate. This procedure is complicated somewhat by the large change in displacement rate experienced beyond the position of the original peak displacement rate. Table 2 shows a comparison of the time-integrated and predicted dose levels experienced at several points along the curves shown in Figure 17.

SUBSURFACE EFFECTS

Near the surface denuded zone, Johnston[5] has occasionally observed an additional peak in the swelling vs. depth curve. An example is shown

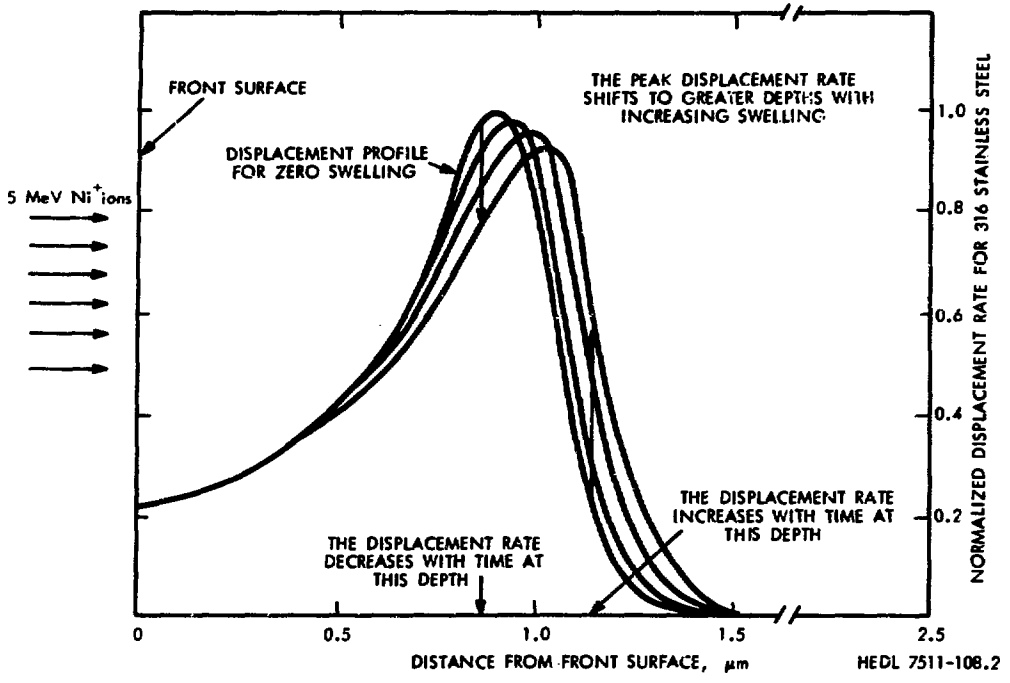

Fig. 15. As Swelling Accumulates, the Instantaneous Displacement Rate Curve is Distorted. Near the front surface, the distortion is negligible, but near the original displacement peak the effect is quite pronounced. The time-averaged dose at a fixed distance from the incident surface may be either greater or smaller than that predicted by the unperturbed curve, depending on the relative position of the original displacement peak.

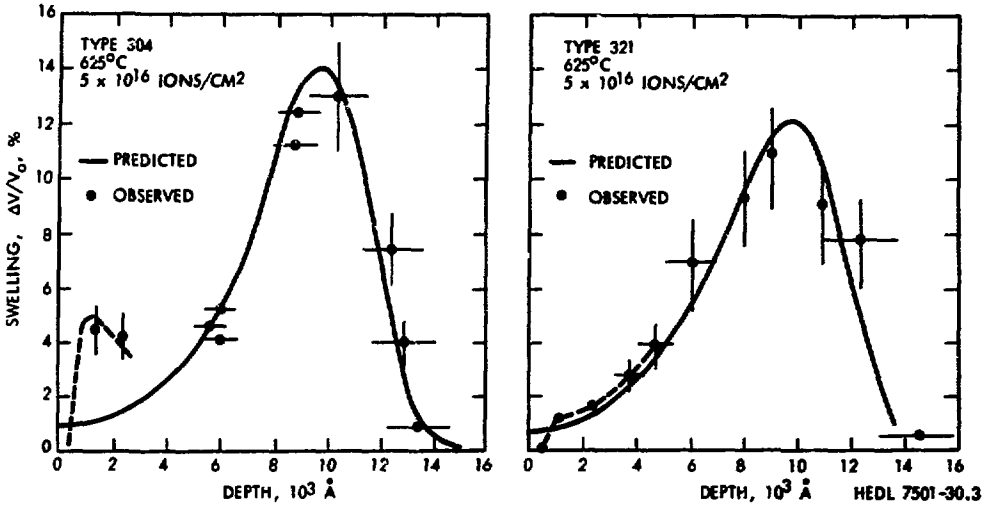

Fig. 16. Comparison of Observed and Predicted Swelling vs. Depth Profiles for 304 and 321 Stainless Steels (Johnston).

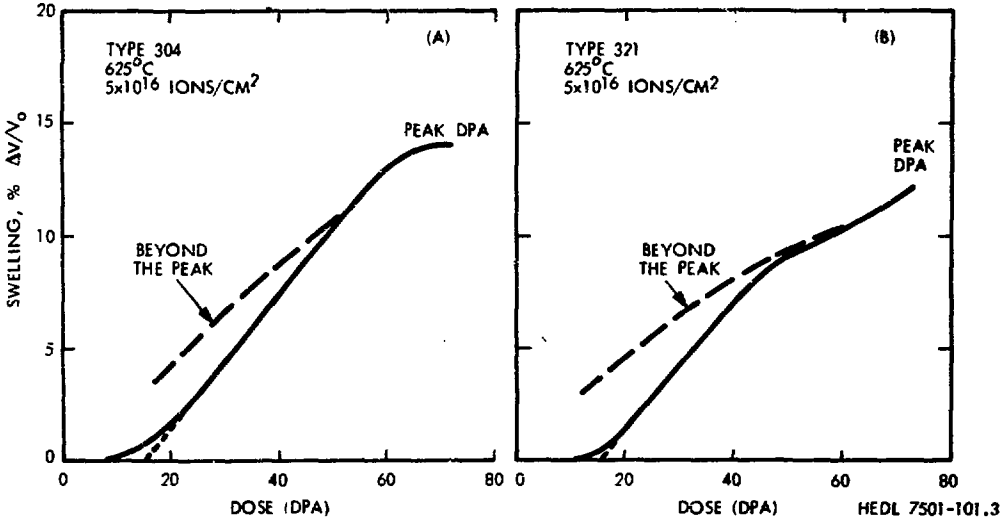

Fig. 17. Swelling vs. Dose Profiles Unfolded from Fig. 15. Note that swelling is initially bilinear but is distorted by the accumulated swelling. The distortion is consistent with the predicted behavior shown in Fig. 16.

Table 2. Apparent Distortion of Linear Swelling Behavior with Accumulating Swelling (Derived from Figure 86)

Swelling (%)	Depth (μm)	Displacement Dose (dpa)		
		Unperturbed	Time Averaged[a]	% Change
Type 304				
5	0.60	32	32	0
13	0.87	60	59	-1.7
14	0.94	68	62	-8.8
14	1.00	72	62	-13.9
12	1.07	56	56	0
8.5	11.7	40	44	+10.0
6.2	12.2	28	36	+28.6
Type 321				
5.4	0.60	34	34	0
9.4	0.80	52	48	-7.7
11.5	0.90	68	56	-11.8
12.2	0.97	73	58	-19.5
9.3	1.12	48	48	0
7.5	1.17	29	38	+31.0
3.0	1.28	11	28	+127.0

a This displacement dose is required to place each data point on the linear portion of the curve. Note that the distortion is always negative below or near the peak, then quickly reverses to positive distortion somewhere beyond the peak.

in Figure 16. In another report,[24] a possible explanation is advanced that involves swelling-induced stress fields, the reversal of the sign of the stress field at the denuded zone interface, and the feedback of the stress state on the local void growth rate. It is anticipated that this phenomenon proceeds concurrently with the incubation effect and internal temperature shift phenomenon described earlier. Therefore, a subsurface peak may or may not be observed, depending on which phenomenon dominates the local swelling behavior.

DISCUSSION

In general, we have shown that the depth-dependence of the swelling profile is not directly proportional to the depth-dependence of the displacement profile. On the other hand, it has been shown here that all observed features of the swelling profile can be explained in terms of phenomena related to displacement rate gradients, their time-dependent histories, stress states which are associated with differential swelling, and perturbation of the experiment by the foil surface. The impact of these phenomena on the interpretation of charged particle experiments varies from minimal effects in most cases to a serious impact in the case of the internal temperature shift for 46.5 MeV Ni^+ and 20 MeV C^+ ion irradiations. The major consequence of this phenomenon is to restrict data normalizations based on the assumption that equal displacement damage generates equal swelling at a given temperature, independent of the local displacement rate.

It should be noted that each of the phenomena explored here in no way detract from the utility of charged particle simulations of neutron environments. Once we have identified each of the variables which are atypical of the neutron environment, it is relatively simple to include their impact in the analysis and in the extrapolation of charged particle data to the neutron environment. In the case of the CTR first wall, these phenomena are not completely atypical; the inner surface of the wall will suffer ion damage as well as neutron damage. The only variable that will be atypical in this case is the rate of ion impingement.

REFERENCES

1. I. Manning and G. P. Mueller, Depth Distribution of Energy Deposition by Ion Bombardment (to be published in Computer Physics Communications).

2. D. G. Doran, et al., Report of the Working Group on Displacement Models and Procedures for Damage Calculations, HEDL-TME 73-76.

3. L. E. Thomas and R. M. Fisher, HVEM Studies of Radiation Swelling of Reactor Steels, International Conference on Physical Metallurgy of Reactor Fuel Elements, Berkely, United Kingdom (Sept. 1973).

4. A. F. Rowcliffe, et al., Swelling and Irradiation-Induced Microstructural Changes in Nickel Base Alloys, ASTM Symposium on Radiation Effects on Structural Materials, Gatlinburg, Tennessee (1974).

5. W. G. Johnston, et al., Depth Distribution of Void Swelling Produced by 5 MeV Nickel Ions, Proceedings, EMSA, St. Louis, Missouri, pp. 358-359 (Aug. 1974).

6. J. A. Hudson, et al., Void Formation in Some Nickel-Aluminum Alloys During 20 MeV C^{++} and 46.5 MeV Ni^{6+} Irradiations, Effects of Radiation Substructure and Mechanical Properties of Metals and Alloys, ASTM STP-529, American Society for Testing and Materials, pp. 326-333 (1973).

7. W. G. Johnston, J. H. Rosolowski, A. M. Turkalo and T. Lauritzen, J. Nucl. Mtls 46, 273 (1973).

8. F. A. Garner and L. E. Thomas, Production of Voids in Stainless Steel by High-Voltage Electrons, Effects of Radiation on Substructure and Mechanical Properties of Metals and Alloys, ASTM STP-529, American Society for Testing and Materials, pp. 303-325 (1973).

9. K. Urban, M. Wilkens and A. Seeger, Application of High Voltage Electron Microscopy to the Study of Voids and Other Point Defect Agglomerates, Proceedings of International Conference, Radiation-Induced Voids in Metals, Albany, New York, pp. 550-562 (1971).

10. N. Q. Lam, S. J. Rothman and R. Sizmann, Rad. Effects 23, 53-59 (1974).

11. S. J. Rothman, N. Q. Lam, R. Sizmann and H. Bisswanger, Rad. Effects 20, 223-227 (1973); also Lam, N. Q., J. Nucl. Mtls. 56, 125-135 (1975).

12. G. L. Guthrie and J. L. Straalsund, Spatial Dependence of Void Growth Rates in the Irradiation of Thin Foils--Theory and Calculations (to be published in Scripta Metallurgica).

13. J. J. Laidler, B. Mastel and F. A. Garner, Swelling in Electron-Irradiated Type 316 Stainless Steel, Properties of Reactor Structural Alloys After Neutron or Particle Irradiation, ASTM STP-570, American Society for Testing and Materials (1975).

14. F. A. Garner and G. L. Guthrie, Evaluation of 20% Cold-Worked 316 Swelling Equation, HEDL-TME 74-4.

15. J. A. Hudson, The Use of 46.5 MeV Ni^+ Irradiations in Void Formation Studies, AERE-R7228.

16. M. D. Mathews, Calculations of the Depth Distribution of Energy Deposition by Ion Bombardment Using the Computer Program of Manning and Mueller, AERE-R7805.

17. J. A. Sprague, et al., J. Nucl. Mtls. 54, 286-298 (1974).

18. T. D. Ryan and A. Taylor, in Proceedings, International Conference on Applications of Ion Beams to Metals, Albuquerque, New Mexico (1973).

19. J. Delaplace, et al., J. Nucl. Mtls. 47, 278 (1973).

20. J. L. Brimhall, H. G. Kissinger and G. L. Kulcinski, in Radiation-Induced Voids in Metals, J. W. Corbett and L. C. Ianniello (eds), USAEC Symposium Series 26, p. 335 (1972).

21. Y. Adda, op. cit., page 31.

22. R. Bullough and R. C. Perrin, in Voids Formed by Irradiation of Reactor Materials, British Nuclear Energy Society, Reading, England, p. 79 (1971).

23. G. R. Odette, D. M. Schwartz and A. J. Ardell, Particle Range and Energy Deposition in Materials Containing Voids (submitted to Rad. Effects).

24. F. A. Garner, G. L. Wire and E. R. Gilbert, Stress Effects in Ion Bombardment Experiments, this conference.

DIMENSIONAL STABILITY OF STAINLESS STEEL AS AFFECTED BY COMPOSITIONAL TRANSMUTATIONS

J. F. Bates
J. O. Schiffgens
M. M. Paxton

Hanford Engineering Development Lab,
Washington, DC

ABSTRACT

One of the major uncertainties involved in the implementation of 316 stainless steel as the material for the first wall of a Controlled Thermonuclear Reactor (CTR) is the question of solid transmutation effects. While the magnitude of these compositional changes can be estimated with reasonable certainty, the physical and metallurgical material perturbations associated with such changes are still largely unknown. The purpose of this report is to present property change data, relative to specific transmutational composition changes, developed from fission reactor irradiations and corresponding unirradiated control tests which can impact CTR design. The effects of composition on the in-reactor behavior of 316 stainless steel are currently being studied by both irradiation-induced swelling experiments conducted in EBR-II and out-of-reactor control studies. These experiments are based on alloy variations from a nominal 316 base steel. In several series of alloys, the composition of a single element and that of iron was varied. Series being studied include variations in C, N, P, S, B, Mn, Cu, Si, Mo, Co, Cr and Ni.

The results indicate that the behavior of 316 stainless steel in a first wall CTR application would undergo no serious detrimental changes due to solid compositional transmutations.

INTRODUCTION

The use of 316 stainless steel as a first wall material for Controlled Thermonuclear Reactors (CTR) would result in chemical changes due to compositional transmutations of constituent elements in the alloy. While the magnitude of these compositional transmutations has been investigated,[1] the resultant effects on the dimensional stability of the steel have not been treated in detail. In the program for the development of the Liquid Metal Fast Breeder Reactor (LMFBR), 316 stainless steel has been employed as a cladding material. Under this program, changes in the dimensional stability of 316 stainless steel as a function of chemical composition have been investigated in some detail. The purpose of this report is to review the effects of composition on the dimensional stability of 316 stainless steel and apply these results to the CTR program. Although the LMFBR program has concentrated on the analysis of 316 stainless steel, the techniques and procedures developed are readily applicable to the analysis of any alloy system.

DESCRIPTION OF EXPERIMENTAL PROGRAM

The data cited were obtained from testing a series of 316 base alloys comprising variations in composition of, in most cases, a single element plus iron. The compositions of the various alloys involved in the experiments discussed in this paper are shown in Table 1. The testing program involves in-reactor tests in the EBR-II to ascertain the effects of composition on irradiation-induced swelling and out-of-reactor tests to determine the effects of composition on lattice dilation (density changes), recrystallization temperature, and tensile properties. The data are reviewed below in light of these property changes.

Lattice Dilation

Included in Table 1 are the densities of the various alloys. The change in density of 316 stainless steel with changes in composition was described in detail in an earlier report.[2] Plots of density versus

TABLE 1

METALLURGICAL VARIABLES ALLOY COMPOSITIONS

ALLOY NO	DENSITY (g/cm^3)	ELEMENT (WEIGHT %)											
CARBON-NITROGEN VARIATIONS		C	Mn	Si	P	S	Cr	Ni	Mo	Cu	Co	B	N
1	7.98131	0.003	0.92	0.40	0.009	0.008	16.95	12.01	2.35	0.10	0.11	0.0011	0.007
3	7.96941	0.047	0.94	0.39	0.010	0.007	16.99	12.05	2.33	0.10	0.12	0.0008	0.050
4	7.963	0.127	0.96	0.38	0.012	0.008	17.06	12.08	2.32	0.10	0.11	0.0010	0.006
5	7.95223	0.128	0.97	0.43	0.011	0.008	17.00	12.10	2.34	0.10	0.11	0.0008	0.111
45	7.9684	0.012	1.12	0.41	0.010	0.007	16.98	12.12	2.31	0.10	0.11	0.0012	0.13
PHOSPHORUS-SULFUR-BORON VARIATIONS													
6	7.96666	0.048	0.92	0.35	0.001	0.004	16.89	11.99	2.36	0.12	0.12	0.0005	0.054
7	7.96796	0.046	0.96	0.37	0.003	0.007	17.06	12.13	2.35	0.10	0.11	0.0005	0.052
8	7.96576	0.046	0.97	0.38	0.003	0.018	17.14	12.14	2.32	0.11	0.11	0.0005	0.054
9	7.96163	0.045	0.96	0.37	0.004	0.036	17.09	12.17	2.32	0.11	0.11	0.0005	0.055
10	7.96973	0.047	0.93	0.37	0.011	0.004	17.09	12.04	2.35	0.11	0.11	0.0005	0.052
11	7.96779	0.045	0.95	0.39	0.021	0.005	16.95	12.03	2.31	0.11	0.12	0.0005	0.054
12	7.96583	0.046	0.93	0.36	0.039	0.004	17.01	12.12	2.33	0.11	0.11	0.0005	0.057
13	7.96495	0.051	0.93	0.40	0.003	0.004	16.95	12.09	2.34	0.11	0.11	0.0012	0.057
14	7.96735	0.046	0.98	0.39	0.003	0.004	17.09	12.10	2.31	0.11	0.11	0.0030	0.054
15	7.96661	0.047	0.96	0.39	0.004	0.004	17.05	12.14	2.32	0.10	0.11	0.0057	0.052
MANGANESE VARIATIONS													
16	7.97462	0.045	0.01	0.43	0.011	0.008	16.92	12.15	2.45	0.10	0.11	0.0011	0.047
17	7.96861	0.046	0.92	0.38	0.009	0.007	17.00	12.07	2.33	0.10	0.11	0.0012	0.052
18	7.9617	0.047	2.04	0.38	0.010	0.008	17.17	11.91	2.21	0.10	0.11	0.0016	0.054
19	7.95103	0.044	3.89	0.37	0.009	0.007	17.03	11.98	2.30	0.10	0.11	0.0012	0.056
COPPER VARIATIONS													
20	7.96913	0.048	0.96	0.40	0.010	0.008	16.92	12.07	2.32	0.01	0.11	0.0010	0.049
22	7.96936	0.044	0.94	0.38	0.009	0.007	16.96	12.04	2.35	0.99	0.11	0.0012	0.052
23	7.97318	0.044	0.95	0.39	0.010	0.008	16.96	12.27	2.35	2.94	0.11	0.0012	0.052
24	7.9758	0.044	0.95	0.39	0.011	0.008	17.00	11.91	2.35	4.47	0.11	0.0013	0.055
SILICON VARIATIONS													
25	7.99698	0.046	0.95	0.01	0.010	0.008	16.88	11.98	2.31	0.10	0.11	0.0011	0.052
26	7.96249	0.045	0.94	0.48	0.009	0.008	17.00	12.12	2.34	0.11	0.11	0.0010	0.054
27	7.92499	0.045	0.94	0.95	0.011	0.007	17.06	12.19	2.35	0.10	0.11	0.0007	0.049
28	7.88573	0.044	0.93	1.47	0.010	0.008	17.07	12.30	2.38	0.10	0.11	0.0007	0.054
29	7.85047	0.045	0.94	1.96	0.010	0.007	17.13	12.39	2.41	0.11	0.11	0.0010	0.050
MOLYBDENUM VARIATIONS													
30	7.9363	0.044	0.99	0.40	0.010	0.007	16.89	12.31	0.01	0.10	0.11	0.0011	0.049
31	7.93893	0.041	0.98	0.38	0.010	0.007	16.86	12.04	0.11	0.10	0.11	0.0011	0.048
32	7.94894	0.045	0.99	0.40	0.010	0.008	16.90	11.99	1.00	0.10	0.11	0.0012	0.049
33	7.97632	0.047	0.92	0.38	0.011	0.008	16.96	12.09	3.03	0.10	0.11	0.0012	0.049
COBALT VARIATIONS													
35	7.96879	0.044	0.96	0.41	0.010	0.007	16.89	12.03	2.31	0.10	0.02	0.0010	0.049
37	7.97283	0.046	0.91	0.41	0.009	0.009	16.97	11.89	2.29	0.10	0.50	0.0010	0.051
39	8.00137	0.042	0.90	0.38	0.011	0.008	17.00	12.04	2.30	0.10	4.45	0.0013	0.049
CHROMIUM-NICKEL VARIATIONS													
40	7.9833	0.045	0.95	0.40	0.010	0.007	14.86	9.96	2.29	0.10	0.12	0.0013	0.050
41	7.99177	0.046	0.96	0.38	0.009	0.007	14.89	12.01	2.35	0.10	0.11	0.0013	0.052
42	7.99584	0.046	1.00	0.39	0.009	0.008	15.13	14.04	2.32	0.10	0.11	0.0008	0.048
43	7.96931	0.047	0.93	0.40	0.009	0.007	16.85	12.12	2.35	0.10	0.11	0.0005	0.052
44	7.9415	0.041	0.90	0.41	0.011	0.007	18.97	12.11	2.35	0.10	0.11	0.0010	0.049

composition exhibited a linear relationship between density and composition for annealed and 20% cold worked material with the slopes of both conditions being nearly identical. The absolute density of the cold worked materials was approximately 0.034% less than the density of the solution treated material, as shown in Figure 1. It was found that variation of some of the elemental concentrations had diverse effects on the densities of the alloys, some increasing and some decreasing the densities. An example of a decrease in the density (lattice dilation) of 316 stainless steel with increasing Mn content is shown in Figure 2.

The density of annealed 316 stainless steel can be described by the following equation:[2]

$$\begin{aligned} \text{density } (g/cm^3) = {} & 8.1145 - 0.1216\ (\%\ C) \\ & - 0.005589\ (\%\ Mn) - 0.07597\ (\%\ Si) \\ & - 0.01155\ (\%\ Cr) + 0.004842\ (\%\ Ni) \\ & + 0.01516\ (\%\ Mo) + 0.001612\ (\%\ Cu) \\ & + 0.007548\ (\%\ Co) - 0.06538\ (\%\ N) \\ & + 1.333\ (\%\ B) - 0.1558\ (\%\ P) - 0.1933\ (\%\ S) \end{aligned} \qquad (1)$$

where all values are in weight percent. The partial molar volumes and size factors of the various elements in stainless steel were also derived from these data and are shown in Table 2.

Irradiation-Induced Swelling

Irradiation-induced swelling of 316 stainless steel has been shown to be strongly dependent on minor alloy constituents.[3] The alloys described in Table 1 were irradiated in EBR-II at temperatures of 370-760°C to fluences approaching 4×10^{22} n/cm^2 (E >0.1 MeV). Several of these specimens are now being reirradiated to extend the fluences out to approximately 10×10^{22} n/cm^2. The irradiation-induced swelling data have been generated for material in the solution annealed and 20% cold worked conditions; as yet, the cold worked material has not achieved any appreciable swelling to allow an assessment of compositional effects. However, data generated from the annealed specimens have shown changes

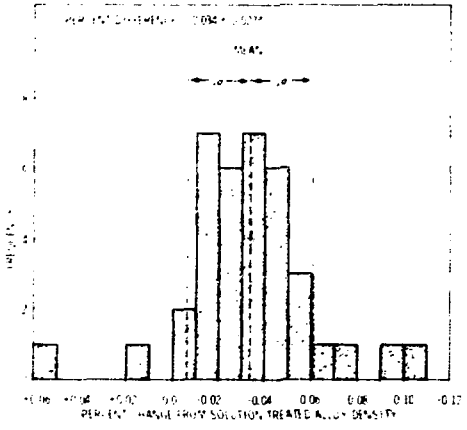

Fig. 1. Histogram of percent difference between densities of cold worked and solution treated alloys.

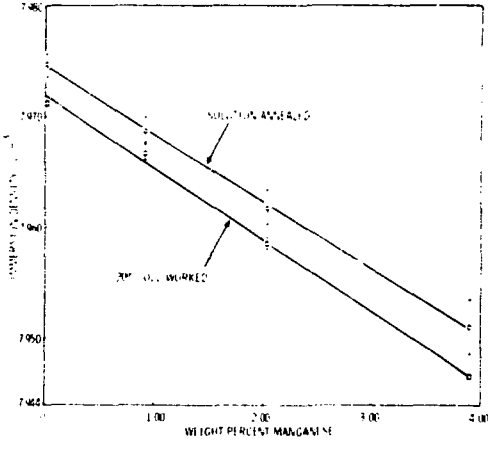

Fig. 2. Effect of manganese content on the immersion density of stainless steel.

TABLE 2

SIZE EFFECT DATA FOR COMPONENTS IN SOLUTION TREATED TYPE 316 STAINLESS STEEL--AS CALCULATED FROM IMMERSION DENSITY DATA*

Element	Wt Pct	Regression Coefficients	At. Wt	Density g/cc	Partial Molar Volume cc/mole	Deviation from Ideal Behavior Pct	Volume Size Factor Pct
Fe	67.029	0	55.87	7.87	6.883	-3.0	-1.8
Mn	0.95	-0.005589	54.938	7.3	7.252	-3.6	3.4
Si	0.4	-0.07597	28.086	2.33	6.823	-43.4	-2.7
Cr	17	-0.01155	51.996	7.2	7.352	1.8	4.8
Ni	12	0.004842	58.71	8.9	6.785	2.8	-3.2
Mo	2.3	0.01516	95.94	10.22	9.526	1.5	35.9
Cu	0.1	0.001612	63.546	8.96	7.667	8.1	9.3
Co	0.1	0.007548	58.9332	8.9	6.559	-0.95	-6.5
P	0.01	-0.1558	30.9738	1.82			
S	0.01	-0.1933	32.064	2			
C	0.05	-0.1215	12.01	3.5	3.780	10.2	53.9
N	0.05	-0.06534	14.0067	1	3.168		45.1
B	0.001	1.333	10.811	2.35			

Computed data for "nominal" alloy (column 1): lattice site volume, Ω = 7.012 cc/mole; density, ρ = 7.965 g/cc; lattice parameter, a = 3.597 Å.

* From Reference 2.

TABLE 3

LATTICE STRAIN DUE TO COMPOSITIONAL TRANSMUTATIONS* OF MANGANESE AND NICKEL

	2 years		10 years		30 years	
	Mn	Ni	Mn	Ni	Mn	Ni
Latttice Strain (Linear)	0.007%	0	0.035%	-0.004%	+0.10%	-0.01%

* The magnitude of the compositional change is based on the University of Wisconsin study (Reference 1).

in levels of concentration of phosphorus, silicon, molybdenum, and carbon to be effective in increasing the swelling resistance of the alloy system. Variations in manganese concentration (of prime interest in the CTR program) exhibited a less pronounced effect, as shown in Figure 3. Other elemental variations such as nickel, sulfur, nitrogen, and boron showed no significant effect on the swelling within the compositional levels investigated.

Mechanical Properties

The effect of alloy composition variations on the 1400°F tensile properties of 20% cold worked Type 316 stainless steel have also been investigated.[4] The 0.2% yield strength for any specific composition can be calculated by the following relationship:

$$\begin{aligned} 0.2\%\ \text{yield strength} = {} & 49{,}840 \\ & + 3258\ (\%\ \text{Molybdenum}) && (0.11 - 3.03\%) \\ & - 57054\ (\%\ \text{Carbon}) && (0.003 - 0.130\%) \\ & - 1307\ (\%\ \text{Copper}) && (0.1 - 4.47\%) \\ & + 42112\ (\%\ \text{Nitrogen}) && (0.007 - 0.134\%) \\ & + 2788\ (\%\ \text{Silicon}) && (0.1 - 1.96\%) \\ & + 790\ (\%\ \text{Cobalt}) && (0.02 - 4.45\%) \\ & - 670\ (\%\ \text{Chromium}) && (14.9 - 19.0\%) \end{aligned} \qquad (2)$$

The numbers in parentheses to the right of the equation show the range of composition over which equation (2) is valid. The standard error of the 0.2% yield strength using equation (2) is 1340 psi. The ductility and the ultimate tensile strength of the alloys were also obtained. An example of the data generated from such studies is shown in Figure 4, which depicts tensile properties versus percent chromium content.

Recrystallization Temperature

Analyses similar to those mentioned above have yielded recrystallization temperatures as a function of composition.[5] For example, the 1000-hour recrystallization temperature of 316 can be represented by the following equation:

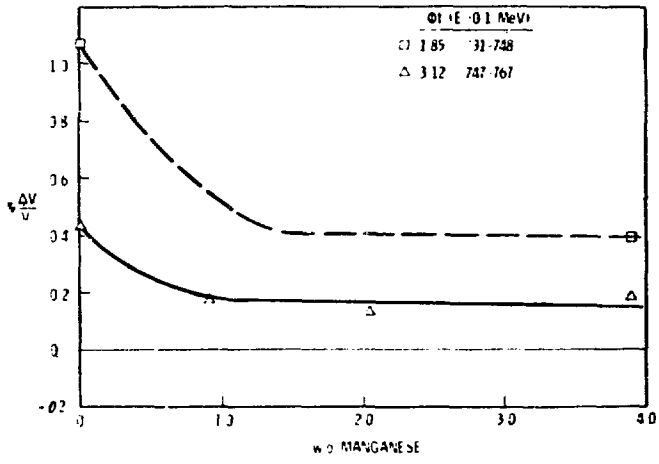

Fig. 3. Swelling in manganese modified stainless steel.

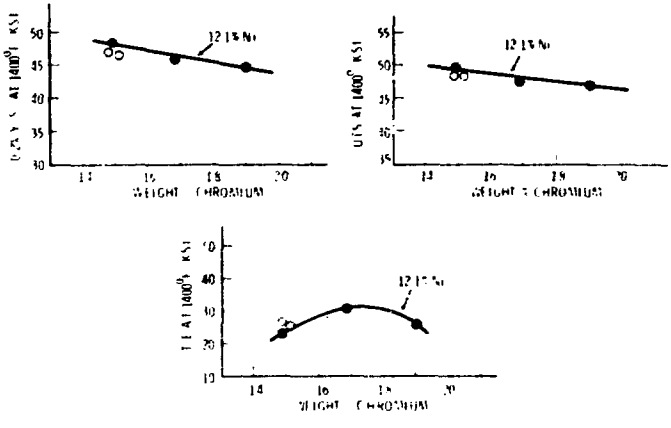

Fig. 4. The effect of chromium variations on the 1400°F tensile properties of 20% cold worked Type 316 stainless steel alloys.

1000 hour recrystallization temperature, °F = 545°F (3)

+ 55.9 (% Silicon)	(0 - 2.0%)
+ 36.8 (% Chromium)	(16.5 - 19.0%)
+ 13.393 (% Boron)	(0 - 0.0057%)
+ 91.5 (% Molybdenum)	(2.0 - 3.0%)

Again, the range of applicable compositions is shown to the right of the equation. It can be observed from equation (3) that few elements affect the recrystallization temperature. The 1-hour and 100-hour recrystallization temperatures were also investigated as shown in Figure 5, which shows recrystallization temperature versus chromium content.

DISCUSSION

The hard neutron spectrum of fusion reactors will not only produce more displacements per neutron than a fission reactor spectrum but will also produce gaseous and solid transmutants at higher rates. These transmutants can not only significantly alter the chemical composition of a component but also alter the rate at which displacement damage affects its dimensions and electrical and mechanical properties. The significance of transmutants on component behavior depends on the function of the component and its chemical composition, as well as the transmutation rate and the character of transmutant-defect interactions. The tolerable amount of transmutation in insulations and superconductors, for example, is expected to be much less than that in common structural alloys such as 316 stainless steel or in simple refractory alloys such as Nb-1Zr.

As noted, the amount of transmutation in a stainless steel exposed to a representative first wall fusion spectrum has been computed.[1] The results of that study show that the elements undergoing the most significant changes in composition are Ni, Mn, Ti and V. Of these elements, Mn and Ni were included in the present series of investigations and the effect of compositional variations of these elements can be evaluated directly. As shown in equations (1)-(3), variations of both Mn and Ni to the levels shown in Table 1 have no effect on the 1400°F tensile properties or on the 1000-hour recrystallization temperature. Both do contribute

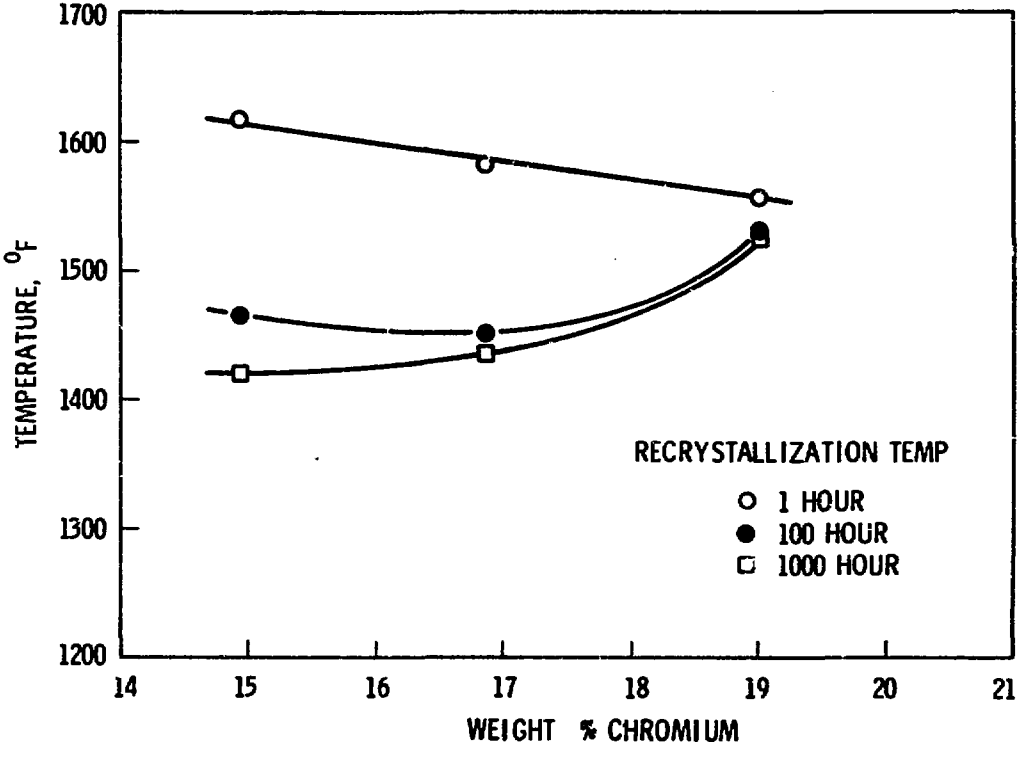

Fig. 5. The effect of chromium variations on the 1, 100 and 1000-hour recrystallization temperature of 20% CW Type 316 stainless steel.

to lattice strain, and these effects are shown in Table 3. However, the effects are small, yielding less than +0.10% cumulative strain after 30 years' operation.

Variations in Mn from 2 to 4 weight percent (the change expected during approximately a 10-year residence time for a typical CTR first wall) did not show a significant change of the magnitude of irradiation-induced swelling. Most of the effect of elemental variations on the irradiation-induced swelling occurs in the process of going from essentially zero percent of the constituents up to some higher content. Once a constant reduction in swelling, from the 0.0 weight percent of the element, is observed, additional small positive changes of the element do not significantly alter this level of swelling.[3,6] We would therefore expect no significant changes to occur in going from 4 to 6 weight percent. The small changes in nickel content produce no significant change in swelling. Therefore, since the swelling versus Mn content is not changing appreciably beyond ∿2% Mn, this particular transmutation should not alter the swelling. The magnitude of swelling could then be estimated from that which would be obtained from a nominal 316 stainless steel. Using a flux of 3.7×10^{15} n/cm^2-sec results in ∿1×10^{22} n/cm^2-yr fluence for the first wall of the CTR. Type 316 stainless steel in the 20% cold worked condition undergoes no significant irradiation-induced density changes below ∿5×10^{22} n/cm^2. Beyond that, the swelling is highly temperature dependent. Thus swelling considerations would suggest a minimum five-year residence time for the first wall of the CTR would be feasible based on Mn and Ni transmutations only.

Let us now consider the effect of increased concentrations of vanadium and titanium. It was shown[6] that elements which tend to be alpha-phase stabilizers of 316 stainless steel also tend to increase the swelling resistance of the alloy. Both Ti and V are alpha stabilizers. Increases in these elements should therefore increase the swelling resistance of the alloy. This has been substantiated in the case of titanium in another investigation,[7] where certain increases in the Ti content were shown to be useful in reducing the swelling.

SUMMARY

Some effects of transmutations of Mn, Ni, Ti and V which would be expected in a CTR 316 stainless steel first wall have been evaluated. Based on the available data and relevant investigations, it is concluded that little or no deleterious effects on the recrystallization temperature or 1400°F tensile properties will be experienced by the steel as a result of these transmutations. Small lattice strains (<0.1% for 30 years' residence time) will be experienced due to changes in Mn and Ni content. The swelling resistance of the alloy would not be altered by changes in Mn and Ni content to the levels discussed in this report. Increases in concentration of V and Ti may result in increased swelling resistance due to α-stabilization.

In conclusion, our results indicate that the behavior of 316 stainless steel in a first wall CTR application would undergo no serious detrimental changes due to solid compositional transmutations.

REFERENCES

1. G. L. Kulcinski (ed.), UWMAK-I, A Wisconsin Toroidal Fusion Reactor Design, UWFDM-68, page VI-D-21 (March 1974).

2. J. L. Straalsund and J. F. Bates, Partial Molar Volumes and Size Factor Data for Alloy Constituents of Stainless Steel, Met. Trans., 5 (February 1974).

3. J. F. Bates, Irradiation-Induced Swelling Variations Resulting from Compositional Modifications of 316 Stainless Steel, Proceedings, International Symposium on Radiation Effects on Structural Materials, Gatlinburg, Tennessee, June 11-13, 1974, to be published as ASTM STP-570.

4. M. M. Paxton, The Effect of Chemistry Variations on the Tensile Properties of 20% Cold Worked 316 Stainless Steel, HEDL-TME 73-34 (March 1973).

5. M. M. Paxton and J. L. Straalsund, The Effect of Chemistry Variations on the Recrystallization Temperature of 20% CW 316 SS, Nucl. Tech., 25, No. 3 (March 1975).

6. J. F. Bates and G. L. Guthrie, A Relationship Between Equivalent Chromium Content and Irradiation-Induced Swelling in Type 316 Stainless Steel, Nucl. Tech., 27, 2 (October 1975).

7. E. E. Bloom, J. M. Leitnaker and J. O. Stiegler, Effect of Neutron Irradiation on the Microstructure and Properties of Titanium Stabilized Type 316 Stainless Steel, submitted for publication in Nucl. Tech. (1975).

AN ANALYSIS OF IRRADIATION WITH TIME-DEPENDENT SOURCES

J. O. Schiffgens
N. J. Graves
D. G. Doran

Hanford Engineering Development Laboratory
Richland, WA 99352

ABSTRACT

Various CTR designs call for pulsed operation with cycle lengths ranging from several seconds to about a hundred minutes, and pulse lengths ranging from nanoseconds to the neighborhood of ninety minutes. Fluctuations in temperature, stress, and damage rate resulting from pulsed reactor operation are expected to significantly affect component life. This paper describes the first phase of an analysis of effects resulting from damage rate fluctuations. Procedures for modeling cluster growth are discussed and the results of calculations of the net growth of gas containing voids during an irradiation cycle are presented. These calculations show that the pulse parameters chosen for reactors and irradiation sources can dramatically alter swelling, and most probably other irradiation effects. For example, if the irradiation pulse length is less than about 10 μsec and the interval between pulses is greater than about ten vacancy mean lives, no void growth is possible in stainless steel regardless of temperature, dislocation density and pulse amplitude (instantaneous displacement rate) provided no voids form in displacement cascades which are large enough to survive the time between pulses.

INTRODUCTION

Anticipated CTR environments[1] present a new range of boundary conditions for the theoretical and experimental analysis of irradiation effects. The hard neutron spectra inherent in D-T fusion reactors will not only produce more displacements per neutron than a fission reactor spectrum but will also produce transmutants (notable H and He) at higher rates. Furthermore, various CTR designs call for pulsed operation with cycle lengths ranging from several seconds (Theta Pinch[2] and Laser[3] reactors) to about a hundred minutes (Tokamak[4-6] reactors) and pulse lengths (burn times) ranging from nanoseconds (Laser reactors) to tens of milliseconds (Theta Pinch reactors) to the neighborhood of 90 minutes (Tokamak reactors). Temperature variations during a cycle may be as small as 50°C in Tokamak reactors and as large as several hundred degress in Theta Pinch reactors. As a result, unique bulk and surface irradiation damage is expected in structural materials exposed to fusion reactor neutrons, and fluctuations in temperature, stress, and damage rate resulting from pulsed reactor operation are expected to significantly affect component life.

In the absence of irradiation facilities which actually simulate CTR environments, irradiation effects data for CTRs will come from experiments with a wide variety of sources. Some of these sources are of a pulsed nature with irradiation cycles ranging from tens of nanoseconds (cyclotrons) to milliseconds (LAMPF). In addition, constant sources may be employed in a pulsed manner. Effective interpretation, correlation, and extrapolation of irradiation data obtained in pulsed systems are essential.

This paper describes the first phase of an investigation of effects resulting from the periodic variation of the damage rate. The effect of cyclic irradiation on the growth of gas containing voids was chosen for analysis at this time because of its relative tractability and the overall significance of voids in altering materials properties. Various first wall structural materials (notably Nb-1% Zr, and PE16 and CW-316 stainless steels) have been considered in conceptual designs of commercial CTRs. In service, first walls are typically expected to withstand integrated neutron exposures in the range of 10^{22} to 10^{23} n/cm^2 at temperatures in the range 500 to 800°C. It is well known that continuous irradiation of such alloys in this temperature range to fast reactor neutron fluences in excess of 10^{22} n/cm^2 results in the formation and growth of voids. Although irradia-

tion effects other than void swelling (such as embrittlement or irradiation enhanced fatigue and/or creep) are likely to be the factors limiting first wall life times, an analysis of void growth will provide valuable insight into the factors affecting damage accumulation during irradiation with time-dependent sources.

No attempt has been made to present a comprehensive model of swelling. The model presented here describes the kinetics of void growth during an irradiation cycle in terms of vacancies and interstitials interacting and diffusing toward stationary sinks. Assuming dislocations are the dominant sinks, the net growth of gas containing voids is calculated as the spatially averaged vacancy and interstitial concentrations vary during the cycle. The general approach taken in this analysis is described in Section II, while the underlying theory is presented in Section III. In Section IV the detailed assumptions incorporated in the model are presented. Identification of significant regimes and initial results of calculations are discussed in Sections V and VI.

GENERAL APPROACH

Initially this research is intended to determine conditions for which cyclic time variations in radiation intensity are likely to substantially affect damage accumulation. Irradiations of interest are those for which the pulse lengths and cycle lengths are short relative to the time required for detectable changes to occur in the dimensional or mechanical properties of structural materials. The quasi-steady state approximation is not applicable to the analysis of mobile defect concentrations throughout such irradiations. Instead, the net effect of mobile defect concentration fluctuations on cluster formation and growth must be determined for each irradiation cycle and the results summed to describe the slowly evolving microstructure.

When the radiation source is on, small mobile defects are produced; their number, type, and spatial distribution are functions of the material and the type and energy of the incident radiation. The effects of pulsing on the evolution of radiation damage is of interest for both neutron and charged particle irradiations. Therefore one must eventually consider any effects that may be due to displacement cascade production as contrasted

with the production of isolated Frenkel pairs. Strictly speaking, only the latter case is considered at this stage of the present study. There are at least two ways in which displacement cascade production may influence the consequences of pulsing an irradiation source. One is simply caused by the inhomogenity of defect production. Given a high enough flux, cascade overlap can become significant. The highest instantaneous fluxes are anticipated for inertial confinement devices. Even in this case, however, cascade overlap, or a flux effect, does not look significant.

The other effect has to do with the production of vacancy clusters within a displacement cascade. Computer simulations of displacement cascade production and short term annealing indicate that only a small fraction of the vacancies are free to escape from the cascade immediately after its production. The simulations indicate that the remainder of the vacancies are present as small vacancy clusters. However, the clustering criteria and the extreme proximity of these small clusters to one another suggest that, on a longer time scale, these clusters could coalesce. Indeed there is experimental evidence that large vacancy clusters, as three-dimensional aggregates or as loops, are formed directly in cascades. These vacancy clusters emit vacancies as a function of time, the rate depending sensitively on the temperature. While they exist, they provide additional annihilation sites for interstitials and effectively extend the average lifetime of vacancies. It has been shown that the existence of these intrinsic vacancy clusters can influence void growth.[7] It has also been shown that they can have a strong influence on void nucleation. It seems clear, then, that the effects produced by the presence of these clusters can be modified by pulsing. A sensitive regime should be where the pulse duration is of the same order as the cluster lifetime.

It is assumed here, for simplicity, that the evolution of the microstructure can be adequately described in terms of the uniform production interaction, and diffusion of point defects. Transmutants, which at the end of their formation process are most likely on lattice sites, diffuse slower than interstitials or vacancies and, with the probable exception of hydrogen, accumulate during irradiation. Hence, transmutants will be assumed stationary during the irradiation cycle, and in future studies

their migration and precipitation will be analyzed separately for incorporation in the model. Precipitated transmutants and other impurities, together with prevailing vacancy and interstitial concentrations, are assumed to completely control void formation and growth.

This paper focuses on the initial growth of gas containing voids. Early in an irradiation, voids are few in number and the average vacancy and interstitial concentration levels are determined by the competition between mutual annihilation during diffusion on the one hand and leakage at dislocations and grain boundaries on the other. In all practical cases, leakage at grain boundaries is insignificant compared to leakage at dislocations.[8] At this point in an irradiation interstitials aggregate to form interstitial dislocation loops, which together with the preirradiation dislocation network, interact with the diffusing defects. As pointed out by others,[9-11] the preferential attraction of dislocations for interstitials is sufficient to bring about the excess of vacancies required to ensure the growth of nucleated voids during continuous irradiation.

Consider the physical processes taking place during an irradiation cycle. At the beginning of the pulse the concentration of both types of defects increases rapidly. However, the concentration of the very mobile interstitials tends to level off quickly as it approaches equilibrium with the existing dislocation network. The relatively slow moving vacancies require much more time to equilibrate with the dislocations; hence, their concentration continues to increase. As the vacancy concentration rises, an increasing fraction of interstitials are removed by annihilation with vacancies, and the interstitial concentration decreases. Consequently, the interstitial concentration should tend to pass through a maximum at a time when the interstitials are in near equilibrium with the dislocations and the vacancy concentration is far from its equilibrium value. If the pulse is long enough, of course, the vacancy and interstitial concentrations reach the values they would have during a continous irradiation having the same defect production rate. At the end of the pulse, the vacancy and interstitial concentrations decrease rapidly, each tending toward its thermal equilibrium value at rates determined by their mobility and the dislocation density. Hence, clusters may form and grow both

during and/or between pulses depending on the factors controlling the vacancy and interstitial concentration levels.

Ideally one would like to obtain a detailed description of the time variation in the spatial distribution of the interacting point defects as they diffuse near each sink type. However, solving the appropriate set of continuity equations for each sink type is impractical, not to mention the difficulty of specifying selfconsistent, interrelated boundary conditions. Matters are considerably simplified if the analysis is separated into three parts. Since the analysis must relate void growth to dislocation density in a meaningful way, it is essential to describe the competition between annihilation and leakage at dislocations. The goal of the first part of this analysis is to obtain the probabilities for vacancy and interstitial leakage as functions of the dislocation density and temperature. The random dislocation configuration of a real solid is approximated by an idealized configuration consisting of a bundle of parallel straight dislocations for which end effects are neglected. The coupled, steady state, continuity equations for vacancies and interstitials, including the interactions between the defects and the stress fields of the dislocations, are solved for the concentration profiles in order to obtain the leakage rates of each and relate them to their average concentrations at the dislocation densities and temperatures of interest.

In the second part of the analysis, it is assumed that vacancy and interstitial leakage rates (for a given temperature, dislocation density and set of defect properties) are proportional to the respective average concentrations at all times. The coupled rate equations which describe the defect balance throughout the cycle in terms of the spatially averaged concentrations are solved to obtain the time dependences of these average concentrations.

The third part of the analysis builds on the first and the second. It is assumed that voids growing among the dislocations may be treated simply as growing in the time varying average concentrations resulting from the annihilation-leakage competition. The fields and the spatial variations in the vacancy and interstitial concentrations near the dislocations are ignored. The uncoupled continuity equations describing

diffusion in the region surrounding the void are solved with the requirement that the average concentration within the region be equal to the average concentration throughout the material at all times.

THEORY

Bombardment with high energy radiation constitutes a volume source of various types of mobile defects resulting in a defect solution that is supersaturated with respect to each defect type. The mobile defects of primary interest are vacancies, interstitials, and the helium and/or hydrogen generated or implanted during irradiation. Consider the region surrounding a defect sink. Within this region an elemental volume of material dV, at any point $\bar{r}$, contains volume sources of all I types of interacting, mobile defects. Let $C_i(\bar{r},t)$ be the number of i^{th} type defects per unit volume within dV at time t. Assuming that the volume contains no stationary sources or sinks, the set of I continuity equations describing the variation in concentration of each i^{th} type defect as a function of position and time is

$$\frac{\partial}{\partial t} C_i(\bar{r},t) = S_i(\bar{r},t) - \bar{\nabla} \cdot \bar{J}_i(\bar{r},t) + R_{iI}(\bar{r},t), \quad i=1,I \tag{1}$$

The equations state that the net rate of accumulation for each i^{th} type defect in dV is equal to the rate of introduction of the defect by its corresponding volume source $S_i(\bar{r},t)$ minus the net rate of flow of the defect from the volume $\bar{\nabla} \cdot \bar{J}_i(\bar{r},t)$, plus the net rate of production of the defect from various reactions and cluster dissociations $R_{iI}(\bar{r},t)$. Since all defects within dV may interact with each other and all clusters may dissociate, the continuity equation for each i^{th} type defect is coupled to those for all others through the $R_{iI}(\bar{r},t)$ term. Extended and essentially stationary defects which act as sources and sinks for the mobile defects are incorporated through the boundary conditions.

For any given calculation, the volume source terms in Eqs. (1) are obtained from a detailed analysis of damage production for the particular irradiation conditions of interest.[12] In this modeling work, the volume source is always assumed to be uniformly distributed, i.e., $S_i(\bar{r},t) = S_i(t)$ and, in this paper, is treated as a rectangular wave

$$S_i(t) = S_i \qquad 0 \le t < t_p, \tag{2}$$
$$= 0 \qquad t_p \le t \le t_c,$$

where t_c is the cycle length, t_p is the pulse length, and S_i is the pulse amplitude.

All potential gradients within the material, whatever the nature of the driving forces, tend to produce a current of the diffusing species with which the gradients interact. These vectors are added to obtain the net current density vector for each defect

$$\bar{J}_i(\bar{r},t) = -D_i \bar{\nabla} C_i(\bar{r},t) - C_i(\bar{r},t) \sum_{q=1}^{Q} \mu_i^q \bar{\nabla} \varepsilon_i^q(\bar{r}), \tag{3}$$

where D_i is the diffusion coefficient, $\bar{\nabla}\varepsilon_i^q$ is the q^{th} potential gradient acting on the defect, μ_i^q is the mobility of the defect in the q^{th} gradient, and Q is the number of potential gradients present. The sense of the driving force $\bar{\nabla}\varepsilon_i^q(\bar{r})$ exerted by the field on the defect is such as to lower the free energy of the material.

The diffusion coefficient in an isotropic crystal is given by

$$D_i = g_i \, a^2 \, \nu_i \exp\left\{S_i^m/k\right\} \exp\left\{-E_i^m/kT\right\} = D_i^o \exp\left\{-E_i^m/kT\right\} \tag{4}$$

where g_i is the geometrical factor, $\underline{a}$ is the lattice parameter, ν_i is the attempt frequency, k is the Boltzmann constant, T is the absolute temperature, and S_i^m and E_i^m are, respectively, the entropy and energy (more accurately enthalpy) of motion. For an impurity whose migration is controlled by some cooperative phenomenon, the free energy of motion is replaced by a free energy of activation, reflecting the probability of occurrence of the particular phenomenon. Though spatial variations may be included,[13] the entropies and energies of motion, and consequently the diffusion coefficients, for the defects considered in this study are taken as spatially constant, evaluated in the absence of a field.

While diffusing toward stationary sinks, the various defects produced by radiation bombardment interact and/or dissociate forming new defects. The diffusion process itself, as well as all reactions ar[illegible]

sociations, may be described in terms of the theory of rate processes.[14] For a system of I defect types interacting through a total of L reactions the stoichiometric equations of mass balance may be written in the generalized form

$$\sum_{i=1}^{I} s_{i\ell}[i] \underset{K_{r\ell}}{\overset{K_{f\ell}}{\rightleftharpoons}} \sum_{i=1}^{I} p_{i\ell}[i], \qquad \ell=1,L \tag{5}$$

where [i] symbolizes the i^{th} type defect, $s_{i\ell}$ and $p_{i\ell}$ are the stoichiometric coefficients of reactant and product [i]'s, respectively, and $K_{f\ell}$ and $K_{r\ell}$ are the reaction rate constants for the forward f and reverse r paths of the ℓ^{th} reaction. Employing this notation, the net rate of formation of the i^{th} type defect by all L reactions may be written as

$$R_i(\bar{r},t) = \sum_{\ell=1}^{L} (p_{i\ell}-s_{i\ell}) \left[K_{f\ell} \prod_{n=1}^{I} \left\{ C_n(\bar{r},t) \right\}^{s_{n\ell}} - K_{r\ell} \prod_{n=1}^{I} \left\{ C_n(\bar{r},t) \right\}^{p_{n\ell}} \right], \tag{6}$$

where $C_n(\bar{r},t)$ is the concentration of the n^{th} type defect in each ℓ^{th} reaction in which i^{th} type defects participate. The rate constants, though taken to be independent of defect concentrations, do depend on the temperature and the thermodynamic properties of the reacting defects.

Reaction rate constants represent the rate of encounter between interacting defects.[15,16] For the j^{th} reaction in which defects of type i and ℓ form a defect of type o, the rate constant is

$$K_{fj} = \frac{\Omega}{2} \left\{ \alpha_{ji} \nu_i \exp\left(S_i^m/k - E_i^m/kT\right) + \alpha_{j\ell} \nu_\ell \exp\left(S_\ell^m/k - E_\ell^m/kT\right) \right\} \tag{7}$$

where α_{ji} and $\alpha_{j\ell}$ are the combinatory numbers, and Ω is the atomic volume. When the reverse path involves dissociation (of say the o^{th} type defect into i and ℓ type defects) the rate constant is

$$K_{rj} = \alpha_{jio} \nu_{io} \exp\left\{ S_i^m/k - (E_i^m + BE_{\ell io})/kT \right\} \tag{8}$$

where, assuming i^{th} defects are more mobile than ℓ^{th} defects, α_{jio} is the combinatory number of the i^{th} defect emitted from an o^{th} cluster, and $BE_{\ell io}$ is the energy characteristic of the binding of defect types i to ℓ in

forming o. The rate constant for dissociation represents the frequency at which a given type of defect breaks away from the cluster.

As with the diffusion coefficients, the rate constans are assumed independent of position in this study. The combinatory numbers appearing in Eqs. (7) and (8) depend on the defect configurations, migration modes, and effective capture radii in the particular crystal. The numbers α_{ji} and $\alpha_{j\ell}$ are determined for each defect by treating one of the defects as stationary and counting all the possible ways that the other can approach it such that the complex of interest forms in a single jump. The number α_{jio} is just the number of sites available to the emitted defect such that dissociation occurs.

Since defect clusters, grain boundaries, and dislocations may act as sources as well as sinks, their boundaries are referred to in this discussion as source-sink boundaries. The treatment of defect diffusion at a source-sink boundary is formally the same as absorption or chemical reaction at a surface. At some point as defects approach a sink they can no longer exist as separate entities and are absorbed by the sink. Hence, a "stability" surface surrounding each sink may be defined by a vector $\bar{r}_b$ from the source-sink center to the nearest metastable defect sites. The rate of diffusion of the i^{th} defect to the boundary is given by the net rate of defect transport across the stability surface of area A_b

$$\bar{u} \cdot \bar{J}_i(\bar{r}_b,t)\, A_b = -\left[\omega_i^{in}(t) - \omega_i^{out}(t)\right], \qquad (9)$$

where $\bar{J}_i(\bar{r}_b,t)$ is the current density vector evaluated at $\bar{r}_b$, $\bar{u}$ is a unit vector normal to the surface at $\bar{r}_b$, and $\omega_i^{in}(t)$ and $\omega_i^{out}(t)$ are the number of i^{th} defects per unit time moving toward and away from the source-sink boundary. As with reactions in general, flow into such a boundary may be considered to proceed through the formation of an activated state, where the rate of flow at any given temperature is determined by the number of defects in the activated state and the velocity at which these travel across the top of the energy barrier defining the activated state. The troughs on either side of the barrier define the bound state and the state corresponding to the nearest (on the average) metastable site. The locus of metastable sites defines the stability surface $r=r_b$. The

expression for $\omega_i^{in}(t)$, the number of the i^{th} defects per unit time crossing this surface while moving toward the boundary,[17] is simply

$$\omega_i^{in}(t) = C_i(r_b,t)\, A_b\, a\, g_i\, \nu_i \exp\left\{S_i^m/k\right\}\exp\left\{-E_i^m/kT\right\}, \tag{10}$$

Similarly, the rate at which i^{th} defects cross the surface while leaving the boundary, assuming all sites of i^{th} defects on the source-sink boundary are energetically equivalent, may be written as

$$\omega_i^{out}(t) = C_{is} A_b\, a\, g_i\, \nu_i \exp\left\{S_i^m/k\right\}\exp\left\{-E_i^m/kT\right\}\exp\left[\frac{dF(n_i)}{dn_i}\frac{1}{kT}\right] \tag{11}$$

where C_{is} refers to the concentration of i^{th} defects at the cluster boundary (not the surface defined by r_b), n_i refers to the number of i^{th} type defects, and $dF(n_i)/dn_i$ refers to the change in free energy associated with the emission of the i^{th} type defect from the cluster. The concentration C_{is} is chosen so that at thermal equilibrium $\omega_i^{in} = \omega_i^{out}$; i.e., C_{is} is set equal to the thermal equilibrium concentration of the i^{th} defect, $\langle C_i \rangle_{eq}$.

Substituting Eqs. (10) and (11) into Eq. (9) yields

$$J(r_b,t) = \frac{1}{a} D_i\, C_i(r_b,t)\left[\frac{\omega_i^{out}(t)}{\omega_i^{in}(t)} - 1\right] \tag{12}$$

where

$$\omega_i^{out}(t)/\omega_i^{in}(t) = C_i^o(t)/C_i(r_b,t), \tag{13}$$

and

$$C_i^o(t) = \langle C_i \rangle_{eq} \exp\left[\frac{dF(n_i)}{dn_i}\frac{1}{kT}\right] \tag{14}$$

When the surrounding defects are in thermal equilibrium with the source-sink boundary, the boundary acts like an ideal reflector, $\omega_i^{out}(t)/\omega_i^{in}(t) = 1$ and $\bar{u} \cdot \bar{J}_i(\bar{r}_b,t) = 0$; for an ideal source, $\omega_i^{in}(t) = 0$ and $\bar{u} \cdot \bar{J}_i(\bar{r}_b,t)$ is positive and independent of the concentration at $\bar{r}_b$; for an ideal sink, $\omega_i^{out}(t) = 0$ and $\bar{u} \cdot \bar{J}_i(\bar{r}_b,t) = -(1/a)D_i\, C_i(\bar{r}_b,t)$, which is equivalent to the requirement that $C_i \to 0$ at a distance $\underline{a}$ behind the stability surface for all times.

Emission of a vacancy at the surface of a gas-containing void changes

the void energy by decreasing its surface and compressing the gas,[18] hence, in the absence of a field

$$\frac{dF}{dn_1} = \frac{d}{dn_1}(4\pi r^2 \gamma) - p\frac{dV}{dn_1} ,$$

$$= \Omega [(2\gamma/r) - p] , \qquad (15)$$

where the volume of the void is $V = 4\pi r^3/3 = n_1\Omega$. The situation is just reversed for interstitial emission so that

$$\frac{dF}{dn_2} = -\Omega [(2\gamma/r) - p] . \qquad (16)$$

ANALYSIS

Diffusion Near Dislocations

The purpose of this portion of the investigation is to calculate leakage rate probabilities at dislocations for vacancies and interstitials. The leakage rate probability $Q_i(t)$ for the i^{th} defect at any time t is just the ratio of the leakage rate $2\pi r_{bi} \rho_d V J_i(r_{bi},t)$ to the total number of defects in excess of the number present at thermal equilibrium $(\langle C_i(t)\rangle - \langle C_i\rangle_{eq})V$, where ρ_d is the dislocation density, V is the volume surrounding the dislocation, $\langle C_i(t)\rangle$ is the spatially averaged concentration within the volume, and $J_i(r_{bi},t)$ is the i^{th} current density at r_{bi} the stability radius about the dislocation for the i^{th} defect. Neglecting transients, which is a good approximation for random distributions of point defects and sinks, the ratio of the current density to the average concentration may be approximated as constant in time. The leakage rate probability becomes, then, a leakage rate constant, which may be written as

$$Q_i = 2\pi r_{bi} \rho_d \frac{J_i(\infty,r_{bi})}{(\langle C_i(\infty)\rangle - \langle C_i\rangle_{eq})} . \qquad (17)$$

This kind of assumption is essential to any rate theory approximation of a diffusion process. It permits the determination of appropriate leakage rate constants through the steady state analysis of vacancies and interstitials interacting and diffusing in the field of a dislocation.

It is assumed that the only mobile defects present are vacancies [1]

and interstitials [2] and that the only reaction they participate in is

$$[1] + [2] \xrightarrow{K} \text{Annihilation.} \tag{18}$$

A numerical solution of the corresponding set of steady state diffusion equations

$$0 = S_i + D_i \bar{\nabla} \cdot \left[\bar{\nabla} C_i(r) + \frac{C_i(r)}{kT} \bar{\nabla} \varepsilon_i(r) \right] - K C_i(r) C_j(r), \quad i,j=1,2 \tag{19}$$

which result from substituting Eqs. (3) and (6) into (1), yields concentration profiles from which average concentrations and current densities at the dislocation are obtained. These profiles are, of course, functions of the production rate, temperature, material and defect properties, and dislocation density. The solution of Eqs. (19) requires specifying the concentration, the normal derivative of the concentration, or some linear combination of the two at the boundaries surrounding the region within which the equations apply. In order to specify boundary conditions, the random dislocation configurations of a real material are approximated by an idealized configuration consisting of a bundle of parallel, straight, equispaced dislocations for which end effects are neglected. Assuming that there is no net transport of defects across the cylindrical surface of radius r_d surrounding each dislocation line [where r_d is equal to one-half the average distance between dislocations, i.e., $r_d = (\pi \rho_d)^{-1/2}$], and since dislocations are, in general, sources as well as sinks, the boundary conditions are taken to be

$$J_i(r) = 0 \qquad \text{at } r = r_d \,, \tag{20-a}$$

and

$$J_i(r) = -\frac{D_i}{a} \left[C_i(r) - \langle C_i \rangle_{eq} \right] \qquad \text{at } r = r_{bi} \,. \tag{20-b}$$

It is the variation in strain energy that dominates the interaction energy terms in Eqs. (19).[19] According to continuum mechanics the average energy corresponding to the interaction between the stress field of an isolated dislocation and that of a point defect is approximated by $\varepsilon_i = A_i/r$, where A_i is a constant representing the strengtn of the interaction with the i^{th} point defect. However, since the dislocations are not isolated it is reasonable to expect their fields, on the average, to cancel

in the neighborhood of r_d, hence, we approximate the interaction energy by

$$\varepsilon_i = A_i\left[\frac{2r_d}{r(2r_d - r)}\right] \tag{21}$$

which varies as A_i/r near the dislocation and has a zero gradient at r_d. Atomistic calculations for copper indicate that the interstitial stability radius r_{b2} is somewhat larger than the core radius (about 7 Å), at which the interaction energy is in the neighborhood of -.03 eV, while the vacancy stability radius r_{b1} is about 5 Å with a corresponding interaction energy < -.005 eV.* For this work we have taken $A_1 = 0$, $A_2 = -.21$ eV Å, and $r_{b1} = r_{b2} = 7$ Å.

The analytic approach employed here involves expressing Eqs. (19) and their boundary conditions in linearized[20] finite difference form and solving the resulting matrix by Gaussian elimination, iterating to convergence. The computer code used to solve these equations, DEPORT-1, can actually treat up to four mobile defects interacting through a variety of reactions.[8] DEPORT-1 consists of a calling program and numerous subroutines and subprograms. The code a) reads various input data and claculates problem parameters (e.g., diffusion coefficients, rate constants, etc.), b) reads or estimates concentrations for use as "initial guesses," c) calculates the band elements[21] of the coefficient matrix and the right hand side vector, d) solves the matrix equation checking for convergence, e) searches for flat regions in the converged concentration profiles, and, if such are found, establishes an improved mesh and repeats the calculation, f) from the converged concentration profiles, calculates current densities at the dislocation, average concentrations, and leakage rate constants for each defect, and g) writes all output in desired form.

---

* These estimates were made using the calculational techniques described in J. O. Schiffgens and D. H. Ashton, J. Appl. Phys. 45, 1023 (1974). In each case only one stability (radius) vector was sought, that for the case where the point defects were on the slip plane approximately midway between the end surfaces (perpendicular to the dislocation line).

Time Variation in Average Concentrations

Having treated the competition between annihilation and leakage at dislocations to obtain leakage rate constants which are functions of temperature, dislocation density, and defect and materials properties, the next step in the analysis is the determination of the time variation in the average concentrations of vacancies and interstitials during the cycle. While a detailed mathematical description of this process is a problem in classical diffusion, the complex configurations of real dislocation networks and loops, and the essentially random distributions of point defects and void nuclei throughout the bulk of the material warrant a simple rate theory formulation.

A numerical solution of the set of coupled time dependent rate equations

$$\frac{d}{dt} \langle C_i(t) \rangle = S_i'(t) - K \langle C_i(t) \rangle \langle C_j(t) \rangle - Q_i \langle C_i(t) \rangle, \quad i,j=1,2 \tag{22}$$

yields the average concentrations of vacancies and interstitials as functions of time during each cycle from the beginning of the irradiation until a stable cycle is established. It is the variation during the stable cycle that is of interest. It is assumed that over the irradiation period to be analyzed the dislocation density does not change substantially and that the average concentration is not affected by the loss of point defects to voids. The point defect production rates during the cycle are

$$S_i'(t) = S_i + ST_i \qquad 0 \leq t < t_p , \tag{23-a}$$

and

$$= ST_i \qquad t_p \leq t \leq t_c , \tag{23-b}$$

where $ST_i = K \langle C_i \rangle_{eq} \langle C_j \rangle_{eq} + Q_i \langle C_i \rangle_{eq}$.

The initial condition is simply

$$\langle C_i(t) \rangle = \langle C_i \rangle_{eq} \qquad i=1,2 \quad \text{at } t = 0. \tag{24}$$

Since temperature variations during cyclic irradiation can significantly alter the evolving microstructure, the temperature dependent quantities K and Q_i are implicit functions of time. Hence, although in

this analysis only constant temperature irradiations are considered, the calculational method employed is general, allowing K and Q_i to be known functions of time. The solutions to Eqs. (22) are obtained by writing them in finite difference form, linearizing the resulting algebraic equations by the same procedure used in solving Eqs. (19), iterating to convergence each time step, then integrating over time. The calculation is terminated when the time variation in the concentrations during successive cycles is unchanging (to within .1 percent). A program PULSE was written to solve Eqs. (22) with the initial conditions expressed in Eqs. (24). The program a) reads irradiation and temperature cycle parameters, b) reads output from DEPORT-1, c) calculates the average concentrations as functions of time, and d) writes and displays output in desired form.

Void Growth

This portion of the analysis is concerned with the solution of Eqs. (1) for vacancies and interstitials diffusing in the neighborhood of a void. It is assumed that the average concentration in the region surrounding the void is at all times equal to the average throughout the material, and that the annihilation term may be expressed in terms of the average concentrations, certainly a reasonable approximation for low void densities.

Elimination of the reaction rate or annihilation term both uncouples and linearizes Eqs. (1). Hence, for isotropic diffusion near a spherical void the continuity equations become

$$\frac{\partial}{\partial t} C_i(r,t) = S_i''(t) + D_i \frac{1}{r^2} \frac{\partial}{\partial r} \left[r^2 \frac{\partial}{\partial r} C_i(r,t) \right] \qquad i=1,2 \ , \tag{25}$$

in which the source terms S_i'' are

$$S_i''(t) = S_i(t) - K\langle C_1(t)\rangle\langle C_2(t)\rangle \ . \tag{26}$$

Consider an average void of radius b(t) at the center of an otherwise sink-free region of radius R, where R is taken to be $(3/4\pi\rho_v)^{1/3}$, with ρ_v being the void density. Appropriate initial and boundary conditions applicable to the solutions of Eqs. (25) for analysis of the void growth during an irradiation cycle are:

$$\text{for } t = 0, \quad b(0) < r < R, \quad C_i(r,0) = f_i(r) \tag{27-a}$$

$$\text{and for } t > 0, \quad r = b(t), \quad J_i[b(t),t] = \frac{1}{a} D_i \left[C_i^0 - C_i(b[t],t)\right] \tag{27-b}$$

$$r = R, \qquad C_i(R,t) = F_i[\langle C_i(t)\rangle, R] \tag{27-c}$$

where $f_i(r)$ refers to the i^{th} defect distribution within R at the beginning of a cycle, $F_i[\langle C_i(t)\rangle,R]$ is the concentration at R such that the average within R is equal to the average throughout the material, and b(t) is the void radius which may change during the cycle, depending on the net flow of matter into the void; i.e.,

$$\frac{d}{dt} b(t) = -\Omega\{J_1[b(t),t] - J_2[b(t),t]\}$$

$$= -\frac{\Omega}{4\pi\, b(t)^2}\{j_1[b(t),t] - j_2[b(t),t]\} \tag{28}$$

In this equation $j_1[b(t),t]$ and $j_2[b(t),t]$ are the rates at which vacancies and interstitials, respectively, flow into the void. Hence, the analysis of void growth during an irradiation cycle requires knowledge of $f_i(r)$ and $\langle C_i(t)\rangle$, and the simultaneous solution of Eqs. (25) and (28). While the general solution of this problem has been formulated, it has not yet been fully programmed.

For certain limited irradiation conditions, a simple straightforward solution has been programmed and may be used to demonstrate the essential features of growth. If the dislocation density and/or temperature are sufficiently high, at the beginning of a radiation pulse the vacancy and interstitial average concentrations rise essentially instantaneously to some known values $\bar{C}_i$ (from the analysis described in Section IV-Time Variation in Average Concentration), remain constant throughout the pulse, then drop to the thermal equilibrium values essentially instantaneously at the end of the pulse. In this case, the total void growth during a pulse and the total void shrinkage between pulses can be described in terms of the effective (or quasi-) steady state current densities. For both time intervals the solutions take the form

$$C_i(r,t) = \phi_i(t) - \theta_i(t) r^2 - \psi_i(t) \frac{1}{r}, \tag{29}$$

where $$\theta_i(t) = \frac{S_i''(t)}{6D_i} , \tag{30}$$

and the only time variation in the concentration profiles during either time interval comes through the change in void radius. Application of the boundary conditions in Eqs. (27-b) and (27-c) yield

$$\psi_i(t) = \frac{b^3 R}{z} \{C_i(R) - C_i^o + \frac{S_i''(t)}{6D_i} [R^2 - b^2 + 2ab]\} , \tag{31}$$

and $$\phi_i(t) = C_i(R) + \frac{S_i''(t)}{6D_i} R^2 + \psi_i(t)\frac{1}{R} , \tag{32}$$

where $z = b[aR + bR - b^2]$, and, for simplicity, the notation for the time dependency of the void radius has been dropped. During the pulse, the concentrations at R are determined by solving

$$\bar{C}_i = \frac{1}{V} \int_b^R C_i(r)\, dV \tag{33}$$

for $C_i(R)$, and between pulses the concentrations at R are

$$C_i(R) = \langle C_i \rangle_{eq} . \tag{34}$$

The steady state concentration profile of the i^{th} defect in the region surrounding a void is given by Eqs. (29) through (34) for both time intervals. Consequently, the rate at which these defects enter the void is given by

$$\begin{aligned} j_i(b) = A_b J(b) &= - 4\pi b^2 D_i \frac{d}{dr} C_i(r)\Big|_{r=b} \\ &= - 4\pi \frac{D_i b^3}{z} \left([C_i(R) - C_i^o] R + \frac{S_i''(t)}{6D_i} (R^3 - 3b^2 R + 2b^3) \right) \end{aligned} \tag{35}$$

and the rate at which they diffuse out of the region defined by R into some other region is

$$\begin{aligned} j_i(R) = A_R J(R) &= - 4\pi R^2 D_i \frac{d}{dr} C_i(r)\Big|_{r=R} \\ &= - 4\pi \frac{D_i b^2 R}{z} \left([C_i(R) - C_i^o] b + \frac{S_i''(t)}{6D_i} (2 \{\frac{a}{b} - \frac{1}{2}\} b^3 + 3bR^2 \right. \\ &\quad \left. - 2 \{\frac{a}{b} + 1\} R^3) \right) \end{aligned} \tag{36}$$

Substitution of Eq. (35) for vacancies and interstitials (i.e., for i=1,2, respectively) into Eq. (28) with the appropriate values for $C_i(R)$ and $S_i''(t)$ yields the net void growth rate for given average vacancy and interstitial concentrations. It is expressed in terms of diffusion coefficients D_i, void parameters C_i^o and b, and the radius of the surrounding sink-free region R, where R and b must be such that flow out of the region to dislocations $j_i(R)$ is very much greater than $j_i(b)$. The change in void radius as a function of time is obtained by numerical solution of the resulting equation. A program, SINK, has been written to solve Eq. (28). The program (a) reads output from DEPORT-1 and PULSE, (b) reads various integration parameters, the void density, the surface energy, and the number of helium atoms in the void, (c) calculates the current densities at the boundaries, the net growth rate, and the void radius, all as functions of time throughout the cycle, and (d) writes and displays all data in desired form.

RESULTS OF CALCULATIONS

The objective of this research is to develop analytic models for the correlation and extrapolation of data on irradiation effects stemming from cyclic variations in radiation intensity. In previous sections, the method of analysis and presently employed calculational techniques were discussed and a model for void growth was presented. Initial results from calculations with the void growth model are described in this section. It is our intention to approximate the behavior of stainless steel. However, appropriate stainless steel defect parameters are not well known and a fairly wide range of values has been used in calculations by various authors.[8-10] The values used in this work are presented in Table 1. At this point, we make no attempt to justify our selection other than to point out that others have used these values and that the results of our calculations with them, as shown below, are reasonable.

It is generally recognized a) that a net flow of vacancies into a bubble or some other void nucleus requires a vacancy excess which can only be sustained if there is a preferential removal of interstitials at alternative sinks, and b) that dislocations, by virtue of the long range interstitial-dislocation interaction, constitute suitable alternative sinks.

TABLE 1

ASSUMED PROPERTIES AND DEFECT PARAMETERS FOR STAINLESS STEEL

Ω	:	Atomic volume (cm^3/at)	1.18×10^{-23}
a	:	Lattice parameter (cm)	3.61×10^{-8}
r_b	:	Stability radius (cm)	7.00×10^{-9}
D_1^o	:	Vacancy Pre-exponential Factor (cm^2/sec)	5.80×10^{-1}
D_2^o	:	Interstitial Pre-exponential Factor (cm^2/sec)	1.00×10^{-3}
E_1^m	:	Vacancy Migration Energy (ev)	1.40
E_2^m	:	Interstitial Migration Energy (ev)	2.00×10^{-1}
E_1^f	:	Vacancy Formation Energy (ev)	1.50
E_2^f	:	Interstitial Formation Energy (ev)	4.00
γ	:	Surface Free Energy (ev/A^2)	8.12×10^{-2}
A_1	:	Vacancy-Dislocation Interaction Constant (evA)	0.00
A_2	:	Interstitial-Dislocation Interaction Constant (evA)	-2.10×10^{-1}
α_1	:	Vacancy-Interstitial Combinatory Number[a]	9.00×10^{2}
α_2	:	Interstitial-Vacancy Combinatory Number[a]	1.80×10^{3}
S_1^f	:	Vacancy Formation Entropy (ev/°K)	4.31×10^{-5}
S_2^f	:	Interstitial Formation Entropy (ev/°K)	0.00

[a]These values are based on the assumption that a vacancy is surrounded by a stability surface containing 75 lattice sites, and that on the average each site has half its nearest neighbors outside the volume enclosed by the surface.

As is evident from Eqs. (28) and (35), a growth function G(t) may be defined such that void growth requires a positive value of G(t). For a dilute solution of large voids it may be readily shown[22] that

$$b\frac{db}{dt} = \Omega G(t) \tag{37}$$

where

$$G(t) = D_1\langle C_1(t)\rangle - D_1\langle C_i\rangle_{eq} - D_2\langle C_2(t)\rangle \ . \tag{38}$$

Hence, it is desirable to begin the analysis of the effects of cyclic variations in damage rate on void growth by determining the combinations of material and operating conditions for which G(t) is positive, then calculate growth rates for a few irradiation conditions.

Before growth could be analyzed the point defect concentration as a function of dislocation density and temperature had to be determined. With DEPORT-1, concentration profiles, average concentrations, and current densities of vacancies and interstitials were calculated for dislocation densities of 5×10^9, 5×10^{10}, and 5×10^{11} cm/cm^3 over the temperature range from 250 to 800°C. Figure 1 shows a sample set of vacancy and interstitial concentration profiles. With a defect production rate of 1×10^{-6} dpa/sec, the concentrations at 500°C are plotted versus the normalized distance from the dislocation line for all three dislocation densities. At this temperature all the profiles are quite flat. Average concentrations obtained from these and other concentration profiles were substituted into Eq. (38) to obtain steady state growth functions. In Figure 2, growth functions for each dislocation density are plotted versus temperature for defect production rates of 1×10^{-6} and 5×10^{-3} dpa/sec, typical of neutron and charged particle irradiations, respectively. The curves for the low production rate exhibit maxima in the range 400 to 580°C. Raising the displacement rate by a factor of 5000 increases the maximum value of the growth function by a factor of ~3500, ~1100, and ~360 for $\rho_d = 5 \times 10^{11}$, 5×10^{10}, and 5×10^9 cm^{-2}, respectively, and shifts the temperature of the maximum upward by 100 to 200°C. The temperatures of maximum growth and their shift with increased displacement rate are in approximate agreement with the experimentally observed behavior of the maxima in stainless steel swelling curves. Voids have not been observed in reactor irradiated

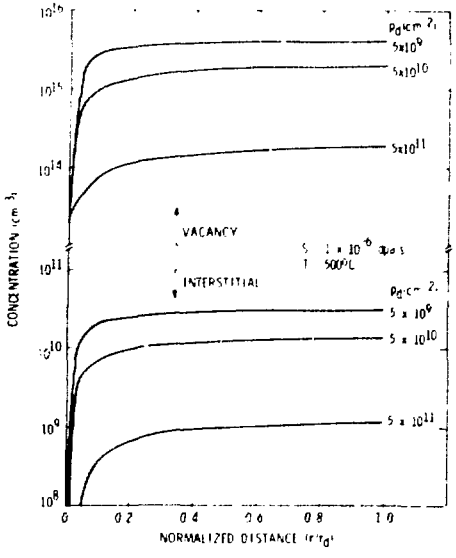

Fig. 1. Vacancy and Interstitial Concentration Profiles.

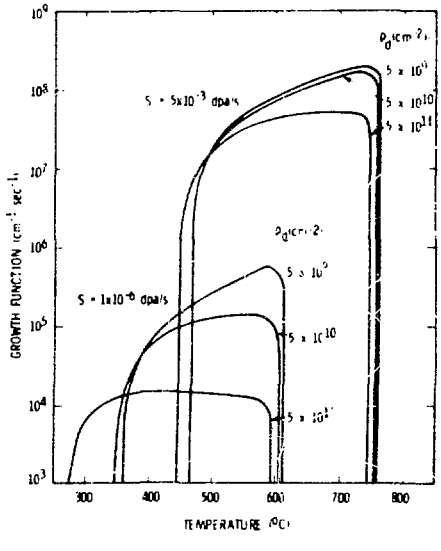

Fig. 2. Growth Function Versus Temperature.

stainless steel at temperatures below 300°C or above about 600°C. On the other hand, voids have been observed in heavy ion and electron irradiated stainless steels at temperatures from 400 to 700°C. Apart from any consideration of cascade effects, the calculations show a significant decrease in the growth function per displacement as the displacement rate is increased, consistant with the rate study conducted at NRL.[23] Note, also, that at low temperatures voids can only grow when the dislocation density is high; for low dislocation densities too few interstitials leak at dislocations for the dislocations to be effective as preferential sinks for interstitials.

Leakage rate constants were obtained by substituting the current densities and corresponding average concentrations into Eq. (17). For convenience in presentation, the leakage rate constants are normalized by dividing by the diffusion coefficient and the dislocation density, $Q_i/D_i\rho_d$. For defect production rates of 1×10^{-6} dpa/sec and 5×10^{-3} dpa/sec, respectively, Figures 3-a and 3-b show plots of $Q_1/D_1\rho_d$ and $Q_2/D_2\rho_d - Q_1/D_1\rho_d$ versus temperature for the three dislocation densities considered. Note that in these calculations, with the parameters listed in Table 1, the $Q_i/D_i\rho_d$ vary with dislocation density and temperature in the region of interest. At high temperatures, the $Q_1D_1\rho_d$ become constant with values in the range 1.25 to 2.75 depending on the dislocation density. For each dislocation density, the quantity $Q_2/D_2\rho_d - Q_1/D_1\rho_d$ is zero at the temperature where $D_1\langle C_1\rangle$ equals $D_2\langle C_2\rangle$ and passes through a maximum with increasing temperature. Over most of the temperature range the difference between the normalized leakage rate constants is slowly changing with values in the range .2 to .8 depending on the dislocation density. These values contrast markedly with constants reported by Brailsford and Bullough,[24] viz, $Q_1/D_1\rho_d = 1$ and $Q_2/D_2\rho_d - Q_1/D_1\rho_d = .02$. The difference is the result of using different defect parameters; Brailsford and Bullough use $E_1^m = 1$ ev, $E_1^f = 1.9$ ev, $A_2 = .1\ kTr_b$, and $K = 10^{16}$ or 10^{17} [our values for K are in the range 10^{13} to 10^{14}, see Eq. (7)]. Note that increasing the displacement rate does little more than shift the curves up in temperature.

With the appropriate annihilation and leakage rate constants Eqs. (16) were solved simultaneously to obtain the average concentrations of vacancies and interstitials as functions of time during the approach to steady state

for each dislocation density at various temperatures. For a defect production rate of 1 x 10^{-6} dpa/sec, plots of $D_1\langle C_1(t)\rangle$ and $D_2\langle C_2(t)\rangle$ versus time for the three dislocation densities at 500°C are presented in Figures 4-a, 4-b, and 4-c. Similar plots are shown for a production rate of 5 x 10^{-3}dpa/sec in Figures 5-a, 5-b, and 5-c. Note that in each case the interstitial concentration increases essentially instantaneously as the interstitials approach equilibrium with the surrounding dislocations. For the lowest dislocation density in Figure 4, a significant fraction of vacancies and interstitials ($\sim$ 85 percent at steady state) are removed by annihilation at this temperature. Correspondingly, the interstitial concentration passes through a maximum and decreases as the relatively slow moving vacancies accumulate. For the higher dislocation densities, Figures 4-b and 4-c, a smaller fraction of vacancies and interstitials are removed by annihilation ($\sim$ 17 and .1 percent, respectively) at this temperature. For the highest dislocation density, the point defect concentrations increase monotonically as they come into equilibrium with the dislocation network nearly independently of each other, interstitials reaching steady state before vacancies.

A general characteristic of all such plots is that initially $D_2\langle C_2(t)\rangle$ is greater than $D_1\langle C_1(t)\rangle$ due to the much higher mobility of interstitials, while at steady state, due to the presence of the biased sinks, the reverse is true. Therefore, at some point t' during the approach to equilibrium these quantities are equal, i.e., $D_2\langle C_2(t')\rangle = D_1\langle C_1(t')\rangle$. The time t' then represents a "zero growth pulse length." For pulse lengths less than t' growth is impossible, provided the only vacancies present during the pulse are those produced during the pulse. That is, the interval between pulses $t_c - t_p$ must be sufficiently long, say 20 times t' (or $\sim$ 10 vacancy mean lives), to drain all vacancies from the material before the beginning of the next pulse. Figures 6 and 7 show plots of the zero growth pulse length versus temperature for each dislocation density. The significance of the plots in Figure 6 is that, for pulse lengths less than 10 microseconds combined with cycle lengths greater than about 20 t', voids should not form or grow in stainless steel at any temperature regardless of the pulse amplitude, unless voids are formed directly in displacement cascades and they are large enough

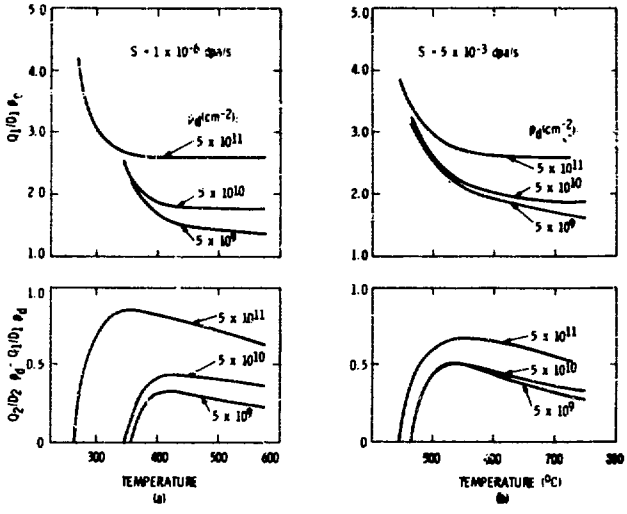

Fig. 3. Normalized Leakage Rate Constants for Vacancies and Interstitials Versus Temperature.

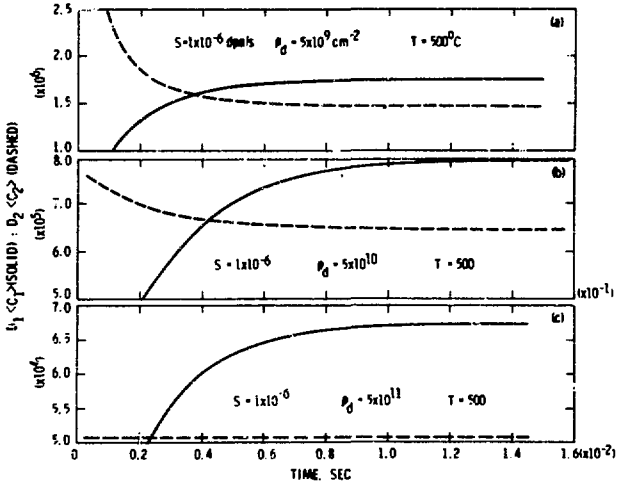

Fig. 4. Plots of $D_1\langle C_1(t)\rangle$ and $D_2\langle C_2(t)\rangle$ Versus Time for a Displacement Rate of 1 x 10^{-6} dpa/sec.

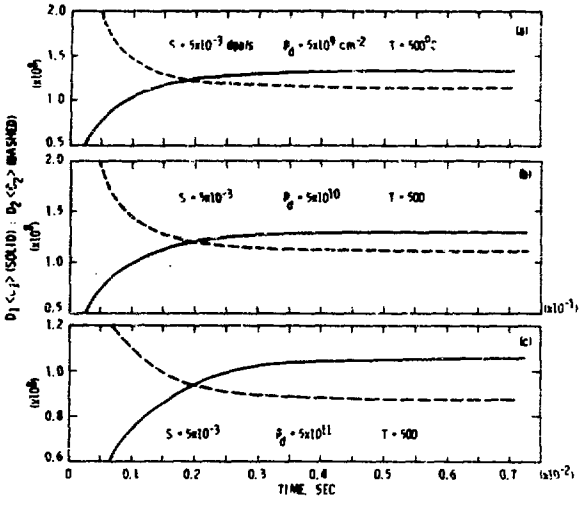

Fig. 5. Plots of $D_1\langle C_1(t)\rangle$ and $D_2\langle C_2(t)\rangle$ Versus Time for a Displacement Rate of 5 x 10^{-3} dpa/sec.

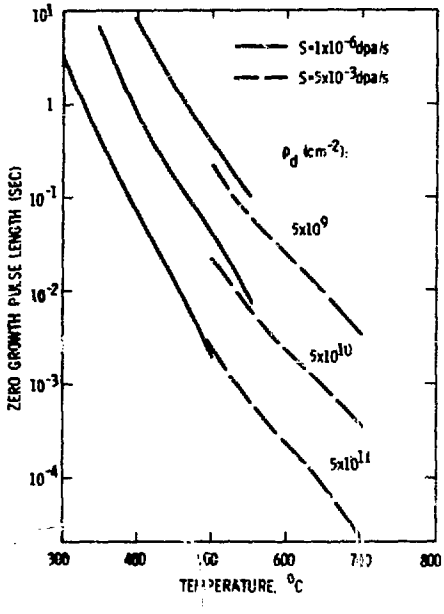

Fig. 6. Zero Growth Pulse Length Versus Temperature for a Vacancy Migration Energy of 1.4 ev.

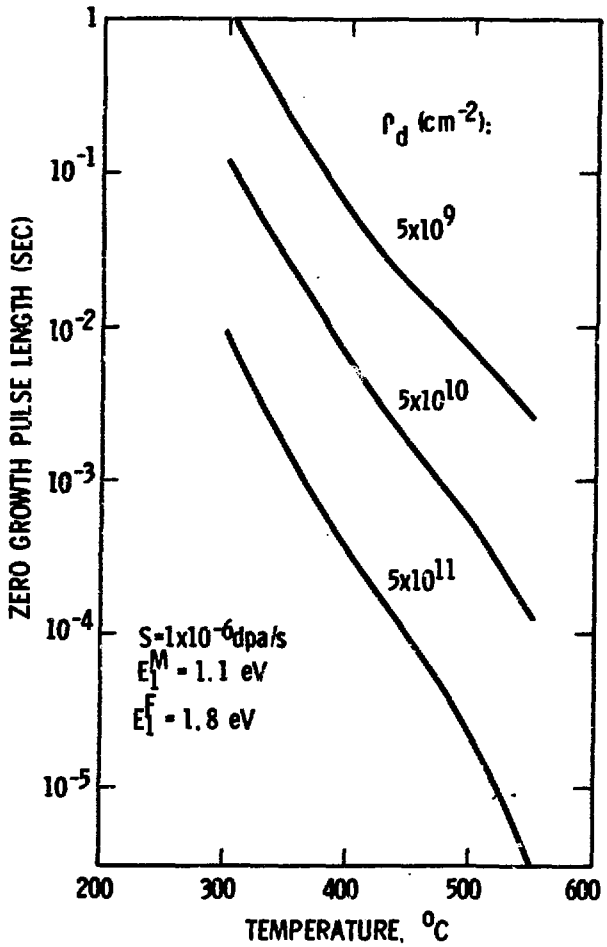

Fig. 7. Zero Growth Pulse Length Versus Temperature for a Vacancy Migration Energy of 1.1 ev.

to survive the interval $(t_c - t_p)$. The plots in Figure 7 are for a vacancy migration energy of 1.1 ev, with all other defect parameters* the same as shown in Table 1. A comparison of Figures 6 and 7, shows the sensitivity of the zero growth pulse length to the vacancy migration energy; a decrease in energy of .3 ev decreases t' by a factor of about 100.

In connenction with pulsed irradiations, four regimes may be readily identified: 1) the pulse is too short for growth to occur during the pulse and the interval between pulses is long enough to permit complete relaxation of the vacancy distribution; 2) the pulse is long enough (and/or its amplitude is large enough) for growth to occur during a pulse, but the shrinkage between pulses is such as to yield no net growth per cycle; 3) growth during the pulse is sufficient so that the void survives the interval between pulses and shows net growth through the cycle; and 4) shrinkage between pulses is negligibly small so that total void growth is just the net growth per pulse summed over all pulses. Specifying the various combinations of parameters which define each regime is complicated by the large number of significant experimental variables (e.g., number and type of nucleation sites, dislocation density, radiation and temperature pulse amplitudes, pulse lengths, and cycle lengths, etc.). At this point, we merely wish to demonstrate the application of the model to growth during a cycle.

In keeping with the approximation employed in arriving at Eq. (29), calculations with the void growth model in its present form are restricted to cases for which the time variations in point defect concentrations may be treated as rectangular pulses.** For example, at 500°C, with a density of void nuclei of 10^{14} cm^{-3}, a dislocation density of 5×10^{10} cm^{-2}, and the defect parameters listed in Table 1, the analysis of growth is limited to pulse lengths greater than a few tenths of a second. For this temperature, void density, and dislocation density, let us consider void growth for two sets of pulse parameters; for case A, t_p = .4 sec and t_c = 10.4 sec and for case B, t_p = 30 sec and t_c = 40 sec. The average displacement rate in each case is taken to be

---

* It is assumed that $E_1^f + E_1^m = 2.9$ ev: hence $E_1^f = 1.8$ ev.

** Work is currently in progress to lift this restriction.

1×10^{-6} dpa/sec. Figures 8 and 9 show the variation in vacancy and interstitial supersaturation for cases A and B, respectively; the pulses are approximately rectangular. With these pulses, the change in void radius during an irradiation cycle was calculated for several void sizes. Figures 10 and 11 show plots of void radii versus time for cases A and B, respectively. In both cases the growth during the pulse decreases with increasing void size and the fraction of new growth lost to shrinkage between pulses decreases. Shrinkage between pulses is less than 1% of the growth during the pulse for void radii greater than about 50Å. Although voids will nucleate more readily in case A than in case B, due to the larger point defect supersaturations, the growth per displacement is much less. From Eq. (37), for a dilute solution of large voids, the change in volume ΔV of a void of radius b for short time intervals Δt is

$$\Delta V = 4\pi\Omega G b \Delta t \tag{39}$$

Accordingly, the percent swelling per dpa for a uniform distribution of voids 50Å in radius during a continuous irradiation with a displacement rate of 1×10^{-6} dpa/sec is .11 percent per dpa. In the limit, when the shrinkage between pulses is essentially zero, the ratio of the change in volume per dpa for a continuous irradiation to that for a pulsed irradiation (for a void of the same size) is just

$$\Delta V_c / \Delta V_p = G_c / (G_p \tau) \tag{40}$$

where G_c and G_p are the growth functions for the average and peak displacement rates respectively, and τ is the (fractional) duty cycle. For case A this ratio is 2.55 and for case B it is 1.05. The ratio is not 1, of course, due to the decrease in efficiency of point defects for sustaining growth as the defect production rate increases, as shown in Figure 2.

SUMMARY

This work has identified four regimes associated with void growth in pulsed systems. The first regime is characterized by two interrelated parameters, a zero growth pulse length t' and a minimum interval between pulses. This analysis shows that if the irradiation pulse length is less

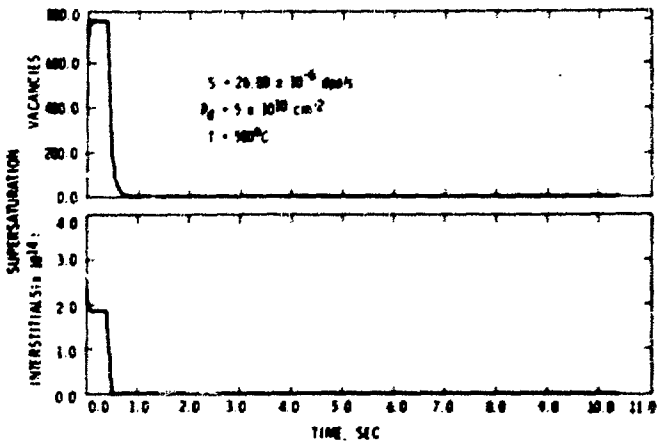

Fig. 8. Vacancy and Interstitial Supersaturations Versus Time for t_p = .4 sec and t_c = 10.4 sec.

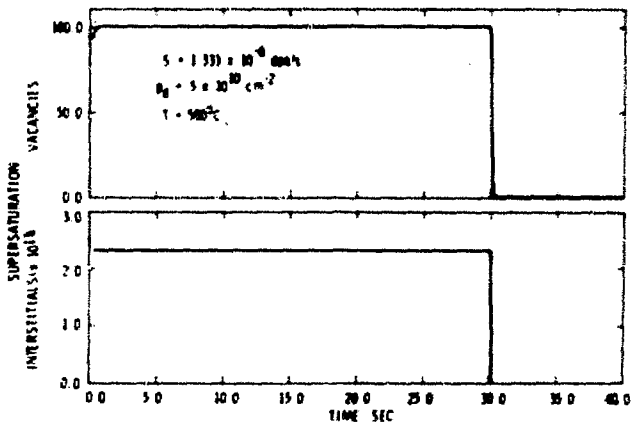

Fig. 9. Vacancy and Interstitial Supersaturations Versus Time for t_p = 30 sec and t_c = 40 sec.

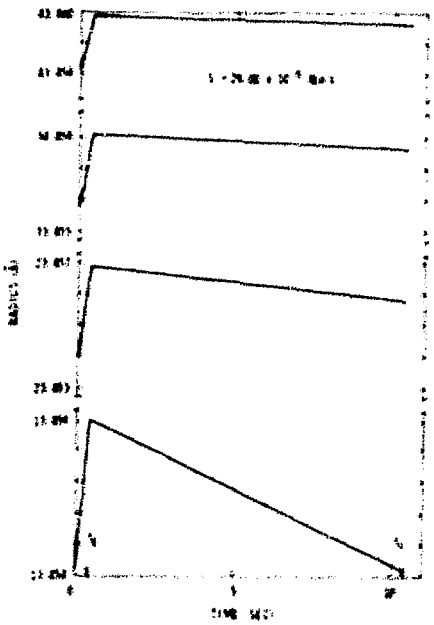

Fig. 10. Void Radius Versus Time During an Irradiation Cycle for t_p = .4 sec and t_c = 10.4 sec.

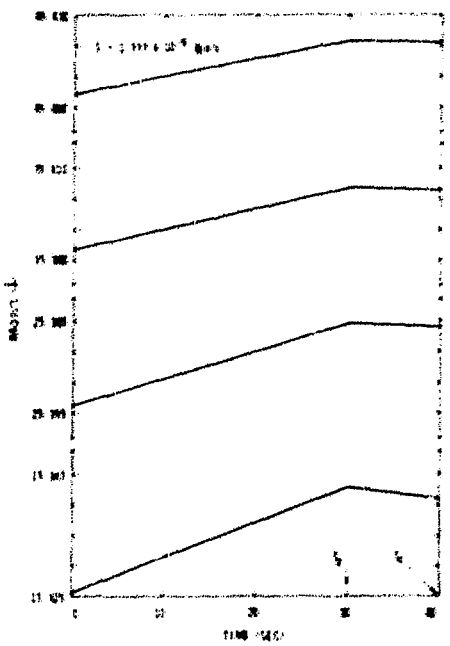

Fig. 11. Void Radius Versus Time During an Irradiation Cycle for t_p = 30 sec and t_c = 40 sec.

than about 10 μsec and the interval between pulses is greater than about 20 t', no void growth is possible in stainless steel regardless of temperature, dislocation density and pulse amplitude (instantaneous displacement rate) provided no voids form in displacement cascades which are large enough to survive the time between pulses.

The second regime is characterized by a pulse amplitude which is large enough for growth on void nuclei but with pulse lengths short enough and/or cycle lengths long enough that void growth during the pulse is completely nullified by the shrinkage between pulses. The third regime is defined by pulse parameters which not only permit voids to grow on given nuclei but for all irradiation times cause more growth during a pulse than shrinkage between pulses. The boundaries for these regimes are more difficult to quantify, as is obvious from the sample calculations presented in this paper. For any given set of pulse and cycle lengths the regime boundaries are complex functions of the physics of void nuclei, the dislocation density, and the temperature and displacement pulse amplitudes.

In the fourth regime, there is essentially no shrinkage between pulses and the total void growth is just the net growth per pulse summed over all pulses. Sample calculations show that, for pulse parameters in the range of interest for CTR design, void growth is significantly altered. For large voids, with a dislocation density of 5×10^{10} cm^{-2}, at 500°C, the rate of change in volume of a void during a continuous irradiation at a displacement rate of 1×10^{-6} dpa/sec is about 2.5 times the rate of change in volume of the same size void during a pulsed irradiation with $t_p = .4$ sec, $t_c = 10.4$ sec, and an average displacement rate of 1×10^{-6} dpa/sec.

In conclusion, these studies show that the pulse parameters chosen for reactors and irradiation sources can dramatically alter swelling, and most probably other irradiation effects.

ACKNOWLEDGMENTS

The authors thank K. M. Zwilsky and T. C. Reuther of the Division of Controlled Thermonuclear Research for their interest in and support of this program. In addition, we are grateful to H. H. Yoshikawa and R. L. Simons

for their helpful comments and suggestions.

This work was performed under the auspices of the United States Energy Research and Development Administration.

REFERENCES

1. F. L. Ribe, Rev. Mod. Phys., 47, 7 (1975).
2. R. A. Krakowski, F. L. Ribe, T. A. Coultas, and A. J. Hatch, eds., "An Engineering Design Study of A Reference Theta-Pinch Reactor", LA-5336 (ANL-8019) March 1974.
3. J. M. Williams and T. G. Frank, "Laser Controlled Thermonuclear Reactor System Studies", LA-5718-MS, September 1974.
4. R. G. Mills, ed., "A Fusion Power Plant", Princeton University Plasma Physics Laboratory, MATT-1050, August 1974.
5. G. L. Kulcinski, ed., "A Wisconsin Toroidal Fusion Reactor Design", University of Wisconsin, UWFDM 68, March 1974.
6. A. P. Fraas, "Conceptual Design of the Blanket and Shield Region and Related Systems for a Full Scale Toroidal Fusion Reactor", Oak Ridge National Laboratory, ORNL-TM-3096 (1973).
7. D. G. Doran, N. J. Graves, E. P. Lippincott, W. N. McElroy, J. O. Schiffgens, and R. L. Simons, "Controlled Thermonuclear Reactor Quarterly Report", HEDL-TME 75-24, December 1974.
8. T. M. Howe and J. O. Schiffgens, Trans. ANS, 16, 74 (1973).
9. R. Bullough, B. L. Eyre, and R. C. Perrin, Nucl. Appl. and Tech. 9, 346 (1970).
10. S. D. Harkness, and Che-Yu Li, Met. Trans. 2, 1457 (1971).
11. H. Wiedersich, Radiation Effects, 12, 111 (1972).
12. D. G. Doran, J. R. Beeler, Jr., N. D. Dudey, and M. J. Fluss, "Report of the Working Group on Displacement Models and Procedures for Damage Calculations", HEDL-TME 73-76, December 1973.
13. J. S. Koehler, Phys. Rev. 181, 1015 (1969).
14. S. Glasstone, K. Laidler, and H. Eyring, Theory of Rate Processes, McGraw-Hill Book Co., New York, 153 (1941).
15. F. R. N. Nabarro, Report of a Conference on Strength of Solids, The Physical Society, London, 75, (1948).
16. J. S. Koehler, M. deJong, and F. Seitz, Proc. of the International Conf. on Crystal Lattice Defects, 18, Suppl. III, 1 (1963).
17. R. Bullough and R. C. Perrin, Proc. of the Sym. on Radiation Damage in Reaction Materials held in Vienna (1969).
18. G. W. Greenwood, A. J. E. Forman, and D. F. Rimmer, J. Nucl. Mat. 4, 305 (1959).

19. A. C. Damask and G. J. Dienes, Point Defects in Metals, Gardon and Breach, New York, 69 (1963).

20. J. F. Holt, Comm. of ACM, 7, 366 (1964).

21. L. Fox, Numerical Solution of Ordinary and Partial Differential Equations, Pergamon Press, London, 68 (1962).

22. D. G. Doran, N. J. Graves, J. O. Schiffgens, and R. L. Simons, "Controlled Thermonuclear Reactor Quarterly Report", HEDL-TME 75-56, March 1975.

23. J. E. Westmoreland, J. A. Sprague, F. A. Smidt, and P. R. Malinberg, "Flux (Dose Rate) Effects for 2.8 MeV $^{58}Ni^{+}$ Irradiations of Pure Ni", Applications of Ion Beams to Metals, Plenum Press, New York, 663 (1974).

24. A. D. Brailsford and R. Bullough, J. Nucl. Mat. 44, 121 (1972).

AUTHOR INDEX